université
PARIS-SACLAY

Performance optimizations at present and future High Energy Colliders

Barbara Dalena

August 23, 2021

These d'Habilitation à Diriger des Recherches

Jury Members

President: president

Referees:
Prof. Riccardo Bartolini (DESY)
Dr. Lucie Linssen (CERN)
Prof. Patrick Puzo (Université Paris-Saclay and CNRS)

Examiners:
Dr. Daniel Schulte (CERN)
Dr. Angeles Faus-Golfe (Université Paris-Saclay and CNRS)
Dr. Roy Aleksan (Université Paris-Saclay and CEA)

Abstract

In the context of the studies for the future high energy accelerators, my personal contribution is explained with references. The projects I have been involved in and their main beam physics challenges are briefly introduced. I had the possibility to work on the optimisation of detectors and accelerators in different phases of several experimental projects: design, technical and running phase. Optimisation is a key aspect to improve the performance of existing systems, in order to explore nuclear and particle physics, or to reach the target realisation of future apparatus. Insights of possible future developments of these beam physics studies are given.

Acknowledgment

For the content of this *habilitaton* and for the competences I reached I have to thanks Ambrogio Pantaleo, Daniel Schulte, Rogelio Tomas, Jacques Payet and Bernhard Holzer. I am indebted to them for all the explanations and stimuli they have always willingly given me, and for the unconditional trust they have always shown in my abilities. All the work presented has been possible thanks also to the tight collaboration of colleagues from INFN, CERN and CEA: Alessandra Filippi, Stefano Piano, Vincenzo Lucherini, Andrea Latina, Michele Modena, Hubert Gerwig, Riccardo De Maria, Stephane Fartoukh, Massimo Giovannozzi, Antoine Chance which provided me either their instruments or their inputs. I greatly acknowledge all BOINC volunteers who supported LHC@Home project, giving for free their CPU time and allowing some of the results presented in this manuscript to be produced. I am also indebted with Vladimir Shiltsev and Frank Zimmermann for having published a comprehensive review of modern and future accelerators that provided me inspiration and references for the introduction and the conclusion of this manuscript. I am also grateful to Luca Bonaventura for careful reading of this manuscript and for stimulating discussions on mathematical aspects of computational physics. I would like to thanks Jerome Schwindling and Pierre Vedrine, my laboratory and department chefs, for their support to the realisation of this document.

During the years described in this thesis, I had the possibility to collaborate with and to guide several post-doc: Giuseppe Simonetti, Diego Faso, Alexey Andronenkov, Hiroyuki Fujioka, Jochem Snuverink, Javier Barranco, Yngve Levinsen and David Boutin. Finally, it was a pleasure for me to work with and to supervise PhD students like Jacob Esberg,

Eduardo Marin, Abele Simona and Thomas Pugnat; and master students as Guillermo Zamudio, Oleg Gabouev and Mehdi Ben Ghali; from all of them I have learnt a lot.

To Nicole and Marco

Contents

List of Figures

List of Tables

Introduction

In 1897 J.J. Thomson discovered that cathodic rays are negatively charged particles with mass smaller than that of the atom using Crookes' cathodic tube [1]. This tube consists of a partially evacuated glass bulb of various shapes, with two metal electrodes, the cathode and the anode, one at either end. When a high voltage is applied between the electrodes, cathode rays (electrons) are projected in straight lines from the cathode. With additional electric and magnetic field, Thomson demonstrated that the cathode rays are negatively charged and have mass-to-charge ratio over a thousand times lower than that of a hydrogen ion (H+). For the first time, electric and magnetic fields were used to study the properties of sub-atomic particles, whose dimensions are out of reach for the most powerful microscopes. In the 1910's, Rutherford, Geiger and Mardsen had the idea to test the Thomson atomic theory bombarding a thin foil of material with a collimated beam of alpha particles [2]. From their observations, they concluded that the atom is almost empty and that the positive charges are concentrated in its centre, contributing to the foundation of a new theory of the atom. For the first time, sub-atomic matter was probed with beam scattering experiments. In 1932, the first nuclear disintegration was possible using protons accelerated with a Cockcroft-Walton DC generator [3, 4]. In 1939, the Nobel Prize was awarded to Ernest O. Lawrence for the invention of the first modern accelerator: the cyclotron [5]. In the following years, accelerators were more and more required to study sub-atomic physics and their development and performance optimisation became soon a specific branch of physics. In order to produce new particles with higher mass (following Einstein's relation $E = mc^2$), the particles needed to be accelerated always to higher

energy. This stimulated the birth of many laboratories around the world and allowed studying the fundamental physics interactions, during the 20^{th} century. The review of the technological developments and physics discoveries made at accelerators is out of the scope of this thesis, but I want to cite the ADA (*Anello Di Accumulazione*) accelerator, which was the first-ever electron–positron particle collider and first electron-positron storage ring, measuring about 1.3 m in diameter. It was designed to store beams of 250 MeV and built in the Frascati National Laboratory in Italy in the 1961 by a group of physicists, lead by Bruno Touscheck [6]. It was soon transferred from Frascati, to Orsay, France, at the Linear Accelerator Laboratory, where it was tested with the laboratory's powerful particle injector and operated for four years [7]. At time of ADA's proposal, American physicists were moving away from using accelerators that sent a beam of particles into a fixed target and instead experimenting with colliding two beams of particles. ADA took this idea to the next level by replacing one of the beams of particles (electrons) with a beam of antiparticles (positrons), something that had never been tested. Even if no major particle physics discovery was reached with ADA, this machine allowed physicists to better understand several aspects of accelerator physics (like the Tousheck effect), and above all it represents the ancestor of a series of particle anti-particle colliders (SPEAR, SPS, Tevatron, LEP) which allowed major discoveries in Physics awarded by many Nobel Prizes.

After one hundred years, particle accelerators are still used to study fundamental physics and, in particular, the properties of the latest particles discovered in 2012 (Higgs Boson) can only be studied using a suitable particle accelerator. Modern colliders are the most sophisticated of all accelerator types and employ the most advanced technologies and beam physics techniques to push their performance.

Precisely at DAΦNE, the second generation descendant of ADA (the first one being Adone), started my research activity in experimental physics during my PhD. At that time my major research interest was the role of strangeness in nuclear and hadronic physics. In particular I was involved in the search for neutron reach Λ-hypernuclei [8, 9],

and for the kaon bound states [10]. These researches are not discussed in the present manuscript. Starting from the end of my PhD, the majority of my research activity focused on optimization methods and beam physics aspects of present and future high energy accelerators. This is the subject of the present *habilitation* which is divided in the three following topics and chapters:

- Luminosity monitoring and impact of detector solenoid;
- Tuning strategies and performance studies of detectors and accelerators;
- Optics optimisation and non linear beam dynamics.

In the following, before to go into the details of the three specific topics, I introduce the accelerators and the experimental project I have worked on.

The FINUDA experiment and the DAΦNE accelerator

The FINUDA (acronym for "FIsica NUcleare a DAΦNE") experiment was an unconventional example of a hypernuclear [1] physics experiment, joining the characteristics of a fixed target experiment, of a tracker in a magnetic field and of an experiment at a collider, carried out in a ϕ-meson factory. The detector was completed in 1998, but its installation on the machine was delayed due to problems of the superconducting coil for the solenoid magnetic field and, mainly, to unexpected drawbacks in the commissioning of the machine. On January 2003, at the beginning of my PhD, the operations devoted to the insertion of the detector in the collider interaction region were started and their completion took about four months. The first roll-in of the detector was done at the end of April 2003. The full detector was calibrated with cosmic rays during six weeks, with magnetic field off and on, in order to measure the alignment and to check the performances of the different sub-detectors. DAΦNE engineering runs were delayed until September 2003, due to a

[1] Hypernuclei are nuclear systems in which one or more nucleons are replaced by one or more hyperons. The most known and studied since longtime are Λ-Hypernuclei, in which a Λ hyperon replaces one neutron of the nucleus.

water supply shortage consequent to the exceptionally hot and dry summer that affected Europe. In October 2003 the first (e^+, e^-) collisions were achieved and first Bhabha [2] events were detected by the FINUDA apparatus, as shown in Fig. 1.

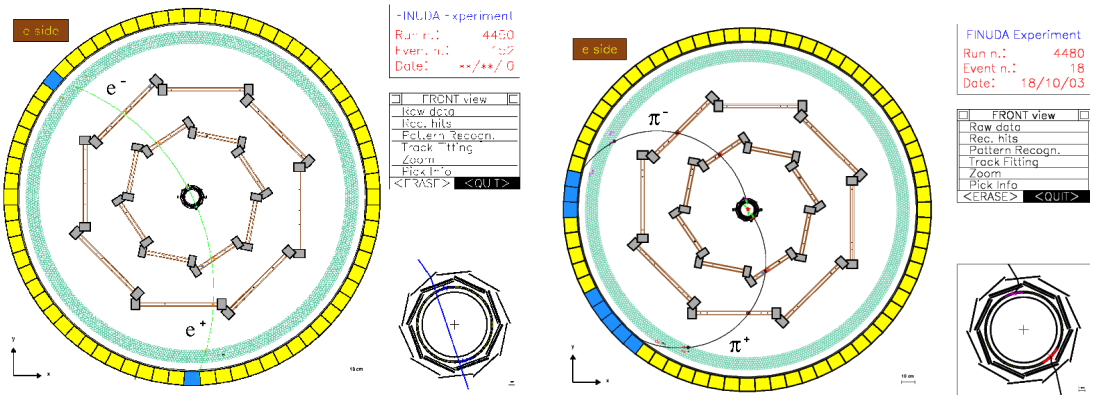

(a) (b)

Figure 1: (a) Front view of the FINUDA display reconstruction software, the e^+e^- pair following Bhabha scattering can be easily recognized. (b) Reconstructed event displayed for $K_S \to \pi^+\pi^-$.

DAΦNE (Double Annular ϕ-factory for Nice Experiments) is a e^+e^- collider running at the center-of-mass energy of the ϕ-meson (1020 MeV). It consists of two rings (Fig. 2), one for electrons and the other for positrons, that overlap in two straight sections where the beams collide. The energy of each beam is 510 MeV, in order to produce the ϕ-meson in the collisions.

The ϕ-particle main decay channels are [11]:

$$\begin{aligned} \Phi &\to K^+ + K^- \quad (49.1 \pm 0.8)\% \\ &\to K_L + K_S \quad (34.1 \pm 0.6)\% \\ &\to \rho\pi \to \pi^+\pi^-\pi^0 \quad (15.5 \pm 0.7)\% \end{aligned} \tag{1}$$

At the luminosity $\mathcal{L} = 10^{32}\text{cm}^{-2}\text{s}^{-1}$, the ϕ-meson is produced at a rate $\sim 4.4 \times 10^2$ s^{-1}, therefore, DAΦNE is a source of $\sim 2.2 \times 10^2$ (K^+K^-) pairs/s, collinear, background free

[2] With Bhabha events we mean $(e^+ + e^- \to e^+ + e^-)$ and $(e^+ + e^- \to e^+ + e^- + \gamma)$, *i.e.* elastic and inelastic (e^+, e^-) scattering.

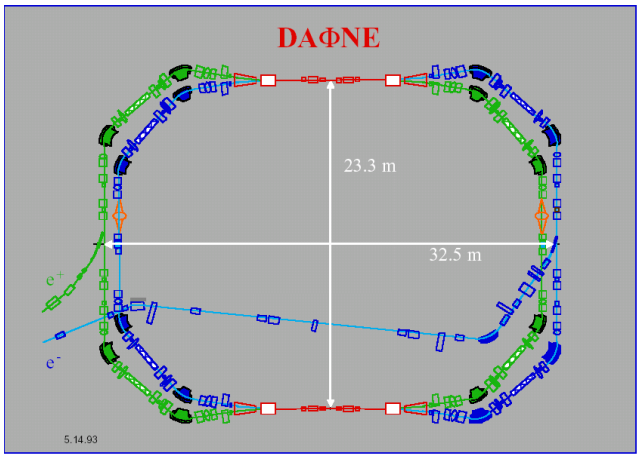

Figure 2: Geometrical design of the DAΦNE main rings (*top view*).

beam energy range	(0.250 ÷ 0.750) GeV
$\theta/2$ (crossing angle)	(10 ÷ 25) mrad
single bunch luminosity	4×10^{30} cm^{-2} s^{-1}
# of bunches per ring	(1 ÷ 120)
# of particles per bunch	8.9×10^{10}
maximum luminosity	5×10^{32} cm^{-2} s^{-1}
crossing frequency	up to 368.25 MHz

Table 1: DAΦNE design values.

and of very low energy ($\sim$ 16 MeV), since the ϕ is produced almost at rest.

Table 1 shows the DAΦNE design values. The beam crossing angle determines a small momentum of the generated ϕ (boost of about 12.3 MeV/c) directed toward the positive x side.

The FINUDA apparatus used the charged low energy kaons to produce strange hyperon stopping the kaons in thin targets, disposed in octagon configuration around the beam pipe after the first two layer of vertex detectors used to identify the kaons couples.

Fig. 3 shows a global view of the apparatus. The layers of the tracker are contained inside a superconducting solenoid (the material used for the coil wire is $NbTi/Cu$) which provides a highly homogeneous (within 2% in the tracking volume) magnetic field of 1.0 T over a cylindrical volume of 146 cm radius and 211 cm length.

Three main regions can be distinguished inside the FINUDA apparatus.

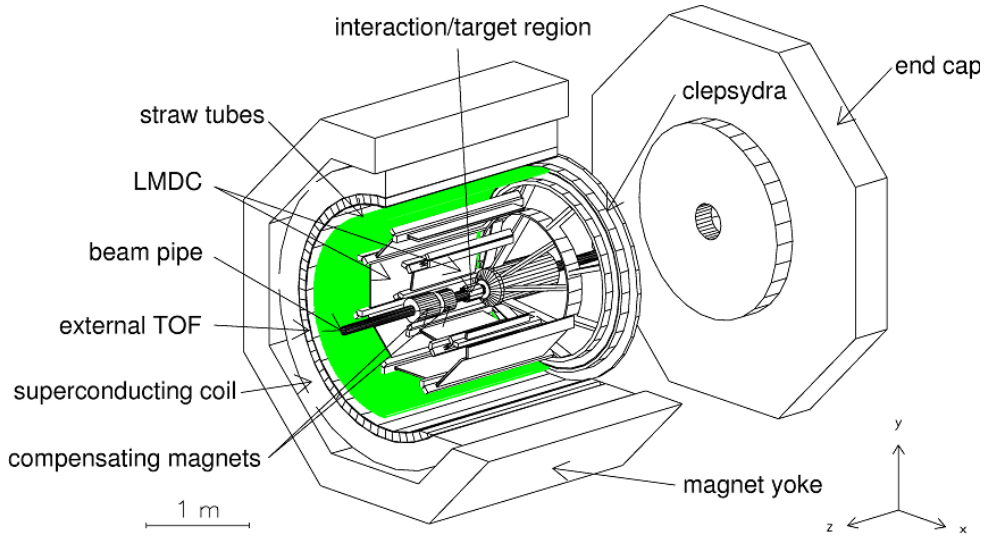

Figure 3: Schematic view of the FINUDA spectrometer.

- *The interaction/target region* which is shown schematically in Fig. 4(a). Here, the highly ionizing (K^+K^-) pairs are detected by a barrel of 12 thin scintillator slabs (TOFINO), surrounding the beam pipe, with a time resolution of a single mean timed slab of $\sigma \sim 250$ ps [12]. The TOFINO barrel is surrounded by an octagonal array of silicon microstrips (ISIM) featuring a spatial resolution $\sigma \sim 30$ μm and an energy resolution on $\Delta E/\Delta x$ for the kaons from $\phi(1020$ MeV) decay of 20% [13]. Thin solid target modules are positioned at a distance of a few millimetres on the external side of the octagon. The task of the ISIM detector is the determination of the (K^+K^-)' s interaction points. The expected precision is some hundreds micrometres, mostly due to multiple scattering in the very last part of the slow kaon trajectory.

- *The external tracking device* which consists of four different layers of position sensitive detectors. It is arranged with a cylindrical symmetry and it is immersed in a He atmosphere in order to reduce the effects of Coulomb multiple scattering.

  The trajectories of charged particles coming from the targets and crossing the tracking system are measured by: (i) a first array of ten double-sided silicon micro-strip modules (OSIM) placed close to target modules (see Fig. 4(a)); (ii) two arrays of

eight planar low-mass drift chambers (LMDC) filled with a (70% He-30% C_4 H_{10}) mixture, featuring a spatial resolution of $\sigma_{\rho\phi} \sim 150\,\mu$m and $\sigma_z \sim 1.0$ cm [14]; (iii) a STRAW tubes detector assembly, composed by six layers of longitudinal and stereo tubes, which provides a spatial resolution of $\sigma_{\rho\phi} \sim 150\,\mu$m and a $\sigma_z \sim 500\,\mu$m [15]. The straw tubes are positioned at 1.1 m from the beams interaction point. With the magnetic field set at 1.0 T, the achieved momentum resolution of the spectrometer, for 270 MeV/c π^-'s, was $\Delta p/p = \sim 0.7\%$ FWHM. It corresponds to an energy resolution ~ 1.0 MeV on hypernuclear spectra and of about 1.6 MeV FWHM on protons emitted in hypernuclear non-mesonic decay.

- *The external time of flight barrel* (TOFONE) which was composed by 72 scintillator slabs, 10 cm thick and 255 cm long, and provided signals for the first level trigger and for the measurement of the time-of-flight of charged and neutral particles, with a time resolution of a single TOFONE slab $\sigma \sim 350$ ps [12]. The detection of neutrons following hypernucleus decay was performed with an efficiency of $\sim 10\%$, an angular acceptance of 70% and an energy resolution of 8-11 MeV FWHM for neutrons of 65-80 MeV.

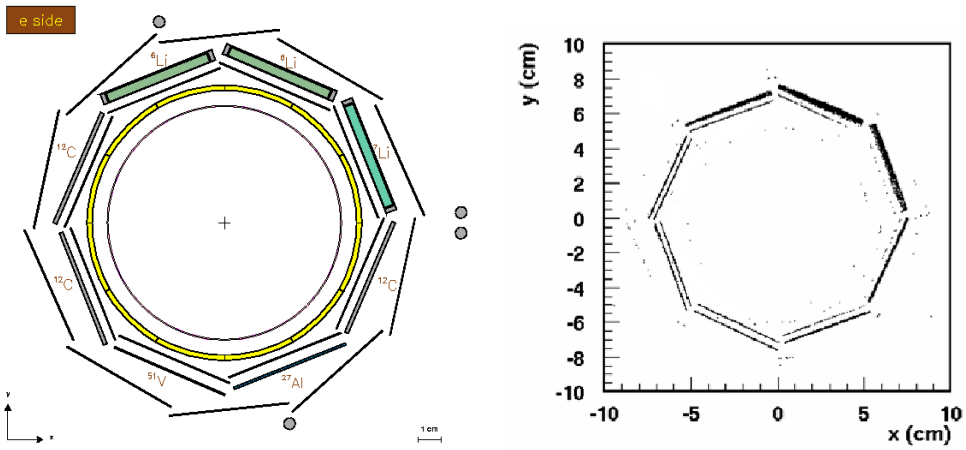

(a) (b)

Figure 4: (a) Schematic view of the interaction/target region. (b) Scatter-plot of the reconstructed y vs x coordinates of the K^- stopping points. Due to the beam crossing angle, an asymmetric distribution of points is reconstructed in the x plane.

With the FINUDA apparatus we were able to define alternatives methods with respect to the standard accelerator ones to monitor and measure DAΦNE parameters, such as luminosity, beam boost and distribution of collision points (the luminosity monitoring will be discussed in particular in chapter 1). As a member of the FINUDA collaboration, I was in charge of the data analysis to search for neutron rich hypernucley [9] and together with the group of the Bari University we had also the responsibility for the TOFONE subdetector and for the analysis of the TOF system (TOFONE + TOFINO) signals (which I discuss in chapter 2).

The e^+e^- Compact LInear Collider

In order to efficiently accelerate electron at energies of the order of 500 GeV, without loosing too much power due to synchrotron radiation, linear colliders have been proposed as next generation e^+e^- colliders. The Compact Linear Collider (CLIC) is a TeV-scale high-luminosity linear e^+e^- collider proposal. It envisions three stages of construction and operation at c.m.e. of 380 GeV, 1.5 TeV, and 3 TeV (Table 2), and a site length ranging between 11 km and 50 km. What makes it distinct from other colliders is its novel two-beam acceleration scheme. Normal Conducting (NC) copper high-gradient 12 GHz accelerating structures are powered by a high-current 1.9 GeV drive beam to efficiently enable an accelerating gradient of 100 MV/m, about three times the gradient of the ILC super conducting cavities [16]. For the first CLIC stage at c.m.e. of 380 GeV, suitable for the Higgs boson and the Top studies, the optimum gradient turns out to be 72 MV/m [17]. Therefore, for this stage an alternative RF power driven option with 12 GHz klystron powering is also being considered [17]. The maximum gradient must be achieved at nominal pulse length and shape (156 ns flat-top, 240 ns full length) and with a breakdown rate (BDR) of less than $\sim 10^{-6}$ (low enough for the reliable operation of some 20000 structures in two linacs); this is one of the CLIC challenges. Figure 5 presents a schematic layout of the CLIC complex at 380 GeV c.m.e. The main spin-polarized e^- beam is produced on a strained GaAs cathode in a conventional RF source and accelerated

to 2.86 GeV. The beam emittance [3] is then reduced in a damping ring. For positron beam production, a dedicated 5 GeV linac sends electrons onto a crystal to produce energetic photons, which in turn hit a second target to produce e^+. These positrons are captured, accelerated to 2.86 GeV and sent through a series of two damping rings. The CLIC RTML (Ring-to-Main-Linac) system transports and accelerates 352 bunches, with 0.5 ns bunch spacing, in each electron and positron beam to 9 GeV, and compresses their bunch lengths to 70 μm r.m.s. (or 44 μm for higher c.m.e.). After the main linacs have accelerated the beams, collimators in the beam delivery system remove any transverse tails and off-energy particles, and finally the final focus magnets compress the beams to the required small transverse sizes at the collision point. After the collision, two post-collision lines transport the spent beams to the beam dumps.

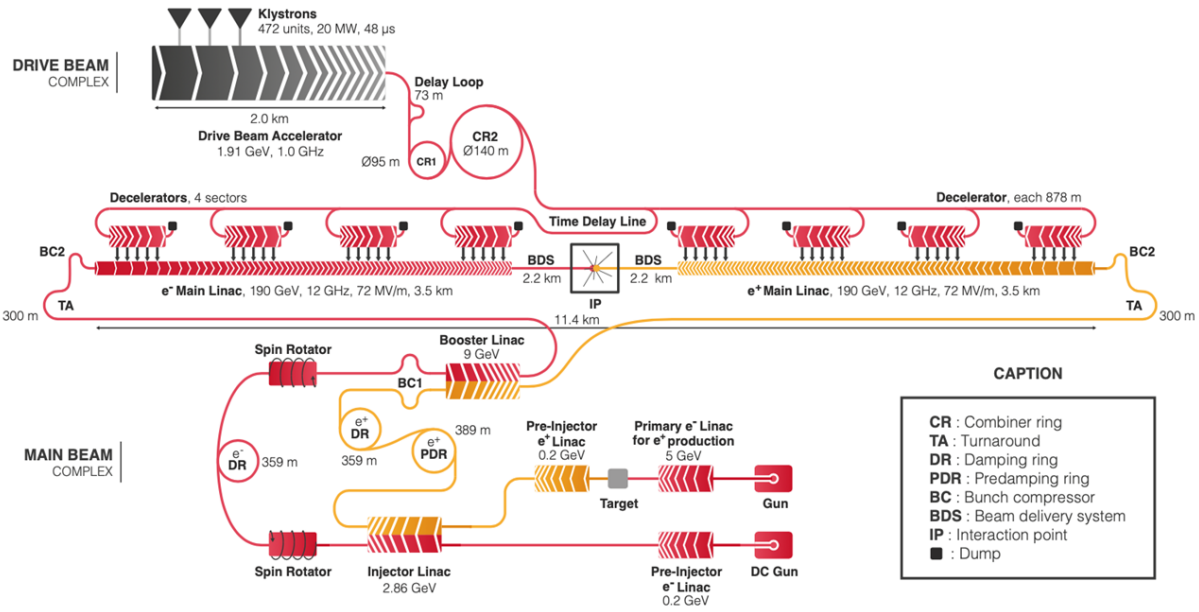

Figure 5: CLIC accelerator complex layout at 380 GeV c.m.e.

The CLIC luminosity critically depends on beam emittances (particularly vertical ones) at the collision point (IP), requiring generation of e^+ and e^- beams with a minimum emittance and their tight preservation during acceleration and focusing. The latter calls

[3] Area of the region in the p_x,x phase space occupied by the particles of a beam [18].

for control of all relevant imperfections, such as:

- pre-alignment of all the main linac and beam delivery system components at the 10 μm level;
- suppression of vibrations of the quadrupoles due to ground motion to the level of 1.5 nm at frequencies above 1 Hz for the main linac (and to 0.2 nm above 4 Hz in the final focus system) [19];
- novel beam-based trajectory tuning methods to minimize the effect of dynamic and static imperfections using sub-micron resolution BPMs [20, 21];
- mitigation of the effect of wakefields caused by high current beams passing through misaligned accelerating structures.

Table 2: Parameters for the CLIC energy stages. The power consumptions for the 1.5 and 3 TeV stages are from the CDR .

Parameter	**Symbol**	**Unit**	**Stage 1**	**Stage 2**	**Stage 3**
Centre-of-mass energy	$\sqrt{s}$	GeV	380	1500	3000
Repetition frequency	f_{rep}	Hz	50	50	50
Number of bunches per train	n_b		352	312	312
Bunch separation	Δt	ns	0.5	0.5	0.5
Pulse length	τ_{RF}	ns	244	244	244
Accelerating gradient	G	MV/m	72	72/100	72/100
Total luminosity	$\mathcal{L}$	10^{34} cm^{-2}s^{-1}	1.5	3.7	5.9
Luminosity above 99% of $\sqrt{s}$	$\mathcal{L}_{0.01}$	10^{34} cm^{-2}s^{-1}	0.9	1.4	2
Main tunnel length		km	11.4	29.0	50.1
Number of particles per bunch	N	10^9	5.2	3.7	3.7
Bunch length	σ_z	μm	70	44	44
IP beam size	σ_x/σ_y	nm	149/2.9	$\sim$ 60/1.5	$\sim$ 40/1
Normalised emittance (end of linac)	ϵ_x/ϵ_y	nm	920/20	660/20	660/20
Normalised emittance (at IP)	ϵ_x/ϵ_y	nm	950/30	—	—
Estimated power consumption	P_{wall}	MW	252	364	589

During my fellow at CERN I was responsible for maintaining and developing simulation codes called PLACET [22] and GUINEA-PIG [23], which are reference codes for the CLIC beam dynamics studies. Using these codes and with other CERN post-docs, master and

PhD students I have contributed to study and to optimize performances in the Beam Delivery System (BDS) and Machine Detector Interface (MDI) areas of the project, as reported in several section of chapters 1 and 2 of this *habilitation*.

The Large Hadron Collider and its upgrades

The superconducting Large Hadron Collider is the world's highest energy collider (see Ref. [24] and references therein). It supports a broad particle-physics program at the energy frontier [25]. Over most of the LHC's 26.7 km circumference, the two counter-rotating hadron beams are contained in two separate vacuum pipes passing through the same superconducting twin-apertures NbTi accelerator magnets. A dipole field of 8.3 T is required to bend hadrons with a momentum of 7 TeV per unit charge in the tunnel; this is 60% higher than in previous accelerators. The LHC beams cross at four IPs, which host two multipurpose high-luminosity experiments, ATLAS and CMS, and two special purpose experiments, ALICE (mainly devoted to heavy-ion physics) and LHCb (B meson physics). With four crossings, as shown in Fig. 6, each beam passes half of a revolution on the outer side, the other half on the inner, so that the circumferences of the two beams are identical. The other four Long Straight Sections (LSS) house the collimation (or beam cleaning) system, the radio frequency (RF) system and beam instrumentation and a system for beam extraction (Dump), see Fig. 6.

In pp collisions the LHC has so far reached a world record luminosity of $2.1\times10^{34}cm^{-2}s^{-1}$, which, within the measurement accuracy, equals the record for e^+e^- colliders still held by KEKB. The LHC can also provide Pb-p collisions, and other ion-ion or ion-proton collisions, at different energies. The highest luminosity is achieved with the smallest possible beam cross-section, a large number of bunches and a high bunch population. Up to 2808 bunches can be filled and accelerated in each beam, the minimum distance between bunches is 25 ns or 7.5 m. Each proton bunch consists of up to 1.7×10^{11} protons. The bunches have a typical length of 7 to 10 cm. At the interaction point the beam has a volume of about 20 microns $\times$ 20 microns $\times$ 8 cm. At 7 TeV, each LHC beam stores an

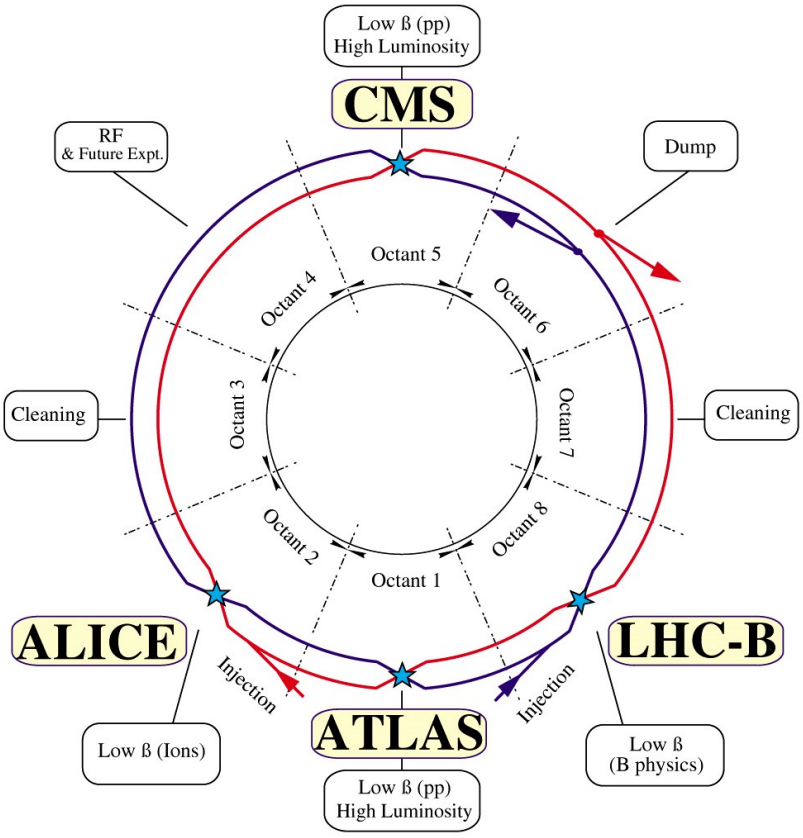

Figure 6: Layout of the LHC double ring, with its eight long straight sections hosting two general and two special-purpose experimental detectors and/or devoted to specific accelerator functions, such as betatron collimation (cleaning), momentum collimation, beam extraction, RF systems and diagnostics. (Image credit: CERN).

energy of up to 360 MJ. Machine protection systems with unprecedented safety levels are required to operate the LHC. This is achieved with a combination of active protection by equipment and beam parameter monitoring, as well as with passive protection by a large number of collimators.

The existing CERN proton accelerator chain provides the beams to the main LHC ring, see Fig. 7. After leaving the source, the protons are first accelerated in a linear accelerator (LINAC2) to 50 MeV. The beams from LINAC2 are further accelerated in the four Proton Synchrotron Booster (PSB) rings to 1.4 GeV, then by the Proton Synchrotron (PS) to 26 GeV. The Super Proton Synchrotron (SPS) at the end of the injection chain delivers protons for the LHC with an energy of 450 GeV through two over 3 km long

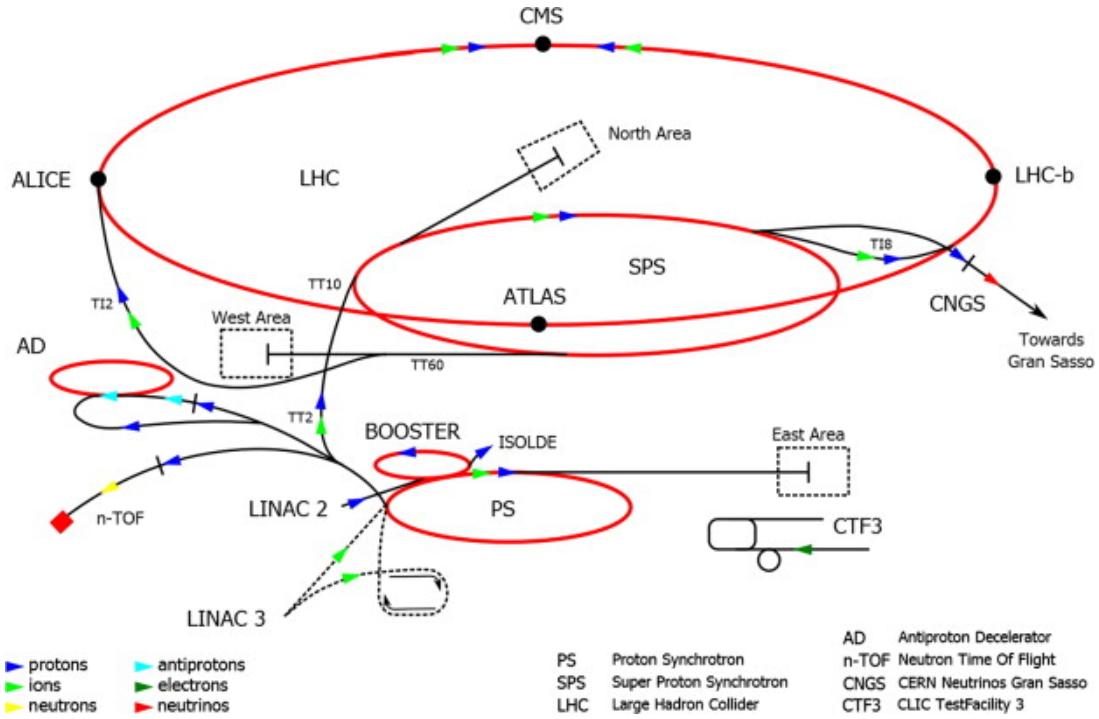

Figure 7: The CERN accelerator complex including the LHC and its injectors. After leaving the source, the protons are first accelerated in LINAC2 before they are passed on to the PS Booster, the PS, the SPS and finally to the LHC.

transfer lines (TI2 and TI8). After the LHC injection phase that lasts 20 to 30 minutes, the beams are accelerated in about 20 minutes using a specially designed superconducting radio-frequency system (RF) to an energy of up to 7 TeV. Sixteen cavities of high-purity niobium deliver an accelerating voltage of up to 16 MV per beam.

It is predicted that the final-focusing quadrupoles around the ATLAS and CMS experiments will be destroyed by radiation from collision debris after a total integrated luminosity of around 300 fb^{-1}. More than half of this value has already been delivered. This provides motivation for the High Luminosity LHC (HL-LHC) upgrade [26], scheduled for around 2025, when the final quadrupole triplets [4] will be exchanged with new ones of larger aperture.

[4] A triplet identify the sequence of final focusing-defocusing-focusing magnets before the beam collision, aiming to produce the target beam sizes at the interaction point. In lepton machines, with different horizontal and vertical beam sizes a doublet of focusing-defocusing quadrupole is used instead.

HL-LHC

The main goal of the LHC upgrade is to achieve an integrated luminosity per year of about 250 fb^{-1}, without exceeding the 400 pile-up event per crossing in the two high luminosity experiments (ATLAS and CMS). Knowing the luminosity recipe for round beams:

$$L = \frac{n_b N_1 N_2 \gamma f_{rev}}{4\pi\beta^* \epsilon_n} F(\phi, \beta^*, \epsilon, \sigma_s) \tag{2}$$

where n_b are the number of bunches, $N_{1,2}$ are the number of proton per bunch, γ is the relativistic factor, f_{rev} is the revolution frequency, β^* is the betatron function [5] at the collision point, ϵ_n is the normalized emittance of the bunches and F is the geometric reduction factor due to the crossing angle ϕ ($F = \frac{1}{\sqrt{1 + (\phi\sigma_s/\sqrt{\beta^*\epsilon})^2}}$). A number of performance optimisation of the LHC complex are required to maximise luminosity, as reported in A.7:

- maximize bunch intensities
- minimize the beam emittance
- minimize beam size at the collision point
- maximize number of bunches
- compensate for 'F'
- Improve machine 'Efficiency'

The higher bunch intensities and the reduction of emittance will be achieved by the injector complex upgrades, with some limitation on the bunch population due to the longitudinal acceptance of the LHC for bunches that are longitudinally stable in the SPS, at injection [26]. The reduction of the beam sizes at the collision point will be possible thanks to new inner triplet magnets with larger aperture and realized in new Nb_3Sn superconducting cables, instead of NbTi cables used for LHC. The maximum number of

[5] β represents the envelope of all particle trajectories at a given position s in a storage ring [27].

bunches that can be transferred from the SPS to the LHC is limited to 288 by machine protection considerations. The compensation for the geometric redaction factor F will be realised installing new equipment in the ring such as the superconducting RF crab cavities [28, 29, 30]. They are deflecting cavities which rotate the beam along the horizontal or vertical axis. In 2018, first beam tests of such crab cavities with protons were successfully performed at the CERN SPS [31]. With all these improvements the instantaneous (or peak) luminosity of about $19 \times 10^{34} cm^{-2} s^{-1}$ could be achieved. Therefore luminosity levelling techniques will be implemented, which allows sustaining the operational luminosity, and the associated event pile-up in the detector, at a constant level over a significant time by means of several methods:

- a gradual reduction of the betatron function at the interaction point (β^*);
- changes in the RF voltage of crab cavities or more sophisticated crabbing schemes [32];
- dynamic bunch-length reduction;
- controlled variation of the transverse separation between the two colliding beams.

FCC-hh

A further increase in the collider size by a factor of about 4 compared with the LHC, i.e., to a circumference of 100 km, yields a c.m.e. of 100 TeV with 16 T dipole magnets technology (Future Circular Collider, hadron version "FCC-hh") [34]. This goal defines the overall infrastructure requirements for the FCC accelerator complex.

Figure 8 indicates the proposed location of the FCC in the Lake Geneva basin, connected to the existing CERN/LHC accelerator complex. The principal structure for the collider is a quasi-circular 97.75 km long tunnel composed of arc segments interleaved with straight sections. Approximately 8 km of bypass tunnels, 18 shafts, 14 large caverns and 12 new surface sites are also planned. The tunnel location and depth were optimized taking into account the local geology. Collider luminosity should ideally increase with the

Table 3: HL-LHC nominal parameters for 25 ns operation for two production modes of the LHC beam in the injectors described in Ref. [33].

Parameter	**Nominal LHC design report**	**HL-LHC standard**	**HL-LHC BCMS**
Beam energy in collision [TeV]	7	7	7
Particles per bunch, $N[10^{11}]$	1.15	2.2	2.2
Number of bunches per beam	2808	2748	2604
Beam current [A]	0.58	1.09	1.03
Crossing angle in ATLAS and CMS	285	590	590
Minimum β^* [m]	0.55	0.15	0.15
Levelled luminosity $[10^{34}cm^{-2}s^{-1}]$	-	5.0	5.0
Virtual Luminosity with crab cavity $[10^{34}cm^{-2}s^{-1}]$	(1.18)	19.54	18.52
ϵ_n [μm]	3.75	2.50	2.50
ϵ_L [eVs]	2.50	2.50	2.50
r.m.s. energy spread [0.0001]	1.13	1.13	1.13
r.m.s. bunch length [cm]	7.55	7.55	7.55
Total loss factor R_0 without crab cavity	0.836	0.305	0.305
Total loss factor R_1 with crab cavity	(0.981)	0.829	0.829
Beam-beam/IP without crab cavity	0.0031	0.0033	0.0033
Beam-beam/IP with crab cavity	(0.0038)	0.0011	0.0011
Events/crossing without levelling and crab cavity	(27)	198	198
Events/crossing with levelling and crab cavity	(27)	138	146

square of the energy, since cross sections decrease as the inverse square of energy. However, due to the nonlinear parton distribution inside the colliding protons, even a lower luminosity can produce exciting physics [35]. The LHC design has already dramatically increased luminosity compared with previous machines. Much higher luminosity still is expected for the proposed FCC-hh. Even higher luminosity can be achieved by reducing the IP beta functions. An ongoing study aims at pushing the FCC-hh β^* down to 5 cm [36]. Like HL-LHC, the crossing angle needs to be increased as the β^* is reduced to mitigate parasitic beam-beam collisions, and to counteract the degradation of luminosity due to the reduction of geometric overlap of the beams FCC-hh will also use novel crab cavities [31].

Future hadron colliders are characterized by record high stored beam energy, rendering machine protection one of the greatest concern. A very challenging multi-stage collimation system is needed to avoid local beam loss spikes near cold magnets, which would

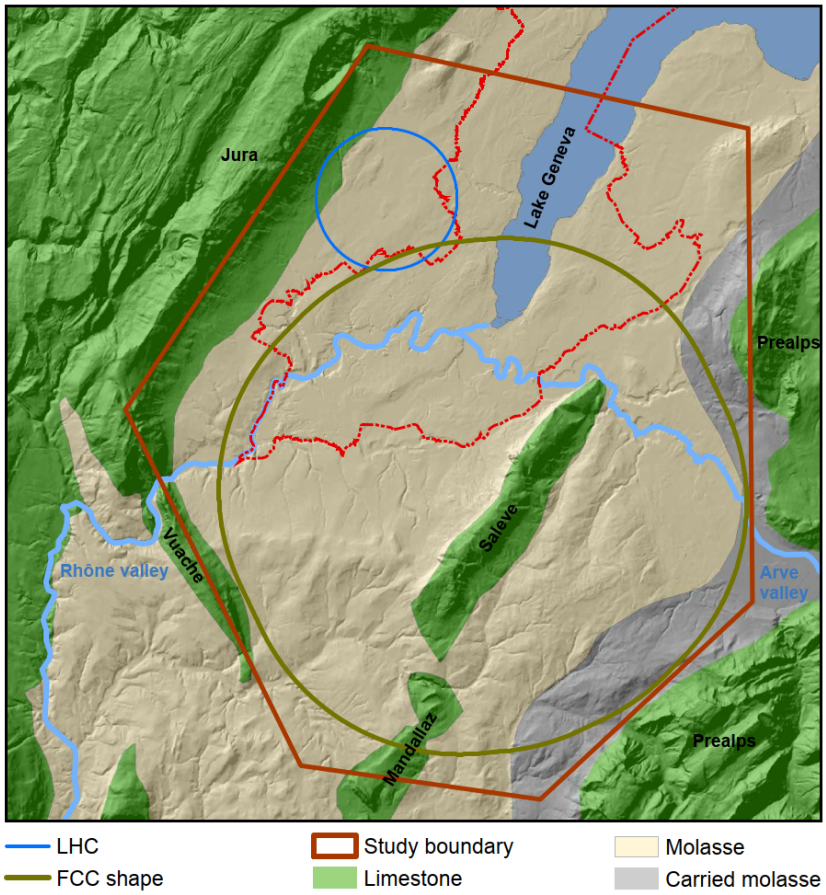

Figure 8: Study boundary (red polygon), showing the main topographical and geological structures, LHC (blue line) and FCC tunnel trace (brown line) [34].

induce magnet quenches. Beam injection and beam extraction are particularly sensitive operations, as injection or dump kickers are among the fastest elements in the machine. The collider design must be robust against the sudden asynchronous firing of a kicker unit. The collimators are likely to be the first element to be hit by the beam in case of any fast failure and must be able to withstand the impact of one or a few bunches. The primary and secondary collimators of the LHC are based on carbon-carbon composite material. For the HL-LHC and future hadron colliders, even stronger materials are being developed and examined, which also feature higher conductivity and, hence, lower "impedance". More advanced options include the use of short bent crystals as primary collimators [37] and the deployment of hollow electron-beam lenses as non-destructible collimators [38], as already considered by the HL-LHC project. Acceptable performance of the collima-

tion system, along with small IP beta function, also requires an excellent optics control. In view of the substantial ring circumference and the associated low momentum compaction, hadron beam intensity in very large accelerators may be limited by conventional instabilities. In particular the resistive wall instability becomes a concern due the low revolution frequency, and TMCI (Transverse Mode Coupling Instability) could appear at injection due to the low synchrotron tune [39, 40]. For future higher-energy hadron colliders, synchrotron radiation damping becomes significant. In such a situation, longitudinal emittance needs to be kept constant during the physics store through controlled longitudinal noise excitation, in order to maintain longitudinal Landau damping [41]. At the same time, the transverse emittance shrinks due to strong radiation damping, while proton intensity rapidly decreases as a result of the "burn-off" due to the high luminosity. For the FCC-hh, the transverse emittance damping time is shorter than the proton burn-off time. As a result, the total beam-beam tune shift increases during the store. At some point, the beam-beam limit is reached, and, from this point onward, the transverse emittance must be controlled by transverse noise excitation, so as to keep the beam-beam tuneshift at, or below, the empirical limit. This limit determines the further luminosity evolution during the store and the optimum run time [42].

Chapter 3 and section 2.2 describe my contribution to these projects. I performed optics design and single particle dynamic study to better understand and to optimize performances of the HL-LHC and FCC-hh colliders. They are the result of a close collaboration with CERN and Politecnico di Milano, and involve the work of several colleagues, post-docs, PhD students and master students.

Chapter 1

Luminosity monitoring and impact of detector solenoid

Luminosity is a key figure in experimental physics, relating the observed number of events of a given process to its cross section. The relation:

$$\mathcal{L}\sigma_c = N_{ev} \tag{1.1}$$

relates the luminosity $\mathcal{L}$, the cross section σ_c [1] of an elementary process in a given part of the phase space defined by experimental selection cuts, and the number of detected events N_{ev} of the process in the same part of the phase space. It is the principal target parameter in the design of a collider, it can be defined by the expression:

$$\mathcal{L} = \frac{N^2}{4\pi\sigma_x\sigma_y} f_{rep} N_b \tag{1.2}$$

where N^2 is the population of the two symmetric bunches, $\sigma_{x,y}$ are the beams widths in the transverse plane (corresponding the the standard deviation in case of Gaussian bunches), f_{rep} is the accelerator repetition rate (or revolution frequency in case of circular colliders), N_b is the number of bunches per train. Usually, for colliders, the integrated and

[1] Probability that a final state happen when two particles collide.

instantaneous (or peak) luminosity can be calculated using the accelerator physics relation of Eq. 1.2 and standard machine parameters, continuously measured by instruments positioned along the rings. This procedure is accurate, but it is not a direct measurement of the luminosity in the specific interaction region. Commonly, in the forward region of detectors in colliders, luminosity is precisely measured with dedicated calorimeters to detect an elementary process whose cross section is well known or can be precisely calculated, such as the Bhabha scattering process for electron-positron colliders or the quasi-elastic scattering for the high energy protons machines. Precision better than per mille level in the luminosity measurement was reached using Bhabha scattering at LEP, thanks to a careful experimental setup, and precise quantum electrodynamics (QED) calculations [43, 44, 45, 46].

Nevertheless, depending on the physical channel of interest or due to competing processes other signals can be more precise or easier to be detected, like in the case of the FINUDA experiment or the case of CLIC at 3 TeV centre of mass energy (c.m.e.).

1.1 DAFNE monitored by FINUDA

With the FINUDA apparatus at the DAΦNE collider we could measure on-line luminosity using both the Bhabha scattering process and the kaons rates, produced by the decay at rest of the Φ meson. To provide the on-line luminosity values in time intervals of the order of few seconds, FINUDA could exploit the counts of the scalers measuring the Bhabha trigger rate. Such counts were transformed in L_{peak} values using a conversion factor obtained from the Bhabha runs where events had been fully reconstructed. There is indeed a fixed relationship between the total counted Bhabha triggers and the total number of Bhabha events reconstructed. This relationship was determined using the FINUDA Monte Carlo code and tuned experimentally at the beginning of FINUDA runs. The luminosity measured with this method, in spite of its larger error with respect to those provided by the reconstruction procedures, was, however, precise enough for the

aim of on-line monitoring the L_{peak} values of DAΦNE luminosity. Moreover, with this method, the values of L_{peak} could also be obtained when the trigger used in the data taking was not the Bhabha one, since no reconstruction of Bhabha events was needed, but only the reading of a dedicated scaler permanently counting the Bhabha trigger conditions occurring during any run. In Fig. 1.1 typical plot of the L_{peak} luminosity measurement provided with the method described above, is given. The figure shows the circulating e^- and e^+ currents, and the instantaneous (peak) and integrated luminosity values as measured by FINUDA during a 2 h period of data taking. For the sake of comparison, the peak luminosity values calculated using accelerator physics relations by means of the data provided by DAΦNE monitoring devices are shown as well.

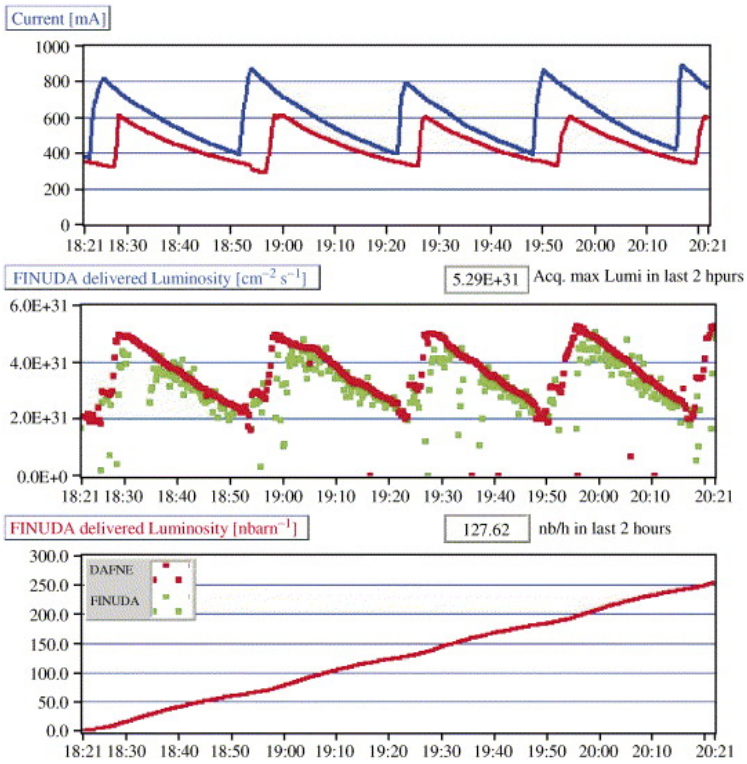

Figure 1.1: The DAΦNE currents (top plot) for $e+$(red) and e^-(blue) beams; the peak luminosity (mid plot) as measured by FINUDA(green points) and provided by DAΦNE (red points), and the DAΦNE integrated luminosity (bottom plot), during a 2 h interval of data taking.

The instantaneous (or peak) machine luminosity was also continuously monitored by counting the reconstructed Bhabha events (offline procedure), as described in detail in

A.1.

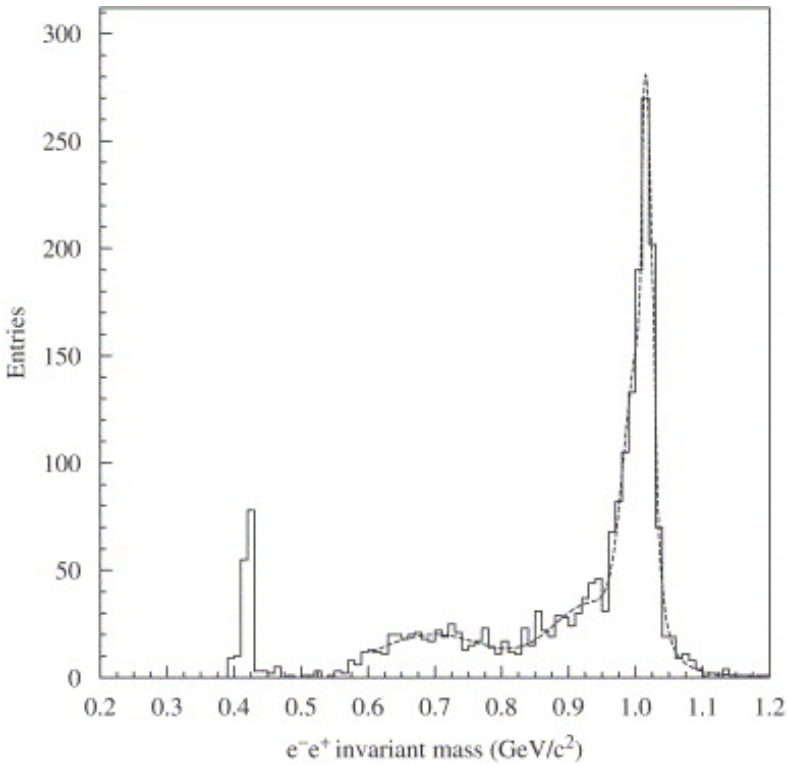

Figure 1.2: Invariant mass of the colliding e^+e^-, as selected and reconstructed in two runs of Bhabha trigger. The main peak at $M_{inv} = 1.019 \pm 0.015 GeV/c^2$ measures the e^+e^- collision energy.

Nevertheless, in the case of the DAΦNE Φ-factory, Bhabha events are not so sensitive to center of mass energy, while kaons production is (the exact energy to produce the Φ is required to be well within ±1 MeV). For such a small energy displacement, the variation of the Bhabha counts or the displacement of the invariant mass [2] Bhabha peak are practically not detectable. Hence, a different method of performing an accurate monitoring of both the luminosity and the c.m. energy had to be employed by FINUDA: the method was based on the complete reconstruction and counting of events coming from the $\phi(1020)$ decay mode into $K^0_S K^0_L$ collected during Bhabha runs. After the K^0_S mass peak has been identified (see low energy part of the spectrum shown in Fig. 1.2), the number of corresponding events $N_{K^0_S}$ was divided by the number N_{Bhabha} of Bhabha events collected

[2]The sum of energies minus the sum of the momenta of two decaying particles leads to the rest mass of the mother particle.

and reconstructed in the same run. This procedure was repeated changing slightly the energy of the two DAΦNE beams at each step. The tuning of the machine at the $\phi(1020)$ energy corresponds to the maximization of the ratio $N_{K_S^0}/N_{Bhabha}$. After the collider has been properly tuned in energy, this ratio is checked at regular time intervals to monitor its stability during the whole period of data taking. Therefore, for the FINUDA experiment the optimum luminosity was reached continuously monitoring and maximising the ratio of the hadronic production from the Φ decay and the Bhabha scattering ($N_{K_S^0}/N_{Bhabha}$). The FINUDA apparatus allowed also to reconstruct other machine parameters; such as the distributions of e^+e^- collision points and the beams boost due to e^+e^- crossing angle, as described in A.1.

1.2 Luminosity monitoring in future electron-positron linear colliders

In future linear lepton colliders, luminometers are foreseen to measure luminosity. The luminometer (LumiCal) is designed as a pair of sampling calorimeters[3] with cylindrical geometry, centred around the outgoing beam axis at $\sim$ 2.5 m from the interaction point (IP) on both sides. In order to reach the target luminosity at future linear colliders, the electron and positron beams will be focused to a few nm in the vertical direction, and a few ten to few hundred nm in the horizontal directions at the interaction point (IP). This results in extremely high local charge densities, and extremely intense EM interaction between the opposing bunches. In case of a charge moving with relativistic velocity v, the component of EM field perpendicular to v scales with the Lorentz factor. At future linear colliders, the Lorentz factor of the bunches is of the order of 10^6 in the lab frame, or 10^{12} in the rest frame of the opposing bunch. Since the bunches have opposite charge signs, the direction of the perpendicular component of the Lorentz force points towards

[3]The calorimeters consist of a number of layers in the longitudinal direction, each layer containing a tungsten disk and a segmented sensor plate. Electromagnetic (EM) showers developing in tungsten are sampled in the sensor plates [47, 48].

Total Luminosity	$[10^{34}\text{cm}^{-2}\text{s}^{-1}]$	5.9
Peak Luminosity	$[10^{34}\text{cm}^{-2}\text{s}^{-1}]$	2.4
repetition freq.	[Hz]	50
bunches/train		312
intra-bunch dist.	[ns]	0.5
particles/bunch	$[10^{10}]$	0.372
bunch length	$[\mu\text{m}]$	44
emittances H/V	[nm]/[nm]	660/20
beam sizes	[nm]/[nm]	45/1

Table 1.1: CLIC parameters at 3 TeV c.m.e. taking into account machine imperfections.

the bunch center. This results in a very strong focusing effect of the bunches (called the pinch effect). The pinch effect enhances the luminosity, but due to the strong bending of the beam particle trajectory, induces emission of intense and energetic EM radiation, called Beamstrahlung, which smears the peak of the luminosity spectrum. In addition to beamstrahlung photons, also QED and quantum chromodynamics (QCD) backgrounds are produced during collision. The relevant processes are: coherent pair production, incoherent pair production and $\gamma\gamma$ to hadrons events. All together they create additional background on the luminosity calorimeter. At CLIC maximum energy (3 TeV in the c.m.) the coherent pair production, the incoherent pair production and hadronic events rates are expected to be high, as shown in Table 1.2 using the parameters reported in table 1.1.

On average two beamstrahlung photons are emitted per beam particle. Their energy distribution is peaked at low values but a significant number of them can reach the nominal beam energy, as shown in Fig. 1.3(left). The deciding parameter, governing the yield of the strong field processes and the shape of the spectrum of the produced leptons, is the Lorentz invariant quantity Υ defined as:

$$\Upsilon^2 = \frac{(F^{\mu\nu}p_\nu)^2}{m^2c^2\mathcal{E}_0^2} \tag{1.3}$$

where $F^{\mu\nu}$ is the electromagnetic field tensor and $p^\nu(\hbar k^\nu)$ is the four-momentum of the impinging lepton (photon) and $\mathcal{E}_0$ is the local electric field in the two bunches reference

frame. At CLIC energies, where the beamstrahlung parameter Υ can be much larger than 0.5, the emitted photons can turn into e^+e^- pairs by interacting with the collective field of the oncoming beam, so called coherent process. The energy spectrum of the produced pair depends on the beamstrahlung parameter, very low energy pairs are created only for high value of Υ. The angular distribution is boosted in the direction of the mother

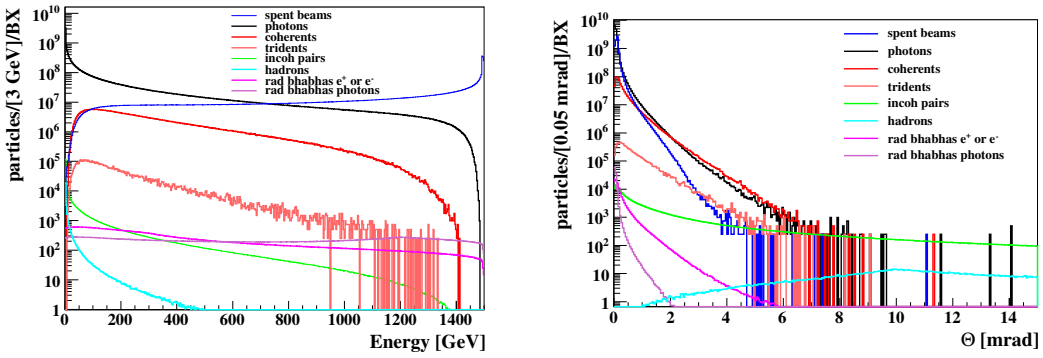

(a) (b)

Figure 1.3: Energy distribution (a) and angular distribution (b) of the particles produced in beam-beam background.

particle of the intermediate photon. The red lines in Fig. 1.3(left) and Fig. 1.3(right) show their expected energy and angular distribution. In CLIC at 3 TeV c.m.e. the coherent pair creation is the dominant process which produces e^+e^- pairs during collision, 6.6×10^8 coherent pairs are expected. Nevertheless at quantum beamstrahlung regime Υ >1 and for very short bunch length the creation of pair may occur by an intermediate virtual photon, in which case the pair production is said to occur by the trident process. The implementation of this process in GUINEA-PIG has been realized with a PhD student and is described in A.3, their production in the GUINEA-PIG code follow the one of the coherent pairs, except for the virtuality of the intermediate photon. The expected energy spectrum and their angular distribution for the nominal CLIC beams are shown by the light-red in Fig. 1.3(left) and Fig. 1.3(right), respectively. As coherent pairs they follow mainly the beam direction while leaving the interaction region. Their angular distribution is well confined in the 10 mrad opening angle of the interaction region beam pipe.

$\Delta E/E_{BS}$	29%
n_γ	2.1 per beam particle
$N_{coherent}$	66×10^7
$N_{trident}$	67×10^5
$N_{incoherent}$	330×10^3
$N_{incoh-muons}$	12.50
$N_{hadrons}$	3.2
$N_{radiative-Bhabhas}$	110×10^3

Table 1.2: Average energy loss due to beamstrahlung and expected beam-beam background rates per bunch crossing for the beam parameters reported in Table 1.1

Most of the low energy incoherent e^+e^- pairs are created at the future linear colliders by individual scattering of particles according to three main processes, the so called Breit-Wheeler ($\gamma\gamma \rightarrow e^+e^-$), Bethe-Heitler ($e^\pm\ \gamma \rightarrow e^\pm\ e^+e^-$) and Landau-Lifshitz ($e^+e^- \rightarrow e^+e^-e^+e^-$) processes. Their are well known QED processes widely described in standard textbooks [49]. The main formulas implemented in GUINEA-PIG are described in [50]. Their expected rate in CLIC at 3 TeV c.m.e. is $\sim 330\times10^3$, lower then the coherent pair one. Having very low energy, they can be highly deflected in the electromagnetic field of the incoming bunch therefore, they can enter in the detector region. The same process can lead to the production of muon pairs as described in [51], the expected number of muons pair is 12.5 per bunch crossing.

Hadronic events are also produced at e^+e^- colliders through the $\gamma\gamma \rightarrow$ hadrons reaction. The cross section is known experimentally up to 200 GeV. Different parameterizations of the cross section with the energy are implemented in GUINEA-PIG, which extrapolate experimental values. According to the one in [52] the expected number of $\gamma\gamma$ collisions per bunch crossing is 3.2 for a center of mass energy of the two photons of > 2 GeV. The energy distribution of the produced hadrons is peaked at low energy and their angular distribution is more central then the incoherent pairs one, allowing them to reach the central detector region.

Radiative Bhabhas is another well known QED process, in which the binary collision

of the electron-positron lead to the emission of a photon in the final state ($e^+e^- \rightarrow e^+e^-\gamma$) [53]. At lowest order the process (in t channel) can be modelled as a two steps reaction: first an e^-/e^+ is substituted by its photon equivalent spectrum, then the compton scattering of the photon on the e^+/e^- is calculated. The expected rate at CLIC is $\sim 110 \times 10^3$. The energy and angular distributions of the scattered e^-/e^+ and photon are shown by the pink and light-pink curve in Fig. 1.3(left) and Fig. 1.3(right). Their energy is spread over a wide range (from 0 up to the nominal beam energy). Their angular distributions are mainly peaked in the very forward direction.
For beam emittances that include budget for imperfections (see Table 1.1) an upper limit for the production rate of all the processes listed above is given in Table 1.2. The actual values depend on the single machine and change during operation.

All these processes under certain conditions may enter in the detector region, generating background in the vertex and forward region detectors, including in particular the Luminometer. The Luminosity measurement by this dedicated instrument might be less accurate and clean than for previous (lower energy) colliders. Furthermore, as already said their rates can vary with the machine configuration, i.e. according to the LINAC and Beam Delivery System imperfections that can generate offsets and aberrations of the colliding beams. In A.2, A.4 a study of the dependence of backgrounds rates and luminosity on beam offsets and aberrations at the collision points is presented. These study have shown that the incoherent processes, such as incoherent pairs and hadronic events, have the same variation of luminosity within 20% (i.e., the correlation between the change of these event rates and the change of luminosity is close to 1), regardless of the aberrations considered. The coherent processes, such as coherent pairs and beamstrahlung, have a different variation with respect to luminosity (i.e. their correlation is far from 1) and present a different variation according to the aberrations too. Therefore, by measuring the variation of the rates of the incoherent processes (with dedicated scalers, like the Bhabha rate or the kaon to Bhabha ratio, in the FINUDA detector) is possible to evaluate the variation in the luminosity with 20% uncertainty, without actually measuring it. The

variation of the rates of coherent processes could be used in combination with the one of incoherent processes to identify the main aberrations of the beams, in dedicated feedback. In practice, it is critical to define a signal that can be easily identified against the other processes. Experimental techniques to detect beamstrahlung photons in the CLIC post-collision line can be found in [54]. The incoherent pairs are produced with relatively small angles with respect to the beam axis, but are deflected by the beam fields. Thus, the pair particles can have large angles and enter in the detector region. The integration of pair energy above a certain angle with respect to the beam axis has been also studied as a potential signal for luminosity optimization in [55]. In CLIC their identification could be more complicated due to the presence of the coherent pairs in the forward region, leptons coming from hadronic events, and Bhabhas. Therefore, in A.4 I have proposed to use the hadronic events as luminosity signal, by looking in particular at its multiplicity in the final state. This signal is of particular interest for the 3 TeV energy stage of CLIC, due to the much smaller production rate at lower energy. Recently, the beamstrahlung photons and incoherent pairs reaching the BeamCal calorimeter (which are available at 380 GeV, as well) have been proven successfully to recover luminosity in more than 90% of machine configurations [56]. The same studies are done and/or foreseen for the lepton option of the future circular colliders. Given the lower energies, the dominant processes in the beam-beam interaction of the future lepton circular colliders are the beamstralhung photon, the incoherent pairs creations and radiative bhabha scattering from beam-beam interaction, and syncrothron radiation and beam-gas scattering beam-induced backgrounds.

I think it could be also interesting to study the possibility to improve the GUINEA-PIG code from a computational point of view. Working for example on the tracking of the low energy pairs, optimizing the speed of the code in order to interface it with multi-turn tracking codes of e^-, e^+ rings. It could be generalized to perform beam-beam studies with other particle species.

1.3 Synchrotron Radiation in the CLIC Detector Solenoids

Another source of beam aberrations and Incoherent Synchrotron Radiation (ISR) at the collision point, not considered in the previous study, is the Detector Solenoid, required by the experiments to reconstruct particle momentum from their bent trajectory. In

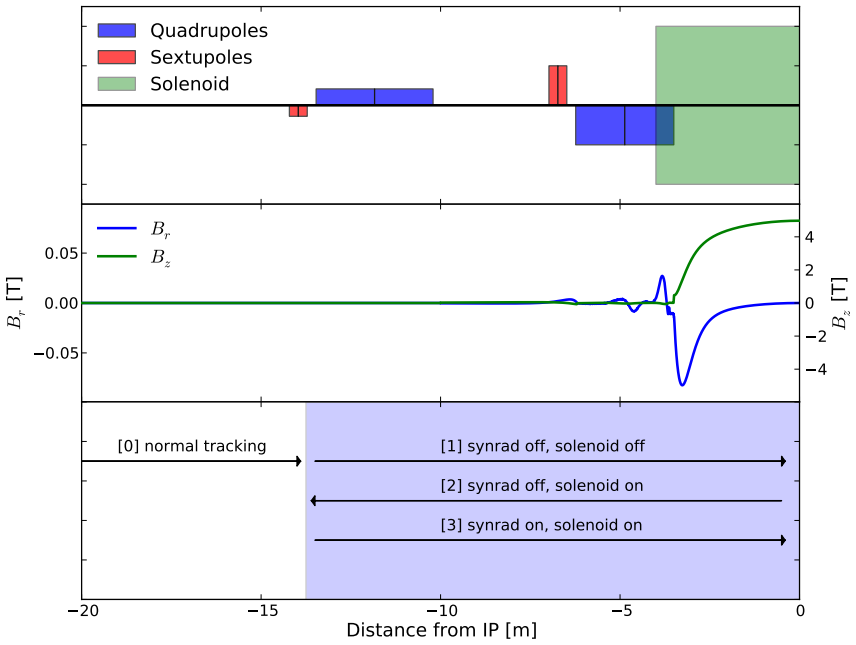

Figure 1.4: Schematic overview of the last 20 m of the final focus in CLIC (top panel). The experimental solenoid (green) is overlapping the QD0 (blue). Sextupoles SD0 and SF1 in red; strengths and signs of quadrupoles/sextupoles are indicated by the size and direction of the bars. In the middle panel the simulated SiD solenoid field is shown. The radial field in blue with values on the left side, and longitudinal field in green with values on the right hand side. In the bottom panel the tracking procedure is visualized.

Fig. 1.4 (top), the final 20 m of the CLIC BDS lattice at 3 TeV c.m.e. for the L* option of 3.5 m, is shown. The residual field from an experimental solenoid typically extends 10˘15 m away from the interaction point (IP), depending on shielding and solenoid design. L* is the distance from the IP to the closest focusing magnet, which is the QD0 for CLIC. In the CLIC at 3 TeV c.m.e. with short L*, the main solenoid field overlaps with the last final focus magnets. This enhances the optical distortions at the IP [57] since the QD0 is, partly inside the experimental solenoid. Special care had to be taken to make sure the

interplay between the solenoid field and the magnet field was minimized. A solenoid will in general have a radial field component on any charged particle off the solenoid center line, with a maximum around the entrance of the solenoid. This is the region of maximum β-function in a linear collider, therefore, the beams are more sensitive to small errors. With a horizontal crossing angle, the horizontal solenoid field component will be larger than the vertical one, resulting in a strong vertical orbit displacement. In CLIC this orbit offset is typically of the order of $10\,\mu$m, for a solenoid field of 4 or 5 Tesla and 1.5 TeV beam energy. The displacement results in a large vertical dispersion at the interaction point (IP). Furthermore, the beams in CLIC are exceptionally flat, which means that any coupling to the vertical plane significantly deteriorates the luminosity. Particles with large angles at the IP have a large displacement from the beam orbit in the region close to the last focusing magnet, where the radial solenoid field is strongest. Hence, the experimental solenoid introduces strong $y{-}x^{'}$ coupling at the IP which must be corrected. Furthermore, due to the high beam energy in CLIC, there is a significant emission of synchrotron radiation as a result of the beam deflection in the solenoid region. The unrecoverable loss is an important concern for CLIC. Optical aberrations can be corrected in several ways; using the final focus magnets, adding skew quadrupoles or compensating solenoid, as done around the FINUDA detector at DAΦNE [58]) or proposed for ILC [57], using dipole orbit corrector integrated into the experiment [59], and finally considering longer L* [60]. In A.5 we presented a new simulation approach which evaluates the effect of the ISR alone without the knowledge of the full compensation. The main concern was the impact of synchrotron radiation emitted in detector solenoid on luminosity that cannot be recovered or compensated. This approach was verified with a semi analytical approach, as well as a more time-consuming study where the full compensation was searched. There are two problems with the full compensation study which were addressed with the new simulation approach. First of all, it is a computationally demanding procedure, requiring on the order of weeks of CPU time to get to the final result. Second, once the result is obtained, one does not know if the remaining luminosity loss is purely due to ISR, or if

there are residual optical aberrations. The procedure to evaluate the luminosity loss due to ISR is described in the lower part of FIG. 1.4, the routine of the symplectic integrator, specifically developed for this tracking study, is briefly described in the appendix of the publication A.5. The beam is first tracked forward without synchrotron radiation, and without the solenoid field present. This provides the optimal beam distribution at the interaction point. The ideal IP beam distribution is tracked backwards through the beam line, with the solenoid field turned on, but still without synchrotron radiation. The result is a beam distribution with a perfect compensation for the coupling introduced by the solenoid field. Finally, the synchrotron radiation is turned on, and the beam is tracked forward through the beam line. The estimated luminosity was compared to a normal tracking of the beam without the solenoid field, but including ISR. Using this approach we evaluated the simulated SiD field maps presented in Fig. 1.4. The loss of peak luminosity due to ISR in the detector solenoid including the antisolenoid was found to be $(4.1 \pm 0.2)\%$ for the SiD detectorsolenoid field map [61], where the error bar is from the calculation of the luminosity in GUINEA-PIG. This result compared well to the result from the semi analytical calculation and from full compensation simulations, as widely discussed in A.5.

The impact on luminosity and on beam-induced background of the relative misalignment between the final focus magnets, the anti-solenoid and the detector solenoid still remains to be evaluated. As well as the interplay of detector solenoid with crab cavity [4], and the impact of vibrations of solenoid and final focus quadrupoles on the beams and luminosity. As for the case of the beam-induced background, the impact of the detector solenoid and its anti-solenoid on the beams is foreseen for the lepton option of the future circular colliders. The tracking procedure developped for CLIC might not be the best solution in the case of circular accelerators, an alternative procedure will be described in section 3.3.

[4]Radio frequency cavity used to rotate the beams in the $x - z$ plane before they collide, in order to maximise the overlap region of two bunches colliding with crossing schemes.

Chapter 2

Tuning strategies and performance studies of detectors and accelerators

With Tuning strategies I mean the mitigation of machine or detector imperfections that can have different origins. In the case of accelerators they are implemented to mitigate the static and dynamics imperfections in linear and circular accelerators. In the case of detector, they can be used to refer to calibration or final settings of the different apparatuses constituting the detector. For example the scintillation barrels, constituting the TOF system of the FINUDA detector, needed temporal synchronisation due to cable lengths differences and cross talk between cables.

In general, dedicated corrections schemes are used for the different cases, which exploit appropriate physics signals to compensate locally or globally the imperfections. Laser signal is used to align time signals from different subdetectors, combination of dipole correctors are employed to recover the orbit in accelerators, or sextupole knobs can be defined to recover beam distortion due to magnets displacements in accelerators. Even if the tuning knobs and signals used as figure of merit can be different for the different problems (detector, linear accelerator or circular accelerators) some common optimization algorithms can be applied (for example Singular Value Decomposition [62] or Simplex [63]). Tuning strategies are important to improve or recover the performance of a detector or an

accelerator, while commissioning it or during the data taking. They are also used in the design phase of a project to define the performance of a detector or an accelerator and to provide tolerances on allowed imperfections for each subsystem. In the following, three examples are given: the synchronization of the TOF system of the FINUDA apparatus, the correction of linear imperfections in linear and circular hadron colliders and the tuning of the CLIC BDS against static imperfections of the magnetic elements.

2.1 Study of the TOF performance of the FINUDA apparatus

Experimental characterisation of scintillation detectors timing performance of the Internal (TOFINO) and External (TOFONE) scintillator barrels used in FINUDA experiment took advantage of detecting synchronous particle pairs produced in the two beams collision, namely e^+e^- pairs from Bhabha scattering and K^+K^- pairs from $\phi(1020)$ decay. Any experimental procedure aimed at timing synchronization of a complex device, composed of arrays of sub-detectors, is based on the detection of synchronous signals, to which a set of reference t_0 timing points is assigned and with respect to which time differences can be measured. In the case of FINUDA TOF detectors, the barrel temporal alignment process was split into two steps: a first rough alignment was performed during data taking by injecting simultaneously laser light pulses to every slab, while alignment refinements were the subject of a second step which took advantage of an offline analysis of the simultaneous hits of synchronous detected particles, namely e^+e^- pairs for the TOFONE detector and K^+K^- pairs for the TOFINO detector. Online laser alignment was carried out by recording the time of the detected laser light with respect to a common reference time, related to the same laser flash. An N_2 laser was employed with an enclosed Dye module, whose details are reported in A.6. The light emitted by the N_2 laser and Dye module combination is fed into a laser to optical fiber coupler connected to a 70 meter long quartz optical fiber. The length of this first optical fiber allowed the laser to be installed

far from the electronic timing equipment, thus avoiding any noise influence. On the other end, this first optical fiber is connected to a connector collimation package feeding a non-polarizing cube beam splitter from which two beams depart separately towards TOFONE (at 0° to the incident beam) and TOFINO (at 90°). Near the cube face opposite to the TOFINO beam a fast photo diode is located at a position allowing it to be triggered by the light diffused within the cube. The timing signal of this photo diode is used as a common reference time for the measurement of the online scintillator t_0's. The TOFINO and TOFONE laser beams are fed to a beam expander facing the individual fibers optics which go to the each scintillator slabs.

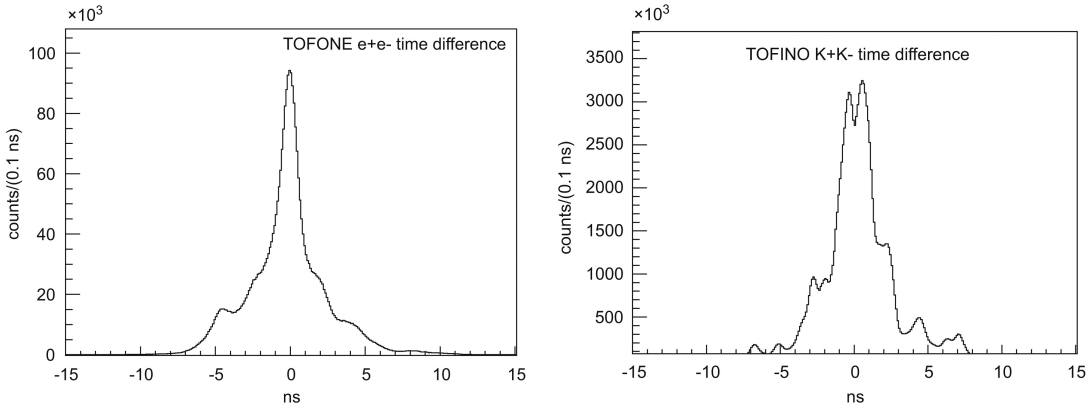

(a) (b)

Figure 2.1: Distribution of the measured time difference of TOFONE e^+e^- pairs (a) and of TOFINO K^+K^- pairs (b), after the online synchronization corrections.

The overall time dispersion of the scintillator barrels were evaluated after the first temporal alignment step, as described above. The results are shown in Fig. 2.1 (a) for TOFONE and in Fig. 2.1 (b) for TOFINO. A greater effort at slab synchronization was still needed, i.e. a better determination of the t_0 values.

During the experiment, the t_0 set in use was frequently measured by flashing the whole scintillation arrays and acquiring the detection time of the laser light by all Light Detection Device (LDDs: i.e. PMT or HPD, more details are in A.6) with respect to the common reference time provided by the photo diode response timing. This technique, carried out while collisions are suspended, is independent of beam status and takes only a few

minutes, and so is very useful for monitoring the stability of the whole TOF system during data taking. Although this stability was in general found to be fairly good, the analysis of sample hit time difference distributions from synchronous particle pairs continued to show differences with respect to the expected average zero value, a sign of still imperfect time alignment due to the presence of some kind of flaw in the alignment procedure. The first investigation showed that the problem was mainly due to crosstalk between neighboring twisted pairs of the flat cables carrying timing signals to the TDC boards, when all the slabs were flashed at the same time. For the second run of the experiment, all TOF signal cables were replaced with new, higher quality and individually shielded twisted pairs, to reduce crosstalk and improve signal integrity and time resolution. Yet the problem persisted, proof of its complex nature. No quick alternative was found for the online refinement of a t_0 laser set. For this reason laser pulsing was used only for the important and frequent stability tests and for a first rough alignment, while a finer synchronization of each scintillator array was carried out by offline hit time data analysis of synchronous particle pairs. The t_0 values could be further refined by using the average features of the hit time difference distributions of synchronous particles impinging in coincidence on correlated slab pairs, as well as the average features of the hit position distributions for particle populations detected symmetrically around $z = 0$. Using the t_0's determined with the laser, the hit time differences obtained from the detection of synchronous particles were used to obtain offsets of the average hit time difference with respect to the expected zero value, as shown in Figs. 9, 10 and 11 of A.6. These offsets were the main known terms for solving the problem of how to refine overall barrel synchronization. For e^+e^- Bhabha pairs detected in TOFONE, there was an experimental azimuthal angle correlation of $\Delta\phi = 130°$ between the two hit slabs, implying a 26 ± 1 slab distance, to be considered either clockwise or counterclockwise, since the first hit could occur in either of the correlated slabs. This angular correlation was obtained by tracking the right- and left-handed helix paths in the magnetic field of the back-to-back scattered e^+e^- Bhabha pairs (see Fig. 1 (a)). This lead to measurements of hit time differences and corresponding offsets of their

mean values with respect to zero. In a similar way, 36 hit time difference measurements for K^+K^- pairs detected in TOFINO could be obtained, each of which provided an offset of the average value from zero. The first 12 were obtained from pure back-to-back events, requiring K^+K^- pairs hitting slabs at $\Delta\phi = 180°$ azimuthal angle difference, the so-called Gap 6 slabs. The other 24 were obtained from extended back-to-back events, in which a K^+K^- pair was detected at $\Delta\phi = 150°$ azimuthal angle difference (in either sense of rotation), the so-called Gap 5 slabs. The Gap 5 slab correlation was obtained by tracking the right- and left-handed helix paths in the magnetic field of some of the back-to-back K^+K^- pairs. Further data useful for the same goal were obtained from hit position distributions of any particle populations detected symmetrically around $z = 0$. A scintillation hit position spectrum in long counters could be obtained from the time difference distribution of left minus right LDD timing, which must by definition be centred at zero for the above particle populations. Adopting the pulsed laser t_0's, a first analysis of hit position distributions was performed. A typical hit position distribution for two TOFONE slabs, obtained with a Bhabha particle hit population symmetrically detected around $z = 0$ (determined using straw tubes [12]) adopting pulsed laser t_0's, is shown in Fig. 2.3(Left). These hit position distributions also presented a total of 72 offsets of the average value from zero, which could be used for the refinement of t_0 values. As for TOFONE, 12 more hit position distribution offsets could be found for TOFINO, using kaons detected symmetrically around $z = 0$, as selected by ISIM [12]. Having collected all the above offset information, a system of equations could be written relating the corrections required to the laser t_0 values and the known offset values:

$$
\begin{aligned}
(t_{0_{Left}} - t_{0_{Right}})_1 &= \delta t_1 \\
(t_{0_{Left}} - t_{0_{Right}})_2 &= \delta t_2 \\
&\vdots \\
(t_{0_{Left}} - t_{0_{Right}})_n &= \delta t_n \\
(t_{0_{Right}} - t_{0_{Left}})_1 &= \delta t_1 \\
(t_{0_{Right}} - t_{0_{Left}})_2 &= \delta t_2 \\
&\vdots \\
(t_{0_{Right}} - t_{0_{Left}})_n &= \delta t_n \\
(t_{0_{Right}} + t_{0_{Left}})_1 - (t_{0_{Right}} + t_{0_{Left}})_{gap_1} &= 2\overline{\delta t_{1,gap_1}} \\
&\vdots \\
(t_{0_{Right}} + t_{0_{Left}})_n - (t_{0_{Right}} + t_{0_{Left}})_{n+gap_1} &= 2\overline{\delta t_{n,n+gap_1}} \\
(t_{0_{Right}} + t_{0_{Left}})_1 - (t_{0_{Right}} + t_{0_{Left}})_{gap_2} &= 2\overline{\delta t_{1,gap_2}} \\
&\vdots \\
(t_{0_{Right}} + t_{0_{Left}})_n - (t_{0_{Right}} + t_{0_{Left}})_{n+gap_2} &= 2\overline{\delta t_{n,n+gap_2}} \\
(t_{0_{Right}} + t_{0_{Left}})_1 - (t_{0_{Right}} + t_{0_{Left}})_{gap_3} &= 2\overline{\delta t_{1,gap_3}} \\
&\vdots \\
(t_{0_{Right}} + t_{0_{Left}})_n - (t_{0_{Right}} + t_{0_{Left}})_{n+gap_3} &= 2\overline{\delta t_{n,n+gap_3}}
\end{aligned}
\tag{2.1}
$$

Where the indexes gap_1, gap_2, gap_3 are the different distance in the TOFONE and TOFINO scintillator barrel described before. This system of equations is over determined, and so a best fit solution was searched for the corrections, based on ROOT classes [64], using a linear least squares search to minimize the $A \cdot x = y$, where A is the $m \times n (m > n)$ matrix with n parameters and m equations. The vector x (the corrections) was determined

with the SVD method.

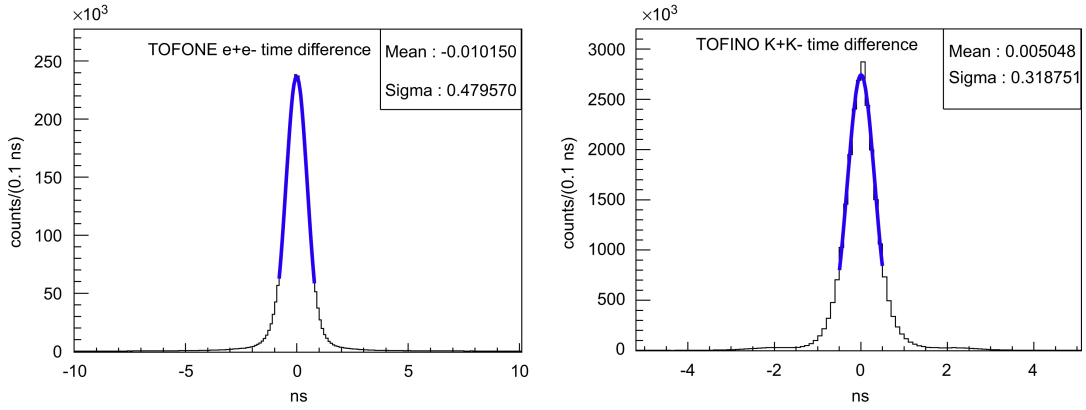

(a) (b)

Figure 2.2: Distribution of the measured time difference of TOFONE e^+e^- pairs (left) and of TOFINO K^+K^- pairs (right) after the offline synchronization corrections. The continuous line is the Gaussian fit with the mean and sigma values shown in the inset.

After finding such a solution, the analysis of the hit time differences for synchronous particle pairs and the one of hit position distributions for particle populations symmetrically detected around $z = 0$ was performed by adopting the offline corrected t_0 values. The results are shown in Fig. 2.2 (a) for all the e^+e^- Bhabha pairs detected in TOFONE, in Fig. 2.2 (b) for all the K^+K^- pairs detected in TOFINO and in Fig. 2.3 (b) for the time difference distributions in the TOFONE slabs.

The mean value of the distributions in Fig. 2.2 is practically always zero, as expected from synchronous particle pairs. The standard deviation σ of the overall TOFONE hit time difference for e^+e^- Bhabha pair distributions (Fig. 2.2 (a)), after offline synchronization, reached a value of ~ 0.48 ns as compared with the several ns obtained after only laser synchronization and with the ~ 0.40 ns of the individual TOFONE slab pairs. The standard deviation σ of the overall TOFINO hit time difference distributions for K^+K^- pairs, comprising all Gap 6 and Gap 5 slab coincidences, after offline synchronization, remained near the average σ value obtained before for single slab pairs (~ 0.31 ns), passing from the several ns time dispersion of Fig. 2.1 (b) to the $\sigma \approx 0.32$ ns of Fig. 2.2 (b), a very significant improvement. The insertion in the calibration data base of the so determined

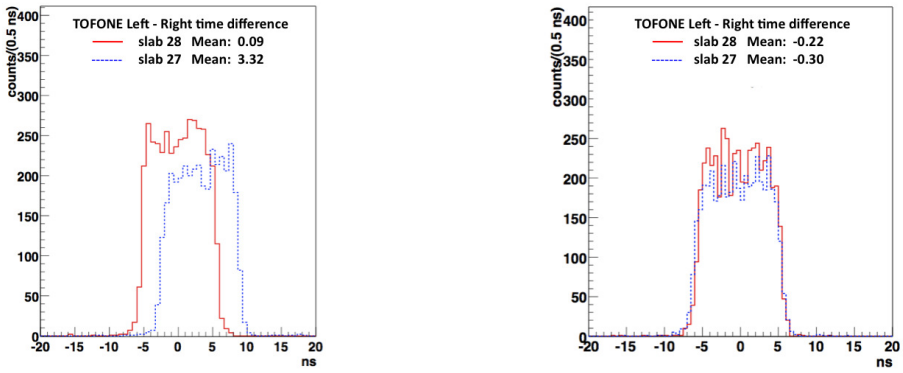

(a) (b)

Figure 2.3: The Left–Right detection time difference distributions for Bhabha particles in two TOFONE slabs, detected symmetrically around z = 0 and determined using straw tubes [12], before (a) and after (b) the offline t_0 corrections.

t_0 offset greatly improved the TOF measurements. These measurements have been a key feature for charged particle identification or for neutron energy reconstruction in many of the physics analysis of the FINUDA collaboration [65, 66, 67, 68, 69].

2.2 Linear imperfections in linear and circular colliders

Alignment errors of the magnets and field errors of the accelerators main components (dipole, quadrupole and their skew equivalents) can lead to errors in beam transport e.g. perturbations in the position, beam sizes or dispersive effects, as well as global parameters like the beam tunes, in circular accelerators. The main contributors to the beam orbit error are the quadrupole position errors in the transverse planes, x and y, and the b_1 dipole component error along the accelerator. The residual orbit z (x or y plane) at a position s is expected to change according to:

$$z_s = \sum_i \sqrt{\beta_s \beta_i} \theta_i sin(\phi_s - \phi_i) \tag{2.2}$$

for an open straight line, and according to:

$$z_s = \sum_i \sqrt{\beta_s \beta_i}\theta_i \frac{cos(\pi Q - |\phi_s - \phi_i|)}{2sin(\pi Q)} \tag{2.3}$$

for a circular accelerator. The index i is the position of the error, θ_i is the equivalent dipole kick generated by the error (integrated dipole field error, dipole roll or a_1 field error and quadrupole displacement), ϕ is the phase advance of the particles at the position of the error and at the generic position s around the accelerator. Q is the tune number in case of circular accelerators. It is worth noticing that, the residual closed orbit will diverge in the case of integer tune.

In uncoupled motion, the main contributions to the beam size error or beta-beating is the b_2 quadrupole component error, in case of circular machine:

$$\left(\frac{\Delta\beta}{\beta}\right)_s \approx \pm \sum_i \frac{\Delta k_i L_i \overline{\beta_i}}{2sin(2\pi Q)} cos(2\pi Q - |\phi_s - \phi_i|) \tag{2.4}$$

where $\Delta k_i L_i$ indicate the equivalent quadrupole integrated strength corresponding to the b_2 field error. $\overline{\beta_i}$ is the average betatron function at the location of the errors, and Q is the betatron tune. In the case of straight lines, one looks for emittance mis-match due to b_1, b_2 field components and quadrupole displacement:

$$\Delta\varepsilon = \frac{1}{2}\left[\pi\Delta_u^2\left(\frac{1+\alpha}{\beta}\right) + \pi\left(\frac{\Delta B}{B\rho}L\right)^2\beta + \Delta K^2\beta^2\varepsilon_0\right] \tag{2.5}$$

where, Δ_u^2 is the quadrupole displacement in the x and y plane, $\frac{\Delta BL}{B\rho}$ is the dipole error and ΔK^2 is the integrated quadrupole gradient error. Skew quadrupole component errors (a_2) and the quadrupole rotation around the longitudinal axis or roll angle can also contribute to β-beating and as a consequence to beam sizes change, that is why β-beating is corrected together with coupling in circular machines [70]. Since the sources of coupling can be many and different in circular machine, usually their effect is described and corrected using the $C^{\pm}$ coefficients or the f_{1001} and f_{1010} generating functions (according to the formalism

used). Their value along the machine include the sum of the contributing sources and characterise the amount of coupling to be corrected [70, 71]. Higher order multipoles impact β-beating through feed-down due to orbit or magnets displacement errors [72].

The main contributions to the dispersion error or dispersion-beating are the a_2 skew quadrupole component error, the quadrupole rotation error around the longitudinal axis (also called roll angle) and sextupole displacement for the vertical dispersion, and the b_2 quadrupole component error for the normalized dispersion:

$$\frac{\Delta D_u(z)}{\sqrt{\beta_u(z)}} = \sum_i \theta(i)\sqrt{\beta_u(i)}sin(\phi(z) - \phi(i)) \tag{2.6}$$

for open lines, and:

$$\frac{\Delta D_u(z)}{\sqrt{\beta_u(z)}} = \frac{1}{2sin(\pi Q_u)} \sum_i \theta(i)\sqrt{\beta_u(i)}cos(\pi Q_u - |\phi(z) - \phi(i)|) \tag{2.7}$$

for circular accelerators. Where the $\theta(i)$ stands for the equivalent kick generated by the different kind of errors (i.e.$\Delta y(i)k_qL(i)$ for quadrupole displacement, $\psi(i)D_u(i)k_qL(i)$ or $D_u(i)a_2(i)$ for quadrupole rotation ψ or the skew quadrupole error, respectively; $\Delta y(i)k_sL(i)$ for sextupole displacement). The index u indicates both x or y planes.

It is very important to be able to correct all these contributions by adding correction elements in the lattice. For this purpose, three different types of correctors are usually inserted in the lattice, together with diagnostic elements, like BPM (Beam Position Monitor), beam profile monitors or emittance measurements instruments:

- Dipole correctors or quadrupole movers to cancel the beam position around the optical axis; the simplest correction scheme is called "one-to-one", it aims at centering the trajectory at the next BPM. More complex schemes can take advantage of redundancy of diagnostic (like MICADO [73]);

- Skew quadrupole correctors or sextupoles movers to cancel the coupling contributions; that can be used to correct locally or globally coupling. They can be powered

individually or in combination of four or five, to define orthogonal knobs;

- Normal quadrupole correctors to correct β-beating and dispersion, and restore the beam tunes to their nominal values in case of circular accelerators;

The main constraint for the correctors when designing an accelerator is its maximum field (which is usually associated with the chosen technology) or the dynamic range of excursion amplitude in case of the elements movers. Therefore, the definition of the correction schemes imply also the definition of the initial errors (static or dynamic field errors and displacement of accelerator elements) that can be tolerated in the accelerators, called tolerances. The figure of merit used to determine the correction strategy and the tolerances on acceptable initial errors is different according to the accelerators, and also according to the type of particle or to its energy. They are mainly related to the stability of the particle motion inside the accelerator: orbit control, physical aperture limitations, particle losses and emittance growth. In this respect, I have tried different approaches to characterise the correction schemes and/or find tolerances:

- analytical methods for statistical analysis of the correction of orbit and coupling [74];
- one-to-one orbit correction, combined with analytical computation of coupling correctors in order to reduce C^- resonance in FCC-hh lattice [75]. Using transport codes it is possible to study statistically several configurations of the lattice according to given errors distributions;
- full tracking simulations with realistic errors in linacs or straight lines [76] [77] [78].

Usually, the correction is found by solving linear system of type $\mathbf{A}\overrightarrow{k} = \overrightarrow{o}$, where $\overrightarrow{k}$ are the correctors strength, $\overrightarrow{o}$ is the set of observable one wants to minimize and $\mathbf{A}$ is the correlation matrix. For example, in the case of the hadron option of the future circular collider, the linear errors correction was applied in a 3-step procedure:

1. Analytical correction of the a_2 contribution to the coupling with skew quadrupoles

Table 2.1: RMS tolerance values of the dipole (Dip), quadrupole (Quad) and beam position monitor (BPM) alignment, in the arcs and dispersion suppressor of the FCC-hh CDR optics. LHC design values taken from [72] are shown for comparison.

Element	Error	Description	Units	FCC	LHC	Comments
Dip	$\sigma(\psi)$	roll angle	mrad	0.50	n/a	LHC value includes $\sigma(\psi)$
	$\sigma(\Delta B/B)$	random b_1	%	0.10	0.08	
	$\sigma(\Delta B/B)$	random b_2	10^{-4} units	0.92	0.80	
	$\sigma(\Delta B/B)$	random a_2	10^{-4} units	1.1	1.6	
	$\sigma(\Delta B/B)$	uncert. a_2	10^{-4} units	1.1	0.50	
Quad	$\sigma(x), \sigma(y)$		mm	0.50	0.36	
	$\sigma(\psi)$	roll angle	mrad	1.0	0.50	
	$\sigma(\Delta B/B)$	random b_2	%	0.10	0.10	
BPM	$\sigma(x), \sigma(y)$		mm	0.30	0.24	relative to quad.
	$\sigma(read)$		mm	0.20	0.50	accuracy

2. Horizontal and vertical orbit correction, (employing SVD algorithm to find individual corrector strength)

3. Tunes correction with trim quadrupoles

A statistical study was performed by generating errors for 200 separate machines, with a different seed for each machine. Each machine was corrected with the aforementioned procedure. The errors were generated using the RMS tolerance values defined for the arc and dispersion suppressor elements according to Table 2.1 and for the insertion elements according to Table 2.2. The tolerances have been estimated for the high luminosity interaction regions and they were considered to be identical in all other insertions.

The following observables were studied at each element position and for each corrected machine:

- Horizontal and vertical residual orbit
- Horizontal and vertical residual angle
- Horizontal and vertical beta-beating $\Delta\beta = (\beta - \beta_{ref})/\beta_{ref}$
- Horizontal and vertical dispersion beating $\Delta D = (D - D_{ref})/\sqrt{\beta_{ref}}$

Table 2.2: RMS tolerance values of the dipole (Dip), quadrupole (Quad) and the beam position monitors (BPM) alignment, in the interaction regions of FCC-hh CDR optics. Values are for injection energy, and they also apply at collision (coll) energy unless specified. The values are used for all elements of the other insertion regions (if applicable).

Element	Error	Description	Units	Triplet	Other	Comments
Dip	$\sigma(\psi)$	roll angle	mrad		1.0	
	$\sigma(\Delta B/B)$	random b_1	%		0.05	
	$\sigma(\Delta B/B)$	random b_2	10^{-4} u.		0.10/1.8	coll (0.10/1.1)
	$\sigma(\Delta B/B)$	random a_2	10^{-4} u.		0.20/0.10	coll (0.10/0.20)
Quad	$\sigma(x), \sigma(y)$		mm	0.20	0.50	Q7 in IR has 0.20
	$\sigma(\psi)$	roll angle	mrad	0.20	0.50	TBD for IR
	$\sigma(\Delta B/B)$	random b_2	%	TBD	0.05	
BPM	$\sigma(x), \sigma(y)$		mm	0.30	0.30	relative to quad.
	$\sigma(read)$		mm	0.05	0.05	accuracy

- Dipole and quadrupole corrector strengths

The study was performed for two settings of the collider, at 3.3 TeV injection energy with a $\beta^\star$ of 4.6 m ("baseline injection"), and at 50 TeV collision energy with a $\beta^\star$ of 0.3 m ("nominal") and crossing scheme. For each observable the mean value, standard deviation and maximum value were computed over the 200 machines. The maximum value distribution was used to obtain the 90-percentile value, the value for which 90% of the data points of a given distribution were included. In other words, the 90-percentile value gave a number for which 90% of the machines did not have an element of the beam line for which this number was exceeded. The 90-percentile values obtained are summarised in Table 2.3.

The results indicate that the residual orbit stays below 1 mm in both planes and for almost all machines. The residual angle did not exceed 35 μrad at injection. At collision the residual angles were very similar. The beta-beating was relatively high at injection, with a 90-percentile value close to 25% in both planes, and well above the target of 10% assumed for beam stay clear calculations (i.e. the mechanical aperture of the machine imposed by beam halo collimation). For collision settings it became significantly higher, up to 34% in horizontal plane and 42% in vertical plane. There was no dedicated

Table 2.3: 90-percentile results obtained for the injection and collision cases for the FCC-hh CDR optics.

Observable	Injection	Collision
Horizontal orbit	0.80 mm	0.79 mm
Vertical orbit	0.73 mm	0.73 mm
Horizontal angle	26 μrad	26 μrad
Vertical angle	25 μrad	27 μrad
Horizontal beta-beating	22 %	34 %
Vertical beta-beating	24 %	42 %
Horizontal dispersion beating	$2.3 \times 10^{-2} \frac{1}{\sqrt{m}}$	$3.6 \times 10^{-2} \frac{1}{\sqrt{m}}$
Vertical dispersion beating	$2.8 \times 10^{-2} \frac{1}{\sqrt{m}}$	$2.7 \times 10^{-2} \frac{1}{\sqrt{m}}$
Hori. orbit correctors strength		4.7 Tm
Vert. orbit correctors strength		4.2 Tm
Skew quadrupoles strength		148 T/m
Trim quadrupoles strength		140 T/m

correction of the beta-beating and residual coupling in these simulations, and the tune correction using the trims did not cancel coupling very efficiently. For comparison in the LHC coupling knobs are used to globally correct residual coupling in the accelerator. The results for the dispersion beating seemed satisfactory at injection, with 90-percentile values below the LHC design values. The horizontal dispersion beating for the collision settings was slightly higher than the value used for the LHC design [72], but, as for β-beating no dedicated correction of dispersion was considered.

In order to improve the efficiency of the correction I would try to:

- put together dispersion, β-beating and coupling corrections in local and global way (like is done operationally in LHC), in order to find optimum correction schemes for the future colliders;

- use of machine learning techniques to define tuning strategy of future accelerators. One could use them for both: look for non-linear matching procedures in the correction strategy or substitute long tracking simulations with artificial intelligence based models.

In order to explore the limits of the old and new correction techniques, their applica-

tion to other kind of machine can be explored. For example, to foreseen high energy lepton machines or to exploring machine based on non-linear optics (like IOTA [79] at FERMILAB), which can run at integer tune but, following Eq. 2.3, standard SVD techniques should hardly converge in finding a solution for the correction.

2.3 CLIC Beam Delivery System tuning

The Beam Delivery of the compact linear collider is a highly non-linear system, which is non trivial to fine tune against static and dynamic imperfections. Conventional beam-based alignment techniques (as described in the previous section) partially succeeded to tune the static imperfections in the CLIC BDS. In particular, they have been proven successful in the collimation section alone while they recover only few percent of luminosity when applied to the CLIC Final Focus System (FFS). This is due to its strong non-linear beam dynamics [80] and very low β function at the IP (β^*) [81].

In A.4 we presented the results of different techniques applied to the CLIC BDS in order to mitigate static imperfections. Detailed studies for dynamic imperfections can be found in [82]. The luminosity loss could be fully recovered by scanning precomputed orthogonal tuning knobs, even if the target of 90% of machine configuration with full luminosity was not reached. The source of the luminosity loss is therefore due to FFS detuning. A fast on-line tuning procedure is required in order to reduce the luminosity loss during operation as well as for the tune-up of the machine. The most successful tuning techniques exploits the luminosity as figure of merit. Therefore, it is mandatory to have a method to estimate luminosity that can be used for machine optimization, which motivates the study reported in section 1.2.

The results of the tuning of the BDS against magnets displacements are summarized in Fig. 2.4 and the most significant numerical values reported in table 2.4. A random Gaussian displacement of each magnet with a σ of 10 μm in the two transverse planes is considered. The number of machines reaching the target luminosity is quite differ-

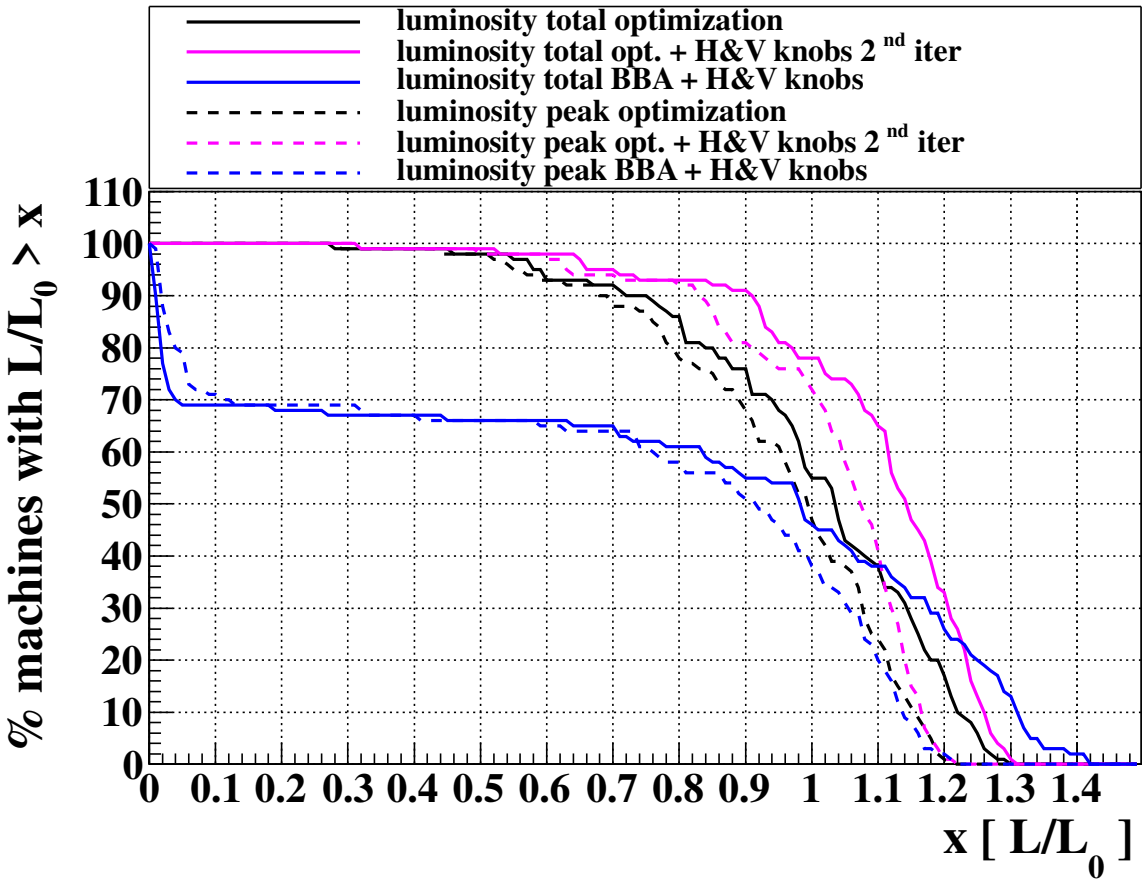

Figure 2.4: Luminosity distribution of 100 machines after three different alignment procedures starting from an initial random pre-alignment of 10 μm.

ent depending on the applied techniques. In order to accommodate for the static and dynamic imperfections the CLIC BDS lattice (with L*=3.5 m) was designed to reach a peak and total luminosity higher than the nominal values, by $\sim$ 20% and $\sim$ 30%, respectively. The target luminosity after the correction for the static imperfections is 110%, the remaining 10%, to reach the design peak luminosity of 120%, is the budget for the dynamic imperfections. Three different procedures have been studied. The Beam Based Alignment (BBA) technique consists of the one-to-one correction followed by Dispersion Free Steering [1] (DFS) [83] in the vertical plane and target DFS in the horizontal one. The assumed BPM resolution in these simulations was 10 nm. These tuning knobs consist of linear combinations of the 5 FFS sextupole displacements built to control the main linear

[1]DFS is a technique that measures the dispersion along the line, using off-energy test beams, and corrects it to zero or to the nominal value. The energy difference of 0.1% is used to measure dispersion.

Technique	# machines [110% of total $\mathcal{L}$]	# machines [110% of peak $\mathcal{L}$]
BBA + Knobs	38	20
luminosity optimization	36	24
luminosity optimization + Knobs	65	40

Table 2.4: Number of machines reaching the target luminosity for the static imperfections in the three combinations of techniques here studied.

aberrations of the beam at the Interaction Point (IP). The possibility to use tuning knobs based on linear combinations of sextupoles displacements had been already explored in CLIC [84]. Knobs that controls the offsets and angles at the IP, the waist shift and the dispersions functions were partially successful. New tuning knobs were built in A.4 using FFS sextupoles displacements, in order to control mainly couplings, dispersions and waist-shift in the two transverse planes [85]. These tuning knobs, applied after BBA, managed to shrink the transverse beam sizes close to the nominal values, recovering up to 50% of luminosity loss in half of the different seeds used in the simulation. Iterations of BBA and tuning knobs improved the correction. The final total and peak luminosity obtained after fifth iterations of this technique for 100 random misaligned machines are shown in Fig. 2.4 (blue line). About 30% of machines reached 110% of CLIC nominal luminosity. Of these about 15% exceed the design value of 130% for the total luminosity, while this was not the case for the peak luminosity. This effect was explained by the smaller horizontal beam size, reached after the BBA+FFS knobs scan, with respect to the nominal value, which causes on one hand the enhancement of total luminosity and on the other hand the emission of more beamstrahlung photons with the consequent increase of average energy loss that smears the luminosity spectrum in the energy peak.

The best tuning performance was obtained by combining luminosity optimization based on the Simplex algorithm and FFS knobs. In the luminosity optimization procedure, all the elements of the FFS were moved in order to maximize luminosity, using the Nedler-Mead algorithm (Simplex). In this case more than 60% of the machines reached 110%

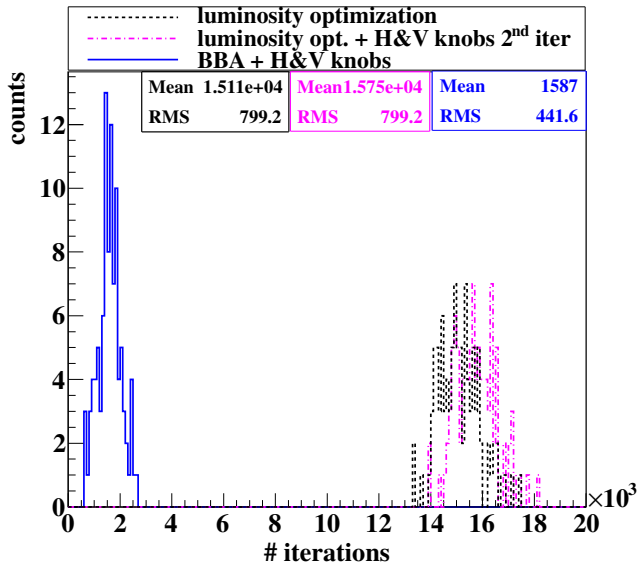

Figure 2.5: Number of luminosity measurements required in the three different alignment procedures in order to reach the results shown in 2.4.

of CLIC total nominal luminosity. It is worth noticing that when the luminosity optimization was combined with tuning knobs about 90% of the machines reach 90% of CLIC nominal total luminosity (Fig. 2.4). Figure 2.5 shows the distribution of the number of iterations required by the techniques presented in Fig. 2.4. The iterations correspond to the number of luminosity measurements required. The number of luminosity measurements needed by the luminosity optimization procedure was one order of magnitude larger than the one required by the BBA+Knobs technique. It is therefore crucial for CLIC to be able to measure luminosity as fast as possible (in the order of seconds) and to be able to tune the system in the most efficient way. This is the main reason motivating the search for a fast luminosity monitoring signal discussed in the first chapter. The use of more sophisticated optimization algorithms and of non linear knobs could improve the overall luminosity results and reduce the number of luminosity measurements required. The final aim is the reduction of the accelerator commissioning and its fine tune time.

Very recently, an improved tuning procedure of two beams and using the incoherent pairs reaching the BeamCal as luminosity monitoring signal, have been proven successfully in fully recover luminosity of more than 90% machine configuration (for the 380 GeV

option) with order of 4000 luminosity evaluations [56]. The improved tuning procedure includes same BBA described before, new sextupole knobs acting on the beam second moments at the interaction point and optimization of sextupoles positions (random walk optimization). To reduce computational time in this random walk optimization procedure a surrogate model of the final focus has been generated using Artificial Neural Networks [86].

Chapter 3

Optics optimization and non linear beam dynamics

The first and necessary step in the conceptual design of an accelerator or in its upgrade is the definition of the optics functions and the study of the single particle dynamics that are able to meet the purpose of the machine (target luminosity for colliders, beam brightness for light sources, etc..). While in most cases consolidated schemes are used for the optics definition (FODO cells, doublet or triplet for final focus, etc...), in each application specific optimizations are required to improve performances (i.e. geological constraints, particles stability, beta* reach, beam cleaning, reducing power consumption's, etc...). In the context of future hadron accelerators at CERN, I have performed optics optimization of the high luminosity interaction region for the luminosity upgrade of LHC (HL-LHC) and studied single particle stability for HL-LHC (section 3.3) and for the hadron option of the Future Circular Collider; see sections 3.1 and 3.2, respectively. In all cases, I have used standard techniques and codes (developed at CERN), but I have also complemented them with my personal code development.

3.1 High luminosity interaction region optics optimization

As already explained in the introduction, the goal of the LHC upgrade project is the production of a total integrated luminosity of approximately 3000 fb^{-1} over the lifetime of the HL-LHC. To achieve this, a considerable reduction of the beta function values at the high luminosity Interaction Points (IP) is needed, aiming for values as low as β^* =15 cm.

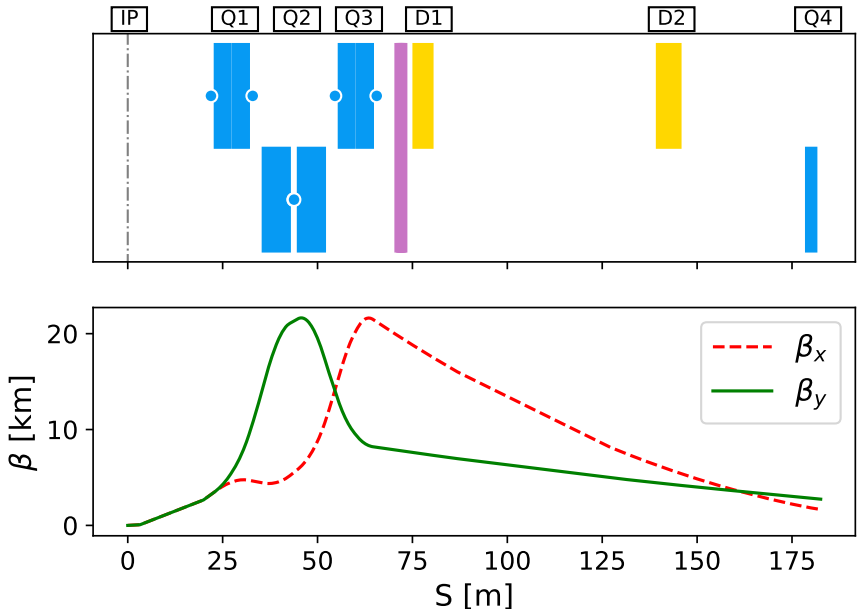

Figure 3.1: Layout (top) and β-function (bottom) of one optics of the high luminosity interaction region for the luminosity upgrade of LHC. Crab cavities are installed between the separation dipole D2 and the first double aperture quadrupole Q4.

The fundamental concept is based on a Achromatic Telescopic Squeezing (ATS) scheme [87], which has been proposed in this context and that allows both the production and the chromatic correction of very low β^* values. This scheme relies essentially on a two-stages. First, a pre-squeeze optics is established by using exclusively the matching quadrupoles of the high luminosity insertions ATLAS and CMS. In a second stage, the β^* value can be further reduced using only the insertions on either side of ATLAS and CMS creating

sizeable β-beating bumps in the four neighbouring sectors. These waves of β-beating create the required β^* reduction and at the same time boost, at constant strength, the efficiency of the chromaticity sextupoles located in the neighbours arc sectors. Therefore, a large optics investigation has been launched to study the flexibility of the overall upgrade optics, taking into account especially the β function value at the first double aperture quadrupole (Q4) in IP1/5 (see Fig. 3.1), where crab cavities are installed. In particular, I have studied three possible directions:

- the possibility to match different maximum triplet gradient;
- the possibility to optimize optics to lower the crab cavity voltage;
- an alternative optics not based on the ATS scheme.

3.1.1 High triplet gradient optics

Based on the quadrupoles triplet that employ different technology (NbTi / Nb_3Sn), gradients between 120 T/m and 170 T/m could be assumed and, accordingly, a variety of different beam optics has been studied. However, not all the boundary conditions (namely the betas in front of Q4) assure the possibility to match the new triplet in the LHC high luminosity interaction regions to the existing arc structure. In order to find acceptable initial boundary conditions, I have developed a tool to scan the optics values in the horizontal and vertical plane at the location of Q4 in a wide range, thus verifying the possibility to match the generated triplet into the arc structure of the two LHC beams. Figure 3.2 shows the area in the β_x and β_y space where an optimal convergence of the matching of the new triplet with the two rings was obtained. It was mainly determined by the constraint imposed by the magnets in the LHC matching sections of the two LHC rings, i.e. Q4 ... Q7 quadrupoles in the interaction region layout − with one of the most critical limits being the maximum allowed strength of the Q7 quadrupole. The solutions plotted in Fig. 3.2 defined the pre-squeeze optics in the sense that − for a given optics parameter at the location of the crab cavities − and for a β-function at the IP of 40 cm, the layout of

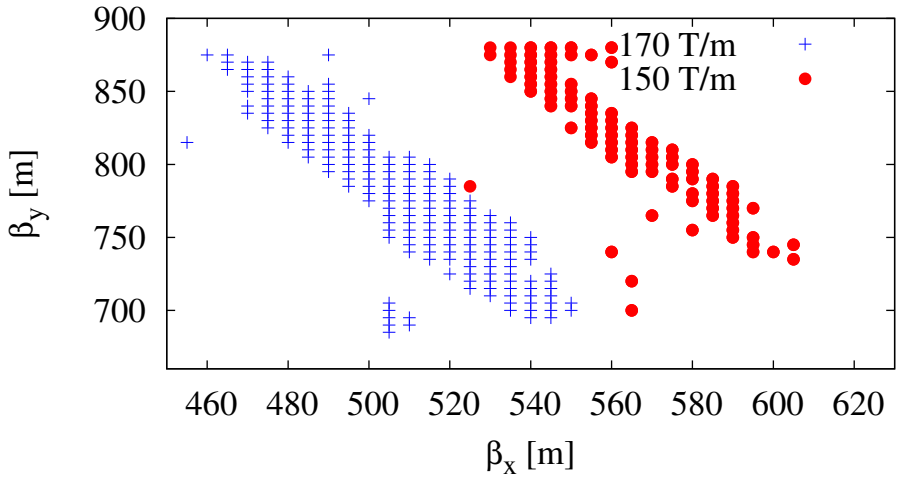

Figure 3.2: Horizontal and vertical β-function in front of Q4, which leads to the convergence of the matching. The plot compares the situation of two different triplet gradients.

the triplet quadrupoles, following a well-defined strategy [88], was determined. However, not all the boundary conditions (namely the beta function values in front of Q4) allowed the possibility to match the new triplet in the LHC high luminosity interaction regions. The successful beam optics shown in Fig. 3.2 are equivalent in terms of maximum beta functions reached in the triplet quadrupoles and natural chromaticity of the lattice. The resulting parameters of the triplet quadrupoles differ only slightly from the pre-defined values in magnet length and maximum feasible gradient of G=170 T/m.

In a more detailed approach, assuming a gradient in the triplet quadruples of G=170 T/m, the convergence of the optics matching has been studied for different β^* values. Again, the optics at the position of Q4 was included as additional boundary condition. Figure 3.3 summarises the results, while a comfortable variety of different beam optics was obtained for the standard value of β^* =40 cm in the pre-squeeze optics, the flexibility of the lattice shrunk if smaller β^* values were aimed for. In the extreme case of β^* =35 cm only in a limited number of possible optics was obtained. More severely, a successful application of the ATS scheme was possible only for pre-squeeze optics that allowed β^*-values larger than β^* =37 cm. For the most promising case with β_x =510 m and β_y =770 m at the location of Q4 (see Fig. 3.2), the properties of the lattice have been studied in more detail,

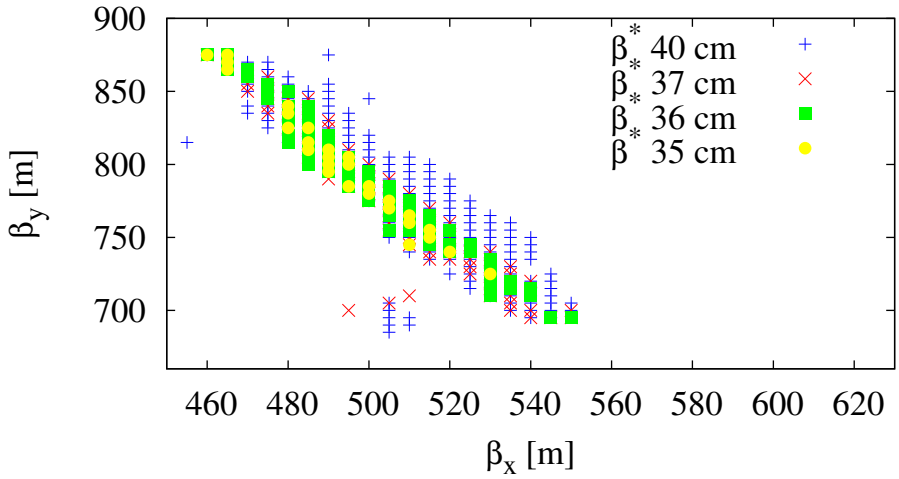

Figure 3.3: Horizontal and vertical β-functions in front of Q4, which lead to the convergence of the matching of the new triplet (170 T/m) with the LHC lattice in the luminosity interaction regions.

including:

- the possibility to combine the optics with the ATS scheme to reduce the β^*-functions from the pre-squeeze values of β^* =40 cm down to the final values of β^* =15 cm;
- the chromatic aberrations;
- the impact of the ATS scheme on the neighbouring LHC sectors.

The chromatic aberration in the case of β^* =15 cm is shown in Fig. 3.4(a), and compared to the baseline lattice. Given the nominal LHC momentum spread of $\Delta p/p$ of 1×10^{-4}, the curve of Fig. 3.4(a) reflects the comfortable momentum acceptance that was obtained. The third order chromaticity is higher with respect to the baseline optics.

The compensation of geometric aberrations of this squeezed optics assured a stability up to 55 σ, where the $3\nu_x$ resonance was crossed, as shown in Fig. 3.4(b).

3.1.2 Matching section layout vs crab cavity voltage

I proposed a promising direction for optimizing the layout of the matching section in the two high luminosity insertions. The main goal of the optimization was the reduction

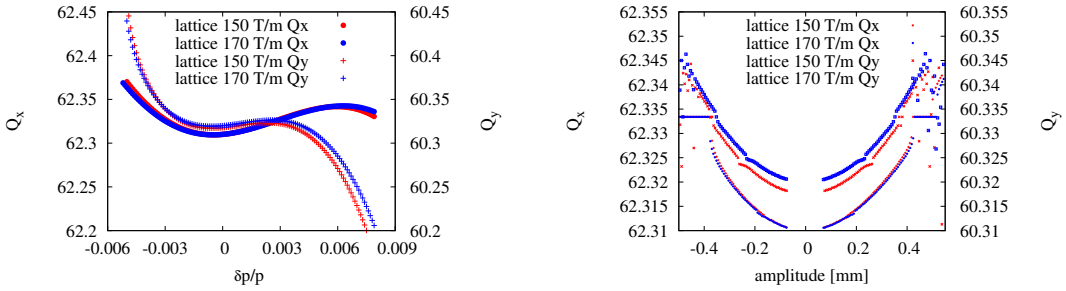

(a) (b)

Figure 3.4: Detuning with momentum (a) and amplitude (b) for different squeezed optics.

of the required crab cavity voltage, in order to leave some margin with respect to the baseline [89]. Three crab cavities providing a total equivalent kick of about 12.5 MV were indeed needed for each of the two beams in the region between D2 and Q4 on either side of the two high luminosity IRs [89]. It can be shown that the crab cavity voltage required to rotate the proton beam by half the crossing angle is given by the following equation:

$$V_{crab} = \frac{cE\theta_c/2}{\omega_{crab}\sqrt{\beta^* \beta_{crab}}} \tag{3.1}$$

where θ_c is the full crossing angle, β_{crab} is the β-function value at the crab cavity location. Therefore, the only method to reduce the required crab cavity voltage was to increase the β function at the crab location, while keeping the same β^* value, the beam energy (E), the position and the frequency (ω_{crab}) of the crab cavity. The β-function can be modified by changing the position and the strength of the magnets in the matching sections. As further constraints to my optimization I have considered:

- compatibility with the ATS optics scheme;
- possibility to design a low β^* optics in non ATS mode, i.e. using the strengths of the IR magnets;
- possibility to realize an injection optics with low β^*.

The optimization of the matching section was performed using the pre-squeeze optics

(first stage of the ATS optics), since the ATS scheme reduced the number of possible configurations of the matching section, due to the stringent conditions imposed on the betatron phase advance between the left and right side and the interaction point, as shown in the previous section.

In the high luminosity matching section optics the Q7 strength was very close to its maximum, while very low gradients were imposed on Q5 and Q6. In order to cure the weakness of Q5 and Q6, we have chosen to put them in triplet configuration with Q4, without moving Q4. To overcome the Q7 limit, a new quadrupole of the same type and polarity as Q7 was added, just in front of the main cryostat of the LHC arc, as sketched in Fig. 3.5. Finally, using the same method described in the previous section, I have iterated the optimization of the new matching section layout several times, increasing the initial β_x, β_y conditions at the crab location at each iteration.

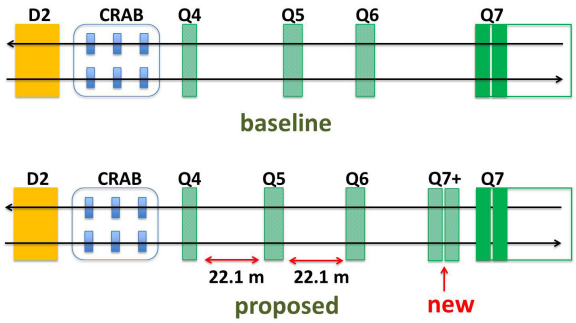

Figure 3.5: First proposed matching section layout (bottom).

This layout would have allowed to design collision optics for HL-LHC whether using the ATS scheme or not [90]. The required crab cavity voltage was reduced by 20-30% with respect to the baseline layout. Moreover, it had the advantage to balance the required voltage between the left and the right side of the IP. The same matching section layout gave more flexibility in collision towards lower β^* even without the ATS scheme, and allowed to realize an optics with β^* of 3 meter at injection, even if some work was still needed to optimize it for apertures.

3.1.3 Alternative matching section layout

Starting from the previous layout and keeping the same constraints imposed before, I have optimized the layout at injection, in order to solve the problem of the apertures in Q6 at injection. This new matching section layout is shown in Fig. 3.6. Q5 was displaced

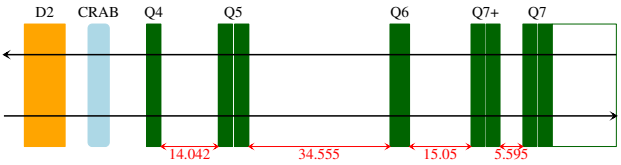

Figure 3.6: Final alternative matching section layout.

towards Q4 with respect to the layout presented in the previous section and the single MQYL type was replaced by 2 MQYY. Q6 was displaced towards Q7+, which is the additional quadrupole introduced with the previous layout. This configuration reduced the β function in Q6 at injection, which was the limit of the previous triplet configuration of Q4, Q5 and Q6.

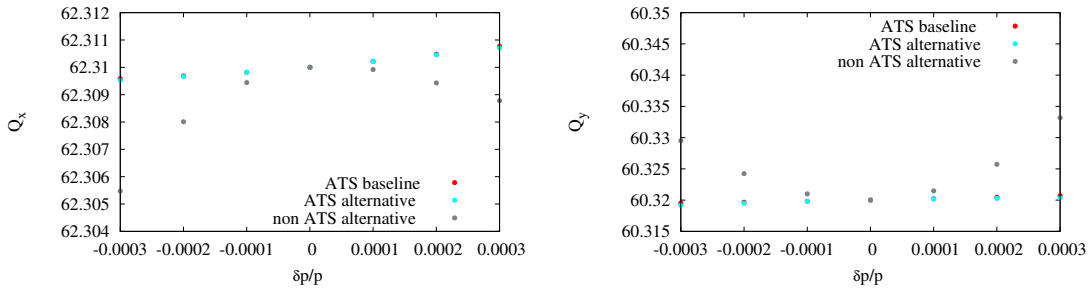

(a) (b)

Figure 3.7: Horizontal (a) and Vertical (b) detuning with momentum for the baseline ATS optics and the alternative matching section layout, the non ATS option of the alternative is also shown.

In the non ATS optics I have corrected the linear chromaticity only, using the LHC sextupoles all together and taking care that their strengths do not exceed the maximum allowed value. Residual second order chromaticity is clearly visible with respect to the ATS optics, see Fig. 3.7. The drawback of this configuration is the additional cost required

by the new hardware [91]. The gain in crab cavity voltage with the best optics option I found was not so high. Moreover, the higher β-function at the crab cavity location could generate higher impedance. Therefore, the project management took soon the decision of adding an additional crab cavity, which guarantees enough margin in the operational voltage. Nevertheless my study provided a tool to search for optics solution in presence of large numbers of constraints, which is the case when matching two different section of complex accelerators. My search of optimum initial conditions for the alternative optics heavily relies on efficient massive use of computer clusters. An interesting option could be to apply non-linear matching methods based on genetic algorithms or machine learning techniques, in order to speed up convergence of matching without the need to scan several initial conditions in parallel. Though they were not selected in the end, my alternatives for the matching sections have pointed out the main optics weakness of the LHC insertion region towards the minimum β^* reach. Some of the solutions proposed have been retained in the conceptual design optics of the hadron option of the future circular collider [36].

3.2 Magnets field quality and single particle dynamics

Once the linear optics of an accelerator are defined, its stability with respect to imperfections must be addressed. In the previous chapter, optimization and correction strategy have been discussed for linear imperfections of circular colliders and linear and non-linear tuning strategies for linear colliders. In this section, we discuss optimization and correction against non-linear imperfections in circular colliders. While the sources of non-linear imperfections can be many, since I deal with single particle dynamics I concentrate exclusively on the magnetic field errors of accelerators magnets. Every magnetic field can be described in terms of the magnetic field expansion [72]:

$$B_y + iB_x = B_{ref} \sum_{n=1}^{\infty} (b_n + ia_n) \left(\frac{x + iy}{R_{ref}} \right)^{n-1} \tag{3.2}$$

where B_{ref} represents the magnetic field at the reference radius R_{ref}, for the principal harmonics. The subscript $n = 1$ refers to dipole, $n = 2$ to a quadrupole and so on. In all dipole or quadrupole magnets a certain number of higher order harmonics ($n > 2$) are present, they are what we mean for non-linear imperfections in circular accelerators. The behaviour of the particles in presence of magnet imperfections cannot be corrected by dedicated feedback. Therefore, it is important to know these field imperfections in advance and to correct them if they reduce, below the safety limit, the region of stable motion of particles in accelerators, which is taken to be equal to the Dynamic Aperture (DA) [1].

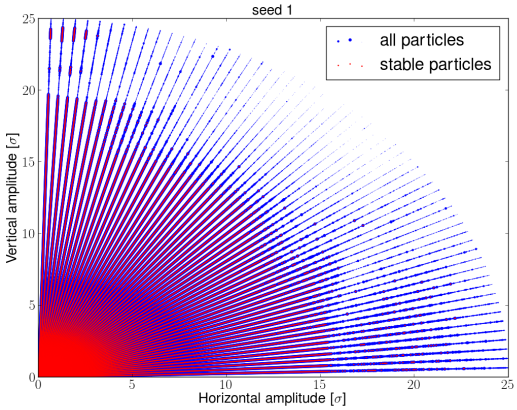

Figure 3.8: Initial amplitude for particles stable after 10^5 revolutions (red) and for all particles (blue) in the injection optics of FCC-hh.

In the case of superconducting magnets, each multipole harmonics entering in the field expansion (a_n and b_n of Eq. 3.2) is modeled as the sum of three contributions:

$$b_n = b_{n_S} + \frac{\xi_U}{1.5} b_{n_U} + \xi_R b_{n_R} \tag{3.3}$$

where ξ_U and ξ_R denote pseudo-random numbers with Gaussian distribution truncated

[1] DA is defined as the area of the stable phase-space region spanned by a particle in an accelerator and it is evaluated using particle tracking simulations [92] or measured by different techniques [93]. The boundary between the stable and chaotic motion is defined tracking particles with different initial conditions (distributed on a polar grid in the $x - y$ phase space) and looking at the initial amplitude that remains stable after 10^n revolutions (see for example Fig. 3.8) or at the evolution of the distance of nearby trajectories (lyapounov exponent).

at 1.5 and 3 σ, respectively. b_{n_S} accounts for systematic field error which are peculiar to the design geometry, thus a common value is assigned to each dipole. b_{n_U} represents field errors coming from the magnet fabrication and assembly, they are called uncertainty. Finally, b_{n_R} is the random field error component which depends on the specific magnet. The computation of the DA is usually very demanding in CPU time, and done on a statistical basis, 60 or 100 different configurations of the machines are simulated to search the initial stable amplitude for each angle scanned in the $x - y$ phase space, as shown in Fig. 3.9. This may require from 1 day to one week or more, depending on the test case and the system of computers used.

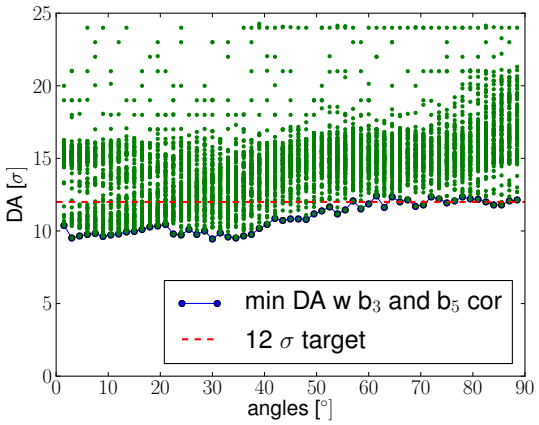

Figure 3.9: DA values at injection computed for 100 seeds and 59 angles in the case of FCC-hh lattice. It includes main dipoles, triplet and separation dipole field errors and the octupole for Landau Damping powered to 15/720 A. The systematic b_3 and b_5 components of the main dipole are locally corrected, as in the LHC machine. Green dots are DA values for each seed and angle. Blue dots represent the minimum DA values for each angle.

I have studied the impact of dipole field quality on the hadron option of future circular colliders, in order to define the sextupole and decapole correction schemes and specifications for the arc sectors, in collaboration with magnets designers [94, 95, 96, 97].

Commonly, DA is computed for an initial momentum offset of the particles equivalent to 2/3 of the RF bucket size [2], which is considered a safe choice. For the FCC-hh, the

[2]The RF bucket is the region of phase stability in the energy-phase phase space [98].

maximum RF bucket is about 4.8×10^{-4}, as given in [18]:

$$\left(\frac{\Delta p}{p}\right)_{max} = \sqrt{\frac{2V_{RF}}{\pi h|\eta_c|cp_0}} \tag{3.4}$$

where V_{RF} is the total RF voltage and $\eta_c = \frac{1}{\gamma_r^2 el} - \alpha_c$ [3] and h is the ring harmonic number [4], c is the speed of light and p_0 is the reference particle momentum. For FCC-hh

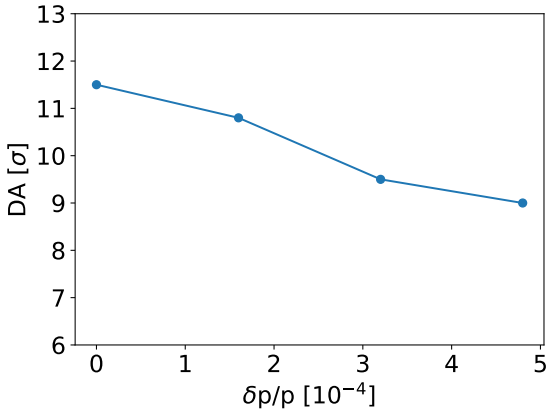

Figure 3.10: Minimum DA over 10^5 turns, 5 directions $\phi = arctan(\epsilon_y/\epsilon_x)$ of the $x-y$ phase space and 60 seeds, as a function of initial momentum offset of the particles, for the injection optics of FCC-hh. The maximum RF bucket size is at $4.8 \times 10^{-4}\Delta p/p$. The Landau damping octupoles current is set to -15/720 A.

at injection, the minimum DA decreases by about 2.5σ moving from zero initial energy offset to the maximum allowed, as shown in Fig. 3.10. The DA results shown in Fig. 3.9 can be improved to be very close to the target value of 12 σ, by providing high quality injected beam with very small energy spread.

Starting from the ensemble of initial amplitude of particles lost in the $x-y$ phase space, shown in Fig. 3.8, DA can be defined following [93]:

$$DA(N) = \frac{2}{\pi}\int_0^{\pi/2} r_s(\theta; N)d\theta \tag{3.5}$$

[3]The momentum compaction factor α_c is the ratio between the relative change in the path length $\Delta L/L$ to the relative difference in momentum $\Delta p/p$

[4]It is an integer number expressed as the ratio between the RF frequency and the particle revolution frequency

where N is the number of revolution of the particle in the accelerator (called turns), r_s is the last stable amplitude (disregarding stability islands non-connected to the origin) and θ is the angle in the $x - y$ phase space. Thus, a value of DA can be calculated for each turn, which is shown in Fig. 3.11 for one configuration of the machine.

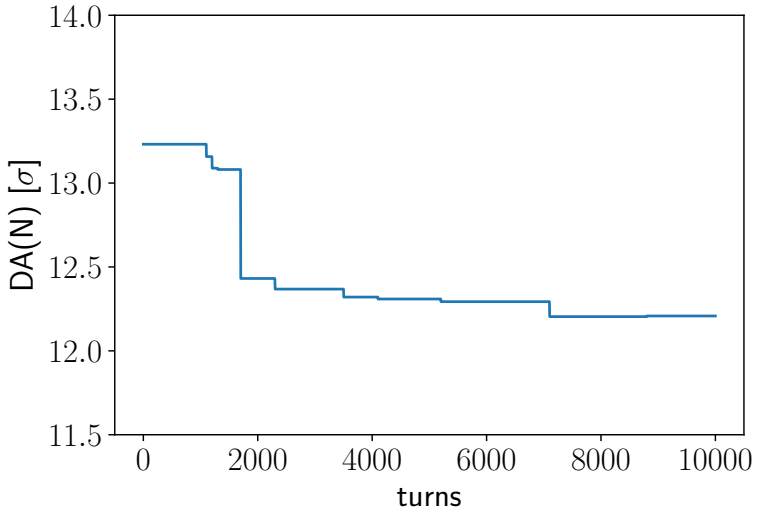

Figure 3.11: Dynamic Aperture as a function of number of revolution in the accelerators (turns), for the injection optics of FCC-hh without Landau Damping Octupoles.

Due to the very demanding time and computer CPU required by these simulations, it would be interesting to see if machine learning and in particular deep learning can be used to emulate long term tracking simulation in order to reduce computational time and be able to perform more cases when defining tolerances on high order multipoles for example, or to be able to extrapolate dynamic aperture to 10^5, and to even more number of revolution of particle in the accelerator, performing the tracking only up to 10^3 or 10^4 turns. Such predictive model could also be used to fit/extrapolate the time evolution of beam intensity measurements for the experimental determination of the DA. For example, the possibility to use Echo State Networks [99] to predict DA at 10^4 or 10^5 turns, knowing its values as a function of turns up to 10^3-10^4 turns, is explored in [100].

Non-linear magnets imperfections impact the detuning with amplitude and momentum as well, therefore the definition of their tolerances may come from limitations given by the allowed tunes changes. In FCC-hh, the estimated arc dipole field quality changes

the tunes in the order of 10^{-3}, which is considered safe. As a comparison beam-beam and octupole for Landau Damping are sources of tune shift and spread of the order 10^{-2}, thus tolerances on dipole field quality are defined using mainly DA simulations. Complementary or alternatively, frequency map analysis is also widely used as figure of merit to define safety limits for magnets imperfections, or to optimize the working point of the accelerator in its design phase [101].

3.3 Impact of quadrupole 3D magnetic field on beam based observables

In the multipole expansion of Eq. 3.2 the B_{ref} value and the b_n, a_n relative harmonics components are usually integrated values, kept constant along the magnet length. This is an approximation, since in real life the field harmonics have a longitudinal distribution which can vary especially at the extremities, as shown in Fig. 3.12.

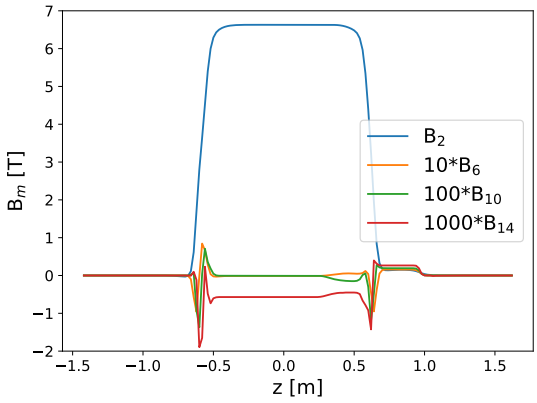

Figure 3.12: Normal longitudinal harmonics sampled at $\Delta z = 2$mm for the prototype of HL-LHC Inner Triplet quadrupole. Courtesy of E. Todesco and S. Izquierdo Bermudez.

I have studied the possibility to quantify the impact of the longitudinal distribution of the harmonics (i.e. of the 3D magnetic field) on beam based observables, like detuning with amplitude and DA (see A.9), focusing on the interaction region quadrupole. In

fact, both detuning with amplitude and DA are very sensible to field errors in the high luminosity insertions, where β-functions can be very high. This study required the effort of defining a new non-linear transfer map [5] to include the 3D magnetic field. The consequent work of analytic and numerical derivation of the field representation and maps has been the subject of 3 internships and 2 PhD thesis.

The study was initially motivated in the context of HL-LHC project, where large betatron functions are foreseen in the final focus magnets, which implies that the beams are more sensible to magnets higher order harmonics. Furthermore, the variation of the betatronic (β) function in a single quadrupole is not so small. Therefore, the computation of beam based quantities like Amplitude Detuning and Dynamic Aperture, can be significantly affected by the approximations of the β-function and of the magnetic field errors.

The starting point of our approach was the choice of a representation of the vector potential entering in the definition of the Hamiltonian, used in the equation of motion of the particle in the quadrupole system. Generalized Gradients based methods are able to include magnetic data, measured or computed, in the non-linear transfer maps [102, 103]. In order to evaluate the non linear fringe field (i.e. of the 3D magnetic field) effect on the long term single particle dynamics, a transfer map of the quadrupoles is required, including the fringe region (i.e. the extremity of the magnet). We computed a symplectic transfer map using Lie Algebra transformations, solving the equation of motion with a $z-$dependent equivalent Hamiltonian. The particle motion in a quadrupole magnetic field, using the longitudinal coordinate as independent variable, can be described with the following dimensionless Hamiltonian $K_{6\mathrm{D}}(x, p_x, y, p_y, s, \delta; z)$:

$$K_{6\mathrm{D}}(x, p_x, y, p_y, s, \delta; z) = -\sqrt{(1+\delta)^2 - (p_x - a_x)^2 - (p_y - a_y)^2} - a_z \tag{3.6}$$

[5] A transfer map is a set of transformations that compute the final positions and momenta of the particle after an element or a sequence of elements, given the initial ones. With non-linear transfer maps we intend a set of transformations that include the higher order harmonics ($n > 2$) of the magnetic element.

where x, p_x, y, p_y are the canonical variables in the transverse plane; a_x, a_y, a_z are the normalised vector potential components of the quadrupole system ($a(x,y,z) = \frac{qA(x,y,z)}{p_0 c}$); s is the curvilinear coordinate; δ is the momentum deviation with respect to the reference momentum $\delta = (p_z - p_0)/p_0$. Being $p_0 \gg p_x + p_y$ for all relativistic particles, the Taylor expansion with respect to $(1+\delta)^2$ can be made. z is the longitudinal coordinate in the quadrupole system used as independent variable instead of time. Moreover, in order to keep the explicit dependence on z in the Hamiltonian, a transformation for the independent variables can be considered such that the 6D equivalent Hamiltonian of Eq. 3.6 becomes the 8 dimensions equivalent Hamiltonian $K_{8\mathrm{D}}(x, p_x, y, p_y, s, \delta, z, p_z; \sigma)$, also given in Ref. [104]:

$$K_{8\mathrm{D}}(x, p_x, y, p_y, s, \delta, z, p_z; \sigma) = p_z - \delta - a_z + \frac{(p_x - a_x)^2}{(1+\delta)^2} + \frac{(p_y - a_y)^2}{(1+\delta)^2} \tag{3.7}$$

where σ is the new independent variable of the system.

The motion of the particles in a magnetic field, using Lie Algebra, is expressed as:

$$\mathcal{M}(\Delta\sigma) = \exp(-L : K_{8\mathrm{D}} :) \tag{3.8}$$

where L is the length of the system described by the equivalent $K_{8\mathrm{D}}$. $: K_{8\mathrm{D}} : f =< K_{8\mathrm{D}}, f >$ is the Lie operator defined by the Poisson brackets [105]. Eq. 3.8 is called the transfer map of the system, it represents the motion of the particle in the system defined by the Hamiltonian $K_{8\mathrm{D}}$. Since the expression of the equivalent Hamiltonian contains the terms $(p_y - a_y)^2$, which is not exactly solvable (integrable), we split the equivalent Hamiltonian in four parts ($K_A = p_z - \delta$, $K_B = -a_z$, $K_C = \frac{(p_x - a_x)^2}{2(1+\delta)}$ and $K_D = \frac{(p_y - a_y)^2}{2(1+\delta)}$) and simplify the not integrable terms using a change of coordinates, as in [104]. Finally, we

obtain the non-linear transfer map at second order, as follow:

$$\begin{aligned}\mathcal{M}(\Delta\sigma) = &\exp(-\tfrac{\Delta\sigma}{2} : K_A :) \exp(-\tfrac{\Delta\sigma}{2} : K_B :) \exp(-\tfrac{\Delta\sigma}{2} : K_C :) \\ &\exp(-\Delta\sigma : K_D :) \exp(-\tfrac{\Delta\sigma}{2} : K_C :) \exp(-\tfrac{\Delta\sigma}{2} : K_B :) \\ &\exp(-\tfrac{\Delta\sigma}{2} : K_A :) + O(\Delta\sigma^3) \\ &= \mathcal{M}_2 + O(\Delta\sigma^3)\end{aligned} \tag{3.9}$$

where $K_{8\mathrm{D}} = K_A + K_B + K_C + K_D$ is the decomposition of the equivalent Hamiltonian. Table 3.1 shows the resulting transformations for the four different terms of the 8 dimensions equivalent Hamiltonian in Eq. 3.7 (see also Ref. [104]).

Table 3.1: Non linear transformations of the four canonical pairs for the four terms of the quadrupole equivalent Hamiltonian.

	$\exp(: K_i :)$	x	p_x	y	p_y	δ	s	z	p_z
K_A	$-\frac{\Delta\sigma}{2}(p_z - \delta)$						$-\frac{\Delta\sigma}{2}$	$+\frac{\Delta\sigma}{2}$	
K_B	$\frac{\Delta\sigma}{2} a_z$		$+\frac{\partial a_z}{\partial x}\frac{\Delta\sigma}{2}$		$+\frac{\partial a_z}{\partial y}\frac{\Delta\sigma}{2}$				$+\frac{\partial a_x}{\partial z}\frac{\Delta\sigma}{2}$
K_C	$-\int a_x dx$		$-a_x$		$-\int \frac{\partial a_x}{\partial y} dx$				$-\int \frac{\partial a_x}{\partial z} dx$
	$-\frac{\Delta\sigma}{2}\frac{p_x^2}{2(1+\delta)}$	$+\frac{p_x \Delta\sigma}{2(1+\delta)}$					$-\frac{p_x^2 \Delta\sigma}{4(1+\delta)^2}$		
	$\int a_x dx$		$+a_x$		$\int \frac{\partial a_x}{\partial y} dx$				$+\int \frac{\partial a_x}{\partial z} dx$
K_D	$-\int a_y dy$		$-\int \frac{\partial a_y}{\partial x} dx$		$-a_y$				$-\int \frac{\partial a_y}{\partial z} dy$
	$-\Delta\sigma\frac{p_y^2}{2(1+\delta)}$			$+\frac{p_y \Delta\sigma}{1+\delta}$			$-\frac{p_y^2 \Delta\sigma}{2(1+\delta)^2}$		
	$\int a_y dy$		$+\int \frac{\partial a_y}{\partial x} dx$		$+a_y$				$+\int \frac{\partial a_y}{\partial z} dy$

In order to include the details of the quadrupole magnetic field, in an accurate and efficient way, we looked for a suitable representation of $\overrightarrow{a}$ in the terms of the map. As already said, Generalized Gradients (functions which depends only on the longitudinal coordinates) allow to express the normalized vector potential $\overrightarrow{a}$ in the form:

$$a_{i,j} = \sum_{i,j} GG_{i,j}(z) x^i y^j \tag{3.10}$$

where the coefficients $GG_{i,j}(z)$ (called Generalized Gradients) depend on the quadrupole longitudinal coordinate z. While the vector potential is expressed as monomials in the x

and y coordinates. The number of terms in the sum depends on the accuracy with which the magnetic field is represented. A more detailed expression of the these coefficients and of their computation starting from 3D realistic magnetic field maps or longitudinal harmonics (shown in Fig. 3.12) is reported in A.8. The degradation in the magnetic field reconstruction accuracy, using Generalized Gradients representation outside the radius of harmonics analysis, is shown in Fig. 3.13. Alternative approximations based on high order finite elements approaches have been investigated in [106], in order to achieve a more reliable description of the particle trajectories in the very large aperture cases. Results are encouraging, but the application of these alternative approaches in accelerator codes implies tracking in cylindrical coordinates.

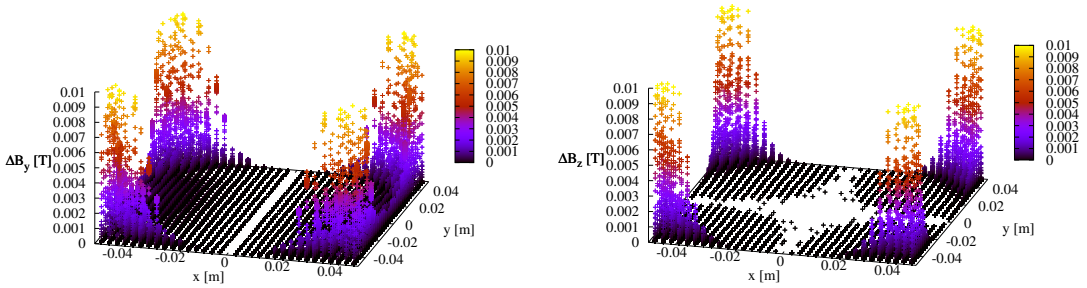

(a) (b)

Figure 3.13: Difference between B_x (a) and B_z (b) magnetic field of ROXIE calculations and the values reconstructed back after the generalised gradients calculation.

Always in A.8, the second order Lie integrator of Eq. 3.9 was compared with higher order both symplectic and not symplectic integrators, showing that for longitudinal step of 2 cm the second order Lie integrator is as accurate and fast as the higher order ones. Therefore, this non-linear transfer map has been implemented in a fortran90 code and interfaced with SixTrack [107]. Details of the map and its integration in the SixTrack code are described in A.9 and in [108].

Basically, the longitudinal distribution of the field is historically not considered or kept constant in the Hard Edge model, even when several subdivisions for the magnet

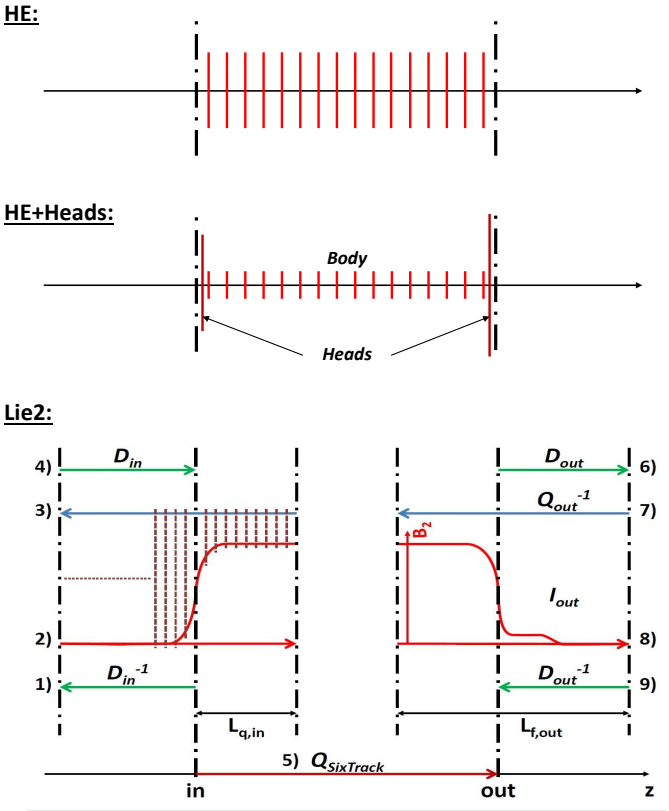

Figure 3.14: Quadrupole longitudinal models. Thin lenses Hard Edge approximation (top panel), Hard Edge plus two equivalent kicks to represent the Heads (central panel) and the novel Lie2 non-linear transfer map (bottom panel). D, D^{-1} are the equivalent drift and anti−drift of the space modelled with the Lie2 integrator I. Q, Q^{-1} are the equivalent quadrupole and anti-quadrupole to cancel the quadrupole component of the space modelled with the Lie2 map.

(called thin lenses) are considered (see Fig. 3.14 top panel). In the Hard Edge approximation the vector potential depends on the two transverse variables (x, y) and the two transverse components are considered to vanish ($A_x = A_y = 0$). The only terms entering in the Hamiltonian are the normal multipole harmonics of the A_z component: $A_z^m = \frac{1}{m} B_m Re[(x + iy)]^m$, similarly for the skew multipole harmonics. In A.9, the classical hard edge approximation is compared to a simple model to account for the longitudinal distribution (shown in the central panel of Fig. 3.14, and called HE+Heads), adding two equivalent kicks at the two extremities of the magnet. The new derived map (called Lie2 and shown in the bottom part of Fig. 3.14) not only improves the longitudinal dependence of the A_z component of the vector potential (considering steps of 2 cm in the longitudinal

direction of the magnet extremities) with respect to the HE+Heads, but describes also the effect of the two transverse components of the vector potential (A_x, A_y). If the symplectic integrator is accurately written in the same coordinates as the HE or the HE+Heads models, the tracking in the central part of the quadrupole can be preserved as it is, and only the fringe field region is treated in the Lie Algebra tracking.

$$D_{in}^{-1} I_{in} Q_{in}^{-1} D_{in} Q_{HE} D_{out} Q_{out}^{-1} I_{out} D_{out}^{-1} \tag{3.11}$$

Equation 3.11 shows the scheme of integration of the Lie Tracking with an existing HE model of the quadrupole, as illustrated into Fig. 3.14 and integrated into SixTrack. In order to avoid over strength counting, an equivalent anti-quadrupole needs to be subtracted after the Lie2 Integrator I_{in}, and the inverse for I_{out}. This has allowed to quantify the impact of a more realistic 3D magnetic field on beam based observables, like amplitude detuning and dynamic aperture. They are used during the commissioning of the machine to control the stability the machine and during the design phase of a project to define tolerances on field errors and specifications on the correctors. The results in the case of the HL-LHC inner triplet quadrupoles are described in detail in A.9. The accurate knowledge of the main field and field errors distribution of the final focus magnets is important to be able to reproduce the long term stability of the machine and the amplitude detuning in numerical simulations. In particular, being able to reproduce accurately the longitudinal profile of each of the harmonics of the final focus magnets is more important than including higher order derivatives (in the case of HL-LHC). The impact on the dynamic aperture of the dodecapole correction can be negligible or amount to about 2σ (number of beam sizes) at 10^4 turns, depending on the model considered. Two σ is well inside the present accuracy (20%) for DA measurements in LHC [93]. Concerning the non-linear correctors strength evaluation, the comparison of the values obtained with the models in Fig. 3.14 shows a dependence on the way one distribute the magnetic length between the central part and the two Heads [109]. First attempts have started to quantify these

effects experimentally by looking at amplitude detuning measurements in the LHC. Results indicate a discrepancy in the correctors strengths between the model which uses the integrated b_4 magnetic field measurements and the beam based values [110]. Moreover, no evidence of b_6 is found from amplitude detuning measurements, even if beneficial effects on beam stability and equipment noise reduction is observed when b_6 correctors are set in the optics [111]. We are presently re−analysing the finite element model of the final focus magnet of LHC, in order to verify if such 3D magnetic field could explain the differences observed in the machine [112, 108].

These experimental evidences trigger two more specific studies:

- which precision on the high order harmonics magnetic measurements can be aimed for ? and with which details in their longitudinal distribution ? R&D studies are on going at CERN on the possibility to precisely measure 3D magnetic field with longitudinally moving rotating coils [113];

- are there other beam-based observable which are more sensitive to 3D magnetic field effects and that can be used to measure and correct non-linear magnetic field imperfections during machine operation? Is the variation of the measured β-beating with the particle amplitude [108, 114] a good candidate to detect more local imperfections ?

Extension of these studies can be done including other type of accelerator elements. For example in HL-LHC, superconducting dipoles are foreseen to replace the present separation dipoles of LHC, being close to the high β region of the high luminosity insertions their field quality also impact beam stability. Using the same generalised gradient representation of the vector potential, the non-linear transfer map for the dipole could also be derived and applied to the interaction region case of HL-LHC. Going further into the future, the same study could be applied to the main arc elements of the hadron option of the future colliders. This could perhaps set further specifications on the longitudinal distribution of the magnets field quality at their design stage. Generalized Gradients rep-

resentation of the vector potential and the Lie2 Integrator could also be used to study the impact of the Detector Solenoid and Anti-Solenoid on the beams, in the FCC-ee interaction region. The simplectic tracking in the Solenoid magnetic field map, presented in the last section of chapter 1, is not suitable for being interfaced with the existing tracking codes adapted to the rings.

Finally, it is natural to question if all these effects and observables are more easily measurable in non-linear optics, like those proposed the IOTA project [79].

Perspectives

Several of today open questions in fundamental physics, like the properties of the Higgs Boson, the existence of supersymmetric particles, the neutrino mass and families and the nature of dark matter can highly profit of the present large hadron collider and future dedicated colliders. The upgrade in High Luminosity of LHC will allow to perform precision measurements of the Higgs and Top properties. To complement and complete HL-LHC measurements, linear and circular electron-positrons colliders are under studies.

The technologies required by both linear and circular e^+e^- colliders are mature now days. Intense past and present R&D, on both Normal Conducting (NC) [17] and Super Conducting (SC) cavities [115], has shown target performance reach for these key components. Performances of the integrated systems can be studied at dedicated test facilities (such as ATF at KEK for linear colliders), in small scale running accelerators (like superKEKB for FCC-ee) and with small size prototypes of a part of the accelerator (like is being done for CLIC and for FCC-ee).

Circular hadron and muon colliders are investigated to explore a new energy domain. Their capability to reach the target performances strongly depends on the available technology in the next decades.

The fundamental step towards future hadron colliders is the possibility to overcome the maximum field of about 8 Tesla of the Nb-Ti magnet technology (for both dipoles and quadrupoles). As already said in the introduction, HL-LHC will be the first project employing Nb_3Sn cables based magnets (for few quadrupoles and dipoles), which can reach 11-12 Tesla peak field. Nevertheless, the high critical current density of 1500 A/mm^2

required to reach the 16 T dipole field can only be possible thanks to the use of Artificial Pinning Centers (APC). Introducing ZrO3 particles (the APCs) into the Nb3Sn strands, the Nb3Sn grain size is effectively reduced, allowing to reach the target critical current density. The APCs decrease magnetization heat during field ramps, improve the magnet field quality at injection, and reduce the probability of flux jumps [116]. Several design and prototypes are planned to be produced and tested as proof of principle of this magnet technology in the next decade.

The dipoles and quadrupoles of the Chinese future hadron collider are foreseen to be made with cables based on an iron-based superconductor, a material discovered at the Tokyo Institute of Technology in the year 2006 [117]. The Chinese R&D goal for the next 10 years is to increase the performance of magnet made of this material by ten times, while simultaneously reducing its cost by an order of magnitude.

In parallel, High Temperature Superconductor insertions and devices are under investigation, which have also application for muon colliders [118] and for drive wind turbine generators [119].

In order to reduce the size and cost of future colliders other less mature technologies are also explored. Since the 1950s plane electron oscillations in plasma are studied [120] and soon it has been understood that they could be used as more compact and efficient acceleration technique, if electron are placed in this plasma-wake longitudinal electric field [121]. Three plasma driver technologies have been explored theoretically and experimentally: short laser pulse [122], short electron bunches [123] and self-modulated high energy proton bunches with an rms bunch length of about 10 cm [124]. The three acceleration techniques have shown impressive progress in the last decades [125, 126, 127]. Multi-TeV e^+e^- colliders design, based on these technologies, already exists, as proposed in Refs. [128, 129]. Nevertheless, there are a number of issues that need to be resolved before these colliders can compete with the more mature designs based on NC and RF technologies: mainly concerning the possibility to reach target beam quality and control, and the positron acceleration (which are de-focused in the plasma wakefield during

acceleration) [130, 131].

Micron-size dielectric accelerating structures can be driven by a laser, and they can support accelerating fields an order of magnitude higher than RF cavities [132]. Despite relatively modest accelerating gradients as compared with plasma, the prospects of using commercial lasers as a power source, and low-cost fabrication lithographic techniques for the production of optical structures have generated interest in dielectric laser acceleration-based electron-positron colliders [133]. The way to achieve high luminosity is to operate at very high repetition rate (order of 20 MHz). This require extensive research and development on laser power generation and distribution to be comparable with CLIC or ILC acceleration systems.

Wake fields in dielectric-lined tube can be induced by short, intense relativistic electron bunches. These fields can be used to accelerate a second electron bunch which followed the driving bunch. The beam accelerating gradient achieved, so far, is some 70 MV/m in 11.7 GHz structures [134]. Application of this concept to colliding beams faces many challenges, such as fabrication of efficient dielectric high gradient RF structures (dielectric-lined tube), drive beam production with bunch charge an order of magnitude greater than typically achieved in common RF guns, and wakefield damping to assure main beam stability and attainment of overall electric power to beam efficiency conversion comparable to that of CLIC [131, 135].

An advanced Normal-Conducting Radio-Frequency (NCRF) C-band linear accelerator (linac) structure to achieve a high gradient has been explored. The accelerating structure features internal manifolds for distributing RF power separately to each cell, permitting the full structure geometry to be designed for high shunt impedance and low breakdown. To optimize for operational constraints, it is advantageous for the structure to be cooled directly by liquid nitrogen (LN). The first operation of a distributed coupling structure at cryogenic temperatures has operated at the nominal gradient of 120 MeV/m [136].

Another emerging technology that stimulated interested for future colliders applications is linac based on the Energy Recovery principle (ERLs) [137]. A green version of

this scheme has been proposed as option for the FCC-ee collider [138] and for $\gamma\gamma$ Higgs factory [139, 140].

Besides technological advances (together with their energy consumption aspects), a key ingredient to reach collider physics performance is our capability to improve beam quality trough a better understanding of beam physics and the application of more advanced techniques to tune, to integrate detectors and accelerator, to optimise and to control these two complex systems. New artificial intelligence techniques, may bring to more efficient correction schemes in terms of performance and cost. At the same time, a more detailed description of the magnetic fields and improved simulation procedures in the accelerator models can help understanding the measurements performed in present accelerators and improving the design of future ones. Following the order in which the topics have been presented in the present *habilitation*, the impact of the relative displacement of the final focus magnets and the Detector Solenoid and anti-solenoid on both the luminosity tuning procedure and on the background rates, in the case of future lepton colliders should be evaluated. In the case of circular colliders, the efficiency of the correction of the linear imperfections could be improved by both trying advanced corrections schemes as done in operation in LHC or by using machine learning techniques to find a better convergence for the correction, which could be valid also for non-linear lattice working at integer tune. In the case of hadron circular colliders surrogate model to substitute long tracking simulations could be searched for, in order to predict dynamic aperture or scan multipole errors to define tolerances on magnets field quality. The 3D non-linear transfer map could be extended to other elements of the accelerators to quantify their impact on different beam based observables.

In order to prove the principle and assure the performance of the next generation accelerators, advanced beam dynamics simulations are essential. They must take into accounts results from experimental R&D campaigns, aiming to improve the knowledge of present and future technologies.

Bibliography

[1] J. J. T. M. F.R.S., "Xl. cathode rays," *The London, Edinburgh, and Dublin Philosophical Magazine and Journal of Science*, vol. 44, no. 269, pp. 293–316, 1897. [Online]. Available: https://doi.org/10.1080/14786449708621070

[2] F. E. Rutherford, "The scattering of α and β particles by matter and the structure of the atom," *Philosophical Magazine Series 6*, vol. 21, pp. 669–688, 1911. [Online]. Available: http://www.math.ubc.ca/~cass/rutherford/rutherford.html

[3] J. D. Cockcroft and E. T. S. Walton, "Experiments with high velocity positive ions.—(i) further developments in the method of obtaining high velocity positive ions." *Proceedings of the Royal Society A*, vol. 136, pp. 619–630, 1932. [Online]. Available: https://royalsocietypublishing.org/doi/pdf/10.1098/rspa.1932.0107

[4] ——, "Experiments with high velocity positive ions. ii.— the disintegration of elements by high velocity protons." *Proceedings of the Royal Society A*, vol. 137, pp. 229–242, 1932. [Online]. Available: https://royalsocietypublishing.org/doi/pdf/10.1098/rspa.1932.0133

[5] "Physics nobel prize web site," http://www.nobelprize.org/prizes/physics/, 2020, accessed: February 27, 2020.

[6] L. Bonolis and G. Pancheri, "Bruno Touschek: Particle physicist and father of the e^+e^- collider," *Eur. Phys. J. H*, vol. 36, pp. 1–61, 2011.

[7] C. Bernardini, "Ada: The first electron-positron collider," *Physics in Perspective*, vol. 6, pp. 156–183, 2004. [Online]. Available: https://link.springer.com/content/pdf/10.1007/s00016-003-0202-y.pdf

[8] B. Dalena, "Search for neutron-rich lambda-hypernuclei with the finuda spectrometer," 2006, phD Thesis. [Online]. Available: https://inspirehep.net/files/66a29e1ddc28845f7da74c0d54198c87

[9] M. Agnello *et al.*, "Production of H-6(Lambda) and H-7(Lambda) with the (K-(stop), pi+) reaction," *Phys. Lett. B*, vol. 640, pp. 145–149, 2006. [Online]. Available: http://www.sciencedirect.com/science/article/pii/S0370269306009178

[10] ——, "Evidence for a kaon-bound state K- p p produced in K- absorption reactions at rest," *Phys. Rev. Lett.*, vol. 94, p. 212303, 2005.

[11] P. A. Z. et al. (Particle Data Group), *The Review of Particle Physics (2020)*. Oxford Academic, 2020. [Online]. Available: http://pdg.lbl.gov

[12] M. Agnello *et al.*, "First results on (Lambda)C-12 production at DAFNE," *Phys. Lett. B*, vol. 622, pp. 35–44, 2005. [Online]. Available: https://doi.org/10.1016/j.physletb.2005.07.002

[13] ——, "Mass discrimination using double-sided silicon microstrip detectors for pions and protons at intermediate energies," *Nuclear Instruments and Methods in Physics Research Section A*, vol. 427, no. 3, pp. 423 – 436, 1999. [Online]. Available: http://www.sciencedirect.com/science/article/pii/S0168900298013321

[14] ——, "Final results of an experimental study of a large-area planar drift chamber filled with a he-based mixture," *Nuclear Instruments and Methods in Physics Research Section A*, vol. 385, no. 1, pp. 58 – 68, 1997. [Online]. Available: http://www.sciencedirect.com/science/article/pii/S0168900297827799

[15] L. Benussi *et al.*, "A 18m2 cylindrical tracking detector made of 2.6m long, stereo mylar straw tubes with 100μm resolution," *Nuclear Instruments and Methods in Physics Research Section A*, vol. 419, no. 2, pp. 648 – 653, 1998. [Online]. Available: http://www.sciencedirect.com/science/article/pii/S0168900298008456

[16] C. Adolphsen *et al.*, "The International Linear Collider Technical Design Report," vol. 3.I and 3.II: Accelerator Baseline Design, 2013. [Online]. Available: https://lss.fnal.gov/archive/test-tm/2000/fermilab-tm-2554.pdf

[17] M. J. Boland *et al.*, "Updated baseline for a staged Compact Linear Collider," 8 2016. [Online]. Available: https://cds.cern.ch/record/2210892/files/Fulltext.pdf

[18] H. Wiedemann, *Particle Accelerator Physics*. Springer, 2007, no. 3^{rd} edition.

[19] C. Collette, K. Artoos, A. Kuzmin, S. Janssens, M. Sylte, M. Guinchard, and C. Hauviller, "Active quadrupole stabilization for future linear particle colliders," *Nuclear Instruments and Methods in Physics Research Section A*, vol. 621, no. 1, pp. 71 – 78, 2010. [Online]. Available: http://www.sciencedirect.com/science/article/pii/S0168900210011174

[20] P. Eliasson and D. Schulte, "Design of main linac emittance tuning bumps for the compact linear collider and the international linear collider," *Phys. Rev. ST Accel. Beams*, vol. 11, p. 011002, Jan 2008. [Online]. Available: https://link.aps.org/doi/10.1103/PhysRevSTAB.11.011002

[21] G. Balik, B. Caron, D. Schulte, J. Snuverink, and J. Pfingstner, "Integrated simulation of ground motion mitigation, techniques for the future compact linear collider (clic)," *Nuclear Instruments and Methods in Physics Research Section A*, vol. 700, pp. 163 – 170, 2013. [Online]. Available: http://www.sciencedirect.com/science/article/pii/S0168900212011631

[22] "Placet," https://gitlab.cern.ch/clic-software/placet.

[23] "Guinea-pig," https://gitlab.cern.ch/clic-software/guinea-pig.

[24] V. Shiltsev and F. Zimmermann, "Modern and future colliders," 2020. [Online]. Available: https://arxiv.org/pdf/2003.09084.pdf

[25] F. Gianotti, M. L. Mangano, T. Virdee *et al.*, "Physics potential and experimental challenges of the lhc luminosity upgrade," *The European Physical Journal C-Particles and Fields*, vol. 39, no. 3, pp. 293–333, 2005.

[26] G. Apollinari, I. Bejar Alonso, O. Bruning, F. P., M. Lamont, L. Rossi, and L. Tavian, "High-luminosity large hadron collider (hl-lhc): Technical design report v. 0.1," CERN, Tech. Rep. CERN Yellow Report: Monograph 2017-007-M, 2017. [Online]. Available: https://doi.org/10.23731/CYRM-2017-004

[27] E. D. Courant and H. S. Snyder, "Theory of the Alternating-Gradient Synchrotron," *Annals of Physics*, vol. 281, no. 1, pp. 360–408, Apr. 2000.

[28] R. Palmer, "Energy scaling, crab crossing and the pair problem," Stanford Linear Accelerator Center, Menlo Park, CA (USA), Tech. Rep. SLAC-PUB-4707, 1988. [Online]. Available: https://www.slac.stanford.edu/pubs/slacpubs/4500/slac-pub-4707.pdf

[29] K. Oide and K. Yokoya, "Beam-beam collision scheme for storage-ring colliders," *Phys. Rev. A*, vol. 40, pp. 315–316, Jul 1989. [Online]. Available: https://link.aps.org/doi/10.1103/PhysRevA.40.315

[30] Y.-P. Sun, R. Assmann, J. Barranco, R. Tomás, T. Weiler, F. Zimmermann, R. Calaga, and A. Morita, "Beam dynamics aspects of crab cavities in the cern large hadron collider," *Phys. Rev. ST Accel. Beams*, vol. 12, p. 101002, Oct 2009. [Online]. Available: https://link.aps.org/doi/10.1103/PhysRevSTAB.12.101002

[31] L. Carver, A. Alekou, F. Antoniou, R. Appleby, H. Bartosik, T. Bohl, G. Burt, R. Calaga, M. Carlà, T. Levens, J. Mitchell, G. Papotti, and C. Welsch, "First

machine development results with HL-LHC crab cavities in the SPS. First machine developments result with HL-LHC crab cavities in the SPS," p. MOPGW094. 4 p, 2019. [Online]. Available: http://cds.cern.ch/record/2696108

[32] S. Fartoukh, "Pile up management at the high-luminosity lhc and introduction to the crab-kissing concept," *Phys. Rev. ST Accel. Beams*, vol. 17, p. 111001, Nov 2014. [Online]. Available: https://link.aps.org/doi/10.1103/PhysRevSTAB.17.111001

[33] G. A. et al., "Beam parameters at lhc injection," 2014. [Online]. Available: https://cds.cern.ch/record/1644771/files/CERN-ACC-2014-0006.pdf

[34] M. Benedikt *et al.*, "Fcc-ee: The lepton collider," *The European Physical Journal Special Topics*, vol. 228, no. 2, pp. 261–623, 2019. [Online]. Available: https://fcc-cdr.web.cern.ch/

[35] ——, "Future circular collider conceptual design report," *The European Physical Journal Special Topics*, vol. 228, 2019. [Online]. Available: https://fcc-cdr.web.cern.ch/

[36] R. Martin, M. I. Besana, F. Cerutti, A. Langner, R. Tomás, E. Cruz-Alaniz, and B. Dalena, "Interaction region design driven by energy deposition," *Phys. Rev. Accel. Beams*, vol. 20, p. 081005, Aug 2017. [Online]. Available: https://link.aps.org/doi/10.1103/PhysRevAccelBeams.20.081005

[37] W. Scandale *et al.*, "Observation of channeling for 6500 gev/c protons in the crystal assisted collimation setup for lhc," *Physics Letters B*, vol. 758, pp. 129–133, 2016. [Online]. Available: https://doi.org/10.1016/j.physletb.2016.05.004

[38] G. Stancari, A. Valishev, G. Annala, G. Kuznetsov, V. Shiltsev, D. A. Still, and L. G. Vorobiev, "Collimation with hollow electron beams," *Phys. Rev. Lett.*, vol. 107, p. 084802, Aug 2011. [Online]. Available: https://link.aps.org/doi/10.1103/PhysRevLett.107.084802

[39] A. Burov, J. Marriner, V. Shiltsev, V. Danilov, and G. Lambertson, "Beam stability issues in very large hadron collider," *Nuclear Instruments and Methods in Physics Research Section A: Accelerators, Spectrometers, Detectors and Associated Equipment*, vol. 450, no. 2-3, pp. 194–206, 2000. [Online]. Available: https://doi.org/10.1016/S0168-9002(00)00261-8

[40] V. D. Shiltsev, "Accelerator physics and technology challenges of very high energy hadron colliders," *International Journal of Modern Physics A*, vol. 30, no. 23, p. 1544001, 2015. [Online]. Available: https://doi.org/10.1142/S0217751X15440017

[41] F. Zimmermann, "Luminosity Limitations at Hadron Colliders," in *Proc. 18th International Conference on High-Energy Accelerators (HEACC'01), Tsukuba, 26–30 March, 2001; also published as CERN-SL-2001-009-AP*, 2001.

[42] M. Benedikt, D. Schulte, and F. Zimmermann, "Optimizing integrated luminosity of future hadron colliders," *Phys. Rev. ST Accel. Beams*, vol. 18, p. 101002, Oct 2015. [Online]. Available: https://link.aps.org/doi/10.1103/PhysRevSTAB.18.101002

[43] C. Opal, "Precision luminosity for z lineshape measurements with a silicon-tungsten calorimeter," *Eur Physics Journal C*, vol. 14, pp. 373–425, 2000.

[44] C. Aleph, "Measurement of the z resonance parameters at lep," *Eur Physics Journal C*, vol. 14, pp. 1–50, 2000.

[45] C. L3, "Measurements of cross sections and forward-backward asymmetries at the z resonance and determination of electroweak parameters," *Eur Physics Journal C*, vol. 16, pp. 1–40, 2000.

[46] A. A. et al., "The present theoretical error on the bhabha scattering cross section in the luminometry region at lep," *Physics Letter B*, vol. 383, pp. 238–242, 1996.

[47] H. Abramowicz *et al.*, "Performance and Molière radius measurements using a compact prototype of LumiCal in an electron test beam," *Eur. Phys. J. C*, vol. 79, no. 7, p. 579, 2019.

[48] M. S. L. Linssen, A. Miyamoto and H. Weerts, "Physics and detectors at clic: Clic conceptual design report (2012)," p. 1202.5940, 2012. [Online]. Available: https://clicdp.web.cern.ch/content/conceptual-design-report

[49] E. L. V.B. Berestetskii and L. Pitaevskii, *Relativistic Quantum Theory.* Pergamon Press, 1971.

[50] D.Schulte, "Study of the electromagnetic and hadronic background in the interaction region of the tesla collider," 1997, phD Thesis. [Online]. Available: http://cds.cern.ch/record/331845/files/shulte.pdf

[51] J. Esberg, U. I. Uggerhøj, B. Dalena, and D. Schulte, "Strong field processes in beam-beam interactions at the Compact Linear Collider," *Phys. Rev. ST Accel. Beams*, vol. 17, no. 5, p. 051003, 2014. [Online]. Available: https://link.aps.org/doi/10.1103/PhysRevSTAB.17.051003

[52] G. Schuler and T. Sjostrand, "A scenario for high energy gamma-gamma interactions," 1996. [Online]. Available: http://cds.cern.ch/record/302680/files/9605240.pdf

[53] D. A. Karlen, "A study of low q^2 radiative bhabha scattering," 1988, phD Thesis.

[54] L. C. D. R. B. Appleby, A. Apyan and E. Gschwendtner, "Clic post-collision line luminosity monitoring," in *Proc. 2nd International Particle Accelerator Conference.* San Sebastian, Spain: JACoW, 2011, paper TUPC027. [Online]. Available: http://accelconf.web.cern.ch/IPAC2011/papers/tupc027.pdf

[55] D. Schulte, "A potential signal for luminosity optimisation in clic," in *Proc. of LINAC 2004*. Lubeck, Germany: JACoW, 2004, paper MOP45. [Online]. Available: https://accelconf.web.cern.ch/l04/PAPERS/MOP45.PDF

[56] J. Ögren, A. Latina, R. Tomás, and D. Schulte, "Tuning the compact linear collider 380 gev final-focus system using realistic beam-beam signals," *Phys. Rev. Accel. Beams*, vol. 23, p. 051002, May 2020. [Online]. Available: https://link.aps.org/doi/10.1103/PhysRevAccelBeams.23.051002

[57] Y. Nosochkov and A. Seryi, "Compensation of detector solenoid effects on the beam size in a linear collider," *Phys. Rev. ST Accel. Beams*, vol. 8, p. 021001, 2005. [Online]. Available: http://link.aps.org/doi/10.1103/PhysRevSTAB.8.021001

[58] C. B. M. Bassetti and C. Milardi, "Solenoidal compensation scheme for an interaction region of an electron-positron collider," in *Proc. of EPAC 1994*. London, England: JACoW, 1994. [Online]. Available: https://accelconf.web.cern.ch/e94/PDF/EPAC1994_1036.PDF

[59] T. M. A. Seryi and B. Parker, "Ir optimization, did and anti-did," SLAC, Stanford, CA, Tech. Rep. SLAC-PUB-11662, 2006. [Online]. Available: http://www.osti.gov/energycitations/product.biblio.jsp?osti_id=876041

[60] A. Seryi, "Near ir ff design including fd and longer l* issues," 2008. [Online]. Available: https://indico.cern.ch/contributionDisplay.py?contribId=283&confId=30383

[61] "Sid detector for ilc." [Online]. Available: http://www.silicondetector.org/

[62] G. Golub and W. Kahan, "Calculating the singular values and pseudo-inverse of a matrix," *Journal of the Society for Industrial and Applied Mathematics Series B Numerical Analysis*, vol. 2, no. 2, pp. 205–224, 1965. [Online]. Available: https://doi.org/10.1137/0702016

[63] G. B. Dantzig, "Origins of the simplex method." [Online]. Available: https://apps.dtic.mil/dtic/tr/fulltext/u2/a182708.pdf

[64] R. Brun and F. Rademakers, "Root - an object oriented data analysis framework," pp. 81–86, 1997. [Online]. Available: http://root.cern.ch

[65] M. Agnello *et al.*, "$\Sigma^- p$ emission rates in K^- absorptions at rest on ^{6}Li, ^{7}Li, ^{9}Be, ^{13}C and ^{16}O," *Phys. Rev. C*, vol. 92, no. 4, p. 045204, 2015. [Online]. Available: https://doi.org/10.1103/PhysRevC.92.045204

[66] ——, "The $A(K^-_{stop}, \pi^{\pm}\Sigma^{\mp})A'$ reaction on p-shell nuclei," *Phys. Lett. B*, vol. 704, pp. 474–480, 2011. [Online]. Available: https://doi.org/10.1016/j.physletb.2011.09.076

[67] ——, "Neutron-proton coincidences from Non-Mesonic Weak Decay of p-shell Λ-hypernuclei and determination of the two-nucleon induced process," *Phys. Lett. B*, vol. 701, pp. 556–561, 2011. [Online]. Available: https://doi.org/10.1016/j.physletb.2011.06.035

[68] ——, "Correlated Lambda t pairs from the absorption of K- at rest in light nuclei," *Phys. Lett. B*, vol. 669, pp. 229–234, 2008. [Online]. Available: https://doi.org/10.1016/j.physletb.2008.09.052

[69] ——, "Correlated Λd pairs from the $K^-_{stop}A \to \Lambda d A'$ reaction," *Phys. Lett. B*, vol. 654, pp. 80–86, 2007. [Online]. Available: https://doi.org/10.1016/j.physletb.2007.08.051

[70] R. T. X. B. J. C. E. Fol and L. Malina, "Imperfections and corrections," in *Proc. of 2018 CERN–Accelerator–School course on Numerical Methods for Analysis, Design and Modelling of Particle Accelerators.* arxiv, June 2020. [Online]. Available: https://arxiv.org/pdf/2006.10661.pdf

[71] J. P. Koutchouk, "Interpretation of the systematic betatron coupling in the lhc and its correction," 1994. [Online]. Available: https://cds.cern.ch/record/267132/files/sl-94-033.pdf

[72] O. S. Brüning and S. D. Fartoukh, "Field Quality Specification for the LHC Main Dipole Magnets," CERN, Geneva, Tech. Rep. LHC-Project-Report-501. CERN-LHC-Project-Report-501, Oct 2001. [Online]. Available: https://cds.cern.ch/record/522049

[73] B. Autin and Y. Marti, ""closed orbit correction of a.g. machines using a small number of magnets," 1973. [Online]. Available: http://cds.cern.ch/record/790199/files/cm-p00040268.pdf

[74] B. D. A. Chance and J. Payet, "Analytical methods for statistical analysis of the correction of coupling due to errors," in *Proc. of 3rd International Particle Accelerator Conference*. JACoW, 2012, pp. 1152 – 1154. [Online]. Available: http://accelconf.web.cern.ch/IPAC2012/papers/tuppc003.pdf

[75] A. C. D. Boutin and B. Dalena, "Optics corrections for fcc-hh," in *Proc. of 10th International Particle Accelerator Conference*. JACoW, 2019, pp. 417 – 419. [Online]. Available: http://accelconf.web.cern.ch/ipac2019/papers/mopmp001.pdf

[76] D. S. et al., "Clic energy scans," in *Proc. of 1st International Particle Accelerator Conference*. JACoW, 2010, pp. 3395 – 3397. [Online]. Available: http://accelconf.web.cern.ch/IPAC10/papers/wepe022.pdf

[77] B. D. et al., "Clic bds tuning, alignment and feedbacks integrated simulations," in *Proc. of 1st International Particle Accelerator Conference*. JACoW, 2010, pp. 3413 – 3415. [Online]. Available: http://accelconf.web.cern.ch/IPAC10/papers/wepe028.pdf

[78] P. N. et al., "Strategy of beam tuning implementation for the saraf mebt and sc linac," in *Proc. of 8th International Particle Accelerator Conference*. JACoW, 2017, pp. 652 – 654. [Online]. Available: http://accelconf.web.cern.ch/ipac2017/papers/mopik057.pdf

[79] V. Danilov and S. Nagaitsev, "Nonlinear accelerator lattices with one and two analytic invariants," *Phys. Rev. ST Accel. Beams*, vol. 13, p. 084002, Aug 2010. [Online]. Available: https://link.aps.org/doi/10.1103/PhysRevSTAB.13.084002

[80] A. L. *et al.*, "Alignment of the clic bds," 2008. [Online]. Available: https://cds.cern.ch/record/1122289/files/CERN-AB-2008-011.pdf

[81] R. T. *et al.*, "Atf2 ultra-low ip betas proposal," 2009. [Online]. Available: https://cds.cern.ch/record/1312198/files/CERN-ATS-2009-092.pdf

[82] J. Pfingstner, K. Artoos, C. Charrondiere, S. Janssens, M. Patecki, Y. Renier, D. Schulte, R. Tomás, A. Jeremie, K. Kubo, S. Kuroda, T. Naito, T. Okugi, T. Tauchi, and N. Terunuma, "Mitigation of ground motion effects in linear accelerators via feed-forward control," *Phys. Rev. ST Accel. Beams*, vol. 17, p. 122801, Dec 2014. [Online]. Available: https://link.aps.org/doi/10.1103/PhysRevSTAB.17.122801

[83] T. Raubenheimer, "A new technique of correcting emittance dilutions in linear colliders," *Nuclear Instruments and Methods in Physics Research Section A*, vol. 306, no. 1, pp. 61 – 64, 1991. [Online]. Available: http://www.sciencedirect.com/science/article/pii/0168900291903027

[84] P. E. *et al.*, "Luminosity tuning at the interaction point," 2006. [Online]. Available: https://cds.cern.ch/record/971872/files/ab-2006-044.pdf

[85] E. Marin, "Design and higher order optimisation of final focus systems for linear colliders," 2012, phD Thesis. [Online]. Available: http://cds.cern.ch/record/1504285/files/CERN-THESIS-2012-218.pdf

[86] J. Ogren, C. Gohil, and D. Schulte, "Surrogate modeling of the clic final-focus system using artificial neural networks," 2020.

[87] S. Fartoukh, "Achromatic telescopic squeezing scheme and application to the lhc and its luminosity upgrade," *Phys. Rev. ST Accel. Beams*, vol. 16, p. 111002, Nov 2013. [Online]. Available: https://link.aps.org/doi/10.1103/PhysRevSTAB.16.111002

[88] R. D. Maria, "Parametric study of the optics options for the hl-lhc project," in *Proc. of 3rd International Particle Accelerator Conference*. JACoW, 2012, pp. 142 – 144. [Online]. Available: http://accelconf.web.cern.ch/IPAC2012/papers/moppc010.pdf

[89] R. D. M. et al., "Hllhcv1.0: Hl-lhc layout and optics model for 150 mm nb_3sn triplets and local crab-cavities," in *Proc. of 4th International Particle Accelerator Conference*. JACoW, 2013, pp. 1358 – 1360. [Online]. Available: http://accelconf.web.cern.ch/IPAC2013/papers/tupfi014.pdf

[90] B. D. et al., "High luminosity lhc matching section layout vs crab cavity voltage," in *Proc. of 4th International Particle Accelerator Conference*. JACoW, 2013, pp. 1328 – 1330. [Online]. Available: http://accelconf.web.cern.ch/IPAC2013/papers/tupfi001.pdf

[91] ——, "Alternative high luminosity lhc matching section layout," in *Proc. of 5th International Particle Accelerator Conference*. JACoW, 2014, pp. 990 – 992. [Online]. Available: http://accelconf.web.cern.ch/IPAC2014/papers/tupro001.pdf

[92] E. Todesco and M. Giovannozzi, "Dynamic aperture estimates and phase-space distortions in nonlinear betatron motion," *Phys. Rev. E*, vol. 53, pp. 4067–4076, Apr 1996. [Online]. Available: https://link.aps.org/doi/10.1103/PhysRevE.53.4067

[93] E. H. Maclean, M. Giovannozzi, and R. B. Appleby, "Innovative method to measure the extend of the stable phase-space region of proton synchrotrons," *Physical Review Accelerators and Beams*, vol. 22, p. 034002, March 2019.

[94] B. D. et al., "First evaluation of dynamic aperture at injection for fcc-hh," in *Proc. of 7th International Particle Accelerator Conference*. JACoW, 2016, pp. 1466 – 1469. [Online]. Available: http://accelconf.web.cern.ch/ipac2016/papers/tupmw019.pdf

[95] ——, "Advance on dynamic aperture at injection for fcc-hh," in *Proc. of 8th International Particle Accelerator Conference*. JACoW, 2017, pp. 2027 – 2030. [Online]. Available: http://accelconf.web.cern.ch/ipac2017/papers/tupva003.pdf

[96] ——, "Dipole field quality and dynamic aperture for fcc-hh," in *Proc. of 9th International Particle Accelerator Conference*. JACoW, 2018, pp. 137 – 140. [Online]. Available: http://accelconf.web.cern.ch/ipac2018/papers/mopmf024.pdf

[97] ——, "Field quality for the hadron option of future circular collider," in *Proc. of 10th International Particle Accelerator Conference*. JACoW, 2019, pp. 4397 – 4400. [Online]. Available: http://accelconf.web.cern.ch/ipac2019/papers/mopmp005.pdf

[98] K. Wille, *The Physics of Particle Accelerator*. Oxford, 2000.

[99] M. Lukoševičius and H. Jaeger, "Reservoir computing approaches to recurrent neural network training," *Computer Science Review*, vol. 3, no. 3, pp. 127–149, 2009. [Online]. Available: https://www.sciencedirect.com/science/article/pii/S1574013709000173

[100] M. B. Ghali and B. Dalena, "A machine learning technique for dynamic aperture computation," in *Proc. 12th International Particle Accelerator Conference*. Campinas, SP, Brazil: JACoW, May 2021, to be publishe on JACow.

[101] J. Laskar, "Frequency map analysis and particle accelerators," in *Proc. of Particle Accelerator Conference*. JACoW, 2003, pp. 378 – 382. [Online]. Available: https://accelconf.web.cern.ch/p03/PAPERS/WOAB001.PDF

[102] M. Venturini and A. J. Dragt, "Accurate computation of transfer maps from magnetic field data," *Nuclear Instruments and Methods in Physics Research A*, vol. 427, pp. 387–392, May 1999. [Online]. Available: https://doi.org/10.1016/S0168-9002(98)01518-6

[103] C. E. Mitchell and A. J. Dragt, "Accurate transfer maps for realistic beam-line elements: Straight elements," *Phys. Rev. ST Accel. Beams*, vol. 13, p. 064001, Jun 2010. [Online]. Available: https://link.aps.org/doi/10.1103/PhysRevSTAB.13.064001

[104] Y. K. Wu, E. Forest, and D. S. Robin, "Explicit symplectic integrator for s-dependent static magnetic field," *Phys. Rev. E*, vol. 68, p. 046502, Oct 2003. [Online]. Available: https://link.aps.org/doi/10.1103/PhysRevE.68.046502

[105] A. J. Draft, F. Neri, G. Rangarajan, D. R. Douglas, L. M. Healy, and R. D. Ryne, "Lie algebraic treatment of linear and nonlinear beam dynamics," *Annual Review of Nuclear and Particle Science*, vol. 38, no. 1, pp. 455–496, 1988. [Online]. Available: https://doi.org/10.1146/annurev.ns.38.120188.002323

[106] A. Simona, "Numerical methods for the simulation of particle motion in electromagnetic fields," 2019, phD Thesis. [Online]. Available: https://mox.polimi.it/publication-results/?id=849&tipo=add_tesi

[107] "SixTrack - 6D tracking code," https://sixtrack.web.cern.ch/SixTrack, jun 2019.

[108] T. Pugnat, "Non linear beam dynamics for the lhc upgrades," 2021, phD Thesis.

[109] B. D. et al., "Updates on the impact of fringe fields on corrector strength," https://indico.cern.ch/event/924095/contributions/3882654/attachments/2057517/3450692/bdalena_updateFringeFields_177HLmeetingWP2.pdf, 2020.

[110] E. H. Maclean, R. Tomás, F. S. Carlier, M. S. Camillocci, J. W. Dilly, J. Coello de Portugal, E. Fol, K. Fuchsberger, A. Garcia-Tabares Valdivieso, M. Giovannozzi, M. Hofer, L. Malina, T. H. B. Persson, P. K. Skowronski, and A. Wegscheider, "New approach to lhc optics commissioning for the nonlinear era," *Phys. Rev. Accel. Beams*, vol. 22, p. 061004, Jun 2019. [Online]. Available: https://link.aps.org/doi/10.1103/PhysRevAccelBeams.22.061004

[111] M. G. E.H. Maclean, F.S. Carlier and R. Tomás, "Report from lhc md 2171: Dynamic aperture at 6.5 tev."

[112] T. P. et al., "3d magnetic field analysis of lhc final focus quadrupole with beam screen," in *Proc. 12th International Particle Accelerator Conference*. Campinas, SP, Brazil: JACoW, May 2021, to be published on JACow.

[113] P. Arpaia, G. Caiafa, and S. Russenschuck, "A Rotating-Coil Magnetometer for Scanning Transversal Field Harmonics in Accelerator Magnets," *Scientific Reports*, vol. 9, no. 1491, pp. 1–11, 2019. [Online]. Available: https://www.nature.com/articles/s41598-018-37371-3#citeas

[114] T. P. et al., "Non-linear variation of the beta-beating measured from amplitude," in *Proc. 12th International Particle Accelerator Conference*. Campinas, SP, Brazil: JACoW, May 2021, to be published on JACow.

[115] D. Reschke, V. Gubarev, J. Schaffran, L. Steder, N. Walker, M. Wenskat, and L. Monaco, "Performance in the vertical test of the 832 nine-cell 1.3 ghz cavities for the european x-ray free electron laser," *Phys. Rev. Accel. Beams*, vol. 20, p. 042004, Apr 2017. [Online]. Available: https://link.aps.org/doi/10.1103/PhysRevAccelBeams.20.042004

[116] X. Xu, M. D. Sumption, and X. Peng, "Internally oxidized nb3sn strands with fine grain size and high critical current density," *Advanced Materials*, vol. 27, no. 8, pp. 1346–1350, 2015. [Online]. Available: https://onlinelibrary.wiley.com/doi/abs/10.1002/adma.201404335

[117] Y. Kamihara, H. Hiramatsu, M. Hirano, R. Kawamura, H. Yanagi, T. Kamiya, and H. Hosono, "Iron-based layered superconductor: Laofep," *Journal of the American Chemical Society*, vol. 128, no. 31, pp. 10 012–10 013, 2006, pMID: 16881620. [Online]. Available: https://doi.org/10.1021/ja063355c

[118] R. Gupta, M. Anerella, G. Ganetis, A. Ghosh, H. Kirk, R. Palmer, S. Plate, W. Sampson, Y. Shiroyanagi, P. Wanderer, B. Brandt, D. Cline, A. Garren, J. Kolonko, R. Scanlan, and R. Weggel, "High field hts r&d solenoid for muon collider," *IEEE Transactions on Applied Superconductivity*, vol. 21, no. 3, pp. 1884–1887, 2011.

[119] C. Lewis and J. Muller, "A direct drive wind turbine hts generator," in *2007 IEEE Power Engineering Society General Meeting*, 2007, pp. 1–8.

[120] J. M. Dawson, "Nonlinear electron oscillations in a cold plasma," *Phys. Rev.*, vol. 113, pp. 383–387, Jan 1959. [Online]. Available: https://link.aps.org/doi/10.1103/PhysRev.113.383

[121] T. Tajima and J. M. Dawson, "Laser electron accelerator," *Phys. Rev. Lett.*, vol. 43, pp. 267–270, Jul 1979. [Online]. Available: https://link.aps.org/doi/10.1103/PhysRevLett.43.267

[122] E. Esarey, C. B. Schroeder, and W. P. Leemans, "Physics of laser-driven plasma-based electron accelerators," *Rev. Mod. Phys.*, vol. 81, pp. 1229–1285, Aug 2009. [Online]. Available: https://link.aps.org/doi/10.1103/RevModPhys.81.1229

[123] M. J. Hogan, "Electron and positron beam–driven plasma acceleration," *Reviews of Accelerator Science and Technology*, vol. 09, pp. 63–83, 2016. [Online]. Available: https://doi.org/10.1142/S1793626816300036

[124] E. Adli and P. Muggli, "Proton-beam-driven plasma acceleration," *Reviews of Accelerator Science and Technology*, vol. 09, pp. 85–104, 2016. [Online]. Available: https://doi.org/10.1142/S1793626816300048

[125] A. R. Maier, N. M. Delbos, T. Eichner, L. Hübner, S. Jalas, L. Jeppe, S. W. Jolly, M. Kirchen, V. Leroux, P. Messner, M. Schnepp, M. Trunk, P. A. Walker, C. Werle, and P. Winkler, "Decoding sources of energy variability in a laser-plasma accelerator," *Phys. Rev. X*, vol. 10, p. 031039, Aug 2020. [Online]. Available: https://link.aps.org/doi/10.1103/PhysRevX.10.031039

[126] M. Litos, E. Adli, J. M. Allen, W. An, C. I. Clarke, S. Corde, C. E. Clayton, J. Frederico, S. J. Gessner, S. Z. Green, M. J. Hogan, C. Joshi, W. Lu, K. A. Marsh, W. B. Mori, M. Schmeltz, N. Vafaei-Najafabadi, and V. Yakimenko, "9 GeV energy gain in a beam-driven plasma wakefield accelerator," *Plasma Physics and Controlled Fusion*, vol. 58, no. 3, p. 034017, feb 2016. [Online]. Available: https://doi.org/10.1088/0741-3335/58/3/034017

[127] E. A. et al., "Acceleration of electrons in the plasma wakefield of a proton bunch," *Nature*, vol. 561, pp. 363–367, September 2018. [Online]. Available: https://doi.org/10.1038/s41586-018-0485-4

[128] W. Leemans and E. Esarey, "Laser-driven plasma-wave electron accelerators," *Physics Today*, vol. 62, no. 3, p. 44, 2009. [Online]. Available: https://doi.org/10.1063/1.3099645

[129] E. Adli, J.-P. Delahaye, S. J. Gessner, M. J. Hogan, T. Raubenheimer, W. An, C. Joshi, and W. Mori, "A beam driven plasma-wakefield linear collider: From higgs factory to multi-tev," 2013.

[130] V. Lebedev, A. Burov, and S. Nagaitsev, "Luminosity limitations of linear colliders based on plasma acceleration," *Reviews of Accelerator Science and Technology*, vol. 09, pp. 187–207, 2016. [Online]. Available: https://doi.org/10.1142/S1793626816300097

[131] D. Schulte, "Application of advanced accelerator concepts for colliders," *Reviews of Accelerator Science and Technology*, vol. 09, pp. 209–233, 2016. [Online]. Available: https://doi.org/10.1142/S1793626816300103

[132] E. P. et al., "Demonstration of electron acceleration in a laser-driven dielectric microstructure," *Nature*, vol. 503, pp. 91–94, November 2013. [Online]. Available: https://doi.org/10.1038/nature12664

[133] R. J. England, R. J. Noble, K. Bane, D. H. Dowell, C.-K. Ng, J. E. Spencer, S. Tantawi, Z. Wu, R. L. Byer, E. Peralta, K. Soong, C.-M. Chang, B. Montazeri, S. J. Wolf, B. Cowan, J. Dawson, W. Gai, P. Hommelhoff, Y.-C. Huang, C. Jing, C. McGuinness, R. B. Palmer, B. Naranjo, J. Rosenzweig, G. Travish, A. Mizrahi, L. Schachter, C. Sears, G. R. Werner, and R. B. Yoder, "Dielectric laser accelerators," *Rev. Mod. Phys.*, vol. 86, pp. 1337–1389, Dec 2014. [Online]. Available: https://link.aps.org/doi/10.1103/RevModPhys.86.1337

[134] J. S. et al., "Recent progress of short pulse dielectric two-beam acceleration," in *Proc. 9th International Particle Accelerator Conference*. Vancouver, Canada: JACoW, 2018, paper TUYGBE3. [Online]. Available: http://accelconf.web.cern.ch/ipac2018/papers/tuygbe3.pdf

[135] C. Jing, "Dielectric wakefield accelerators," *Reviews of Accelerator Science and Technology*, vol. 09, pp. 127–149, 2016. [Online]. Available: https://doi.org/10.1142/S1793626816300061

[136] K. L. Bane, T. L. Barklow, M. Breidenbach, C. P. Burkhart, E. A. Fauve, A. R. Gold, V. Heloin, Z. Li, E. A. Nanni, M. Nasr, M. Oriunno, J. M. Paterson, M. E.

Peskin, T. O. Raubenheimer, and S. G. Tantawi, "An advanced ncrf linac concept for a high energy e^+e^- linear collider," 2019.

[137] M. Tigner, "A possible apparatus for electron clashing-beam experiments," *Il Nuovo Cimento*, vol. 37, no. 3, pp. 1228–1231, Jun. 1965.

[138] V. N. Litvinenko, T. Roser, and M. Chamizo-Llatas, "High-energy high-luminosity e+e- collider using energy-recovery linacs," *Physics Letters B*, vol. 804, p. 135394, May 2020. [Online]. Available: http://dx.doi.org/10.1016/j.physletb.2020.135394

[139] S. A. Bogacz, J. Ellis, L. Lusito, D. Schulte, T. Takahashi, M. Velasco, M. Zanetti, and F. Zimmermann, "Sapphire: a small gamma-gamma higgs factory," 2012.

[140] J. Gronberg, "The photon collider," *Reviews of Accelerator Science and Technology*, vol. 07, pp. 161–175, 2014. [Online]. Available: https://doi.org/10.1142/S1793626814300084

Appendix A

Publications

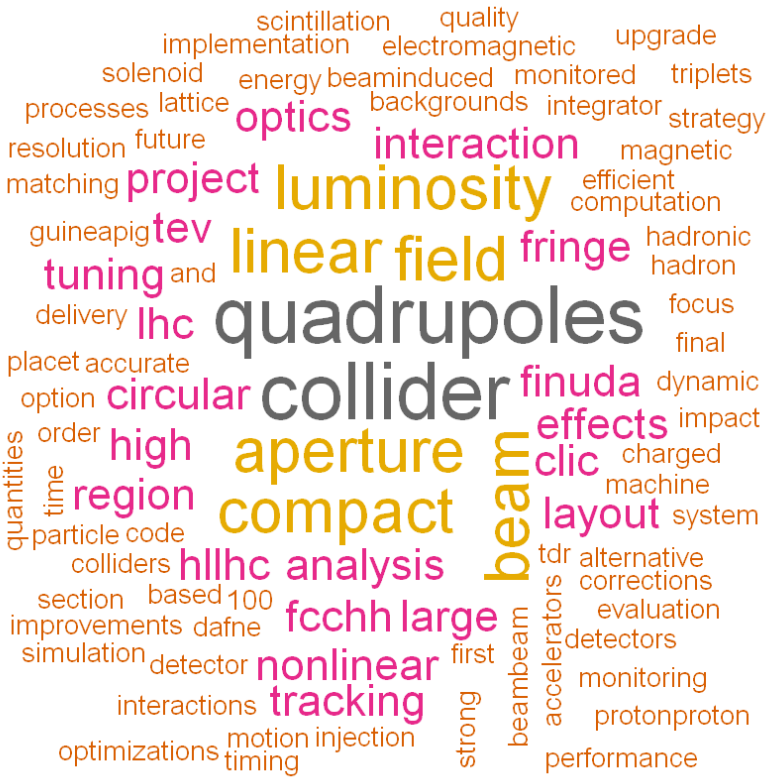

A.1 DAFNE monitored by FINUDA

Available online at www.sciencedirect.com
ScienceDirect
ELSEVIER
Nuclear Instruments and Methods in Physics Research A 570 (2007) 205–215
NUCLEAR INSTRUMENTS & METHODS IN PHYSICS RESEARCH Section A
www.elsevier.com/locate/nima

Technical note

DAΦNE monitored by FINUDA

M. Agnello[a,b], L. Benussi[c], M. Bertani[c], H.C. Bhang[d], S. Bianco[c], G. Bonomi[e,f], E. Botta[b,g], M. Bregant[h,i], T. Bressani[b,g], L. Busso[b,j], D. Calvo[b], P. Camerini[h,i], P. Cerello[b], B. Dalena[k,l], F. De Mori[b,g], G. D'Erasmo[k,l], D. Di Santo[k,l], D. Elia[l], F.L. Fabbri[c], D. Faso[b,j], A. Feliciello[b], A. Filippi[b], V. Filippini[f,⋆], R. Fini[l], M.E. Fiore[k,l], H. Fujioka[m], P. Gianotti[c], N. Grion[i], B. Kang[d], A. Krasnoperov[n], V. Lucherini[c,*], V. Lenti[l], V. Manzari[l], S. Marcello[b,g], T. Maruta[q], N. Mirfakhrai[o], O. Morra[b,p], T. Nagae[q], H. Outa[r], E. Pace[c], M. Pallotta[c], M. Palomba[k,l], A. Pantaleo[l], A. Panzarasa[f], V. Paticchio[k], S. Piano[i], F. Pompili[c], R. Rui[h,i], G. Simonetti[k,l], H. So[d], V. Tereschenko[n], S. Tomassini[c], R. Wheadon[b], A. Zenoni[e,f]

[a]*Dip. di Fisica Politecnico di Torino, Via Duca degli Abruzzi 24, Torino, Italy*
[b]*INFN Sez. di Torino, via P. Giuria 1, Torino, Italy*
[c]*Laboratori Nazionali di Frascati dell'INFN, via E. Fermi 40, Frascati, Italy*
[d]*Department of Physics, Seoul National University, 151-742 Seoul, South Korea*
[e]*Dip. di Meccanica, Università di Brescia, via Valotti 9, Brescia, Italy*
[f]*INFN Sez. di Pavia, via Bassi 6, Pavia, Italy*
[g]*Dip. di Fisica Sperim., Università di Torino, via P. Giuria 1, Torino, Italy*
[h]*Dip. di Fisica, Univ. di Trieste, via Valerio 2, Trieste, Italy*
[i]*INFN, Sez. di Trieste, via Valerio 2, Trieste, Italy*
[j]*Dip. di Fisica Generale, Università di Torino, via P. Giuria 1, Torino, Italy*
[k]*Dip. di Fisica, Univ. di Bari, via Amendola 173, Bari, Italy*
[l]*INFN Sez. di Bari, via Amendola 173, Bari, Italy*
[m]*Department of Physics, University of Tokyo, Bunkyo, Tokyo 113-0033, Japan*
[n]*JINR, Dubna, Moscow region, Russia*
[o]*Department of Physics, Shahid Behesty University, 19834 Teheran, Iran*
[p]*INAF-IFSI Sez. di Torino, C.so Fiume, Torino, Italy*
[q]*High Energy Accelerator Research Organization (KEK), Tsukuba, Ibaraki 305-0801, Japan*
[r]*RIKEN, Wako, Saitama 351-0198, Japan*

Received 27 June 2006; received in revised form 12 September 2006; accepted 21 September 2006
Available online 9 November 2006

Abstract

The FINUDA spectrometer, devoted to hypernuclear physics and installed on the DAΦNE two rings collider at the Laboratori Nationali di Frascati, is able to monitor the relevant machine parameters, as luminosity, collision vertexes, c.m. energy and transversal momentum boost, during the process of data taking to study hypernuclear physics without affecting it. The collider parameters relevant to optimize the machine performances to the needs of the experiment are measured both on-line and offline in a run-to-run basis, in an efficient, redundant way, allowing the continuous extraction of reliable and cross-checked information on the machine working conditions.

PACS: 21.80.+a; 41.75.Ht; 41.85.Ew; 41.85.Qg

Keywords: Λ hypernuclei; Luminosity; Collider parameters

*Corresponding author. Tel.: +39 694932408; fax: +39 69403559.
E-mail address: vincenzo.lucherini@lnf.infn.it (V. Lucherini).
⋆Deceased.

0168-9002/$ - see front matter © 2006 Elsevier B.V. All rights reserved.
doi:10.1016/j.nima.2006.09.113

1. Introduction

The aim of the FINUDA experiment is the systematic study of hypernuclear formation and decay using low energy stopped K^-. The FINUDA apparatus is a high acceptance, high resolution spectrometer whose unique feature is that of employing a low energy K^- beam produced by the decay of ϕ mesons generated in the interaction of the e^+ and e^- beams circulating in a two ring collider, DAΦNE, at the Frascati National Laboratories of INFN.

Indeed, the DAΦNE collider [1] is optimized in performance and energy to collide e^+ and e^- beams of 510 MeV energy, in order to produce $\phi(1020)$ mesons almost at rest. The $\phi(1020)$ decays with BR = 0.49 into a pair of back-to-back K^-K^+ mesons with momenta of 127 MeV/c. Thanks to these peculiar features, very thin targets ($0.21-0.38\,g/cm^2$) can be used to stop the K^-. Therefore, the deterioration of the momentum resolution of the emitted particles, due to the target crossing, is minimized, contrarily to all the other experiments employing extracted kaon and also pion beams. Moreover, the hadronic background, already intrinsically low in an electromagnetic machine, can be further reduced by triggering on the specific topology and momentum of the K^-K^+ pairs coming from the $\phi(1020)$ decay.

The FINUDA spectrometer consists of a non-focusing, superconducting solenoid ($B = 1.0$ T, $\varnothing = 240$ cm) located around the thin (500 μm, $\varnothing = 10$ cm) beam pipe of DAΦNE and instrumented with several arrays of tracking detectors and two scintillator barrels, arranged with axial symmetry around the axis of the apparatus. The innermost scintillator barrel (TOFINO) is placed just around the beam pipe and is composed by 12 thin (2.3 mm thickness, 20 cm length) scintillator slabs, whereas the outer barrel (TOFONE) is composed by 72 thick large scintillator slabs (10 cm thickness, 255 cm length) and is placed in outermost position, just close to the magnet cryostat. The two scintillator barrels are used for triggering and time of flight (t.o.f.) measurements, while TOFONE detects also neutral particles.

The momentum resolution of the spectrometer is optimized for the prompt π^- coming from Λ-hypernucleus formation (260−270 MeV/c) and is presently 0.6% FWHM. The apparatus is also able to detect the hypernucleus decay products and, quite in general, the charged particles produced in the K^- (and K^+) interactions on the target nuclei. In the FINUDA interaction region up to eight different thin (about 200 mg/cm^2) targets can be installed, between two co-axial arrays of bi-dimensional Si micro-strip, detectors, 400 μm thick and 20 cm long. The internal array (ISIM) allows to measure the crossing point of the K^- (K^+) coming from the $\phi(1020)$ decay close to the targets, while the external array (OSIM) measures the crossing points of the outgoing charged particles resulting from kaon interactions in the targets. The Si micro-strip arrays provide also particle identification by dE/dX measurement.

The tracking of the charged particles in the spectrometer volume, between the vertex region and the outer scintillator barrel, is performed by means of two co-axial octagonal layers of low mass drift chambers (LMDC) followed by six circular layers of thin-walled straw tubes (STRAW), two layers of which are arranged along the apparatus axis, the other two couples of layers are tilted by ±15° relative to the axis of the apparatus, for stereo reconstruction of the crossing track trajectory. The whole FINUDA tracking volume is filled with Helium gas, in order to minimize the effect of the multiple scattering on the particle trajectories. A more detailed description of the FINUDA setup, shown in Fig. 1, is given in Ref. [2].

The first level trigger of the FINUDA apparatus is based on the fast signals coming from the two scintillator barrels and is produced by a selectable combination of defined hit topologies and energy deposition in the slabs. In particular, the latter condition allows for the recognition of highly ionizing particles, like low energy kaons, at trigger level, against the minimum ionizing ones. Proper scalers record the counts of the different detected trigger conditions, during the data taking.

The unconventional way in which the K^- beam is produced in DAΦNE imposes severe constraints to the

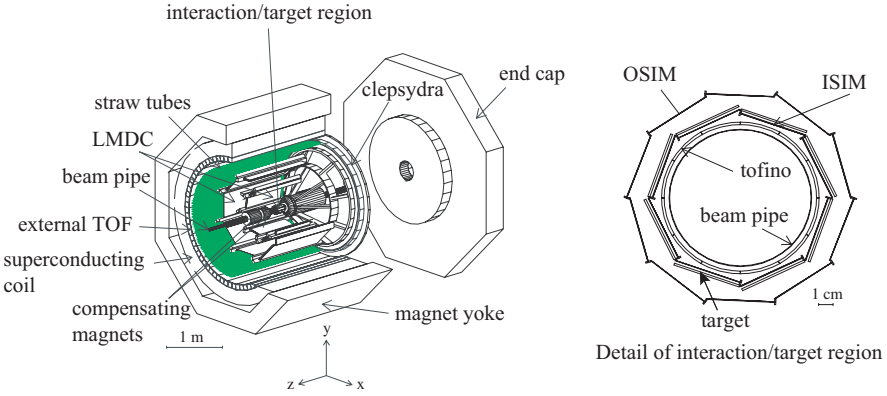

Fig. 1. The FINUDA setup. Left: overall 3D view; right: 2D view of the vertex–target region.

machine performances, in order to fit at best the specific needs of FINUDA. The critical parameters to be optimized are: the machine luminosity at the c.m. energy of 1020 MeV, the K^- and K^+ fluxes, the positions of the e^+e^- collision vertexes, which must be aligned at the center of the spectrometer to provide the maximum apparatus acceptance. Moreover, the usual machine parameters, as stability and a low level of background, need also to be achieved and continuously monitored.

In this paper, we describe how the FINUDA apparatus is able to measure the relevant machine parameters, allowing the performances of DAΦNE to be continuously monitored and optimized, during the data taking and without disturbing it. The experimental data here referred to, have been taken during the first FINUDA run on DAΦNE, started on December 1st 2003, after a period of machine tuning and detector debugging, and lasted till March 22, 2004, cumulating an overall integrated luminosity of $\mathscr{L}_{\text{int}} = 250\,\text{pb}^{-1}$ (debugging and data taking).

2. Monitoring DAΦNE parameters

2.1. Machine luminosity and energy

The most important machine parameter to be monitored is the luminosity of the collider. The luminosity $\mathscr{L}$ is defined, as usual, as the quantity to be multiplied by the cross-section σ of a given process to obtain the number of events expected from that process. It is related, in the case of a collider, to several machine parameters as the beam currents, the number of bunches, the transversal sizes of the circulating beams, the RF, and so on.

We can speak of instantaneous luminosity, $\mathscr{L}_{\text{inst}}$, in which case the product $\mathscr{L}_{\text{inst}}\sigma$ gives the counting rate expected for the process whose cross-section is σ; the units of $\mathscr{L}_{\text{inst}}$ are, therefore, $\text{cm}^{-2}\,\text{s}^{-1}$. We can also speak of the integrated luminosity in a given time interval ΔT, $\mathscr{L}_{\text{int}}$, in which case the product of $\mathscr{L}_{\text{int}}\sigma$ gives the total number of events collected during ΔT for the process whose cross-section is σ. The units for $\mathscr{L}_{\text{int}}$, in this case, are simply the units of the inverse of a cross-section, cm^{-2} or a multiple like nb^{-1} or pb^{-1}.

FINUDA is able to measure and monitor the machine luminosity, both $\mathscr{L}_{\text{inst}}$ and $\mathscr{L}_{\text{int}}$, exploiting different and independent physical processes occurring after e^+e^- collisions:

(1) counting e^+e^- scattering events (Bhabha events) provided by a dedicated trigger and reconstructed by the apparatus; the cross-section of the Bhabha process is well known [3] and rather flat with energy around the nominal energy value of DAΦNE; the counting of the Bhabha events detected by the apparatus allows the number of e^+e^- collisions and hence the beam luminosity to be directly evaluated;
(2) counting the K^0_S events, produced by the $\phi(1020)$ decay into $K^0_S K^0_L$ (BR = 0.34), filtering inside the Bhabha trigger and reconstructed by the apparatus; the cross-section of this process is well known [4], but strongly dependent on the machine energy, let us say on the position on the ϕ resonance, which is only 4.43 MeV wide. Therefore, the counting of reconstructed K^0_S events allows not only the luminosity to be evaluated and compared with the value obtained from the Bhabha events, but also the machine energy to be measured and monitored;
(3) during the data taking the luminosity and machine energy can also be monitored by counting the number of K^+K^- pairs from the decay of the $\phi(1020)$, as recorded by the hypernuclear trigger and reconstructed by the apparatus.

The Bhabha scattering [3] is a collision of the DAΦNE e^+e^- beams proceeding through the following channels:

$$e^+e^- \rightarrow e^+e^-(n\gamma). \quad (1)$$

The Bhabha scattering is called elastic if the number n of γ-rays is zero, and inelastic if there is at least one ($n = 1$) γ-ray. In case of elastic or highly elastic (i.e. with a *soft* energy emitted γ-ray) Bhabha scattering, the e^+e^- pair in the final state will be emitted back-to-back and have the same or very similar momenta, close to the 510 MeV/c of the circulating beams. Fig. 2 shows, as an example, a typical highly elastic Bhabha event recorded by the FINUDA spectrometer and reconstructed and fitted by the FINUDA reconstruction procedures.

Such events are selected using a dedicated trigger, called Bhabha trigger, requiring the fulfillment of the following

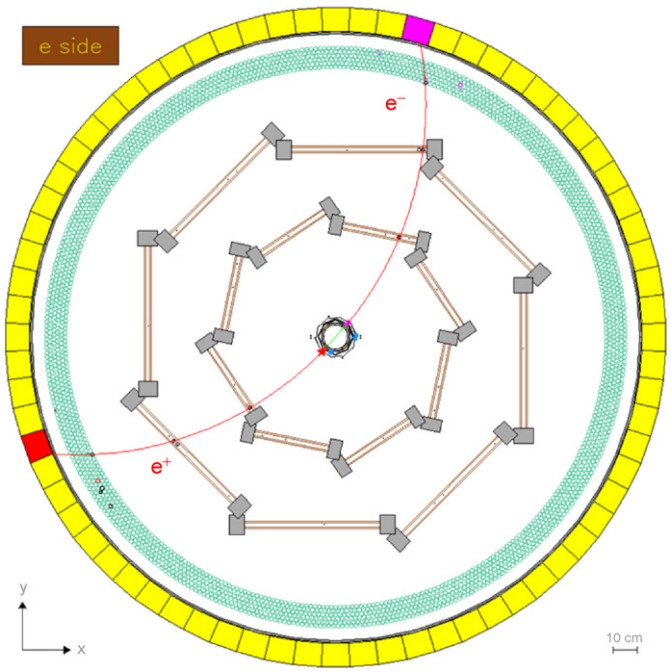

Fig. 2. Highly elastic Bhabha event $e^+e^- \rightarrow e^+e^-$ recorded by the FINUDA spectrometer. The reconstructed momenta of the e^+ and e^- track are 512 and 492 MeV/c, respectively.

criteria: (a) two opposite (back-to-back) coincident hits, with minimum ionizing energy deposition, in the slabs of TOFINO scintillator barrel; (b) coincidence with at least two hits in the slabs of the TOFONE scintillator barrel; (c) time coincidence window between TOFINO and TOFONE hits: 4−18 ns. The geometrical acceptance of the FINUDA apparatus (from 45° to 135° polar angle) and these trigger conditions allow to collect a number of Bhabha pairs corresponding to about 700 nb of integrated Bhabha cross-section. It is worth reminding that the Bhabha cross-section strongly depends on the polar angle and has not a finite total value, but diverges at zero polar angle. With a nominal luminosity of $\mathscr{L}_{\text{inst}} = 5 \times 10^{31}\,\text{cm}^{-2}\,\text{s}^{-1}$, about 35 Hz Bhabha events are accepted by the trigger and recorded by the apparatus.

Other types of events, coming mainly from the $\phi(1020)$ decays, can filter through the Bhabha trigger as defined above, since their topologies basically fulfill, with lower efficiencies, the same criteria:

- $e^+e^- \to \phi \to K^0_S K^0_L$ followed by K^0_S decay $K^0_S \to \pi^+\pi^-$,
- $e^+e^- \to \phi \to \rho\pi$ followed by $\rho^{\pm 0}$ decay into two pions,
- $e^+e^- \to \phi \to \pi^+\pi^-\pi^0$,
- $e^+e^- \to \phi \to K^+K^-$ followed by $K^+ \to \mu^+\nu$, $K^+ \to \pi^+\pi^0$.

Among the mentioned processes, the $K^0_S \to \pi^+\pi^-$ decay gives the main contribution to the background of the Bhabha trigger. The other processes are efficiently rejected by the trigger or have lower branching ratios; their contributions to the total counts have anyway to be considered for an accurate evaluation of the luminosity. Finally, thanks to the selectivity of the trigger, the machine e.m. background hardly fulfills the trigger conditions and can be completely neglected.

In Fig. 3, an event $\phi \to K^0_S K^0_L$ followed by $K^0_S \to \pi^+\pi^-$, recorded with the Bhabha trigger and reconstructed by the FINUDA reconstruction procedure is shown.

The topologies of the two types of events (Bhabha and K^0_S decay) are very similar. The charged π's from a low momentum $K^0_S (\approx 110\,\text{MeV}/c)$ are also nearly back-to-back and mimic the trigger feature of the Bhabha events. The different average momenta of the produced π's, 206 MeV/c, instead of 510 MeV/c for the Bhabha events, do not prevent events from K^0_S decay to satisfy the trigger conditions. Simply, the K^0_S decay events will be collected with less efficiency respect to the Bhabha events, due to the higher curvature of the π's in the high magnetic field of FINUDA, hampering them to reach the external TOFONE scintillator barrel.

The instantaneous machine luminosity was continuously monitored by counting the reconstructed Bhabha events, in time intervals ΔT, and evaluating the following formula:

$$\mathscr{L}^{\text{Bhabha}}_{\text{inst}} = \frac{N^{\text{rec}}_{\text{Bhabha}}/\Delta T}{[\sigma_{\text{Bhabha}} \times \varepsilon_{\text{trig}} \times \varepsilon_{\text{rec}}]_{\theta > \theta_0} \times \varepsilon_{\text{detec}}} \qquad (2)$$

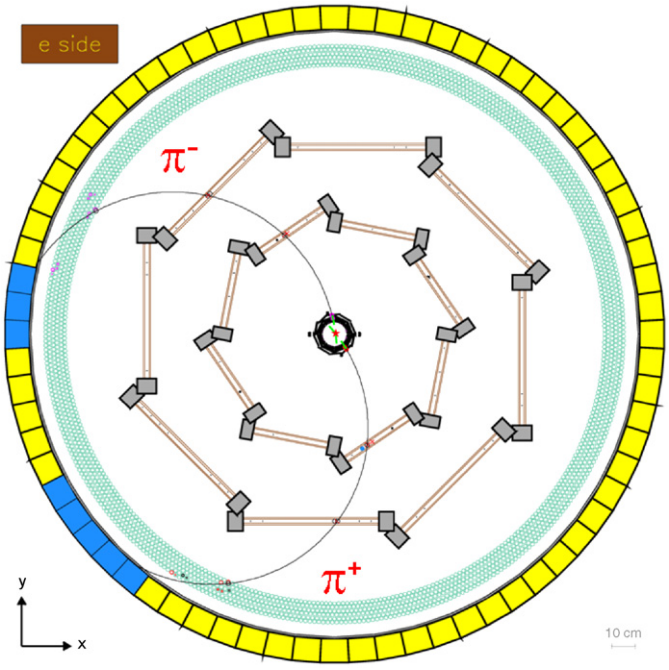

Fig. 3. Event $e^+e^- \to \phi$, $\phi \to K^0_L K^0_S$, $K^0_S \to \pi^+\pi^-$ recorded by the FINUDA spectrometer.

where $N^{\text{rec}}_{\text{Bhabha}}$ is the number of the Bhabha events reconstructed by the apparatus, σ_{Bhabha} is the Bhabha cross-section for emission polar angles larger than $\theta_0 = 30°$ (relative to the beam direction), $\varepsilon_{\text{detec}}$ is the global apparatus efficiency estimated with cosmic ray calibrations, and $\varepsilon_{\text{trig}}$ and ε_{rec} are the trigger and reconstruction efficiencies for Bhabha events. These efficiencies are calculated by the FINUDA Monte Carlo program using the Bhabha event generator from Ref. [5] and accounting for the beam characteristics. The values of $\varepsilon_{\text{trig}}$ and ε_{rec} for Bhabha events turn out to be 0.31 and 0.81, respectively.

The instantaneous machine luminosity was also calculated using the K^0_S decay events filtered inside the Bhabha trigger, by means of a formula similar to the relation (2):

$$\mathscr{L}^{K^0_S}_{\text{inst}} = \frac{N^{\text{rec}}_{K^0_S}/\Delta T}{[\sigma_\phi \times \text{BR}_{(K^0_S K^0_L)} \times \varepsilon_{\text{trig}} \times \varepsilon_{\text{rec}}] \times \varepsilon_{\text{detec}}} \qquad (3)$$

where $N^{\text{rec}}_{K^0_S}$ is the number of the K^0_S events reconstructed by the apparatus, σ_ϕ is the effective cross-section for the formation of the ϕ ($\sigma_\phi = 3.26\,\mu\text{b}$), $\text{BR}_{(K^0_S K^0_L)}$ is the branching ratio for the decay of the ϕ into $K^0_S K^0_L$, $\varepsilon_{\text{detec}}$ is the global apparatus efficiency, estimated with cosmic ray calibrations, and $\varepsilon_{\text{trig}}\,(= 0.29)$ and $\varepsilon_{\text{rec}}\,(= 0.78)$ are the trigger and reconstruction efficiencies, respectively, for K^0_S events calculated using the FINUDA Monte Carlo code.

The reconstruction of the events fulfilling the Bhabha trigger conditions was performed using two different procedures. A simple and robust one, called *single arm* procedure, was used mainly in the phase of the machine and apparatus commissioning. With this procedure, all hits generated by the two charged prongs of the triggered

events in the FINUDA detectors were fitted by only a single curved trajectory. The advantages of such a method are: (i) a high reconstruction efficiency for Bhabha events (larger than 90%); (ii) the use of several spatial points (up to 10) to reconstruct the *single arm* trajectory; (iii) the insensitivity to detector inefficiencies and possible single detector failures; (iv) the high rate of reconstructed events. At the nominal luminosity of $\mathscr{L}_{\text{inst}} = 5 \times 10^{31}\,\text{cm}^{-2}\,\text{s}^{-1}$, a rate of about 30 Hz of reconstructed Bhabha events are expected.

In Fig. 4 the momentum distribution of the *single arm* tracks reconstructed in the FINUDA apparatus, after a 10 min typical run with Bhabha trigger, is shown. The larger momentum peak around 500 MeV/c corresponds to elastic and highly elastic Bhabha events, whereas the smaller peak around 200 MeV/c corresponds to K^0_S events filtered inside the Bhabha trigger. Events in between the two peaks are mainly due to other processes, in particular to the $\rho^0\pi^0$ one. This process gives indeed a not negligible trigger rate, since it has a large branching ratio and produces energetic and almost back-to-back charged pions, the ρ^0 being produced almost at rest.

By counting the number of events in the Bhabha and K^0_S peaks and applying the relations (2) and (3), respectively, the value of the machine luminosity $\mathscr{L}_{\text{inst}}$ can be evaluated on-line from two different and independent physical processes. The results obtained were always in good relative agreement and nicely compatible with the luminosity evaluated by the machine staff. Moreover, since the K^0_S process depends not only on the instantaneous luminosity, but also on the centering of the machine energy on the ϕ resonance, the ratio between the contents of the two peaks allowed also the machine energy to be roughly monitored on-line during the machine commissioning phase.

The described *single arm* procedure is very efficient, robust and fast. However, it is not very accurate and has been complemented by a second reconstruction procedure, called *double arm* procedure, in which the two opposite charged arms of the triggered event are both reconstructed and accurately fitted. Results of the procedure have already be shown in Figs. 2 and 3 for a Bhabha and a K^0_S event, respectively. This procedure is slower, since it requests both tracks to be accurately measured, but allows the complete kinematics of the event to be reconstructed: the momentum of each prong with resolution of the order of few per mil, the vertex of the event (if any), the invariant mass of the two system of two tracks, according to a given mass hypothesis.

In Fig. 5 the invariant mass distribution for events with two opposite charged particles, collected during two runs with Bhabha trigger, is shown, in the hypothesis that the two tracks are e^+e^- pairs. The peak at the highest mass corresponds to highly elastic Bhabha processes. The machine collision energy during these runs as measured by the position of this peak results $M_{\text{inv}} = 1.019 \pm 0.015\,\text{GeV}/c^2$. The narrow peak at the lowest mass corresponds to the events from $K^0_S \to \pi^+\pi^-$: the peak is displaced from the nominal K^0_S mass simply due to the use of the electron mass instead of the pion one in the invariant mass formula. The broad structure in between the two main peaks corresponds to the decay of the $\rho^0(770) \to \pi^+\pi^-$ coming from the $\phi \to \rho\pi$ decay.

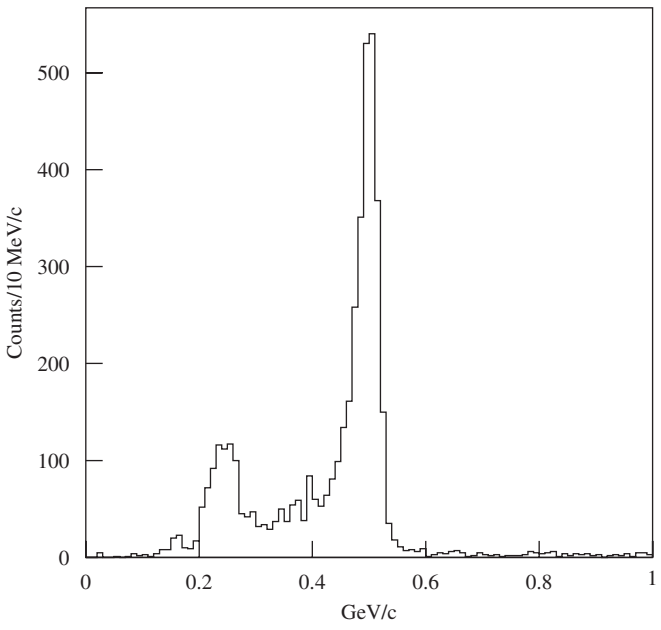

Fig. 4. The momentum distribution of *single arm tracks* reconstructed by FINUDA in a 10 min run with Bhabha trigger. The peak around 500 MeV/c corresponds to elastic and highly elastic Bhabha events. The other one, around 200 MeV/c, corresponds to K^0_S events filtered through the Bhabha trigger.

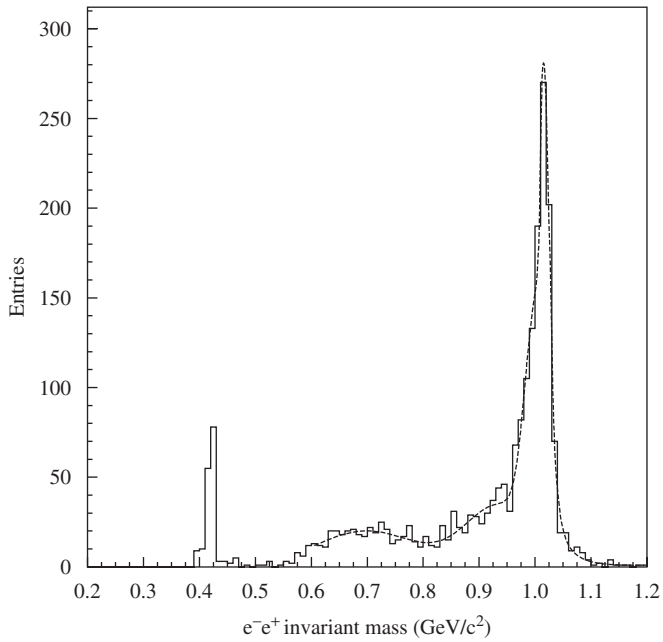

Fig. 5. Invariant mass of the (e^+e^-) system. The main peak at $M_{\text{inv}} = 1.019 \pm 0.015\,\text{GeV}/c^2$ measures the e^+e^- collision energy. This figure is obtained summing two Bhabha trigger runs to increase the statistics.

The analysis is performed offline, after the end of the run, analyzing the collected data and performing the complete reconstruction of the events. The Bhabha trigger runs have normally a statistics of 20 000 events which, at the typical (average) instantaneous luminosity $\mathscr{L}_{\text{inst}} = 4 \times 10^{31}\,\text{cm}^{-2}\,\text{s}^{-1}$, are collected in a time ΔT of $\approx$10 min.

In Fig. 6 the invariant mass is shown for the $\pi^+\pi^-$ mass hypothesis on events belonging to the same runs. The narrow peak at $M_{\text{inv}} = (0.496 \pm 0.002)\,\text{GeV}/c^2$ corresponds to the decay of the K^0_S, in good agreement with the PDG mass of the K^0_S, $M_{K^0_S} = 0.4977\,\text{GeV}/c^2$. The position and the width of the peak provide information on the absolute calibration and on the global mass resolution of the spectrometer. The wide bump on the right of the K^0_S peak corresponds, as already mentioned, to the decay of the $\rho^0(770) \to \pi^+\pi^-$.

The two above described methods (*single* and *double arm* procedures) provide a cross check of the measured values of the average luminosities, after a time interval ΔT of at least several minutes. This information is very useful but the delivering rate is not always fast enough to serve all the needs of the experiment. Due to the specific features of DAΦNE, the lifetimes of the beams are of the order of few tens of minutes, and the lifetime of the luminosity of their collision even shorter. Due to this fact, in order to properly tuning the machine and continuously checking its working conditions, the luminosity values must be known on an on-line basis. In other terms, instantaneous luminosities values or, at least, luminosities averaged in time intervals of the order of few seconds, must also be provided in order to be useful for the optimization of DAΦNE performance to the FINUDA needs.

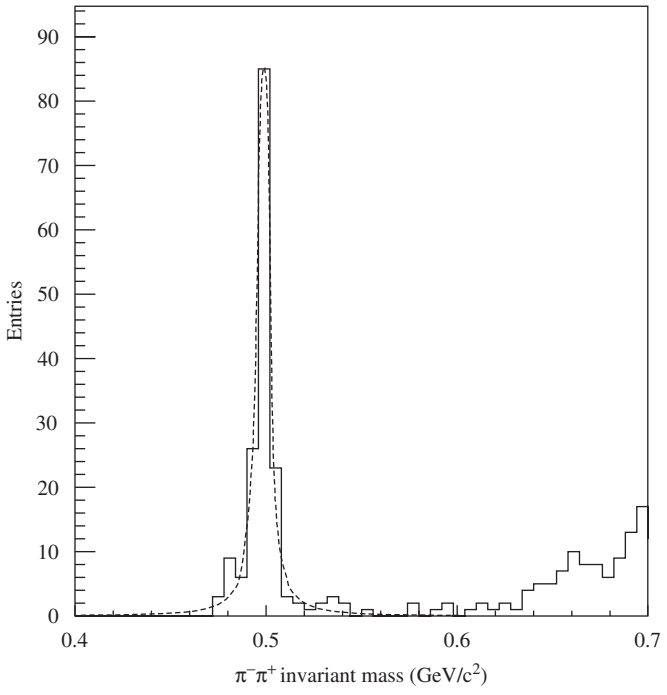

Fig. 6. Invariant mass of the $(\pi^+\pi^-)$ system. The narrow peak at $M_{\text{inv}} = 0.496 \pm 0.002\,\text{GeV}/c^2$ corresponds to the $K^0_S \to \pi^+\pi^-$ decay. This figure is obtained summing two Bhabha trigger runs to increase the statistics.

One possibility to obtain these instantaneous values is to calculate them using accelerator physics relations and standard machine parameters, continuously measured by instruments positioned along the rings. This procedure is accurate, but it is not a direct measurement of the luminosity in the FINUDA interaction region. A direct measurement can, however, be provided by the same FINUDA detectors.

To provide the on-line luminosity values in time intervals of the order of few seconds, FINUDA can exploit the counts of the scalers measuring the Bhabha trigger rate. Such counts are transformed in $\mathscr{L}_{\text{inst}}$ values using a conversion factor obtained from the Bhabha runs where events have been fully reconstructed. There is indeed a fixed relationship between the total counted Bhabha triggers and the total number of Bhabha events reconstructed with the above described procedure. This relationship has been determined using the FINUDA Monte Carlo code and tuned experimentally at the beginning of FINUDA runs, in order to find and optimize the conversion factor; then it has been used to provide the on-line values of the machine luminosity based on the Bhabha trigger rate.

The luminosity measured with this method, in spite of its larger error respect to those provided by the reconstruction procedures, is, however, precise enough for the aim of on-line monitoring the $\mathscr{L}_{\text{inst}}$ values of DAΦNE luminosity. Moreover, with this method, the values of $\mathscr{L}_{\text{inst}}$ can be obtained also when the trigger used in the data taking is not the Bhabha one since, in regime conditions, no reconstruction of Bhabha events is needed, but only the reading of a dedicated scaler permanently counting the Bhabha trigger conditions occurring during any run. The conversion factor (evaluated as 0.17) was periodically checked during the run period to verify its stability.

In Fig. 7a typical plot of the $\mathscr{L}_{\text{inst}}$ luminosity measurement provided with the method described above, is given. The figure shows the circulating e^- and e^+ currents, and the instantaneous and integrated luminosity values as measured by FINUDA during a 2 h period of data taking. For the sake of comparison, the instantaneous luminosity values calculated using accelerator physics relations by means of the data provided by DAΦNE monitoring devices are shown as well.

The luminosity measured using Bhabha events, both with the on-line and the offline methods, is, however, not very sensitive to the actual machine energy setting. Indeed, the behavior of the Bhabha cross-section is rather flat with c.m. energy and the determination of the true mass of the Bhabha system invariant mass is affected by radiative corrections. It is, however, pivotal for FINUDA to work exactly at the c.m. energy corresponding to the mass of the ϕ meson, to get the maximum flux of (K^-, K^+) pairs from its decay. In fact, with a width of the ϕ meson of only 4.43 MeV (FWHM), there is a loss of charged kaon beam

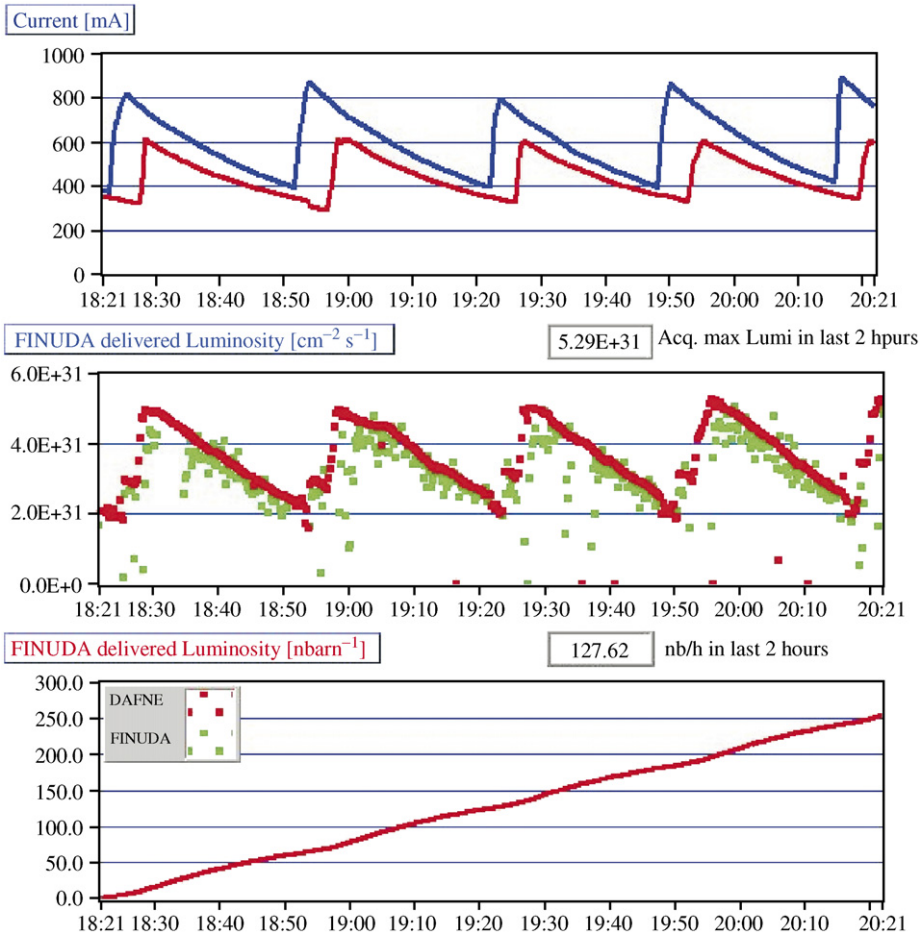

Fig. 7. The DAΦNE currents (top plot) for e^+ (red) and e^- (blue); the corresponding instantaneous luminosities (mid plot) as measured by FINUDA (green points) and provided by DAΦNE (red points), and the DAΦNE integrated luminosity (bottom plot), during a 2 h interval of data taking.

intensity of a factor 2 if the energy of both beams is displaced, for instance, of ± 1 MeV only from the nominal 510 MeV value. For such a small energy displacement, the variation of the Bhabha counts or the displacement of the invariant mass Bhabha peak are practically not detectable.

Hence, a different method of performing an accurate monitoring of both the luminosity and the c.m. energy had to be employed by FINUDA: the method is based on the complete reconstruction and counting of events coming from the $\phi(1020)$ decay mode into $K^0_S K^0_L$ collected during Bhabha runs. After the K^0_S mass peak has been identified (see Fig. 5), the number of corresponding events $N_{K^0_S}$ is divided by the number N_{Bhabha} of Bhabha events collected and reconstructed in the same run. This procedure is repeated changing slightly the energy of the two DAΦNE beams at each step. The tuning of the machine at the $\phi(1020)$ energy corresponds to the maximization of the ratio $N_{K^0_S}/N_{\text{Bhabha}}$. After the collider has been properly tuned in energy, this ratio is checked at regular time intervals to monitor its stability during the whole period of data taking. In Fig. 8 the ratio $N_{K^0_S}/N_{\text{Bhabha}}$ is shown during the whole data taking period of FINUDA. As it can be seen, after an initial period of beam tuning, the ratio remains roughly constant, demonstrating the stability of DAΦNE c.m. energy at the mass of the ϕ meson.

2.2. Measurement of the DAΦNE beam boost

FINUDA is able to monitor another important parameter of the DAΦNE machine: the transversal boost of the generated $\phi(1020)$ mesons. DAΦNE is a two rings collider and, due to this particular feature, in the FINUDA interaction region the e^+ and e^- beams do not collide exactly head on, but form a crossing angle different from zero and amounting to about 25 mrad. Due to this crossing angle, the $\phi(1020)$ mesons are not produced at rest, but have a small transversal momentum (boost) of 12.3 MeV/c. In the case of the FINUDA interaction point, the vector momentum is directed outward with respect to the center of the rings.

This small total momentum of the ϕ affects, of course, also the momenta of the (K^-, K^+) produced in the ϕ decay. Indeed, if the ϕ decay occurred at rest, the kaon momenta would be 127 MeV/c, independently from their direction, and their angular distribution would be symmetric around the e^+, e^- beam axis. The presence of a transversal beam

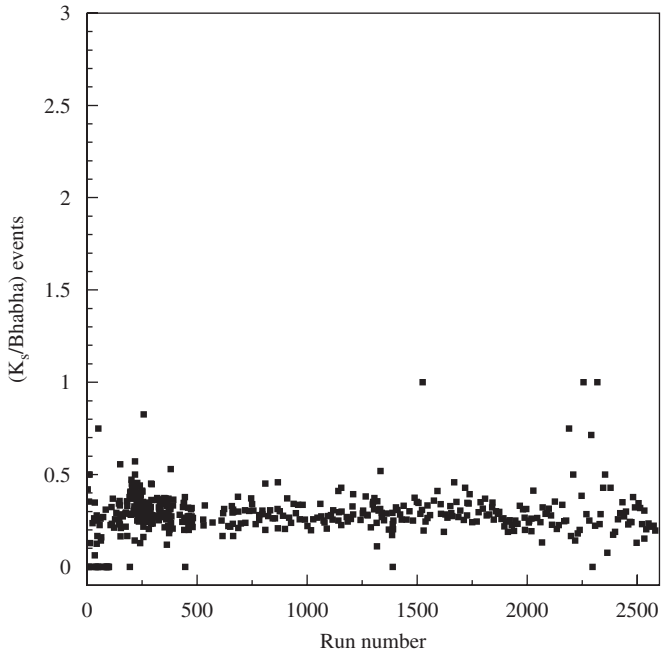

Fig. 8. Ratio of the counts of the reconstructed events in the K^0_S peak over the corresponding counts of the reconstructed events in the Bhabha peak, as a function of the run number, during the whole period of the FINUDA data taking, including also debugging, test and short runs.

boost changes the values of the kaon momenta making them dependent on the azimuthal angle of emission: the momenta are slightly increased in the boost direction and decreased in the opposite one. Moreover the kaon emission distribution is modified and is no longer axially symmetric.

These features of the DAΦNE kaon beam are of big relevance for FINUDA, which is optimized to study interactions of stopped kaons in thin targets of different materials. Due to the low momentum of the generated charged kaons, their energy loss in crossing the beam pipe, the TOFINO scintillator, the silicon micro-strips of the vertex detector and the target materials is huge and increasing highly non-linearly during the slowing down. Therefore, a variation of the beam crossing angle, and consequently of the momenta of the charged kaons, could change their range, and modify their stopping distribution inside the targets.

In fact, the thicknesses of the different targets have been determined in order to have the K^- stopping point distribution as close as possible to their outward surface, in order to minimize the amount of residual target material crossed by the outgoing particles and, consequently, the perturbation of their momentum to be measured in the spectrometer. In extreme cases, the charged kaons may not even stop in the thin targets, either stopping before or passing through them.

For this reason, it is of paramount importance for FINUDA to check, during the data taking, that the beam boost remains constant and stable at the nominal value. The monitor of the stability of the beam boost is performed, by FINUDA, on a run-to-run basis, by means of a set of events periodically collected using the Bhabha trigger prescaled to the main hypernuclear trigger. To this aim, a sample of Bhabha events, fully reconstructed and recognized as highly elastic by the values of the momenta of both positive and negative prongs close to 510 MeV/c, is selected. For each event, the reconstructed momenta of the e^+ and of the e^- are then vectorial added and the magnitude of the resulting total momentum is calculated.

The magnitude of the total momentum of the event may differ from zero due to several reasons, a part from the presence of the total beam boost: radiative losses of the electron or positron, deviations of the trajectories due to multiple scattering or errors in the reconstruction. The distribution, however, of the values of the magnitude of the total e^+ and e^- momentum should show a minimum value, that corresponds to the magnitude of the boost of the not perfectly head-on (e^+e^-) collision. This minimum value should be zero in case the Bhabha reaction was due to e^+ and e^- with momenta of equal magnitude and colliding exactly head on, and should correspond to the boost of the DAΦNE e^+e^- beams, in the FINUDA interaction region, when different from zero.

In Fig. 9 the distribution is shown of the magnitude of the total momentum of the positive and negative reconstructed tracks of Bhabha highly elastic events. The straight line fit to the shoulder of the distribution allows to determine, by its intersection with the momentum axis, the boost of DAΦNE. In this example, it amounts to about 12.5 MeV/c, as expected from e^+ and e^- beam interaction with the nominal crossing angle of 25 mrad. This procedure

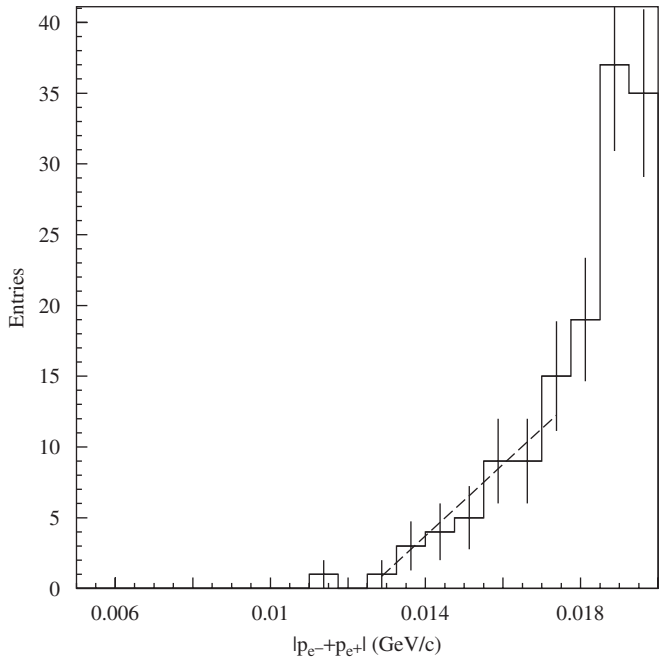

Fig. 9. Distribution of the magnitude of the vectorial sum of the e^+ and e^- momenta in Bhabha trigger runs. The intersection of the dashed line with the abscissa axis gives the value of the DAΦNE boost momentum. In order to increase the statistics in the shoulder region, five consecutive Bhabha runs have been summed up.

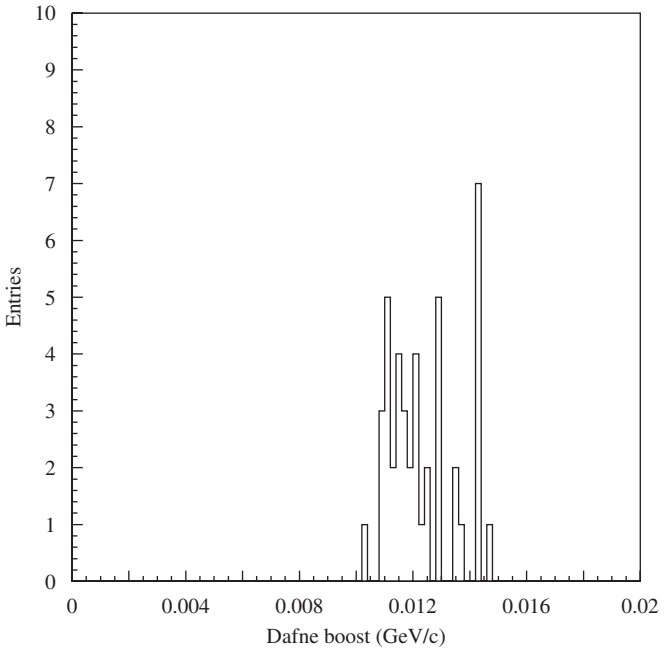

Fig. 10. The distribution of the DAΦNE boost momentum measured by FINUDA during the whole period of data taking (consecutive Bhabha trigger runs have been summed up five by five increasing the statistics to better determine the boost value).

has been performed systematically during the whole data taking, to check the value of the DAΦNE boost.

The result of this monitoring is plotted in Fig. 10 for the whole data taking period and shows how FINUDA is able to measure the boost value of DAΦNE during the data taking. This information can be used during the data analysis to improve the event reconstruction.

2.3. *Distribution of the* e^+e^- *collision points*

FINUDA is also able, on a run-to-run basis, to monitor both the distribution of the e^+e^- collision points and the distribution of the $\phi(1020)$ decay vertexes, using two different types of events. This information is relevant, since the limited extension along the beam axis of the FINUDA vertex region and the geometry of its tracking volume, symmetrical around the e^+e^- axis and covering a polar angle of acceptance from about 45° to 135°, require to center the spot of the e^+e^- collisions in the middle of the spectrometer, in order to maximize its geometrical acceptance.

The distribution of the e^+e^- collision points can be measured, especially during the commissioning phase, using the reconstruction of the Bhabha events with the *single arm* procedure. In fact, each *single arm* trajectory, which averages the trajectories of the two single e^+e^- prongs, crosses the horizontal plane in which the e^+e^- beams are contained. This crossing point is a good estimation of the e^+e^- collision point, where the two prongs are generated. It is worth reminding, in fact, that the DAΦNE collision spot is essentially distributed along the beam axis z and in the transverse direction x, since in the vertical direction y its spread is just 20 μm.

In Fig. 11 the distributions of the x and z coordinates of the e^+e^- collision spot, obtained with the fast *single arm* procedure in only one run of $\Delta T = 10$ min, are shown, together with the corresponding scatter plot. It should be worth noticing that the x distribution obtained with this method is not corrected for the boost effect; this can be seen from the mean value of the x distribution, which is displaced in the $+x$ (i.e. boost) direction.

The distribution of the $\phi(1020)$ decay vertexes may be obtained, during the data taking, by the accurate reconstruction of the origin vertexes of the K^+K^- pairs. The reconstruction procedure of the K^+K^- trajectories is based on a two helix algorithm that accounts for the average value of the mass of the $\phi(1020)$ and for the e^+e^- beam crossing angle (25 mrad). The algorithm determines, event by event, the ϕ formation point and the two kaon directions and momenta, solving possible ambiguities. Input information to the procedure are the interaction points of the two kaons on the ISIM micro-strips facing the two TOFINO fired slabs. The hits of the kaons on ISIM are recognized, against the hits of the other particles, thanks to the high specific ionization of the very slow kaons.

The exact K^+K^- trajectories and stopping points are then calculated by a tracking procedure based on the GEANE tracking package [6] and starting from the ϕ formation point and the K^- and K^+ directions and momenta. The procedure accounts for the geometrical structure and the material composition

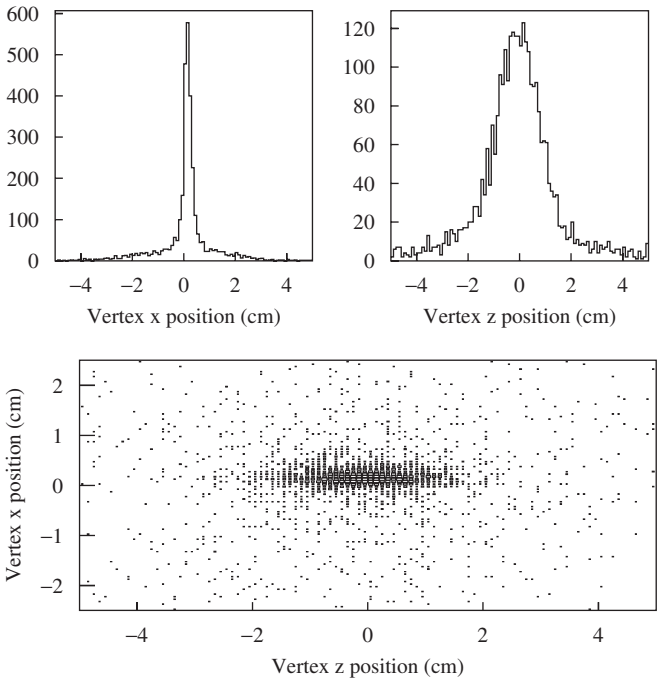

Fig. 11. Distributions of the x (top left) and z (top right) e^+e^- collision points as reconstructed by FINUDA with the *single arm* procedure in one Bhabha trigger run. Bottom: the corresponding x vs. z scatter plot.

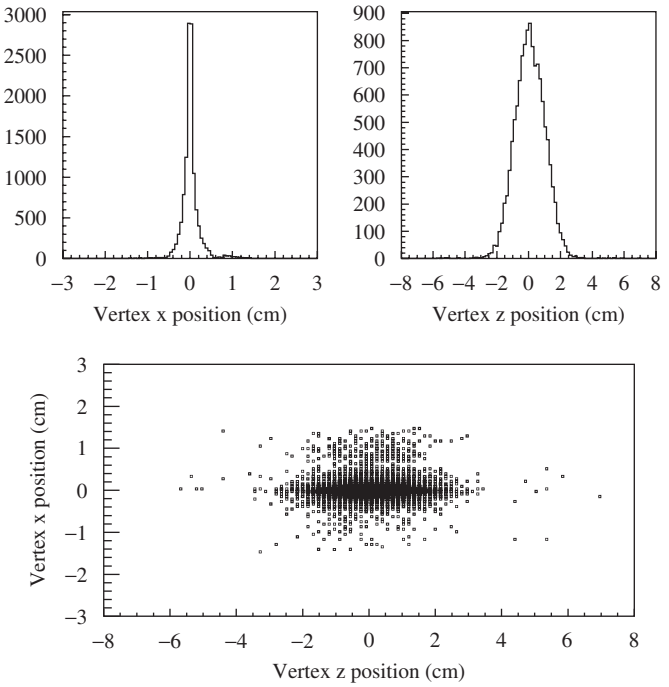

Fig. 12. Distributions of the x (top left) and z (top right) ϕ vertexes as reconstructed by FINUDA with the *double arm* procedure in runs using the trigger optimized for hypernucleus event selection. Bottom: the corresponding x vs. z scatter plot.

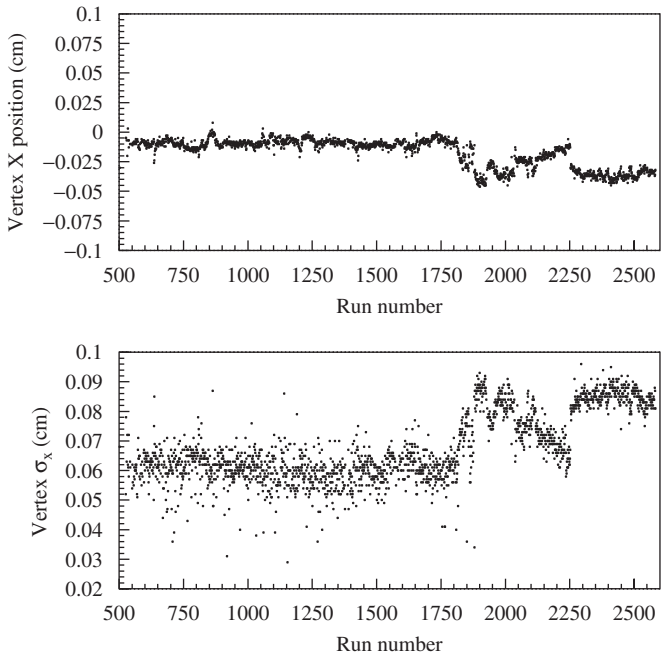

Fig. 13. The centroid (top) and the σ (bottom) of the x distribution of the ϕ vertexes as a function of the run number during the FINUDA data taking period.

of the vertex region, accurately described in the FINUDA Monte Carlo program. As an example of the result obtained, the distributions of the K^-K^+ origin vertexes, in a typical run, are shown in Fig. 12. In the picture, the horizontal transverse x and longitudinal z distributions of

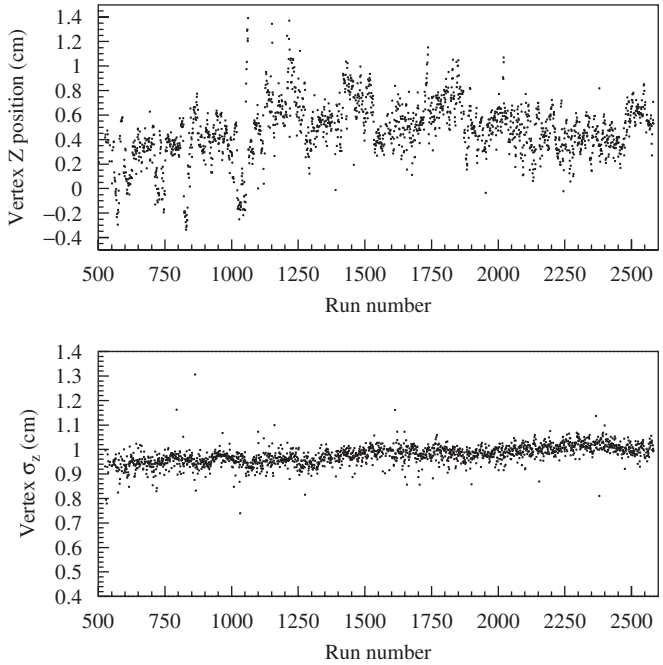

Fig. 14. The centroid (top) and the σ (bottom) of the z distribution of the ϕ vertexes as a function of the run number during the FINUDA data taking period.

the $\phi(1020)$ vertexes are shown, as well as the x vs. z scatter plot. It should be noted that, with the *double arm* procedure, the boost effect is properly taken into account and, correspondingly, the x distribution is centered at the origin.

By means of this last procedure, the stability in position and width of the $\phi(1020)$ decay vertex distribution was monitored during the whole data taking. In Fig. 13 (Fig. 14), the center and the sigma of the transversal-x (longitudinal-z) coordinates of the vertexes during the whole period of FINUDA data taking are plotted, showing the pretty good stability of the $e^+e^- \rightarrow \phi(1020)$ generation positions in DAΦNE.

3. Conclusions

The FINUDA spectrometer, devoted to hypernuclear physics, employs, for the first time, an e^+e^- collider to provide the primary K^- beam. The apparatus is able, during the normal data taking, to provide also information on the machine performances: instantaneous luminosity, total beam boost, distribution of e^+e^- collision points. This information, provided to the machine staff on-line and off-line, in a run-to-run basis and in a continuous way, allows for the optimization, the stability control and background reduction of the DAΦNE accelerator. Moreover, the information on the DAΦNE performance is provided without perturbing the ordinary collection of data for the primary physical aims of the experiment.

Acknowledgments

We intend to acknowledge the DAΦNE machine staff for their skillful handling of the collider and the FINUDA technical staff for the assistance during all the stages of the experiment. We also acknowledge the authors of the *Babayaga* program for the generation of the Bhabha events for their help and advice.

References

[1] C. Milardi, et al., DAΦNE operation with the FINUDA experiment, in: Proceedings of the Ninth European Particle Accelerator Conference (EPAC 2004), Lucerne, Switzerland, 5–9 July 2004, p. 233.
[2] M. Agnello, et al., Phys. Lett. B 622 (2005) 35.
[3] H.J. Bhabha, Proc. Roy. Soc. A 154 (1936) 195.
[4] Particle Data Group, Phys. Lett. B 592 (2004) 309.
[5] C.M. Carloni Calame, C. Lunardini, G. Montagna, O. Nicrosini, F. Piccinini, Nucl. Phys. B 584 (2000) 459.
[6] V. Innocente, et al., GEANE: Average Tracking and Error Propagation Package, CERN Program Library, W5013-E, 1991.

A.2 Beam-induced backgrounds in the CLIC 3 TeV CM energy interaction region

Beam-induced backgrounds in the CLIC 3 TeV CM energy interaction region

B. Dalena[1,2], J. Esberg[2,3] and D. Schulte[2]

1- CEA/SACLAY, DSM/Irfu/SACM - 91191 Gif-sur-Yvette - France
2- CERN - Geneva - Switzerland
3- Department of Physics and Astronomy, Aarhus University, Denmark

Luminosity spectrum and accelerator background levels strongly influence the experimental conditions and have an important impact on detector design. The expected rates of the main beam-beam products at CLIC 3 TeV CM energy, taking into account for machine imperfections, are computed. Among the other machine-induced background the photon fans from the Incoherent Synchrotron Radiation (ISR) photons emitted in the final doublet are evaluated.

1 Introduction

In the design of the CLIC interaction region the background levels need to be carefully taken into account, since their rates are expected to be high because of the high energy and high luminosity foreseen. Two main sources of background can be identified: those coming from the beam interactions before and after the collision point, the so called machine backgrounds, and those arising from beam-beam effects, so called beam-beam background. In this paper we review the main beam-beam products in order to give an upper limit to their expected rates, the impact on the luminosity spectrum is also discussed. The distribution of their expected energy and angle are shown. Furthermore we discuss the impact of ISR photons coming from the final doublet on the CLIC interaction region.

Total Luminosity	$[10^{34}\text{cm}^{-2}\text{s}^{-1}]$	5.9
Peak Luminosity	$[10^{34}\text{cm}^{-2}\text{s}^{-1}]$	2.4
repetition freq.	[Hz]	50
bunches/train		312
intra-bunch dist.	[ns]	0.5
particles/bunch	$[10^{10}]$	0.372
bunch length	$[\mu\text{m}]$	44
emittances H/V	[nm]/[nm]	660/20
beam sizes	[nm]/[nm]	45/1

Table 1: CLIC parameters taking into account machine imperfections.

In order to achieve the required luminosity the two beams at the future linear colliders are focused to very small sizes, see Table 1. In electron-positron collisions the electromagnetic field of each bunch will focus the other, leading to an enhancement of total luminosity (so-called Pinch effect). At the same time due to the strong bending of their trajectory, the beam particles emit high-energy photons (called beamstrahlung photons), which smear the peak of the luminosity spectrum, as shown in Fig. 1.

In addition to beamstrahlung photons also QED and QCD backgrounds are produced during collision. The relevant processes are: coherent pair production, incoherent pair production and $\gamma\gamma \to$ hadrons events. They are briefly described in the next section. The pairs produced in the coherent processes can contribute to luminosity $\sim$4% of the total luminosity comes from these pairs mainly in the low energy tail of the spectrum. They can also create collisions where an electron, from a coherent pair produced in the positron beam, collides with the electron beam (and vice versa for a positron). The contribution of these

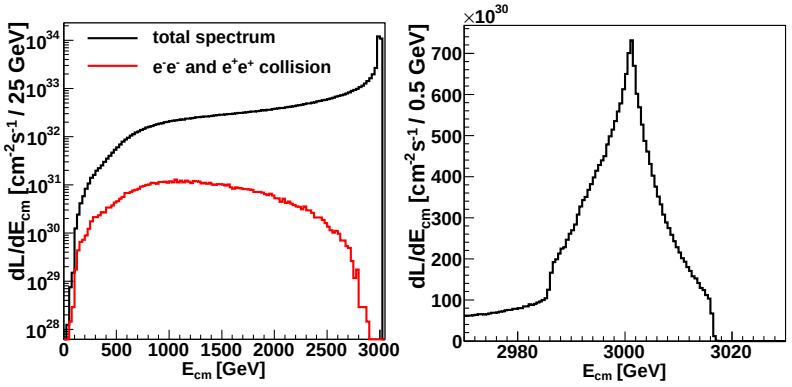

Figure 1: Luminosity spectrum for nominal CLIC 3 TeV CM energy parameters.

type of collisions to the luminosity is ∼1%, which correspond to the red line showed in Fig. 1.

2 Beam-Beam backgrounds at 3 TeV CM energy

The beam-beam backgrounds rates are computed using the GUINEA-PIG code [1]. In the simulations we use realistic bunch shapes coming from the full tracking of the two beams in the LINAC and the BDS systems toward the Interaction Point (IP). For this purpose the C++ version of the code [2] has been extensively reviewed and further developed. The beam-beam effects and processes that can be studied by GUINEA-PIG are: emission of beamstrahlung photons, coherent processes such as creation of pairs particles in the strong electromagnetic field of the two bunches, and incoherent processes such as incoherent pairs creation and hadronic events. Other QED processes such as Bhabhas can be simulated as well.

Due to the strong focusing forces generated by the electromagnetic field during interaction, quite a lot of energy goes in the emission of synchrotron radiation photons, so called beamstrahlung photons, generating the long energy tail in the spent beam distribution. On average two beamstrahlung photons are emitted per beam particle. Their energy distribution is peaked at low values but a significant number of them can reach the nominal beam

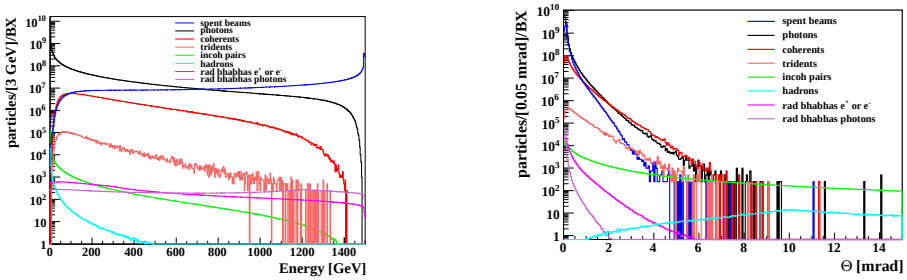

Figure 2: Energy distribution (left) and angular distribution (right) of the particles produced in beam-beam background.

energy, as shown in Fig. 2(left). At CLIC energies, where the beamstrahlung parameter Υ can be much larger than 0.5, the emitted photons can turn into e^+e^- pairs by interacting with the collective field of the oncoming beam, so called coherent process. The energy spectrum of the produced pair depends on the beamstrahlung parameter, very low energy pairs are created only for high value of Υ. The angular distribution is boosted in the direction of the mother particle of the intermediate photon. The red lines in Fig. 2(left) and Fig. 2(right) show their expected energy and angular distribution. In CLIC the coherent pair creation is the dominant process which produces e^+e^- pairs during collision, 6.6×10^8 coherent pairs are expected. Nevertheless at quantum beamstrahlung regime Υ >1 and for very short bunch length the creation of pair may occur by an intermediate virtual photon, in which case the pair production is said to occur by the trident process. The recent implementation of this process in GUINEA-PIG++ is described in [3], their production in the code follow the one of the coherent pairs, except for the virtuality of the intermediate photon. The expected energy spectrum and their angular distribution for the nominal CLIC beams are shown by the light-red in Fig. 2(left) and Fig. 2(right), respectively. As coherent pairs they follow mainly the beam direction while leaving the interaction region. Their angular distribution is well confined in the 10 *mrad* opening angle of the interaction region beam pipe.

Most of the low energy e^+e^- pairs are created at the future linear colliders by individual scattering of particles according to three main processes, the so called Breit-Wheeler ($\gamma\gamma \rightarrow e^+e^-$), Bethe-Heitler ($e^\pm\ \gamma \rightarrow e^\pm\ e^+e^-$) and Landau-Lifshitz ($e^+e^- \rightarrow e^+e^-e^+e^-$) processes. Their are well known QED processes widely described in standard textbooks [4]. The main formulas implemented in GUINEA-PIG are described in [5]. Their expected rate in CLIC is $\sim 330\times10^3$, lower then the coherent pair one. Having very low energy, they can be highly deflected in the electromagnetic field of the incoming bunch therefore, they can enter in the detector region. The same process can lead to the production of muon pairs as described in [3], the expected number of muons pair is 12.5 per bunch crossing.

Hadronic events are produced at e^+e^- colliders through the $\gamma\gamma \rightarrow$ hadrons reaction. The cross section is known experimentally up to 200 GeV. Different parameterizations of the cross section with the energy are implemented in GUINEA-PIG. According to the one in [6] the expected number of $\gamma\gamma$ collisions per bunch crossing is 3.2 for a center of mass energy of the two photons of $>$ 2 GeV. The energy distribution of the produced hadrons is peaked at low energy and their angular distribution is more central then the incoherent pairs one, allowing them to reach the central detector region.

$\Delta E/E_{BS}$	29%
n_γ	2.1 per beam particle
$N_{coherent}$	66×10^7
$N_{trident}$	67×10^5
$N_{incoherent}$	330×10^3
$N_{incoh-muons}$	12.50
$N_{hadrons}$	3.2
$N_{radiative-Bhabhas}$	110×10^3

Table 2: Average energy loss due to beamstrahlung and expected beam-beam background rates per bunch crossing for the beam parameters reported in table 1.

Radiative Bhabhas is another well known QED process, in which the binary collision of the electron-positron lead to the emission of a photon in the final state ($e^+e^- \rightarrow e^+e^-\gamma$) [7]. At lowest order the process (in t channel) can be modeled as a two steps reaction: first an e^-/e^+ is substituted by its photon equivalent spectrum, then the compton scattering of the photon on the e^+/e^- is calculated. The expected rate at CLIC is $\sim110\times10^3$. The energy and angular distributions of the scattered e^-/e^+ and photon are shown by the pink and light-pink curve in Fig. 2(left) and Fig. 2(right). Their

energy is spread over a wide range (from 0 up to the nominal beam energy). Their angular distributions are mainly peaked in the very forward direction.
All the expected beam-beam background rates we have studied are summarized in Table 2. The emittance values considered in the simulations include the budgets for imperfections. The actual values depend on the single machine and change during operation.

2.1 Machine imperfections and background rates

If machine imperfections are well controlled the final emittance of the two beams can be lower then the one reported in Table 1, leading to a high luminosity and high background rate. The overall correlation of the background rates with the horizontal and vertical emittance of the two beams has been studied in [8]. In the following we report the evaluation of an upper limit of the rate of the two backgrounds of interest for the detectors, such as incoherent pairs and hadronic events. For this purpose we track the two beams in the Main LINAC and the BDS considering realistic imperfections and nominal beam parameters at the entrance of the LINAC, using the tracking code PLACET [9]. We consider here machine imperfections in the vertical plane only, which is the most critical one due to the very small emittance. The vertical emittance at the entrance of the main LINAC is 10 nm and the machine imperfections considered in the simulation are reported in Table 3.

imperfections	dim.	value
BPM vert. offset	μm	14
BPM resolution	μm	0.1
accelerating structure vert. offset	μm	7
accelerating structure vert. tilt	μrad	142
quadrupole vert. offset	μm	17
quadrupole vert. roll	μrad	100
beam parameters	dim.	value
Bunch charge N	particles	3.72e+09
Bunch length σ_z	μm	44
hor. emittance $\gamma\epsilon_x$	nm	660
vert. emittance $\gamma\epsilon_y$	nm	10

Table 3: Values of the machine imperfections and beam parameters used in the main LINAC simulations.

These imperfections are enough to bring the vertical emittance of the nominal beams to growth up to several order of magnitude if no correction scheme is applied to the machines. When the Beam-Based-Alignment (BBA), described in [10], is applied to the machines the average emittance growth at the end of the ML stays well below five nm, which is the budget for static imperfections in the main LINAC. We steer the beams coming from the corrected linacs into the BDS, and track them to the IP, without any imperfections in the BDS. The bunch shapes, so obtained, are used to compute luminosity and background rates again. This procedure allow us to evaluate the effect of imperfections in the Main Linac only on the luminosity and on the background rates. Moreover since further machine imperfections in the BDS would only lower the luminosity and background rates, this assumption ensure that we estimate a maximum value for the background rates.

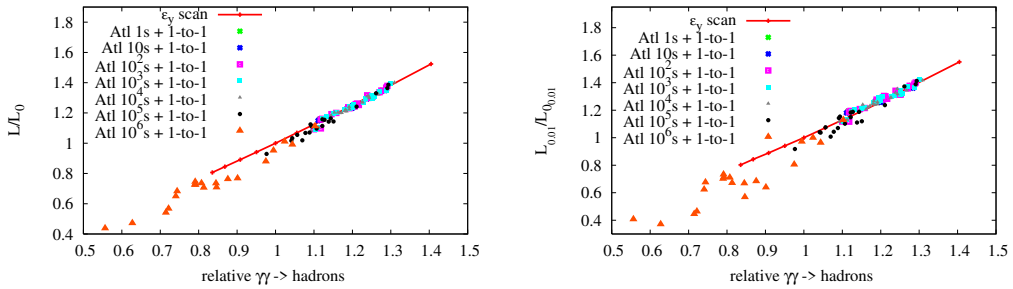

Figure 3: Total luminosity L(left) and Peak luminosity $L_{0.01}$(right) vs number of $\gamma\gamma \rightarrow$ hadrons events, normalized to the nominal values, for perfect machines and different vertical emittance values, and for corrected machines and nominal vertical emittance.

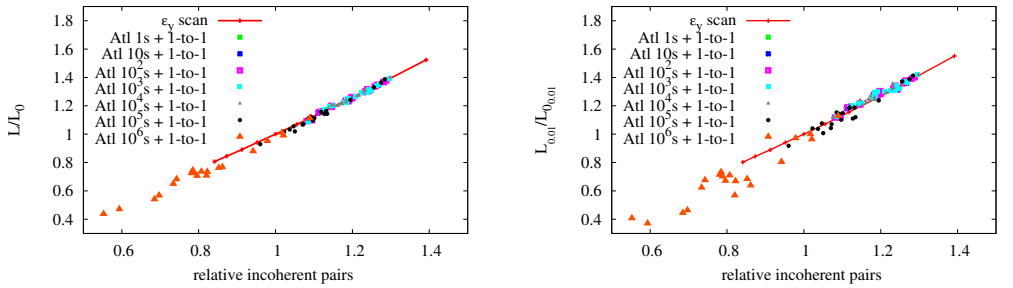

Figure 4: Total luminosity L(left) and Peak luminosity $L_{0.01}$(right) vs number of incoherent pairs events, normalized to the nominal values, for perfect machines and different vertical emittance values, and for corrected machines and nominal vertical emittance.

The cases of perfect machines and scaled beam emittances, as in Figs. 3 and 4 are compared with the cases of corrected machines and initial nominal beam parameters. The Total and Peak luminosities are shown in separeted plots. We define Peak Luminosity the luminosity contained into ±1% around the 3 TeV CM peak.
The correlation between luminosity and background rates variations is linear for both the background types considered, and it stays linear for both total(L) and peak($L_{0,01}$) luminosity. The fluctuation in the variation of luminosity and background rates for the corrected machines is on average ∼5%, indicating that different emittance values can be reached by the different machines after the linac BBA correction. In these simulations the mean luminosity reached by the corrected machines is about 30% higher than the values reported in Table 1, and on average 25% more background with respect to the values in Table 2. When 10^6 s of ground motion is applied to the Main LINAC the luminosity and background rates start to fluctuate more around the linear behavior (the fluctuations of the background rates are $> 15\%$). The majority of the machines have a relative low luminosity while still a significant number of hadronic events and incoherent pairs can be produced. Even though the background rates stay below the values quoted in Table 2. A safety margin of 50% more luminosity and 40% more background (for both hadronic events and incoherent pairs) can

be defined. Detectors should thus be able to handle this level in order not to have to reduce luminosity to reduce background.

3 Synchrotron Radiation photons from the final doublet

In order to provide an acceptable cleaning efficiency of the desired beam halo the collimation apertures are determined from the following conditions:

1. minimize the synchrotron radiation photons emitted in the first final quadrupole magnet which can hit the 2nd final quadrupole (QD0);

2. minimize the beam particles that can hit either QF1 or QD0.

Macroparticles with high transverse amplitude are tracked using the code PLACET [9], taking into account the emission of synchrotron radiation and all the non linear elements of the system. The particles positions and angles have been checked at the entrance, in the middle and at the exit of QF1 and QD0. The dangerous particles are efficiently removed for collimator apertures of $< 15\ \sigma_x$ in the horizontal plane and of $< 55\ \sigma_y$ in the vertical plane. Therefore we define 15 σ_x and 55 σ_y as the collimation depths [11].

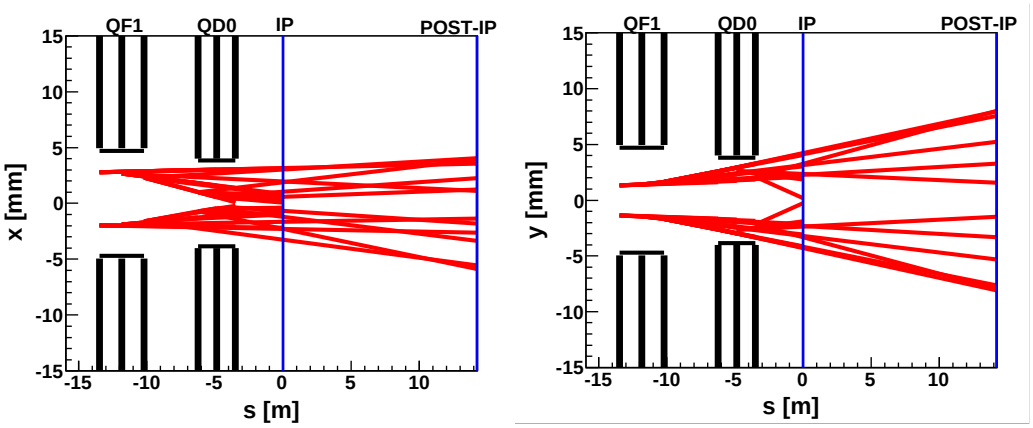

Figure 5: Incoherent Synchrotron radiation photon fans at 3 TeV.

Fig. 5 shows the residual synchrotron radiation fans from the final quadrupoles QF1 and QD0 to the IP for an envelop covering 15 and 55 standard deviations in x and in y, respectively. At the IP the photon cone is inside a cylinder of radius of five mm, which is well inside the beam pipe aperture. Therefore, in principle, they are not an issue of concern for the detectors.

The distribution of the expected energy of the radiated photons in the final doublet for a perfect machine and nominal beam parameters is shown in Fig. 6. The spectrum is peaked at very low energy, i.e. < 1 MeV, with an energy tail up to ~ 1 GeV. The number of radiated photons is ~ 1 for beam particle. An internal shielding of the beam pipe in the final doublet magnets region should be foreseen.

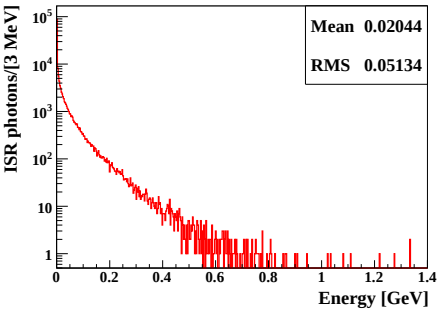

Figure 6: Energy of synchrotron radiation photons emitted in the final doublet.

4 Conclusion

Beam-beam effects at CLIC 3 TeV CM energy have been reviewed. The expected production rates, their energy and angular distribution evaluated. A safety margin of 40% of the background processes of interest for the detectors is estimated. The ISR photon fans coming from the final doublet is shown to be well inside the beam pipe aperture at the IP, considering the nominal collimation depths. Their energy distribution is peaked at few MeV.

References

[1] D. Schulte, *Beam-Beam Simulations with GUINEA-PIG*, ICAP98, Monterey, CA, USA (1998).

[2] G. Le Meur *et al.*, *Description of GUINEAPIG++, the C++ upgraded version of the GUINEA-PIG beam-beam simulation program*, EUROTeV-Report-2008-067.

[3] J. Esberg, *Simulations of the interaction point for the TeV-scale e^+e^- colliders* IPAC'11 proceeding.

[4] for example: V.B. Berestetskii, E.M. Lifshitz and L.P. Pitaevskii, *Relativistic Quantum Theory*, Pergamon Press (1971).

[5] D. Schulte, *Study of the Electromagnetic and Hadronic Background in the Interaction Region of the TESLA Collider*, PhD-thesis, TESLA 97-98(1997).

[6] G.A. Schuler and T. Sjostrand, *gamma-gamma Physics at Linear Colliders*, CERN-TH/96-119 (1996).

[7] D.A. Karlen, *A Study of low Q^2 radiative bhabha scattering*, PhD-thesis, SLAC-235 (1988).

[8] B. Dalena and D. Schulte, *Beam-Beam background in CLIC in presence of imperfections*, IPAC10, Kyoto, Japan (2010).

[9] D. Schulte *et al.*, *Simulation Package based on PLACET*, CERN/PS, 2001/028.

[10] D. Schulte, *Beam-based alignment in the new CLIC main linac*, PAC09, Vancouver, Canada (2009).

[11] J. Resta Lopez *et al. Status report of the baseline collimation system of CLIC*, arXiv:1104.2426 and arXiv:1104.2431.

A.3 Strong field processes in beam-beam interactions at the Compact Linear Collider

Strong field processes in beam-beam interactions at the Compact Linear Collider

J. Esberg,[1,2] U. I. Uggerhøj,[1] B. Dalena,[2] and D. Schulte[2]

[1]*Department of Physics and Astronomy, Aarhus University, Ny Munkegade 120, 8000 Aarhus C, Denmark*

[2]*CERN, CH-1211 Geneva 23, Switzerland*

(Received 27 January 2013; published 27 May 2014)

The demand for high luminosity in the next generation of linear e^+e^- colliders necessitates extremely dense beams, giving rise to strong fields at the collision point, and therefore the impact of the field on the physical processes occurring at the interaction point must be considered. These processes are well described by the interaction of the individual lepton with the field of the oncoming bunch, and they depend strongly on the beamstrahlung parameter Υ which expresses the field experienced by the lepton in units of the critical field. In this paper, we describe calculations and simulations of strong field processes—also of higher order—at the interaction point.

DOI: 10.1103/PhysRevSTAB.17.051003 PACS numbers: 12.20.−m, 13.40.Em, 13.40.Ks, 13.66.De

I. INTRODUCTION

High precision measurements of possible new physics to be discovered at the CERN LHC are only achievable by a lepton machine due to the noncompositeness nature of the initial particles. In addition to being able to perform precision measurements of the Higgs particle, that measurements have shown exists [1,2], a high center-of-momentum (CM) electron-positron collider would possess potential for precision measurements of additional exotic particles in the high mass range, and in this respect, high energy is the key. Energy loss to synchrotron radiation dictates that a light lepton (e^+e^-) collider must be linear if the wall plug efficiency is to be acceptable.

In order to reach significant luminosity, the particle bunches must be very dense. This leads to the presence of strong fields in the rest frame of the particles in the opposing bunch. These fields may approach, or even exceed, the critical field value $\mathcal{E}_0 = m^2c^3/e\hbar = 1.32 \times 10^{16}$ V/cm. Thus, strong field processes may become important, as they, for example, lead to a significant reduction of the beam energy at the time of collision.

The deciding parameter, governing the yield of the strong field processes and the shape of the spectrum of the produced leptons, is the Lorentz invariant quantity Υ defined from

$$\Upsilon^2 = \frac{(F^{\mu\nu}p_\nu)^2}{m^2c^2\mathcal{E}_0^2}, \tag{1}$$

where $F^{\mu\nu}$ is the electromagnetic field tensor and p^μ ($\hbar k^\mu$) is the four-momentum of the impinging lepton (photon). In a frame where the field is solely electric and transverse to the particle motion, this reduces to $\Upsilon = \gamma\mathcal{E}/\mathcal{E}_0$ where $\gamma = E/mc^2$ is the Lorentz factor of the impinging particle ($\hbar\omega/mc^2$ in case of a photon) and $\mathcal{E}$ the local electric field, both measured in the same reference frame, for example, the laboratory. At the Compact Linear Collider (CLIC), an average value of the strong field parameter is $\bar{\Upsilon} \simeq 4$.

The program GUINEA-PIG [3] is one among several codes that can simulate the beam-beam dynamics and background production of a linear collider. The method of simulation is via a particle-in-box approach. Recently, the program was further developed [4] to object oriented C++ code that includes some spin effects and a new method of generating beamstrahlung. The present studies are based on development and usage of this code, with a strong link to experimental results. A more detailed description of a wide range of the topics can be found in [5].

II. THE CLIC PROJECT

Two very central keywords in the design of a e^+e^- collider are energy and luminosity. Nearly all components of such a machine are meant to increase one or both of these. While achieving the energy is often a matter of scaling of components, increasing luminosity for a fixed energy requires a wide range of precision instruments and submachines. In the effort to achieve the required energy and luminosity, the CLIC project strives towards the limiting boundaries of technology and physics in a multitude of ways, with, for example, high frequencies generated by interleaving bunches and a two-beam approach to acceleration. An extensive description can be found in [6] and key parameters can be found in Table 1.

An approximate expression for the instantaneous luminosity one can achieve with Gaussian bunches is

$$\mathcal{L}_0 = \frac{N^2}{4\pi\sigma_x\sigma_y} f_{\text{rep}} N_b \tag{2}$$

where N is the number of particles per bunch, $\sigma_{x,y}$ are the transverse bunch widths at the interaction point (IP), f_{rep} is the linac repetition frequency, and N_b is the number of bunches per train.

The deciding parameter for strong field effects in a collider is approximately given by [7]

$$\langle \Upsilon \rangle = \frac{5}{6} \frac{\gamma N r_e^2}{\alpha \sigma_z (\sigma_x + \sigma_y)}, \tag{3}$$

in this context known as the beamstrahlung parameter, with r_e being the classical electron radius, and σ_z the length of the beams at the IP. The yield and radiation characteristics of strong field processes depend strongly on the parameter Υ. In particular, the spectrum and yield of photons from the IP (beamstrahlung) naturally depends on this parameter.

When Eq. (3) is compared to the expression for the luminosity Eq. (2), one sees that high luminosity and high beamstrahlung parameter are intimately connected.

Since the beam size at the interaction point is $\sigma_{x,y} = \sqrt{\epsilon_{x,y}\beta^*_{x,y}}$, where β^* is the beta function at the IP, the small vertical emittance ϵ_y makes luminosity very sensitive to vertical beam displacements. Furthermore, $\sigma_y/\sigma_x \ll 1$, in order to keep luminosity (2) high while beam-beam effects relatively low [see Eq. (3)], so the beams are shaped like horizontal sheets of particles. Since $\sigma_y = 1$ nm at the IP, the final focusing superconducting quadrupole, QD0, must be stabilized with subnanometer precision—an extraordinary technological challenge.

A crossing angle between the beams is necessary with the current time structure of the train of bunches in order to avoid precollisional scattering. Since this means that incoming and outgoing beams are physically separated, the design of postcollision lines is simplified and the feedback and corrector systems are transversely separate. Crab cavities must be used, since the planned crossing angle for CLIC is much larger than the transverse to longitudinal beam ratio, $\sigma_x/\sigma_z \ll 20$ mrad. These cavities give the front and rear end of a bunch opposite transverse kicks which rotate the bunch in its average rest frame, recovering luminosity.

If the beta function varies significantly within the bunch length at the IP, the bunches are focused such that they have nominally hourglass-like shapes during interaction. This would also reduce luminosity significantly. However, the effect can, at least in theory, be mitigated by varying the focus of different transverse slices of the bunches, so-called traveling focus. Another option would be to decrease the bunch length in a tradeoff for a larger beamstrahlung parameter, Υ.

III. BEAM-BEAM EFFECTS

The electric field of one bunch is boosted by the Lorentz factor γ when observing it in the laboratory frame. When moving to the rest frame of one bunch, the Lorentz boosted field of the oncoming bunch is enhanced by a factor $2\gamma^2 - 1$, meaning that immensely strong electromagnetic fields exist in this frame. If the bunches are very dense and energetic, the field of one bunch is able to deflect the oncoming bunch significantly. This force focuses one bunch on the other during crossing, an effect that naturally

TABLE I. E_{cm}: CM energy; $\mathcal{L}$: total luminosity; $\mathcal{L}_{99\%}$: luminosity within 1% of the nominal CM energy; f_{rep}: repetition frequency; N_b: number of bunches per train; t_b: time between bunches; N: number of particles per bunch; $\gamma\epsilon_{x,y}$: horizontal, vertical normalized emittance; $\beta_{x,y}$: horizontal, vertical beta function at the IP; $\sigma_{x,y,z}$: horizontal, vertical, longitudinal beam size at the IP; $\delta_{e,p}$: relative electron/positron energy spread; α_c: crossing angle; f_{rf}: accelerating radio frequency.

	CLIC 3 TeV	CLIC 500 GeV	ILC 500 GeV	ILC 1 TeV
E_{cm} [GeV]	3000	500	500	1000
$\mathcal{L}$ [10^{34} cm^{-2} s^{-1}]	5.9	2.3	1.8[a]	4.9
$\mathcal{L}_{99\%}$ [10^{34} cm^{-2} s^{-1}]	2	1.4	1.13	2.23
f_{rep} [Hz]	50	50	5	4
N_b	312	354	1312	2450
t_b [ns]	0.5	0.5	554	366
N [10^9]	3.72	6.8	20	17.4
$\gamma\epsilon_x/\gamma\epsilon_y$ [nm rad]	660/20	2400/25	10000/35	10000/30
β_x/β_y [mm]	6.9/0.068	8/0.1	11/0.48	11.0/0.23
σ_x/σ_y [nm]	45/1	202/2.3	474/5.9	335/2.7
σ_z [μm]	44	72	300	225
δ_e/δ_p [%]	0.29/0.29	0.35/0.35	0.125/0.70	0.085/0.047
α_c [mrad]	20	20	14	20/2
f_{rf} [GHz]	11.994	11.994	1.3	1.3
$\langle\Upsilon\rangle$	4.9	0.21	0.062	0.20

[a]With waist shift, no traveling focus.

causes growth of the total luminosity. On the other hand the strong radiation resulting from the deflection causes energy loss that means that the mean collision energy is not the double beam energy, but the luminosity becomes a wide spectrum extending to low energies.

The decrease in effective beam size and following enhancement of luminosity can be quantified through the introduction of so-called disruption parameters [8,9]

$$D_{x,y} = \frac{2Nr_e\sigma_z}{\gamma\sigma_{x,y}(\sigma_x + \sigma_y)}. \quad (4)$$

The disruption parameters determine the characteristics of the beam-beam dynamics. The weak disruption regime, when $D \lesssim 0.5$, the intermediate regime when $0.5 \lesssim D \lesssim 5$, and strong disruption is when $D \gtrsim 5$ [9]. In the weak disruption regime, the focal point lies beyond the oncoming bunch, while it moves inside the oncoming bunch in the intermediate regime. In the strong disruption, or "pinching" regime, the central part of one bunch is essentially confined to the oncoming one. In the strong pinching regime, the interaction point may become unstable. One can empirically calculate the beam size as a function of the disruption parameters in the stable disruption regimes.

A. Central background processes

The total power of the main beam is 14 MW for CLIC at 3 TeV CM. This power should be disposed of properly and valuable information should be extracted from the spent beam as well. Approximately 29% of the beam power is converted into beamstrahlung photons i.e. about 4 MW. They have relatively small polar angles (< 5 mrad) and will therefore all exit through the postcollisional beam pipe. Equally, the dominant process of e^+e^- pair production, the coherent pair production, makes the disrupted beam include low energy pairs with angles of emergence from the IP < 10 mrad; see Fig. 1.

The production of secondary particles has two sides; as well as being a source of background, they provide useful signals for diagnostics, feedback, and luminosity optimization. The primary sources for a fast and direct luminosity signal are the incoherent pairs produced in binary collisions between particles such as e^+e^-, $e^+\gamma$, $e^-\gamma$, or $\gamma\gamma$. They are abundant and their numbers are proportional to luminosity. They have large production angles and thus populate an area of phase space which is otherwise unoccupied. This makes the incoherent pair signal a clean one.

Beamstrahlung from the interaction region has proven a useful diagnostics tool. More specifically it is useful for minimizing the beam sizes at the IP [3]. In the main dump, the physical separation from the charged beam allows for selective conversion of the beamstrahlung photons into muons, that can be counted in a Cherenkov detector behind the main dump. This is a useful signal for monitoring luminosity, and will provide feedback signals for the beam delivery system to maintain high luminosity.

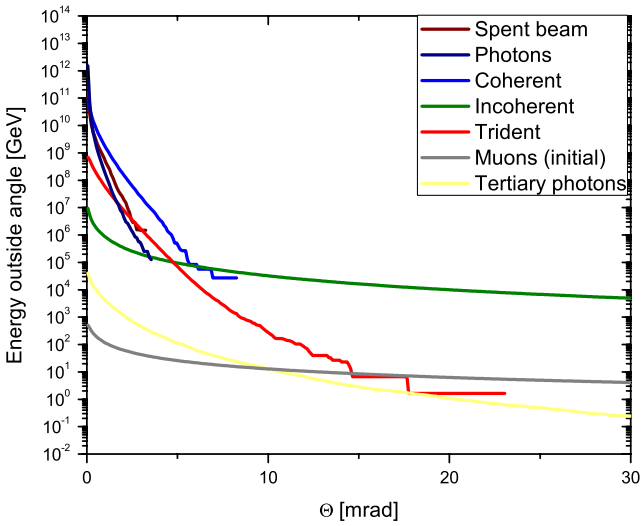

FIG. 1. Energy distributions of the disrupted particles produced at the IP as functions of angular cut. The muons shown here do not include the effect of disruption.

B. Beamstrahlung

Beamstrahlung, emitted from the IP, is confined to relatively small angles as seen in Fig. 1. In the current versions of GUINEA-PIG and GUINEA-PIG++, the radiation is emitted exactly in the direction of the radiating particle. This is approximately true for very energetic photons, but at very low frequencies $\omega \ll \omega_c$, the emission angle is $\theta \approx (2\omega_c/\omega)^{1/3}/\gamma$. The number of photons emitted is approximately [8,10,11]

$$n_\gamma = \frac{5}{2}\frac{\alpha^2}{r_e^2\gamma}\frac{\sigma_z\Upsilon}{\sqrt{1+\Upsilon^{2/3}}}, \quad (5)$$

which is roughly proportional to N/σ_x for $\Upsilon \ll 1$, where N is the number of particles per bunch, and α is the fine structure constant. Recent experimental investigations [12] have shown that the emission of synchrotronlike radiation in the strong field regime $0.05 < \Upsilon < 7$ is well described by theory. The generation of beamstrahlung in GUINEA-PIG++ closely follows that of CAIN [13], and there is an option to include spin-flip transitions via the Sokolov-Ternov mechanism. In the C version of the program, spin is not part of the properties of electrons.

C. Coherent pairs

Coherent pairs are the pairs generated from the conversion of beamstrahlung photons in the beam-beam field. The number of created coherent pairs in a constant field, applicable in the IP of a collider, is approximately

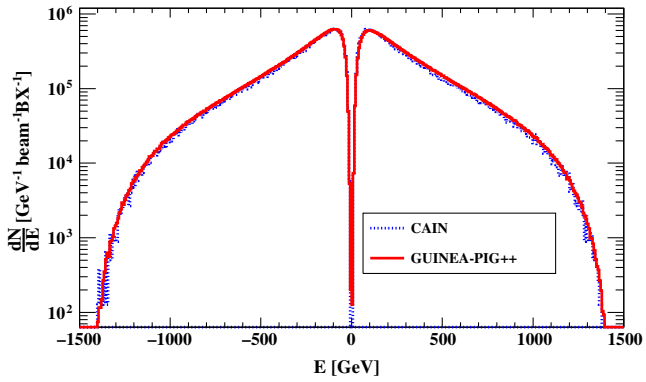

FIG. 2. Comparison between spectra of coherent pairs produced by CAIN and GUINEA-PIG++. The sign of the energy corresponds to the sign of the charge.

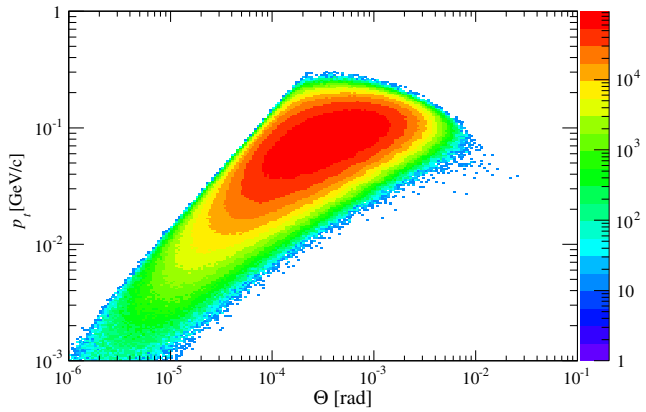

FIG. 3. Distribution of same-charge (defocused) coherent pairs after one bunch crossing using the 3 TeV CLIC baseline design parameters. On the z axis is the number of particles in each bin, per bunch crossing.

$$n_p = \frac{4\sqrt{3}}{25\pi}\left(\frac{\alpha\sigma_z}{\lambda\!\!\!^{-}_c\gamma}\Upsilon\right)^2\Xi(\Upsilon) \tag{6}$$

where several expressions for the auxillary function Ξ exist [8,14–16]. Chen and Telnov [15] give the approximate expression

$$\Xi(\Upsilon) = 0.5\exp[-16/(3\Upsilon)], \quad \Upsilon \ll 1, \tag{7}$$

$$\Xi(\Upsilon) = 2.6\Upsilon^{-2/3}\ln(\Upsilon), \quad \Upsilon \gg 1, \tag{8}$$

where $\lambda\!\!\!^{-}_c = \hbar/mc$ is the reduced Compton wavelength. The quadratic dependence on the bunch length for a fixed Υ reflects the fact that photons creating the pairs must be created before the photon can convert. Generation of pairs in GUINEA-PIG++ once again closely follows the implementation in CAIN [13]. As can be seen in Fig. 2, the two programs agree on the spectra of produced coherent pairs.

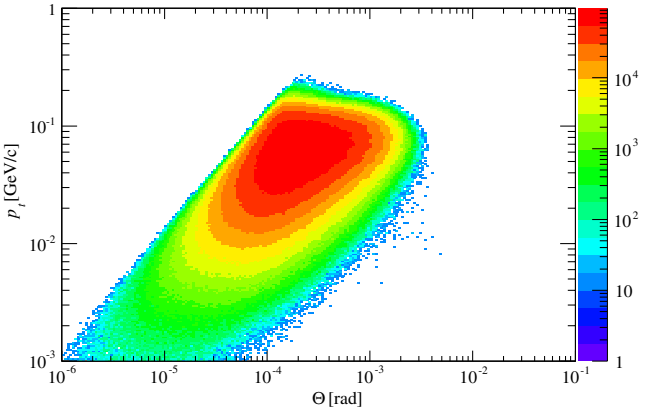

FIG. 4. Distribution of opposite-charge (focused) coherent pairs after one bunch crossing using the 3 TeV CLIC baseline design parameters. On the z axis is the number of particles in each bin, per bunch crossing.

This is a valuable cross-check of the generators of coherent pairs as well as of bremsstrahlung photons.

The kinematic distribution of the coherent pairs can be seen in Figs. 3 and 4. The angles of these particles are relatively well confined meaning that cutting away these particles in the postcollisional line is achievable. The sign of the charge of the produced particles determines weather it is defocused or pinched by the oncoming beam which then in turn determines the postcollitional characteristics of the occupied phase space. The particles with the same charge as the opposing beam reach the largest angles due to the defocusing nature of the force they experience. These particles emerge from the IP with maximum polar angles of approximately $\sqrt{4\ln D_x/\epsilon + 1 D_x\sigma_x^2/(\sqrt{3}\sigma_z^2\epsilon)}$ [3] with ϵ being the particle energy relative to the beam energy.

IV. TRIDENTS

Because the QED critical field is of a magnitude such that an electron will gain an energy of mc^2 by moving a reduced Compton wavelength, it is not surprising that spontaneous emission of pairs by an electron in such a field is expected. One could say that virtual pairs associated with the electron field will be able to reach the mass shell in fields of such magnitudes. The direct trident process $e^- + \mathcal{E} \to e^- + \mathcal{E} + e^- + e^+$ represented by the Feynman diagram in Fig. 5 is the emission of an electron/positron pair in a strong field [17] without intermediate steps.

Events where an electron produces a pair in the interaction with an electromagnetic field may proceed either through the sequential process where the electron emits a real photon that converts into a pair, or directly where the intermediate stage contains a virtual photon. A recent measurement of trident events from both amorphous and crystalline matter may be found in [18]. In fact, energetic

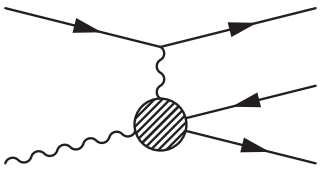

FIG. 5. Feynman diagram for the direct trident process used for the Weizsäcker-Williams calculation. The incoming wavy line represents the coherent interaction of many particles—described as a homogeneous field—with the electron.

particles interacting with an oncoming crystal (as seen from the frame of the particle) closely resembles the situation of particles interacting with an oncoming bunch. As stated by Blankenbecler and Drell in their seminal paper [19] "…we find it convenient to work in the rest frame of the pulse which transforms into a very long narrow 'string' of N charges," directly reminiscent of the string of charges constituting a crystal. An introduction to particle interactions in crystalline matter at high energies can be found in [20].

Many conventions for the naming of produced pairs exist—especially when not only interactions with the field are considered. The term "trident" may refer only to the direct trident process, also known as magnetic electroproduction, but in some contexts it refers to the union of the sets "sequential tridents" and "direct tridents" due to the three-prong track of the reaction products when they are subject to a magnetic field.

In GUINEA-PIG "incoherent pairs" refers to pairs produced in binary collisions. One of the possibilities for a pair producing collision is one between two leptons i.e. the Landau-Lifshitz process. This looks strikingly similar to the amorphous trident production mechanism via a virtual photon. However, incoherent pairs also include photon-photon or photon-lepton collisions. All these processes are shown in Fig. 6.

Here we will distinguish between direct tridents (magnetic electroproduction) and sequential tridents (coherent pairs). Finally, "incoherent tridents" means Landau-Lifshitz-like pairs, i.e. resulting from binary collisions between two leptons—or in material media between a nucleus and a lepton.

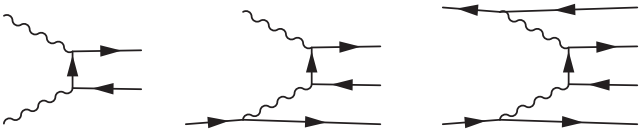

FIG. 6. Feynman diagrams for incoherent pairs and incoherent muons. From left to right: the Breit-Wheeler, Bethe-Heitler, and Landau-Lifshitz processes. For each of these u-channel diagrams, there is a corresponding t-channel diagram (which means connecting each photon to the opposite virtual fermion vertex).

A. Direct tridents in colliders

The sequential trident events are important when considering the design of a TeV scale linear e^+e^- collider: they are the result of beamstrahlung photons converting in the strong field of the oncoming bunch and may contribute ~10% of the total charge after the bunch crossing. Likewise, the result of the conversion of virtual photons in the field of the oncoming bunch, direct trident events, may be significant and can be analyzed using a Weizsäcker-Williams calculation.

The subject of equivalent-quanta trident production in a homogenous field has been studied by several authors [21] or in crystals using the Weizsäcker-Williams method [22]. Decreasing the bunch lengths in order to minimize the hourglass effect could be an attractive way of increasing luminosity when the bunches are tightly focused. However, since the strong field parameter is proportional to $1/\sigma_z$ this would increase the strong field parameter making the quantum nature of the IP more pronounced. The direct trident process depends strongly on the strong field parameter and could potentially become a dominant channel for pair creation. Furthermore, the emitted electrons and positrons can be of rather low energies [23] compared with coherent pairs, which means that they could emerge from the IP with rather large angles.

Not many analytical expressions for the yield exist [15,23–26], and to the knowledge of the authors, a single conversion probability in closed form, valid in the intermediate range $\Upsilon \approx 1$ does not exist. However, estimates do exist and according to [15,27] the total number of created direct tridents is

$$n_{\mathrm{tr}} = \frac{4\sqrt{3}}{25\pi}\left(\frac{\alpha\sigma_z\Upsilon}{\gamma\lambda\!\!\!^{-}_c}\right)\Omega(\Upsilon), \tag{9}$$

where σ_z is the bunch length and

$$\Omega(\Upsilon) = 2.6\alpha\ln(\Upsilon), \quad \Upsilon \gg 1. \tag{10}$$

This expression, however, fails at small energies. In order to mitigate, we here use a Weizsäcker-Williams calculation [28].

The spectrum of virtual photons can be estimated to first order using [28,29]

$$\frac{\mathrm{d}n_v}{\mathrm{d}x} = \frac{\alpha}{2\pi}\frac{1+(1-x)^2}{x}\ln\left(\frac{q^2_{\mathrm{max}}}{q^2_{\mathrm{min}}}\right), \tag{11}$$

$x = \hbar\omega/E_0$, E_0 being the energy of the emitting particle. An integration of the virtual photon spectrum from q^2_{min} to q^2_{max} has been done creating a cutoff at these virtualities. For the purpose of this article and the GUINEA-PIG++ calculations, this spectrum is used with $q^2_{\mathrm{max}} = m^2$ and $|q_{\mathrm{min}}|^2 = x^2m^2$ [25]; see Fig. 7 .

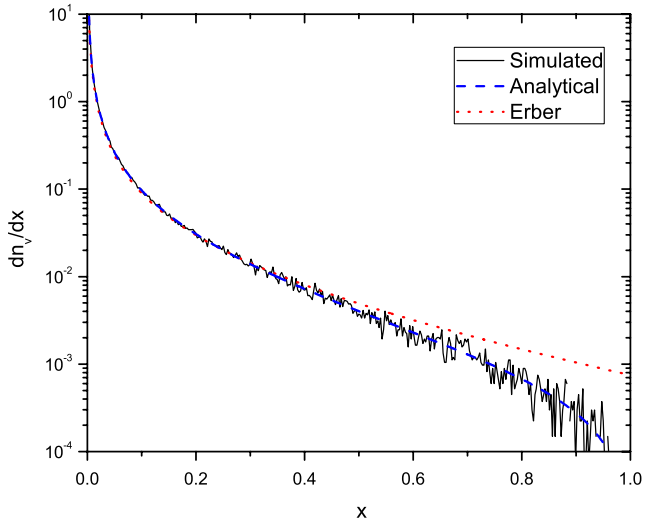

FIG. 7. Spectrum of virtual photons used for generating direct tridents, $x = \hbar\omega/E_0$. The expression (11) ("analytical") exhibits a cutoff in the maximum energy, which is clearly more physical than the semiclassical spectrum ("Erber") from [14].

The total number of virtual photons carried by an electron is then approximately $n_v \approx \alpha \ln^2(x_{\min})/\pi$ for $x_{\min} \ll 1$. For the sake of calculations $x_{\min} = 10^{-5}$ was chosen as a default, ensuring that the simulation is valid for all currently considered collider designs since the smallest energy of the produced particles is higher than this fraction of the primary electron energy [23].

Since the relevant virtualities are very small, the virtual photon has near on-shell properties. Therefore it can be assumed to convert in the external field with the probability and spectrum of an unpolarized photon on the mass shell, $q^2 = 0$. The total cross section can be parametrized by [13]

$$p = 0.23\alpha \frac{mc^2}{\hbar\omega} \frac{\Delta z}{\lambda_c} \kappa e^{-8/3\kappa} (1 + 0.22\kappa)^{-1/3}, \tag{12}$$

where $\kappa = x\Upsilon$, the strong field parameter of the photon, while the photon converts with the differential probability [24]

$$\frac{\mathrm{d}p}{\mathrm{d}x'} = \frac{\alpha}{\sqrt{3}\pi} \frac{\Delta z}{\lambda_c} \frac{mc^2}{\hbar\omega} \times \left(\frac{x'^2 + (1-x')^2}{x'(1-x')} K_{2/3}(\xi) + \int_\xi^\infty K_{1/3}(y)\mathrm{d}y \right), \tag{13}$$

where $x' = E_-/\hbar\omega$ is the electron fraction of the photon energy and $\xi = \frac{2}{3\kappa} \frac{1}{x'(1-x')}$. Also Eq. (13) has been tested successfully by experiments utilizing crystalline targets [30,31].

Special numerical techniques are needed to sample from this function. An easily invertible approximate expression for the integral of this function can be used to determine the sampled energy [13], while the real expression (13) is used to correct the cross section. This method of determining the energy follows the method described in [13]. For Monte Carlo simulation purposes, the exact expression for the differential probability is evaluated using interpolations of the modified Bessel functions $K_{2/3}$ and the integral of $K_{1/3}$.

In extreme fields, one finds corrections to the virtual photon spectrum. Here, we only mention the possible corrections without applying them to real simulations. The maximum magnitude of the virtuality chosen above is the squared center-of-mass energy. An additional correction to the minimal virtuality arises from the recoil of the electron $q^2_{\min} \approx m^2(x^2\Upsilon)^{2/3}$ when $(\Upsilon/x)^{1/3} \gg 1$. This effect gives rise to the mechanism of magnetic suppression, for example, relevant for bremsstrahlung [32], but this cut is not used for the direct trident generation.

Because of the continuous nature of the process, the probability of photon conversion in a single step is attenuated when the linear probability gets large

$$p' = 1 - e^{-p}. \tag{14}$$

This means that in simulations with large Υ, the step size should not be too large to ensure that a linear expansion of (14) is valid.

In order to determine any effects on the beam particles, the energy of the producing electron is modified if the virtual photon converts, and the direct tridents are added to the luminosity calculation as well as the bunch field calculation of GUINEA-PIG++.

B. Results of simulation

A comparison between a version of the direct trident generator with constant Υ and expressions from [14,15] is seen in Fig. 8. Clearly, the approximate expressions are not adequate for determining the yield at the threshold for quantum effects around $\Upsilon = 1$. In Erber's seminal paper [14] a semiclassical Weizsäcker-Williams approximation is used for the virtual photon spectrum. This spectrum weighs more on high energies than Eq. (11) which explains the difference at $\Upsilon < 1$ and the similarity at $\Upsilon \gg 1$. The spectra coincide completely at low energies as can be verified analytically. The Weizsäcker-Williams approximation used here is much better in the intermediate range besides being valid in the quantum regime.

Figures 11, 12, and 9 show the results of a full CLIC 3 TeV simulation using realistic input distributions. The amount of direct tridents is 3.6×10^6 per beam per bunch crossing or approximately one per mil of the total initial bunch charge. By comparison, the coherent pairs contribute with 2 orders of magnitude more charge. The smallness of the yield of direct tridents means that the parameter region, where this ratio is 1, is quite far from any realistic CLIC parameter set.

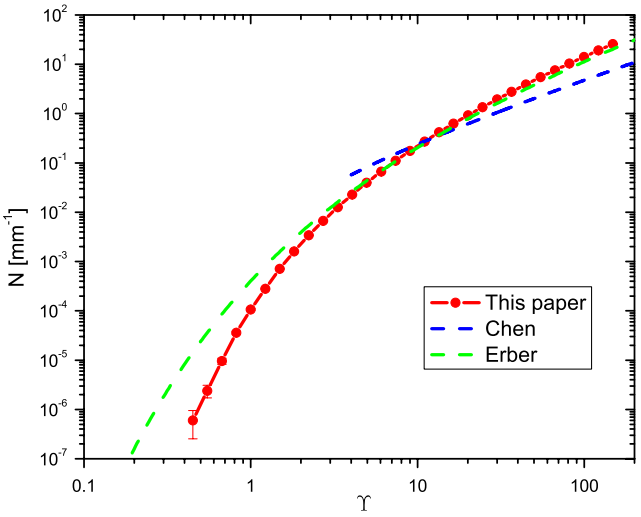

FIG. 8. Total yield of direct tridents at a primary energy of 250 GeV. Red: Monte Carlo simulation, this paper. Blue dashed: approximate expression by Chen [15]. Green dotted: Erber [14]. Note that the Chen and Erber curves are shown outside of their respective regions of validity.

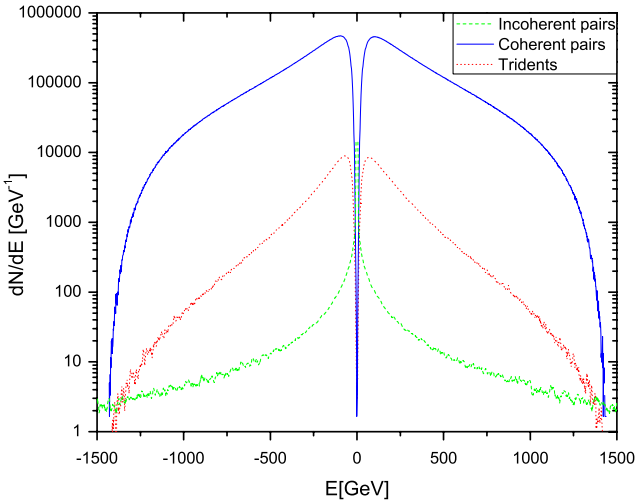

FIG. 9. Spectrum of the various pair production mechanisms after full beam crossing simulation.

The development of the yield of the direct tridents closely follows that of the coherent pairs with respect to a vertical offset of the beams since they are both strong field processes. This means that vertical offsets will not vary the relative composition of produced strong field pairs significantly.

This study, using Gaussian beams in the CLIC nominal parameter range, is seen in Fig. 10. Here, it becomes evident that the bunches must become prohibitively short if direct tridents are to be produced in large numbers.

The incoherent pair production mechanism produces approximately 1.5×10^5 particles per beam per bunch crossing. Because of the nature of the process and since the spectrum is peaked at energies just above the electron mass, these particles can emerge from the interaction region at very large angles. This makes them suitable for luminosity monitoring. The large difference in the spectrum and angles of these pairs in comparison to the direct trident process lies in the assumption of complete field coherence in the production of a direct trident. If, however, a single electron interacts coherently with several particles, but not a continuous field, neither of these models for pair production will be sufficient. In the laboratory frame, the density of electrons/positrons is of the same order as in solid matter, which means that the scattering centers are close.

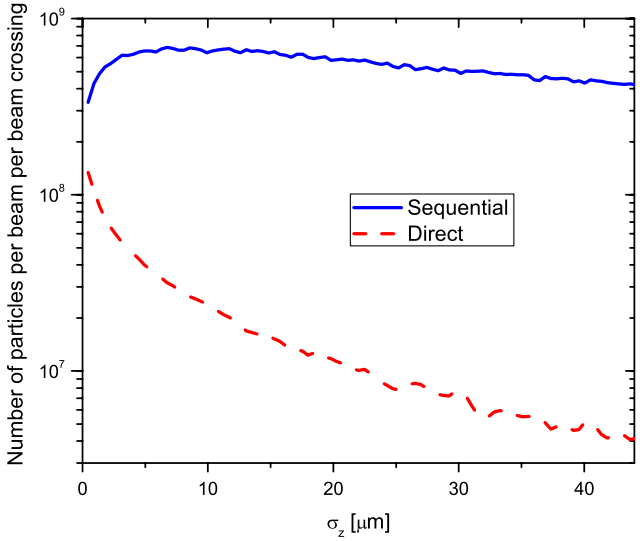

FIG. 10. Bunch length dependence of the yield of the coherent pair production mechanisms. The bunch charge is kept constant.

The angular distribution of the direct tridents is narrower than that of the incoherent pairs and the energies not as low as those of the incoherent pairs. Even so, there was an area of phase space that the coherent pairs did not occupy, while the same area was populated by incoherent pairs. This, before the tridents were simulated, allowed for an almost complete separation of these pairs by positioning the lumical at a certain polar angle. The direct tridents narrow the window in angle$/p_t$, meaning that they should be kept in mind when designing the forward detector which is intended for luminosity monitoring utilizing incoherent pairs [33].

Thus, a generator of direct trident that is valid in the quantum mechanical as well as in the intermediate $\Upsilon \approx 1$ regime has been developed. This generator has been applied to beam-beam simulations relevant for CLIC. The impact on any proposed 3 TeV CLIC design is small when compared to other processes of e^+e^- pair creation but may become significant in the limit of short bunches. The kinematic characteristics of the produced particles are not unlike those of sequential tridents. Since the relative

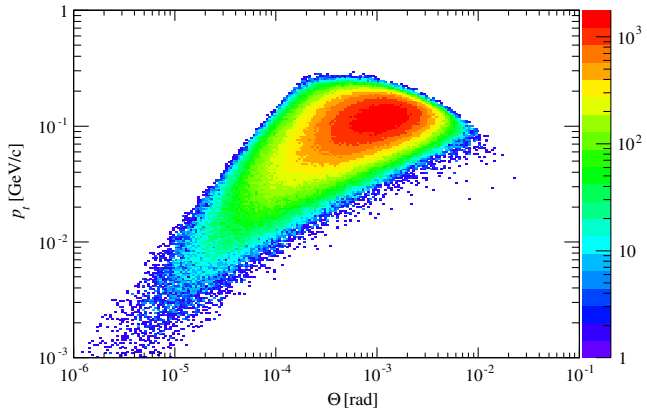

FIG. 11. Distribution of same-charge (defocused) direct tridents after one bunch crossing using the 3 TeV CLIC baseline design parameters. On the z axis is the number of particles in each bin, per bunch crossing. May be compared with the distribution of coherent pairs shown in Figs. 3 and 4.

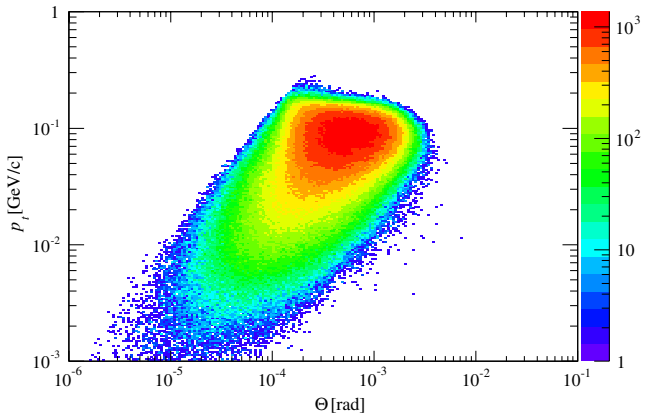

FIG. 12. Same as Fig. 11 but for opposite-charge (focused) particles.

contribution of the direct tridents to the postcollisional bunch charge is small, this will mean that they are most likely difficult to distinguish from the coherent pairs in a detector. Varying the bunch length will, however, alter the ratio of the yields of these processes.

The physics performance potential of the detector is limited by background processes. Beam-beam induced backgrounds include minijets from $\gamma-\gamma$ collisions, coherent pairs, and incoherent pairs as well as incoherent muons and direct trident pairs. The presence of these processes influences the design of the detector and the event selection algorithms in various ways. A great number of these processes are implemented in GUINEA-PIG and GUINEA-PIG++. They include Bhahba scattered particles and radiative Bhabha events, bremsstrahlung photons, minijets, and initial state radiation [34].

The strong field effects at the IP may further modify the vertices of key physics processes, for example, W pair production. This process may be useful in polarimetry measurements [35] if one measures the left-right asymmetry of the produced W's. The strong field effects on these matters have not been extensively studied.

V. LUMINOSITY SPECTRUM

The energy loss due to beamstrahlung—and other mechanisms—means that a substantial fraction of collisions will occur at lower energies than the nominal CM energy. Furthermore, collisions involving coherent pairs will contribute to luminosity at lower energies. The luminosity spectrum is seen in Fig. 13. The quantum nature of beamstrahlung is naturally very important to take into account. The ratio of the luminosity within 1% of the nominal center-of-mass energy to the total luminosity is 34%, while the ratio would be in the vicinity of 17% if the particles radiated with the classical synchrotron probability. This very significant difference has recently been corroborated by experiment [12].

A. Properties of produced particles

The simulated production angles of various beam particles can be seen in Fig. 1; see, for example, also [34]. This provides some information of the dynamics of each single process. Generally, incoherent processes extend to large angles since the center-of-mass frame is approximately the laboratory.

During active stabilization of the beams, rather large offsets of the beams with respect to one another can be expected. Luminosity and effective fields experienced by a beam particle are in particular very sensitive to vertical offsets since the beams are "flat." The change of amount of produced particles with this offset then gives insight to the instantaneous luminosity. The behavior of some yields can be seen in Fig. 14. For coherently produced particles,

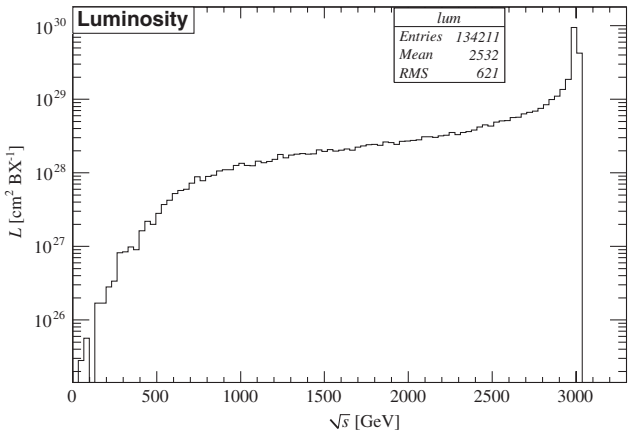

FIG. 13. CLIC nominal luminosity spectrum at ideal conditions; the spectrum includes contributions from coherent pairs and initial state radiation.

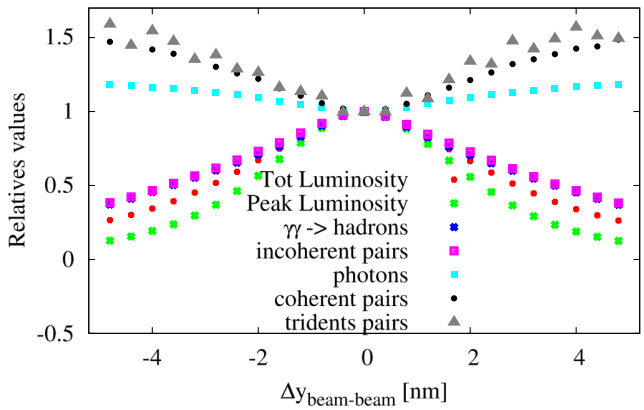

FIG. 14. Dependence of various relative yields on vertical offset between colliding bunches normalized to production at perfect conditions. The average strong field increases with this offset, increasing the yield of strong field processes. Peak luminosity refers to the amount of luminosity within 1% of the nominal collision energy. $\gamma\gamma \rightarrow$ hadrons refers to the amount of hadronic events from collisions between real or virtual photons.

the yield increases with offset due to increase in the field while the incoherently produced particle yields decrease. If coherently produced charged particles were to be used as luminosity signals, spectral information is furthermore needed. This is so, since the spectra change significantly with the field which in turn will affect the detection efficiency.

VI. DEPOLARIZATION

Ideally, the colliding beams of a future collider should be longitudinally polarized, meaning that the spin vectors of beam particles should have an average longitudinal direction in space. The strong field beam-beam effects could potentially partially destroy this polarization, partly due to the deflection of the beam particles that will cause strong spin precession, and partly due to the radiative spin-flip process.

Electron sources that utilize the band structure of gallium arsenide (GaAs) will be able to produce highly polarized beams when struck by circularly polarized photons. Further refinements of such sources that introduce a periodic deformation of the surface—a so-called super lattice—promise to be able to produce highly polarized (~90%) electrons [36].

A possible source of positrons would utilize a storage ring able to Compton-backscatter photons. This gives rise to photons of high energy and high degree of polarization. The scattered photons would then be converted to pairs using a solid target that could possibly be crystalline [37].

The spin should be vertical before the particles are entering damping rings and the ring to main linac line, since the subsequent magnetic deflection would otherwise cause spin precession. This is achieved in spin rotators that utilize the spin precession to orient the average spin. Before the main linac, the spin is intended to be rotated back to the longitudinal direction of the main linac for the collisions.

A. The T-BMT equation

The T-BMT equation [38,39] describes the dynamics of the classical spin in a homogeneous electromagnetic field.

If this mechanism would be the only one governing the spin dynamics of the interaction point, total depolarization would be $\langle D \rangle = (\gamma a)^2/2[\Delta\theta_{x,\mathrm{rms}}^2 + \Delta\theta_{y,\mathrm{rms}}^2]$ where $\Delta\theta_{\mathrm{rms}}$ is the rms deflection angle of the beam particles and a is the anomalous magnetic moment of the electron [40]. Since $\Delta\theta_{\mathrm{rms}} \approx 50\ \mu$rad [41], we would expect an average depolarization of approximately 6% from spin precession alone. However, the strong field greatly reduces the magnitude of depolarization from this mechanism.

B. High field correction to the anomalous magnetic moment

Although not very well known, the anomalous magnetic moment of the electron, a, is not a universal constant [42]. In strong fields this quantity is modified due to a change in the mass operator. The theoretical value of a is changed to

$$a(\Upsilon) = \frac{\alpha}{2\pi}\int_0^\infty \int_0^\infty \frac{v}{1+v^3}\sin\left(\frac{v}{\Upsilon}\left[z+\frac{z^3}{3}\right]\right)\mathrm{d}v\mathrm{d}z, \quad (15)$$

or approximately

$$a(\Upsilon) = \begin{cases} \frac{\alpha}{2\pi}\left(1-12\Upsilon^2\left[\ln\left(\frac{1}{\Upsilon}\right)-1.957\right]\right) & \Upsilon \ll 1 \\ \frac{\alpha}{9\sqrt{3}}\Gamma(1/3)(3\Upsilon)^{-2/3}\left(1+6\frac{\Gamma(2/3)}{\Gamma(1/3)(3\Upsilon)^{-2/3}}\right) & \Upsilon \gg 1 \end{cases}. \quad (16)$$

GUINEA-PIG++ and CAIN use more elaborate, but identical, approximate expressions to calculate the anomalous magnetic moment on the fly. These expressions coincide when $\Upsilon = 0.6125$. So for Υ above this value the lower expression is used while the upper expression is used for calculation of the magnetic moment when $\Upsilon > 0.6125$. The function implemented in these programs can be seen in Fig. 15. If the magnetic moment were constant, the majority of the T-BMT spin precession would take place in regions of high fields, but the nonlinear reduction of a counteracts this effect meaning that the spin precession part of the depolarization in the CLIC interaction region is significantly suppressed.

C. Sokolov-Ternov spin flip

Another source of depolarization is the radiation emission. When Υ becomes of the order one, a significant portion of the radiation emission originates from the

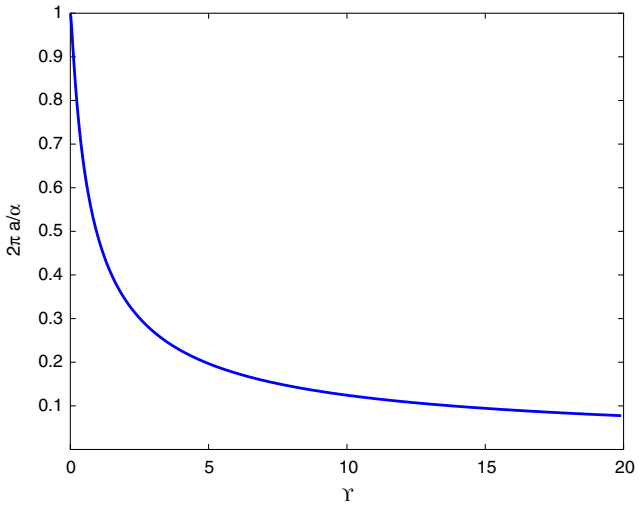

FIG. 15. The strong field dependence (16) of the anomalous magnetic moment of the electron.

electron reversing its spin. The already existing implementation of the spin-flip process on the radiating electron in GUINEA-PIG++ is very closely related to the one described in the CAIN manual [13]. It has been confirmed that the implementation reproduces the result described in [43], even though there was until recently a problem with the normalization of the spin vector. The significance of the spin-flip process in strong fields has also been observed experimentally in crystals [44].

An estimate for the beam-beam depolarization including the Sokolov-Ternov process is given by Yokoya and Chen in [40]. Using analytic expressions from this article, one can estimate the total depolarization due to spin-flip radiation to approximately 8.5% when one takes the deflection parameters into account [their Eq. (45)]. When $\Upsilon \ll 1$, this article furthermore gives the convenient estimate for the Sololov-Ternov driven depolarization as $(7/27)n_\gamma\langle\Upsilon\rangle^2$, where n_γ is the number of synchrotron photons per beam particle, but since the low-field condition is not fulfilled for CLIC this estimate has not gotten much use in this case.

D. Simulations of depolarization for CLIC

When doing simulations using GUINEA-PIG++ and using realistic input beams, one gets the total depolarizations listed in Table II. In this case depolarization for the spent beams is defined as $1-\langle S_z\rangle$ while the luminosity weighted depolarization is calculated as $1-\sqrt{\langle S_{z1}S_{z2}\rangle}$. Here, S_z are the longitudinal components of the spin vector ($|S_z|=1$) and the numerical indices correspond to the bunch to which the colliding particle belongs. The numbers presented here have been cross-checked with the results obtained in [43], and found to agree.

Because the Sokolov-Ternov (ST) mechanism dominates the CLIC depolarization, one would expect that the particles least influenced by synchrotron radiation are the ones that are least depolarized [33,45]. This tendency can be seen in Fig. 16, where it is apparent that the energy dependence
of depolarization is strong. If one is able to isolate the collisions occurring within the 1% of nominal center-of-mass energy, the luminosity weighted depolarization for these collisions is reduced to only 0.5‰, an almost negligible number compared to the few percent that one would expect for the total depolarization.

TABLE II. Simulated total depolarizations for CLIC 3 TeV. The beams are assumed to be completely longitudinally polarized before collision.

Total depolarizations	BMT	BMT + ST
Spent beam	0.33%	6%
Luminosity weighted	8.9e-2%	3%

Since the deflection and mean strong field parameter increases with offset between the colliding beams, one would expect the depolarization to increase accordingly. In Fig. 17 the offset dependence of depolarization is shown to be rising significantly with vertical offset, but in the 1% luminosity peak, the luminosity weighted depolarization remains relatively small although not entirely negligible anymore with offsets in the order of a few nanometers.

In conclusion, the nonlinear strong field effects at the interaction point tend to favor depolarizations that are quite small. And in the interesting energy region, the depolarization is significantly smaller than estimated in analytical formulas [40]. This means that other sources, for example, the beam delivery system, are likely to account for an equal or greater degree of depolarization of the luminosity peak in a linear collider operating in the strong field regime.

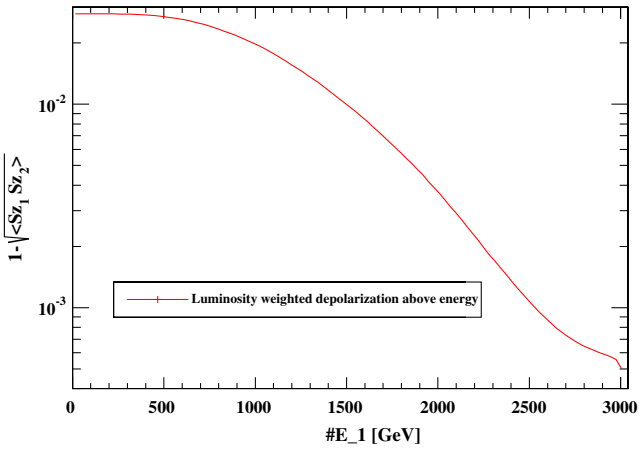

FIG. 16. The CLIC depolarization as function of a cut in the lower CM energy.

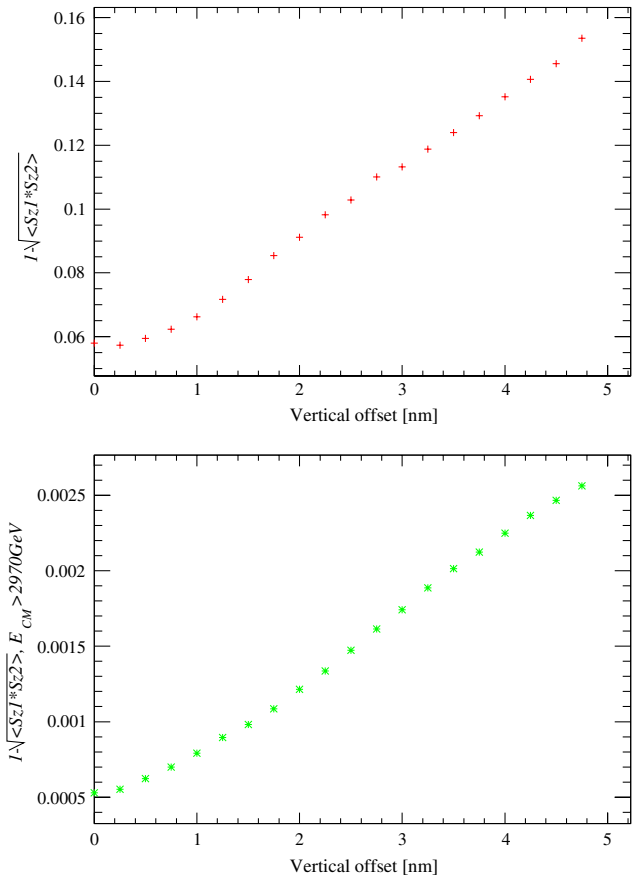

FIG. 17. Depolarization as function of vertical offset using Gaussian input beams. Top: total depolarization. Bottom: depolarization within 1% of the nominal CM energy.

E. Spin measurements

It is essential that the spin is known at collision time. However, the large difference between average depolarization and depolarization in the luminosity peak could make measurements of the postcollisional spin less useful. Such measurements would most likely measure the average polarization of the bunches. Therefore, a thorough knowledge of the behavior of the spin dynamics is essential, and simulations will have to interplay with measurements in order to obtain full knowledge of the luminosity weighted depolarization. A method for measuring the average spin would be to pass the beams through a circularly polarized laser beam and look at the Compton scattered photons. The shape of that spectrum is highly dependent on the orientation of the spin vector of the electron. Some deconvolution might be possible in order to determine the energy dependent depolarization.

VII. INCOHERENT MUON PAIRS

Very clean signals for detection of physics events are provided by muons. This is due to their large penetration depth which makes it possible to separate practically all background events in the muon chambers surrounding the detectors. Muon pairs will however also be produced incoherently, where the virtual lepton is a muon. They extend to rather large angles creating background muon signals. This makes knowledge of their abundance and kinematics important.

A. Method of generation

Muons are generated almost identically to the incoherent pairs in GUINEA-PIG++ as in Fig. 6 where the only difference is their mass. This description of the muon generator here will follow the one in [3]. The Breit-Wheeler process where two photons collide can be simulated while the Bethe-Heitler (colliding one photon and one lepton) and Landau-Lifshitz (colliding two leptons) processes can be done utilizing a Weizsäcker-Williams calculation replacing the lepton by its virtual photon flux.

This procedure gives the well-known total cross section of

$$\sigma_{\mathrm{BW}} = \frac{\pi r_\mu^2 m_\mu^2 c^2}{s} \times \left[\left(2+\frac{2}{\gamma^2}-\frac{1}{\gamma^4}\right)\ln\left(\frac{1+\beta}{1-\beta}\right)-\left(2+\frac{2}{\gamma^2}\right)\beta\right]. \quad (17)$$

The procedure for Breit-Wheeler muon generation is first to transform from the lab frame to the CM frame of the photons and hence also of the muons, then evaluate Eq. (17). Inversion of the differential cross section leads to determination of the pair production angles, and thus a complete determination of the kinetics of the final state. For the additional two processes, Landau-Lifshitz and Bethe-Heitler, the method of virtual quanta is employed. For muon production (as well as for incoherent pair production) the maximum virtuality of the photons is chosen as $E_{\mathrm{cm}}/4$.

The muon production cross section should approach the well-tested incoherent pair production at high transverse momenta $p_t > m_\mu c$ since the mass contribution to the produced pair energies in the CM frame is negligible in this case. Thus, it was tested that the produced muon cross section coincides with the cross section for the incoherent pairs at high p_t as seen in Fig. 18.

Although the muons have been allowed to emit synchrotron radiation in the simulation, they are not allowed to affect any beam particles or fields after they are produced.

The produced muon pairs were added to the tracking of beam pairs in GUINEA-PIG++. The tracking algorithm has not been fully verified for nonrelativistic particles and since muon pairs are produced with energies not much above their mass, one should use muon tracking in the current implementation of muon tracking with caution. Therefore the user can optionally store the produced pairs before beam-beam tracking, and the tracking of muons is optional. Since synchrotron radiation is highly unlikely

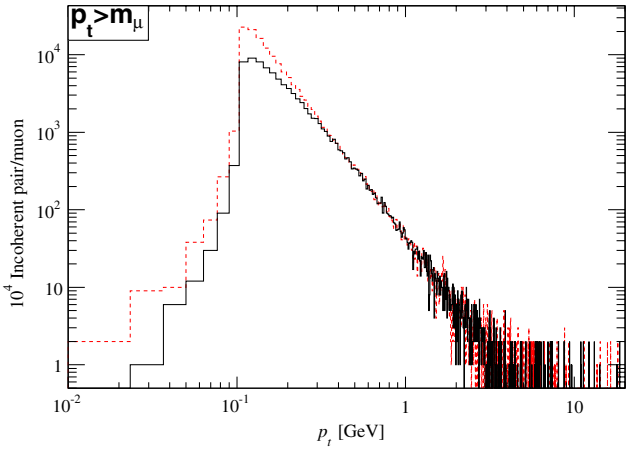

FIG. 18. Comparison of the transverse momentum of incoherent electrons and muons. Cross sections have been scaled up by 10^4 to decrease simulation time. At production time, the cut $p_t > m_\mu c$ has been employed. Red dashed line indicates incoherent electrons. Black solid line indicates incoherent muons.

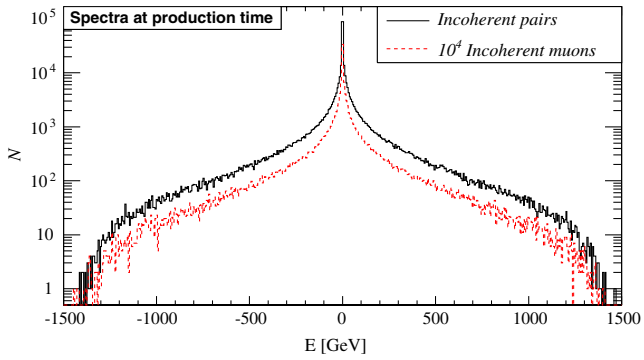

FIG. 19. Spectrum of incoherent muons at the time of production. The sign of the energy corresponds to the muon charge sign. The muon cross section is scaled up by a factor 10^4, taking $(m_\mu/m_e)^2 = 4 \times 10^4$ into account, to decrease simulation time.

for muons, the beam-beam interaction hardly affects the muon spectrum.

For CLIC, the total number of produced muon pairs per bunch crossing is 12.5. Of these particles 0.6 are produced through the Breit-Wheeler process, 8.0 through the Bethe-Heitler mechanism, and 3.9 from the Landau-Lifshitz process. Their spectrum is seen in Fig. 19, and their production angles can be seen in Fig. 1.

B. *s*-channel muons

To ensure that no other processes contribute significantly to the muon pair production cross section, it was checked that *s*-channel muons would not be of importance. The leading order processes are

$$e^+ + e^- \to \gamma \to \mu^+ + \mu^-, \tag{18}$$

$$e^+ + e^- \to Z_0 \to \mu^+ + \mu^-, \tag{19}$$

where the intermediate particle is a virtual gauge boson. The first process gives rise to an s^{-1} dependent cross section while the second process gives rise to the familiar Breit-Wigner resonance around the Z_0 mass of 91 GeV.

The total *s*-channel cross section can be found in [46,47]. A very rough integration of the $1/s$ shape in the range 30–150 GeV reveals that the photon diagram contribution to the cross section in this range is ≈20 pb while the Z_0 diagram contribution in this range is of the order of 1 nb.

Looking at the luminosity spectrum in Fig. 13, one clearly sees that there is not enough luminosity at CLIC in the vicinity of the Z_0 resonance to make it worthwhile to include *s*-channel diagrams in the simulation. An upper bound of the luminosity in the Z_0 range is 10^{-6} nb^{-1} per bunch crossing, meaning that approximately 10^{-6} muons per bunch crossing would be produced via these mechanisms. Therefore, these events can safely be excluded from simulations.

VIII. TERTIARY PHOTONS

At present, several produced particles could provide excellent fast luminosity signals. These particles include beamstrahlung photons and large p_t hadronic events [48]. Here, we propose another fast luminosity signal arising from optical photons.

Synchrotron radiation emitted from incoherent pairs share the large angles of these particles, and could potentially supply information about luminosity and/or reach unintended parts of the detector. Therefore, it was decided to simulate the creation and the properties of these "tertiary photons." Their kinematic information was saved to a separate output file of GUINEA-PIG++.

The angles of the tertiary photons can be found in Fig. 1, where the large production angles are apparent. In Fig. 20 is seen the azimuthal information for these particles, where their trajectories have been projected onto a transverse

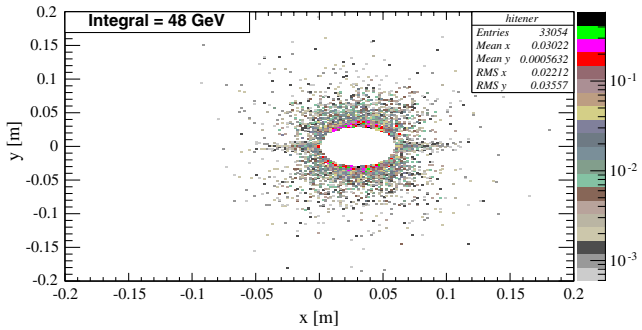

FIG. 20. Spatial distribution of energy deposited by the tertiary photons at a transverse plane 3 m from the IP. Only photons with production angles above 20 mrad are displayed here.

plane 3 m from the IP. The 10 mrad width of the beam pipe has been cut away revealing that the energy deposition in the detector is very small and in the vicinity of 48 GeV per bunch crossing. This number should be compared to 27 TeV for the incoherent pairs, 2200 GeV for the coherent pairs and 880 GeV for direct trident pairs, respectively.

The energy of the tertiary photons can be very low as seen in Fig. 21. In fact, the spectrum extends to energies below those of optical photons. These photons are readily detected, and could provide information about the instantaneous luminosity. In Fig. 22, the rather strong correlation between the tertiary photon yield and luminosity is seen. Since the process is partly incoherent and partly a result of the interaction with the field, the dependence of tertiary photons with some imperfection could potentially be quite complex. But there seems to be a direct proportionality between luminosity and tertiary photon counts. Furthermore they are sufficiently abundant for detection and hence also for fast luminosity monitoring.

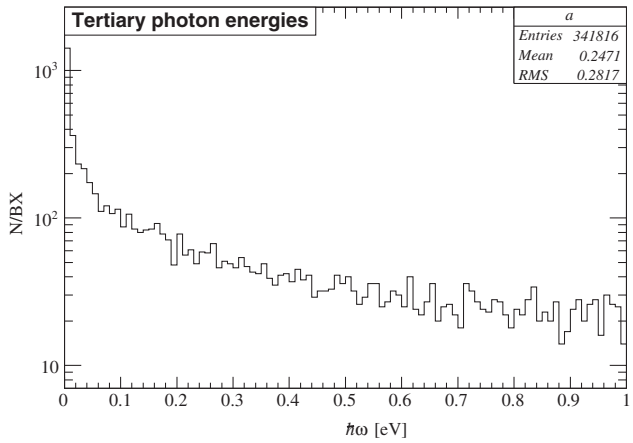

FIG. 21. Low-energy part of the tertiary photon spectrum.

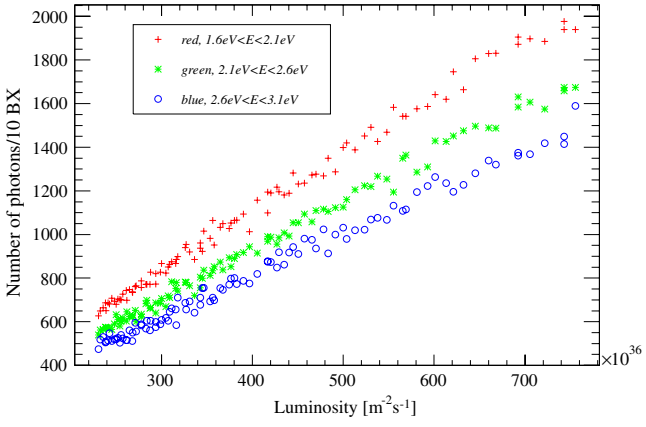

FIG. 22. Correlation between luminosity and number of tertiary photons (per 10 bunch crossings) when the size of one beam is varied. Each color in the optical region corresponds to an energy bin of 0.5 eV width.

Since the tertiary photons are not affected by the solenoid field, the azimuthal information about their distribution could prove very useful. And there might be some useful spectral information to be found in the tertiary photons. This would be due to the fact that a larger average beam-beam field, induced by some imperfection and experienced by the incoherent pairs, would increase the critical frequency of synchrotron radiation.

The low-energy photon background from other pairs at the interaction point would have to be determined in order to assess the feasibility of using the tertiary photons as a luminosity signal. Especially the direct trident pairs would be able to emit light at rather large angles. Since direct trident pairs in CLIC are more abundant than incoherent pairs, there is a chance that photons from these particles would create a large background. However, synchrotron photons from these particles will not extend to very large angles, so in all likeliness there is an angular cut above which only tertiary photons would be seen. Searches for background radiation would also include an estimate of the synchrotron yield from the interaction with the detector solenoid field. If these particles turn out to be of interest, the inclusion of an emission angle, as opposed to the current implementation, where the photons have the direction of the emitting electron, would be essential.

Finally, the vertex detectors are in all likeliness not sensitive to these photons. However, the spectrum of tertiary photons is very wide and some frequencies of the light could potentially trigger signals in them.

IX. CONCLUSIONS

New processes have been implemented and simulated in GUINEA-PIG. These new additions have been tested along with previously implemented ones. In particular, a Weizsäcker-Williams calculation of the direct trident process that is valid in the quantum mechanical as well as in the intermediate $\Upsilon \approx 1$ regime has been implemented. This simulation has been applied to beam-beam simulations relevant for the next generation linear colliders. The impact on any proposed 3 TeV CLIC design is small when compared to other processes of e^+e^- pair creation but may become significant in the limit of short bunches. The kinematic characteristics of the produced particles are not unlike those of sequential tridents (coherent pairs). Because the relative contribution of the direct tridents to the postcollisional bunch charge is small, this will mean that they are most likely difficult to distinguish from the coherent pairs in a detector without varying the bunch length. Depolarization due to beam-beam effects is below the percent level in the luminosity peak for CLIC at 3 TeV. The explanation is partly due to diminishment of the electron anomalous magnetic moment and partly due to lack of beamstrahlung from the most energetic particles. Approximately 12.5 μm will be emitted per bunch crossing

due to binary collisions which have been cross-checked with high p_t results of incoherent pairs.

Incoherent pairs will emit synchrotron in the visible regime that extends to large polar angles. As optical photons are easily manipulated, they might be efficiently detected and used to monitor luminosity effectively and fast.

[1] ATLAS Collaboration, Phys. Lett. B **716**, 1 (2012).
[2] CMS Collaboration, Phys. Lett. B **716**, 30 (2012).
[3] D. Schulte, Doctorate, Universität Hamburg, 1996.
[4] C. Rimbault *et al.*, Report No. EuroTeV-Report-2007-056, 2007.
[5] J. Esberg, Ph.D. thesis, Aarhus University, 2012.
[6] CLIC Collaboration, CERN Report No. CERN-12-007, 2012.
[7] R. Noble, Nucl. Instrum. Methods Phys. Res., Sect. A **256**, 427 (1987).
[8] P. Chen, Report No. SLAC-PUB-5914, 1992.
[9] P. Chen and K. Yokoya, Phys. Rev. D **38**, 987 (1988).
[10] K. Yokoya and P. Chen, Lect. Notes Phys. **400**, 415 (1991).
[11] K. Yokoya, Nucl. Instrum. Methods Phys. Res., Sect. A **251**, 1 (1986).
[12] K. K. Andersen, J. Esberg, H. Knudsen, H. D. Thomsen, U. I. Uggerhøj, P. Sona, A. Mangiarotti, T. J. Ketel, A. Dizdar, and S. Ballestrero (CERN NA63 Collaboration), Phys. Rev. D **86**, 072001 (2012).
[13] K. Yokoya and P. Chen, SLAC-PUB-4692, 1988; K. Yokoya, *User's Manual of CAIN, Version 2.35 (2003).*
[14] T. Erber, Rev. Mod. Phys. **38**, 626 (1966).
[15] P. Chen and V. I. Telnov, Phys. Rev. Lett. **63**, 1796 (1989).
[16] K. A. Thompson and P. Chen, AIP Conf. Proc. **472**, 260 (1999).
[17] J. Esberg and U. I. Uggerhøj, J. Phys. Conf. Ser. **198**, 012007 (2009).
[18] J. Esberg, K. Kirsebom, H. Knudsen, H. D. Thomsen, E. Uggerhøj, U. I. Uggerhøj, P. Sona, A. Mangiarotti, T. J. Ketel, A. Dizdar, M. M. Dalton, S. Ballestrero, and S. Connell (CERN NA63 Collaboration), Phys. Rev. D **82**, 072002 (2010).
[19] R. Blankenbecler and S. D. Drell, Phys. Rev. D **36**, 277 (1987).
[20] U. I. Uggerhøj, Rev. Mod. Phys. **77**, 1131 (2005).
[21] V. N. Baier, V. M. Katkov, and V. M. Strakhovenko, *Sov. J. Nucl. Phys.* ***53****, 632 (1991).*
[22] J. C. Kimball and N. Cue, Phys. Rep. **125**, 69 (1985).
[23] K. A. Thompson and P. Chen, Report No. SLAC-PUB-7776, 1998.
[24] V. N Baier, V. M. Katkov, and V. M Strakhovenko, *Electromagnetic Processes at High Energies in Oriented Single Crystals* (World Scientific, Singapore, 1998).
[25] D. White, Phys. Rev. D **24**, 526 (1981).
[26] D. White, Phys. Rev. D **26**, 10 (1982).
[27] V. I. Ritus, Nucl. Phys. **B44**, 236 (1972).
[28] V. B. Berestetskii, E. M. Lifschitz, and L. P. Pitaevskii, *Relativistic Quantum Theory*, Course of Theoretical Physics Vol. 4 (AIP, New York, 1971), part 1.
[29] V. M. Budnev, I. F. Ginzburg, G. V. Meledin, and V. G. Serbo, Phys. Rep. **15**, 181 (1975).
[30] K. Kirsebom *et al.*, Nucl. Instrum. Methods Phys. Res., Sect. B **135**, 143 (1998).
[31] V. N. Baier and V. M. Katkov, Phys. Lett. A **346**, 359 (2005).
[32] V. N Baier and V. M. Katkov, *Sov. Phys. Dokl.* ***17****, 1068 (1973).*
[33] A. Miyamoto, M. Stanitzki, H. Weerts, and L. Linssen Report No. CERN-12-008, 2012.
[34] B. Dalena, J. Esberg, and D. Schulte, *2011 Proceedings of the International Workshop on Future Linear Colliders, arXiv:1202.0563.*
[35] M. Woods, Report No. SLAC-PUB-8397, 2000.
[36] T. Nishitani *et al.*, J. Appl. Phys. **97**, 094907 (2005).
[37] X. Artru, R. Chehab, M. Chevallier, and V. Strakhovenko, Phys. Rev. ST Accel. Beams **6**, 091003 (2003).
[38] L. H. Thomas, Nature (London) **117**, 514 (1926).
[39] V. Bargmann, L. Michel, and V. L. Telegdi, Phys. Rev. Lett. **2**, 435 (1959).
[40] K. Yokoya and P. Chen, Report No. SLAC-PUB-4692, 1988.
[41] A. Ferrari, V. Ziemann, R. B. Appleby, and M. Salt, Phys. Rev. ST Accel. Beams **12**, 021001 (2009).
[42] V. N. Baier, V. M. Katkov, and V. M. Strakhovenko, *Lett. Nuovo Cimento* ***15****, 5 (1976).*
[43] C. Rimbault *et al.*, Report No. EUROTeV-report-2008-066, 2008.
[44] K. Kirsebom, U. Mikkelsen, E. Uggerhøj, K. Elsener, S. Ballestrero, P. Sona, and Z. Z. Vilakazi, Phys. Rev. Lett. **87**, 054801 (2001).
[45] J. Esberg, D. Schulte, U. I. Uggerhøj, and B. Dalena, CLIC-Note-2011-934, 2011.
[46] F. A. Berends, R. Kleiss, and S. Jadach, Nucl. Phys. **B202**, 63 (1982).
[47] U. Becker, Nucl. Phys. B, Proc. Suppl. **19**, 333 (1991).
[48] B. Dalena, J. Barranco, A. Latina, E. Marin, J. Pfingstner, D. Schulte, J. Snuverink, R. Tomás, and G. Zamudio, Phys. Rev. ST Accel. Beams **15**, 051006 (2012).

A.4 Beam delivery system tuning and luminosity monitoring in the Compact Linear Collider

Beam delivery system tuning and luminosity monitoring in the Compact Linear Collider

B. Dalena, J. Barranco, A. Latina, E. Marin, J. Pfingstner, D. Schulte, J. Snuverink, R. Tomás, and G. Zamudio

CERN, Geneva, Switzerland

(Received 17 November 2011; published 30 May 2012)

Emittance preservation in the beam delivery system (BDS) is one of the major challenges in the Compact Linear Collider (CLIC). The fast detuning of the final focus optics requires an on-line tuning procedure in order to keep luminosity close to the maximum. In this paper we discuss different tuning techniques to mitigate the displacement of magnets in the CLIC BDS and in particular in the final focus system. Some of them require a fast luminosity measurement. Here we study the possibility to use beam-beam background processes at CLIC 3 TeV c.m. energy as a fast luminosity signal. In particular, the hadron multiplicity in the detector region is investigated.

DOI: 10.1103/PhysRevSTAB.15.051006 PACS numbers: 41.75.Ht, 29.27.Fh, 41.60.−m

I. INTRODUCTION

In order to achieve high luminosity in the Compact Linear Collider (CLIC) nanometer beam sizes at the interaction point (IP) are required. One of the major challenges of this future linear collider is the preservation of the transverse emittances from the damping ring to the IP. Amongst the most critical sources of emittance growth are static and dynamic imperfections along the main linac (ML) and the beam delivery system (BDS). These are the systems where the tolerances on magnet misalignment and errors are tighter (~ 10 μm for the static and fraction of nm for the dynamic imperfections). The tuning of the static imperfections do not require any fast procedure except for the last part of the Final Focus System (FFS), when the push-pull scenario is considered. The tuning of the dynamic imperfections needs to be done at faster time scales, in order to keep luminosity stable during operation. Integrated simulations of ML and BDS including ground motion lead to a luminosity loss of the order of 10% after about 1 hour [1].

Traditionally, by the tuning of a linear collider, we understand the full correction procedure in order to bring the system to its ideal performance, as described in [2]. In this paper we discuss the mitigation against static magnet displacements in the BDS. Thus, in the following the word tuning will assume this meaning. The main reason to consider only magnet displacements is because of their relevance in the dynamic case, and common solutions can be adopted in the two cases. Moreover, we consider the BDS and in particular the FFS, due to the known difficulty to tune the system [3]. The origin of this behavior comes from the strong contribution of nonlinear terms in the design of the FFS optics [4] and the increasing difficulty in tuning the system with a very low β function at the IP, as expected from simulations and empirically tested [5]. Furthermore, the integrated simulation of ML and BDS including ground motion shows that the source of the luminosity loss is the fast detuning of the FFS optics. In fact, the luminosity loss can be fully recovered by adding to the orbit control feedback the scan of precomputed orthogonal knobs [1]. The knobs and the first results achieved in the tuning of the BDS will be presented in Sec. II. The tuning procedures we studied exploit luminosity as a figure of merit. Therefore it is mandatory to have a method to estimate the luminosity. Note that the luminosity measurements needed by the tuning procedure are not necessarily a measurement of the luminosity value. For the purpose of this tuning it can be a signal whose rate scales like luminosity (with imperfections considered).

The measurement of luminosity in e^+e^- colliders is usually done by detecting radiative Bhabhas ($e^+e^- \rightarrow e^+e^-\gamma$) [6] in the detector's forward region. In CLIC at 3 TeV c.m. energy there is no energy window where the electrons or positrons can be separated from the spent beam low energy tails or the incoherent pairs energy distribution, as shown in Fig. 1. The low angle Bhabhas have a lower event rate than radiative Bhabhas at the CLIC c.m. energy. Moreover, these methods need from 7 to 70 minutes in order to reach 1% precision in the measurement of the luminosity [7]. The fast detuning of the machine is then not compatible with this technique.

The possibility to use secondary particles emitted during the beam-beam interaction to monitor luminosity at CLIC has already been proposed [8]. In particular, the possibility to use the beamstrahlung photons as a fast luminosity signal has been exploited in [9]. The measurement of the beam sizes at the IP, using incoherent pairs both alone or in combination with beamstrahlung, has been explored in [10]. In the following, the results in terms of CLIC BDS performances are presented, according to the different

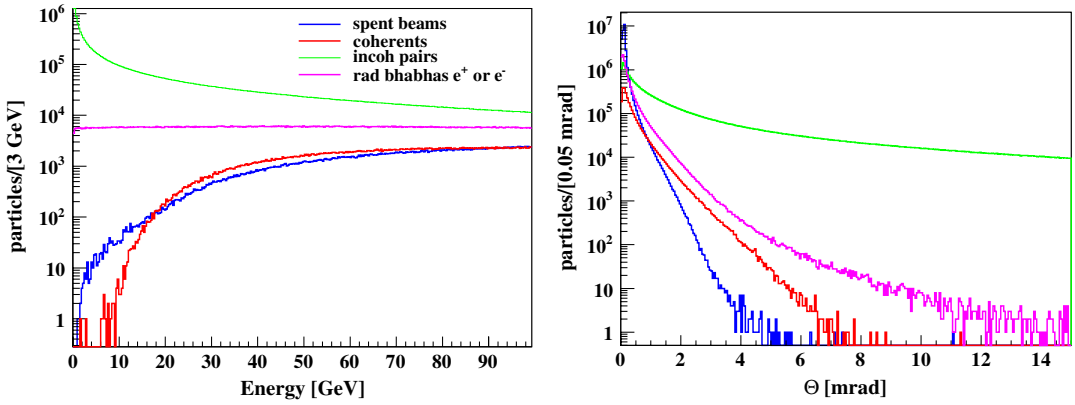

FIG. 1. Energy distribution up to 100 GeV of the spent beam and the different beam-beam interaction products (left). Angular distribution at the interaction point of the spent beam and the different beam-beam interaction products (right). The distributions are not normalized with respect to their rates.

techniques studied. The beam-beam background processes and their correlations with luminosity are studied, considering several beam aberrations at the IP. Finally, a new potential signal from the $\gamma\gamma \rightarrow$ hadrons process is assessed for tuning purposes.

II. BDS TUNING

In order to mitigate effects due to static and dynamic imperfections, the CLIC BDS lattice (with $L^* = 3.5$ m) is designed to reach a peak and total luminosity higher than their nominal values, by ~20% and ~30%, respectively. The peak luminosity is defined as the luminosity in a region of $\pm 1\%$ around the 3 TeV peak. Half of the 20% peak luminosity is the budget for the static imperfections, the other half for the dynamic errors.

Table I shows the values of the peak and total luminosities obtained by tracking the beams in the ML and BDS (using the tracking code PLACET [11]) and computing them with GUINEA-PIG [12], the corresponding nominal values are reported in parenthesis. The main beam parameters and the corresponding background rates are reported in Table I as well. In the following we present the first results of the tuning of the static imperfections in the CLIC BDS. Detailed studies for dynamic imperfections can be found in [13].

TABLE I. Main parameters of CLIC at $E_{\rm cm} = 3$ TeV accounting for imperfections. Nominal peak and total luminosity are in brackets. The background is per bunch crossing, beamstrahlung photons are per beam particle.

Total luminosity (nominal) $\mathcal{L}$	$[10^{34}\ \mathrm{cm}^{-2}\,\mathrm{s}^{-1}]$	7.7 (5.9)
Peak luminosity (nominal) $\mathcal{L}$	$[10^{34}\ \mathrm{cm}^{-2}\,\mathrm{s}^{-1}]$	2.4 (2.0)
Repetition frequency f_r	[Hz]	50
Bunches per train N_b		312
Distance between bunches Δ_y	[ns]	0.5
Particles per bunch N	$[10^{10}]$	0.372
Bunch length σ_z	$[\mu\mathrm{m}]$	44
Emittances $\gamma\epsilon_x/\gamma\epsilon_y$	[nm]/[nm]	660/20
Beam sizes σ_x^*/σ_y^*	[nm]/[nm]	45/1
Beamstrahlung photons/particle n_γ		2.1
Incoherent pairs $N_{\rm pairs}$	$[10^3]$	330
Coherent pairs $N_{\rm coh}$	$[10^7]$	33
Hadronic events N_H	$E_{\gamma\gamma_{\rm cm}} > 5$ GeV	2.8

In the simulations we assume that all the magnets of the BDS or FFS (except for the bending magnets) are randomly displaced in the two transverse planes (x and y) with a Gaussian distribution of $\sigma = 10$ μm, which is defined to be the prealignment tolerance for this study. This value is a first estimate, which is very close to the value used in the main linac alignment [14]. In this study identical e^+e^- machines are simulated. The three techniques studied to recover from the magnets displacements are: beam based alignment (BBA), of the entire BDS, combined with FFS sextupole knobs; luminosity optimization of the FFS; the latter combined with sextupole knobs.

The BBA technique consists of the 1-to-1 correction [15] followed by dispersion-free steering (DFS) [16] in the vertical plane and target DFS in the horizontal one. In the 1-to-1 correction, the beam is steered through the center of the beam position monitors (BPMs). DFS is a technique that measures the dispersion along the line, using off-energy test beams, and corrects it to zero or to the nominal value. An energy difference of 0.1% is used to measure dispersion. The assumed BPM resolution in these simulations is 10 nm. This value is a first estimate of the required BPM resolution.

The possibility to use tuning knobs based on linear combinations of sextupole displacements has been already explored in CLIC [9]. New tuning knobs are built here using FFS sextupole displacements, in order to control mainly coupling, dispersion, and waist shift in the two transverse planes. The five sextupoles of the FFS are used to construct 10 linear knobs by their horizontal and vertical displacements. Assuming the BDS without errors,

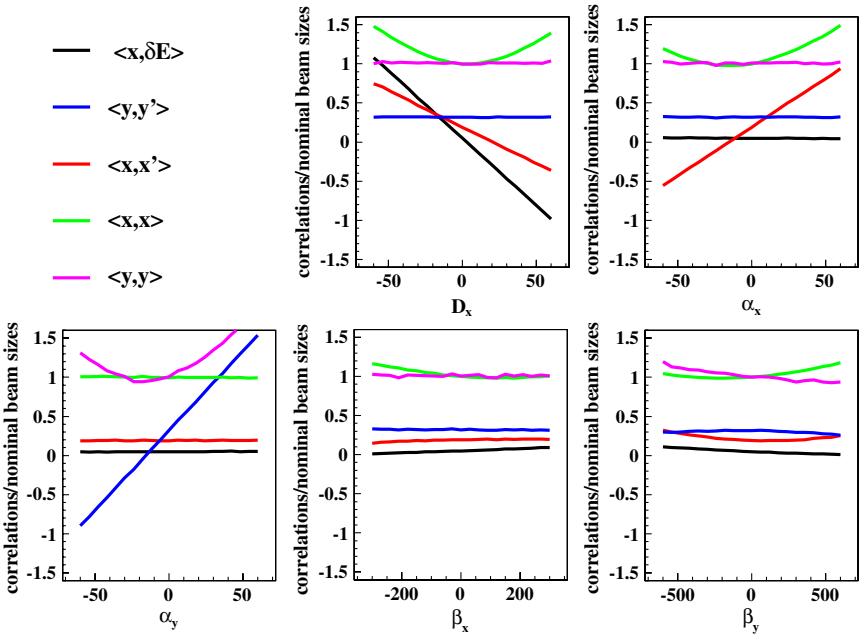

FIG. 2. Beam covariances at the IP as a function of the horizontal knobs scan. The range of the scan in units of μm is shown in Fig. 6.

a single sextupole is moved by 0.1 μm at a time. For each sextupole displacement the variations of the chosen set of aberrations are evaluated, and corresponding 5×5 response matrices M_x and M_y are built. The knobs correspond to the columns of the inverted matrices. The chosen set of knobs used to build M_x are: the two β at the IP, the two α and horizontal dispersion. The knobs in M_y are $\langle x, y\rangle$, $\langle x', y\rangle$, $\langle x', y'\rangle$, vertical dispersion, and vertical angular dispersion. These sets of knobs control the spectrum of the expected beams aberrations. Figures 2 and 3 show the effects of the knobs on the beam covariances at the IP, when they are scanned individually.

Despite the orthogonality condition with which they are built, these first knobs show a multiknobs behavior, whereby the knob constructed to control one aberration can act on another one. For example, the β knobs that change the α ($\langle x, x'\rangle$ and $\langle y, y'\rangle$) at the IP as well. Nevertheless, all the knobs contribute to the overall

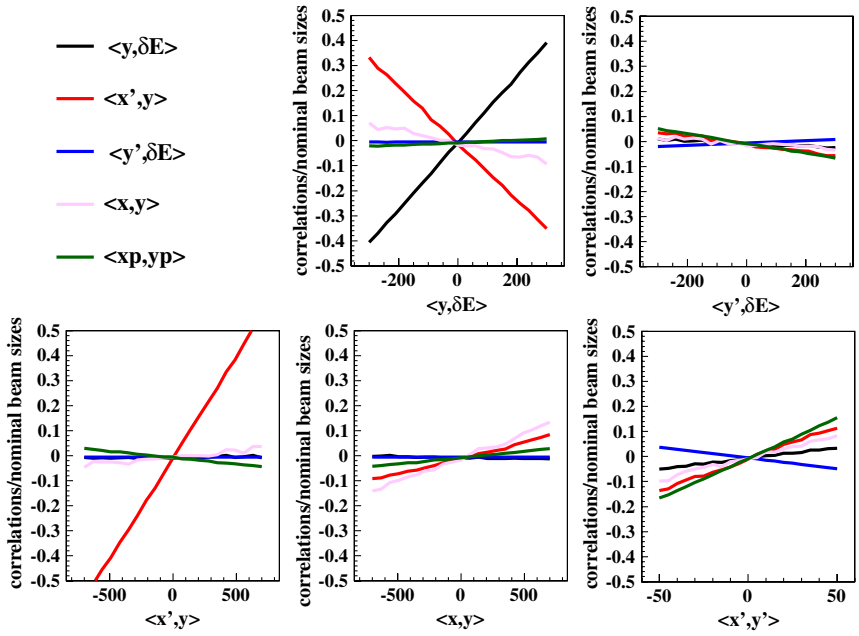

FIG. 3. Beam covariances at the IP as a function of the horizontal knobs scan. The range of the scan in units of μm is shown in Fig. 6.

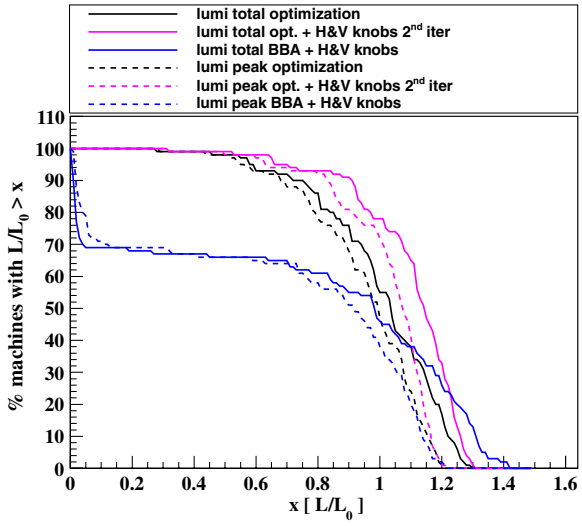

FIG. 4. Luminosity distribution of 100 machines after three different alignment procedures starting from an initial random prealignment of 10 μm. Full lines are the total luminosity values, dashed lines for the peak luminosity.

optimization procedure giving an increase of luminosity each time they are scanned. An optimization of such knobs to improve their orthogonality is planned for the future.

In the luminosity optimization procedure, the horizontal and vertical positions of the misaligned elements of the FFS (except for the bending magnets) are changed in order to maximize luminosity, using the Nedler-Mead algorithm (Simplex).

The results of the tuning of the BDS against magnet displacements are summarized in Fig. 4 for 100 machines and the most significant numerical values reported in Table II.

The BBA technique has proven successful in the CLIC collimation section alone, while it fails when the FFS is also considered [3]. Iterations of BBA combined with tuning knobs improve the correction. The final total and peak luminosity obtained after fifth iterations of BBA and tuning knobs for the 100 machines are shown in Fig. 4 (blue line). About 35% of the machines reach 10% more luminosity than the nominal value, which is

TABLE II. Number of machines reaching the target luminosity for the static imperfections in the three combinations of techniques here studied.

Technique	# machines [110% of total $\mathcal{L}$]	# machines [110% of peak $\mathcal{L}$]
BBA + knobs	38	20
Luminosity optimization	36	24
Luminosity optimization + knobs	65	40

the budget for static imperfections in the BDS. Of these, about 15% exceed the 30% more total luminosity we expect by design, while this is not the case for the peak luminosity. This effect is explained by the smaller horizontal beam size that is reached after the BBA and FFS knobs scan with respect to the nominal value. This causes, on one hand, the enhancement of total luminosity, and, on the other hand, the emission of more beamstrahlung photons with the consequent increase of average energy loss that smears the luminosity spectrum in the energy peak. With the luminosity optimization technique alone 36 machines reach the target of 10% more luminosity than nominal value. The best tuning performance is obtained by combining luminosity optimization and FFS knobs. In this case more than 60% of the machines reach the target value. It is worth noticing that about 90% of the machines reach 90% of CLIC nominal total luminosity.

Figure 5 shows the distribution of the number of iterations required by the techniques presented in Fig. 4. The iterations correspond to the number of luminosity measurements required. The number of luminosity measurements needed by the luminosity optimization procedure is 1 order of magnitude larger than the one required by the BBA combined with the Knobs technique. It is therefore crucial for CLIC to be able to measure luminosity as fast as possible (in the order of seconds) and to be able to tune the system in the most efficient way. The use of more sophisticated optimization algorithms and nonlinear knobs could improve the overall luminosity results and reduce the number of luminosity measurements required.

In the following, we concentrate on the definition of fast luminosity signals. For this purpose the beam-beam background processes and their correlation with the main sources of luminosity degradation are presented.

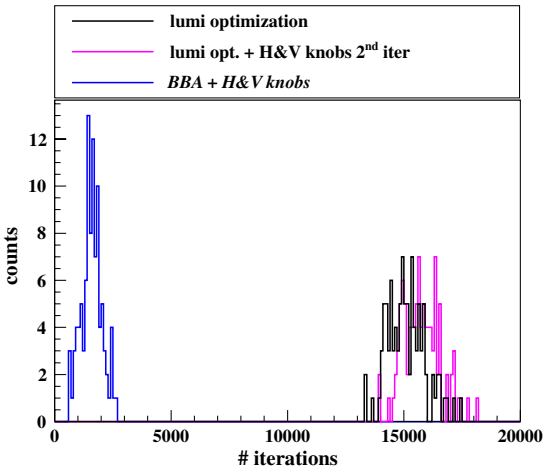

FIG. 5. Number of luminosity measurements required in the three different alignment procedures in order to reach the results shown in 4.

III. BEAM-BEAM BACKGROUND

Because of the high energy and high luminosity foreseen at CLIC the background rates due to the beam-beam interaction are expected to be high. The relevant processes are: the emission of beamstrahlung photons, the coherent pair production, the incoherent pair production, and the hadronic events. A detailed description of those processes can be found in [17].

Their expected rates in CLIC at 3 TeV c.m. energy are reported in Table I. The actual values of luminosity and background depend on the single machine and can change during operation. A first study of the variation of the background rates with the offsets of the two beams and the emittance growth has been presented in [18]. All the background rates show the same behavior in case of horizontal offsets and horizontal emittance growth of the two beams at the IP, following luminosity variations. In the case of vertical offsets and vertical emittance growth, the coherent processes show a different behavior with respect to luminosity. These processes are due to the interaction of photons with the electromagnetic field produced by the bunches, which is strongly dominated by the larger horizontal beam size and increase with small vertical offsets, as shown in [18]. In the following we show in more detail the dependence of the backgrounds and luminosity on the specific beam aberrations at the IP. These are the same aberrations we used to define the sextupole knobs in the previous section.

Luminosity signals and colliding beam parameters

We present here a study of the variation of different signals from beam-beam interaction, according to 10 different beam aberrations at the IP. The size of the aberrations has been chosen to produce a luminosity loss of about 30%. The six Signals (S) we have defined are: (i) coherent pairs from the two beams (coherent); (ii) average beamstrahlung photons from the two beams $[(n_{\gamma 1} + n_{\gamma 2})/2]$; (iii) difference of beamstrahlung photons from the two beams normalized to their sum $(1.0 - |\Delta n_\gamma / \Sigma n_\gamma|)$; (iv) ratio of beamstrahlung photons from the two beams $(n_{\gamma 2}/n_{\gamma 1})$; (v) total number of $\gamma\gamma \rightarrow$ hadrons events (hadrons); (vi) total incoherent pairs from the two beams (incoherent).

The two beams are transported to the IP as described in the previous section. In this case the sextupoles of one beam line are displaced according to the linear knobs introduced in Sec. II, generating the beam phase space distortion at the IP. The second beam line instead is kept perfectly aligned.

Figure 6 shows the relative change of the six signals and of the peak and total luminosity by scanning the five horizontal knobs. The colored lines correspond to parabolic fits through the data points. The optimum luminosity values coming from the parabolic fits of the six signals reproduce the maximum value of luminosity with a relative accuracy of the order of 10^{-3}. The numerical uncertainties are about 2% in the case of incoherent pairs and hadronic events and about 6% in

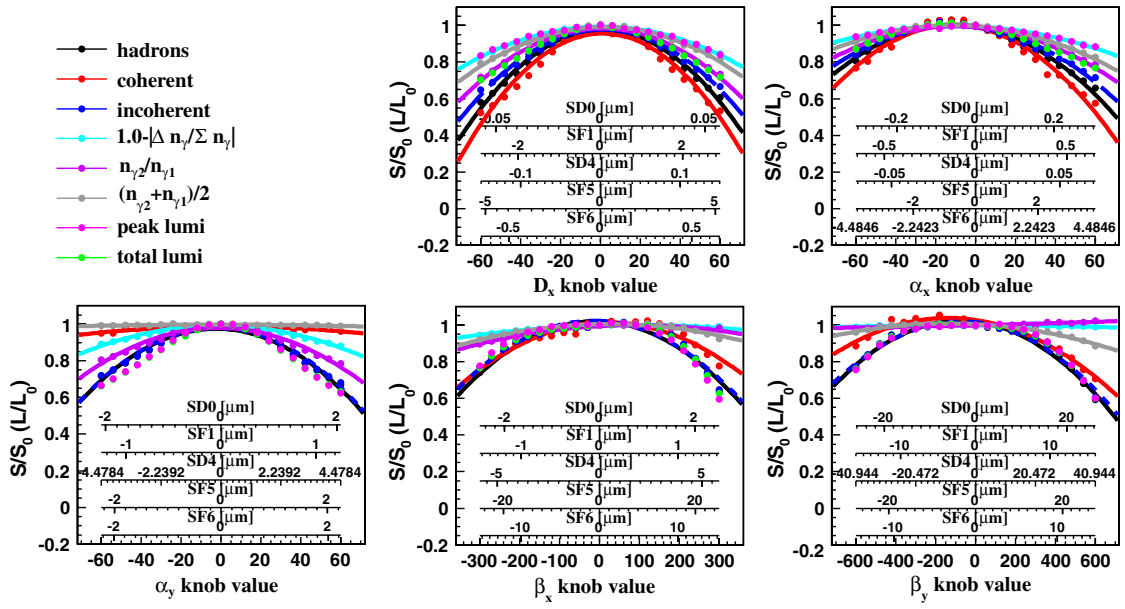

FIG. 6. Scan of the horizontal tuning knobs. The points show the change of luminosity (L/L_0) and beam-beam background (S/S_0) rates (normalized to their nominal values), according to horizontal dispersion, α and β functions in the two planes. The lines represent the fit through the background rates points. The lines corresponding to the fit through the points of the total and peak luminosity are not shown.

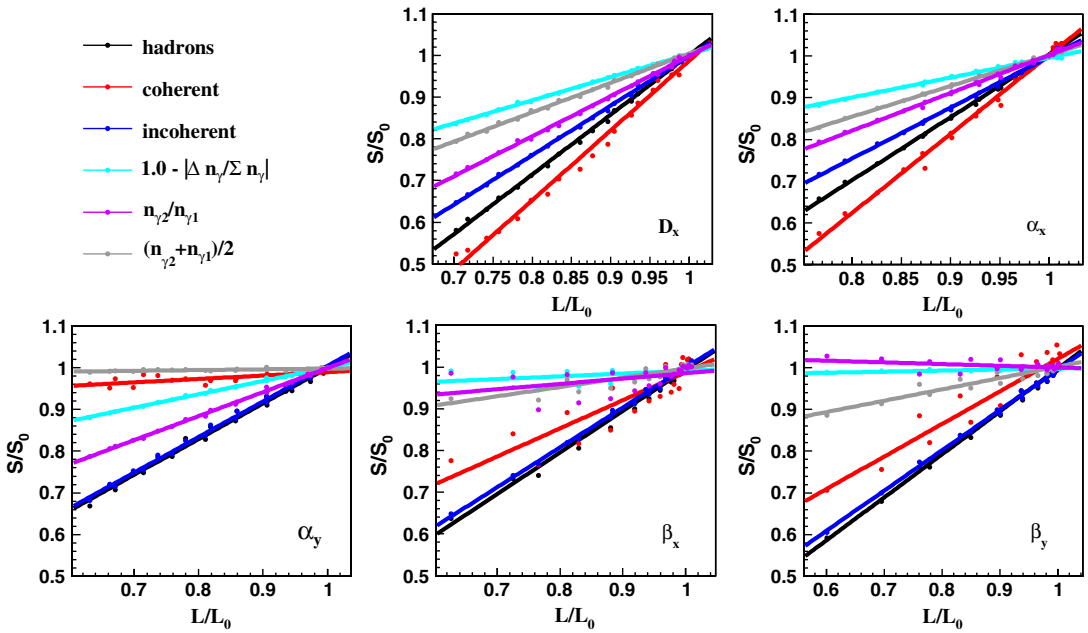

FIG. 7. Beam-beam background signal correlation with total luminosity for the scan of the five horizontal knobs shown in Fig. 6.

the case of beamstrahlung and coherent processes. Figure 7 shows a fairly linear correlation of the six signals to the total luminosity in this range of scan of the knobs. The angular coefficients [that we name $\Delta(S/S_0)/\Delta(L/L_0)$] obtained from the linear fits of the data points are shown in Fig. 8. A value of $\Delta(S/S_0)/\Delta(L/L_0)$ equal or close to 1 means that the variation of the luminosity and of the corresponding background signal are equal. The incoherent pairs signal presents an angular coefficient close to 1 (within 20% uncertainty) for all five horizontal aberrations considered. The relative hadronic events rate shows the same behavior as the incoherent pairs except for

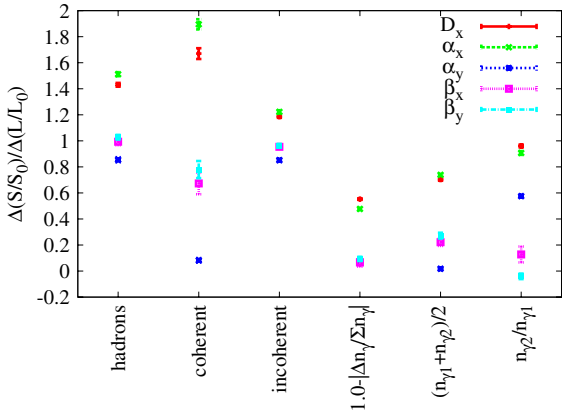

FIG. 8. Relative change of the six signals with total luminosity coming from the angular coefficient of the fit shown in Fig. 7.

horizontal dispersion and horizontal waist shift. In these two cases in fact the horizontal beam size increase leads to the reduction of beamstrahlung photons, hence to the decrement of γ available for the $\gamma\gamma \rightarrow$ hadrons reaction. The relative change of these two types of processes follow the luminosity variation within 20% uncertainty independently of the beam aberrations.

Figures 9–11 show the same analysis, when we scan the five vertical knobs. The behavior of background signals vs luminosity is similar to the horizontal case.

In summary, the incoherent processes, such as incoherent pairs and hadronic events, have the same variation of luminosity within 20% (i.e., the correlation between the change of these event rates and the change of luminosity is close to 1), regardless of the aberrations considered. The coherent processes, such as coherent pairs and beamstrahlung, have a different variation with respect to luminosity (i.e. their correlation is far from 1) and present a different variation according to the aberrations too. Therefore, by measuring the variation of the rates of the incoherent processes it is possible to evaluate the variation in the luminosity with 20% uncertainty. The variation of the rates of coherent processes could be used in combination with the one of incoherent processes to identify the main aberrations of the beams, in dedicated feedback.

In practice, it is critical to define a signal that can be easily identified against the other processes. Experimental techniques to detect beamstrahlung photons in the CLIC post collision line can be found in [19]. The incoherent pairs are produced with relatively small angles with respect to the

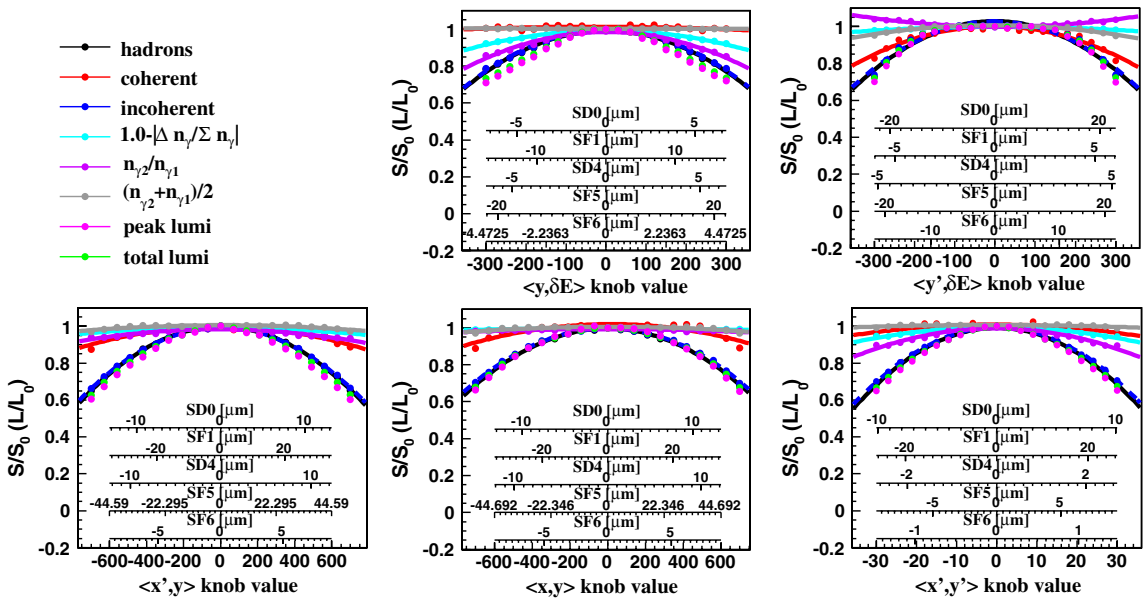

FIG. 9. Scan of the vertical tuning knobs. The points show the change of luminosity (L/L_0) and beam-beam background (S/S_0) rates (normalized to the nominal value), according to vertical dispersion, angular dispersion, and couplings. The lines represent the fit through the background rate points. The lines corresponding to the fit through the points of the total and peak luminosity are not shown.

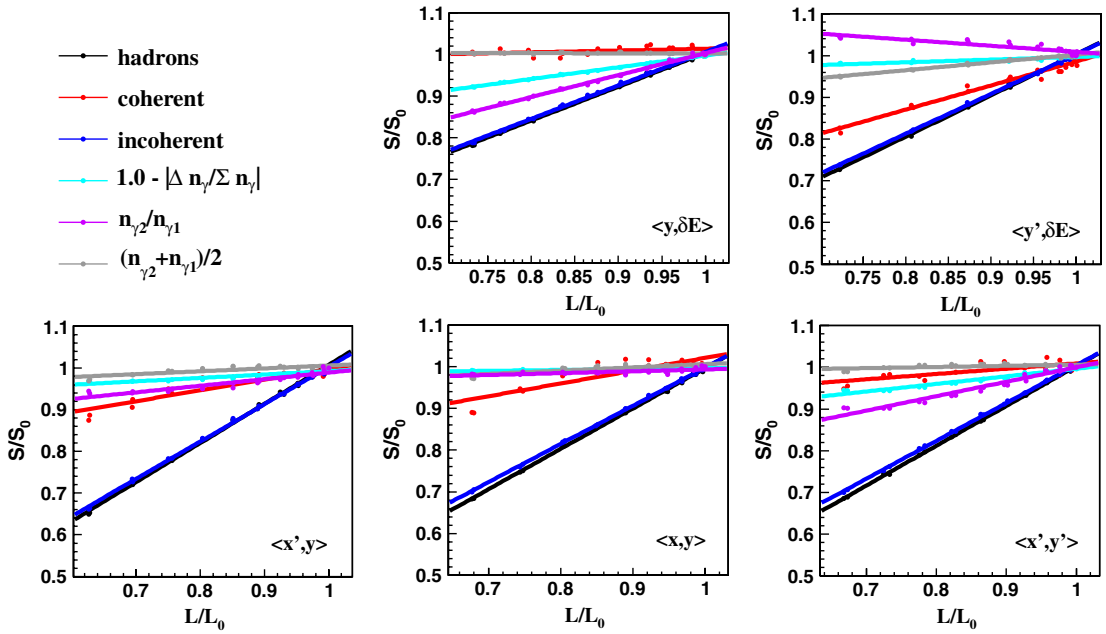

FIG. 10. Beam-beam background signal correlation with total luminosity for the scan of the five vertical knobs shown in Fig. 9.

beam axis, but are deflected by the beam fields. Therefore, the pair particles can have large angles. The integration of pair energy above a certain angle with respect to the beam axis has been studied as a potential signal for luminosity optimization in [8]. In CLIC their identification could be more complicated due to the presence of the coherent pairs in the forward region, leptons coming from hadronic events, and Bhabhas. In the following we discuss further the hadronic events signal by looking in particular at its multiplicity in the final state of the process.

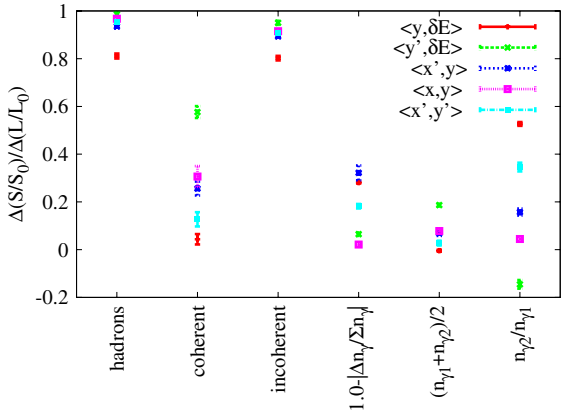

FIG. 11. Relative change of the six signals with total luminosity coming from the angular coefficient of the fit shown in Fig. 10.

IV. HADRONIC EVENTS

Hadrons at linear colliders are produced by the process $e^+e^- \to \gamma\gamma \to$ hadrons. The total $\gamma\gamma \to$ hadrons cross section is known experimentally up to 200 GeV in the center of mass energy. The simplest model of the energy dependence of the $\gamma\gamma \to$ hadrons cross section (σ) is the vector meson dominance one. The model assumes that the photon resonates to a hadronic state (a ρ) with a certain probability [20], with the energy dependence expressed as

$$\sigma = 211 \text{ nb} \cdot \left(\frac{s}{\text{GeV}}\right)^{\epsilon} + 215 \text{ nb} \cdot \left(\frac{s}{\text{GeV}}\right)^{\mu} \qquad (1)$$

where $\epsilon = 0.0808$ and $\mu = 0.4525$ [21]. GUINEA-PIG implements the above parametrization of the total $\gamma\gamma \to$ hadrons cross section. An electron or positron is replaced by the appropriate number of photons from the equivalent spectrum. The energies of the two colliding photons can be stored in a file which can be loaded as input to PYTHIA [22], or an equivalent code, to generate the hadrons.

Detectable signals for this process can be the hadron multiplicity and/or their deposited energy in the detector region. The total and single particles average multiplicity in the final state of the $\gamma\gamma \to$ hadrons collision as shown in Fig. 12 (left). The average total multiplicity is dominated by the photons and charged pions, while the leptons and the other hadrons multiplicity is close to zero in all the events analyzed. Figure 12 (right) shows the total energy distribution. In order to define a region where the hadron multiplicity can be easily identified and detected against the other background sources, two different p_T cuts are applied to the charged particles in order to ensure that they can travel in the forward detector region or in the detector main tracking region, considering a B field of 5 Tesla. Following [23], we consider tracks with $p_T > 0.050$ GeV and $27 \text{ mrad} < \theta < 117$ mrad for the forward region and tracks with $p_T > 0.160$ GeV and $117 \text{ mrad} < \theta < 1.57$ rad for the main tracking region.

The 27 mrad condition for the forward region is due to the envelope of the incoherent pairs while traveling in the detector solenoid magnetic field. We track the particles with a helix up to different longitudinal positions, taking into account the CLIC crossing angle. The incoherent pair particle positions in the XY plane, at $z = 2.65$ m from the IP, are shown in Fig. 13 (left). A circle containing the majority of the particles is defined "by eye" at each longitudinal position. The points so determined and the definition of the two angular cuts are shown in Fig. 13 (right).

The resulting multiplicity distributions of all the charged particles and that of the hadrons, according to the selected angles and momenta, are shown in Fig. 14. The multiplicities integrated over 1, 10, and 20 trains are shown. Almost all the multiplicity from $\gamma\gamma$ collision consists of charged hadrons. The mean value of the distribution over 20 trains is determined with about 1% fluctuation. Taking into account the 20% uncertainty in the correlation of this signal with luminosity, as shown in Figs. 8 and 11, this gives an estimation of luminosity variations within 1.2% precision. Moreover, given the CLIC repetition rate

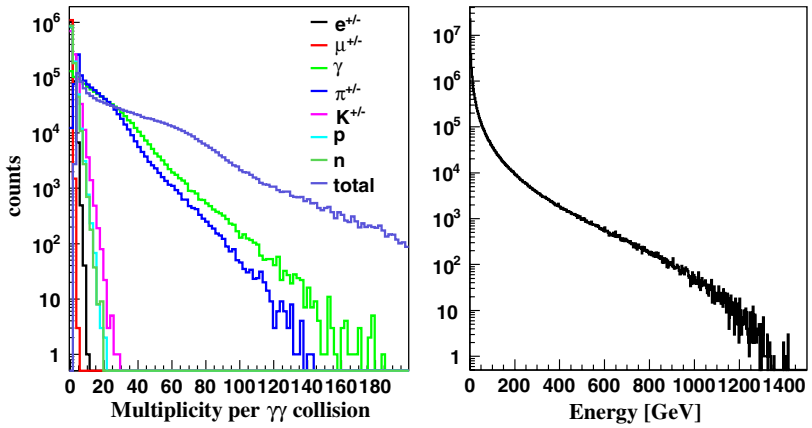

FIG. 12. Average particles multiplicity and energy for a single $\gamma\gamma$ collision.

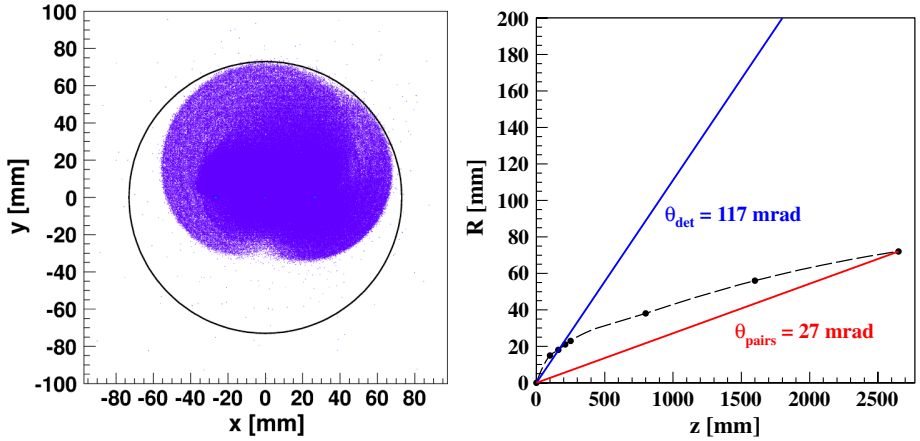

FIG. 13. Incoherent pair particle positions, at $z = 2.65$ m from the IP, for a constant B field of 5 T (left). Definition of the two regions for the $\gamma\gamma \rightarrow$ hadrons multiplicity detection (right). The blue line represents the main tracking region acceptance. The black points and the dashed line represent the incoherent pairs envelop. The red line is the angular cut we define to separate the hadronic events from the incoherent ones.

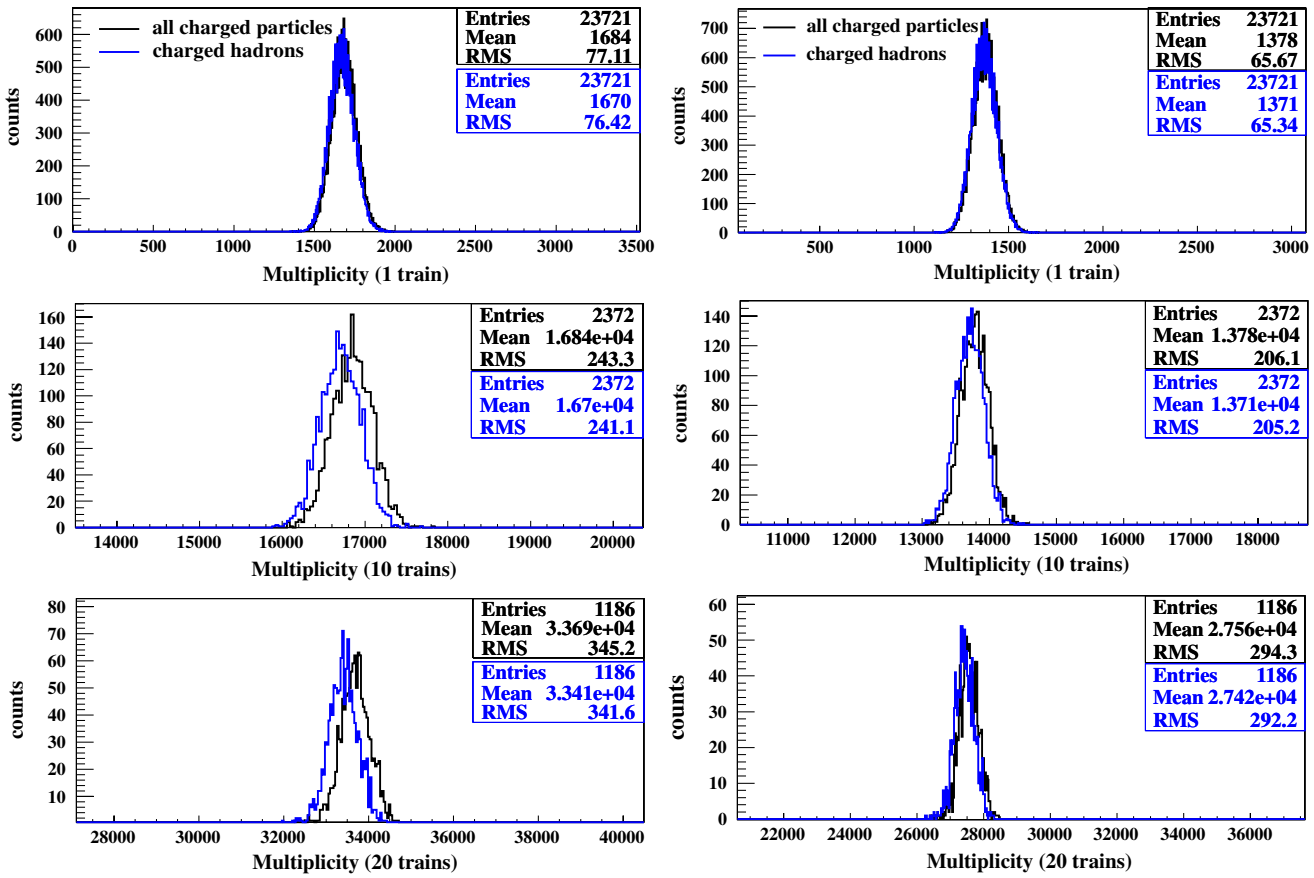

FIG. 14. Integrated charged particles and charged hadrons multiplicity over 1, 10, and 20 CLIC trains with $p_T > 0.050$ GeV/c and $0.027 < \theta < 0.117$ rad (left), and with $p_T > 0.160$ GeV/c and $0.117 < \theta < 1.57$ rad (right).

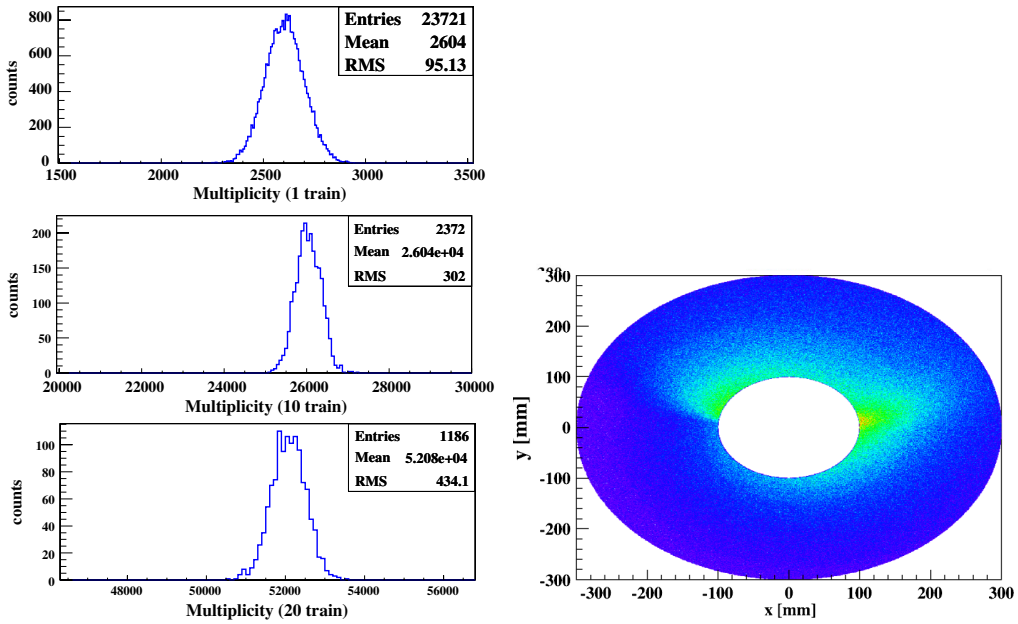

FIG. 15. Integrated particle multiplicity over 1, 10, and 20 CLIC trains in a disk of inner radius of 10 cm and outer radius of 30 cm at 2.6 m from the IP. The scatter plot of the X, Y positions of the particles in the defined disk is shown on the right.

(50 Hz) 20 trains correspond to 0.4 seconds. Requiring a total time ≤ 0.1 s for the readout electronics and signal elaboration, one luminosity measurement should take about 0.5 s.

Considering the number of particles intercepting a disk of 10 cm inner radius and 30 cm outer radius at 2.6 m from the IP, the rms fluctuation on the mean is of the order of 1% integrating over 10 trains only [Fig. 15 (left)]. This corresponds to about 0.3 s for one luminosity measurement. The two-dimensional distribution of the x and y positions at the disk (after the tracking in a uniform magnetic field of 5 Tesla) is shown in Fig. 15 (right). Taking into account the number of iterations that requires a luminosity measurement in the procedures studied here, the total time needed to tune the BDS, starting from a random Gaussian displacement of the FFS magnet of 10 μm, would be about 10 min when the BBA technique in combination with the FFS sextupoles knobs are applied, even with low success rate. The total time required to tune the BDS with the luminosity optimization technique is instead of the order of 2 hours. The full CLIC detector model is not considered in these simulations. The actual amount of material and the interaction of these particles with matter should be considered in order to define the best region of detection of the multiplicity minimizing the number of bunches to be integrated in the definition of the trigger signal.

V. CONCLUSIONS

In order to mitigate the static imperfections in the CLIC BDS different techniques have been applied. The first results show that their combination gives 90% of CLIC nominal total luminosity in 90% of the cases. Among them 65% reach the target luminosity of 110%. In particular, for the first time sextupole knobs are successfully and systematically used within CLIC FFS tuning. Tuning knobs and the luminosity optimization technique require a fast luminosity measurement. For this purpose, the possibility to use $\gamma\gamma \rightarrow$ hadrons background has been investigated. The first study of the charged particle multiplicity from this process in the vertex-tracking and/or in the forward region of the detector shows that it could provide a signal for a fast luminosity measurement in less than 1 s with $\sim$1% precision. Given the number of luminosity measurements needed by the different alignment techniques here considered, the full tuning of the CLIC BDS against magnet displacements can be achieved in the range between about 10 min and 2 hours.

[1] J. Pfingstner and J. Snuverink (to be published); CLIC Conceptual Design Report (CDR) [http://project-clic-cdr.web.cern.ch/project-CLIC-CDR].
[2] G. White *et al.*, in *Proceedings of the International Particle Accelerator Conference, Kyoto, Japan* (ICR, Kyoto, 2010), WEOBMH01
[3] A. Latina *et al.*, Report No. CERN-AB-2008-011; Report No. CLIC-Note-753; Report No. EUROTeV-Report-2008-040.
[4] R. Tomás, Phys. Rev. ST Accel. Beams **9**, 081001 (2006).
[5] R. Tomás *et al.*, Report No. CERN-ATS-2009-092; Report No. EuCARD-CON-2009-058; Report No. CLIC-Note-792.

[6] D. A. Karlen, Ph.D. thesis, Stanford University [Report No. SLAC-325, 1988].
[7] D. Schulte, at the CLIC 08 workshop at CERN, 2008.
[8] D. Schulte, Report No. CLIC CERN-AB-2004-068; Report No. CLIC-Note-600.
[9] P. Eliasson *et al.*, Report No. CERN-AB-2006-044; CLIC Report No. 660; EUROTeV Report No. 2006-039.
[10] T. Tauki and K. Yokoya, Phys. Rev. E **51**, 6119 (1995).
[11] D. Schulte *et al.*, Report No. CERN/PS 2001/028.
[12] D. Schulte, CERN-PS-99-014-LP; CLIC-Note-387.
[13] J. Snuverink *et al.*, in Proceedings of the International Particle Accelerator Conference, San Sebastian, Spain, 2011, TUPC023.
[14] D. Schulte *et al.*, in Proceedings of the Particle Accelerator Conference, Vancouver, Canada, 2009, TH6PFP045 .
[15] Chris Adolphsen *et al.*, in *Proceedings of the 1989 Particle Accelerator Conference, Chicago, IL* (IEEE, New York, 1989), p. 977.
[16] T. Raubenheimer and R. Ruth, Nucl. Instrum. Methods Phys. Res., Sect. A **302**, 191 (1991).
[17] D. Schulte, Ph.D. thesis, University of Hamburg [Report No. TESLA 97-98, 1997].
[18] B. Dalena and D. Schulte, Reports No. CERN-ATS-2010-080, CLIC-Note-835.
[19] R. B. Appleby, A. Apyan, L. C. Deacon, and E. Gschwendtner, in Proceedings of the International Particle Accelerator Conference, San Sebastian, Spain, 2011, TUPC027.
[20] P. Chien, T. L. Barklow, and M. E. Peskin, Phys. Rev. D **49**, 3209 (1994).
[21] G. A. Schuler and T. Sjöstrand, Report No. CERN-TH/96-119, 1996.
[22] T. Sjöstrand, S. Mrenna, and P. Skands, J. High Energy Phys. 05 (2006) 026.
[23] D. Dannheim and A. Sailer, CERN LCD-Note-2011-021.

A.5 Impact of detector solenoid on the Compact LInear Collider luminosity

Impact of detector solenoid on the Compact Linear Collider luminosity performance

Y. Inntjore Levinsen,* B. Dalena,† R. Tomás, and D. Schulte

CERN, Geneva, Switzerland

(Received 10 December 2013; published 27 May 2014; publisher error corrected 19 June 2014)

In order to obtain the necessary luminosity with a reasonable amount of beam power, the Compact LInear Collider (CLIC) design includes an unprecedented collision beam size of $\sigma_y = 1$ nm vertically and $\sigma_x = 45$ nm horizontally. With exceptionally small and flat beams, the luminosity can be significantly degraded due to the combination of the experimental solenoid field and a large crossing angle. The two main effects reducing the luminosity are y-x′-coupling and an increase of vertical dispersion. Additionally, incoherent synchrotron radiation (ISR) from the orbit deflection created by the solenoid field increases the beam emittance and results in unrecoverable luminosity degradation. A novel approach to evaluate the ISR effect from a realistic solenoid field without knowledge of the full compensation of the geometric aberrations is presented. This approach is confirmed by a detailed study of the correction techniques to compensate the beam optics distortions. The unrecoverable luminosity loss due to ISR for CLIC at 3 TeV has been evaluated, and found to be around 4% to 5% for the solenoid design under study.

DOI: 10.1103/PhysRevSTAB.17.051002 PACS numbers: 29.20.Ej, 29.27.-a, 41.85.Lc

I. INTRODUCTION

The Compact Linear Collider (CLIC) is an accelerator design based on normal conducting components. In order to obtain the required luminosity with reasonable power consumption, short bunch separation (0.5 ns) and small β^* are needed. A post-collision beam line for the spent beam and the main beam-beam products is necessary, which requires a large crossing angle of around 20 mrad [1]. A large crossing angle is also required to mitigate the effects of the parasitic bunch collisions between the incoming and outgoing beam, but is not the limiting factor for CLIC [1].

Relevant parameters for the CLIC beam delivery system (BDS) are shown in Table I. A detailed overview of the CLIC BDS can be found in [[2], Chap. 3.5]. The CLIC final focus system has strict tolerances, and the BDS is optimized taking higher order terms into consideration [3–7]. Compensation of beam distortions in the BDS, such as static and dynamic misalignments, has proven to be quite challenging [2,8].

In Fig. 1, the final 20 m of the CLIC BDS lattice is shown. The residual field from an experimental solenoid typically extends 10–15 m away from the interaction point (IP), depending on shielding and solenoid design. L^* is the distance from the IP to the closest focusing magnet, which is the QD0 for CLIC. Due to the short L^* required to reach the luminosity target, the main solenoid field overlaps with the last final focus magnets, which enhances the optical distortions at the IP [9]. The QD0 is partly inside the experimental solenoid. Special care has to be taken to make sure the interplay between the solenoid field and the magnet field is minimized.

A solenoid will in general have a radial field component on any charged particle off the solenoid center line, with a maximum around the entrance of the solenoid. This is the region of maximum β-function in a linear collider, and the beams are more sensitive to small errors. With a horizontal crossing angle, the horizontal solenoid field component will be larger than the vertical one, resulting in a strong vertical orbit displacement. In CLIC this orbit offset is typically on the order of 10 μm, for a solenoid field of 4–5 T and 1.5 TeV beam energy. The displacement results in a large vertical dispersion at the interaction point (IP). Furthermore, the beams in CLIC are exceptionally flat,

TABLE I. CLIC BDS parameters [2]. Peak luminosity is defined as the luminosity in the 1% energy peak.

Parameter	Value
Maximum beam energy	1.5 TeV
L^*	3.5 m
β^* (x/y)	10/0.07 mm
Crossing angle	20 μrad
IP beam size (x/y)	45/1 nm
IP beam divergence (x/y)	7.7/10.3 μrad
Bunch length	44 μm
Nominal peak luminosity	2.5×10^{34} cm^{-2} s^{-1}

*yngve.inntjore.levinsen@cern.ch
†Present address: CEA/SACLAY, DSM/Irfu/SACM F-91191 Gif-sur-Yvette, France.

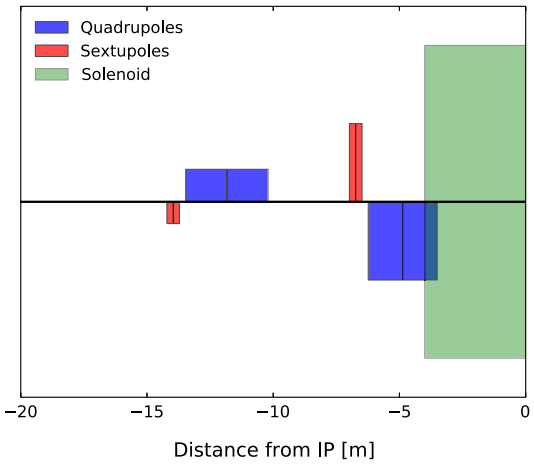

FIG. 1. The final 20 m of the CLIC final focus system. The 4 m long experimental solenoid is marked in green. The final doublet quadrupoles are marked in blue, and the sextupoles in red. The height of the bars indicate their relative strength and polarity.

which means that any coupling to the vertical plane significantly deteriorates the luminosity.

Particles with large angles at the IP have a large displacement from the beam orbit in the region close to the last focusing magnet, where the radial solenoid field is strongest. Hence, the experimental solenoid introduces strong y-x′ coupling at the IP which must be corrected.

Due to the high beam energy in CLIC, there is a significant emission of synchrotron radiation as a result of the beam deflection in the solenoid region. Earlier similar studies have shown an unrecoverable luminosity loss due to ISR of up to 25%, depending on the detector solenoid design [2,10].

The unrecoverable loss is an important concern for CLIC. Optical aberrations can be corrected in several ways; using the final focus magnets, adding skew quadrupoles, using an antisolenoid [9], dipole orbit corrector integrated into the experiment [11], and longer L^* [12].

We present a new simulation approach which evaluates the effect of the ISR alone without the knowledge of the full compensation. This approach is verified with a semi-analytical approach, as well as a more time-consuming study where the full compensation is found.

For the latter study, the tuning methods described in [8] are used to compensate for optical distortions introduced by the experimental solenoid field. A realistic design of the solenoid and antisolenoid is used [13]. Similar correction schemes have been explored for. e.g., the NLC [9], but at lower beam energies which means synchrotron radiation effects are less significant.

There are two problems with the full compensation study which are addressed with the new simulation approach. First of all, it is a computationally demanding procedure, requiring on the order of weeks of CPU time to get to the final result. Second, once the result is obtained, one does not know if the remaining luminosity loss is purely due to ISR, or if there are residual optical aberrations.

II. EXPERIMENTAL SOLENOID FIELD

Two detectors will be running in a push-pull configuration in CLIC. In the conceptual design report it is foreseen that one detector will follow the SiD design [14], while the second detector will have The International Large Detector (ILD) design [15]. An important difference in the two magnet designs is the peak longitudinal field, which is 4 T for the ILD detector magnet,

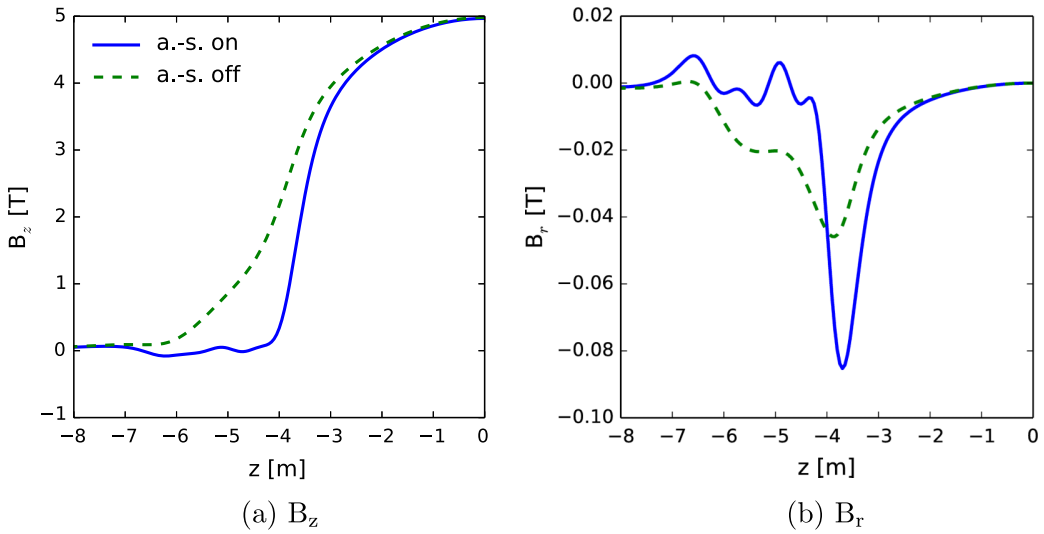

(a) B_z (b) B_r

FIG. 2. The longitudinal (a) and radial (b) SiD solenoid field with (blue, solid) and without (green, dashed) antisolenoid, along a beam line with a 10 μrad inclination with respect to the solenoid axis. The QD0 entrance is at 3.5 m, and the IP is at 0 m.

and 5 T in the SiD case. Nevertheless, previous studies have found that the luminosity loss from the two detector designs is fairly similar due to the relative increase in stray fields from the ILD solenoid compared to the SiD solenoid [10].

The longitudinal and radial fields along the beam line for the SiD detector magnet are shown in Fig. 2, both with (blue, solid) and without (green, dashed) the antisolenoid [14]. For all detector designs currently considered, the antisolenoid is foreseen to be integrated into the CLIC detector. This is in contrast to, e.g., the International Linear Collider (ILC) [16], where the antisolenoid is integrated into the QD0 design [17]. The antisolenoid significantly reduces the longitudinal field inside the QD0, increasing the radial field at the entrance of the QD0 (at 3.5 m). This reduces the optical aberrations originating from the combination of the quadrupolar field of the QD0 and the solenoid stray fields [9].

In this paper we discuss only the $L^* = 3.5$ m lattice design. An increase of L^* to around 6–8 m has been considered in order to have the QD0 outside the detector [12,18]. This would have the benefit of an improved mechanical stability of the QD0 since it would be attached to the tunnel ground/beam line. It would further reduce the interference between the QD0 and the experiment, both in terms of taking up physical space for detector components, and in terms of magnetic field interplay. The downside of a longer L^* is primarily reduced luminosity. A different L^* is expected to significantly impact the result of the studies presented here.

III. SEMIANALYTICAL APPROACH

The problem of evaluating the luminosity loss due to the detector solenoid can be divided into two parts. The first part consists of the evaluation and the correction of the optical distortions, which should be possible to correct for by using the antisolenoid and tuning knobs. The second part, the ISR from the vertical orbit deflection, increases the beam emittance. This emittance increase cannot be compensated for, and can be considered a minimum luminosity loss for a given solenoid design.

From Refs. [19,20], we have the following estimate for the increase of vertical beam size due to synchrotron radiation

$$(\Delta\sigma_y^{\mathrm{SR}})^2 = C_E\gamma^5 \int_0^\infty \frac{R_{36}^2(z)}{|\rho(z)|^3}\mathrm{d}z, \tag{1}$$

where

$$C_E = \frac{55}{24\sqrt{(3)}} r_e\lambda_e = 1.26\times 10^{-27}. \tag{2}$$

Here, R_{36} is the transport matrix element 36 for the given slice $\mathrm{d}z$ to the IP, γ is the relativistic gamma, and $\rho(z)$ is the radius of curvature at z. r_e and λ_e are the electron classical and Compton radius, respectively. The beam size increase should be added in quadrature to the initial beam size.

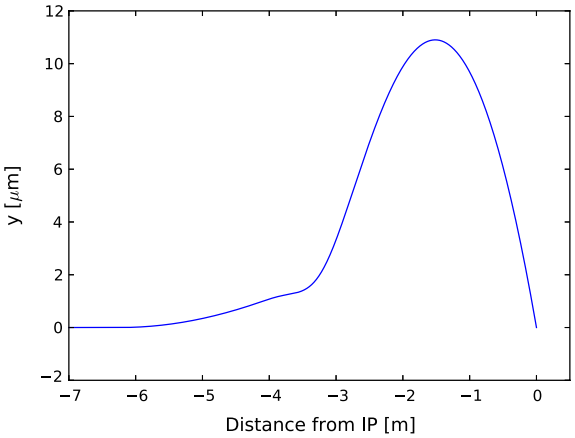

FIG. 3. The vertical orbit of the last 7 m before the IP given in μm. The QD0 is displaced vertically in order to get the orbit to end at $y = 0$.

We calculate the $R_{36}(z)$ by tracking backwards an off-momentum particle (+4 GeV) from the IP under the assumption that the dispersion at the IP is 0. $\rho(z)$ is calculated numerically from the orbit shown in Fig. 3. The estimate from this analytical formula then gives us

$$\Delta\sigma_y^{\mathrm{SR}} = 0.36\ \mathrm{nm}, \tag{3}$$

for the solenoid field map which has the antisolenoid included.

The initial core 1 sigma beam size is about 1 nm in CLIC, which means an increase of 6.4%. If we assume that luminosity is inversely proportional to beam size, we get a luminosity loss of 6%. If we instead use the rms vertical beam size which is around 1.3 nm, we get a relative increase to the beam size of around 3.7%. However, for the peak luminosity [21] in particular, the core beam size is usually considered to be the more relevant parameter. This is an encouraging result, considering that up to 25% luminosity loss due to ISR caused by the solenoid was expected for the nominal CLIC machine [2].

Estimating luminosity loss only via beam size growth has a considerable level of uncertainty. The tails of the beam typically increase the rms beam size, while not affecting luminosity as significantly. For this reason, we always use GUINEA-PIG [23] to simulate the luminosity in our tracking studies.

IV. DETERMINISTIC APPROACH

A novel simulation approach is proposed, which separately evaluates the losses from ISR alone, before the full compensation is known. The procedure to evaluate the luminosity loss due to ISR is described in the lower part of

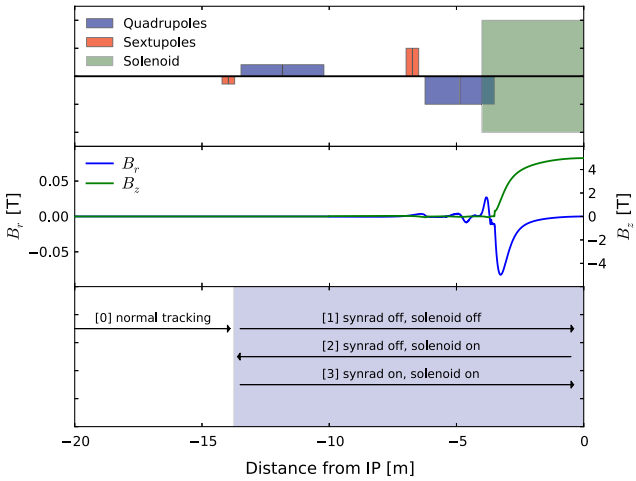

FIG. 4. Schematic overview of the last 20 m of the final focus in CLIC in the upper third. The experimental solenoid (green) is overlapping the QD0 (blue). Sextupoles SD0 and SF1 in red. strengths and signs of quadrupoles/sextupoles are indicated by the size and direction of the bars. In the middle the simulated SiD solenoid field is shown. The radial field in blue with values on the left side, and longitudinal field in green with values on the right-hand side. In the bottom plot the tracking procedure is visualized.

Fig. 4, where the tracking including the solenoid field is done using the new 4th order symplectic integrator described in the Appendix. The beam is first tracked forward without synchrotron radiation, and without the solenoid field present. This provides the optimal beam distribution at the interaction point. The ideal IP beam distribution is tracked backwards through the beam line, with the solenoid field turned on but still without synchrotron radiation. The result is a beam distribution with a perfect compensation for the coupling introduced by the solenoid field. Finally, the synchrotron radiation is turned on, and the beam is tracked forward through the beam line. The estimated luminosity is compared to a normal tracking of the beam without the solenoid field, but including ISR.

Using this approach we evaluated the simulated SiD field maps presented in Fig. 2. The loss of peak luminosity due to ISR in the detector solenoid including the anti-solenoid is found to be $(4.1 \pm 0.2)\%$, where the error bar is from the calculation of the luminosity in GUINEA-PIG. This result compares well to the result from the semianalytical calculation.

Without the antisolenoid, we find a luminosity loss of around 5%. 1% of additional luminosity would not alone be

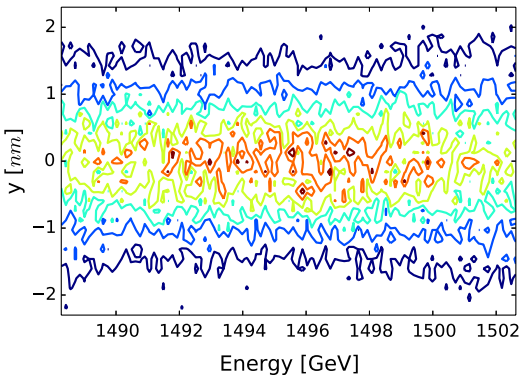

(a) No solenoid

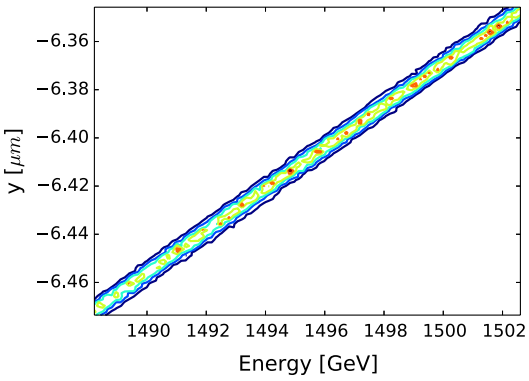

(b) With solenoid

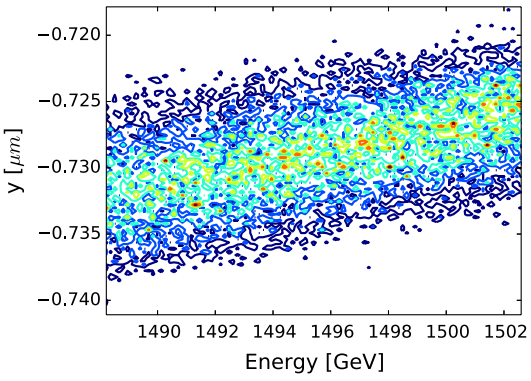

(c) With solenoid+anti-solenoid

FIG. 5. The vertical dispersion with and without solenoid field. No coupling is present in the baseline (a). The solenoid alone introduces a strong coupling (b), most of which is corrected by the antisolenoid (c). Additionally, the solenoid is producing a strong orbit deflection. In (b) the average vertical position is 6.4 μm off center.

enough to justify the installation of an antisolenoid which significantly complicates the detector design. However, the most important purpose of the antisolenoid is to protect the permanent magnet material in the QD0 and allow it to safely reach its high gradient. The antisolenoid also makes the compensation easier, as it decouples the solenoid field from the field inside the QD0 [9]. With an alternative larger L^* of 6 m or more [18], where the QD0 is outside the detector, the need for an antisolenoid could be reassessed.

V. FULL COMPENSATION

The main distortions responsible for the luminosity loss are vertical dispersion and y-x′ coupling, shown in Figs. 5 and 6. From these results it is evident that the antisolenoid alone is not able to fully compensate the optical distortions caused by the main solenoid field. With the solenoid alone on the order of 1% of nominal luminosity remains, before any compensation of the beam distribution is applied. When we add the antisolenoid the luminosity increases by an order of magnitude, but is still far off acceptable performance. Other compensation methods are required in addition to the antisolenoid, in order to fully recover the luminosity.

In order to recover the residual optical distortions induced by the main solenoid field we can use knobs based on transversal sextupole displacement in addition to the antisolenoid. These linear combinations of displacements of the five sextupoles in the CLIC final focus system ideally give 5 degrees of freedom for correcting coupling and dispersion terms (vertical displacements), and 5 for correcting focusing and dispersion terms (horizontal displacements). The main couplings caused by the experimental solenoid are vertical dispersion and y-x′ coupling, both corrected by vertical knobs. The knobs have been proven successful when applied to the tuning against magnet misalignment of the CLIC final focus, as reported in [8]. Additionally, a vertical displacement of QD0 is effective at correcting the vertical offset and dispersion at the IP. We also add horizontal displacement and roll of the QD0, for more local corrections. With the same three knobs for QF1, we have a total of 17 knobs to recover the residual luminosity loss due to the given experimental solenoid and antisolenoid design.

In our simulation, each knob is evaluated separately. We start with the QD0 knobs, then QF1, then the vertical sextupole knobs, and finally the horizontal knobs. For each knob we make a parabolic fit of the luminosity as a function

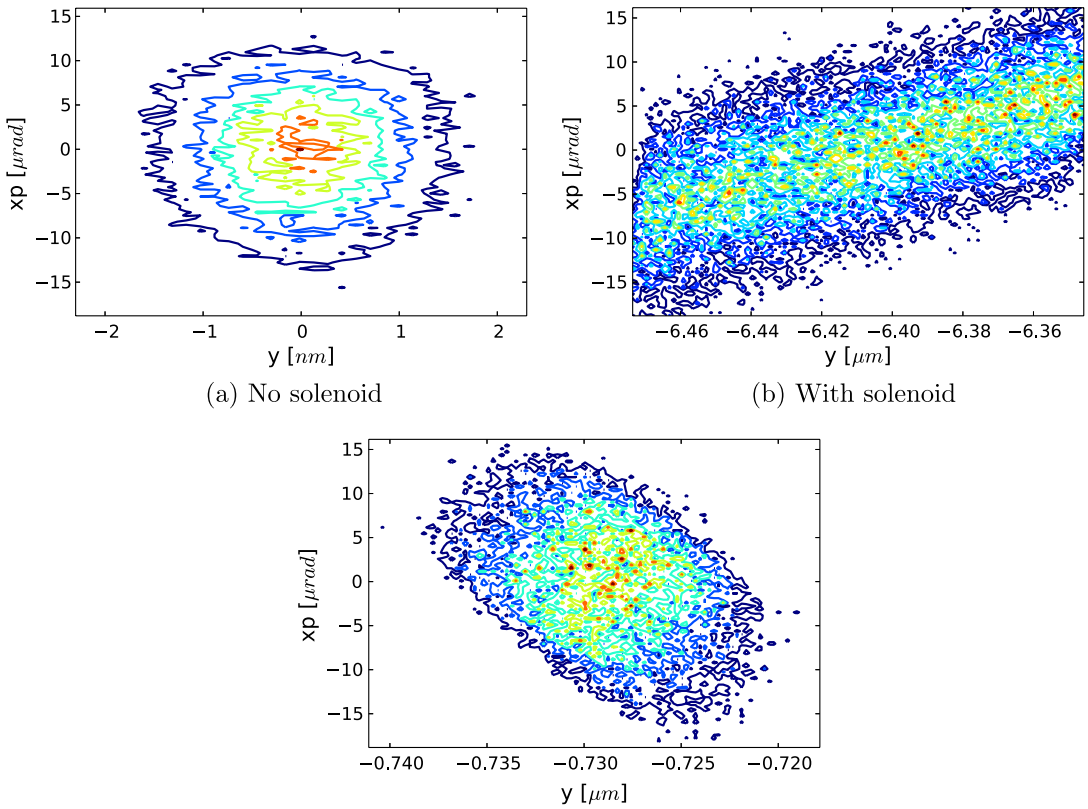

(a) No solenoid

(b) With solenoid

(c) With solenoid+anti-solenoid

FIG. 6. The y-x′ coupling with and without solenoid field. The observations are similar to those observed for the vertical dispersion in Fig. 5.

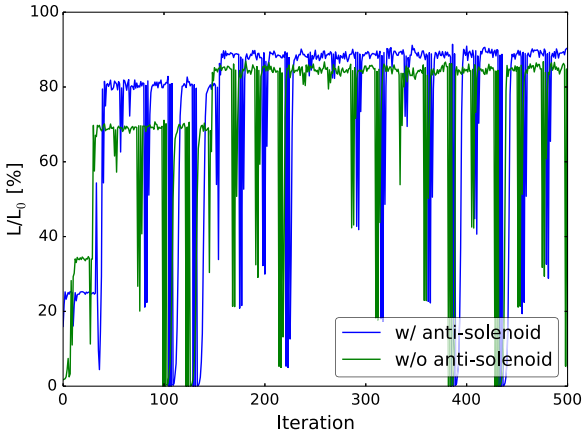

FIG. 7. The luminosity as a function of the number of iterations. The results when including the antisolenoid (blue) are significantly better than the results without (green). 100% is defined as the luminosity without solenoid field.

of the knob value and move the magnets accordingly. This is repeated with smaller and smaller steps to make sure we are close to the optimum. We iterate over the entire algorithm a few times to make sure we have at least found a local optimum. Note that we have not taken into account any magnet imperfections or misalignments in these simulations. ISR is still activated, which means that we expect to reach a luminosity of about 96% with the antisolenoid compared to the beam line without solenoid field included, based on the result from the deterministic simulation.

In Fig. 7 we see the resulting luminosity as a function of iterations. Each dip corresponds to the iteration where the algorithm moved to a new knob. We see that most of the aberrations are corrected after the first round of QD0 and vertical sextupole knobs. Without the antisolenoid, it is not possible to obtain the same luminosity level. The number of iterations to reach optimal luminosity is about the same.

We find a luminosity loss of $(8.0 \pm 1.6)\%$ with the antisolenoid in these simulations. Including the error bars, this fits well with both the semianalytical estimate of 6%, and the deterministic approach which estimated 4% luminosity loss. The results give us confidence that the deterministic approach makes valid assumptions for evaluating the luminosity loss due to ISR alone.

In Fig. 8 the vertical dispersion and y-x′ coupling can be seen with the full compensation. Only dipolar and quadrupolar terms have been used for this compensation. A check was made keeping ISR off for the entire simulation. The routine then completely canceled out the optical aberrations using only these linear elements. While one can then conclude that the solenoid itself introduces mostly linear coupling terms, the solenoid in combination with ISR can lead to nonlinear effects that may require nonlinear correctors. Indeed, the limitation of a tuning-based algorithm is the lack of knowledge about the absolute optimal luminosity.

VI. CONCLUSIONS

A novel simulation approach for estimating the irreversible luminosity loss from incoherent synchrotron radiation produced by the experimental solenoid in a high energy lepton collider has been developed. The results are compatible with the slower and more complicated simulations to find the full compensation, and consistent with a semianalytical estimate of the beam size growth. This method obtains in a deterministic way the optimal luminosity that can be achieved if the correction is perfect.

For the current SiD design for CLIC, we find that we can expect a luminosity loss due to incoherent synchrotron radiation of $(4.1 \pm 0.2)\%$. This is at the optimistic end of the scale given in the conceptual design report, and is a promising result for the CLIC design effort. The antisolenoid reduces the losses due to ISR by approximately 1%, and strongly reduces the optical distortions. We have shown

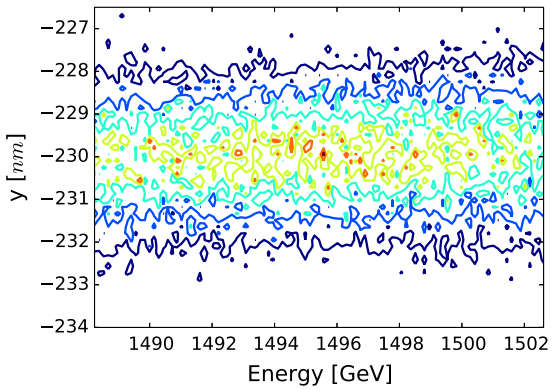

(a) Vertical dispersion

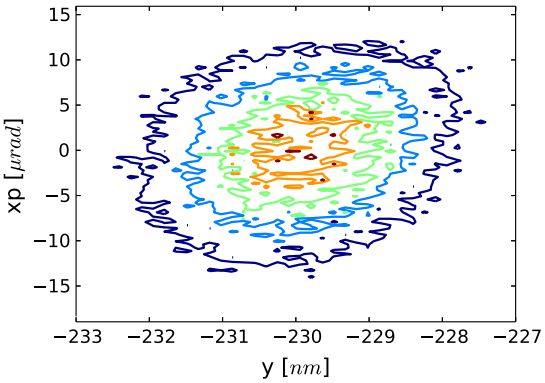

(b) y-x′ coupling

FIG. 8. The vertical dispersion and y-x′ coupling with the optimal knobs. This should be compared to the reference distribution shown in Figs. 5(a) and 6(a).

through a full simulation that the beam delivery system provides enough flexibility to correct for the optical distortions introduced by the solenoid and its overlap with the last focusing magnet.

ACKNOWLEDGMENTS

The authors would like to express their thanks to Michele Modena, Hubert Gerwig, Antonio Bartalesi, and Alexander Aloev for all their help with the field map simulations and fruitful discussions. We would also like to thank Andrea Latina and Jochem Snuverink for valuable help implementing the code into PLACET. Finally, we would like to thank Paul Anton Letnes for carefully reading through and correcting the English grammar.

APPENDIX: TRACKING ROUTINE

We have implemented a 4th order symplectic integrator in the particle tracking code PLACET [24,25], with a user defined step length. The sum of magnetic fields from beam line elements and solenoid field map is used to calculate the Lorentz force at each location of a kick. With the appropriate choices for drifts and kicks, it can be shown numerically that this integrator is in fact of 4th order [26]. This integrator allows us to track the beam through a combination of beam line elements and added field map (solenoid field), something that was not possible previously.

The new integrator has been compared to the other independent tracking routines already available in PLACET (excluding the solenoid field map) and was found to be in good agreement. The 4th order integrator has also been independently compared to a Lie tracking routine [27].

In Fig. 9 the error in the vertical position at the interaction point is shown as a function of the step length used. Each set of initial coordinates is tracked with multiple step lengths. The error is estimated as the final position at the interaction point with the given step length compared to using a much shorter step length. For each step length we then get an average error for N initial coordinates as

$$\mathrm{avg}(|\Delta y|) = \frac{\sum_{i=1}^{N} |\Delta y_i|}{N}. \tag{A1}$$

The vertical beam size at the interaction point is approximately 1 nm, so the error should be well below this value. Hence, step lengths lower than 1 cm are acceptable. The results presented in this paper are obtained using a step length of 1 mm.

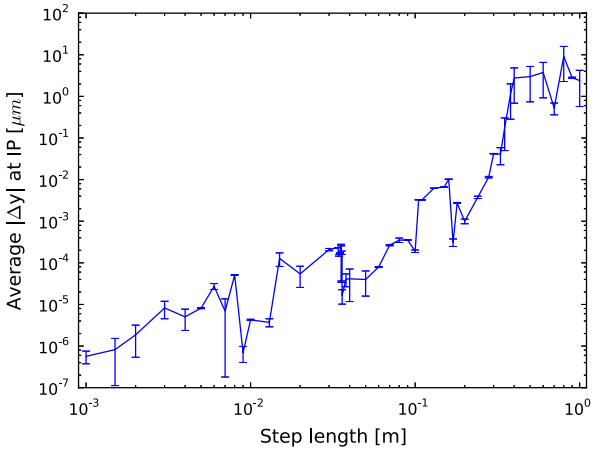

FIG. 9. The difference in vertical position as a function of step length is evaluated for 4000 initial positions, using the formulas defined in Eq. (A1). The trajectory with shortest step length (0.2 mm) is used as reference.

[1] D. Schulte and F. Zimmermann, *19th IEEE Particle Accelerator Conference, Chicago, USA, 2001*, CLIC-Note-484.
[2] The CLIC Collaboration, Technical Report, 2012; http://clic-study.org/accelerator/CLIC-ConceptDesignRep.php.
[3] P. Raimondi and A. Seryi, Phys. Rev. Lett. **86**, 3779 (2001).
[4] R. Tomás, Phys. Rev. ST Accel. Beams **9**, 081001 (2006).
[5] E. Marin Lacoma, R. Tomás, and Y. Koubychine, Ph.D. thesis, Barcelona, IEEC, 2012; http://cds.cern.ch/record/1504285.
[6] E. Marin, R. Tomás, P. Bambade, K. Kubo, T. Okugi, T. Tauchi, N. Terunuma, J. Urakawa, A. Seryi, R. White *et al.*, Phys. Rev. ST Accel. Beams **17**, 021002 (2014).
[7] J. Barranco Garcia, R. Tomás Garcia, and E. Marin, Phys. Rev. ST Accel. Beams **16**, 041001 (2013).
[8] B. Dalena, J. Barranco, A. Latina, E. Marin, J. Pfingstner, D. Schulte, J. Snuverink, R. Tomás, and G. Zamudio, Phys. Rev. ST Accel. Beams **15**, 051006 (2012).
[9] Y. Nosochkov and A. Seryi, Phys. Rev. ST Accel. Beams **8**, 021001 (2005).
[10] B. Dalena, D. Schulte, and R. Tomás, in *Proceedings of the International Particle Accelerator Conference, Kyoto, Japan* (ICR, Kyoto, 2010); Reports No. CERN-ATS-2010-081; CLIC-Note-831, p. 3.
[11] A. Seryi, T. Maruyama, and B. Parker, SLAC Technical Report No., 2006; http://www.osti.gov/energycitations/product.biblio.jsp?osti_id=876041.
[12] A. Seryi, *Near IR FF design including FD and longer L* issues*, http://cds.cern.ch/record/1216866.
[13] D. Swoboda, B. Dalena, and R. Tomas, CERN Technical Reports No. CERN-OPEN-2010-016; CLIC-Note-815, 2009; http://cds.cern.ch/record/1266884
[14] H. Aihara, P. Burrows, and M. Oreglia, arXiv:0911.0006v1.
[15] ILD Concept Group, *ILD Letter of Intent, http://ilcild.org/documents/ild-letter-of-intent (2010).*
[16] ILC Technical Report, 2013; https://www.linearcollider.org/ILC/Publications/Technical-Design-Report.
[17] B. Parker, M. Anerella, J. Escallier, and P. He, in *Proceedings of the 22nd Particle Accelerator Conference, PAC-2007, Albuquerque, NM* (IEEE, New York, 2007).
[18] G. Zamudio and R. Tomás, CERN Technical Report No. CLIC-Note-882, 2010; http://cds.cern.ch/record/1368480.
[19] P. Tenenbaum, J. Irwin, and T. O. Raubenheimer, Phys. Rev. ST Accel. Beams **6**, 061001 (2003).

[20] B. Parker and A. Seryi, Phys. Rev. ST Accel. Beams **8**, 041001 (2005).
[21] The peak luminosity is defined as luminosity produced by collisions within 1% of the energy peak. See discussion in, e.g., [22], Chap. 2.1.1.
[22] L. Linssen, A. Miyamoto, M. Stanitzki, and H. Weerts, arXiv:1202.5940v1.
[23] D. Schulte, in *5th International Computational Accelerator Physics Conference, Monterey, CA, USA, 1998*, CLIC-Note-387, pp. 127–131.
[24] A. Latina, E. Adli, H. Burkhardt, Y. Renier, G. Rumolo, D. Schulte, and R. Tomás, in *Proceedings of the 11th European Particle Accelerator Conference, Genoa, 2008* (EPS-AG, Genoa, Italy, 2008).
[25] A. Latina, E. Adli, B. Dalena, D. Schulte, and J. Snuverink, CERN Technical Report No. CERN-ATS-2012-166, 2012; http://cdsweb.cern.ch/record/1463325.
[26] E. Forest and R. D. Ruth, Physica D: Nonlinear Phenomena **43**, 105 (1990).
[27] B. Dalena *et al.*, *IPAC'14, Dresden, Germany, 2014*.

A.6 Timing resolution of the FINUDA scintillation detectors

Nuclear Instruments and Methods in Physics Research A 603 (2009) 276–286

Contents lists available at ScienceDirect

Nuclear Instruments and Methods in Physics Research A

journal homepage: www.elsevier.com/locate/nima

Timing resolution of the FINUDA scintillation detectors

B. Dalena [a,1], G. D'Erasmo [a], D. Di Santo [a], E.M. Fiore [a], M. Palomba [a], G. Simonetti [a], A. Andronenkov [b], A. Pantaleo [b,*], V. Paticchio [b], D. Faso [c]

[a] Dipartimento Interateneo di Fisica, Universitá di Bari and INFN Sezione di Bari, via Amendola 173, 70126 Bari, Italy
[b] INFN Sezione di Bari, via Amendola 173, 70126 Bari, Italy
[c] Dipartimento di Fisica Generale dell'Universitá di Torino and INFN Sezione di Torino, via P. Giuria 1, 10125 Torino, Italy

ARTICLE INFO

Article history:
Received 28 August 2008
Received in revised form
5 February 2009
Accepted 6 February 2009
Available online 28 February 2009

Keywords:
FINUDA
Scintillation detectors
Timing resolution
TOF

ABSTRACT

Experimental characterizations of scintillation detectors timing performance of the internal (TOFINO) and external (TOFONE) scintillator barrels used in FINUDA experiment are presented.

The measurements take advantage of detecting synchronous particle pairs produced in the reactions, namely e^+e^- pairs from Bhabha collisions between the primary beams and K^+K^- pairs from $\phi(1020)$ decay.

The method used for synchronizing the multiple detectors constituting the scintillator barrels is also described as being carried out in two steps: a rough one online by the injection of laser light pulses flashing the scintillators all together, and a fine one offline exploiting the timing features of e^+e^- and K^+K^- pairs.

1. Introduction

The FINUDA experiment performed two distinct runs at the INFN Frascati (Rome—Italy) National Labs, the first in 2003–2004 and the second in 2006–2007, to investigate the formation and decay of Hypernuclei and the anti-kaon nucleon clusters produced by stopping—within thin solid targets—the slow K^- coming out from e^+e^- collisions at ϕ-factory DAΦNE, as reported in Refs. [1–3] and references therein.

The experiment employs a large acceptance and high momentum resolution magnetic spectrometer equipped with a Time-Of-Flight (TOF) system composed of two scintillator barrels: the internal one, named TOFINO and built as two distinct devices (TOFINO1 and TOFINO2) employed in the two runs, and the external one, named TOFONE. A description of these detectors has already been given [1–9], but it is worth reporting here some details concerning the behaviour of the TOF system during the data taking, mainly regarding the timing performance of the two arrays, together with the techniques used for their overall timing synchronization.

The goal of FINUDA was to attain measurements of the TOFONE–TOFINO TOF with an overall timing resolution, due both to detector timing performance and to barrel synchronization, better than 1 ns FWHM.

2. TOFINO construction details

The TOFINO (internal TOF) detector, located close to the beam pipe (Fig. 1), is the first detector hit by kaons. It is a cylindrical array of 12 scintillator slabs (see Table 1), this shape maximizing its geometrical acceptance. Each slab is connected on both sides to short plastic light guides which bring the scintillation light to the Light Detection Devices (LDDs). Pictures of the fully assembled TOFINO1 and TOFINO2 detectors are shown in Figs. 2 and 3 which highlight their similar constructions.

As already stated before, the technical features of the detector have already been described [2,5–9], hence only the most important issues related to the TOFINO development and performances will be summarized in this section. Notice in Fig. 1 the Internal Silicon Microstrip (ISIM) detectors [2], which use two-dimensional information to precisely track the spatial coordinates of the kaons just as they leave the TOFINO.

Since the TOFINO is installed in a region characterized by the presence of a 1.0 T magnetic field parallel to the z axis, the whole TOFINO mechanical structure is made of aluminium, which allows also to avoid sizable scattering effects on bulk heavy material. The presence of a high magnetic field led also to the choice of proximity focusing Hybrid Photo Diodes (HPDs) in TOFINO1, on account of their insensitivity to a magnetic field along their axis [5–7,9], and of Hamamatsu Fine Mesh photomultiplier tubes (PMTs) in TOFINO2, on account of their low sensitivity to magnetic fields up to 1.0 T, and higher intrinsic current gain [10–13].

The slabs are thin in order to minimize kaon energy loss and ensure that kaons stop as close as possible to the outgoing surface

* Corresponding author. Tel.: +39 0805443186; fax: +39 0800999509.
E-mail address: ambrogio.pantaleo@ba.infn.it (A. Pantaleo).
[1] Present address: CERN, CH-1211 Geneva 23, Switzerland.

0168-9002/$ - see front matter © 2009 Elsevier B.V. All rights reserved.
doi:10.1016/j.nima.2009.02.025

of the targets, thus reducing multiple Coulomb scattering of the emitted pions and preserving their high energy resolution.

Kaons coming from the DAΦNE interaction region, on account of their low momentum and high rest mass value, release more energy inside the TOFINO slabs than Bhabha scattered electrons or positrons, which are minimum ionizing particles (MIPs). The ratio between the energy loss in the TOFINO1 slabs of the K^+K^- pairs coming from ϕ decay and that of the e^+e^- pairs coming from Bhabha scattering was calculated by means of a dedicated simulation [7] to be 8.1 ± 0.2. The results of this simulation (represented by the continuous line) were compared to the experimental data reported in Fig. 4, in which the charge amplitude spectrum is relative to the HPD of the TOFINO1 slab # 1 on the electron beam entrance side (see Fig. 1). The deposited energy is directly related to the scintillation light which, partly attenuated while propagating towards side LDDs, generates photoelectrons (PEs) at the LDDs' photocathode. The number of PEs generated in TOFINO1 HPDs for central ($z = 0$) events is 28 ± 5 for MIPs and 230 for kaons [6,9].

Although particles crossing TOFINO2's thinner scintillators deposit less energy, the number of PEs generated in TOFINO2's LDDs for central events is near 75 for MIPs and 660 for kaons [8, Fig. 2.7]. The ratio of kaon PEs to MIP PEs is almost the same as in TOFINO1, but the numbers of PEs are higher, mainly on account of:

- a more favourable photocathode diameter value (17 compared to 13 mm);
- the removal of the last bend of the light guide (PMT parallel to the light guide whereas the HPD was parallel to the scintillator);
- shorter light guides (78 compared to 87 mm) and
- a possible deficit of useful PEs in TOFINO1 HPDs, like the one already observed [14] for focussing HPDs, but not reported yet for proximity focussing HPDs.

The clear separation between QDC (charge to digital converter) signals coming from electrons and kaons allowed us to discriminate between them by using different discriminator levels and to develop fast triggers for candidate back-to-back K^+K^- and e^+e^- pair events.

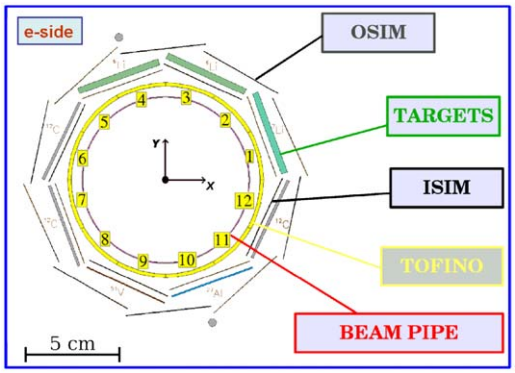

Fig. 1. The FINUDA interaction region scheme (electron beam entrance side, called e-side, view). The reference frame origin at the centre of the FINUDA apparatus (centre of the colliding beams) and z corresponding to the axis of the beam pipe.

3. TOFONE construction details

The TOFONE external scintillator barrel consists of 72 slabs mounted near the magnet cryostat (see Fig. 1 in [1] and Fig. 5). Each slab of the array is a trapezoidal bar of plastic scintillator (see Table 1) joined at both ends to 90° lucite reflecting prisms with conical adapters and 5 cm diameter 1 m long cylindrical light guides, in order to keep the PMTs outside the magnetic field of the FINUDA apparatus. Fig. 6 shows an exploded schematic view of the main pieces constituting one TOFONE slab assembly.

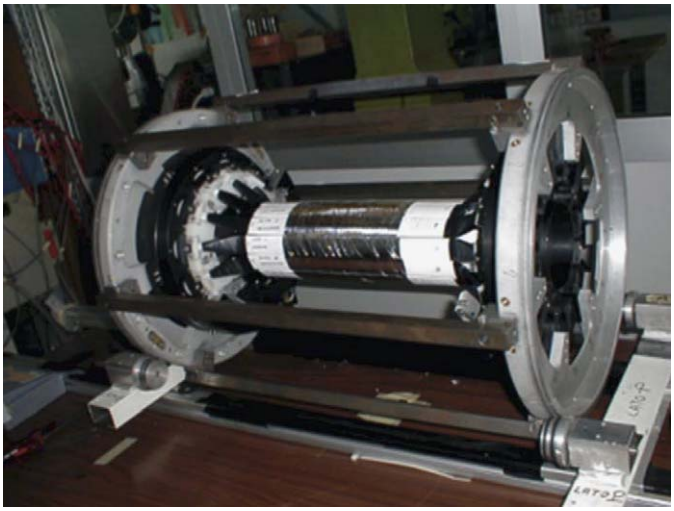

Fig. 2. The assembled TOFINO1 detector.

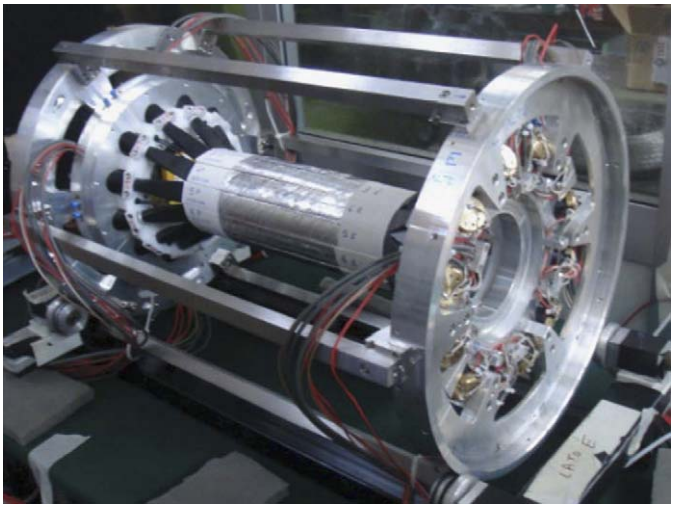

Fig. 3. The assembled TOFINO2 detector.

Table 1
Main features of TOFONE, TOFINO1 and TOFINO2.

	Scintillator	Dimensions of slabs (mm)	Light guides length (mm)	LDD	Photocathode diameter (mm)
TOFONE	BC 408	$2550 \times (116 + 107)/2 \times 100$	1000	PMT, Photonis XP2020	44
TOFINO1	NE 102A	$200 \times 31 \times 2.3$	87	HPD, DEP PP0350F	13
TOFINO2	EJ 130 (BC 420)	$200 \times 31 \times 1.8$	78	PMT, Hamamatsu R5505	17

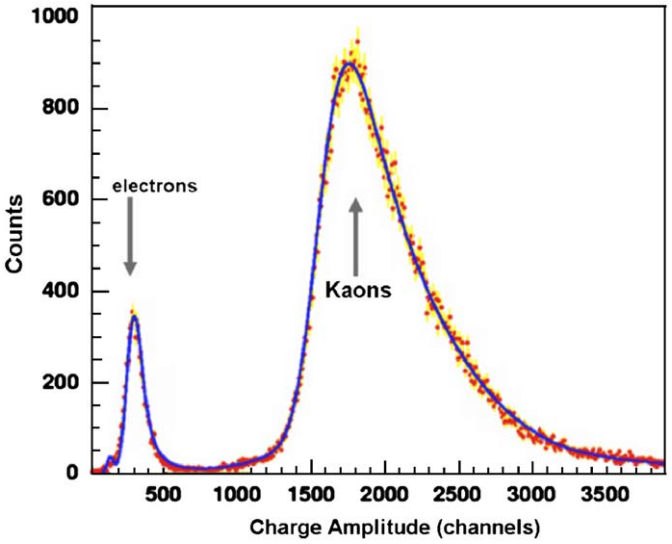

Fig. 4. TOFINO1 charge amplitude spectrum of detected electrons and kaons (QDC pedestal, electron peak and kaon peak at channel 140, 344 and 1720, respectively).

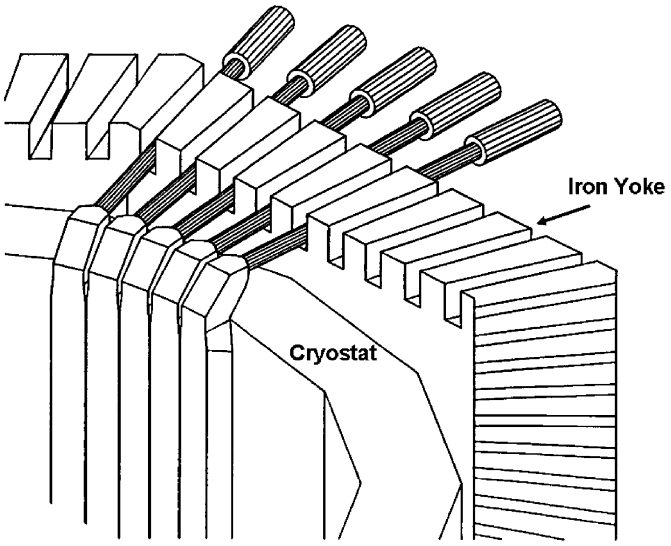

Fig. 5. Details of the TOFONE slab mounting against the cryostat and of the light guide paths through the magnet yoke.

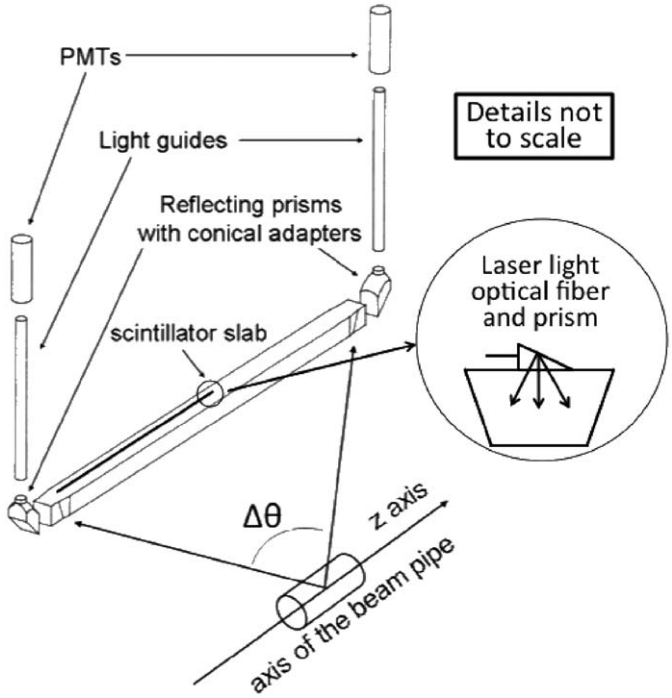

Fig. 6. Exploded schematic view of a TOFONE slab assembly. The z axis of the reference frame (axis of the beam pipe) and the polar angular range $\Delta\theta$ of the detected particles are shown.

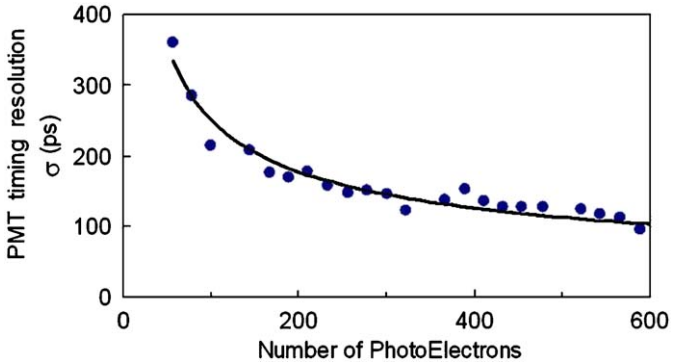

Fig. 7. XP2020 PMT timing resolution standard deviation versus photoelectron number, obtained using γ–γ pairs from ^{60}Co decay. The statistical errors are smaller than the circles used.

For the measurement of the mean time and for a position estimation [4], the light produced is read out at both ends of the scintillator. The detector is enveloped in aluminium foil for more efficient light collection, and sealed against external light with black tape. The use of an air-plastic separation surface, before the aluminium foil, is also responsible for the scintillation light attenuation function, measured [4] with cosmic rays.

The PMTs are XP2020 from Photonis (once Philips). They are operated at a typical voltage of −2200 V using hybridized voltage divider bases [15] following the CERN NP-Division voltage divider base Mod. 4238 (CERN-NP drawing 4238-25A1) [1], and housed in metal containers with μ-metal to shield from the residual magnetic field (less than 100 G).

Fig. 1 in [1] gives a good idea of the overall TOFONE placement within the FINUDA multi-detector apparatus. Details of the exit paths of the light guides out of the iron yoke of the magnet are shown here in Fig. 5. Charged particles entering the TOFONE from its inner face (see Fig. 6) are always detected also by an array of straw tubes [2] placed just before it, able to precisely track their spatial coordinates by means of two-dimensional information.

4. TOFINO and TOFONE LDDs intrinsic timing resolution

The intrinsic timing resolution achieved by TOFINO1 HPDs and associated electronics is reported in [9]. Its dependence on the number of PEs is summarized by Fig. 6 in [9], from which the relevant numerical values are taken. For instance, for the 230 PEs produced by kaon events an intrinsic timing resolution of 150 ps is found.

The intrinsic timing resolution achieved by TOFINO2 R5505 PMTs versus the number of PEs is reported in Fig. 1 in [10]. From the same, an intrinsic timing resolution of 20 ps is found for the 660 PEs produced by kaon events.

The intrinsic timing resolution achieved by TOFONE XP2020 PMTs versus the number of PEs has not been reported yet and therefore is described below. It is expected to have a $1/\sqrt{N}$ dependence on the number N of PEs, at least for not too small values of N, and it is related to the particular PMT + voltage divider base + adopted high voltage assembly. In order to study a dependence on the number of PEs, a scale calibration is needed for the charge collected at the anode compared with the number of PEs generated at the cathode, which is equivalent to measuring the PMT gain. In Appendix A, the different methods used to measure PMT gain are reported and the typical gain of our XP2020 PMT + base, operated at -2200 V, is $(6.9 \pm 0.2) \times 10^6$. Using this value, the timing resolution as a function of the number of PEs detected at the XP2020 cathodes is determined by means of γ–γ pairs from a ^{60}Co source. The γ rays are detected in two small cylindrical (diameter, 5 cm; height, 2 cm) BC 408 plastic scintillators, which are read out by our XP2020 PMTs + base assemblies, operated at -2200 V, and their coincidence time spectrum is recorded. The charge calibrated spectra of the anode pulses are also collected. The spectra are dominated by Compton scattering because of the low photoelectric and pair production cross-sections of the plastic scintillator for γ-rays at these energies. All the measurements are taken within narrow bins of the collected Compton charge spectra and hence without time walk effects due to the electronic timing discriminators. XP2020 PMT timing resolution σ values, taken from the standard deviation of the coincidence time peak of the pair of identical PMTs and directly measured, versus the number of PEs, up to ~600 PEs, are shown in Fig. 7. The $1/\sqrt{N}$ dependence best fitted to these experimental σ points is, in ps units, $2490/\sqrt{N}$.

5. TOFINO and TOFONE experimental timing resolution with synchronous particles

The timing performances of both scintillator barrels were measured taking advantage of synchronous particle pairs, namely e^+e^- pairs from Bhabha scattering of the primary beams and K^+K^- pairs from $\phi(1020)$ decay. The former pair reaches both barrels while the latter stops inside the targets. The choice of e^+e^- pairs from Bhabha scattering is therefore mandatory for TOFONE timing performance measurements. As already said, e^+e^- pairs (MIPs) generate too few PEs in TOFINO for optimum timing performance. By contrast, K^+K^- pairs, which deliver the start signal of TOF measurements, in TOFINO LDDs generate enough PEs (~230 in TOFINO1 HPDs and ~660 in TOFINO2 PMTs) to achieve a very good intrinsic timing (see Fig. 6 in [9] and Fig. 1 in [10]). They are therefore the natural candidates for TOFINO timing performance studies. A typical experimental spectrum of the amplitudes of Bhabha scattered electrons or positrons in a TOFONE slab near $z = 0$ is presented in Fig. 8, where the peak shown corresponds to about 200 PEs. The Bhabha events detected far from $z = 0$ have a PE production ranging from ~100 to 500 (Appendix B), similar to the one produced by kaons in TOFINO1 HPDs.

In principle, the two particles of the chosen pair arrive into two different slabs of the detector barrel at the same time. If the hit time on the slab is obtained by evaluating the mean time between left and right scintillation light detection, the main position dependence of the hit time on the slab is cancelled out (except for a small residual part presented in Appendix C, which worsens the time resolution), and it becomes simpler to measure distributions of the hit time difference between two mean-timed correlated slabs. Hit time difference experimental distributions between two selected TOFONE and TOFINO slabs, respectively, produced either in run #1 or in run #2, presented practically the same results, in spite of the different LDDs used in the TOFINO, of the different constant fraction discriminators (CFDs) used for both barrels in the two runs (details below), and of the geometrical variations of TOFINO2 with respect to TOFINO1. For this reason only a sample of such experimental distributions coming from run #2 will be shown. Typical hit time difference distributions between two barrel slabs are reported in Figs. 9–11, for the particle pairs of

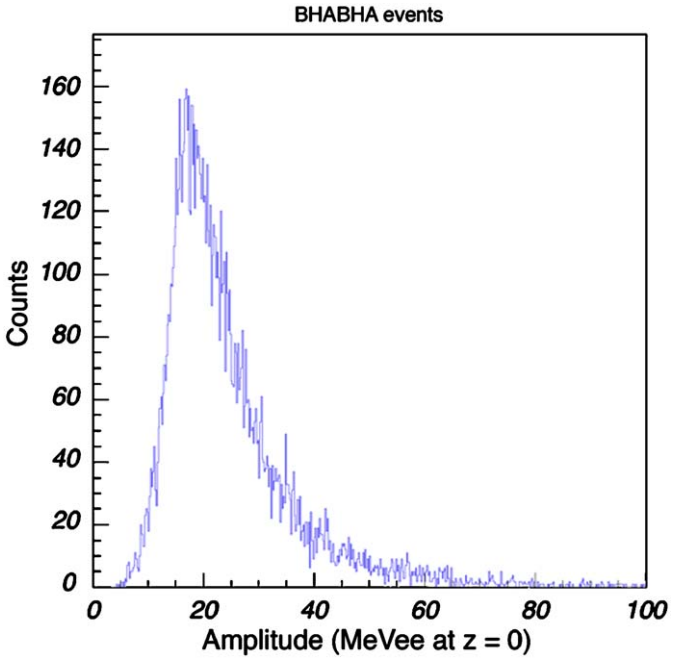

Fig. 8. Spectrum of amplitudes, in MeV electron equivalent light units (MeVee) [1], of Bhabha e^+e^- detected at $z = 0$ in TOFONE.

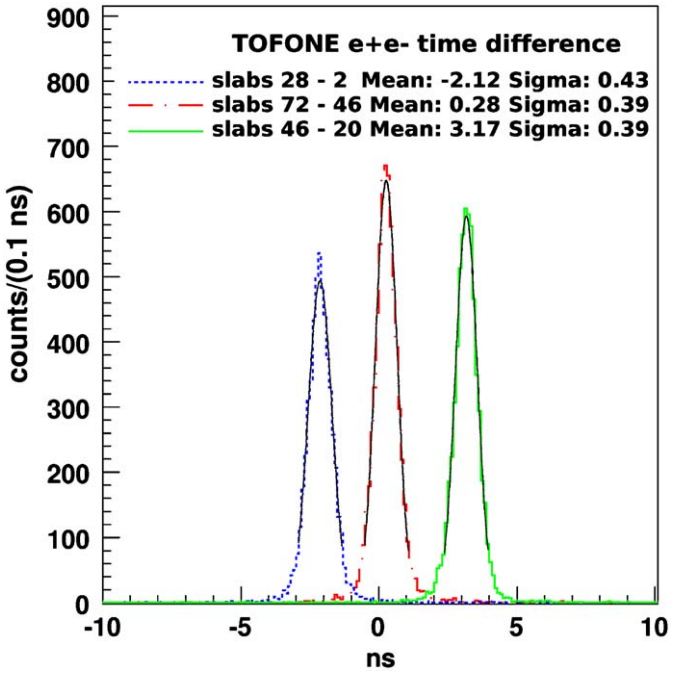

Fig. 9. Difference distribution of the hit times of e^+e^- Bhabha pairs between three $|\Delta\phi| = 130^\circ$ azimuthal angle difference experimentally correlated pairs of TOFONE slabs. This angular correlation is obtained by tracking the right- and left-handed helix paths in the magnetic field of the back-to-back scattered e^+e^- Bhabha pairs (see Fig. 2 in [16]).

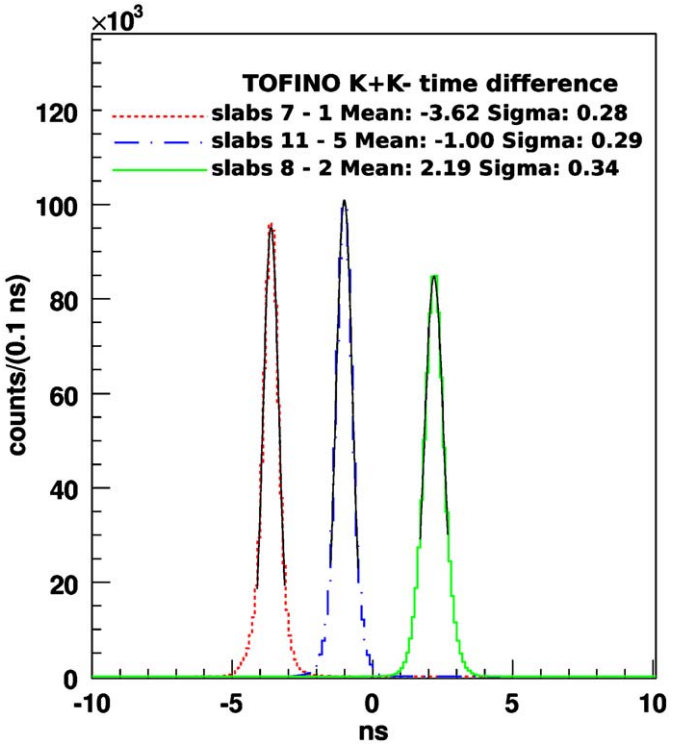

Fig. 10. Difference distribution of the hit times of K^+K^- pairs between three $\Delta\phi = 180^\circ$ azimuthal angle difference experimentally correlated pairs of TOFINO slabs.

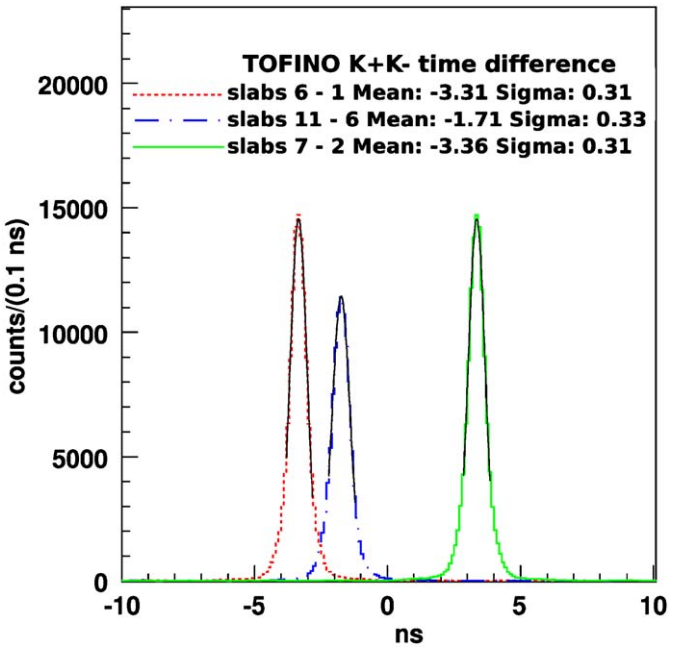

Fig. 11. Difference distribution of the hit times of K^+K^- pairs between three $|\Delta\phi| = 150^\circ$ azimuthal angle difference experimentally correlated pairs of TOFINO slabs. This angular correlation is obtained by tracking the right- and left-handed helix paths in the magnetic field of some of the back-to-back K^+K^- pairs.

interest. The standard deviation of the distributions shown is typically $\sigma \approx 0.40$ ns for the TOFONE and $\sigma \approx 0.31$ ns for the TOFINO. Their average values, different from zero, are connected with the need to refine the barrel synchronization, as will be shown hereafter.

Both σ results above are to be related to the intrinsic time dispersion of the respective LDDs operating with a high number of PEs, as already said. Using error propagation formulas, it can be shown that the standard deviation σ of the hit time difference between two mean-timed slabs in the barrel is equivalent to that of a single LDD. Specifically, if T_1, T_2, T_3 and T_4 are the times of the four identical LDDs involved with respect to the common reference time and σ is the standard deviation of all of them, then the hit time difference is $(T_1 + T_2 - T_3 - T_4)/2$ (where the reference time cancels out) and $\sqrt{4\sigma^2}/2 = \sigma$ its standard deviation. With a number of PEs between 100 and 500, for a single HPD or XP2020 PMT, and between 300 and more than 1000 for a single R5505 PMT, LDDs are characterized by intrinsic timing resolutions all having σ values below 0.2 ns ([9,10] and Fig. 7 of the present work). The quoted experimental results are poorer than that and therefore need to be explained by the geometric and kinematical details of the interactions, by the residual electronic walk versus pulse amplitude of the constant fraction timing discriminators and by the residual positional dependence of the mean time, as attempted below by means of Monte Carlo (MC) simulations.

6. The MC simulation of synchronous particle pairs

A program, FIDAMC [2], based on GEANT [17], simulates the paths of particles produced inside or outside the FINUDA detector. Among the experimental conditions which can influence the quality of timing, FIDAMC already considers:

- the e^+e^- beam energy spread ($E_e = 510$ MeV with $\sigma_E = 0.5$ Mev [16]),
- the finite dimensions of the volume in which the $\phi(1020)$ is produced and decays, or in which the e^+e^- beams undergo a Bhabha collision ($\sigma_x = 1.45$ mm; $\sigma_y = 21.1$ μm and $\sigma_z = 2.0$ cm around zero [16]; refer to Fig. 1 for the reference frame),
- a finite boost of ~12.3 MeV/c momentum along x in both runs, arising from a small crossing angle between the colliding beams.

Among the other experimental conditions that can influence the quality of timing, the new effects simulated in FIDAMC for our timing studies were:

(1) The attenuation of the scintillation light transmitted along the z coordinate (length) of the slabs of the external (TOFONE) and internal (TOFINO1 or TOFINO2) scintillator barrels, normalized to unity at the centre of the slab ($z = 0$), using the attenuation functions, respectively, taken from Refs. [4,5,18], with a finite amplitude resolution of ~30% FWHM in the collected scintillation signal for the best agreement of the simulated amplitude spectra with the experimental ones [1,7,8]; here we report only, from Refs. [4,5,18], the light attenuation length values for TOFONE: 181 cm; TOFINO1: 29 cm and TOFINO2: 20 cm.
(2) The intrinsic statistical timing uncertainty connected to the PEs generated at LDDs by the attenuated scintillation light (Fig. 7, and [9,10]).
(3) The adoption of a semi-empirical evaluation of the time dispersion introduced by light propagation through total internal reflection along the scintillators and light guides towards the left and right LDDs.
(4) The explicit consideration of the measured time walk corrections due to the Camac CFDs employed, the measured dependences of which are shown versus pulse height in Fig. 12. In particular for run #1, the Camac CFDs employed were mod. C208 (for TOFONE) and C671 (for TOFINO1), both

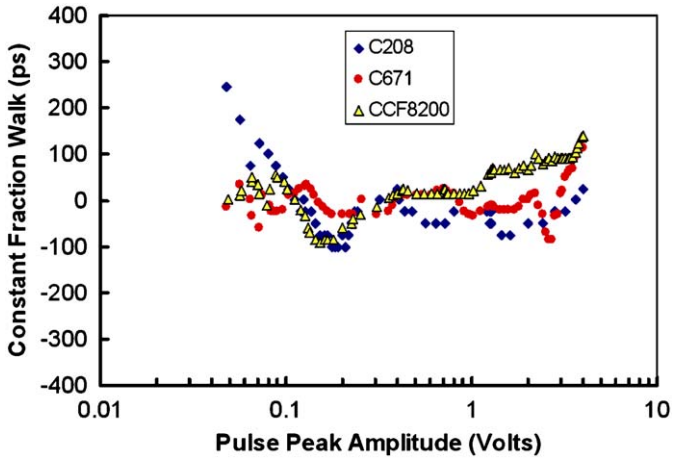

Fig. 12. Mod. C208, Mod. C671 and Mod. CCF8200 Camac constant fraction discriminators measured residual walk functions versus pulse peak amplitude. The statistical errors are smaller than the symbols used.

manufactured by CAEN, Italy, while for run #2 only one Camac CFD model was used, mod. CCF8200 (for both TOFONE and TOFINO2), manufactured by ORTEC, USA.

(5) The experimental residual position dependence of the mean time as shown in Appendix C.

The simulated hit time differences for e^+e^- Bhabha pairs scattered into two TOFONE slabs and detected with a threshold level corresponding to an "attenuated" light amplitude of 6 MeVee (MeV electron equivalent [1]) light units, are characterized by a quasi-Gaussian distribution having a standard deviation σ which increases when the different phenomena described above (identified in subscript with the same numbers as in the above list) are taken into account, according to the relation:

$$\sigma^2 = \sigma_{1,2}^2 + \sigma_3^2 + \sigma_4^2 + \sigma_5^2. \quad (1)$$

The attenuation of scintillation light in its way to the lateral collection (with the finite amplitude resolution of the collected signal) and the intrinsic XP2020 PMT time resolution contribute together on average a $\sigma_{1,2} \approx 180$ ps. The light transmission through total internal reflection in the scintillator and in the light guides determines a σ_3 ranging from 90 (for $z = 0$ hits) to 230 ps (for $|z| = 127.5$ cm hits). These values were estimated by comparing the results of simulations without this specific time dispersion against the experimental results of the *Left–Right* time detection measurements of e^+e^- Bhabha pair hits, z selected by means of straw tube signals [2] in coincidence. e^+e^- Bhabha pair events characterized by TOFONE hits having a high value of $|z|$ are greatly favoured by the angular distribution of the Bhabha scattering cross-section. The residual timing walk of the Camac CFDs contributes on average a $\sigma_4 \approx 50$ ps in run #1 and a $\sigma_4 \approx 40$ ps in run #2. The positional dependence of the mean time measurement affects the timing spread of e^+e^- Bhabha pairs with a $\sigma_5 \approx 205$ ps. Having taken into account all the above contributions, the simulated distribution of the hit time differences of e^+e^- Bhabha pairs in the TOFONE has a $\sigma \approx 360$ ps in both runs, closer to the experimental results than that of the intrinsic time distribution of the TOFONE PMTs.

The simulated hit time difference of K^+K^- pairs is also found in the TOFINO to be represented by a quasi-Gaussian distribution having a σ which increases when the various different phenomena above are introduced into the simulation. In a similar way as before, the simulated hit time differences of K^+K^- pairs in the TOFINO have a standard deviation as in Eq. (1) where, giving the same meaning to the symbols and for run #1 and run #2, respectively, $\sigma_{1,2} \approx 160$ (run #1) and ≈ 40 (run #2) ps, $\sigma_3 \approx 250$ (run #1) and ≈ 275 ps (run #2) (almost independent from $|z|$) as deduced by comparing simulations without this time dispersion against the experimental results of the *Left–Right* time detection measurements for K particles, where z is determined by ISIM [2], $\sigma_4 \approx 30$ (run #1) and ≈ 20 (run #2) ps and $\sigma_5 \approx 18$ ps (for both runs). Taken together, these contributions provide an overall simulated distribution of the hit time differences for K^+K^- pairs in the TOFINO with a $\sigma \approx 299$ (run #1) and ≈ 279 (run #2) ps, again much closer to the experimental results than those of the intrinsic time distributions of the TOFINO LDDs.

The different values of the various contributions to the TOFINO timing resolution with respect to those of the TOFONE are essentially due:

- in the case of $\sigma_{1,2}$, to the better intrinsic timing resolution of HPDs and R5505 PMTs with respect to that of XP2020 PMTs, at the inherent PE numbers involved;
- in the case of σ_3, to the different geometry of the slabs (slab length up to 111 times the depth for TOFINO, as compared to the ~25 times value for TOFONE) and light guides (light guide length equal to 20 times their diameter for TOFONE while only ~6 times on average for TOFINO with the diameter gradually shrinking to connect to the scintillator slab depth);
- in the case of σ_4, to the different range in Volts adopted for the amplitude of the electronic pulses to be fed into the CFDs, namely 0.6–1.3 V for the TOFINO and 0.35–2.3 V for the TOFONE;
- in the case of σ_5, to the very different lengths of the respective slabs.

7. Barrel synchronization. Description of the method

Any experimental procedure aimed at timing synchronization of a complex device, composed of arrays of sub-detectors, is based on the detection of synchronous signals, to which a set of reference t_0 timing points is assigned and with respect to which time differences can be measured. In the case of FINUDA TOF detectors, the barrel time alignment process was split into two steps: a first rough alignment was performed during data taking by injecting simultaneous laser light pulses to every slab, while alignment refinements were the subject of a second step which took advantage of an offline analysis of the simultaneous hits of synchronous detected particles, the same as those used in the previous section for timing resolution performance studies, namely e^+e^- pairs for TOFONE and K^+K^- pairs for TOFINO.

7.1. Online laser light injection procedure

Online laser alignment was carried out by recording the time of the detected laser light with respect to a common reference time, related to the same laser flash. An N_2 laser was employed with an enclosed Dye module. The N_2 laser provides UV light which directly pumps the Dye module containing a Littrow grating dye configuration cavity and emits light at a longer wavelength, (500 ± 3) nm, which is a good compromise between optical attenuation in the scintillator and in the optical fibers (see below) and good sensitivity of the LDDs, and with a spectral band width of 0.6% (see Table 2).

The light emitted by the N_2 laser and Dye module combination is fed (see Fig. 13) into a laser to optical fiber coupler (OZ Optics Ltd., Canada, P.N. HPUC-25-500-M-6.6GR) connected to a 0.39 NA Multimode 600 μm core 70 m long quartz optical fiber (mod. FT-600-EMT, ThorLabs Inc., USA) with SMA905 connectors.

Table 2
Main features of the N_2 laser and Dye module.

N_2 laser: mod. LN203C, Laser Photonics, USA	
UV light wavelength	337.1 nm
Energy per pulse	90 μJ
Pulse duration	600 ps FWHM
Frequency	[10–50] Hz
Dye module: LD2S, PRA Laser Inc. Canada	
Absorbed light wavelength	337.1 nm
Emitted light wavelengths	(500 ± 3) nm

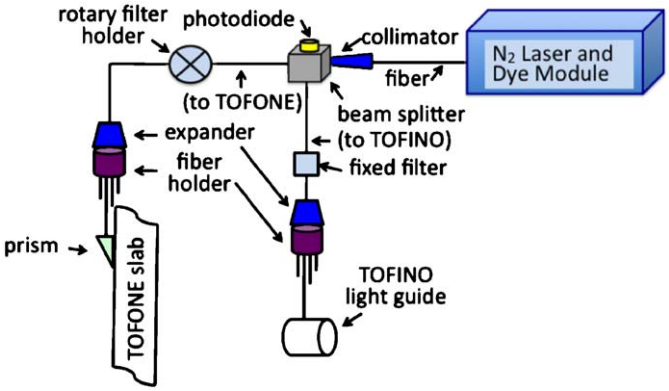

Fig. 13. Scheme of the FINUDA laser light injection system. The injection in the TOFONE by means of small reflecting prisms is indicated (see also Fig. 6).

The length of this first optical fiber allowed the laser to be installed far from electronic timing equipment, thus avoiding any noise influence on the same. At its other end, this first optical fiber is connected to an SMA connector collimation package (mod. F230SMA-A, ThorLabs Inc., USA) feeding a non-polarizing cube beam splitter (mod. 05BC16NP.2, Newport Inc., USA) from which two beams depart separately towards TOFONE (at 0° to the incident beam) and TOFINO (at 90°). Near the cube face opposite to the TOFINO beam a fast photodiode (mod. AEPX65, Centronic Inc., USA) is located at a position allowing it to be triggered by the light diffused within the cube. The timing signal of this photodiode is used as a common reference time for the measurement of the online scintillator t_0's. The TOFINO split beam is then attenuated by a fixed neutral density filter having a convenient transmitted light fraction and fed to a beam expander (mod. T81-20X, Newport Inc., USA) facing a holder of 24 equal length 300 μm diameter quartz optical fibers (mod. LT60/HCP300/SMA-3SMA, Fort Fibre Ottiche, Italy). These fibers feed, at the other end, the TOFINO individual slabs through holes drilled into each of the side light guides.

The TOFONE split beam, instead, is attenuated by means of a rotary filter holder, holding various transmission neutral density filters for studies with different amounts of light injection. It is then fed to a beam expander similar to the one above, facing a fiber holder lodging the 72 equal length 1 mm diameter plastic optical fibers which go to the individual slabs of the external scintillator barrel. Light injection from each fiber to each slab is accomplished by means of a 90° reflecting small plastic prism glued to the end of the fiber and to the centre of the slab face contiguous to the cryostat (see Figs. 5 and 6). This mounting allows the transmission of equal amounts of light from one fiber to both lateral PMTs.

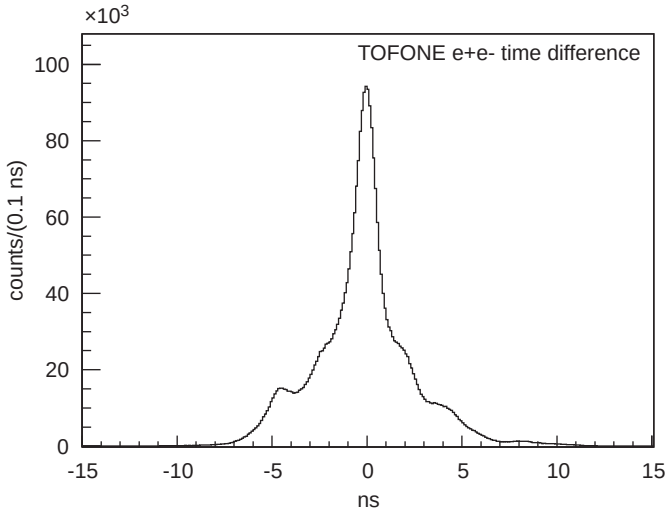

Fig. 14. Distribution of the measured hit time difference for e^+e^- Bhabha pairs detected in all the slabs of the TOFONE, after the online laser synchronization.

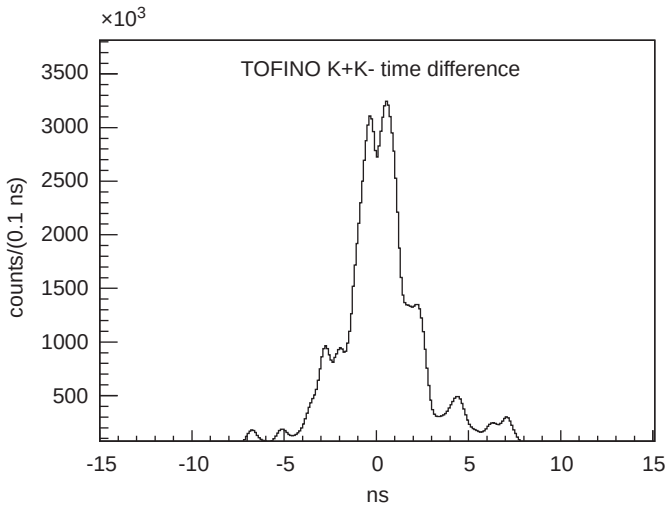

Fig. 15. Distribution of the measured hit time differences for K^+K^- pairs detected in all the slabs of the TOFINO, after the online laser synchronization.

The overall time dispersions of the scintillator barrels were evaluated after the first time alignment step, as described above. The results are shown in Fig. 14 for TOFONE and in Fig. 15 for TOFINO.

It is evident that a greater effort at slab synchronization was still needed, i.e. a better determination of the t_0 values.

During the experiment, the t_0 set in use was frequently measured by flashing the whole scintillation arrays and acquiring the detection time of the laser light by all LDDs with respect to the common reference time provided by the photodiode response timing. This technique, carried out while collisions are suspended, is independent of beam status and takes only a few minutes, and so is very useful for monitoring the stability of the whole TOF system during data taking. Although this stability was in general found to be fairly good, the analysis of sample hit time difference distributions from synchronous particle pairs continued to show differences with respect to the expected average zero value, a sign of still imperfect time alignment due to the presence of some kind of flaw in the alignment procedure. The first investigation showed the problem was mainly due to crosstalk between neighbouring twisted pairs of the flat cables carrying timing signals to the TDC

boards, when all the slabs were flashed at the same time. For the second run, all TOF signal cables were replaced with new, higher quality and individually shielded twisted pairs, to reduce crosstalk and improve signal integrity and time resolution. Yet the problem persisted, proof of its complex nature. No quick alternative was found for the online refinement of a t_0 laser set. For this reason laser pulsing was used only for the important and frequent stability tests and for a first rough alignment, while a finer synchronization of each scintillator array was carried out by offline hit time data analysis of synchronous particle pairs.

7.2. Offline synchronous particle pair analysis procedure

The t_0 values can be further refined by using the average features of the hit time difference distributions of synchronous particles impinging in coincidence on correlated slab pairs, as well as the average features of the hit position distributions for particle populations detected symmetrically around $z=0$. Using the t_0's determined with the laser, the hit time differences obtained from the detection of synchronous particles are used to obtain offsets of the average hit time difference with respect to the expected zero value, as shown in Figs. 9–11. These offsets are the main known terms for solving the problem of how to refine overall barrel synchronization.

For e^+e^- Bhabha pairs detected in TOFONE, there is an experimental azimuthal angle correlation of $\Delta\phi = 130^\circ$ between the two hit slabs, implying a 26 ± 1 slab distance, to be considered either clockwise or counterclockwise, since the first hit can occur in either of the correlated slabs. This angular correlation is obtained by tracking the right- and left-handed helix paths in the magnetic field of the back-to-back scattered e^+e^- Bhabha pairs (see Fig. 2 in [16]). This leads to 432 measurements of hit time differences and corresponding offsets of their mean values with respect to zero.

In a similar way, 36 hit time difference measurements for K^+K^- pairs detected in TOFINO can be obtained, each of which provides an offset of the average value from zero. The first 12 are obtained from pure back-to-back events, requiring K^+K^- pairs hitting slabs at $\Delta\phi = 180^\circ$ azimuthal angle difference, the so-called Gap 6 slabs. The other 24 are obtained from "extended" back-to-back events, in which a K^+K^- pair is detected at $\Delta\phi = 150^\circ$ azimuthal angle difference (in either sense of rotation), the so-called Gap 5 slabs. The Gap 5 slab correlation is obtained by tracking the right- and left-handed helix paths in the magnetic field of some of the back-to-back K^+K^- pairs.

Further data useful for the same goal are obtained from hit position distributions of any particle populations detected symmetrically around $z=0$. A scintillation hit position spectrum in long counters can be obtained from the time difference distribution of left minus right LDD timing, which must by definition be centred at zero for the above particle populations. Adopting the pulsed laser t_0's, a first analysis of hit position distributions was performed. A typical hit position distribution for two TOFONE slabs, obtained with a Bhabha particle hit population symmetrically detected around $z=0$ (determined using straw tubes [2]) adopting pulsed laser t_0's, is shown in Fig. 16. As can be seen from Fig. 16 (values of the Mean in the inset), these hit position distributions also present a total of 72 offsets of the average value from zero, which can be used for the refinement of t_0 values. As for TOFONE, 12 more hit position distribution offsets can be found for TOFINO, using kaons detected symmetrically around $z=0$, as selected by ISIM [2].

Having collected all the above offset information, a system of equations can be written relating the corrections required to the laser t_0 values and the known offset values. This system of equations is overdetermined, and so a best fit solution is achieved for the corrections, based on ROOT class TDecompSVD [19], using a linear least squares search to minimize the $A \cdot x = y$, where A is the $m \times n$ ($m > n$) matrix with n parameters and m equations with y known values. The vector x (the corrections) is determined with the SVD (Singular Value Decomposition) method.

After finding such a solution, the analysis of the hit time differences for synchronous particle pairs and the one of hit position distributions for particle populations symmetrically detected around $z=0$ was performed by adopting the offline

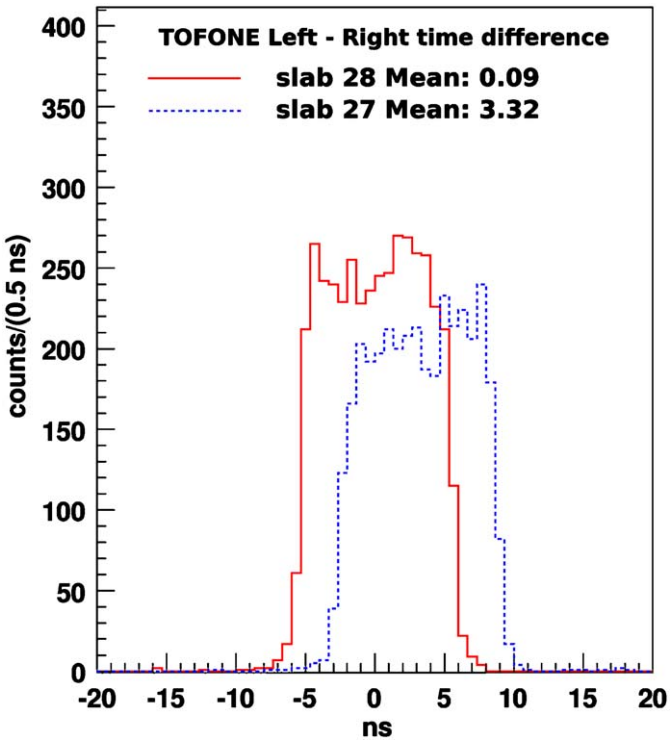

Fig. 16. Online distributions of the *Left–Right* detection time difference for Bhabha particles in two TOFONE slabs, detected symmetrically around $z=0$ and determined using straw tubes [2].

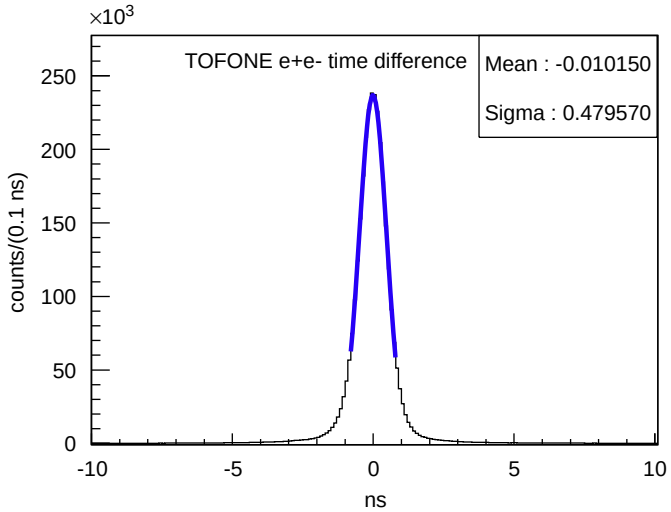

Fig. 17. Distribution of the measured hit time difference for e^+e^- Bhabha pairs detected in all the slabs of the TOFONE, after the offline synchronization corrections. The continuous line is the Gaussian fit having the mean and sigma values shown in the inset.

corrected t_0 values. The results are shown in Fig. 17 (for all the e^+e^- Bhabha pairs detected in TOFONE), in Fig. 18 (for all the K^+K^- pairs detected in TOFINO) and in Fig. 19 (in which the hit position distributions from Fig. 16 are corrected).

The mean value of the distributions in Figs. 17 and 18 is practically always zero, as expected from synchronous particle pairs. The standard deviation σ of the overall TOFONE hit time difference for e^+e^- Bhabha pair distributions (Fig. 17), after offline synchronization, reaches a value of ~0.48 ns as compared with the several ns obtained after only laser synchronization and with the ~0.40 ns of the individual TOFONE slab pairs. The standard deviation σ of the overall TOFINO hit time difference distributions for K^+K^- pairs (Fig. 18), comprising all Gap 6 and Gap 5 slab coincidences, after offline synchronization, remains near the average σ value obtained before for single slab pairs (~0.31 ns), passing from the several ns time dispersion of Fig. 15 to the $\sigma \approx$ 0.32 ns of Fig. 18, a very significant improvement.

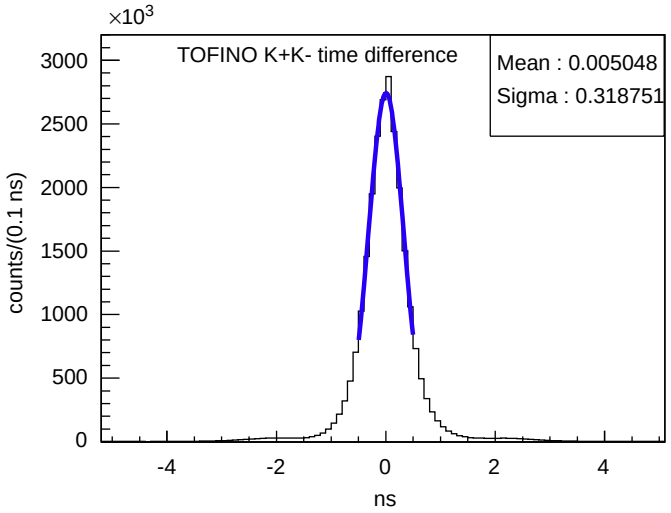

Fig. 18. Distribution of the measured hit time difference for K^+K^- pairs detected in all the slabs of the TOFINO, after the offline synchronization corrections. The continuous line is the Gaussian fit having the mean and sigma values shown in the inset.

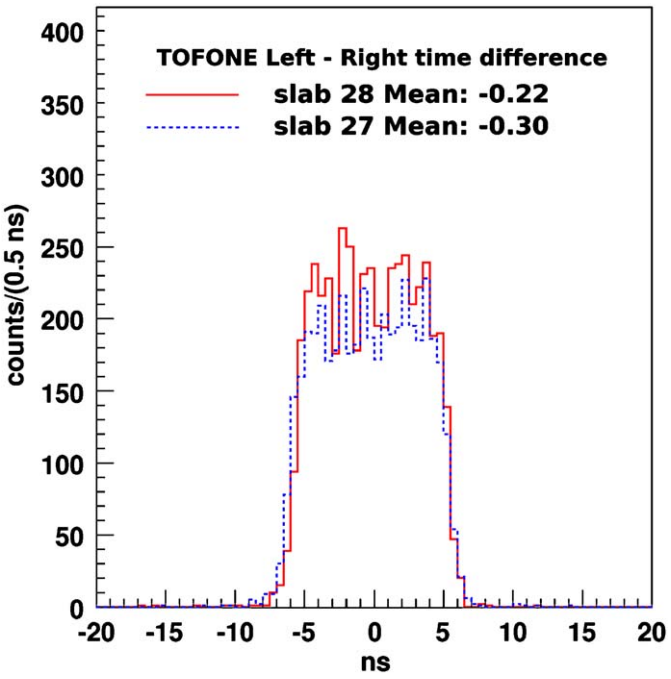

Fig. 19. The *Left–Right* detection time difference distributions of Fig. 16, after the offline t_0 corrections.

8. Conclusion

All the coincidence time distributions measured for pairs of synchronous particles detected in the internal and external scintillator barrels gave dispersion results greater than expected from LDD intrinsic timing resolutions at the inherent number of PEs produced, on account of the detection geometry of the barrels, of the beam energy spread, boost and finite dimension interaction volume, of the scintillation light attenuation influencing the PEs produced, of the time dispersion caused by scintillation light propagation through total internal reflection, of the time walk of the Camac CFDs and of the residual position dependence of the mean time measurements. The MC simulation here carried out explains the time dispersion results for specific pairs of coincident slabs within ~90% for TOFONE and an average of ~93% for TOFINO, so much better experimental results could not have been obtained for both barrels. On the other hand, the synchronization procedure for the overall barrels proved to be a more crucial point for TOFONE than for TOFINO: in fact, although the offline procedure presented here achieved good results compared with the online one, a 20% worsening of the overall TOFONE timing resolution with respect to specific coincident slab measurements still persists. The reason for this difference in behaviour between the two barrels is probably connected to their very different geometrical dimensions, which in the case of TOFONE adversely affect its timing properties. Nevertheless, using the overall timing resolution standard deviation results shown for the two scintillator barrels we obtain a FWHM dispersion for the TOFONE–TOFINO TOF measurement (i.e., the measurement of the delay between any mean timed TOFONE slab and any mean timed TOFINO slab) of less than 0.95 ns, in agreement with the goal of the FINUDA experiment.

Acknowledgement

Thanks are due to Mr. Gaetano Antuofermo, Mr. Pasquale Cariola, Mr. Michele Franco, Mr. Giuseppe Iacobelli, Mr. Michele Sacchetti and Mr. Pietro Vasta for technical assistance and to the DAΦNE machine staff for their skilful handling of the collider.

Appendix A. Measurement of PMT gain.

As already shown in Fig. 7, the intrinsic time resolution of a PMT is related to the number of PEs generated at its photocathode by the impinging light flash.

To obtain an evaluation of the number of PEs generated by the scintillation light collected from a particular detection event in the TOFONE scintillators, knowledge of the XP2020 PMT gain is needed, which depends on the PMT model + voltage divider base design details + operating voltage assembly. Unless a particular type of voltage divider base design is adopted among the ones suggested by the PMT manufacturer, in which case the gain values as a function of the applied voltage can be taken from the PMT manufacturer data sheets, the gain of a specific PMT + base assembly, at the particular high voltage used (here typically −2200 V), has to be measured.

Different methods are employed for this measurement, some of which take advantage from pulsed illumination of the

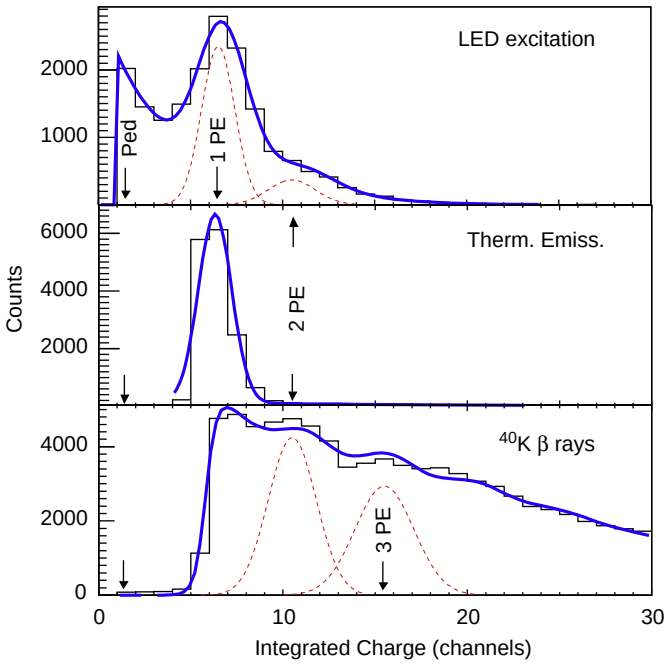

Fig. A1. The XP2020 PMT anode charge from a small photoelectron number cathode excitation events collected on the same charge scale for PMT gain studies.

photocathode by very low light intensity levels emitted by an LED. The resulting charge spectrum at the anode allows the details of the charge distribution to be related to definite numbers of PEs generated at the cathode and hence to deduce the gain. The lower the light intensity level, the higher the excitation probability of 1 PE events. The logical pulse triggering the light flash emission can be used to enable the event acquisition. This cuts the contributions from the thermionic emission and any other inclusive excitation of the cathode (cosmic rays, natural radioactivity, etc.), and a charge spectrum results only from gated events. A spectrum obtained with a low intensity light source is shown in Fig. A1 (top), to which a curve has been fitted (following the methods of [20]) containing a main contribution from 1 PE emission plus minor contributions from 2 and 3 PEs emission. The pedestal is connected with failures of the logical trigger to excite the light source.

A second measurement of PMT gain is performed by taking only the inclusive charge spectrum of the dark current pulses collected at the anode. In fact, if the PMT cannot receive light from outside, it can detect only the single PE pulses from cathode thermionic emission and the very low amplitude pulses (1–20 PEs) from the Cherenkov light in the tube glass bulb caused by γ ray emission from the ^{40}K contained in the glass itself. Cathode thermionic emission usually dominates, unless the PMT has been darkened for a long time and/or its temperature has been sufficiently decreased. In any case, the measurement of the charge collected from various PE events can be performed adopting a suitable threshold level, as can be seen from Fig. A1 (middle) and (bottom), in which the fitted curves ([20] with an added threshold function implemented here for the "bottom" case) take into account events characterized by a different number of PEs at the cathode, of which only the prevailing underlying distributions are individually shown. As can be seen, in all the measurements shown the collected anode charge can be related to the small number of PEs originating the detected event (arrows). Considering the average charge values needed for a 1 PE increase (with a charge conversion coefficient of 0.25 pC/channel) divided by the value of the electron charge, our XP2020 PMT gain is obtained as $(6.9 \pm 0.2) \times 10^6$.

Appendix B. XP2020 PMT PE number

A typical experimental spectrum of the amplitudes of Bhabha scattered electrons or positrons in a TOFONE slab near $z = 0$ is presented in Fig. 8. The number of PEs generated by the light yield of the peak can be evaluated from the following. The TOFONE scintillation light pulses reaching XP2020 PMT photocathodes from centrally ($z = 0$) detected Bhabha events produce PMT anode current pulses which are charge integrated and calibrated in MeVee (MeV electron equivalent) light units [1]. Their current yield is ~20 mA at the peak (~1 mA/MeVee gain setting [1]) and their time length is ~5 ns HWHM, data which, once the XP2020 PMT gain is known, allow to deduce the PEs corresponding to the events of interest. The peak in Fig. 8 corresponds in this way to about 200 PEs.

The Bhabha events detected far from $z = 0$ are characterized by a greater energy deposition on account of their oblique crossing of the scintillator. These energy depositions produce more scintillation light, even better collected by the nearer PMT (with respect to the ones from central events) and sufficiently well collected by the farther PMT, with a PE production ranging from ~100 to 500.

Appendix C. Positional dependence of the mean time measurements.

The positional dependence of the mean time measurement from a TOFONE or a TOFINO slab (i.e. the average value of their Left and Right LDD times) was studied by means of cosmic ray (for TOFONE) and highly collimated β ray (for TOFINO) measurements, carried out using extra TOFONE and TOFINO detection modules (outside the FINUDA apparatus). The cosmic ray events were triggered by the coincidence between a pair of scintillator pads, selecting their crossing directions and impact positions on the TOFONE module. By contrast, the β ray events from a ^{90}Sr/^{90}Y radioactive source were triggered by the coincidence between the TOFINO module itself and a very small scintillator pad, the latter giving the pulse leading edge starting the timing measurements. The many cosmic ray events taken with the FINUDA apparatus cannot be used for this study because of the common reference time employed for any timing measurement in FINUDA, which is given by the mean time of a TOFONE or a TOFINO slab. In fact this

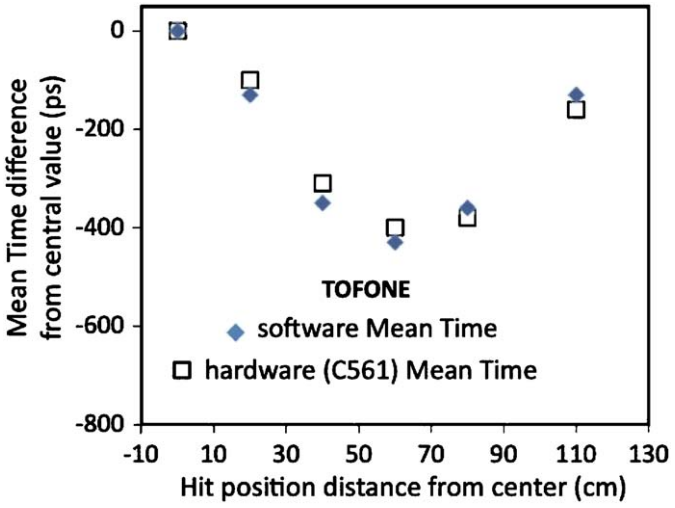

Fig. C1. The dependence on impact position z of the experimental mean time between *Left* and *Right* PMTs, in a TOFONE slab. The average time is evaluated either by software or by hardware (Caen C561) treatment. $z = 0$ for central position. The statistical errors are smaller than the symbols used.

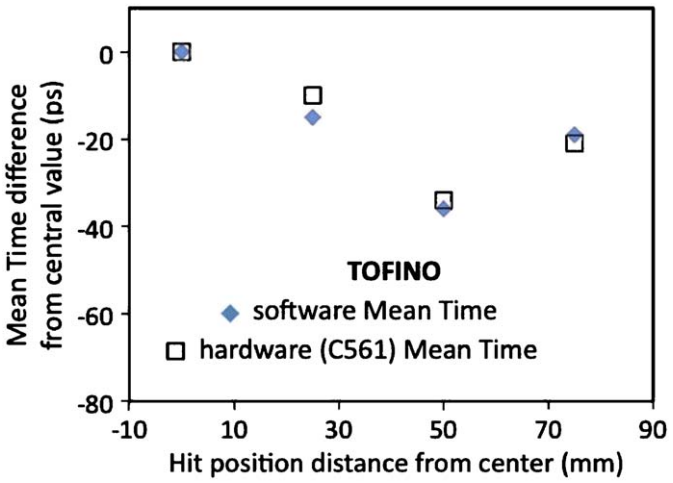

Fig. C2. The dependence on impact position z of the experimental mean time between *Left* and *Right* LDDs, in a TOFINO slab. The average time is evaluated either by software or by hardware (Caen C561) treatment. $z = 0$ for central position. The statistical errors are smaller than the symbols used.

reference time, which does not cancel out in mean time measurements of a single slab as it does in the measurement of the time difference between two mean timed slabs, is itself affected by the dependence under investigation. In the above measurements carried out for the TOFONE module care was taken to reproduce, with respect to FINUDA experimental conditions, the MIP energy deposition in the scintillator and the detection threshold, to avoid possible different contributions to PMT timing response by light collected from different light collection paths. It was not possible to take the same care for the TOFINO measurements: in fact in FINUDA experiments kaons in TOFINO deposited higher energies than MIPs and were detected with a higher threshold, a condition that cannot be reproduced with radioactive sources or cosmic rays. The TOFINO study was therefore carried out in MIP experimental conditions. Nevertheless, on account of the small length of TOFINO slabs, a limited positional dependence for its mean time, like the one shown below, would probably have been measured in any experimental conditions. The cited specific measurements gave the TOFONE and TOFINO positional dependence of the mean time shown in Figs. C1 and C2, which were used in the MC simulation.

Both measured trends resemble those shown in the inset of Fig. 9 in [21] and in Fig. 2 in [22], characterized by a higher mean time value at $z = 0$, while differ from the one shown to the right part of Fig. 7 in [23], having a smaller mean time value at $z = 0$. A higher mean time value for central hits can be connected to a smaller apparent speed of light transmission to both scintillator sides, a condition usually established for sufficiently distant sides (i.e. at a great distance from hit position, in units of the average transverse dimension of the slab). In this situation, for non-central hit positions one of the scintillator sides is always far enough, while the other, nearer to the hit position, can be reached by the scintillation light with a slightly higher apparent speed (depending on z). This higher speed is effective, however, only on the shorter transmission distance involved within the scintillator, a mechanism explaining the trend here shown. By contrast, a lower mean time value for central hits can be connected to a slightly higher apparent speed of light transmission to both scintillator sides, which in this case cannot yet be considered "far enough" to reach with a lower apparent speed of light transmission. In Ref. [23], the different refraction indexes of the scintillator (GSO(Ce)) and coating used and the lack of light guides may have contributed to the results reported.

References

[1] A. Pantaleo, et al., Nucl. Instr. and Meth. A 545 (2005) 593 (and references therein).
[2] M. Agnello, et al., Phys. Lett. B 622 (2005) 35.
[3] M. Agnello, et al., Nucl. Phys. A 804 (2008) 151.
[4] L. Celano, et al., Nucl. Instr. and Meth. A 392 (1997) 304 (and references therein).
[5] V. Filippini, et al., Nucl. Instr. and Meth. A 424 (1999) 343.
[6] V. Filippini, et al., Nucl. Instr. and Meth. A 457 (2000) 279.
[7] D. Faso, Ph.D. Graduation Thesis in Physics, Turin University, XVII Cycle, 2004, unpublished.
[8] H. Fujioka, Ph.D. Graduation Thesis, Department of Physics, University of Tokyo, March 2008, unpublished.
[9] L. Busso, et al., Nucl. Instr. and Meth. A 432 (1999) 436.
[10] V.A. Grigorév, et al., Instr. Exp. Technol. 43 (2000) 750.
[11] A.V. Akindinov, et al., Instr. Exp. Technol. 46 (2003) 345.
[12] M. Bonesini, et al., Nucl. Instr. and Meth. A 567 (2006) 200.
[13] M. Bonesini, et al., Nucl. Instr. and Meth. A 572 (2007) 465.
[14] Marek Moszynski, et al., Nucl. Instr. and Meth. A 356 (1995) 270.
[15] G.C. Bonazzola, et al., Nucl. Instr. and Meth. A 356 (1995) 270.
[16] M. Agnello, et al., Nucl. Instr. and Meth. A 570 (2007) 205 (and references therein).
[17] R. Brun, GEANT detector description and simulation tool, CERN Program Library Long Writeup W5013, 1994.
[18] T. Maruta, University of Tokyo, 2005 TOFINO tests at KEK, private communication.
[19] ROOT framework documentation at: ⟨http://root.cern.ch⟩ ROOT class TDecompSVD documentation at: ⟨http://root.cern.ch/root/html/TDecompSVD.html⟩.
[20] E.H. Bellamy, et al., Nucl. Instr. and Meth. A 339 (1994) 468.
[21] B. Adeva, et al., Nucl. Instr. and Meth. A 491 (2002) 41.
[22] E. Liatard, G0 Collaboration Report, G0 Document 82-v1, G0-99-016, 1999 ⟨www.npl.uiuc.edu/exp/G0/docs/docs.html#1999⟩.
[23] T. Tamagawa, et al., Nucl. Instr. and Meth. A 562 (2006) 120.

A.7 HL-LHC TDR: Chapter 2, Machine Layout and Performance

Chapter 2

Machine Layout and Performance

D. Angal-Kalinin[1], R. Appleby[2], G. Arduini[3], D. Banfi[4], J. Barranco[4], N. Biancacci[3], D. Brett[2], R. Bruce[3], O. Brüning[3], X. Buffat[3], A. Burov[5], Y. Cai[6], R. Calaga[3], A. Chancé[7], M. Crouch[2], B. Dalena[7], H. Day[3], R. de Maria[3], J. Esteban Muller[3], S. Fartoukh[3], M. Fitterer[3], O. Frasciello[8], M. Giovannozzi[3], W. Herr[3], W. Höfle[3], B. Holzer[3], G. Iadarola[3], J.M. Jowett[3], M. Korostelev[9], K. Li[3], E. McIntosh[3], E. Métral[3], A. Mostacci[10], N. Mounet[3], B. Muratori[1], Y. Nosochkov[6], K. Ohmi[11], Y. Papaphilippou[3], S. Paret[12], J. Payet [7], T. Pieloni[3], J. Qiang[12], T. Rijoff[3], L. Rossi[3], G. Rumolo[3], B. Salvant[3], M. Schaumann[3], E. Shaposhnikova[3], D. Shatilov[13], C. Tambasco[3], R. Tomás[3], A. Valishev[5], M.-H. Wang[6], R. Wanzenberg[14], S. White[3], A. Wolski[9], O. Zagorodnova[14], C. Zannini[3], F. Zimmermann[3] and M. Zobov[8]*

[1]ASTeC, STFC, Daresbury Laboratory, Warrington, UK
[2]UMAN, The University of Manchester and the Cockcroft Institute, Warrington, UK
[3]CERN, Accelerator & Technology Sector, Geneva, Switzerland
[4]EPFL, Lausanne, Switzerland
[5]FNAL, Fermi National Accelerator Laboratory, Batavia, USA
[6]SLAC, National Accelerator Laboratory, Menlo Park, USA
[7]CEA/SACLAY, DSM/Irfu/SACM, Gif-sur-Yvette, France
[8]INFN-LNF, Rome, Italy
[9]University of Liverpool, Liverpool, UK
[10]University of Rome "La Sapienza", Rome, Italy
[11]KEK, Tsukuba, Japan
[12]LBNL, Lawrence Berkeley National Laboratory, Berkeley, USA
[13]BINP, Novosibirsk, Russia
[14]DESY, Deutsches Elektronen-Synchrotron, Hamburg, Germany

2 Machine layout and performance

2.1 Performance goals (nominal scheme)

The goal of the High Luminosity upgrade of the LHC is to deliver an integrated luminosity of at least 250 fb^{-1} per year in each of the two high-luminosity general-purpose detectors, ATLAS and CMS, located at the interaction points (IP) one and five, respectively. The other two experiments, ALICE and LHCb with detectors located at IP2 and IP8 respectively, are expecting to collect integrated luminosities of 100 pb^{-1} per year (of proton–proton data) and 5 fb^{-1} to 10 fb^{-1} per year, respectively [1]. No operation for forward physics experiments is expected after the upgrade.

The ATLAS and CMS detectors will be upgraded to handle an average number of pile-up events per bunch crossing of at least 140, corresponding to an instantaneous luminosity of approximately 5×10^{34} cm^{-2} s^{-1} for operation with 25 ns beams at 7 TeV, for a visible cross-section σ_{vis} = 85 mb. The detectors are also expected to handle a line density of pile-up events of 1.3 events per mm per bunch crossing. ALICE and LHCb will be upgraded to operate at instantaneous luminosities of up to 2×10^{31} cm^{-2} s^{-1} and 2×10^{33} cm^{-2} s^{-1}, respectively.

The HL-LHC upgrade project aims to achieve a 'virtual' peak luminosity that is considerably higher than the maximum imposed by the acceptable event pile-up rate, and to control the instantaneous luminosity

* Corresponding author: Gianluigi.Arduini@cern.ch

during the physics fill ('luminosity levelling') so that the luminosity production can be sustained over longer periods to maximize the integrated luminosity.

A simplified but realistic model of the luminosity evolution has been developed [2] taking into account the beam population N_{beam} reduction due to the collisions (the so called 'burn-off') in n_{IP} collision points with instantaneous luminosity L_{inst},

$$\frac{\mathrm{d}N_{\text{beam}}}{\mathrm{d}t} = -n_{\text{IP}}\sigma_{\text{tot}}L_{\text{inst}}\,, \tag{2-1}$$

where σ_{tot} is the total hadron cross-section (here assumed to be 100 mb). No other sources of intensity reduction or emittance blow-up are considered in this model. Figure 2-1 shows the expected yearly integrated luminosity as a function of the 'virtual' peak luminosity for three different values of the luminosity at which levelling is performed (see Section 1.2.3). In this figure the corresponding optimum fill length T_{fill} (i.e. the length of time for each fill that will maximize the average luminosity production rate) is also shown. In order to estimate the annual integrated luminosity, we assume a minimum turnaround time $T_{\text{turnaround}}$ of 3 hours (see Chapter 16), a scheduled physics time T_{physics} for luminosity production of 160 days per year, with N_{fills} successful physics fills of duration T_{fill}, and a performance efficiency of 50% (this was 53.5% in 2012) where [3]:

$$\eta = N_{\text{fills}}\frac{T_{\text{turnaround}}+T_{\text{fill}}}{T_{\text{physics}}} \times 100\% \tag{2-2}$$

In order to reach the goal of integrating 250 fb^{-1}/year levelling must be performed at luminosities larger than 5×10^{34} cm^{-2} s^{-1} and peak virtual luminosities of more than 20×10^{34} cm^{-2} s^{-1}. Furthermore, the performance efficiency must be at least 50% and the typical fill length must be comparable with the estimated optimum fill length (for comparison the average fill length during the 2012 run was 6.1 hours). In this respect, levelling to higher luminosities will be beneficial because it would make it easier to reach and even exceed the integrated luminosity goal, with fill lengths comparable to the fill lengths of the 2012 run.

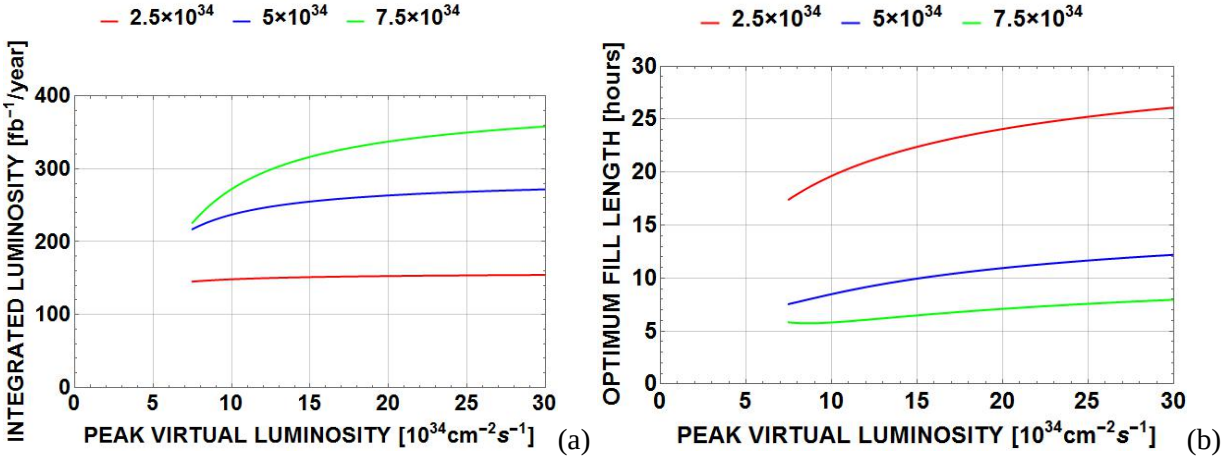

Figure 2-1: (a) Expected annual integrated luminosity; (b) optimum fill length as a function of the 'virtual' peak luminosity for three different values of the luminosity at which levelling is performed. A circulating current of 1.1 A (corresponding to $N_{\text{beam}} = 6.1 \times 10^{14}$ p), a minimum turnaround time of 3 hours and a performance efficiency η of 50% have been assumed. Only burn-off for a total hadron cross-section of 100 mb has been considered for the estimate of the beam population and virtual luminosity evolution. Two high-luminosity interaction points have been assumed.

2.1.1 Parameter space and basic parameter choices

The instantaneous luminosity L is given by

$$L = \frac{n_{\text{b}}N^2 f_{\text{rev}}\gamma}{4\pi\beta^*\varepsilon_{\text{n}}}R(\beta^*, \sigma_z, d_{\text{bb}}) \tag{2-3}$$

The r.m.s. normalized emittance ε_n in collision is assumed here to be equal for the two beams and for the horizontal and vertical planes. The Twiss beta function β^* in collision at the IP determines, together with the normalized emittance, the r.m.s. beam size $\sigma^* = \sqrt{\varepsilon_n \beta^*/\gamma}$ at the IP (assuming that the contribution to the beam size due to the dispersion and the momentum spread of the beam can be neglected). Here and below it is assumed that the relativistic factor $\beta = 1$.

A crossing angle is needed to separate bunches immediately upstream and downstream of the collision point. This leads to a reduced geometric overlap between the colliding beams, and hence to a reduction in luminosity. The crossing angle needs to be increased when reducing the β^* in order to maintain a sufficiently large normalized beam–beam separation d_{bb}. The luminosity is also reduced by the 'hourglass effect' that arises from the increase of the beta function upstream and downstream of the interaction point along the bunch longitudinal distribution. The hourglass effect is enhanced by a reduction in β^* and by an increase in bunch length. The luminosity reduction factor R in Eq. (2-3) takes both the crossing angle and the hourglass effect into account.

Equation (2-3) shows the parameters that can be varied to maximize the instantaneous luminosity. The considerations that constrain their values are briefly discussed below [4, 5]:

- The maximum number of bunches nb is limited by the minimum time interval between bunch crossings at the IP that can be handled by the detectors: this is limited to 25 ns. The maximum number of bunches that can be injected in the LHC is also limited by the following.
    - The maximum number of bunches that can be transferred safely from the SPS to the LHC due to the maximum energy that can be deposited on the injection protection absorber (TDI) in case the LHC injection kicker is not firing. The present limitation for the TDI is considered to be a maximum of 288 bunches per SPS extraction for the ultimate bunch population [6].
    - The rise-time of the injection kickers in the SPS and LHC, extraction kickers in the PS and SPS, and abort gap kicker in the LHC.
    - The need for injecting one train consisting of a few bunches (typically 12 nominal bunches for 25 ns spacing) before injecting one nominal train for machine protection considerations [7]. For the same reason the last train must have the maximum number of bunches.
    - The constraints imposed by the experiments: the need for non-colliding bunches for background evaluation, and a sufficient number of collisions for lower luminosity experiments [1].
- The maximum bunch population N is limited in the LHC by the onset of the single bunch transverse mode coupling instability (TMCI), expected to occur at 3.5×10^{11} p/bunch [8].
- The total current of the beam circulating in the LHC, $I_{beam} = e n_b N f_{rev}$ (where e is the proton charge), is expected to be limited to 1.1 A by the cryogenic power available to cool the beam screen. This assumes that a secondary electron yield (SEY) as low as 1.3 can be reached in the beam screen, to limit the heat load due to the electron cloud in the arcs, and additional cryogenic plants are installed in Points 1, 4 and 5 [4, 9].
- The beam brightness $B \equiv N/\varepsilon_n$ is limited by the following considerations [4].
    - The total head-on beam–beam tune shift $\Delta Q_{bbho} \propto N/\varepsilon_n$ is expected to be limited to 0.02–0.03 based on experience gained (from operations and dedicated experiments) during LHC Run 1. Its value is reduced in a similar fashion to the luminosity in the presence of a crossing angle [10].
    - Intra-beam scattering induces transverse and longitudinal emittance blow-up, particularly at injection (low energy) but also in the acceleration, squeeze, and collision phases. The evolution of the beam emittances can be described by the equations,

$$\frac{1}{\tau_H} = \frac{1}{\varepsilon_{nH}} \frac{d\varepsilon_{nH}}{dt} \text{ and } \frac{1}{\tau_L} = \frac{1}{\varepsilon_L} \frac{d\varepsilon_L}{dt} \text{ with } \frac{1}{\tau_d} \propto \frac{N}{\gamma \varepsilon_{nH} \varepsilon_{nV} \varepsilon_L} \text{ and } d = \text{H, L,} \quad (2\text{-}4)$$

where $\varepsilon_{\mathrm{nH,V}}$ are the r.m.s. normalized horizontal and vertical emittances. Here we assume that vertical dispersion and coupling are negligible so that the vertical emittance blow-up can be neglected.

The minimum β^* is limited by [5]:

- The aperture at the triplet, taking into account that the maximum β function β_{max} at the triplet increases in inverse proportion to β^*, and that the crossing angle θ_c required to maintain a sufficiently large normalized beam–beam separation d_{bb} to minimize the long-range beam–beam tune spread ΔQ_{bbLR} is $\theta_{\mathrm{c}} = d_{\mathrm{bb}}\sqrt{\varepsilon_n/\gamma\beta^*}$;
- The maximum β function at the triplet that can be matched to the regular optics of the arcs within the distance available in the matching section between the triplets and the arcs;
- The strengths of the arc sextupoles available to correct the chromaticity generated by the triplets (proportional to β_{max}) and, in general, the nonlinear chromaticities and off-momentum beta beating.

For a round optics (i.e. with equal β^* in the horizontal and vertical planes) in the presence of a crossing angle and at constant normalized long-range beam–beam separation d_{bb}, the increase in luminosity saturates for values of $\beta^* < \sigma_z$, as shown in Figure 2-2, because of the corresponding reduction of the luminosity reduction factor R. The effect of the geometric reduction due to the crossing angle can be counteracted by means of crab cavities operated at the LHC main RF frequency [11] as shown in Figure 1-6. The comparison of the two plots of Figure 2-2 also shows that the effect of crab cavities in enhancing the peak virtual luminosity becomes negligible, for β^* greater than 30–40 cm.

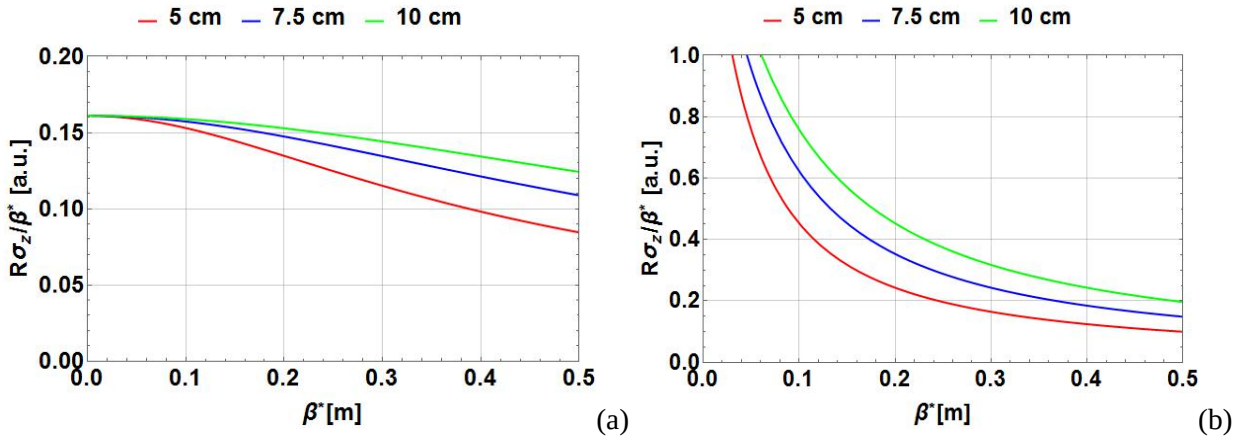

Figure 2-2: Parameter $R\sigma_z/\beta^*$ vs. β^* for different bunch lengths for a round optics and constant normalized long-range beam–beam separation d_{bb} (a) without crab cavities and (b) with crab cavities. The small effect of RF curvature in the crab cavities is not included.

Even after their planned upgrades, the injectors will also constrain the parameters of the beam that can be expected in the LHC in collision. First, there is a maximum current $I_{\mathrm{RF}} \approx 2N_{\mathrm{SPS}}\, e/T_{\mathrm{bb}}$ (where N_{SPS} is the bunch population in the SPS and T_{bb} is the bunch spacing) that can be accelerated per SPS cycle due to RF power limitations in the power amplifiers, power couplers and feeder lines of the main 200 MHz RF system. This maximum current is 2.6 A corresponding to $N_{\mathrm{SPS}} = 2.0 \times 10^{11}$ particles at SPS extraction [12, 13]. The total number of bunches is also limited to 288 due to the thermal load on the power lines. Second, the brightness of the LHC beam in the injectors is expected to be limited by space charge effects at injection in the PSB, PS, and SPS. From present experience it is expected that the maximum brightness of the LHC beams after the full injector upgrade will be $B_{\mathrm{SPS}} \sim 1.5 \times 10^{11}$ p/μm [13].

Table 2-1 shows the beam parameters at collision, selected on the basis of the above considerations [3, 14]. The parameters in the table are consistent with the above constraints with the exception of the requested bunch population that can be delivered within the longitudinal acceptance of the LHC at injection. To avoid longitudinal instabilities in the SPS, a controlled longitudinal emittance blow-up needs to be applied for high bunch population, which would lead to bunches that are longer than acceptable for clean capture in the LHC with the main 400 MHz RF system (even with the maximum 200 MHz RF voltage available in the SPS at extraction). The identification of the elements contributing to the longitudinal impedance in the SPS and the reduction of their impedance might allow for this limit to be increased. In that case, the requirements in terms of bunch population for the HL-LHC could be met.

Table 2-1: HL-LHC nominal parameters for 25 ns operation [14] for two production modes of the LHC beam in the injectors described in Ref. [3].

Parameter	**Nominal LHC (design report)**	**HL-LHC (standard)**	**HL-LHC (BCMS)**
Beam energy in collision [TeV]	7	7	7
Particles per bunch, N [10^{11}]	1.15	2.2	2.2
Number of bunches per beam	2808	2748	2604
Number of collisions in IP1 and IP5[*]	2808	2736	2592
N_{tot} [10^{14}]	3.2	6.0	5.7
Beam current [A]	0.58	1.09	1.03
Crossing angle in IP1 and IP5 [μrad]	285	590	590
Normalized long-range beam–beam separation [σ]	9.4	12.5	12.5
Minimum β^* [m]	0.55	0.15	0.15
ε_n [μm]	3.75	2.50	2.50
ε_L [eVs]	2.50	2.50	2.50
r.m.s. energy spread [0.0001]	1.13	1.13	1.13
r.m.s. bunch length [cm]	7.55	7.55	7.55
IBS horizontal [h]	105	18.5	18.5
IBS longitudinal [h]	63	20.4	20.4
Piwinski parameter	0.65	3.14	3.14
Total loss factor R_0 without crab cavity	0.836	0.305	0.305
Total loss factor R_1 with crab cavity	(0.981)	0.829	0.829
Beam–beam/IP without crab cavity	0.0031	0.0033	0.0033
Beam–beam/IP with crab cavity	0.0038	0.011	0.011
Peak luminosity without crab cavity [10^{34} cm^{-2} s^{-1}]	1.00	7.18	6.80
Virtual luminosity with crab cavity $L_{peak} \times R_1/R_0$ [10^{34} cm^{-2} s^{-1}]	(1.18)	19.54	18.52
Events/crossing without levelling and without crab cavity	27	198	198
Levelled luminosity [10^{34} cm^{-2} s^{-1}]	-	5.00[†]	5.00[†]
Events/crossing (with levelling and crab cavities for HL-LHC)[‡]	27	138	146
Maximum line density of pile-up events during fill [event/mm]	0.21	1.25	1.31
Levelling time [h] (assuming no emittance growth)[‡]	-	8.3	7.6
Number of collisions in IP2/IP8	2808	2452/2524[**]	2288/2396[**]
N at LHC injection [10^{11}][††]	1.20	2.30	2.30
Maximum number of bunches per injection	288	288	288
N_{tot}/injection [10^{13}]	3.46	6.62	6.62
ε_n at SPS extraction [μm][‡‡]	3.40	2.00	<2.00[***]

[*]Assuming one less batch from the PS for machine protection (pilot injection, Transfer line steering with 12 nominal bunches) and non-colliding bunches for experiments (background studies, etc.). Note that due to RF beam loading the abort gap length must not exceed the 3 μs design value.
[†]For the design of the HL-LHC systems (collimators, triplet magnets, etc.), a margin of 50% on the stated peak luminosity (corresponding to the ultimate levelled luminosity) has been agreed.
[‡]The total number of events/crossing is calculated with an inelastic cross-section of 85 mb (also for nominal), while 100 mb is still assumed for calculating the proton burn off and the resulting levelling time.
[**]The lower number of collisions in IR2/8 compared to the general-purpose detectors is a result of the agreed filling scheme, aiming as much as possible at a democratic sharing of collisions between the experiments.
[††]An intensity loss of 5% distributed along the cycle is assumed from SPS extraction to collisions in the LHC.
[‡‡]A transverse emittance blow-up of 10–15% on the average H/V emittance in addition to that expected from intra-beam scattering (IBS) is assumed (to reach 2.5 μm of emittance in collision for 25 ns operation).
[***]For the BCMS scheme emittances down to 1.7 μm have already been achieved at LHC injection, which might be used to mitigate excessive emittance blow-up in the LHC during injection and ramp.

2.2 Proposed systems upgrades and improvements

The high luminosity configuration requires upgrades of numerous systems. In some cases, existing systems would not be able to face the increasingly harsh conditions that the highest luminosity performance will generate. Accelerated wear and radiation damage are serious concerns. Many changes will be necessary just in order to allow the machine to continue to run in a regime of nominal or ultimate luminosity. For certain systems, replacements could be made with equipment achieving better performance, rather than with spares of the same specification. This performance 'improvement' goes well beyond the basic consolidation that is already planned for the LHC.

For other systems, replacement, although triggered by technical reasons, is the chance to carry out a complete change of layout or performance and may be considered to be a real upgrade. The most striking example is the replacement of the inner triplet magnets with new magnets of different technology based on a Nb_3Sn superconductor. This will constitute the backbone of the upgrade. Another case is the replacement of a good part of the present collimation system with an improved design with lower impedance jaws.

In other cases, new equipment not included in the present LHC layout will be installed in order to increase performance, either in terms of peak luminosity or availability. The most important example is the superconducting RF crab cavities, which are of a compact design as required for the HL-LHC, comprising a completely new development and a first for a proton collider. A further example is the installation of a collimation system in the continuous cryostat in the dispersion suppressors.

In this section, we compile a list of the systems that will require an upgrade or at least a serious improvement in performance, to face the ambitious challenge of the High Luminosity LHC.

2.2.1 Insertion region magnets

It is expected that the LHC will reach an integrated luminosity of approximately 300 fb^{-1} by 2022, resulting in doses of up to 30 MGy to some components in the high luminosity interaction regions. The inner triplet quadrupoles should withstand the radiation resulting from 400 fb^{-1} to 700 fb^{-1}, but some nested-type corrector magnets could fail at around 300 fb^{-1}. The most likely failure mode is sudden electric breakdown, entailing serious and long repairs. Replacement of the triplet must be anticipated before radiation damage reaches the level where serious failure is a significant possibility.

The replacement can be coupled with an increase in the quadrupole aperture to allow room for an increase in the luminosity via a lower β^*. However, larger aperture inner triplet (IT) quadrupoles and the increased luminosity, with consequent higher radiation levels, imply the redesign of the whole interaction region (IR) zone. This redesign includes larger D1 and D2 dipoles, a new electrical feedbox (DFBX), and much better access to various components for maintenance. In addition, larger aperture magnets in the matching sections will be required, as well as a redesign of the collimation system in the high luminosity insertions.

To maximize the benefit of such a long shutdown, this work must be complemented by a series of improvements and upgrades for other systems, and must be coupled with a major upgrade of the experimental

detectors. Both the machine and the detectors must be partially redesigned in order to withstand the expected level of integrated luminosity. The upgrade should allow the delivery of 3000 fb^{-1}, i.e. one order of magnitude greater than the nominal LHC design goal.

It is clear that the change of the inner triplets in the high luminosity insertions is the cornerstone of the LHC upgrade. The decision for the HL-LHC has been to rely on the success of the advanced Nb_3Sn technology, which provides access to magnetic fields well beyond 9 T, allowing the maximization of the aperture of the IT quadrupoles. A 15-year-long study led by the DOE in the US under the auspices of the US LARP programme (see Chapter 1, Section 1.3.2), and more recently by other EU programmes, has shown the feasibility of Nb_3Sn accelerator magnets. For the HL-LHC, some 24 IT Nb_3Sn quadrupoles are needed: they all feature a 150 mm aperture and an operating gradient of 140 T/m, which entails more than 12 T peak field on the coils. The Q1 and Q3 quadrupoles each consist of a pair of 4 m long magnets, while Q2a and Q2b each consist of a single unit almost 7 m long (see Chapter 3, Section 3.2). The same Nb_3Sn technology will be used to provide collimation in the DS, which will be achieved by replacing a number of selected main dipoles with two shorter 11 T Nb_3Sn dipoles (see Chapter 11 Section 11.3). A collimator will be installed between the shorter dipoles (see, for example, Ref. [15] and references therein).

In addition to the IT quadrupoles, there are four new D1/D2 separation/recombination dipole pairs, a number of matching section (MS) quadrupoles, not only in IR1 and IR5, but also in IR6, and a smaller number of lattice sextupoles that can be made using well-known Nb-Ti technology (see Tables 2-3 and 2-4). These magnets will feature a larger aperture and will be exposed to higher radiation doses if not properly protected, and thus will be more challenging than the present LHC equivalents (see Chapter 3).

The corrector packages in the IT and in the MS regions need to be significantly upgraded to increase aperture and (where needed) strength. Some 70 corrector magnets of various orders (from dipole for orbit correction to dodecapole skew correctors) and typology (from superferric to nested cos theta) have to be installed with the new larger IR magnets.

2.2.2 TAXS/TAXN absorbers

The change of the IT aperture will require replacement of the TAS, the first absorber on either side of the high luminosity interaction points. The TAS protects the downstream magnets from collision debris. Its aperture roughly scales with the IT aperture. The new absorber, named TAXS, will have an aperture of 54 mm (compared with 30 mm in the present TAS), and will have to withstand a flux of particles five times larger than in the present nominal design. In the current LHC, the TAS is probably the most highly activated component of the whole machine. The baseline choice at present is to replace the TAS with the TAXS during LS3 (see Chapter 8).

Given the fact that the experimental detectors have reduced the size of the vacuum chamber by nearly 50% (from 55 mm down to about 35 mm) it is clear that all challenges at the machine–detector interface are increased. This includes keeping background radiation in the detectors at acceptable levels.

2.2.3 Crab cavities

Superconducting (SC) RF crab cavities (CC) in the HL-LHC are needed in order to compensate for the geometric reduction factor, thus making the very low β^* fully useful for luminosity. HL-LHC crab cavities are beyond the state-of-the-art in terms of their unconventional, compact design, which cannot be achieved with the well-known geometry of an elliptical cavity. They also demand a very precise control of the phase of the RF (to better than 0.001°) so that the beam rotation given before collision is exactly cancelled on the other side of the interaction point (IP). The crab cavities will also pose new challenges for machine protection. Compact crab cavities will be installed on both sides of IP1 and IP5 without additional magnetic doglegs (as in IP4 for the accelerating cavities). Each cavity is designed to provide a transverse kick voltage of 3.4 MV. There are four crab cavities per beam on each side of the IP. They will be assembled in cryomodules, each containing two cavities. All four cavities may be used to rotate the beam in the crossing plane; alternatively, a single

cryomodule (two cavities) can be used for this task, with the cavities in the second cryomodule providing a deflection in the orthogonal plane, enabling the so-called crab kissing scheme for reducing the pile-up density [16]. At present, the baseline is to use all crab cavities for geometric compensation, i.e. rotation in the crossing plane.

The first-generation, proof-of-principle, compact crab cavities have recently been tested successfully (see Chapter 4). However, a second generation with machine-oriented characteristics are now under construction by LARP, CERN, and UK institutions (Lancaster University, STFC, and the Cockcroft Institute). A full cryomodule will be tested in the SPS before LS2, to investigate experimentally the effect on a proton beam and to gain the necessary experience in view of LHC operation.

2.2.4 Collimation

The collimation system has been designed for the first phase of LHC operation. It is currently operating according to design. However, the impedance of the collimation system may need to be reduced if beam instabilities are triggered at intensities close to, or just above, nominal. Hints of this behaviour have been already seen during Run 1: only operation near nominal conditions can dismiss or validate this hypothesis.

Safe handling of a beam of 1 A or more, with beta functions at collision beyond the design value, will constitute new territory. The triplet must remain protected during the large change of the collision beam parameters (β^* transition from 6 m to 10–15 cm). This will be one of the most critical phases of HL-LHC operation: just the beam halo itself could be beyond the damage limit. An upgrade of the collimation system is thus required. The main additional needs associated with the upgrade are a better precision in alignment and materials capable of withstanding higher power.

A second area that will require special attention in connection with the collimation system is the dispersion suppressor (DS), where leakage of off-momentum particles into the first and second main superconducting dipoles has already been identified as a possible LHC performance limitation. The most promising concept is to substitute an LHC main dipole with a dipole of equal bending strength (120 T·m) obtained by a higher field (11 T) and shorter magnetic length (11 m) than those of the LHC dipoles (8.3 T and 14.2 m). The space gained is sufficient for the installation of special collimators. This system is already needed for Run 3 ion operation in the DS region around IP2 following the upgrade of ALICE in LS2. It might also be needed in the DS around IP7 for HL-LHC operation. The requirements in other insertion regions have yet to be assessed.

2.2.5 New cold powering

While a considerable effort is under way to study how to replace the radiation-sensitive electronics boards with radiation-hard cards, another solution is also being pursued for special zones: removal of the power converters and electrical feedboxes (DFBs), delicate equipment associated with the continuous cryostat, out of the tunnel. Besides improving LHC availability (fewer interruptions, faster interventions without the need for tunnel access), radiation dose to personnel would be reduced as well.

Removal of power converters and DFBs to locations far from the beam line, and possibly to the surface, is only possible through the use of a novel technology: superconducting links (SCLs) made out of high-temperature superconductors (YBCO or Bi-2223) or MgB_2 superconductors. Regions where this radical solution will be needed because of the high radiation load on electronics, and/or the ‘as low as reasonably achievable’ principle (ALARA), have been identified.

- The long straight section of IP7 where a 500 m cable rated at 20 kA is needed.
- The high luminosity insertion regions IR1 and IR5, where much higher current cables (150 kA and 164 kA) are needed for the IT magnets and the magnets in the MS region (i.e. from D2 to Q6). In this latter case, the superconducting cable will link the magnets with power converters on the surface, with

significant challenges to the cryogenics and system integration resulting from the 100 m or so difference in altitude.

2.2.6 Enhanced machine protection and remote handling

Various systems will become a bottleneck with aging of the machine and higher performance beyond the 40 fb^{-1} to 60 fb^{-1} per year envisaged in the original LHC design. One such system is the quench protection system (QPS) of the superconducting magnets. The QPS should:

i) become fully redundant in case of power loss;

ii) allow low energy discharge on quench heaters and easy adaption of the detection thresholds;

iii) provide an interlock for the quench heater discharge based on a sensor for quench heater integrity.

In general, the QPS will need a complete renovation after 2020.

Machine protection will have to be improved, and not just because of the higher beam energy and energy density: it will have to cope with very fast events generated, for example, by crab cavities and by a possible increase of the events generated by falling particles (UFOs).

The LHC has not been designed specifically for remote handling. However, the level of activation from 2020, and even earlier, requires careful study and development of special equipment to allow replacement of collimators, magnets, vacuum components, etc. according to the ALARA principle. While full robotics are difficult to implement given the conditions, remote manipulation, enhanced reality, and supervision are the key to minimizing the radiation dose to personnel.

2.2.7 New cryogenics plants and distribution

To increase the flexibility for intervention and rapid restoration of availability (i.e. to minimize loss of integrated luminosity) it will be useful to install a new cryogenics plant in P4 for a full separation between superconducting RF and magnet cooling. This should be done during LS2, to avoid a possible weak zone for Run 3. The new plant should also be able to provide cooling to new cryogenic equipment under consideration for IP4, i.e. a new SCRF harmonic system and the hollow e-lens for halo control, which requires a superconducting solenoid. For the time being, these two systems are not in the baseline; however, they constitute interesting options under study.

A further consolidation that is deemed necessary in the long term is the separation between the cooling of the inner triplets and the few stand-alone superconducting magnets in the MS from the magnets of the arc. The present coupling of IR and arc magnets means that an intervention in the triplet region requires warm-up of the entire sector (an operation of three months, not without risk).

New power plants will be needed to cope with higher heat deposition from the high luminosity points. In particular, given the luminosity-driven heat load in the cold magnets, and the cooling of superconducting crab cavities at 1.9 K, the power (at 4.2 K) of the new cryo-plant in IP1 and IP5 will have to be in the 15–18 kW range. The cooling scheme includes separation, with possible interconnection, between arc and IR cryogenics to gain in flexibility.

2.2.8 Enhanced beam instrumentation

Improving beam instrumentation is a continuous task during routine operation of an accelerator. The HL-LHC will require improved or new equipment to monitor and act on proton beams with more challenging parameters than those of the LHC. A short illustrative list includes the following.

- New beam loss monitors for the IT quadrupoles.
- A radiation-tolerant Application-Specific Integrated Circuit (ASIC) for the beam loss monitoring system.

- A new beam position monitoring system, including a high-resolution orbit measurement system, and high-directivity strip-line pick-ups for the insertion regions.
- Emittance measurement: while improving the present system, a new concept-based beam gas vertex emittance monitor is envisaged for the HL-LHC.
- Halo diagnostics to control the halo in order to minimize losses (and especially loss peaks) in the presence of a beam with a stored energy close to 0.7 GJ. Synchrotron radiation imaging, and possibly wire scanners, appear to be the only candidates for halo monitoring in the HL-LHC.
- Diagnostics for crab cavities: electromagnetic pick-ups and streak cameras are being studied for beam shape monitoring.
- Luminosity measurements with new radiation-hard devices (located in the new TAXN) capable of withstanding the radiation level, which will be ten times higher.

2.2.9 Beam transfer and kickers

The higher beam current significantly increases the beam-induced power deposited in many elements, including the injection kicker magnets in the LHC ring. New designs for several components in the dump system devices will probably be needed because of the increased energy deposition in the case of direct impact, and because of an increased radiation background, which could affect the reliability of this key machine protection system.

A non-exhaustive list of the elements that could need an improvement or a more radical upgrade (based on the experience from Run 2) is given below.

- Injector kicker magnets (better cooling of the magnets to cope with beam-induced heating, different type of ferrites with higher critical temperature, coating of ceramic tubes to reduce SEY to suppress e-cloud effects).
- Beam dump block TDE with its N_2 overpressure system and window VDWB: if these are not compatible with HL-LHC intensities, extension of the dilution pattern may be the only practical and safe solution, implying the installation of additional dilution kicker systems MKB (up to 50%).
- Injection absorber, auxiliary protection collimators, protection masks.
- Beam dump absorber system.

2.3 Baseline optics and layout

2.3.1 Basic optics and layout choices for the High Luminosity insertions

The current baseline optics design (HLLHCV1.1) has evolved from the previous LHC Upgrade Phase I project [17–19]. A realistic, cost-efficient and robust (achromatic) implementation of low β^* collision optics requires the deployment of the Achromatic Telescopic Squeeze (ATS) scheme, together with the installation of insertion magnets of larger aperture [20–24]. Successful validation tests of the ATS with beam were achieved in 2011–2012 [25–29] in very specific conditions (low intensity, no crossing angle to save aperture, etc.). The corresponding number, type, and specifications of the new magnets to reach low β^* [20, 21] were then endorsed by the project (see, for example, [30] and references therein).

The historical development of the optics design is summarized in Ref. [31]; here, only the last three parts of this long chain are mentioned, namely the so-called SLHCV3.1b [32], HLLHCV1.0 [33], and HLLHCV1.1 (current baseline) optics. SLHCV3.1b uses ATS optics based on 150 T/m Nb_3Sn triplets and displacement of D2 for crab cavity integration [32]. HLLHCV1.0 is similar to SLHCV3.1b, but with a new triplet layout based on 140 T/m Nb_3Sn triplets [33]. HLLHCV1.1, the new baseline, is based on HLLHCV1.0, but with some modifications to take into account the results of design studies for D2, energy deposition studies for the passive

protection of the superconducting elements, hardware integration studies, and updated naming conventions [34, 35], and corresponding optical configurations.

Table 2-2 presents an overview of the main features of the three layouts and of the corresponding optical configurations.

Table 2-2: Main HL-LHC optics variants currently under study. The baseline collision optics corresponds to $\beta^* = 15$ cm in both transverse planes (round optics) with a full crossing angle of 590 μrad. Other collision optics are available, round or flat, for dedicated studies.

	SLHC V3.1b	**HLLHCV1.0**	**HLLHCV1.1 (Baseline)**
Collision β^* IP1, IP5	Round: 15cm, (10 cm, 33 cm, 40 cm). Flat: 30/7.5cm, (20/5 cm) with HV, VH crossing.	Round: 15cm, (10 cm). Flat: 30/7.5cm, (20/5 cm) with HV, VH crossing. Complete squeeze.	
Pre-squeeze β^* IP1, IP5	40 cm, (2 m)	44 cm, (3 m) transition strengths.	44 cm
Injection β^* IP1, IP5	5.5 m (11 m)	6 m, (11 m, 18 m)	6 m (15 m)
Triplet gradient	150 T/m	140 T/m	140 T/m
Triplet magnetic length	Q1–Q3: 7.685 m Q2: 6.577 m	Q1–Q3: 4.002 m × 2 Q2: 6.792 m	Q1–Q3: 4.00 m × 2 Q2: 6.8 m
Triplet corrector package	Nested triplet nonlinear corrector package with new a_5, b_5, a_6 corrector coils	Superferric, non-nested, nonlinear corrector package.	
Insertion region dipoles	D2 moved towards the IP by 15 m. For version HLLHCV1.1 the magnetic length of D1 [40] and D2 has been shortened.		
Insertion region quadrupoles	MQYY type for Q4 in IR1, IP5. Q5 moved towards arc by 11 m. MQYL type for Q5 in IR1, IR5, IR6. Additional MS in Q10 of IR1 and IR5.	MQYY type for Q4 in IR1, IR5. Q5 moved towards the arc by 11 m. MQYL type for Q5 in IR1, IR5, IR6. Additional MS in Q10 of IR1 and IR5.	MQYY type for Q4 in IR1, IR5. Q5 moved towards arc by 11 m. Q4 moved towards arc by 8 m. MQY at 1.9 K type for Q5 in IR1, IR5. Double MQY for Q5 in IR6. Additional MS in Q10 of IR1 and IR5.
Crab cavities	3		4

The current baseline layout incorporates various optimizations, and in particular has been made compatible with the latest hardware parameters and constraints. The magnetic elements in the region between the IP and Q4 (Figure 2-3) have been positioned to optimize the strength requirements for the magnets and for ancillary equipment. For instance, moving the Q4 quadrupole changes the value of the beta functions at the location of the crab cavities, thus improving their efficiency.

In the triplet region (Figure 2-3, which is in the range of approximately 20 m to 80 m) the Q1 and Q3 magnets are split into two and the dipole corrector magnets (used to create the crossing and separation schemes) are implemented in a nested configuration for both planes. The corrector package close to Q3 consists of superferric magnets. The specifications and performance of the non-linear correctors (used to compensate the field quality effects of the triplets and D1 separation dipoles on both sides of the IP) are reported in Refs. [36, 37]. Detailed numerical simulations indicate that additional corrector types are needed to cope with the pushed

performance of the HL-LHC, so the layout of the correctors will not be a simple carbon copy of the existing layout. Inclusion of the field quality of the D2 separation dipole has been considered, but is not trivial, due to the two-in-one structure of the D2.

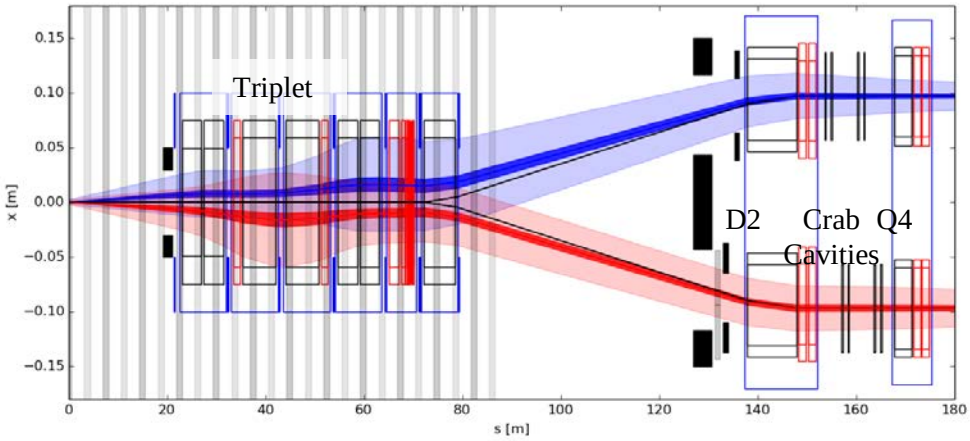

Figure 2-3: Overall layout of the insertion region between the IP and Q4. The dark blue and red areas represent the 2 σ beam envelope. The light regions correspond to a 12 σ value of the beam envelope for an emittance of 3.5 μm with a tolerance of 20% for beta-beating and 2 mm of closed orbit distortion. The shaded grey areas in the triplet region represent the locations of the parasitic beam–beam encounters.

The block of two separation dipoles has been changed with respect to the nominal LHC layout, decreasing their separation. The D2 area is particularly delicate for several reasons. First, there are space constraints because of the need for protection devices such as the absorber for neutral debris from the collisions. Second, the transverse separation is not yet optimal, leading to a reduction in the amount of iron between the two apertures of the D2, as well as to reduced beam and mechanical apertures because of the large values of the beta functions at this point. Downstream of D2, the situation is not much easier, as the crab cavities impose tight constraints on the space between D2 and Q4, as well as on the values of the beta functions.

Detailed work has been performed to specify the strengths of dipole orbit correctors in the triplets and the D2 and Q4 magnets [38, 39]. Initially, the required strength needed too long correctors, mainly because of the need to close the bumps at the D2 dipole in order to avoid a non-zero closed orbit at the location of the crab cavities. Detailed analysis of the RF aspects allowed the tight constraints to be relaxed (0.5 mm of closed orbit distortion can be tolerated at the crab cavities when operating and 2–3 mm when the cavities are made transparent to the beam). The design now includes a correction scheme with magnets that are 1.5–2.5 m long. This makes it possible to close the orbit bumps further downstream from the D2 separation dipoles, thus reducing their overall strength. In the current layout, Q4 is a new magnet with a larger aperture, MQYY, while Q5 is a MQY-type (the Q4 of the present LHC) operating at 1.9 K to provide the required gradient.

The implementation of the ATS scheme in the HLLHCV1.0 requires hardware changes in other parts of the LHC ring. In particular, an additional lattice sextupole (MS) magnet should be installed in Q10 in IR1 and IR5. Moreover, Q5 in IR6 should be upgraded. The current baseline layout envisages the installation of a second MQY-type quadrupole close to each existing Q5.

Table 2-3 lists the key parameters of the quadrupoles (new or refurbished) to be installed in IR1 and IR5, while Table 2-4 gives the corresponding parameters for the separation dipoles and orbit correctors. Table 2-5 gives the parameters for the multipolar correctors.

Table 2-3: New or refurbished quadrupoles for HL-LHC, all operating at 1.9 K. The orientation of the rectellipse aperture (*R*) [40] can be changed to optimize the mechanical aperture.

	Inner triplet (single aperture)			**Matching section (two-in-one)**		
Magnet	Q1	Q2	Q3	Q4	Q5	Q6
Number	2	2	2	1	1	1
Type	MQXFA	MQXFB	MQXFA	MQYY	MQY	MQML
Magnetic length [m]	4.0	6.8	4.0	3.8	3.4	4.8
Gradient [T/m]	140	140	140	115	200	200
Coil aperture [mm]	150	150	150	90	70	56
Aperture separation [mm]	-	-	-	194	194	194
Beam screen (BS) shape	Octagon	Octagon	Octagon	Rectellipse	Rectellipse	Rectellipse
BS aperture (H/V) [mm]	98/98	118/118	118/118	64/74	44/57.8	35.3/45.1
Mechanical tolerances (R/H/V) [mm] [41]	0.6/1/1	0.6/1/1	0.6/1/1	0.84/1.26/0.6	0.84/1.26/0.6	As built

Table 2-4: New dipole magnets for HL-LHC, all operating at 1.9 K. The orientation of the rectellipse (*R*) aperture can be changed to optimize the mechanical aperture. The orbit correctors can be nested or consecutive as indicated.

	Separation/recombination dipoles		**Orbit correctors**			
Assembly	D1	D2	Corrector package	Q2	D2	Q4
Number per side per insertion	1	1	1 [HV nested]	2 [HV nested]	2 [HV consec.]	2 [HV consec.]
Type	MBXF	MBRD	MCBXFA	MCBXFB	MCBRD	MCBYY
Magnetic length [m]	6.27	7.78	2.2	1.2	1.5	1.5
Integrated field [T m]	35	35	4.5	2.5	4.5	4.5
Coil aperture [mm]	150	105	150	150	100	100
Aperture separation [mm]	n/a	188	-	-	194	194
BS shape	Octagon	Octagon	Octagon	Octagon	Octagon	Rectellipse
BS aperture (H/V) [mm]	118/118	84/84	118/118	118/118	79/79	64/74
Mechanical tolerances (R/H/V) [mm]	0.6/1/1	0.84/1.36/1	0.6/1/1	0.6/1/1	0.84/1.36/1	0.84/1.26/ 0.6

Table 2-5: New multipolar superferric correctors for HL-LHC, all operating at 1.9 K.

Number	**1**	**1**	**1**	**1**	**1**	**1**	**1**	**1**	**1**
Number of poles	4	12	12	10	10	8	8	6	6
Normal/skew	Skew	Normal	Skew	Normal	Skew	Normal	Skew	Normal	Skew
Type	MQSXF	MCTXF	MCTSXF	MCDXF	MCDSXF	MCOXF	MCOSXF	MCSXF	MCSSXF
Magnetic length [m]	0.807	0.43	0.089	0.095	0.095	0.087	0.087	0.111	0.111
Integrated field [mT·m] at 50 mm	1000	86	17	25	25	46	46	63	63
Coil aperture [mm]	150	150	150	150	150	150	150	150	150
BS shape	Octagon	Octagon	Octagon	Octagon	Octagon	Octagon	Octagon	Octagon	Octagon
BS aperture (H/V) [mm]	118/118	118/118	118/118	118/118	118/118	118/118	118/118	118/118	118/118
Mechanical tolerances (R/H/V) [mm]	0.6/1/1	0.6/1/1	0.6/1/1	0.6/1/1	0.6/1/1	0.6/1/1	0.6/1/1	0.6/1/1	0.6/1/1

As already mentioned, protection devices are required for the new layout of the IR1 and IR5 regions. The current LHC layout has only a TAS in front of Q1, to protect this magnet from collision debris, and a TAN to protect D2 from the neutrals produced at the IP. For the HL-LHC, these two devices will have to be upgraded to withstand much larger luminosities. Furthermore, additional masks are envisaged to protect other magnets in the matching section. A summary of the characteristics of these devices can be found in Table 2-6.

Table 2-6: New absorbers for HL-LHC, all operating at 1.9 K. The orientation of the rectellipse aperture can be changed to optimize the mechanical aperture.

	Inner triplet (single aperture)	**Matching section (two-in-one)**			
Absorber	TAS	TAN	Mask D2	Mask Q5	Mask Q6
Aperture	1	2	2	2	2
Type	TAXS	TAXN	TCLMA	TCLMB	TCLMC
L [m]	1.8	3.5	0.5	1.0	1.0
Aperture separation [mm]	n/a	149–159	188	194	194
Aperture (H/V) [mm]	54/54	80/80	84/84	44/57.8	35.3/45.1
Mechanical tolerances (R/H/V) [mm]	2/0.5/0.5	0.6/1/1	0.6/1/1	0.6/1/1	0.6/1/1

Figure 2-4 shows example optics configurations for injection and collision. Several configurations can be provided apart from the nominal (i.e. round) optics.

Table 2-7 gives the main sets of β^* values (including the optical parameters corresponding to the ion runs). Since IR2 and IR8 are running with increased strength of the triplets at injection, a so-called pre-squeeze has to be applied at top energy to reduce the strength of the triplets at constant value of beta function at the IP.

The transition between the various optical configurations has been studied in detail [42, 43]. The sequence of gradients during the squeeze is available, and will be used to perform first estimates of the hysteresis effects. Moreover, it will be possible to evaluate the time required to accomplish the squeeze, which is essential information to determine specifications for the required power converters. Work is in progress to address these two points; results are expected in the coming months.

Finally, it is worth mentioning additional studies that have looked at alternative layouts. Options have been studied based on triplets using 120 T/m and 170 T/m gradients [44, 45], and an additional Q7 for crab

cavity kick enhancements [46] without upgrading the matching section layout [47]. The latest results can be found in Ref. [48].

There are numerous constraints on the layout of components, arising from various considerations. The constraints and the associated issues are described in Chapter 15.

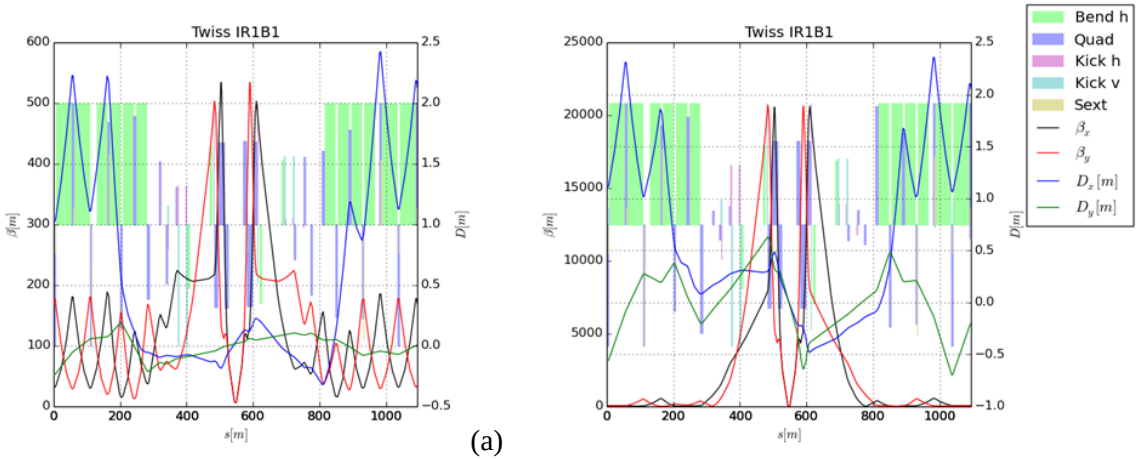

(a) (b)

Figure 2-4: Optical functions at (a) injection and (b) collision. Note the different vertical scales: at collision, the beta functions in the triplets are large, to provide the low β^* at the IP.

Table 2-7: Available optical configurations for the baseline layout. IR3 and IR7 are not reported here as they have static optics from injection to collision and do not take part in the ATS scheme. Some alternative configurations (other than the nominal) are also shown.

Optics	**IR1**	**IR5**	**IR2**	**IR8**	**IR4**	**IR6**
Injection	β^* = 6 m, inj.	β^* = 6 m, inj.	β^* = 10 m, inj.	β^* = 10 m, inj.	Inj.	Inj.
End of ramp	β^* = 6 m	β^* = 6 m	β^* = 10 m	β^* = 10 m	Inj.	Inj.
Pre-squeeze	β^* = 44 cm	β^* = 44 cm	β^* = 10 m	β^* = 3 m	Inj.	Inj.
Collision round	β^*_{ATS} = 15 cm	β^*_{ATS} = 15 cm	β^* = 10 m, ATS (3×, 3×)	β^* = 3 m, ATS (3×, 3×)	ATS (3×, 3×)	ATS (3×, 3×)
Collision ions	β^* = 44 cm	β^* = 44 cm	β^* = 50 cm	β^* = 50 cm	Inj.	Inj.
Collision VDM	β^* = 30 m	β^* = 30 m	In preparation	In preparation	Inj.	Inj.
Alternative configurations						
Collision Flat	β^*_{ATS} = 7.5/30 cm	β^*_{ATS} = 30/7.5 cm	β^* = 10 m, ATS (6×,1.5×)	β^* = 3 m, ATS (6×,1.5×)	ATS (1.5×, 6×)	ATS (1.5×, 6×)
Collision FlatHV	β^*_{ATS} = 30/7.5 cm	β^*_{ATS} = 7.5/30 cm	β^* = 10 m, ATS (1.5×, 6×)	β^* = 3 m, ATS (1.5×, 6×)	ATS (6×,1.5×)	ATS (6×,1.5×)
Collision sRound	β^*_{ATS} = 10 cm	β^*_{ATS} = 10 cm	β^* = 10 m, ATS (4.5×, 4.5×)	β^* = 3m, ATS (4.5×, 4.5×)	ATS (4.5×, 4.5×)	ATS (4.5×, 4.5×)
Collision sFlat	β^*_{ATS} = 5/20 cm	β^*_{ATS} = 20/5 cm	β^* = 10 m, ATS (9×, 4.5×)	β^* = 3 m, ATS (9×, 4.5×)	ATS (4.5×, 9×)	ATS (4.5×, 9×)
Collision sFlatHV	β^*_{ATS} = 20/5 cm	β^*_{ATS} = 5/20 cm	β^* = 10 m, ATS (4.5×, 9×)	β^* = 3 m, ATS (4.5×, 9×)	ATS (9×, 4.5×)	ATS (9×, 4.5×)

2.3.2 Target field quality and dynamic aperture

The dynamic aperture (DA) has been used since the initial steps of the design of the LHC [40] to determine the required field quality of the various magnet classes. For computation of the DA in the HL-LHC, particles are tracked over 10^6 or 10^5 turns, depending on whether beam–beam effects are included or neglected, respectively. The initial momentum co-ordinate is set to two-thirds of the bucket height (2.7×10^{-4} and 7.5×10^{-4} for collision and injection energy, respectively). Sixty implementations of the random components in the magnets, corresponding to sixty realizations of the LHC lattice, are considered in the numerical

simulations. Eleven phase space angles have routinely been used (although for special studies up to 59 values have been probed), while thirty particle-pairs per 2 σ amplitude step have been used. All these parameters have been specified during the design stage of the LHC. Since then, the amount of available computing power has increased, thanks to the increased CPU power of the CERN batch system and because of the use of volunteer-based computing resources [49]: this has enabled an increase of the number of directions considered in the studies, making the DA estimate more accurate. Note that the number of turns and random seeds affects the accuracy of the DA calculation, which is at least 0.1 σ in this case.

For reference, the multipole expansion used to describe the magnetic field is given as [40]:

$$B_y + iB_x = B_{\mathrm{ref}} \sum_{n=1}^{\infty} (b_n + \mathrm{i}a_n) \left(\frac{x+\mathrm{i}y}{r_0}\right)^{n-1}, \tag{2-5}$$

where B_x, B_y, and B_{ref} are the transverse magnetic field components and the reference field, respectively. The coefficients a_n, b_n are the skew and normal field components, and r_0 is a reference radius. In the framework of the LHC studies the magnetic errors are split into three components, namely mean (*S*), uncertainty (*U*), and random (*R*), such that a given multipole is obtained by:

$$b_n = b_{n_S} + \frac{\xi_U}{1.5} b_{n_U} + \xi_R b_{n_R}, \tag{2-6}$$

where ξ_U, ξ_R are Gaussian-distributed random variables cut at 1.5 σ and 3 σ, respectively. The ξ_U variable is the same for all magnets of a given class, but changes from seed to seed and for the different multipoles. On the other hand, ξ_R also changes from magnet to magnet.

The target value of the DA differs between injection and collision energies. At injection, where the beam–beam effects can be safely neglected, the focus is on the impact of magnetic field quality. For the LHC design [40], a target value of 12 σ (for a normalized emittance of 3.75 μm) was assumed. The best model of the LHC, including the measured field quality of the magnets and the sorting of magnets, provides a DA slightly lower than 11 σ [50]. No signs of issues due to DA limitations have been observed during operation or dedicated studies in Run 1, although operation at high intensity has been conducted with beams with an emittance smaller than nominal (2–2.5 μm rather than 3.75 μm).

At top energy, beam–beam effects cannot be neglected and the DA has to be evaluated, including both magnetic field imperfections and head-on and long-range beam–beam phenomena (see Section 2.4.2). Hence, the approach taken consists of probing the impact on DA of the field quality of the new magnets, asking that all new magnets have an impact on the DA that is in the shadow of the triplet quadrupoles. Eventually, the beam–beam effects are also included, providing the final DA value.

Studies for the field quality of the new magnets started from the top energy configuration and with an earlier version of the layout, namely the so-called SLHCV3.1b [32]. This allowed first estimates of the required field quality to be derived, which were then improved by including consideration of the injection energy, where the beam size reaches its maximum and the field quality is worse, due to the persistent current effect. The newer layout HLLHCV1.0 [33] has been used following its release.

In the numerical simulations consideration is made of the machine as built, i.e. the best knowledge of the measured magnetic errors is assigned to the magnets as installed, while, for the magnets that will be replaced according to the upgrade plans, the expected error table, with statistical assignment of errors, is used. This is the baseline configuration of the LHC ring to which magnetic field errors of other classes of magnets can be selectively added.

In these studies the acceptable minimum DA was set to about 10.5 σ at top energy, based on experience from the LHC. The DA calculation was performed using long-term tracking in SixTrack [51, 52], neglecting beam–beam effects. Determination of the required field quality based on DA computations is intrinsically a non-linear problem. The field quality obtained from electromagnetic simulations is used as an initial guess. Then, optimization of the field quality essentially involves determining the Jacobian of the DA as a function of the multipoles around the initial value of field quality. For this reason, it is of paramount importance to have

a reliable estimate of the expected field quality from detailed electromagnetic simulations and measurements (see Chapter 3). The resulting error tables can be found in the official optics repositories [53, 54] and are also collected in Ref. [55].

The previous IT specifications at 7 TeV [56] were updated to take into account the additional IT correctors for $a_5,\ b_5, a_6$ errors. It is worth mentioning that in all the studies reported in this document, the IT correctors have been considered as ideal devices, i.e. exactly correcting the field quality of the IT and D1 magnets, without any error due to uncertainty in the transfer function of the correctors. These specifications will be referred to as IT_errortable_v66. An estimate of the D1 field quality is based on magnet design and referred to as D1_errortable_v1 [57]. Due to the evolution of the D2 dipole design, three versions of the D2 field quality were used in the study: these are referred to as D2_errortable_v3, _v4 [58], and _v5 [59]. The D2 low-order terms at 7 TeV are shown in Table 2-8. Estimates for the Q4 and Q5 magnets are based on a scaling of the measured field of the existing MQY quadrupole and referred to as Q4_errortable_v1 and Q5_errortable_v0, respectively.

Table 2-8: Evolution of low order terms of the estimated D2 field quality at 7 TeV ($r_0 = 35$ mm).

n	a_{nS}	a_{nU}	a_{nR}	b_{nS}	b_{nU}	b_{nR}
D2_errortable_v3						
2	0.0	0.679	0.679	65.0	3.000	3.000
3	0.0	0.282	0.282	-30.0	5.000	5.000
4	0.0	0.444	0.444	25.0	1.000	1.000
5	0.0	0.152	0.152	-4.0	1.000	1.000
6	0.0	0.176	0.176	0.0	0.060	0.060
D2_errortable_v4						
2	0.0	0.679	0.679	25.0	2.500	2.500
3	0.0	0.282	0.282	3.0	1.500	1.500
4	0.0	0.444	0.444	2.0	0.200	0.200
5	0.0	0.152	0.152	-1.0	0.500	0.500
6	0.0	0.176	0.176	0.0	0.060	0.060
D2_errortable_v5						
2	0.0	0.679	0.679	1.0	1.000	1.000
3	0.0	0.282	0.282	1.0	1.667	1.667
4	0.0	0.444	0.444	-3.0	0.600	0.600
5	0.0	0.152	0.152	-1.0	0.500	0.500
6	0.0	0.176	0.176	2.0	0.060	0.060

The SLHCV3.1b collision optics features $\beta^* = 15$ cm. The desired minimum DA (among all seeds and phase angles) at collision energy is about 10 σ. Tracking simulations performed with the error table IT_errortable_v66 and without the D1, D2, Q4 and Q5 magnetic errors give $DA_{\min} = 10.4\ \sigma$, which is acceptable. Note that $DA_{\min}$ stands for the minimum DA over all seeds and angles, while DA_{ave} represents the minimum over all angles of the DA averaged over the seeds.

As a next step, the impact on DA of the field quality in the D1, D2, Q4 and Q5 magnets was verified. The Q4 and Q5 estimated magnetic errors produced negligible effect on the DA, hence their field quality is acceptable. Impact of the D1 estimated errors is mostly due to the relatively large allowed multipoles b_{n_S}. It is found that the largest DA reduction is caused by b_{7S} and b_{9S}. The low-order D1 errors have negligible effect since they are compensated for by the included IT correctors of order *n* between 3 and 6. To reduce the impact of b_{7S} and b_{9S} while keeping them realistic, it is proposed to reduce them by a factor of 2 (to 0.2 and −0.295, respectively) relative to D1_errortable_v1.

Two versions of the estimated D2 field quality were used for the SLHCV3.1b tracking: D2_errortable_v3 and D2_errortable_v4.These tables were produced during successive iterations of the field quality optimization. The b_2 to b_4 terms are rather large due to field saturation. These terms showed a strong impact on the DA. The b_2 affected the linear optics by increasing β^*, thus resulting in a too optimistic DA value. To avoid this effect,

the b_2 was set to zero for subsequent tracking campaigns, on the assumption that it can be reduced by appropriate design and that β^* will be corrected after measurements. It is found that the D2 b_3 and b_4 have a strong effect on the DA. Effects of feed-down due to the orbit in the straight D1 and D2 magnets were found to be very small. To maintain the DA_{min} close to 10 σ, b_3 and b_4 must be reduced by an order of magnitude relative to D2_errortable_v3. These terms had been, indeed, much improved in the updated error table, D2_errortable_v4 (see Table 2-8). Following the tracking results, the proposed further adjustment for D2_errortable_v4 is to reduce b_2 to about 1 unit and b_{3S} from 3.0 to 1.5. The resulting DA_{min} and DA_{ave} at 7 TeV, with all new magnet errors and adjustments, are 9.90 σ and 11.64 σ, respectively, which is still acceptable.

The β^* for SLHCV3.1b lattice at 450 GeV is 5.5 m, with peak beta functions in the IR magnets lower by a factor of 35 than those in the collision optics. Beam sizes in these magnets are also reduced even though the emittance is larger by a factor of 16. Therefore, the impact of field errors of the new magnets will be much smaller, and the use of the IT correctors is a priori not needed: these results are confirmed by tracking studies. Hence, their field quality at injection based on the present estimates is acceptable. The resulting DA_{min} and DA_{ave} with all errors are 10.16 σ and 10.5 σ, respectively, and are also acceptable. Another option of the injection optics, with β^* of 11 m, was verified and showed very similar DA.

The injection DA, however, is about 1 σ smaller than the DA of the nominal LHC. Since it is not limited by the IR magnets, other improvements (e.g. in the arcs) may need to be considered. Possible options include a larger integer tune split and adjustment of the working point. Tune scans indicate an effect of the 7th order horizontal resonance close to the current tune (62.28, 60.31). Reducing the horizontal and vertical tunes by about 0.01 would increase the DA by about 0.5 σ.

HLLHCV1.0 is the latest version of the HL-LHC lattice that has been considered in numerical simulations so far. Some of the differences relative to the SLHCV3.1b include: a longer IT with a lower gradient of 140 T/m and higher peak beta function (7%) at collision, adjusted orientation of magnets in the cryostat, new IT corrector positions, and different phase advance between IP1 and IP5. Using the previously optimized field quality of the new magnets, the collision DA of the HLLHCV1.0 lattice is reduced by about 1 σ relative to the SLHCV3.1b, i.e. with DA_{min} and DA_{ave} of 8.8 σ and 10.4 σ, respectively. A stronger impact of the D2 b_3 and b_4 terms of the previously adjusted D2_errortable_v4 was noticed. Since b_{3S} had been already reduced in this table, the next step was to reduce b_{4S} by half. This improved the DA to DA_{min} = 9.1 σ and DA_{ave} = 11.1 σ. Further improvement was achieved when using the most recent D2 field estimate D2_errortable_v5 [59] (see Table 2-8), where the b_2 and b_3 terms are reduced at the expense of somewhat larger higher-order terms. In this case, DA_{min} = 9.8 σ and DA_{ave} = 12.5 σ, as shown in Figure 2-5(a), which is acceptable and rather comparable to the DA of the SLHCV3.1b. The reasons for such noticeable improvement will need to be further analyzed.

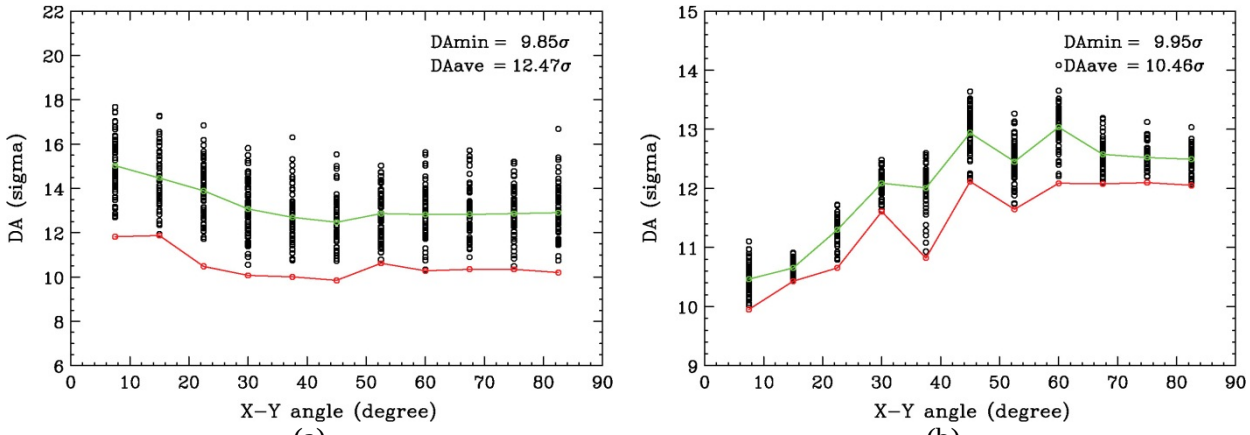

Figure 2-5: DA of HLHCV1.0. (a) DA at 7 TeV with adjusted estimated field quality of new magnets. (b) DA at 450 GeV with estimated field quality of new magnets. The r.m.s. beam size is that corresponding to a normalized emittance of 3.75 μm.

The β^* at injection for HLLHCV1.0 is 6.0 m, comparable to SLHCV3.1b. The impact of the field errors in the new magnets on the DA was verified and found to be insignificant (similar to SLHCV3.1b). The resulting DA with all errors (DA_{min} = 9.9 σ and DA_{ave} = 10.5 σ) is acceptable, see Figure 2-5(b).

Field quality and dynamic aperture studies will be pursued in the future along several lines, including:

- dedicated studies to assess the impact of field quality of IT, D1, D2, Q4 and Q5 on linear optics, knowing that the distortion of the optical parameters can stem from both the b_2 component and the feed-down from b_3 and a_3 via the crossing scheme bumps;
- dedicated studies (ongoing) to assess the maximum tolerable ripple in the power converters of the IT quadrupoles and magnets in the matching section [60];
- specification of crab cavity field quality: preliminary results [61–64] seem to indicate that the estimated field quality should be good enough to prevent any impact on the DA;
- assessment of the impact of fringe fields for the large aperture magnets, including the new IT quadrupoles and the separation dipoles.

Regarding fringe fields, the quadrupolar component has already been considered and found non-problematic in Ref. [65]. Preliminary analytical results [66] indicate that, albeit small, the detuning with amplitude induced by the fringe fields is not completely negligible, thus calling for a second level of study. This should include long-term numerical simulations to study the non-linear effects generated. This opens the wide field of symplectic integration as, in the presence of 3D magnetic fields, the standard approach based on multipoles cannot be applied. Work is underway to study the best integration schemes and their implementation [67, 68], before starting the real numerical work.

2.4 Performance

2.4.1 Beam stability

The impedance in the HL-LHC, shown in Figure 2-6 [69], is not dramatically higher than in the LHC. Molybdenum-coated secondary collimators could decrease the total impedance by more than a factor of 2. However, special caution should be given to devices in high beta regions and unshielded elements.

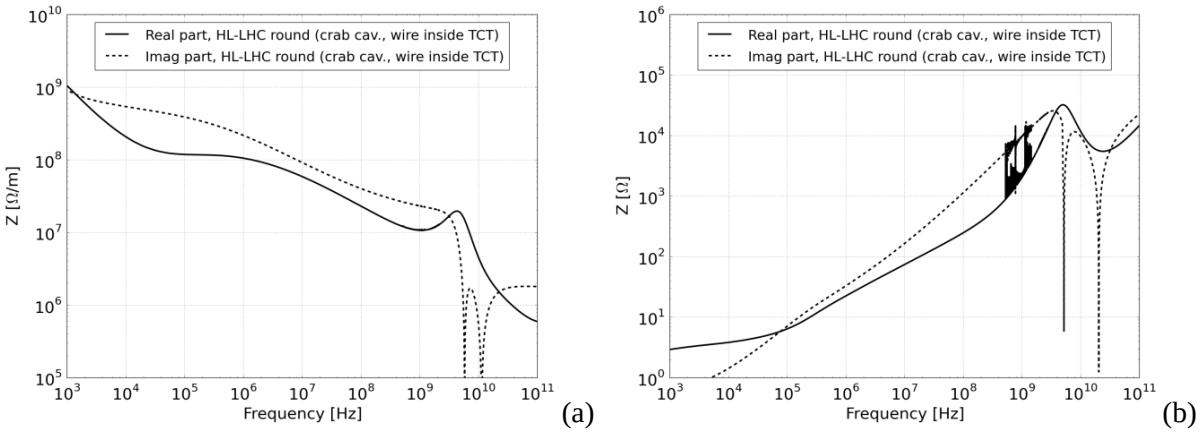

Figure 2-6: (a) First estimate of the horizontal dipolar impedance of HL-LHC, including both crab cavities and beam–beam wire compensators. The vertical dipolar impedance is similar to the horizontal. (b) Longitudinal impedance.

Longitudinal instabilities are not expected to be an issue in the HL-LHC [70]. Single bunch measurements in the LHC at 4 TeV showed an intensity threshold at 1×10^{11} p/b, for an RF voltage of 12 MV and a longitudinal emittance of 1 eVs (4 σ bunch length of 0.8 ns, scaled from the measurement of the full

width at half maximum). Scaling to HL-LHC parameters (16 MV, 2.5 eVs) leads to an intensity threshold of ~3.4×10^{11} p/b. A double RF system is therefore not needed for beam stability in the longitudinal plane. However, a high harmonic RF system [71–77] in bunch shortening mode could provide an additional margin for longitudinal stability; in bunch lengthening mode, by flattening the bunch profile, a high harmonic RF system could reduce intra-beam scattering (IBS) emittance growth rates, beam-induced heating, and pile-up density. A preliminary cavity design for the 800 MHz RF system exists [78]. Recently, the use of a low harmonic RF system in the LHC (200 MHz) as the fundamental RF system has been suggested [79] since:

- it would allow to accept larger longitudinal emittance and therefore larger bunch population from the SPS after its upgrade;
- it could help to reduce IBS, beam-induced heating, and e-cloud effects;
- together with the existing 400 MHz RF system, it could be used for luminosity and pile-up levelling;
- it also has a beneficial effect for ions and the momentum slip-stacking scheme in the SPS [80].

A new design has been proposed for a compact superconducting cavity [81]. The compatibility of this scheme with 400 MHz crab cavities or the possibility of installing 200 MHz crab cavities needs to be studied further if this scenario is to be considered. Finally, the expected benefits of a double RF system should be weighed against the impedance increase and the possible reduced reliability.

Transverse instabilities are a concern based on the experience of the LHC Run 1, during which a transverse instability at the end of the betatron squeeze could not be cured [70]. While transverse mode coupling instabilities (TMCI) thresholds well exceed the nominal HL-LHC bunch population both at injection and at high energy, to achieve transverse single-beam stability the collimators will need to be coated with 5 μm of molybdenum [70], and the transverse damper must be able to damp coupled-bunch instabilities up to the maximum frequency (20 MHz). Figure 2-7 shows the expected HL-LHC single-beam stability limits for different scenarios with a transverse damper. If the instabilities observed in 2012 are mainly single-bunch (and therefore beyond the range of the damper), we will not be able to stabilize the HL-LHC beams in the case of the standard material collimators and RF dipole crab cavities. However, beam stability could be recovered with molybdenum-coated collimators. This assumes that the transverse damper can damp all coupled-bunch modes otherwise we will not be able to stabilize the HL-LHC beams for any scenario. It is thus clear that the operation of the transverse damper is vital for HL-LHC. The situation improves with the negative polarity of the Landau octupoles but the results are qualitatively the same.

In Figure 2-7, stability thresholds are plotted versus transverse emittance, assuming the fully squeezed ATS optics (with 15 cm β^* in both planes) [25]. The high beta functions greatly enhance the impedance contribution from crab cavities compared to the un-squeezed flat-top situation. The design of the crab cavities has to be carefully evaluated and optimized with regard to the high-order modes (HOMs), to minimize the contribution to the coupled-bunch instabilities. The coupled-bunch modes will have to be stabilized by the transverse damper; the damper specifications will therefore have to be finalized once the design of the crab cavities is more advanced (at present, the impedance model of the crab cavities is quite coarse and needs to be improved). During the squeeze, the tune spread (providing Landau damping) could be increased if the ATS can be implemented starting from $\beta^* = 2$ m, thanks to the enhanced beta functions in the arcs. This effect would improve very significantly the situation in terms of stability. In reality, the situation will be even less critical because of luminosity levelling, as the smallest β^* will be reached only at a lower intensity. All these effects should be studied in more detail in the future.

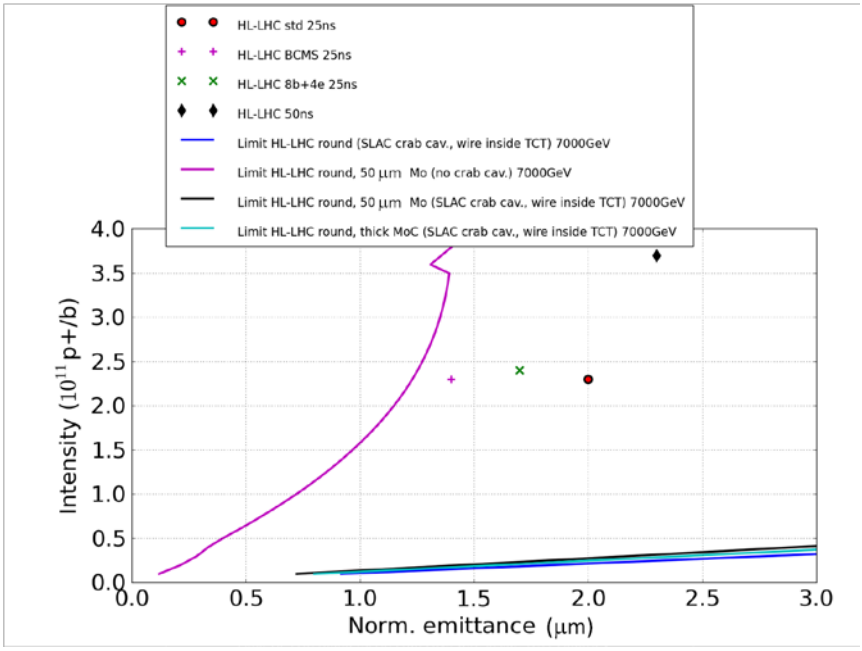

Figure 2-7: Single-beam (25 ns) intensity limit vs. transverse emittance with transverse damper (50-turn damping time) at top energy, for a chromaticity $Q' \sim 15$ for the two extreme cases (CFC collimators with ODU/SLAC crab cavities and Mo-coated collimators without crab cavities) and for positive polarity of the Landau octupoles.

With an additional 800 MHz RF system, the bunch-shortening mode should be preferred from the point of view of transverse beam stability as, even at low chromaticity, beam stability could be reached [70]. However, the operating mode that has been envisaged until now is bunch lengthening to create flat bunches; for that reason alternative scenarios (e.g. bunch flattening by band-limited RF phase noise on the main 400 MHz system) should be studied.

The effect of the electron cloud on beam stability still needs to be assessed. Induced heat loads from the electron cloud are discussed in Section 2.4.3.

Based on experience from LHC Run 1, the interplay between impedance, Landau octupoles, and beam–beam is expected to play an important role in defining the stability limits. A first estimate of the stability diagram for the fully squeezed optics (β^* = 15 cm) in the presence of both octupoles and long-range beam–beam can be found in Ref. [82]. The stable region with octupoles only increases for β^* below 40 cm, and is about 2.5 times larger with the ATS compared to the nominal optics, due to the larger beta functions at the octupoles. As is the case for the LHC, negative octupole polarity (negative amplitude detuning) is preferred for single-beam stability. On the other hand, compensation between negative amplitude detuning from the octupoles and positive amplitude detuning from long-range beam–beam leads to a reduction of the stable region during the squeeze [83]. Below a certain beam–beam separation, positive octupole polarity starts to give larger stable regions and is therefore preferred. Some details of the simulation still need to be checked. However, the proposed operational scenario for the HL-LHC is first to bring the beams into collision, and then to squeeze. By taking advantage in this way as soon as possible of the large amount of Landau damping provided by head-on beam–beam interactions, this should remove possible instability issues arising from long-range beam–beam during the betatron squeeze, while keeping negative octupole polarity (which is better for single-beam stability).

2.4.2 Beam–beam effects

The beam–beam interaction is known to be an important factor limiting the performance reach of present particle colliders. Two of the most significant effects of beam–beam interactions are: (i) the induced particle

losses that decrease the beam lifetime, create a high background load for physics experiments, and elevated heat and radiation load on the collimation system; and (ii) the degradation of beam quality manifesting itself through the beam size blow-up that decreases the luminosity delivered to particle physics experiments.

Owing to the extensive theoretical and simulation campaign during the design of the LHC collider, the beam–beam effects in the present machine are well controlled [84]. However, the HL-LHC represents a quantitative as well as a qualitative leap into unknown territory with respect to beam–beam effects. The baseline configuration makes use of some novel concepts that have not so far been used to their full extent in hadron colliders, and thus require careful evaluation. The concepts related to beam–beam effects are: (i) luminosity levelling by variation of the beta function at the IPs; (ii) tilting bunches in the main IPs with the use of RF crab cavities; (iii) significantly high value of the head-on beam–beam tune shift.

Hence, the expected impact of beam–beam interactions on HL-LHC machine performance has been evaluated in order to provide an insight into possible limitations. The studies were mostly performed with the use of the weak–strong approximation and employed the SixTrack and Lifetrack codes, which have been successfully used for the design and optimization of past and existing colliders [85, 86]. Both codes are capable of calculating the area of stable motion in phase space (the dynamic aperture), and hence a direct comparison of the results is possible. The performance reach for weak–strong codes is a few million turns, which is equivalent to a few minutes of machine time. Where necessary, strong–strong simulations with BeamBeam3D, COMBI and a code by K. Ohmi [87–99] were carried out.

In the evaluation of the HL-LHC, the criteria used for establishing satisfactory beam dynamics behaviour were the same as in the LHC design study. In particular, the target value for the one-million turn DA was 6 σ (for the nominal HL-LHC emittance of 2.5 μm) or more. The motivation for the choice of such a margin is explained in Ref. [85]. In short, the beam–beam driven diffusion at small amplitudes is quite slow, and the 10^6 turns of tracking typically does not represent the real long-term stability boundary. In the majority of studies, the 6 σ DA corresponds to a true stability boundary of about 4 σ with the appearance of chaotic spikes [85]. Benchmarking of the simulations with machine studies seem to indicate that losses and reduction of beam lifetime start to appear only at values of the crossing angle for which the simulated dynamic aperture is as low as 4 σ [89, 90]. However, it must be noted that other studies indicate that the simulations of the dynamic aperture of the installed LHC overestimate the dynamic aperture by 20–30% [94].

In the baseline HL-LHC scenario (25 ns spacing), bunches will begin colliding with 2.2×10^{11} p/b and transverse normalized emittance of 2.5 μm. The bunches will be tilted by crab cavities at each of the two main IPs to ensure head-on collisions despite the trajectories crossing at an angle. The luminosity will be levelled at the constant value of 5×10^{34} cm^{-2} s^{-1} by varying the beta function from ~69 cm at the beginning of the fill to 15 cm at the end, in the case of constant crossing angle of 590 μrad. Assuming negligible transverse emittance growth, the separation of beams at parasitic crossings will thus vary from 26 σ at the beginning of the fill to 12.5 σ at the end. Hence, from the point of view of beam–beam effects, three stages can be distinguished over the course of a fill.

- Beginning of fill (β^* = 69 cm, $N = 2.2 \times 10^{11}$ p/b): weak long-range interactions (26 σ separation) and strong head-on interactions, characterized by beam–beam tune shift ξ = 0.031 (assuming head-on collisions in LHCb), determined by beam brightness $B \sim N/\varepsilon$. Since optics with β^* = 69 cm were not readily available, simulations were performed with β^* = 40 cm, which, with the nominal initial intensity, corresponds to a significantly enhanced beam–beam effect (worst-case scenario). The bunch intensity at the specified levelled luminosity is $N = 1.7 \times 10^{11}$ p/b.
- Middle of fill (β^* = 33 cm, $N = 1.5 \times 10^{11}$ p/b): appreciably large long-range and head-on interactions.
- End of fill (β^* = 15 cm, $N = 1.1 \times 10^{11}$ p/b): weak head-on (ξ = 0.015 due to the particle burn-off in collisions) and relatively strong long-range (12.5 σ separation).

All simulations were performed with lattice version SLHCV3.1b. In addition to IR1 and IR5, the beams also collide with a finite angle at IR8 (LHCb), which further enhances the negative impact of the head-on

beam–beam effects on the dynamics. The long-range effects are weaker thanks to the beneficial effects of the β^* levelling [92]. Multipole errors in the IR magnets were included in the simulations as specified in Ref. [94]. A parametric study was performed to establish the robustness of the baseline HL-LHC scenario [93] and in order to determine the optimal crossing angle. Figure 2-8 shows the dependence of the minimum DA value on the crossing angle at IP1 and IP5 for different bunch intensities. The dashed lines indicate the minimum target DA and the nominal crossing angle. For the operational cases described above, the DA is always largely above 6 σ.

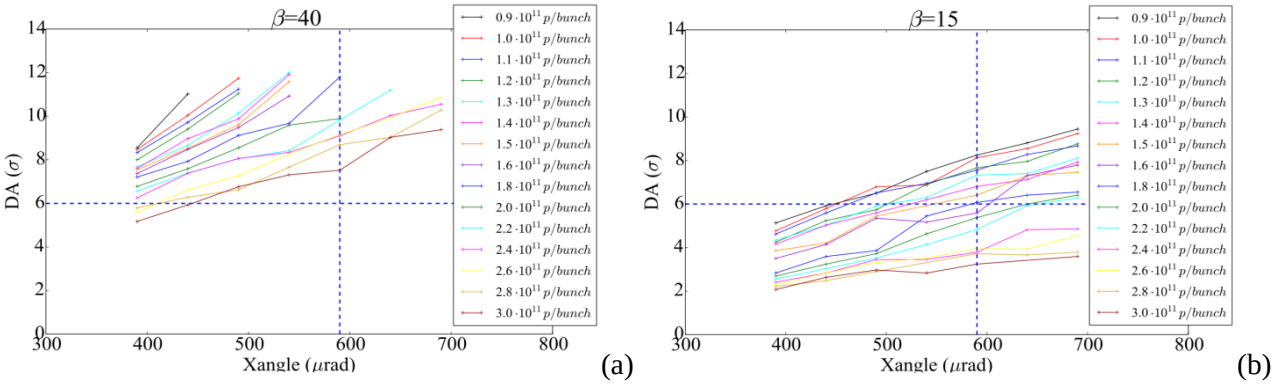

(a) (b)

Figure 2-8: Minimum DA for (a) $\beta^* = 40$ cm optics and (b) $\beta^* = 15$ cm optics as a function of crossing angle for different bunch intensities. The r.m.s. beam size corresponds to a normalized emittance of 2.5 µm.

Pacman effects [95, 97] have been evaluated and shown not to have a significant impact on DA and luminosity. The pacman effects are expected to be strongest at the end of the fill (β^* = 15 cm), and will be weaker than the nominal LHC case due to a larger beam–beam separation (12.5 σ compared to 9.5 σ). With an intensity of $N = 1.1 \times 10^{11}$ p/b and a long-range beam–beam separation of 12.5 σ one expects a maximum offset at IP1 and IP5 of about 0.15 σ. The spread over the bunch train is of the same order, 0.1–0.2 σ. The long-range variations at IP1 and IP5 result in a very small asymmetry in the tune footprint, and no impact on long-term tracking has been noticed [93].

The results of weak–strong simulations confirm the robustness of the baseline HL-LHC scenario with respect to beam lifetime and particle losses, and suggest that a significant margin exists that would allow either a decrease of the crossing angle to approximately 450 µrad, or operation at higher values of levelled luminosity [95].

Beam–beam effects can induce beam emittance growth and related luminosity lifetime degradation via a variety of mechanisms. Weak–strong simulations of multi-particle bunches were used to evaluate the emittance growth due to beam–beam related betatron resonances. The results predict that the luminosity lifetime due to beam–beam effects will be more than 80 h even in the worst case [98]. A more significant mechanism of emittance degradation can be related to the interplay between the nonlinearity of the beam–beam interaction and various sources of noise. In particular, the phase errors of crab cavities and the ripple of dipole magnet power supplies lead to fluctuations in beam–beam separation. Strong–strong beam–beam simulations have been carried out for the HL-LHC parameters with a large crossing angle and crab cavity compensation [99, 100]. A detailed damper model was included in the simulations. Both β^* levelling and crab cavity levelling were simulated including crab cavity noise and dipole power supply ripple [100]. For white random phase noise in the crab cavities, simulations suggest that the r.m.s. noise amplitude should be kept around the level of 3×10^{-5} rad in order to maintain a luminosity lifetime of 24 h. This tolerance limit might over-estimate the crab cavity phase noise level since the real phase error will have some spectral distribution different from white noise. For the present studies the spectrum was sampled at a number of frequencies near the betatron frequency. Simulations suggest that strong emittance growth would occur with noise frequencies near the fractional tune of 0.30 and 0.31. The phase errors with those frequencies should be kept as small as possible. The 600 Hz dipole noise was found to have negligible effect on the beam emittance

2.4.3 Beam-induced heat load on the cryogenic system

Both impedance and the e-cloud induce heat loads on the cryogenic system [70]. The impedance-induced heat loads with the HL-LHC beam parameters [14] for several key systems are summarized in Table 2-9. In the analysis it is assumed that no forward physics detectors (e.g. ALFA and TOTEM) will be installed during the HL-LHC era. The impedance-induced heat loads for the different types of beam screens vs. temperature are summarized in Table 2-10.

Electron cloud effects should be mitigated by beam-induced scrubbing in the arcs (experience from Run 2 will be vital in that respect) and by low secondary emission yield (SEY) coatings and/or clearing electrodes in the new insertion regions, intended to keep the heat loads within the cooling capacity [70]. Similar actions will be required for the beam screen of the triplets/D1 in IR2 and IR8.

Figure 2-9 shows the heat load from the e-cloud vs. bunch intensity for both an arc dipole and an arc quadrupole, for different SEYs. Provided that a low SEY is achieved, the increased bunch intensity should be acceptable for heat load, but the effect on the beam stability still needs to be assessed. The aim of the scrubbing run is to reach a SEY of ~1.3 in the arc main magnets: this applies for both LHC and HL-LHC, because the dependence of the SEY threshold on bunch intensity in the dipoles is weak. It is worth noting that the quadrupoles have a threshold below 1.1, which cannot be reached by scrubbing. The detrimental effects of the electron cloud in the LHC (heat load in cold regions and emittance blow-up) can be partly mitigated by using specially conceived filling patterns. The underlying idea is to use the flexibility of the injector complex to build bunch trains in LHC with long enough gaps interspersed, to prevent the build-up of an electron cloud along the beam. An alternative scenario (referred to as 8b+4e) based on beams with 25 ns spacing has been conceived to reduce the electron cloud effects in the HL-LHC, if needed, in its initial phase of operation following the upgrade [101] and has been considered as part of the HL-LHC operational scenarios [3]. Operation with a 200 MHz main RF system would allow for longer bunches and would have a positive impact also on the e-cloud [79]. The impact of the bunch length on the e-cloud will be studied experimentally during the coming Run 2 (e.g. to reduce emittance blow-up at low energy).

Table 2-9: Summary of the impedance-induced heat load computations for several key systems

Element	**Expected heat load [W]**	**Conclusion/comment**
Equipment with RF fingers [102]	Negligible for conforming RF fingers.	Robust mechanical and quality control required during the installation phase.
Experimental beam pipes (resonant modes) [103–107]	ATLAS: no significant mode expected. ALICE: potentially* more than 1 kW. CMS: potentially* more than 350 W. LHCb: potentially* more than 250 W.	During Run 2, the temperature should be closely monitored in the large-diameter regions of ALICE, CMS, and LHCb. The impact of these potential expected heat loads on hardware integrity and outgassing should be assessed.
All types of beam screens [104] and Table 2-10	See Table 2-10, where the power losses have been computed vs. temperature (between 20 K and 70 K).	The effects of the beam screen longitudinal weld, the two counter-rotating beams, and the magneto-resistance have been taken into account. Decoupling of the cryogenics for the IR elements and the RF will provide more margin for acceptable heat load in the arcs.
Triplet beam position monitors [109]	~0.2 W/m for the (most critical) 50 ns beam.	This assumes no interferences between the two beams' electromagnetic fields (worst case) and copper coating.
New collimators with integrated BPMs and ferrites [110]	~100 W (of which ~5 W to 7 W would be dissipated in the ferrites, and ~4 W to 6 W in the RF fingers).	More thorough simulation studies as well as bench measurements are under way to confirm these results. This should be acceptable.
Injection kickers (MKIs) [111, 112]	Between ~125 W/m and ~191W/m (based on measurements of 9 MKIs	It is of the order of heat loads estimated with pre-LS1 parameters for the old MKI8D (i.e. before the third

	upgraded to have the full complement of 24 screen conductors). For comparison, most of the MKIs before LS1 had a power deposition of ~ 70 W/m (which did not limit LHC operation).	Technical Stop of 2012) which had a 90° twist in the screen conductors and that had a power deposition of ~160 W/m, based on measurements of impedance during LS1. This required significant time to cool-down after physics fills. For the HL-LHC we are looking at: (i) further reducing the power deposition; (ii) improving the cooling; (iii) using high Curie point ferrites.
Crab cavities [113]	In the multi kW range if the longitudinal modes overlap with beam harmonic frequencies.	The design should allow detuning the longitudinal modes from multiples of 20 MHz by ~0.5 MHz.
Injection protection dump (TDI) [106]	The present design already suffers from beam-induced heating (in the kW range for the injection settings) with nominal LHC parameters due to inefficient cooling.	The present design of the TDI is not compatible with the HL-LHC parameters and a new design is being studied, with installation foreseen for LS2.
Synchrotron radiation monitor (BSRT) [114]	The power deposited in the ferrite absorbers (heated at ~ 250°C to 350°C according to simulations and measurements) during 2012 operation could not be efficiently transferred, leading to damage.	A new design is being studied and installed during LS1. The usability of this design for HL-LHC will need to be assessed after LS1.

*If the longitudinal modes overlap with beam harmonic frequencies.

Table 2-10: Impedance-induced heat loads for the different types of beam screens (including the effects of the longitudinal weld, two counter-rotating beams, and the magneto-resistance) vs. temperature: values are given for the 25 ns beam and for the 50 ns beam (in parentheses).

Power loss [W/m]	**20 K**	**30 K**	**40 K**	**50 K**	**60 K**	**70 K**
Q1 (49 mm, 6.9 T)	0.23 (0.28)	0.24 (0.31)	0.28 (0.35)	0.34 (0.43)	0.40 (0.51)	0.47 (0.59)
Q2–Q3 (59 mm, 8.3 T)	0.19 (0.24)	0.20 (0.26)	0.23 (0.29)	0.28 (0.35)	0.33 (0.42)	0.38 (0.49)
D1 (59 mm, 5.6 T)	0.17 (0.22)	0.19 (0.24)	0.22 (0.28)	0.27 (0.34)	0.32 (0.41)	0.38 (0.48)
D2 (42 mm, 4.5 T)	0.25 (0.32)	0.27 (0.34)	0.32 (0.40)	0.39 (0.50)	0.47 (0.59)	0.54 (0.69)
Q4 (32 mm, 3.7 T)	0.34 (0.43)	0.37 (0.47)	0.44 (0.56)	0.54 (0.68)	0.64 (0.81)	0.74 (0.94)
Q5 (22 mm, 4.4 T)	0.59 (0.74)	0.63 (0.80)	0.72 (0.91)	0.86 (1.09)	1.01 (1.28)	1.16 (1.46)
Q6 (17.7 mm, 3.5 T)	0.79 (0.99)	0.84 (1.06)	0.96 (1.22)	1.14 (1.44)	1.32 (1.68)	1.51 (1.91)
Q7 (17.2 mm, 3.4 T)	0.82 (1.03)	0.87 (1.11)	1.00 (1.26)	1.18 (1.49)	1.37 (1.74)	1.56 (1.98)

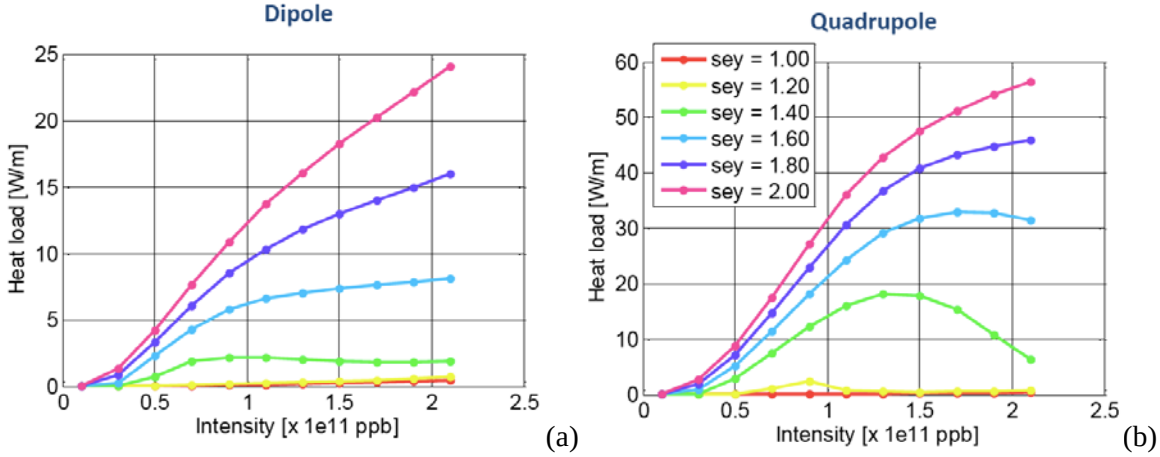

Figure 2-9: Heat load from e-cloud in the arc main magnets as a function of bunch intensity and SEY

Figure 2-10 shows the expected heat load along the triplet in IP1 and IP5 for different SEY values. The least efficient build-up (lower heat load) occurs at the locations of the long-range encounters (vertical dashed

lines). Note that the values in the D1 dipole are comparable to or higher than the values in the quads. The comparison of the heat load from the e-cloud for the current LHC and the future HL-LHC triplets shows that the larger bunch population and larger chamber size lead to a larger heat load by a factor ~3, for the HL-LHC [69] (for the same SEY, a similar energy of multipacting electrons, and a larger number of impacting electrons). For IP2 and IP8, scaling the results also leads to an increase of the heat load from the e-cloud by a factor ~3, but detailed simulations remain to be done. Unlike IP1 and IP5, the cryostats in IP2 and IP8 already include D1 (about 10 m long).

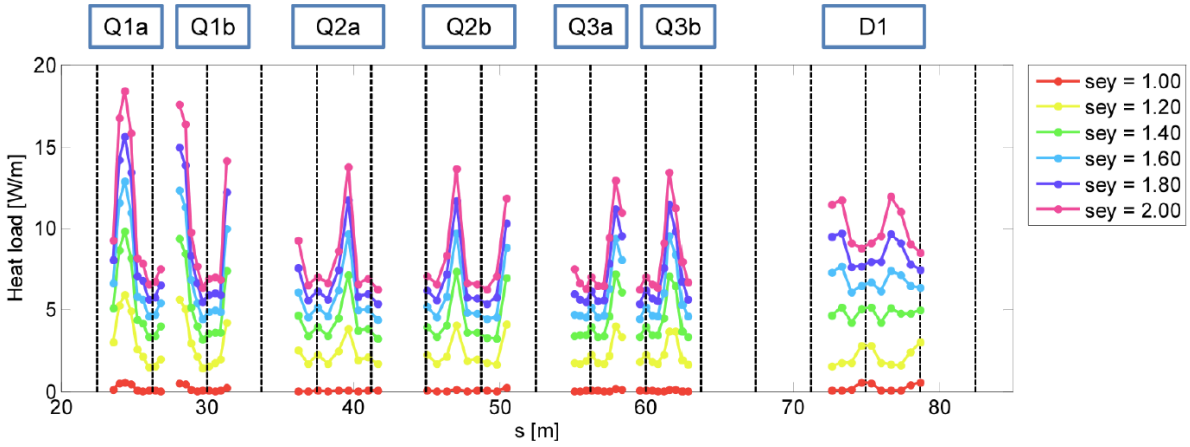

Figure 2-10: Heat load from the e-cloud along the future HL-LHC triplets

Understanding e-cloud build-up in the matching section requires the study of a large number of configurations (beam screen shape and dimensions, magnetic field configuration, beam size, beam position, etc.). Parametric studies will be performed to assess which of these dependencies strongly impact e-cloud build-up. Some preliminary simulations revealed that the beam size and the magnetic field have a small but non-negligible impact. The next step will be to try and disentangle these two effects. The effect of the beam position will then have to be studied in detail.

2.4.4 Luminosity performance

The peak performance at 7 TeV has been estimated in Table 2-1. The estimate of the integrated luminosity requires determining the luminosity evolution during a fill. The beam intensity evolution has been evaluated taking into account burn-off due to luminosity considering a total cross-section of 100 mb [115, 116], and an additional (unknown) source of intensity loss with a lifetime of 200 h (based on experience during 2012 [117]).

The emittance evolution has been determined including: intra-beam scattering (IBS) (based on Run 1 experience, no coupling has been assumed); radiation damping; and an additional (unknown) source of vertical emittance blow-up with a lifetime of 40 h (based on observations during Run 1). A finite difference method in steps of 5 min has been implemented to model the intensity evolution and the evolution of the IBS lifetime as a function of the bunch population. Figure 2-11, Figure 2-12 and Figure 2-13 show the evolution of the main parameters for two cases of levelling, corresponding to a pile-up of 140 and 210, for the standard filling scheme with parameters listed in Table 2-1. In the estimates the worst case scenario (with respect to the head on beam–beam tune spread) of β^* levelling in IP1, IP5, and IP8 has been considered. Full compensation of the crossing angle by crab cavities has been included for IP1 and IP5. The crossing angle is assumed to be constant during the fill. Alternative (or complementary) luminosity levelling scenarios include:

- crossing angle variation to increase the geometric reduction factor at the beginning of the fill;
- crab cavity RF voltage variation to have a partial crossing angle compensation at the beginning of the fill;
- dynamic bunch length reduction;
- controlled variation of the transverse separation of the two colliding beams.

Options 1 and 2 have the disadvantage of increasing the line pile-up density at the start of the fill.

The performance estimates for the two cases considered (pile-up 140 and 210) are listed in Table 2-11. The parameters used for the estimates of the HL-LHC integrated performance are listed in Table 2-12. The operation at the higher pile-up limit is appealing because it allows higher integrated luminosity while keeping the optimum fill length to values already obtained in 2012; however, in this case, the maximum pile-up density exceeds the target pile-up density limit of 1.3 events/mm/crossing. This could be reduced by increasing the bunch length. A more elegant solution could be provided by the crab-kissing scheme [16] and/or by the implementation of flat-beam optics with a smaller crossing angle (provided that long-range effects can be kept under control, perhaps by the implementation of long-range compensation schemes). These alternative scenarios will be described below.

Table 2-11: Integrated performance estimate for levelling scenarios at pile-up levels of 140 (PU 140) and 210 (PU 210) events/crossing, respectively.

	Levelling time [h]	**Optimum fill length [h]**	**Integrated Lumi [fb^{-1}/y] for η = 50%, optimum fill length IP1/IP5/IP8/IP2**	**Maximum mean pile-up density [events/mm/ crossing] in IP1/IP5**	**Maximum mean pile-up [events/ crossing] in IP1/IP5**
PU 140	8.1	9.4	261/8.9/0.105	1.25/140	140
PU 210	4.25	6	331/7.8/0.092	1.81/210	210

Table 2-12: Parameters assumed for HL-LHC performance estimate

Scheduled physics time for p–p luminosity production/year (T_{phys}) [days]	**160**
Minimum turnaround time [h]	3
Performance efficiency – goal [%]	50
Pile-up limit IP1/IP5 [events/crossing]	140/200
Pile-up limit IP8 [events/crossing]	4.5
Pile-up density limit – IP1/IP5 [events/mm/crossing]	1.3
Visible cross-section IP1/IP2/IP5 [mb]	85
Visible cross-section IP8 [mb]	75 [118]

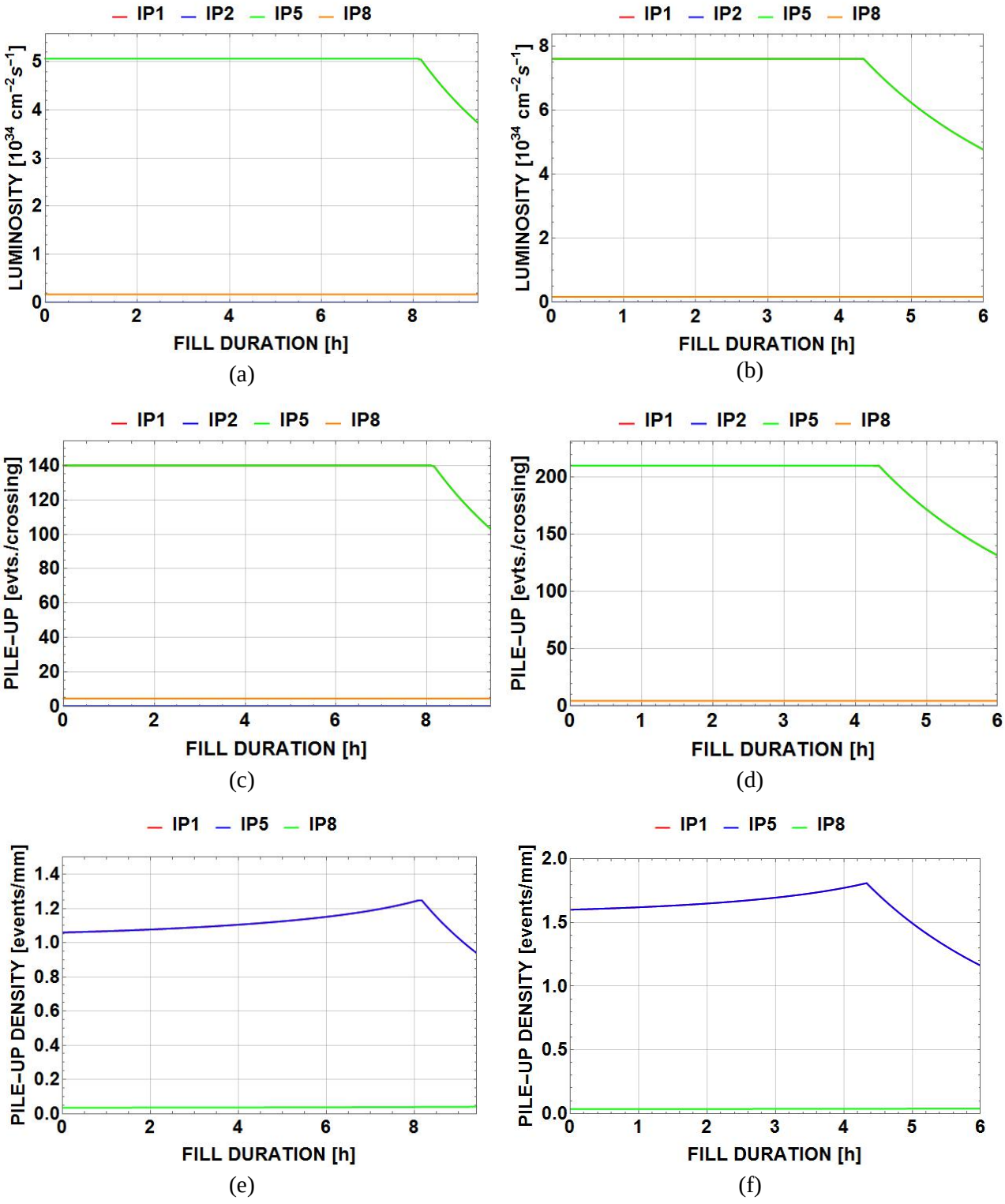

Figure 2-11: Evolution of Luminosity, pile-up and pile-up density assuming levelling at 140 events/crossing (a, c, e) and 210 events/crossing (b, d, f) in IP1 and IP5. The small effects of RF curvature in the crab cavities is not included.

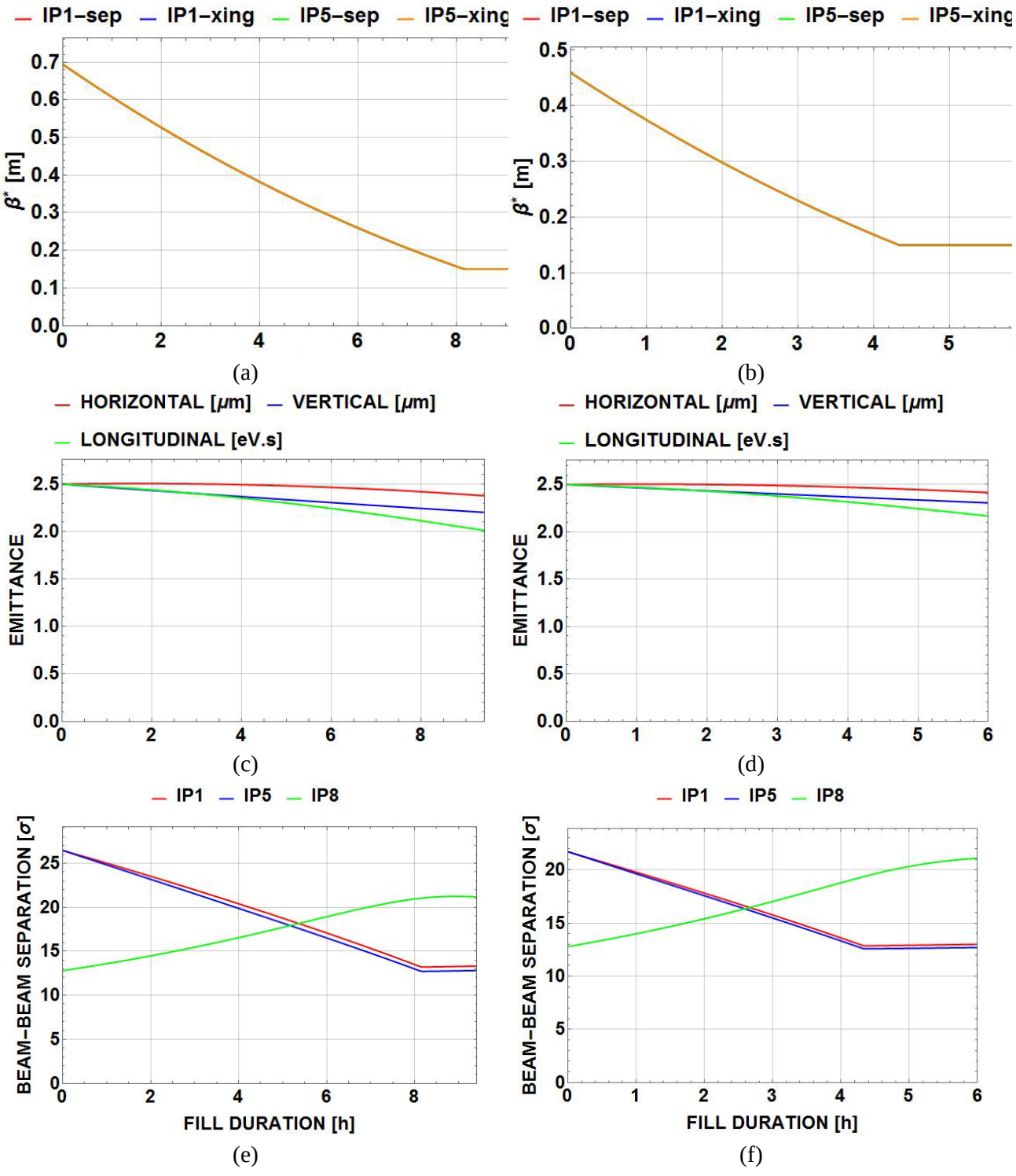

Figure 2-12: Evolution of β^*, emittance and long-range beam–beam normalized separation (d_{bb}) for levelling at 140 (a, c, e) and at 210 events/crossing (b, d, f) in IP1 and IP5.

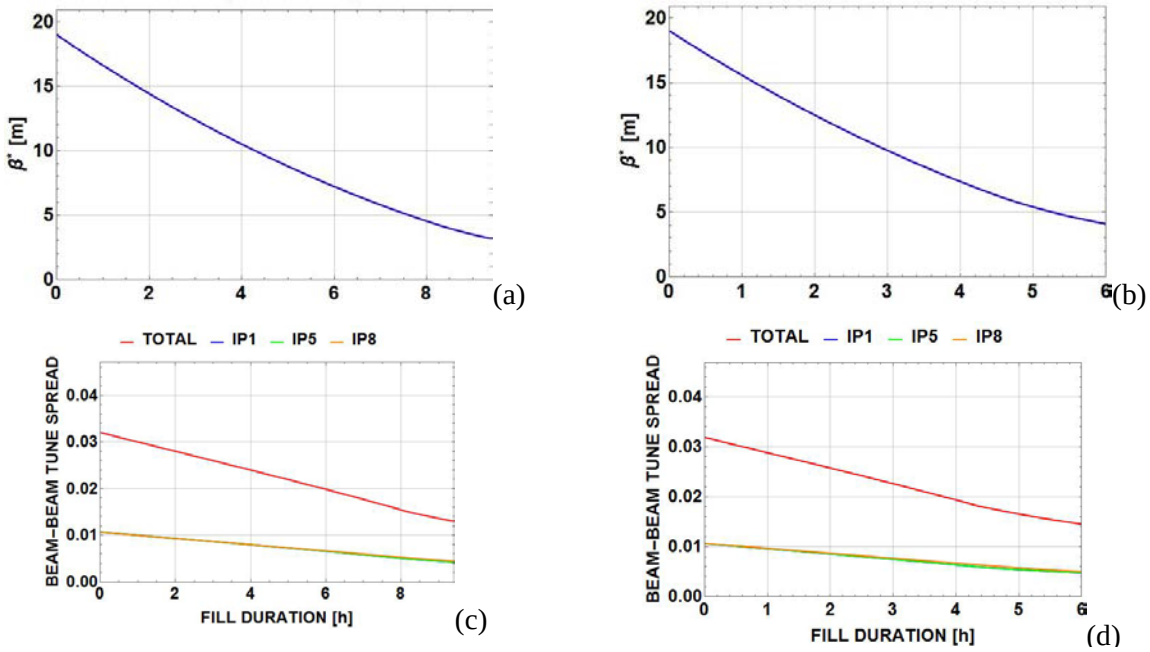

Figure 2-13: Evolution of β^* in IP8, head-on beam–beam tune spread assuming levelling at 140 events/crossing (a, c) and at 210 events/crossing (b, d) in IP1 and IP5.

2.5 Variants and options

The HL-LHC project includes the study of various alternatives to the present baseline configuration with the aim either of improving the potential performance of the machine or of providing options for addressing possible limitations or changes in parameters (see Figure 2-14).

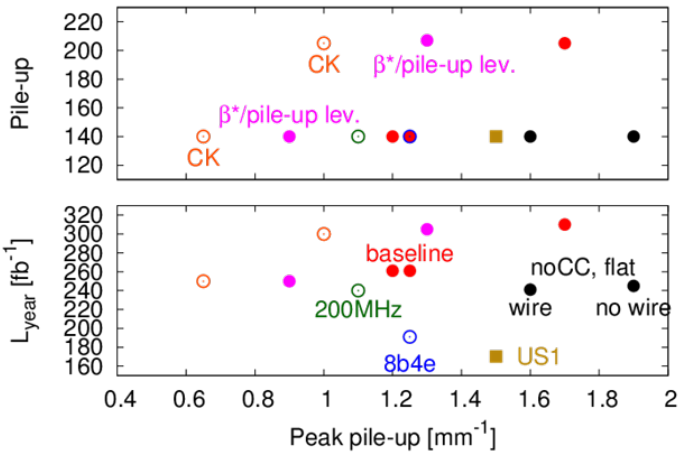

Figure 2-14: Performance expectation of different alternatives. The red markers represent the baseline scenarios (flat or round) for different target of total pile-up (140 and 200 events per crossing). In the case of the crab cavities are absent (black marker) annual integrated luminosity could be recovered by using flat optics for an increase of the peak pile-up density that can be limited with long-range compensators. The crab-kissing scheme (magenta markers) on the other hand offers the target annual luminosity with the means to control the pile-up density and to reduce it considerably with respect to the nominal scheme. Peak pile-up density can also be levelled with β^* (magenta markers). If e-cloud effects needs to be mitigated, a 200 MHz RF system or the 8b+4e filling schemes (green and blue markers) could be deployed.

2.5.1 Pile-up density management

The crab-kissing scheme ([16, 119] and references therein) would allow either improvement of the data quality by reducing the peak pile-up density at a constant integrated luminosity, or an increase of the integrated luminosity at constant total pile-up or levelled luminosity (see orange markers in Figure 2-14). At present, implementation of the crab-kissing scheme would require changes to the layout of the crab cavities, to allow bunch deflections in different planes. Also, a flat optics with beam–beam long-range compensator would need to be implemented. These changes are not completely compatible with the nominal scheme because the crab cavity voltage is insufficient to provide the required deflections in both planes; however new optics solutions are being explored to keep the crab-kissing scheme and the nominal configuration mutually compatible.

If crab kissing is not available it would still be possible to level peak pile-up density using β^* with different total pile-up targets (see magenta markers in Figure 2-14). In this scenario a flat longitudinal profile is assumed to be reachable through use of a second harmonic RF system or phase modulation as in the case of crab kissing. In the absence of flat longitudinal profiles one could expect an increase in the peak pile-up of about 10%.

2.5.2 Alternative scenarios

A compact 200 MHz RF system could be installed ([79] and references therein) in the LHC, potentially allowing an increase in the injected intensity from the SPS, although further studies are needed to confirm what could be achieved. Such a system, together with a 400 MHz system, could offer the means to increase the bunch length (e.g. 15 cm) to reduce electron cloud effects, reduce IBS growth rates, and provide flat longitudinal bunch charge density (see green markers in Figure 2-14).

If the e-cloud severely limits the beam current with 25 ns bunch spacing, the 8b+4e [79] filling scheme would allow comparable beam current at the cost of lower levelled luminosity with constant total pile-up. The 8b+4e scheme can provide about 2.3×10^{11} p/b with 1900 bunches [3], halfway between the corresponding 50 ns and 25 ns configurations, and therefore resulting in a performance reach between those two extremes (see blue markers in Figure 2-14).

In the absence of crab cavities, it may still be possible to implement some measures to limit the loss of performance [20]. By increasing β^* in the crossing plane and decreasing it in the separation plane, one could limit the impact of the geometric reduction factor thanks to the reduction of the necessary crossing angle (see rightmost black marker in Figure 2-14). However, a large crossing angle in units of σ is still needed (12 σ for the lower $\beta^* = 30$ cm) because of the partial loss of the IR1/IR5 long-range beam–beam (LRBB) interaction compensation (i.e. passive compensation from the non-symmetric alternating crossing between IP1 and IP5). However, an LRBB compensator could potentially allow 10 σ separation, therefore restoring the luminosity compared to the nominal scenario at the cost of some increase in pile-up density (see the leftmost black marker in Figure 2-14). Similarly, a staged upgrade scenario for which the replacement of the matching section is postponed (see Refs. [120, 47] and references therein) could still benefit from flat beam optics, although with a limited reach of β^* in the non-crossing plane (about 20 cm) but with the potential of reaching about 170 fb^{-1} per year (see dark yellow markers in Figure 2-14). In this context, a design for a movable TAXN that could be adapted to different β^* values would offer the best radiation protection for the downstream elements in all these scenarios, regardless of the chosen optics configurations.

2.6 The HL-LHC as a nucleus–nucleus collider

The LHC's second major physics programme provides nucleus–nucleus collisions to ALICE, CMS and ATLAS, and proton–nucleus collisions to these three experiments and, in addition, to LHCb. The overall goal of the programme is ultimately to accumulate 10 nb^{-1} of Pb–Pb luminosity during the whole LHC operating period after Run 2 [80, 121]. The p–Pb requirement will be for approximate equivalence in terms of integrated nucleon-pair luminosity [80, 122, 123]. The heavy-ion programme may also require short p–p runs at specific energies to provide reference data; the luminosity requirement will be similar (see 16.6). Nuclei other than

$^{208}Pb^{82+}$ have not been requested by the experiments but remain as possible options with potential performance to be evaluated.

The heavy-ion luminosity upgrade aims at increasing integrated rather than peak luminosity and is therefore focused mainly on injecting the maximum beam current possible. With the expected upgrade to remove the event rate limit of the ALICE experiment, luminosity levelling will no longer be a necessity but may be employed to mitigate the rapid luminosity decay due to the large electromagnetic cross-sections [80, 124]. Low values of β^* are required at three or four interaction points so the ATS will not be used. The main elements of the heavy-ion luminosity upgrade should be in place a few years before those of the proton–proton part of the project.

Upgrades to the heavy-ion injector chain [125] would normally aim to increase the number of bunches and the intensity per bunch, but these two quantities are not independent. Injecting long trains from the SPS lengthens the injection plateau in the SPS, subjecting some bunches to higher losses from the effects of intra-beam scattering, space charge, and RF noise [126]. On the other hand, injecting a larger number of short trains from the SPS increases the average bunch intensity but leaves more gaps in the LHC bunch train and increases the LHC's injection time, reducing overall efficiency and subjecting some bunches to more emittance growth at LHC injection. In all cases, there is a broad distribution of bunch parameters in collision in the LHC. Optimization of the injection and filling schemes has to take all these interdependencies into account [126] and will likely have to be done anew each year as a function of injector performance.

The present performance estimates are nevertheless based on an injection scheme that assumes that the maximum 12 PS batches of four bunches are assembled into a batch in the SPS, with a 50 ns bunch spacing achieved by slip-stacking. This is repeated 26 times to assemble a train of 1248 bunches in the LHC (practical filling scheme details will reduce this by some percent, depending on the experiment) and yielding a distribution of individual bunch-pair luminosities at the start of colliding beams as shown in Figure 2-15. Simulation of the evolution of these individual bunches, taking into account luminosity burn-off, IBS, and radiation damping [126] leads to the total luminosity shown in Figure 2-16. Depending on the turnaround time (between beam dump and the next declaration of stable beams for physics), the fill length can be optimized to give the ideal average daily luminosity shown.

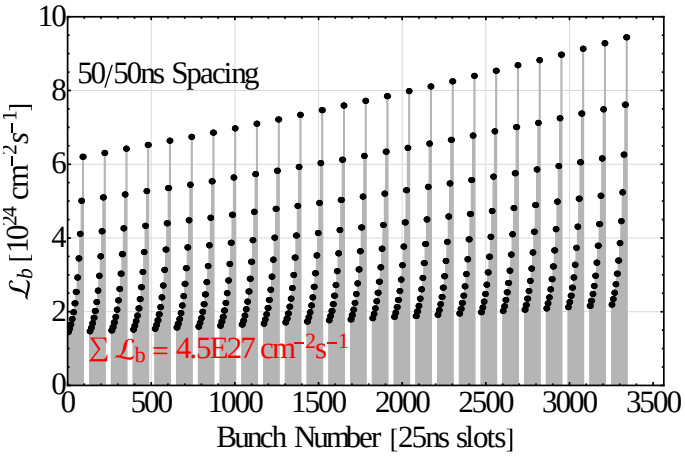

Figure 2-15: Initial luminosity for each colliding bunch pair along the full train in the LHC

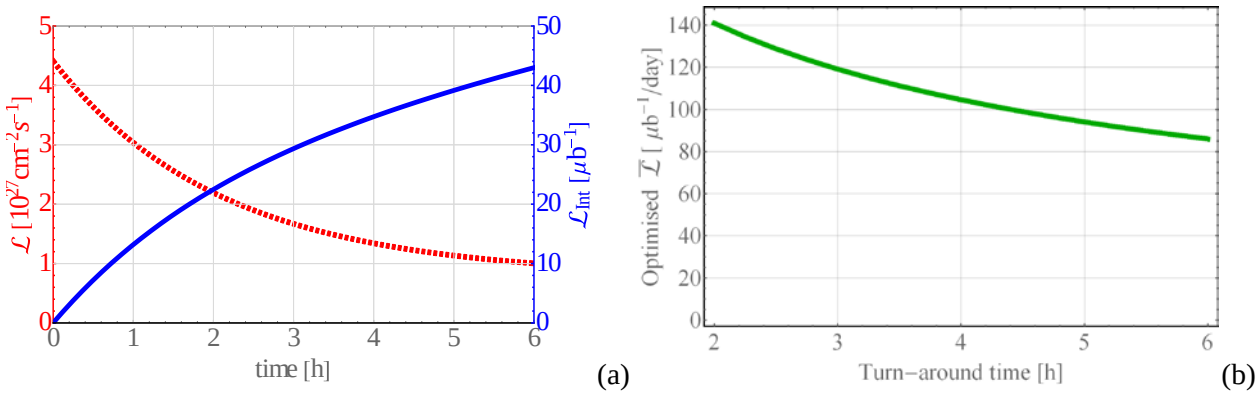

Figure 2-16: (a) Total luminosity (red) and integrated luminosity (blue) during a fill starting with the bunch-pair luminosities shown in Figure 2-15. (b) Average luminosity per day as a function of turnaround time (dump to next stable beams) when fill lengths are optimized, with lengths varying between 3 h and 6 h, with the luminosity dependence shown in the left plot.

The rapid luminosity decay is due to the large cross-sections of electromagnetic processes in the collisions [126, 127]. The peak luminosity is expected to be substantially above the quench limit from losses due to the bound-free pair-production process; and new collimators are foreseen in the dispersion suppressors to absorb these secondary beams emerging from the interaction points (see Chapter 5, Section 5.2). Intensity limitations may also arise from losses due to collimation inefficiency, which is higher for ion beams, due to the more complicated nuclear interactions with collimators [128, 129].

The 50 ns bunch spacing introduces close parasitic beam–beam encounters near to the ALICE experiment, which may require the half-crossing angle to be increased beyond the 60 µrad limit imposed for optimum operation of the zero-degree calorimeters. The minimum acceptable at the low Pb bunch charge will be determined empirically [80]. The crossing angles for ATLAS and CMS are unrestricted and can be taken over from proton operation.

The principal beam parameters determining the luminosity are summarized in Table 2-13. Other parameters will be similar to those given in Ref. [130]. Further potential gains in luminosity may come from improved injector performance and, possibly, a cooling system [131] in the LHC.

Table 2-13: Average values of principal beam parameters at start of physics

Parameter	**Value**
Number of bunches per beam	1248
Normalized transverse emittance (average)	1.6 µm
Optical function at interaction point	0.5 m
Crossing angle at ALICE experiment	60 µrad
Bunch population (average)	1.04×10^8
Bunch length	0.1 m
Peak luminosity	4.5×10^{27} cm^{-2} s^{-1}

2.7 Acknowledgements

The volunteers of the LHC@home project are warmly acknowledged for their generous contribution of CPU time for the numerical simulations of dynamic aperture. Furthermore, we would like to express our gratitude to E. McIntosh for his continuous support for the numerical simulations and the SixTrack code.

2.8 References

[1] R. Jacobsson, Future wishes and constraints from the experiments at the LHC for the proton–proton programme, ICFA Mini-Workshop on Beam-Beam Effects in Hadron Colliders (BB2013), CERN,

Geneva, Switzerland, 18 - 22 Mar 2013, Eds. W. Herr and G. Papotti, CERN-2014-004 (2014), p. 167–176.

[2] O.S. Brüning and F. Zimmermann, Parameter space for the LHC High Luminosity Upgrade, Proc. 3rd International Particle Accelerator Conf., New Orleans, 20–25 May 2012, Eds. C. Petit-Jean-Genaz and J. Corbett, p. 127–129.

[3] G. Arduini, O. Brüning, R. De Maria, R. Garoby, S. Gilardoni, B. Goddard, B. Gorini, M. Meddahi, G. Rumolo and R. Tomás, Beam parameters at LHC injection, CERN-ACC-2014-0006 (2014).

[4] O.S. Brüning, HL-LHC parameter space and scenarios, Proc. Chamonix 2012 Workshop on LHC Performance, Chamonix, France, 6–10 Feb 2012, Ed. C. Carli, CERN-2012-006 (2012), p. 315–324.

[5] S. Fartoukh and F. Zimmermann, The accelerator physics challenges CERN-ACC-2014-0209 (2014).

[6] V. Kain, Concerns with low emittance beams operation, LHC Performance Workshop, Chamonix, France, 22–25 September 2014, http://indico.cern.ch/event/315665/session/5/contribution/22/material/slides/0.pdf

[7] V. Kain *et al.*, Injection protection – Are we taking it seriously? How can we make it safer?, Proc. 2nd Evian Workshop on LHC Beam Operation, Evian, France, 7–9 December 2010, Ed. B. Goddard, p. 143–149.

[8] E. Métral, Pushing the limits: Beam, Proc. Chamonix 2011 Workshop on LHC Performance, Chamonix, France, 24–28 January 2011, Ed. C. Carli, CERN-ATS-2011-005, p. 252–260.

[9] R.W. Assmann, Implications of higher intensities in the LHC, Proc. Chamonix 2011 Workshop on LHC Performance, Chamonix, France, 25–29 January 2010, Ed. C. Carli, CERN-ATS-2010-026, p. 328–333.

[10] X. Buffat, R. Giachino, W. Herr, G. Papotti, T. Pieloni, R. Calaga and S.M. White, Observation of coherent beam-beam effects in the LHC, Proc. 2nd International Particle Accelerator Conf., San Sebastian, Spain, 4 - 9 Sep 2011, pp.TUPZ029 .

[11] R. Calaga, R. Tomas and F. Zimmermann, LHC Crab-Cavity Aspects and Strategy, Proc. 1st International Particle Accelerator Conf., Kyoto, Japan, 23–28 May 2010, Eds. A. Noda, C. Petit-Jean-Genaz, V. Schaa, T. Shirai and A. Shirakawa, p. 1240–1242.

[12] E. Shaposhnikova, E. Ciapala and E. Montesinos, Upgrade of the 200 MHz RF System in the CERN SPS, CERN-ATS-2011-042, Proc. 2nd International Particle Accelerator Conf., S. Sebastian, Spain, 4–9 September 2011, Eds. C. Petit-Jean-Genaz, A. Blanco, I. Etxebarria, F. Perez, A. Wolski and V. Schaa, p. 214–216.

[13] H. Bartosik, G. Iadarola, Y. Papaphilippou, G. Rumolo and E. Shaposhnikova, Can we ever reach the HL-LHC requirements with the injectors?, Review of LHC and Injector Upgrade Plans Workshop, Archamps, 29–31 October 2013. https://indico.cern.ch/event/260492/session/4/contribution/18/material/paper/0.pdf

[14] HL-LHC Parameter and Layout Committee Parameter table v 4.1.0 (27/8/2014). https://espace.cern.ch/HiLumi/PLC/_layouts/xlviewer.aspx?id=/HiLumi/PLC/SiteAssets/Parameter%20Table.xlsx

[15] R. Bruce, A. Marsili and S. Redaelli, Cleaning performance with 11 T dipoles and local dispersion suppressor collimation at the LHC, 5th International Particle Accelerator Conference, Dresden, Germany, 15 - 20 Jun 2014, pp.MOPRO042.

[16] S. Fartoukh, Pile-up density management at HL-LHC and the crab-kissing scheme, HL-LHC brainstorming coordination meeting, July 2013. http://indico.cern.ch/conferenceDisplay.py?confId=263083

[17] S. Fartoukh, Optics challenges and solutions for the LHC insertion upgrade phase I, Workshop on LHC Performance, Chamonix, France, 25–29 January 2010, CERN-sLHC-PROJECT-Report-0038, pp. 262–290.

[18] S. Fartoukh, Layout and optics solution for the LHC Insertion Upgrade Phase I, 1st International Particle Accelerator Conference, Kyoto, Japan, 23 - 28 May 2010, pp.THPE018.

[19] S. Fartoukh, R. Tomás and J. Miles, Specification of the closed orbit corrector magnets for the new LHC inner triplet, CERN-sLHC-PROJECT-Report-0030 (2009).

[20] S. Fartoukh, Towards the LHC Upgrade using the LHC well-characterized technology, CERN-sLHC-PROJECT-Report-0049 (2010).

[21] S. Fartoukh, Breaching the phase I optics limitations for the HL-LHC, CERN-sLHC-PROJECT-Report-0053 (2011).

[22] S. Fartoukh, An achromatic telescopic squeezing (ATS) scheme for the LHC upgrade, 2nd International Particle Accelerator Conference, San Sebastian, Spain, 4 - 9 Sep 2011, pp.WEPC037.

[23] S. Fartoukh, B. Goddard, W. Höfle, M. Lamont, R. de Maria, R. Miyamoto, G. Müller, L. Ponce, S. Redaelli, R. Steinhagen, M. Strzelczyk, R. Tomás, G. Vanbavinckhove and J. Wenninger, The achromatic telescopic squeezing scheme: Basic principles and first demonstration at the LHC, 3rd International Particle Accelerator Conference 2012, New Orleans, LA, USA, 20 - 25 May 2012, pp.1978.

[24] S. Fartoukh, Achromatic telescopic squeezing scheme and application to the LHC and its luminosity upgrade, *Phys. Rev. Spec. Top. Accel. Beams* **16** (2013) 111002.

[25] S. Fartoukh, G. Vanbavinckhove, M. C. Alabau Pons, R. Alemany Fernandez, R. Assmann, A. Butterworth, M. Giovannozzi, B. Goddard, P. Hagen, W. Höfle, D. Jacquet, R. de Maria, R. Miyamoto, G. Müller, S. Redaelli, R. Steinhagen, M. Strzelczyk, R. Suykerbuyk, E. Todesco, R. Tomás, W. Venturini, J. Wenninger and F. Zimmermann, The achromatic telescopic squeezing (ATS) MD part I, CERN-ATS-Note-2011-033 MD (2011).

[26] S. Fartoukh, M. Lamont, R. De Maria, R. Miyamoto, G. Müller, L. Ponce, S. Redaelli, M. Strzelczyk, R. Tomás, G. Vanbavinckhove, J. Wenninger, M. Albert, R. Giachino, M. Giovannozzi, B. Goddard, P. Hagen, W. Höfle, V. Kain, A. Macpherson, L. Normann, G. Papotti, R. Steinhagen, D. Valuch and D. Wollman, The achromatic telescopic squeezing (ATS) MD part II, CERN-ATS-Note-2011-060 MD (2011).

[27] S. Fartoukh, R. Tomás, B. Goddard, W. Höfle, D. Jacquet, G. Kruk, M. Lamont, R. de Maria, R. Miyamoto, G. Müller, M. Pojer, L. Ponce, S. Redaelli, N. Ryckx, R. Steinhagen, M. Strzelczyk, G. Vanbavinckhove and J. Wenninger, The achromatic telescopic squeezing (ATS) MD part III, CERN-ATS-Note-2011-132 MD (2011).

[28] S. Fartoukh, V. Kain, Y. Levinsen, E. Maclean, R. de Maria, T. Persson, M. Pojer, L. Ponce, P. Skowronski, M. Solfaroli, R. Tomás and J. Wenninger, The 10 cm beta* ATS MD, CERN-ATS-Note-2013-004 MD (2013).

[29] S. Fartoukh, First demonstration with beam of the Achromatic Telescopic Squeezing (ATS) scheme, 2012 Workshop on LHC Performance, Chamonix, France, 6–10 February 2012, pp. 128–134.

[30] E. Todesco, H. Allain, G. Ambrosio, G. Arduini, F. Cerutti, R. De Maria, L. Esposito, S. Fartoukh, P. Ferracin and H. Felice *et al.*, A first baseline for the magnets in the High Luminosity LHC insertion regions, CERN-ACC-2014-0036 (2014).

[31] S. Fartoukh and R. De Maria, Database of baseline scenarios and variants: Milestone: MS17, CERN-ACC-2014-0069 (2014).

[32] S. Fartoukh and R. De Maria, Optics and layout solutions for HL-LHC with large aperture Nb_3Sn and Nb-Ti inner triplets, 3rd International Particle Accelerator Conference 2012, New Orleans, LA, USA, 20 - 25 May 2012, pp.145.

[33] R. De Maria, S. Fartoukh, A. Bogomyagkov and M. Korostelev, HLLHCV1.0: HL-LHC layout and optics models for 150 mm Nb_3Sn Triplets and local crab-cavities, 4th International Particle Accelerator Conference, Shanghai, China, 12 - 17 May 2013, pp.1358.

[34] R. Calaga and R. De Maria *et al.*, 9th HL-LHC PLC meeting (2014). https://indico.cern.ch/event/315418/

[35] M. Giovannozzi *et al.*, Optics and layout update, 3rd Joint HiLumi LHC– 22nd LARP Collaboration Meeting, 7–8 May 2014, BNL, USA. https://indico.bnl.gov/conferenceDisplay.py?confId=730

[36] M. Giovannozzi, S. Fartoukh and R. De Maria, Specification of a system of correctors for the triplets and separation dipoles of the LHC upgrade, 4th International Particle Accelerator Conference, Shanghai, China, 12 - 17 May 2013, pp.2612.

[37] M. Giovannozzi, S. Fartoukh and R. De Maria, Initial models of correction systems, CERN-ACC-2014-0010 (2014).

[38] M. Fitterer, Budget for HL-LHC Orbit Correctors, HSS meeting 14 April 2014. http://ab-dep-abp.web.cern.ch/ab-dep-abp/HSS/HSS_meetings/2014/20140414/HSSMeeting14042014.pdf

[39] M. Fitterer and R. De Maria, IT BPM tolerances for HL-LHC orbit correction, HSS meeting 26 May 2014. http://ab-dep-abp.web.cern.ch/ab-dep-abp/HSS/HSS_meetings/2014/20140526/HSSMeeting26052014.pdf

[40] O. S. Brüning, P. Collier, P. Lebrun, S. Myers, R. Ostojic, J. Poole and P. Proudlock (Eds.), LHC Design Report, v.1: The LHC Main Ring, CERN-2004-003-V-1 (2012).

[41] J.-B. Jeanneret, Geometrical tolerances for the qualification of LHC magnets, LHC Project Report 1007 (2007).

[42] M. Korostelev, A. Wolski, R. De Maria and S. Fartoukh, Optics Transition between Injection and Collision Optics for the HL-LHC Upgrade Project, 4th International Particle Accelerator Conference, Shanghai, China, 12 - 17 May 2013, pp.1460.

[43] M. Korostelev, Transition between injection optics and collision optics (including ATS squeeze), 3rd Joint HiLumi LHC-LARP Annual Meeting, 11–15 November 2013. https://indico.cern.ch/event/257368/session/11/contribution/31

[44] R. De Maria, Parametric study of optics options for the HL-LHC project, 3rd International Particle Accelerator Conference 2012, New Orleans, LA, USA, 20 - 25 May 2012, pp.142.

[45] B.J. Holzer, R. De Maria, S. Fartoukh, A. Chancé, B. Dalena, J. Payet, A. Bogomyagkov, R. B. Appleby, S. Kelly, M. B. Thomas, L. Thompson, M. Korostelev, K. M. Hock, A. Wolski, C. Milardi, A. Faus-Golfe and J. Resta Lopez, Optics design and lattice optimisation for the HL-LHC, 4th International Particle Accelerator Conference, Shanghai, China, 12 - 17 May 2013, pp.1385. https://cds.cern.ch/record/1558908

[46] B. Dalena, J. Payet and A. Chancè, R. De Maria, S. Fartoukh, High Luminosity LHC matching section layout vs crab cavity voltage, 4th International Particle Accelerator Conference, Shanghai, China, 12 - 17 May 2013, pp.1328.

[47] M. Fitterer, R. Bruce, R. De Maria and S. Fartoukh, Optics Considerations for PIC and US1 scenarios for HL-LHC in the framework of the RLIUP review, CERN-ACC-NOTE-2014-0031 (2014).

[48] B. Dalena, J. Payet, A. Chancé and R. De Maria, Alternative high luminosity LHC matching section layout, 5th International Particle Accelerator Conference, Dresden, Germany, 15 - 20 Jun 2014, pp.990.

[49] M. Giovannozzi *et al.*, LHC@Home: A Volunteer computing system for Massive Numerical Simulations of Beam Dynamics and High Energy Physics Events, 3rd International Particle Accelerator Conference 2012, New Orleans, LA, USA, 20 - 25 May 2012, pp.505.

[50] S. Fartoukh and M. Giovannozzi, Dynamic aperture computation for the as-built CERN Large Hadron Collider and impact of main dipoles sorting, *Nucl. Instrum. Methods Phys. Res.*, A **671** (2012) 10–23.

[51] F. Schmidt, SixTrack – Version 4.2.16 – Single particle tracking code treating transverse motion with synchrotron oscillations in a symplectic manner – Users' reference manual, CERN/SL/94-56 (AP) update (2012).

[52] SixTrack web site http://sixtrack-ng.web.cern.ch/sixtrack-ng/

[53] https://espace.cern.ch/HiLumi/WP2/task4/SitePages/Home.aspx and afs/cern.ch/eng/lhc/optics/SLHCV3.1b/errors/

[54] https://espace.cern.ch/HiLumi/WP2/task4/SitePages/Home.aspx and /afs/cern.ch/eng/lhc/optics/HLLHCV1.0/errors/

[55] R. de Maria, S. Fartoukh, M. Giovannozzi, E. McIntosh, Y. Nosochkov, Y. Cai and M.-H. Wang, HiLumi LHC Deliverable Report: Magnet Field Quality Specifications, CERN-ACC-2014-0295 (2014).

[56] Y. Nosochkov, Y. Cai, M.-H. Wang, R. de Maria, S. Fartoukh, M. Giovannozzi and E. McIntosh, Optimization of Triplet Quadrupoles Field Quality for the LHC High Luminosity Lattice at Collision Energy, 4th International Particle Accelerator Conference, Shanghai, China, 12 - 17 May 2013, pp.1364.

[57] https://espace.cern.ch/HiLumi/WP3/SitePages/MBXF.aspx

[58] https://espace.cern.ch/HiLumi/WP3/SitePages/D2.aspx

[59] E. Todesco, private communication (2014).

[60] M. Fitterer, R. De Maria and M. Giovannozzi, Powering requirements for HL-LHC triplet, WP2 task leader meeting 18 July 2014. https://indico.cern.ch/event/323862/contribution/2/material/slides/1.pdf

[61] Yi-Peng Sun, R. Assmann, J. Barranco, R. Tomás, T. Weiler, F. Zimmermann, R. Calaga and A. Morita, Beam dynamics aspects of crab cavities in the CERN Large Hadron Collider, *Phys. Rev. ST Accel. Beams* **12** (2009) 101002.

[62] J. Barranco García *et al.*, Study of multipolar RF kicks from the main deflecting mode in compact crab cavities for LHC, 3rd International Particle Accelerator Conference 2012, New Orleans, LA, USA, 20 - 25 May 2012, pp.1873.

[63] D. R. Brett *et al.*, Comparison of Taylor maps with RF multipoles in a thin lens 6D tracking code, Proc. 4th International Particle Accelerator Conference, Shanghai, China, 12 - 17 May 2013, Eds. Z. Dai, C. Petit-Jean-Genaz, V. Schaa, C. Zhang, pp. 2687-2689.

[64] R. Appleby *et al.*, Modelling and long term dynamics of crab cavities in the LHC, 5th International Particle Accelerator Conference, Dresden, Germany, 15 - 20 Jun 2014, pp.1578.

[65] S. Kelly, M.B. Thomas, R. Appleby, L. Thompson, B. Holzer, R. De Maria and S. Russenschuck, Study of the impact of fringe fields of the large aperture triplets on the linear optics of the HL-LHC, 4th International Particle Accelerator Conference, Shanghai, China, 12 - 17 May 2013, pp.2642.

[66] A. Bogomyagkov *et al.*, Analysis of the non-linear fringe effects of large aperture triplets for the HL LHC project, Proc. 4th International Particle Accelerator Conference, Shanghai, China, 12 - 17 May 2013, pp.2615.

[67] B. Dalena *et al.*, Fringe fields modelling for the High Luminosity LHC large aperture quadrupoles, 5th International Particle Accelerator Conference, Dresden, Germany, 15 - 20 Jun 2014, pp.993.

[68] S. Jones, D. Newton and A. Wolski, Initial estimate of fringe field effects in HL-LHC using frequency map analysis, 5th International Particle Accelerator Conference, Dresden, Germany, 15 - 20 Jun 2014, pp.1067.

[69] E. Métral, Initial estimate of machine impedance, CERN-ACC-2014-0005 (2014).

[70] E. Métral, Initial estimates of intensity limitations, CERN-ACC-2014-0074 (2014).

[71] O. Brüning *et al.*, LHC luminosity and energy upgrade: A feasibility study, LHC Project Report 626 (2002).

[72] F. Ruggiero and F. Zimmermann, Luminosity optimization near the beam-beam limit by increasing the bunch length or crossing angle, CERN-SL-2002-005-REV (AP) (2002).
[73] F. Ruggiero and F. Zimmermann, Possible scenario for an LHC upgrade, Proc. HHH 2004 Workshop, Geneva, November 2004, CARE-Conf-05-002-HHH.
[74] T. Linnecar and E. Shaposhnikova, An RF system for Landau damping in the LHC, LHC Project Note 394 (2007).
[75] C. Bhat, Bunch shaping in the LHC: A quick look, CERN 97th LMC meeting, 22 June 2011.
[76] T. Mertens *et al.*, Emittance growth, debunching and integrated luminosity in the LHC with a higher harmonic RF system, CERN-AT-Note-2011-071 PERF (2011).
[77] D. Shatilov and M. Zobov, On the possibility of utilizing flat longitudinal beam profiles to increase the luminosity in collisions with large Piwinski angle, 14 April 2012, unpublished note. https://espace.cern.ch/HiLumi/WP2/task4/Shared%20Documents/flat_long_en.docx
[78] L. Ficcadenti *et al.*, Summary of the 800 MHz RF design, CERN meeting on High Harmonic RF System Review, 27 May 2013. https://indico.cern.ch/event/254151/
[79] R. Tomas *et al.*, HL-LHC: Exploring alternative ideas, Review of LHC and Injector Upgrade Plans Workshop (RLIUP), Archamps, France, 29–31 October 2013.
[80] J.M. Jowett *et al.*, Future heavy-ion performance of the LHC, Review of LHC and Injector Upgrade Plans Workshop (RLIUP), Archamps, France, 29–31 October 2013.
[81] R. Calaga *et al.*, A proposal for a compact 200 MHz SC-RF system for the LHC.
[82] C. Tambasco *et al.*, Beam-beam and octupoles stability diagrams in the betatron squeeze for HL-LHC optics, CERN Beam-Beam meeting, 21 August 2014, CERN-ACC-SLIDES-2014-0089.
[83] S. Fartoukh, The sign of the LHC octupoles, CERN LMC meeting, 11 July 2012. https://espace.cern.ch/lhc-machine-committee/Presentations/1/lmc_141/lmc_141h.pdf
[84] W. Herr, Observations of beam-beam effects in the LHC in 2011, Chamonix 2012 Workshop on LHC Performance (2012).
[85] Y. Luo and F. Schmidt, Dynamic aperture studies for LHC optics Version 6.2 at Collision, LHC Project Note 310 (2003).
[86] A. Valishev *et al.*, Simulation of beam-beam effects and Tevatron experience, *JINST* **7** (2012) P12002.
[87] J. Qiang *et al.*, A parallel particle-in-cell model for beam–beam interaction in high energy ring colliders, *J. Comp. Phys*. **198** (2004) 278.
[88] T. Pieloni, Ph.D. thesis, EPFL, 2008.
[89] W. Herr, X. Buffat, R. Calaga, R. Giachino, G. Papotti, T. Pieloni and D. Kaltchev, Long range beam-beam effects in the LHC, CERN-2014-004, pp. 87–92 (2014).
[90] T. Pieloni, X. Buffat, D. Banfi, J. Barranco, G. Arduini, E. Mounet, N. Mounet, S.M. White and J. Qiang, Two beam effects, Proc. 5th EVIAN workshop, Evian, France, 2–4 June 2014. Eds. B. Goddard, S. Dubourg, CERN-ACC-2014-0319 (2014), pp. 69-79.
[91] T. Pieloni, Levelling Scenarios: present and future prospectives, LARP-HiLumi Meeting INFN Frascati, Frascati, Italy, 14–16 November 2012. https://indico.cern.ch/event/183635/session/10/contribution/100
[92] X. Buffat, D. Banfi, G.R. Coombs, W. Herr and T. Pieloni, Beam-Beam Effects in Different Luminosity Levelling Scenarios for the LHC, Proc. 5th International Particle Accelerator Conference, Dresden, Germany, 15 - 20 June 2014, Eds. C. Petit-Jean-Genaz, G. Arduini, P. Michel and V.R.W. Schaa, pp. 1061-1063.
[93] D. Banfi, J. Barranco, T. Pieloni and A. Valishev, Weak-Strong Beam-Beam Simulations for the HL-LHC, Proc. 5th International Particle Accelerator Conference, Dresden, Germany, 15 - 20 June 2014, Eds. C. Petit-Jean-Genaz, G. Arduini, P. Michel and V.R.W. Schaa, pp. 3079-3081.

[94] M. Giovannozzi, Dynamic Aperture: Simulations vs. Experiments and first DA results in the LHC, 14th HiLumi WP2 Task Leader Meeting, 27 August 2013.
https://indico.cern.ch/getFile.py/access?contribId=2&resId=0&materialId=slides&confId=267840.

[95] T. Pieloni *et al.*, Beam-beam effects and limitations in the HL-LHC, LARP-HiLUMI Collaboration Meeting, 7–9 May 2014, Brookhaven National Laboratory.

[96] M. Giovannozzi *et al.*, Dynamic aperture performance for different collision optics scenarios for the LHC luminosity upgrade, Proc. 4th International Particle Accelerator Conference, Shanghai, China, 12 - 17 May 2013, Eds. Z. Dai, C. Petit-Jean-Genaz, V. Schaa, C. Zhang, pp. 2609-2611.

[97] T. Pieloni *et al.*, Preliminary studies of beam-beam long-range effects: Orbit, tune, chromaticity for HL-LHC, 35th HiLumi WP2 Task Leader Meeting, 10 October 2014.

[98] A. Valishev *et al.*, Preliminary estimates of beam-beam effects, HiLumi LHC Milestone Report, CERN-ACC-2014-0066 (2014).

[99] K. Ohmi, Beam-beam effects under the influence of external noise, CERN-2014-004 (2014) pp. 69–74 (2014).

[100] J. Qiang *et al.*, Strong-strong beam-beam simulation for LHC upgrade, Proc. 5th International Particle Accelerator Conference, Dresden, Germany, 15 - 20 June 2014, Eds. C. Petit-Jean-Genaz, G. Arduini, P. Michel and V.R.W. Schaa, pp. 1006-1009.

[101] H. Damerau, LIU: Exploring Alternative Ideas, Review of LHC and Injector Upgrade Plans workshop (RLIUP), Archamps, France, 29–31 October 2013.

[102] E. Métral *et al.*, Lessons learnt and mitigation measures for the CERN LHC equipment with RF fingers, Proc. 4th International Particle Accelerator Conference, Shanghai, China, 12 - 17 May 2013, Eds. Z. Dai, C. Petit-Jean-Genaz, V. Schaa, C. Zhang, pp. 1802-1804.

[103] R. Veness *et al.*, Specification of new vacuum chambers for the LHC experimental interactions, Proc. 2nd International Particle Accelerator Conference, San Sebastian, Spain, 4 - 9 Sep 2011, Eds. C. Petit-Jean-Genaz, A. Blanco, I. Etxebarria, F. Perez, A. Wolski and V. Schaa, pp. 1584-1586.

[104] B. Salvant *et al.*, RF Analysis of ALICE, LHCb and AFP, 10th CERN LEB Technical Meeting, 15 June 2012.

[105] R. Wanzenberg and O. Zagorodnova, Calculation of wakefields and higher order modes for the new design of the vacuum chamber of the CMS experiment for the HL-LHC, CERN-ATS-Note-2013-018 TECH (2013).

[106] B. Salvant *et al.*, Heat load from impedance on existing and new hardware in the LHC era, Joint HiLumi LHC-LARP Annual Meeting, Daresbury, UK, 11–15 November 2013.

[107] B. Salvant *et al.*, Impedance of new ALICE beam pipe, CERN internal TREX meeting, 31 July 2014.

[108] E. Métral and C. Zannini, Temperature effects on image current losses in the HL-LHC triplets – Part 2, 33rd HiLumi WP2 Task Leaders Meeting, CERN, 5 September 2014.
https://indico.cern.ch/event/323863/

[109] N. Mounet *et al.*, Impedance considerations for the design of the triplet/D1 beam screen, Technical Meeting on Vacuum for HL-LHC, CERN, 5 March 2014.

[110] E. Métral *et al.*, Expected impedance and heat load of the present design of the HL- LHC BPMs, 28th HiLumi WP2 Task Leaders Meeting, CERN, 23 May 2014.

[111] H. Day *et al.*, TCTP summary of power loss and heat load calculations (with attention paid to the heat load of the ferrite damping material), LHC collimation working group, 1 October 2012.

[112] H. Day,Ph.D. thesis, Manchester University, 2013.

[113] B. Salvant *et al.*, Impedance aspects of crab cavities, HiLumi-LHC/LARP Crab Cavity System External Review, BNL, USA, 5–6 May 2014.

[114] M. Wendt, Wakefield analysis of the LHC BSRT mirror holder, CERN Internal Impedance Meeting, 9 September 2013.

[115] G. Antchev *et al.*, Luminosity-independent measurements of total, elastic and inelastic cross sections at $\sqrt{s}$=7 TeV, CERN-PH-EP-2012-353 (2012).

[116] G. Antchev *et al.*, Luminosity-independent measurements of the proton–proton total cross section at $\sqrt{s}$=8 TeV, CERN-PH-EP-2012-354 (2012).

[117] G. Arduini *et al.*, PICS: What do we gain in beam performance, Review of LHC and Injector Upgrade Plans Workshop, Archamps, 29–31 October 2013.
https://indico.cern.ch/event/260492/session/3/contribution/16/material/slides/7.pdf

[118] R. Jacobsson, private communication (2014).

[119] S. Fartoukh, Pile up management at the High Luminosity LHC and introduction to the crab-kissing concept, CERN-ACC-2014-0076 (2014).

[120] O. Brüning *et al.*, HL-LHC: How to achieve upgrade scenario 1 goals in the LHC? Proc. Review of LHC and Injectors Upgrade Plans Workshop, Archamps, France, 2013.

[121] J.M. Jowett, R. Alemany-Fernandez, R. Assmann, P. Baudrenghien, G. Bellodi, S. Hancock, M. Lamont, D. Manglunki, S. Redaelli, M. Sapinski, M. Schaumann, M. Solfaroli, R. Versteegen, J. Wenninger and D. Wollmann, Heavy ions in 2012 and the programme up to 2022, Proc. Chamonix 2012 Workshop on LHC Performance, CERN-2012-006 (2012).

[122] C.A. Salgado, J. Alvarez-Muniz, F. Arleo, N. Armesto and M. Botje *et al.*, Proton–nucleus collisions at the LHC: Scientific opportunities and requirements, *J. Phys.* **G39** (2012) 015010.

[123] J.M. Jowett, R. Alemany-Fernandez, P. Baudrenghien, D. Jacquet, M. Lamont, D. Manglunki, S. Redaelli, M. Sapinski, M. Schaumann, M. Solfaroli, Camillocci, R. Tomas, J. Uythoven, D. Valuch, R. Versteegen and J. Wenninger Proton nucleus collisions in the LHC, Proc. 4th International Particle Accelerator Conference, Shanghai, China, 12 - 17 May 2013, Eds. Z. Dai, C. Petit-Jean-Genaz, V. Schaa, C. Zhang, pp.49-51.

[124] R. Bruce, D. Bocian, S. Gilardoni and J.M. Jowett, Beam losses from ultraperipheral nuclear collisions between $^{208}Pb^{82+}$ ions in the large hadron collider and their alleviation, *Phys. Rev.ST Accel. Beams* **12** (2009) 071002.

[125] M. Bodendorfer, Ions: Baseline, Studies Plan and Strategy for Pending Options, Proc. Chamonix 2014 Workshop on LHC Performance, Chamonix, France, 22–25 September 2014, Ed. M. Draper, CERN–2015–002, pp. 192-197.

[126] M. Schaumann, Semi-empirical model for optimising future heavy-ion luminosity of the LHC, Proc. 5th International Particle Accelerator Conference, Dresden, Germany, 15 - 20 June 2014, Eds. C. Petit-Jean-Genaz, G. Arduini, P. Michel and V.R.W. Schaa, pp. 1033–1035.

[127] J.M. Jowett, H.-H. Braun, M.I. Gresham, E. Mahner and A.N. Nicholson, *et al.*, Limits to the performance of the LHC with ion beams, Proc. 9th European Particle Accelerator Conference, Lucerne, Switzerland, 5 – 9 July 2004, Eds. J. Chrin, C. Petit-Jean-Genaz, J. Poole, C. Prior, H.-A. Synal, pp. 578–580.

[128] H.-H. Braun, R.W. Assmann, A. Ferrari, J.-B. Jeanneret, J.M. Jowett and I.A. Pshenichnov, Collimation of heavy ion beams in LHC, Proc. 9th European Particle Accelerator Conference, Lucerne, Switzerland, 5 – 9 July 2004, Eds. J. Chrin, C. Petit-Jean-Genaz, J. Poole, C. Prior, H.-A. Synal, pp. 551–553.

[129] H.-H. Braun, A. Fassò, A. Ferrari, J.M. Jowett, P.R. Sala and G.I. Smirnov, Hadronic and electromagnetic fragmentation of ultrarelativistic heavy ions at LHC, *Phys. Rev. ST Accel. Beams* **17** (2014) 021006.

[130] O. S. Brüning, P. Collier, P. Lebrun, S. Myers, R. Ostojic, J. Poole and P. Proudlock (Eds.), LHC Design Report, v.1: The LHC Main Ring, CERN-2004-003-V-1 (2012) Chapter 21. "The LHC as a Lead Ion Collider", Tables 21.1-21.3.

[131] M. Schaumann *et al.*, Potential of stochastic cooling of heavy ions in the LHC, Proc. 5th International Particle Accelerator Conference, Dresden, Germany, 15 - 20 June 2014, Eds. C. Petit-Jean-Genaz, G. Arduini, P. Michel and V.R.W. Schaa, pp. 76–78.

A.8 High order time integrator for the simulation of charged particle motion in magnetic quadrupoles

Computer Physics Communications 239 (2019) 33–52

Contents lists available at ScienceDirect

Computer Physics Communications

journal homepage: www.elsevier.com/locate/cpc

High order time integrators for the simulation of charged particle motion in magnetic quadrupoles

Abele Simona [a,*], Luca Bonaventura [a], Thomas Pugnat [b], Barbara Dalena [b]

[a] MOX – Modelling and Scientific Computing, Dipartimento di Matematica, Politecnico di Milano, Via Bonardi 9, 20133 Milano, Italy
[b] CEA, Irfu, DACM, Université Paris-Saclay, F-91191 Gif-sur-Yvette, France

ARTICLE INFO

Article history:
Received 18 May 2018
Received in revised form 19 January 2019
Accepted 23 January 2019
Available online 7 February 2019

Keywords:
Magnetic fields
Particle accelerators
Hamilton equations
Symplectic methods
High order ODE methods

ABSTRACT

Magnetic quadrupoles are essential components of particle accelerators like the Large Hadron Collider. In order to study numerically the stability of the particle beam crossing a quadrupole, a large number of particle revolutions in the accelerator must be simulated. This requires to preserve numerically invariants of motion over a long time interval and entails a substantial computational cost, mostly related to the repeated evaluation of the magnetic vector potential. In this paper, in order to reduce this cost, we first consider a specific gauge transformation that allows to reduce significantly the number of vector potential evaluations. We then analyse the sensitivity of the numerical solution to the interpolation procedure required to compute magnetic vector potential data from gridded precomputed values at the locations required by high order time integration methods. Finally, we compare several high order integration techniques, in order to assess their accuracy and efficiency for these long term simulations. Explicit high order Lie methods are considered, along with implicit high order symplectic integrators and conventional explicit Runge–Kutta methods. Among symplectic methods, high order Lie integrators yield optimal results in terms of cost/accuracy ratios, but non-symplectic Runge–Kutta methods perform remarkably well even in very long term simulations. Furthermore, the accuracy of the field reconstruction and interpolation techniques appears to be the limiting factors for the accuracy of the particle tracking procedures.

1. Introduction

Magnetic quadrupoles are key components of particle accelerators that are used to focus particle beams. In high energy circular accelerators, the quality of their magnetic fields can influence the overall beam stability. The beam stability is measured in terms of the dynamic aperture, defined as the region in the phase space outside which a particle is considered as lost from the beam. The dynamic aperture is estimated by solving numerically the Hamilton equations describing the particle trajectories for a large number of accelerator revolutions (typically, more than 10^5). Therefore, it is important to use very efficient time integration methods which also guarantee good long-term preservation of dynamical invariants of motion. The action of a quadrupole can be approximately described using a linear combination of the position and momenta of the particles at the inlet that yields the position and momenta at the outlet [1]. This approach yields a good approximation if the particles travel near the quadrupole centre (small apertures) and it is exact in regions where the magnetic field is constant along the longitudinal axis z and only the main quadrupole field is present. In realistic cases, however, the magnetic field has a more complex structure which involves non-uniformity along z and harmonics of higher order, see e.g. [2]. These inhomogeneities of the field at the quadrupole ends, known as fringe field, can lead to a nonlinear dependency of the position and momenta of the particles at the outlet from the position and momenta at the inlet. In this paper, we focus on the numerical problems encountered when modelling these nonlinear dependencies in an accurate and efficient way, as necessary for the design of the large aperture quadrupoles foreseen for the HL-LHC project [3]. The accurate numerical solution of the complete Hamilton equations is mandatory in this case. A preliminary study on the applicability of second-order methods based on the Lie algebra integrators proposed in [4] has been carried out in [5] for the case of a realistic quadrupole. A wide class of methods approximates the nonlinear effects in each element by means of transfer maps, which are functions that represent a nonlinear relation between position and momenta of the particles at the inlet and at the outlet, respectively. These methods typically introduce strong approximations on the field shape, such as the Hard Edge model, that allow then to integrate the Hamilton equations and obtain an expression for a symplectic transfer map. An example

* Corresponding author.
E-mail addresses: abele.simona@polimi.it (A. Simona), luca.bonaventura@polimi.it (L. Bonaventura), thomas.pugnat@cea.fr (T. Pugnat), barbara.dalena@cea.fr (B. Dalena).

https://doi.org/10.1016/j.cpc.2019.01.018
0010-4655/

of such method, that does not consider the z-dependence of the field, is the thin model used in SixTrack [6], the code developed at CERN to simulate the whole accelerator. Another example is the one introduced in [2], where only the quadrupolar component of the field is considered and modelled as a Hard Edge with a nonlinear contribution which takes into account the effect of the fringe field in the Hard Edge limit. In this work, we consider instead methods that numerically integrate the Hamilton equations. These methods are often computationally expensive and they are strongly affected by the representation of the field. In particular, a standard way of representing the field is by locally interpolating a set of sampled values on a 3D grid (see e.g. [7,8]). In this work we instead rely on the more efficient representation based on the generalized gradients [9], combined with a wide range of techniques for the integration of Hamilton equations. The aim is to accurately describe the real magnetic field (for which computed or measured field maps are required) and its effect on the particles. In particular, the focus is on critical elements for the overall beam stability, such as the final focus quadrupoles in the HL-LHC [10]. As a first step, we consider a specific gauge transformation that allows to reduce by approximately 50% the computational cost of each vector potential evaluation, thus significantly enhancing the efficiency of any numerical approximation method employed for the particle trajectory simulation. We then compare several high order integration techniques, which allow to maintain sufficiently high accuracy even with relatively large integration step values, in order to assess their accuracy and efficiency for these long-term simulations. Explicit high order Lie methods [4] are considered along with implicit high order symplectic integrators [11] and more conventional, non-symplectic explicit Runge–Kutta methods.

In the case of realistic vector potentials, the errors induced by the vector potential reconstruction and interpolation become significant and reduce the highest possible accuracy that can be attained. Furthermore, since in realistic cases the magnetic vector potential evaluation is more costly, numerical methods which require less evaluations, such as the second-order Lie method, appear to be more competitive. On the other hand, experiments with idealized fields show that, if these errors could be reduced, higher order methods could be advantageous and the speed gain obtained with the horizontal-free Coulomb gauge would enhance their efficiency. In particular, the explicit fourth-order Runge–Kutta appears to be the most efficient method and the fourth-order Lie the most efficient among symplectic methods. A particularly interesting aspect of the results obtained is the fact that non-symplectic methods appear to be competitive with symplectic ones even on relatively long integrations, when stability of the computed trajectories and energy conservation are considered. Indeed, the spurious energy losses appear to be more closely related to the errors in the representation of the magnetic vector potential than to those introduced by the time integrators. This unexpected result warrants more detailed investigation.

A detailed outline of the paper is as follows. In Section 2, we introduce the Hamiltonian that describes the motion of a charged particle inside a magnetic quadrupole and the corresponding Hamilton equations. In Section 3, the numerical methods used in this work are briefly reviewed, along with the specific issues that arise when the vector potential values are only available at given sampling intervals, so that appropriate interpolation procedures must be employed if high order methods are to be applied. In Section 4, we review the approach employed to represent the magnetic vector potential. We also show how the non-uniqueness of the vector potential can be exploited to identify a gauge that allows to reduce the number of vector potential evaluations. Numerical results for a simple vector potential that can be expressed analytically are presented in Section 5. An assessment of time integration methods on a realistic case is presented in Section 6. In Section 7, we estimate the impact of approximation errors on the accurate representation of the nonlinear relationship between outlet and inlet dynamical parameters and we compare the results with those of the thin lens model, currently used in SixTrack [6]. Finally, some conclusions are drawn in Section 8, where we also discuss possible developments of this work.

2. Charged particle motion in magnetic quadrupoles

Magnetic quadrupoles are devices in which a stationary magnetic field with cylindrical symmetry is generated. Near the quadrupole centre, where the particles travel, the field is a solution of the Maxwell equations in the vacuum and in absence of charges and currents

$$\begin{aligned} \nabla\cdot\boldsymbol{E} &= 0 \qquad & \nabla\cdot\boldsymbol{B} &= 0 \\ \nabla\times\boldsymbol{E} &= 0 \qquad & \nabla\times\boldsymbol{B} &= 0. \end{aligned} \tag{1}$$

Since the magnetic field $\boldsymbol{B}$ is irrotational and conservative on simply connected domains, there exist a magnetic scalar potential ψ and a magnetic vector potential $\boldsymbol{A}$ such that $\boldsymbol{B} = \nabla\times\boldsymbol{A} = \nabla\psi$. The magnetic scalar potential is defined up to constants and the magnetic vector potential is defined up to gradients of scalar functions, so that given a scalar function λ and defining $\boldsymbol{A}' = \boldsymbol{A} + \nabla\lambda$, one has $\nabla\times\boldsymbol{A}' = \nabla\times(\boldsymbol{A}+\nabla\lambda) = \nabla\times\boldsymbol{A} = \boldsymbol{B}$. A gauge transformation $\boldsymbol{A}' = \boldsymbol{A} + \nabla\lambda$ does not change the magnetic field but can yield a more convenient representation of the vector potential for specific purposes. The second Maxwell equation can be rewritten as

$$0 = \nabla\cdot\boldsymbol{B} = \nabla\cdot(\nabla\psi) = \Delta\psi\ , \tag{2}$$

which means that the scalar potential satisfies the Laplace equation. Many high accuracy numerical methods are available to solve this equation starting from appropriate boundary conditions and taking into account also the real geometry of the accelerator, see e.g. [12,13]. However, in the approach most commonly used in accelerator physics, see e.g. [9,14], the magnetic vector potential $\boldsymbol{A}$ is represented by a power series in the transversal coordinates, whose coefficients are functions of the longitudinal coordinate. A detailed presentation of this approach is given in Section 4.

The motion of a charged particle in a magnetic quadrupole is described in terms of its position $\boldsymbol{q}(t) = (x,\ y,\ z)^T$ and its canonical momentum $\boldsymbol{p}(t) = \left(p_x,\ p_y,\ p_z\right)^T$. In the case of a high energy particle accelerator, the particles speed is very close to the speed of light. The relativistic Hamiltonian is given by

$$\mathcal{H}(\boldsymbol{q},\ \boldsymbol{p}) = \sqrt{m^2c^4 + c^2\|\boldsymbol{p} - Q\,\boldsymbol{A}(\boldsymbol{q})\|^2}, \tag{3}$$

where m denotes the rest mass of the particle, c is the speed of light and Q the particle charge [15]. The mechanical momenta are denoted by $\boldsymbol{p}^M = m\gamma\boldsymbol{v}$, where $\boldsymbol{v}$ is the particle speed and $\gamma = 1/\sqrt{1-\|\boldsymbol{v}\|^2/c^2} = 1/\sqrt{1-\beta^2}$ is the Lorentz factor. The canonical momenta $\boldsymbol{p}$ are related to the mechanical momenta through:

$$\boldsymbol{p} = \boldsymbol{p}^M + Q\,\boldsymbol{A}(\boldsymbol{q}). \tag{4}$$

The physical trajectory in the phase space $\boldsymbol{w}(t) = (\boldsymbol{q},\ \boldsymbol{p})^T$ is the one for which the action

$$\mathcal{B}[\boldsymbol{w}] = \int \boldsymbol{p}\cdot\dot{\boldsymbol{q}} - \mathcal{H}\,\mathrm{d}t \tag{5}$$

is stationary. Notice that, since the vector potential is stationary, the Hamiltonian is constant:

$$\frac{\mathrm{d}\mathcal{H}}{\mathrm{d}t} = \frac{\partial\mathcal{H}}{\partial t} = 0\ . \tag{6}$$

As a consequence, using (4), it is possible to see that the mechanical momentum module is constant:

$$\text{const} = \mathcal{H} = \sqrt{m^2 c^4 + c^2 \left\| \boldsymbol{p}^M \right\|^2} \quad \rightarrow \quad \left\| \boldsymbol{p}^M \right\| = \text{const} \,. \tag{7}$$

As a first step, it is useful to work with dimensionless variables. We choose a reference length L, a reference momentum module p^0, and a reference magnetic field intensity B, we rescale

$$\boldsymbol{Q} = \frac{\boldsymbol{q}}{L} \,, \quad \boldsymbol{P} = \frac{\boldsymbol{p}}{p^0} \,, \quad T = \frac{c}{L} t \,, \quad \widetilde{\boldsymbol{A}} = \frac{\boldsymbol{A}}{B L} \tag{8}$$

and we consider the dimensionless action $\widetilde{\mathcal{B}} = \mathcal{B}/\left(L p^0\right)$ to which is associated the dimensionless Hamiltonian:

$$\widetilde{\mathcal{H}} = \frac{\mathcal{H}}{p^0 c} = \frac{\gamma}{D_1} = \sqrt{\frac{1}{D_1^2} + \left\| \boldsymbol{P} - D_2 \widetilde{\boldsymbol{A}} \right\|^2} \,, \tag{9}$$

where D_1 and D_2 are two dimensionless coefficients:

$$D_1 = \frac{p^0}{m c} \,, \qquad D_2 = \frac{Q B L}{p^0} \,. \tag{10}$$

Exploiting (4), it is possible to introduce another constant quantity δ, which is the relative deviation of the mechanical momentum module with respect to the reference momentum p^0:

$$\delta = \frac{\left\| \boldsymbol{p}^M \right\| - p^0}{p^0} = \sqrt{\frac{D_1^2 \, \widetilde{\mathcal{H}}^2 - 1}{D_1^2}} - 1 \,. \tag{11}$$

Introducing the state vector $\boldsymbol{w} = \left(\boldsymbol{Q}^T, \, \boldsymbol{P}^T\right)^T$, the relativistic Hamilton equations can be written as

$$\begin{aligned} \dot{\boldsymbol{w}} &= \boldsymbol{J} \, \nabla \widetilde{\mathcal{H}}(\boldsymbol{w}) \\ &= \begin{bmatrix} \dfrac{\left(\boldsymbol{P} - D_2 \widetilde{\boldsymbol{A}}(\boldsymbol{Q})\right)}{\sqrt{1/D_1^2 + \left\| \boldsymbol{P} - D_2 \widetilde{\boldsymbol{A}}(\boldsymbol{Q}) \right\|^2}} \\ \dfrac{D_2}{\sqrt{1/D_1^2 + \left\| \boldsymbol{P} - D_2 \widetilde{\boldsymbol{A}}(\boldsymbol{Q}) \right\|^2}} \, \mathcal{J}_{\widetilde{\boldsymbol{A}}}^{\boldsymbol{Q}}(\boldsymbol{Q})^T \left(\boldsymbol{P} - D_2 \widetilde{\boldsymbol{A}}(\boldsymbol{Q})\right) \end{bmatrix} . \end{aligned} \tag{12}$$

Here the dot denotes the total derivative with respect to T, we denote $\mathcal{J}_{\widetilde{\boldsymbol{A}}}^{\boldsymbol{Q}}(\boldsymbol{Q}) = \partial \widetilde{\boldsymbol{A}} / \partial \boldsymbol{Q}$ and we set

$$\boldsymbol{J} = \begin{bmatrix} \boldsymbol{0} & \boldsymbol{I} \\ -\boldsymbol{I} & \boldsymbol{0} \end{bmatrix} , \tag{13}$$

where $\boldsymbol{0}$, $\boldsymbol{I}$ are the zero and identity matrix, respectively. For the specific problem at hand, it is convenient to assume that the Z axis is the symmetry axis of the quadrupole and to use the longitudinal coordinate Z as independent variable instead of time. To see this change of independent variable it is useful to consider the action

$$\widetilde{\mathcal{B}} = \int_{T_0}^{T_f} \left[P_x \frac{\mathrm{d}X}{\mathrm{d}T} + P_y \frac{\mathrm{d}Y}{\mathrm{d}T} + P_z \frac{\mathrm{d}Z}{\mathrm{d}T} - \widetilde{\mathcal{H}} \right] \mathrm{d}T \,. \tag{14}$$

Since the particle travels at high speed in the Z direction, $\dfrac{\mathrm{d}Z}{\mathrm{d}T} \neq 0$ and a change of integration variable can be done:

$$\int_{Z_0}^{Z_f} \left[P_x \frac{\mathrm{d}X}{\mathrm{d}Z} + P_y \frac{\mathrm{d}Y}{\mathrm{d}Z} + P_z - \widetilde{\mathcal{H}} \frac{\mathrm{d}T}{\mathrm{d}Z} \right] \mathrm{d}Z \,. \tag{15}$$

Using (9), it is possible to express P_z as a function of the other variables:

$$P_z = \sqrt{\widetilde{\mathcal{H}}^2 - \frac{1}{D_1^2} - \left(P_x - D_2 \widetilde{A}_x\right)^2 - \left(P_y - D_2 \widetilde{A}_y\right)^2} + D_2 \widetilde{A}_z \tag{16}$$

and to consider $-P_z$ as a new Hamiltonian $\mathcal{F}$ and $\left(T, \, -\widetilde{\mathcal{H}}\right)$ as a canonical pair. For our purposes, it is more convenient to use the momentum deviation variable δ (11) instead of $-\widetilde{\mathcal{H}}$, we therefore apply a canonical transformation using the following generating function:

$$G_2\left(X, \, Y, \, T, P_x, P_y, \delta; Z\right) = X P_x + Y P_y + \delta \left(Z - \frac{\gamma}{D_1 \, \delta} T \right) . \tag{17}$$

Recalling that

$$(\delta + 1)^2 = \frac{\left\| \boldsymbol{p}^M \right\|^2}{\left(p^0\right)^2} = \frac{\gamma^2 \beta^2}{D_1^2} = \frac{\gamma^2 - 1}{D_1^2} \,, \tag{18}$$

we see that

$$\begin{aligned} \gamma &= \sqrt{D_1^2 (\delta + 1)^2 + 1} \,, \\ -\widetilde{\mathcal{H}} &= \frac{\partial G_2}{\partial T} = -\frac{\gamma}{D_1} \,, \\ \ell &= \frac{\partial G_2}{\partial \delta} = Z - \frac{D_1 (\delta + 1)}{\gamma} T = Z - \beta \, T \,, \\ \mathcal{F}_2 &= \mathcal{F} + \frac{\partial G_2}{\partial Z} = \mathcal{F} + \delta \,. \end{aligned} \tag{19}$$

So, we end up with a system ruled by the following Hamiltonian:

$$\begin{aligned} \mathcal{F}_2(\boldsymbol{w}; \, Z) \, = \, & -\sqrt{(\delta + 1)^2 - \left(P_x - D_2 \widetilde{A}_x\right)^2 - \left(P_y - D_2 \widetilde{A}_y\right)^2} \\ & - D_2 \widetilde{A}_z \, + \delta, \end{aligned} \tag{20}$$

where $\boldsymbol{w} = \left(X, \, Y, \, \ell, P_x, P_y, \delta\right)$ are the dynamical variables. The system associated to the Hamiltonian $\mathcal{F}_2$ is not autonomous anymore since such Hamiltonian explicitly depends on the independent variable Z through the vector potential $\widetilde{\boldsymbol{A}}(X, \, Y, \, Z)$. In order to study an equivalent autonomous system, we can use a trivial change of independent variable $\sigma(Z) = Z$ and introduce another action

$$\mathcal{C}[\boldsymbol{w}] = \int_{\sigma_0}^{\sigma_f} \left[P_x \frac{\mathrm{d}X}{\mathrm{d}\sigma} + P_y \frac{\mathrm{d}Y}{\mathrm{d}\sigma} + \delta \frac{\mathrm{d}\ell}{\mathrm{d}\sigma} + P_z \frac{\mathrm{d}Z}{\mathrm{d}\sigma} - \widetilde{\mathcal{K}} \right] \mathrm{d}\sigma \,, \tag{21}$$

where

$$\begin{aligned} \widetilde{\mathcal{K}}(\boldsymbol{w}; \, \sigma) \, = \, & -\sqrt{(\delta + 1)^2 - \left(P_x - D_2 \widetilde{A}_x\right)^2 - \left(P_y - D_2 \widetilde{A}_y\right)^2} - D_2 \widetilde{A}_z \\ & + P_z + \delta \end{aligned} \tag{22}$$

and $\boldsymbol{w} = \left(X, \, Y, \, \ell, \, Z, \, P_x, \, P_y, \, \delta, \, P_z\right)$. For relativistic particles, the momenta in the transversal plane are much smaller than the total momentum module, i.e.

$$(1 + \delta)^2 \gg \left(P_x - \widetilde{A}_x\right)^2 + \left(P_y - \widetilde{A}_y\right)^2 .$$

Therefore, the so called paraxial approximation can be introduced, that amounts to substituting the square root in Eq. (22) with its Taylor expansion truncated at the first order:

$$\begin{aligned} \widetilde{\mathcal{K}} &= -\sqrt{(\delta + 1)^2 - \left(P_x - D_2 \widetilde{A}_x\right)^2 - \left(P_y - D_2 \widetilde{A}_y\right)^2} - D_2 \widetilde{A}_z \\ &\quad + P_z + \delta \\ &= -(\delta + 1) \sqrt{1 - \frac{\left(P_x - D_2 \widetilde{A}_x\right)^2}{(\delta + 1)^2} - \frac{\left(P_y - D_2 \widetilde{A}_y\right)^2}{(\delta + 1)^2}} - D_2 \widetilde{A}_z \\ &\quad + P_z + \delta \\ &\approx -(\delta + 1) \left(1 - \frac{\left(P_x - D_2 \widetilde{A}_x\right)^2}{2(\delta + 1)^2} - \frac{\left(P_y - D_2 \widetilde{A}_y\right)^2}{2(\delta + 1)^2} \right) - D_2 \widetilde{A}_z \\ &\quad + P_z + \delta \\ &= -1 + \frac{\left(P_x - D_2 \widetilde{A}_x\right)^2}{2(\delta + 1)} + \frac{\left(P_y - D_2 \widetilde{A}_y\right)^2}{2(\delta + 1)} - D_2 \widetilde{A}_z + P_z = \mathcal{K} \,. \end{aligned} \tag{23}$$

In this work, we will use a reference length $L = 1$ m, a reference field magnitude B such that the dimensionless coefficient $D_2 = 1$ and we will use as a reference the momentum of a proton with rest mass $m_0 \sim 938\,\mathrm{MeV/c^2} \sim 1.67 \times 10^{-27}$ kg and total energy $E = 7\,\mathrm{TeV} \sim 1.12 \times 10^{-6}$ J. Therefore the reference momentum module is given by:

$$p^0 = 7\,\mathrm{TeV}\beta/c \sim 3.74 \times 10^{-15}\,\mathrm{kg\,m/s}\,. \tag{24}$$

Considering the approximate Hamiltonian (23) and $D_2 = 1$, the resulting Hamilton equations are:

$$\dot{\boldsymbol{w}} = \boldsymbol{J}\,\nabla\mathcal{K} = \begin{bmatrix} \dfrac{P_x - \widetilde{A}_x}{\delta + 1} \\ \dfrac{P_y - \widetilde{A}_y}{\delta + 1} \\ -\dfrac{\left(P_x - \widetilde{A}_x\right)^2}{2(\delta+1)^2} - \dfrac{\left(P_y - \widetilde{A}_y\right)^2}{2(\delta+1)^2} \\ \dfrac{\partial \widetilde{A}_x}{\partial X}\dfrac{\left(P_x - \widetilde{A}_x\right)}{\delta+1} + \dfrac{\partial \widetilde{A}_y}{\partial X}\dfrac{\left(P_y - \widetilde{A}_y\right)}{\delta+1} + \dfrac{\partial \widetilde{A}_z}{\partial X} \\ \dfrac{\partial \widetilde{A}_x}{\partial Y}\dfrac{\left(P_x - \widetilde{A}_x\right)}{\delta+1} + \dfrac{\partial \widetilde{A}_y}{\partial Y}\dfrac{\left(P_y - \widetilde{A}_y\right)}{\delta+1} + \dfrac{\partial \widetilde{A}_z}{\partial Y} \\ \dfrac{\partial \widetilde{A}_x}{\partial Z}\dfrac{\left(P_x - \widetilde{A}_x\right)}{\delta+1} + \dfrac{\partial \widetilde{A}_y}{\partial Z}\dfrac{\left(P_y - \widetilde{A}_y\right)}{\delta+1} + \dfrac{\partial \widetilde{A}_z}{\partial Z} \end{bmatrix}. \tag{25}$$

Moreover, it can be noticed that the Hamiltonian does not depend on ℓ, so that the partial derivative of $\mathcal{K}$ with respect to ℓ is zero. As a consequence, δ is a constant of motion, equal to the initial value, denoted by the subscript 0, δ_0. If the evolution of the variable ℓ is not needed, the canonical pair $(\ell,\ \delta)$ can be neglected, considering δ_0 as a parameter and reducing again the size of the phase space. In this case, the Hamiltonian is still given by (23) but, since the dynamical variables are now $\boldsymbol{w} = \left(X,\ Y, Z,\ P_x,\ P_y,\ P_z\right)$, the Hamilton equations become:

$$\dot{\boldsymbol{w}} = \boldsymbol{J}\,\nabla\mathcal{K} = \begin{bmatrix} \dfrac{P_x - \widetilde{A}_x}{\delta_0 + 1} \\ \dfrac{P_y - \widetilde{A}_y}{\delta_0 + 1} \\ \dfrac{\partial \widetilde{A}_x}{\partial X}\dfrac{\left(P_x - \widetilde{A}_x\right)}{\delta_0+1} + \dfrac{\partial \widetilde{A}_y}{\partial X}\dfrac{\left(P_y - \widetilde{A}_y\right)}{\delta_0+1} + \dfrac{\partial \widetilde{A}_z}{\partial X} \\ \dfrac{\partial \widetilde{A}_x}{\partial Y}\dfrac{\left(P_x - \widetilde{A}_x\right)}{\delta_0+1} + \dfrac{\partial \widetilde{A}_y}{\partial Y}\dfrac{\left(P_y - \widetilde{A}_y\right)}{\delta_0+1} + \dfrac{\partial \widetilde{A}_z}{\partial Y} \\ \dfrac{\partial \widetilde{A}_x}{\partial Z}\dfrac{\left(P_x - \widetilde{A}_x\right)}{\delta_0+1} + \dfrac{\partial \widetilde{A}_y}{\partial Z}\dfrac{\left(P_y - \widetilde{A}_y\right)}{\delta_0+1} + \dfrac{\partial \widetilde{A}_z}{\partial Z} \end{bmatrix}. \tag{26}$$

A further simplification can be achieved noticing that P_z is decoupled from the other dynamical variables, so that its computation can be neglected if we are only interested in the dynamics of the transversal variables, reducing the number of equations (26) to the four ones associated to X, Y, P_x and P_y.

3. Review of high order numerical methods for ODE problems

In this section, some high order numerical methods for the solution of a first order system $\dot{\boldsymbol{y}}(t) = \boldsymbol{f}(t, \boldsymbol{y})$ will be reviewed, in view of their application to the solution of the Hamilton equations. A more detailed presentation of the relevant numerical methods can be found for example in [11].

An important feature of Hamiltonian flows is their symplectic property, which can be defined more precisely as follows.

Definition 3.1. A differentiable map $\boldsymbol{g} : U \to \mathbb{R}^{2d}$, where $U \subset \mathbb{R}^{2d}$ is an open set, is called symplectic if:

$$\mathcal{J}_{\boldsymbol{g}}(\boldsymbol{w})^T \boldsymbol{J}\,\mathcal{J}_{\boldsymbol{g}}(\boldsymbol{w}) = \boldsymbol{J} \qquad \forall \boldsymbol{w} \in U\,,$$

where $\mathcal{J}_{\boldsymbol{g}}$ is the Jacobian matrix of $\boldsymbol{g}$ and $\boldsymbol{J}$ is the matrix (13).

When this property is preserved by the numerical method, i.e., if the one-step map $\Phi_{\Delta t} : y_0 \mapsto \Phi_{\Delta t}(y_0) = y_1$ is symplectic, quadratic invariants of motion are preserved, thus ensuring in principle a good behaviour for long-term simulations. The first symplectic techniques that will be considered are Runge–Kutta methods, which can be written in general as

Definition 3.2. Let $b_i,\ a_{ij}\ (i,\ j = 1,\ \ldots,\ s)$ be real numbers and let $c_i = \sum_{j=1}^{s} a_{ij}$. A s-stage Runge–Kutta method is given by:

$$\begin{aligned} \boldsymbol{y}_{n+1} &= \boldsymbol{y}_n + \Delta t \sum_{i=1}^{s} b_i \boldsymbol{f}(t_n + \Delta t\, c_i, \boldsymbol{u}_i) \\ \boldsymbol{u}_i &= \boldsymbol{y}_n + \Delta t \sum_{j=1}^{s} a_{ij} \boldsymbol{f}(t_n + \Delta t\, c_j,\ \boldsymbol{u}_j), \quad i = 1,\ \ldots,\ s\,. \end{aligned} \tag{27}$$

Runge–Kutta methods are often summarized via the so called Butcher tableau, in which all the coefficients are arranged as:

$$\begin{array}{c|ccc} c_1 & a_{1,1} & \cdots & a_{1,s} \\ \vdots & \vdots & \ddots & \vdots \\ c_s & a_{s,1} & \cdots & a_{s,s} \\ \hline & b_1 & \cdots & b_s \end{array}\,.$$

A Runge–Kutta method is explicit if $a_{ij} = 0$ for $j \geq i$. The following theorem gives a sufficient condition for a Runge–Kutta method to be symplectic [11].

Theorem 1. *If the coefficients of a Runge–Kutta method satisfy:*

$$b_i\, a_{ij} + b_j\, a_{ji} = b_i\, b_j \quad \forall i,\ j = 1,\ \ldots,\ s \tag{28}$$

then the method is symplectic.

Gauss methods are particular implicit Runge–Kutta methods, some of which satisfy the condition of Theorem 1 and are thus symplectic. The midpoint method can be interpreted as the second-order Gauss method, characterized by the Butcher tableau

$$\begin{array}{c|c} \frac{1}{2} & \frac{1}{2} \\ \hline & \frac{1}{2} \end{array}\,.$$

The fourth-order Gauss method, considered in this paper, is characterized by the Butcher tableau

$$\begin{array}{c|cc} \frac{1}{2} - \frac{\sqrt{3}}{6} & \frac{1}{4} & \frac{1}{4} - \frac{\sqrt{3}}{6} \\ \frac{1}{2} + \frac{\sqrt{3}}{6} & \frac{1}{4} + \frac{\sqrt{3}}{6} & \frac{1}{4} \\ \hline & \frac{1}{2} & \frac{1}{2} \end{array}\,.$$

The sixth-order Gauss method is instead characterized by the Butcher tableau

$$\begin{array}{c|ccc} \frac{1}{2}-\frac{\sqrt{15}}{10} & \frac{5}{36} & \frac{2}{9}-\frac{\sqrt{15}}{15} & \frac{5}{36}-\frac{\sqrt{15}}{30} \\ \frac{1}{2} & \frac{5}{36}+\frac{\sqrt{15}}{24} & \frac{2}{9} & \frac{5}{36}-\frac{\sqrt{15}}{24} \\ \frac{1}{2}+\frac{\sqrt{15}}{10} & \frac{5}{36}+\frac{\sqrt{15}}{30} & \frac{2}{9}-\frac{\sqrt{15}}{15} & \frac{5}{36} \\ \hline & \frac{5}{18} & \frac{4}{9} & \frac{5}{18} \end{array} .$$

Implicit methods require the solution of a nonlinear system of equations at each time step. This can be done using either the Newton or the fixed-point method. Even though Newton's method is usually superior, numerical results show that the latter is faster. This behaviour can be justified by the fact that, for the problems at hand, both methods require a small number of iterations to achieve convergence, but the Newton method implies higher initial costs related to the evaluation of Jacobian matrix, see e.g. the discussion in [11]. Also the best known fourth-order explicit Runge–Kutta method has been considered in this work. This method is not symplectic and it is characterized by the Butcher tableau

$$\begin{array}{c|cccc} 0 & & & & \\ \frac{1}{2} & \frac{1}{2} & & & \\ \frac{1}{2} & 0 & \frac{1}{2} & & \\ 1 & 0 & 0 & 1 & \\ \hline & \frac{1}{6} & \frac{1}{3} & \frac{1}{3} & \frac{1}{6} \end{array} .$$

If $\mathcal{H}$ is the Hamiltonian ruling the evolution of an autonomous system, then the exact solution of the Hamilton equations can be formally represented as

$$\boldsymbol{w}(t) = \exp\left(t : -\mathcal{H} : \right)\boldsymbol{w}_0. \tag{29}$$

Here, the notation of Eq. (12) is used, : : denotes the Lie operator and the exponentiation of a Lie operator is called Lie transformation [9]. The methods based on Lie algebra techniques most widely applied in accelerator physics employ a second-order approximation of the Lie transformation. Higher order Lie methods are then built using the procedure introduced by Yoshida in [16] and further discussed in [4]. The first step is to split the Hamiltonian $\mathcal{H}$ into s solvable parts

$$\mathcal{H} = \sum_{i=1}^{s} \mathcal{H}_i$$

such that $\exp\left(: \mathcal{H}_i :\right)$ can be computed exactly for $i = 1, \ldots, s$. This is true if $: \mathcal{H}_i :$ is nilpotent of order two (i.e. $: \mathcal{H}_i :^k \boldsymbol{w} = \boldsymbol{0}$ for $k \geq 2$), because in this case the exponential series reduces to a finite sum. A second order approximation is then given by

$$\begin{aligned} &\exp\left(\Delta t : -\mathcal{H} : \right) = \\ &\quad = \exp\left(\frac{\Delta t}{2} : -\mathcal{H}_1 : \right)\exp\left(\frac{\Delta t}{2} : -\mathcal{H}_2 : \right) \\ &\quad \ldots \exp\left(\Delta t : -\mathcal{H}_s : \right)\exp\left(\frac{\Delta t}{2} : -\mathcal{H}_{s-1} : \right) \\ &\quad \ldots \exp\left(\frac{\Delta t}{2} : -\mathcal{H}_1 : \right) + o\left(\Delta t^2\right). \end{aligned} \tag{30}$$

Denoting by $\mathcal{M}_2(\Delta t)$ the approximation (30) and by $\mathcal{M}_{2n}(\Delta t)$ an approximation of order $2n$, an approximation of order $2n+2$ can be built as follows

$$\mathcal{M}_{2n+2}(\Delta t) = \mathcal{M}_{2n}(\alpha_1\, \Delta t)\mathcal{M}_{2n}(\alpha_0\, \Delta t)\mathcal{M}_{2n}(\alpha_1\, \Delta t)\,, \tag{31}$$

where $\alpha_0 = -\dfrac{2^{1/2n+1}}{2-2^{1/(2n+1)}}$ and $\alpha_1 = \dfrac{1}{2-2^{1/(2n+1)}}$. In this work, methods of order 4 and 6 have been considered, with (α_0, α_1) pairs given by

$$\left(-\frac{2^{1/3}}{2-2^{1/3}},\ \frac{1}{2-2^{1/3}}\right) \quad \text{and} \quad \left(-\frac{2^{1/5}}{2-2^{1/5}},\ \frac{1}{2-2^{1/5}}\right),$$

respectively.

Taking into account the discussion in Section 2, the map $\mathcal{M}_2$, applied to $\boldsymbol{w}_n$ yields the following algorithm

$$\begin{aligned}
\boldsymbol{w}_{n+1/11} &= \boldsymbol{w}_n + \frac{\sigma}{2}\left(0,\ 0,\ \frac{\partial \widetilde{A}_z}{\partial X},\ \frac{\partial \widetilde{A}_z}{\partial Y}\right)^T; \\
\boldsymbol{w}_{n+2/11} &= \boldsymbol{w}_{n+1/11} + \left(0,\ 0,\ \widetilde{A}_x,\ \int \frac{\partial \widetilde{A}_x}{\partial Y}\,\mathrm{d}X\right)^T; \\
\boldsymbol{w}_{n+3/11} &= \boldsymbol{w}_{n+2/11} + \frac{\sigma}{2}\left(\frac{P_x}{1+\delta_0},\ 0,\ 0,\ 0\right)^T; \\
\boldsymbol{w}_{n+4/11} &= \boldsymbol{w}_{n+3/11} + \left(0,\ 0,\ -\widetilde{A}_x,\ -\int \frac{\partial \widetilde{A}_x}{\partial Y}\,\mathrm{d}X\right)^T; \\
\boldsymbol{w}_{n+5/11} &= \boldsymbol{w}_{n+4/11} + \left(0,\ 0,\ +\int \frac{\partial \widetilde{A}_y}{\partial X}\,\mathrm{d}Y,\ +\widetilde{A}_y\right)^T; \\
\boldsymbol{w}_{n+6/11} &= \boldsymbol{w}_{n+5/11} + \sigma\left(0,\ \frac{P_y}{1+\delta_0},\ 0,\ 0\right)^T; \\
\boldsymbol{w}_{n+7/11} &= \boldsymbol{w}_{n+6/11} + \left(0,\ 0,\ -\int \frac{\partial \widetilde{A}_y}{\partial X}\,\mathrm{d}Y,\ -\widetilde{A}_y\right)^T; \\
\boldsymbol{w}_{n+8/11} &= \boldsymbol{w}_{n+7/11} + \left(0,\ 0,\ \widetilde{A}_x,\ \int \frac{\partial \widetilde{A}_x}{\partial Y}\,\mathrm{d}X\right)^T; \\
\boldsymbol{w}_{n+9/11} &= \boldsymbol{w}_{n+8/11} + \frac{\sigma}{2}\left(\frac{P_x}{1+\delta_0},\ 0,\ 0,\ 0\right)^T; \\
\boldsymbol{w}_{n+10/11} &= \boldsymbol{w}_{n+9/11} + \left(0,\ 0,\ -\widetilde{A}_x,\ -\int \frac{\partial \widetilde{A}_x}{\partial Y}\,\mathrm{d}X\right)^T; \\
\boldsymbol{w}_{n+1} &= \boldsymbol{w}_{n+10/11} + \frac{\sigma}{2}\left(0,\ 0,\ \frac{\partial \widetilde{A}_z}{\partial X},\ \frac{\partial \widetilde{A}_z}{\partial Y}\right)^T.
\end{aligned} \tag{32}$$

In the case of particle motion inside a magnetic quadrupole, the ODE system is given by (26). In many practical applications, only the magnetic vector potential values, sampled at equally spaced locations in Z, are available. On the other hand, all the methods introduced require the magnetic vector potential evaluation at Z values different from the sampled ones. For some methods, like the midpoint and explicit Runge–Kutta method, only the evaluation at $Z = Z_n + \Delta Z/2$ is required, so that interpolation of the sampled data can be avoided if a ΔZ is employed for computation that is twice that of the data. However, in general an interpolation is needed in order to provide the magnetic vector potential A evaluated at the points needed by each specific ODE solver. This introduces a further source of error whose quantification is not a straightforward task. Some proposals to compute intermediate values will be compared in Section 5, extending the preliminary results in [17].

4. Representation of the magnetic vector potential

In this section, the approach used in this work for the reconstruction of the magnetic vector potential will be introduced. The reader is referred to [9] for a complete presentation of this technique. Due to the geometry of the quadrupole, it is natural to describe its magnetic field using cylindrical coordinates $(\rho,\ \theta,\ z)$. Due to the periodicity of the field in the angular variable θ, it is then possible to expand the angular dependence using Fourier series

$$\boldsymbol{B}(\rho,\ \theta,\ z) = \sum_{m=1}^{\infty} \boldsymbol{B}_m(\rho,\ z)\sin\left(m\,\theta\right) + \boldsymbol{A}_m(\rho,\ z)\cos\left(m\,\theta\right). \tag{33}$$

The field harmonics $\boldsymbol{A}_m$ and $\boldsymbol{B}_m$ are the basis of the vector potential approximation. Exploiting the quadrupole symmetries, it is possible to show that only the harmonics associated to certain

values of m are different from zero, in particular those with $m = 2(2j+1)$ for $j \geq 0$. The magnetic scalar potential ψ satisfies the Laplace equation (2). This allows to derive from (33) the representation

$$\begin{aligned}\psi(\rho,\,\theta,\,z) &= \sum_{m=1}^{\infty}\sin(m\theta)\sum_{\ell=0}^{\infty}(-1)^{\ell}\frac{m!}{2^{2\ell}\ell!(\ell+m)!}\rho^{2\ell+m}C_{m,s}^{[2\ell]}(z)\\ &+\sum_{m=1}^{\infty}\cos(m\theta)\sum_{\ell=0}^{\infty}(-1)^{\ell}\frac{m!}{2^{2\ell}\ell!(\ell+m)!}\rho^{2\ell+m}C_{m,c}^{[2\ell]}(z)\\ &=\sum_{m=1}^{\infty}\psi_{m,s}+\psi_{m,c}=\psi_s+\psi_c\,,\end{aligned} \tag{34}$$

where $C_{m,s}^{[2\ell]}(z)$ (and $C_{m,c}^{[2\ell]}(z)$) are known functions called normal (skew) generalized gradients. The radial component of the harmonics $A_{\rho,m}$ and $B_{\rho,m}$ (see Eq. (33)), measured at a certain radius R_{an}, also known as radius of analysis, is denoted from now on simply by A_m and B_m. They can be used to compute the generalized gradients using the following formula

$$\begin{aligned}C_{m,c}^{[n]}(z) &= \frac{i^n}{2^m m!}\frac{1}{\sqrt{2\pi}}\int_{-\infty}^{+\infty}\frac{k^{m+n-1}}{I'_m(R_{an}\,k)}\widehat{A}_m(R_{an},\,k)\,e^{ikz}\,\mathrm{d}k\,,\\ C_{m,s}^{[n]}(z) &= \frac{i^n}{2^m m!}\frac{1}{\sqrt{2\pi}}\int_{-\infty}^{+\infty}\frac{k^{m+n-1}}{I'_m(R_{an}\,k)}\widehat{B}_m(R_{an},\,k)\,e^{ikz}\,\mathrm{d}k\,.\end{aligned} \tag{35}$$

Here, I'_m denotes the modified Bessel function of the first kind, while $\widehat{A}_m(R_{an},\,k)$ and $\widehat{B}_m(R_{an},\,k)$ denote the Fourier transforms of $A_m(R_{an},\,z)$ and $B_m(R_{an},\,z)$, respectively. It is possible to express different quantities, such as the harmonics or the magnetic potentials, using either the normal or the skew generalized gradients. Depending on which generalized gradient is used, these quantities are labelled as normal (s) or skew (c). Also the magnetic vector potential be defined using normal and skew terms:

$$\boldsymbol{A}=\sum_{m=1}^{\infty}(\boldsymbol{A}^{m,s}+\boldsymbol{A}^{m,c})\,. \tag{36}$$

Using the generalized gradients, it is possible to derive the expression for a first vector potential gauge, called azimuthal-free gauge, for which $A_\varphi \equiv 0$:

$$\begin{aligned}A_x^{m,s} &= \cos(\theta)\frac{\cos(m\theta)}{m}\sum_{\ell=0}^{\infty}\frac{(-1)^{\ell}m!}{2^{2\ell}\ell!(\ell+m)!}C_{m,s}^{[2\ell+1]}(z)\rho^{2\ell+m+1}\,;\\ A_x^{m,c} &= -\cos(\theta)\frac{\sin(m\theta)}{m}\sum_{\ell=0}^{\infty}\frac{(-1)^{\ell}m!}{2^{2\ell}\ell!(\ell+m)!}C_{m,c}^{[2\ell+1]}(z)\rho^{2\ell+m+1}\,;\\ A_y^{m,s} &= \sin(\theta)\frac{\cos(m\theta)}{m}\sum_{\ell=0}^{\infty}\frac{(-1)^{\ell}m!}{2^{2\ell}\ell!(\ell+m)!}C_{m,s}^{[2\ell+1]}(z)\rho^{2\ell+m+1}\,;\\ A_y^{m,c} &= -\sin(\theta)\frac{\sin(m\theta)}{m}\sum_{\ell=0}^{\infty}\frac{(-1)^{\ell}m!}{2^{2\ell}\ell!(\ell+m)!}C_{m,c}^{[2\ell+1]}(z)\rho^{2\ell+m+1}\,;\\ A_z^{m,s} &= -\frac{\cos(m\theta)}{m}\sum_{\ell=0}^{\infty}(2\ell+m)\frac{(-1)^{\ell}m!}{2^{2\ell}\ell!(\ell+m)!}C_{m,s}^{[2\ell]}(z)\rho^{2\ell+m}\,;\\ A_z^{m,c} &= \frac{\sin(m\theta)}{m}\sum_{\ell=0}^{\infty}(2\ell+m)\frac{(-1)^{\ell}m!}{2^{2\ell}\ell!(\ell+m)!}C_{m,c}^{[2\ell]}(z)\rho^{2\ell+m}\,.\end{aligned} \tag{37}$$

If we require that a vector potential is divergence-free $\nabla\cdot\widehat{\boldsymbol{A}}=0$, we obtain the so called Coulomb gauge. The symmetric Coulomb gauge $\widehat{\boldsymbol{A}}$ belongs to this category and can be expressed as

$$\begin{aligned}\widehat{A}_x^{m,s} &= \frac{\cos((m+1)\theta)}{2}\sum_{\ell=0}^{\infty}\frac{(-1)^{\ell}m!}{2^{2\ell}\ell!(\ell+m+1)!}C_{m,s}^{[2\ell+1]}(z)\\ &\quad\times\rho^{2\ell+m+1}\,;\\ \widehat{A}_x^{m,c} &= -\frac{\sin((m+1)\theta)}{2}\sum_{\ell=0}^{\infty}\frac{(-1)^{\ell}m!}{2^{2\ell}\ell!(\ell+m+1)!}C_{m,c}^{[2\ell+1]}(z)\\ &\quad\times\rho^{2\ell+m+1}\,;\\ \widehat{A}_y^{m,s} &= \frac{\sin((m+1)\theta)}{2}\sum_{\ell=0}^{\infty}\frac{(-1)^{\ell}m!}{2^{2\ell}\ell!(\ell+m+1)!}C_{m,s}^{[2\ell+1]}(z)\\ &\quad\times\rho^{2\ell+m+1}\,;\\ \widehat{A}_y^{m,c} &= \frac{\cos((m+1)\theta)}{2}\sum_{\ell=0}^{\infty}\frac{(-1)^{\ell}m!}{2^{2\ell}\ell!(\ell+m+1)!}C_{m,c}^{[2\ell+1]}(z)\\ &\quad\times\rho^{2\ell+m+1}\,;\\ \widehat{A}_z^{m,s} &= -\cos(m\theta)\sum_{\ell=0}^{\infty}\frac{(-1)^{\ell}m!}{2^{2\ell}\ell!(\ell+m)!}C_{m,s}^{[2\ell]}(z)\rho^{2\ell+m}\,;\\ \widehat{A}_z^{m,c} &= \sin(m\theta)\sum_{\ell=0}^{\infty}\frac{(-1)^{\ell}m!}{2^{2\ell}\ell!(\ell+m)!}C_{m,c}^{[2\ell]}(z)\rho^{2\ell+m}\,.\end{aligned} \tag{38}$$

The x and the y component can be written as follows

$$\begin{aligned}\widehat{A}_x^{\widetilde{m},s} &= \cos(\widetilde{m}\,\theta)\sum_{\ell=0}^{\infty}\frac{(-1)^{\ell}\widetilde{m}!}{2^{2\ell}\ell!(\ell+\widetilde{m})!}B_{\widetilde{m},s}^{[2\ell]}(z)\rho^{2\ell+\widetilde{m}}\,;\\ \widehat{A}_x^{\widetilde{m},c} &= \sin(\widetilde{m}\,\theta)\sum_{\ell=0}^{\infty}\frac{(-1)^{\ell}\widetilde{m}!}{2^{2\ell}\ell!(\ell+\widetilde{m})!}B_{\widetilde{m},c}^{[2\ell]}(z)\rho^{2\ell+\widetilde{m}}\,;\\ \widehat{A}_y^{\widetilde{m},s} &= \sin(\widetilde{m}\,\theta)\sum_{\ell=0}^{\infty}\frac{(-1)^{\ell}\widetilde{m}!}{2^{2\ell}\ell!(\ell+\widetilde{m})!}B_{\widetilde{m},s}^{[2\ell]}(z)\rho^{2\ell+\widetilde{m}}\,;\\ \widehat{A}_y^{\widetilde{m},c} &= -\cos(\widetilde{m}\,\theta)\sum_{\ell=0}^{\infty}\frac{(-1)^{\ell}\widetilde{m}!}{2^{2\ell}\ell!(\ell+\widetilde{m})!}B_{\widetilde{m},c}^{[2\ell]}(z)\rho^{2\ell+\widetilde{m}}\,,\end{aligned} \tag{39}$$

where $\widetilde{m}=m+1$ and

$$\begin{aligned}B_{\widetilde{m},s}^{[2\ell]}(z) &= \frac{1}{2\widetilde{m}}\,C_{\widetilde{m}-1,s}^{[2\ell+1]}(z)\,;\\ B_{\widetilde{m},c}^{[2\ell]}(z) &= -\frac{1}{2\widetilde{m}}\,C_{\widetilde{m}-1,c}^{[2\ell+1]}(z)\,.\end{aligned}$$

Finally, via a gauge transformation $\bar{\boldsymbol{A}}=\widehat{\boldsymbol{A}}+\nabla\lambda$, a new form of the vector potential can be derived, such that $\bar{A}_x\equiv 0$. The derivation of this so called horizontal-free Coulomb gauge is described in detail [9] and summarized in the following. As it will be shown later in this section, the property $\bar{A}_x\equiv 0$ implies that using this representation for the vector potential leads to a significant reduction in the computational cost of each right hand side evaluation in the numerical solution of system (26).

Notice that a gauge transformation is equivalent to a canonical transformation, see e.g. [18]. In particular, if we consider a Hamiltonian $\mathcal{K}$, similar to (23), with vector potential $\boldsymbol{A}$ and dynamical variables $\boldsymbol{q}$ and $\boldsymbol{p}$ then, using a new vector potential $\boldsymbol{A}'=\boldsymbol{A}+\nabla\lambda$ we obtain a Hamiltonian $\mathcal{K}'$ in the same form of $\mathcal{K}$ with dynamical variables:

$$\begin{aligned}\boldsymbol{Q} &= \boldsymbol{q}\,;\\ \boldsymbol{P} &= \boldsymbol{p}+Q\nabla\lambda\,,\end{aligned} \tag{40}$$

where Q denotes again the particle charge. To derive the horizontal free Coulomb gauge transformation, we build a harmonic function

λ as

$$\lambda = \sum_{m=0}^{\infty} \left[\sin(m\theta)\lambda_{m,c} + \cos(m\theta)\lambda_{m,s} \right], \tag{41}$$

where

$$\lambda_{m,c} = \sum_{\ell=0}^{\infty} \frac{(-1)^{\ell} m!}{2^{2\ell}\ell!(\ell+m)!} L_{m,c}^{[2\ell]}(z)\rho^{2\ell+m},$$

$$\lambda_{m,s} = \sum_{\ell=0}^{\infty} \frac{(-1)^{\ell} m!}{2^{2\ell}\ell!(\ell+m)!} L_{m,s}^{[2\ell]}(z)\rho^{2\ell+m},$$

and the coefficients $L_{m,s/c}^{[2\ell]}(z)$ are related to the coefficients $C_{m,s/c}^{[2\ell]}(z)$ by the following relations

$$\begin{aligned} L_{m+1,s}^{[2\ell]}(z) &= \frac{1}{m+1}\left[\frac{1}{4m} L_{m-1,s}^{[2\ell+2]}(z) - B_{m,s}^{[2\ell]}(z)\right] \\ L_{m+1,c}^{[2\ell]}(z) &= \frac{1}{m+1}\left[\frac{1}{4m} L_{m-1,c}^{[2\ell+2]}(z) - B_{m,c}^{[2\ell]}(z)\right] \end{aligned} \tag{42}$$

and $L_{m,s/c}^{[0]}(z) \equiv 0$ for $m \leq 2$. It is possible to show that $\partial_x \lambda_{s/c} = -\widehat{A}_x^{s/c}$ leading to the desired horizontal-free Coulomb gauge:

$$\begin{aligned} &\bar{A}_x^s = 0 \quad \bar{A}_x^c = 0\,; \\ &\bar{A}_y^s = \widehat{A}_y^s + \partial_y \lambda_s\,; \\ &\bar{A}_y^c = \widehat{A}_y^c + \partial_y \lambda_c\,; \\ &\bar{A}_z^s = \widehat{A}_z^s + \partial_z \lambda_s\,; \\ &\bar{A}_z^c = \widehat{A}_z^c + \partial_z \lambda_c\,, \end{aligned} \tag{43}$$

where

$$\begin{aligned} \partial_y \lambda_{m,c} = &-\sum_{\ell=0}^{\infty} \frac{(-1)^{\ell}}{2^{2\ell}\ell!(\ell+m)!} \left\{ (m+1) L_{m+1,c}^{[2\ell]} + \frac{1}{4m} L_{m-1,c}^{[2\ell+2]} \right\} \\ &\times \rho^{2\ell+m} \cos(m\theta)\,; \\ \partial_y \lambda_{m,s} = &-\sum_{\ell=0}^{\infty} \frac{(-1)^{\ell}}{2^{2\ell}\ell!(\ell+m)!} \left\{ (m+1) L_{m+1,s}^{[2\ell]} + \frac{1}{4m} L_{m-1,s}^{[2\ell+2]} \right\} \\ &\times \rho^{2\ell+m} \sin(m\theta)\,, \end{aligned} \tag{44}$$

and $\partial_z \lambda$ is obtained from (41):

$$\begin{aligned} \partial_z \lambda = &\sum_{m=0}^{\infty} \sin(m\theta) \sum_{\ell=0}^{\infty} \frac{(-1)^{\ell} m!}{2^{2\ell}\ell!(\ell+m)!} L_{m,c}^{[2\ell+1]}(z)\rho^{2\ell+m} \\ &+ \sum_{m=0}^{\infty} \cos(m\theta) \sum_{\ell=0}^{\infty} \frac{(-1)^{\ell} m!}{2^{2\ell}\ell!(\ell+m)!} L_{m,s}^{[2\ell+1]}(z)\rho^{2\ell+m}\,. \end{aligned} \tag{45}$$

All the previous vector potential descriptions, when expressed in Cartesian coordinates, take the form

$$\boldsymbol{A}(x, y, z) = \sum_{i,j} \boldsymbol{a}_{i,j}(z)\, x^i y^j\,, \tag{46}$$

where the coefficients $\boldsymbol{a}_{i,j}(z)$ depend on the longitudinal coordinate z. In practical cases, the series expansions in the previous formulae are truncated to a finite number of terms, which depends on the number of harmonics used to describe the field, while the maximum number of generalized gradients derivatives ND determines the range of the indices i and j in (46). Therefore, for a given $z = \widehat{z}$ value, the evaluation time of (46) is proportional to the number of coefficients $\boldsymbol{a}_{i,j}(\widehat{z})$ retained, which can therefore be used to estimate the computational cost entailed by each representation.

Table 1
Number of vector potential coefficients using the harmonics $m \in \{2, 6, 10, 14\}$, for different gauges and number of generalized gradients derivatives.

		ND = 2		ND = 16	
		Normal	Skew	Normal	Skew
A_x	AF	20	16	112	105
	HFC	0	0	0	0
A_y	AF	20	16	112	105
	HFC	20	20	119	112
A_z	AF	40	36	128	120
	HFC	44	32	135	113
TOT	AF	80	68	352	330
	HFC	64	52	254	225
	HFC/AF	0.80	0.76	0.72	0.68

Table 2
Number of function evaluation for each vector potential component (left) and ratio of function evaluations between horizontal free Coulomb gauge (HFC) and azimuthal free gauge (AF), for standard symplectic methods (first row) and Lie algebra based methods (second row). Numbers refer to the case of harmonics $m \in \{2, 6, 10, 14\}$ and $ND = 16$ generalized gradient derivatives.

	Number of evaluations			Ratio HFC/AF	
	A_x	A_y	A_z	Norm	Skew
$\boldsymbol{J}\nabla\mathcal{K}$	3	3	2	0.666	0.646
$\mathcal{M}_2$	8	4	4	0.539	0.517

Using the horizontal-free gauge, all the terms in the previous series expansions corresponding to the x component of the vector potential are null, while the number of terms corresponding to the other two components is similar in the Coulomb and horizontal free gauges. A possible set of harmonics which describe the field of a quadrupole is $m \in \{2, 6, 10, 14\}$. The number of coefficients required by the magnetic vector potential at a specific z location, in different gauges, using such set of harmonics and different generalized gradient derivatives are shown in Table 1.

It can be noticed that the horizontal-free Coulomb gauge requires in general between 20% and 25% less coefficients with respect to the azimuthal-free gauge.

The effective reduction in computational cost achievable by this reformulation is however dependent on the specific features of each numerical method. Indeed, Runge–Kutta methods require the evaluation of the right hand side of Hamilton equations $\boldsymbol{J}\nabla\mathcal{K}$, while Lie methods evaluate the map $\mathcal{M}_2$. Therefore, the speed-up of Runge–Kutta and Lie methods, achieved with the different gauges, is related to the number of vector potential coefficients required by $\boldsymbol{J}\nabla\mathcal{K}$ and $\mathcal{M}_2$, respectively. In Table 2, the number of evaluations of each vector potential component required by $\boldsymbol{J}\nabla\mathcal{K}$ and by $\mathcal{M}_2$ are shown. Moreover, in the last columns, the ratios between the number of vector potential coefficients using the horizontal-free Coulomb gauge and the azimuthal-free gauge are shown, when considering harmonics $m \in \{2, 6, 10, 14\}$ and $ND = 16$. It can be noticed that the map $\mathcal{M}_2$, and therefore Lie methods, benefit more from the change of gauge, because they require more evaluations of the A_x component. The overall efficiency of each method also depends on the total number of evaluations of $\boldsymbol{J}\nabla\mathcal{K}$ or $\mathcal{M}_2$ required at each step. These are reported in Table 3. Moreover, it is important to notice that implicit methods require a certain number of fixed point iterations, between 5 and 8, that increase significantly their computational cost per time step. For a comprehensive efficiency comparison, the total computational cost of each method must be compared to the accuracy level it allows to achieve and to the accuracy level that is actually required for accelerator design. This comparison will be attempted in Sections 5 and 6.

In the following sections, only normal quadrupoles will be considered (i.e. with null skew generalized gradients), so that the notation will be simplified using $C_m^{[n]}$ instead of $C_{m,s}^{[n]}$.

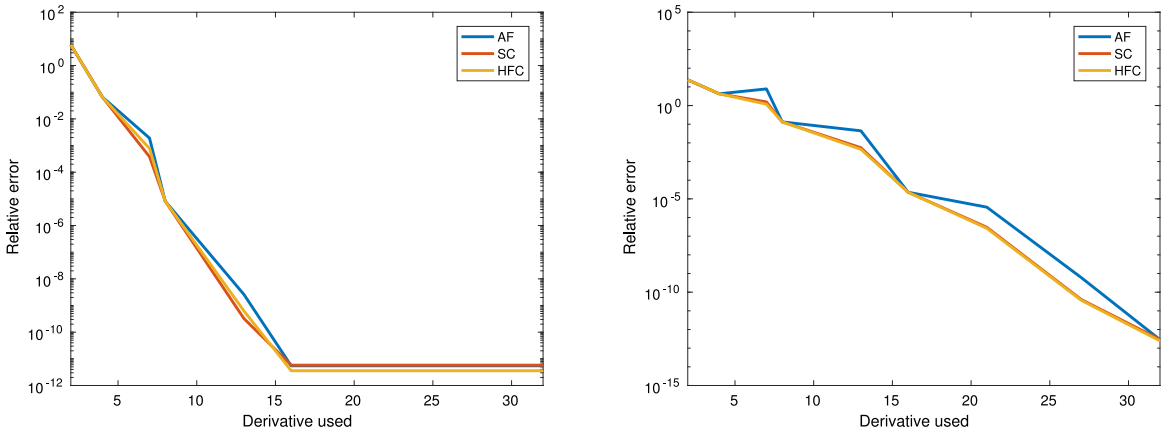

Fig. 1. Relative error in the Maxwell equation with respect to the number of generalized gradient derivatives used. Positions $(X_0, Y_0) = (0, 0.01)$ (left) and $(X_0, Y_0) = (0, 0.04)$ (right). Second order harmonic B_2 of realistic case (Section 6).

Table 3
Number of evaluations of $\boldsymbol{J}\nabla\mathcal{K}$ or $\mathcal{M}_2$ required by each numerical method. N_{fp} denotes the number of fixed point iterations required by implicit methods.

	$\boldsymbol{J}\nabla\mathcal{K}$	$\mathcal{M}_2$
midPoint	$1 \cdot N_{fp}$	
rk4	4	
gauss4	$2 \cdot N_{fp}$	
gauss6	$3 \cdot N_{fp}$	
lie2		1
lie4		3
lie6		9

A final remark concerns one important consequence of the previously introduced vector potential representation. The vector potential expressions (37), (38) and (43) are truncated at a finite number of terms ND. As a consequence, many equations that the vector potential should satisfy only hold up to terms associated to the first generalized gradient derivatives that have been neglected, i.e. $C^{[ND+1]}_{m,s/c}(z)$. If ND is an even number, all the vector potential gauges produce exactly the same magnetic field, which satisfies the Maxwell equation

$$\nabla \times \nabla \times \boldsymbol{A} = \boldsymbol{j}^{SP} ,$$

where $\boldsymbol{j}^{SP}$ is a spurious current that depends on the generalized gradients only through the generalized gradient derivatives of order $ND+1$. This implies that, generally, the largest contributions to these currents will be concentrated in the fringe field. For example, using only two derivatives of $C_2^{[0]}(Z)$, the spurious currents are:

$$\boldsymbol{j}^{SP} = \begin{bmatrix} \frac{1}{6}\left(X^3 - 3X\,Y^2\right)C_2^{[3]}(Z) \\ -\frac{1}{6}\left(Y^3 + 3Y\,X^2\right)C_2^{[3]}(Z) \\ 0 \end{bmatrix} . \tag{47}$$

The magnitude of this error can be measured using the following quantity:

$$\frac{\max_Z\left(\|\nabla \times \nabla \times \boldsymbol{A}(X_0,\, Y_0,\, Z)\|_2\right)}{\max_Z\left(\|\boldsymbol{A}(X_0,\, Y_0,\, Z)\|_2\right)} , \tag{48}$$

where (X_0, Y_0) refers to a fixed position in the transversal plane. In Fig. 1, we show the behaviour of the error (48) for two different transversal positions, one closer to the quadrupole axis and another further away. The results refer to vector potentials in different gauges, computed considering a second order harmonic B_2 coming from a realistic design of a quadrupole (see Section 6). It can be noticed that the error in the different gauges coincides if ND is an even number, coherently with the fact that the magnetic fields are identical. Furthermore, the error is larger at locations further from the quadrupole centre and reaches a saturation level when a sufficiently large number of generalized gradient derivatives are used. It is unclear to which extent this approximation error, which is far from negligible at larger distances from the quadrupole axis, entails a limitation for the accuracy that tracking algorithms can achieve. Mimetic methods like those presented in [13] guarantee that a discrete equivalent of $\nabla \times \nabla \times \boldsymbol{A} = 0$ is exactly satisfied, so that they could represent a potentially interesting alternative to the techniques described in this section.

As a final remark we notice that, in the use of Eq. (35), particular attention has to be devoted to the computation of the input harmonics. If harmonics that do not go to zero sufficiently fast at the boundaries are employed, significant errors in the field description may result. For example, even if the harmonics vanish at the boundaries, the computed generalized gradients, and thus the vector potential, may not vanish as well, causing a discrepancy between the canonical and the mechanical momenta in a region where they should coincide. In our experience, these issues can be avoided by appropriate extension of the harmonics data by sufficiently large regions filled with zero values.

5. Numerical experiments with an analytic magnetic vector potential

In this section, Eqs. (26) will be solved for the case of a simple vector potential, whose expression is given by a polynomial with just a few nonzero coefficients. It is important to notice that this configuration is not completely realistic, since this vector potential does not exactly satisfy the Maxwell equation $\nabla \times \nabla \times \boldsymbol{A} = 0$. As discussed in the previous section, this leads to spurious residual currents on the right hand side of this equation, which are however not accounted for in Eqs. (26). In spite of this inconsistency, this benchmark is useful to assess the impact of the interpolation procedure mentioned in Section 3, since the simple analytic expression can also be computed cheaply online and comparison between results obtained with and without interpolation can be carried out.

A set of scaled vector potentials in different gauges is built using Eqs. (37), (38) and (43) and employing only the $C_2^{[0]}(Z)$ function defined as follows. We first set

$$\sigma(x) = \begin{cases} 0 & x \in (-\infty, -1] \\ \frac{1}{2}\left[1 + \mathrm{erf}\left(\tan\frac{\pi}{2}\,x\right)\right] & x \in (-1, 1) \\ 1 & x \in [1, +\infty) \end{cases} \tag{49}$$

where erf denotes the error function, defined as

$$\mathrm{erf}\,(x) = \frac{2}{\sqrt{\pi}}\int_0^x e^{-t^2}\mathrm{d}t .$$

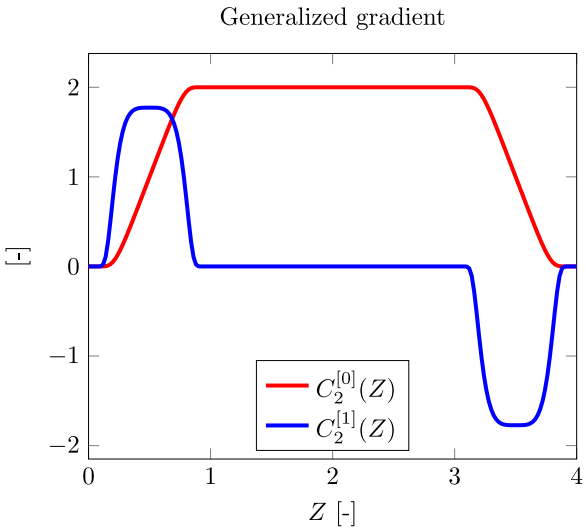

Fig. 2. Analytic generalized gradient and its derivative.

Using (49), the function $C_2^{[0]}(Z)$ is then defined as

$$C_2^{[0]}(Z) = \begin{cases} \alpha \left[\sigma\left(-1 + 2\,\dfrac{Z}{L_1}\right) \right. \\ \quad \left. + \sigma\left(1 - 2\,\dfrac{Z - Z_2}{L_2}\right) \right] - \alpha & Z \in (0,\ Z_{MAX}) \\ 0 & \text{otherwise.} \end{cases} \tag{50}$$

Here, the coefficient α is the plateau value of $C_2^{[0]}(Z)$, Z_{MAX} denotes the total field length, L_1, L_2 are the widths of the regions in which the field is not constant and Z_2 denotes the location of the second of these regions, the first being located at $Z = 0$ (see Fig. 2). In this work, the value α in (50) has been chosen equal to $6 \cdot 10^{-4}$ with $L_1 = L_2 = 0.9$ and $Z_2 = 3.1$. The initial conditions for the transversal positions and momenta of the particle are set to $\boldsymbol{w}_0 = (0.02,\ -0.04,\ 0,\ 0)$ and $\delta_0 = 0$. A reference solution is computed using the exact vector potential and the MATLAB ODE solver `ode45` with a maximum $\Delta Z^{ref} = \Delta Z^{data}/10$ and a relative error tolerance of 10^{-13}.

In Fig. 3, the errors obtained with the different ODE methods are presented, in the case in which no interpolation is used and the magnetic vector potential is computed exactly at each required location. The errors on the X, Y coordinates behave very similarly and the same is true for the corresponding moments, but the errors on transversal momenta are larger than those on positions. As long as the errors are above the tolerance chosen for the reference solution, both second and fourth order solvers behave in agreement with theoretical expectations, while sixth order solvers only seem to display the expected error decay for sufficiently small values of the interval ΔZ. Furthermore, very similar errors are obtained for second and fourth order methods for the largest ΔZ employed. We attribute these facts to the poor resolution of the larger gradient areas at the beginning and at the end of the idealized quadrupole. This effect can also be seen in the numerical results of Section 6. It gives a clear indication that there is an upper limit to the value ΔZ that can be employed, independently of the accuracy of the solver employed.

In order to study the impact of different interpolation techniques in the more realistic case in which the vector potential is only available as sampled data, the analytic vector potential obtained from (50) is sampled on a fine mesh with $\Delta Z^{data} = 0.002$ over the interval $[0, 4]$. For each given position along the Z axis where the vector potential is not available, we employ (a) the value at the last previously available gridded location (`previous`), (b) the value at the nearest gridded location available (`nearest`), (c) the average of the nearest available potential values (`interval`) (d) a cubic spline interpolation (`spline`). The results of this comparison are reported in Fig. 4. Only results obtained with the sixth-order Gauss method are displayed, since the highest order methods are those most affected by the accuracy of the field interpolation. It can be noticed that all interpolation methods limit the overall accuracy of the time integrator, to a larger or lesser extent. Ideally, an interpolator of the same order of the time integration method should be employed. On the other hand, spline interpolation seems to be sufficient to achieve errors comparable to those of the exact potential evaluation in most cases.

In order to compare the efficiencies of the methods employed, we report in Fig. 5 the behaviour of the error as a function of the CPU time required by each method for a given resolution. Since the interpolation stage is done off-line, the CPU time required does not depend on the interpolation method employed. Among the ODE methods, the fourth-order explicit Runge–Kutta method gives the best results, followed by the sixth-order Gauss method and the fourth-order Lie method. Among the symplectic methods, the fastest method is the second-order Lie one, but it has a relatively low accuracy.

As mentioned in the introduction, the beam stability assessment requires long-term simulations. In order to verify the solution quality in this framework, the phase-space orbits of a particle which travels through a sequence of focusing–defocusing quadrupole couples are measured. This test is carried out considering a sequence of 3000 consecutive quadrupole couples and an integration step of $\Delta Z = 0.08$. All the numerical methods produced stable orbits in this test. As an example, in Fig. 6 the results for the fourth-order Lie method are reported. Remarkably, the non-symplectic fourth-order Runge–Kutta method gives results entirely analogous to those of the other (symplectic) methods considered, see Fig. 7.

6. Numerical experiments with a realistic vector potential

In this section, Eqs. (26) will be solved for the case of a magnetic vector potential that corresponds to the design of a realistic quadrupole. The harmonics $m = 2, 6, 10, 14$, at a radius of analysis of 0.05 and sampled at $\Delta Z^{data} = 0.02$ (Fig. 8) are provided by numerical simulations performed by the FEM/BEM software ROXIE [19], developed at CERN to design the accelerator magnets. The presence of connectors on one side of the quadrupole causes asymmetries in the harmonics along the Z axis and the presence of skew harmonics. The generalized gradients are computed using up to 16 derivatives. We will consider the case of a particle quite far from the quadrupole axis: indeed, the initial conditions for the transversal positions and momenta are set to $\boldsymbol{w}_0 = (0.02,\ -0.04,\ 0,\ 0)$ and $\delta_0 = 0$. Using the horizontal-free Coulomb gauge, we obtain a gain in efficiency quite in agreement with the estimates given in Section 4, see Tables 4 and 5. In the following, only the results with the horizontal-free Coulomb gauge and using cubic spline interpolation of gridded data are reported.

The error comparisons are shown in Fig. 9. In order to measure the methods' accuracy, the absolute error on the positions and the momenta at the quadrupole exit are used, because these values are useful to understand if the nonlinear effects, mentioned in the introduction, can be described correctly. The trend is similar to those seen in the previous sections, but with a general worsening in accuracy. The longer integration steps imply that the fringe field region is not sampled in a sufficiently accurate way, thus

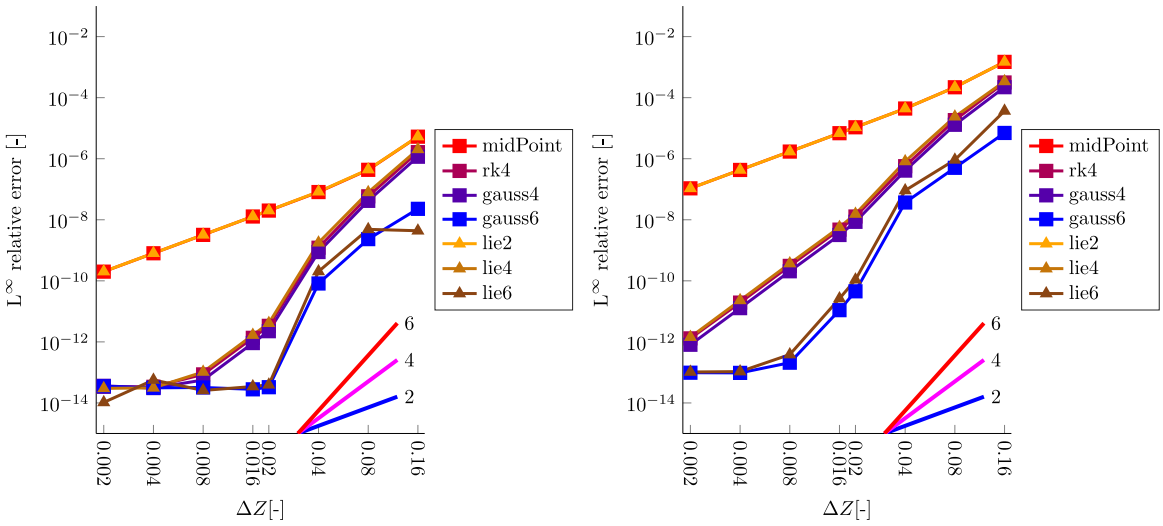

Fig. 3. Test case with analytically defined vector potential. Convergence behaviour in the l_∞ norm of different ODE methods for X (left) and P_y (right) when exact vector potential values are employed at all intermediate steps. The straight lines in the bottom right corner denote theoretical slopes for different convergence orders.

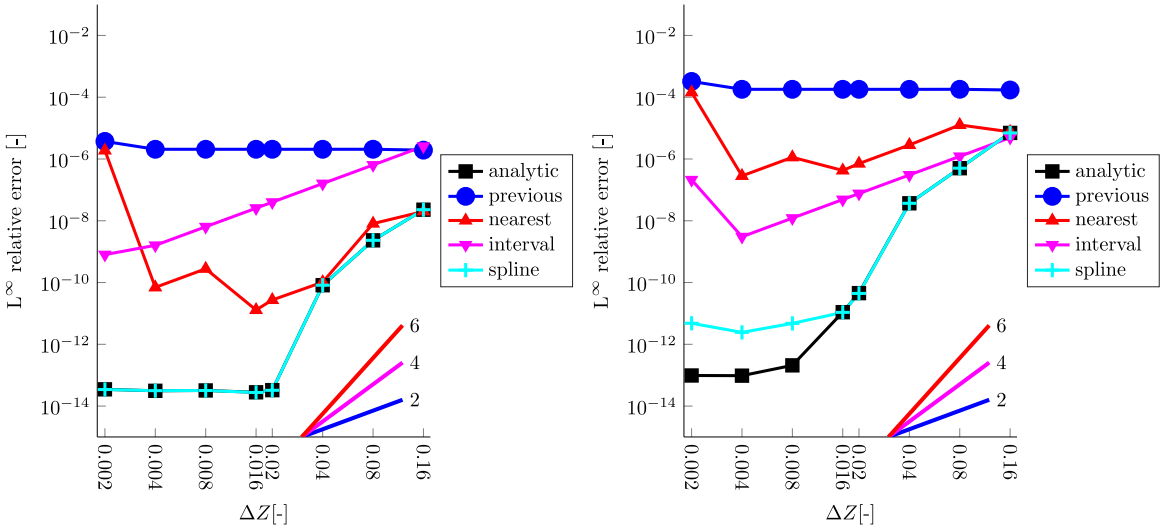

Fig. 4. Test case with analytically defined vector potential. Convergence behaviour in the l_∞ norm of different ODE methods for X (left) and P_y (right) when reconstructed vector potential values are employed at all intermediate steps. The straight lines in the bottom right corner denote theoretical slopes for different convergence orders.

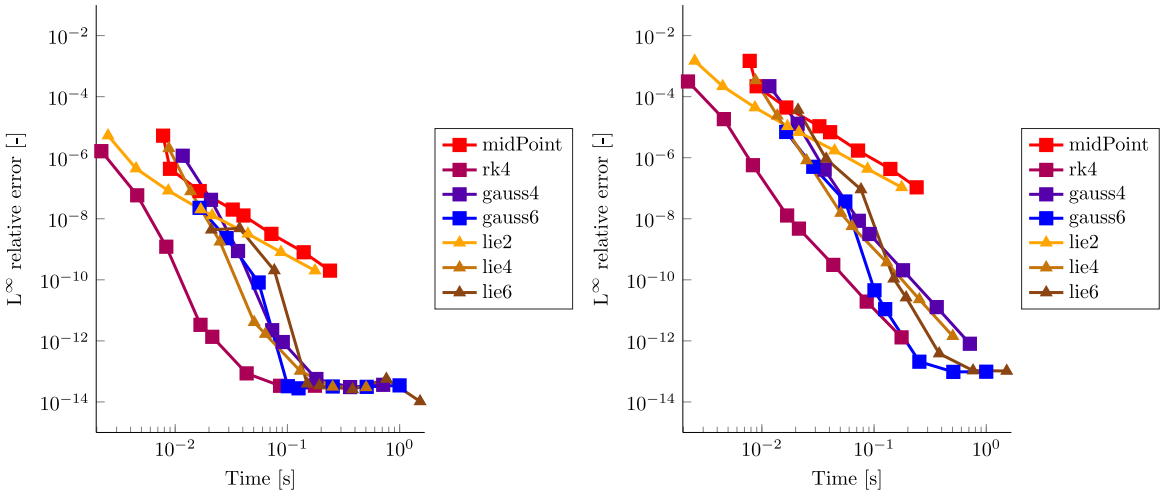

Fig. 5. Analytic case, no interpolation. Efficiency comparison between ODE methods for X (left) and P_y (right).

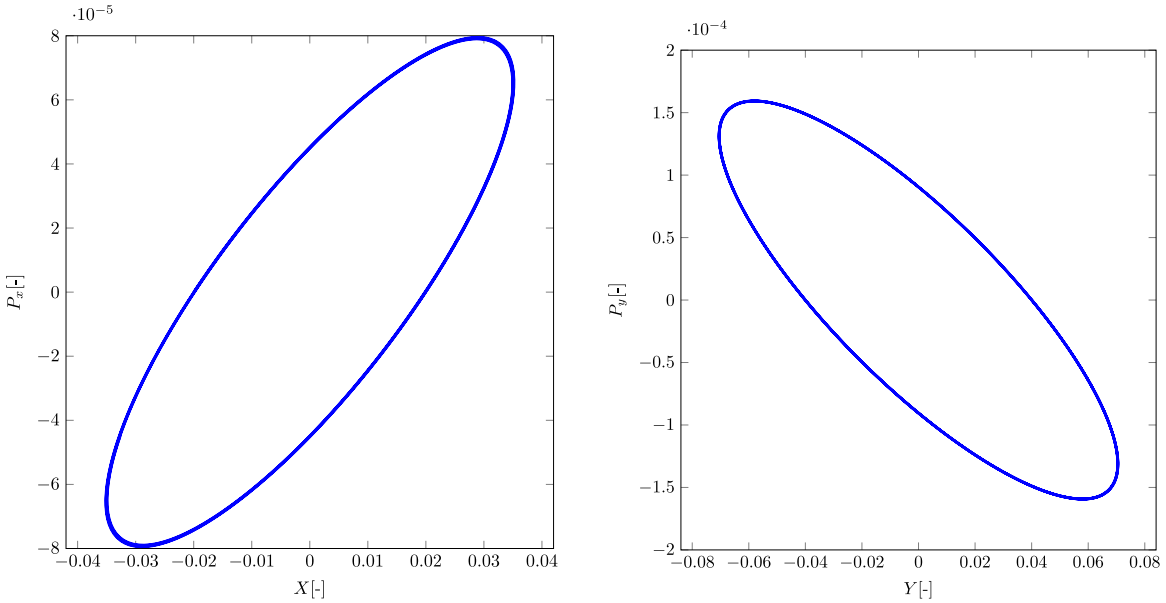

Fig. 6. Analytic case, cubic spline interpolation. Phase-space trajectories in the (X, P_x) (left) and (Y, P_y) (right) planes, $X_0 = -0.02$, $Y_0 = 0.04$. Fourth-order Lie method.

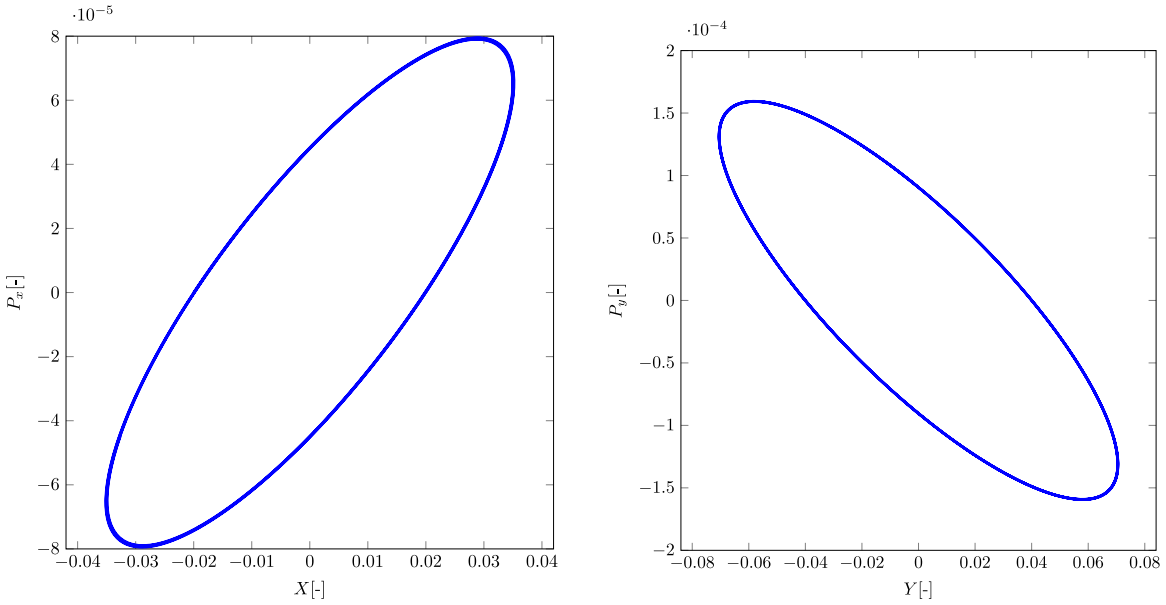

Fig. 7. Analytic case, cubic spline interpolation. Phase-space trajectories in the (X, P_x) (left) and (Y, P_y) (right) planes, $X_0 = -0.02$, $Y_0 = 0.04$. Fourth-order explicit Runge–Kutta method.

Table 4
Realistic case. CPU time and speed-up obtained using different vector potential gauges and the fourth-order explicit Runge–Kutta method.

ΔZ [–]	Time [s]		Ratio [–]
	AF	HFC	HFC/AF
0.02	0.0599	0.0341	0.5704
0.04	0.0271	0.0166	0.6131
0.08	0.0133	0.0084	0.6348
0.16	0.0071	0.0043	0.6041
Average			**0.606**

Table 5
Realistic case. CPU time and speed-up obtained using different vector potential gauges and the fourth-order Lie method.

ΔZ [–]	Time [s]		Ratio [–]
	AF	HFC	HFC/AF
0.02	0.0966	0.0548	0.5680
0.04	0.0474	0.0256	0.5401
0.08	0.0241	0.0132	0.5477
0.16	0.0118	0.0068	0.5726
Average			**0.557**

preventing the correct description of the field and the achievement of the theoretical convergence orders for the numerical methods. The final error drop in the high-order methods can be due to the fact that the reference solution has been computed using the same starting vector potential data and only a finer mesh of interpolated values. In order to compare the efficiencies of the methods employed, we plot in Fig. 10 the behaviour of the error as a function of the CPU time required by each method for a given resolution.

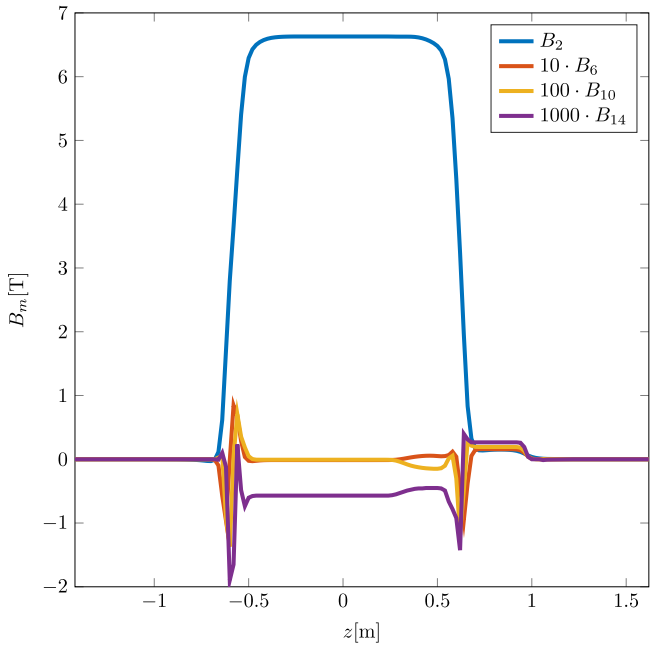

Fig. 8. Realistic case. Normal harmonics sampled at $\Delta z^{data} = 0.02$ m. Courtesy of E. Todesco and S. Izquierdo Bermudez.

In this case, as discussed before, the large ΔZ^{data} of the input data limits the possibility of achieving high accuracies, therefore there is no clear advantage in the use of high order methods and the second-order Lie method is the most efficient.

Finally, we check the beam stability looking at the phase-space orbits of a particle which travels through a sequence of focusing–defocusing quadrupole couples. This test is carried out considering a sequence of 24 000 consecutive quadrupole couples and an integration step of $\Delta Z = 0.04$. In this case it is possible to notice, see Figs. 11 and 12, that the numerically approximated trajectories, rather than identifying a well defined orbit, span a wide region in the (X, P_x) phase space.

We attribute this inaccuracy to the numerical errors induced by evaluation of vector potential polynomial terms with high degree, which result from using various harmonics and many generalized gradient derivatives. In fact, using only the second order harmonic and two generalized gradient derivatives (Fig. 13), or considering a motion closer to the quadrupole axis (Fig. 14), where the high degree polynomial terms are less important, it is possible to obtain stable orbits similar to the ones obtained in the analytical case presented in Section 5. It is especially noteworthy that, in spite of its lack of symplectic properties, the classical fourth order RK method does not appear to behave differently from the symplectic ones (Figs. 15 and 16).

In order to study the long term behaviour of the numerical methods, we also simulate the motion of a particle through 50 000 focusing–defocusing quadrupole pairs using an integration step

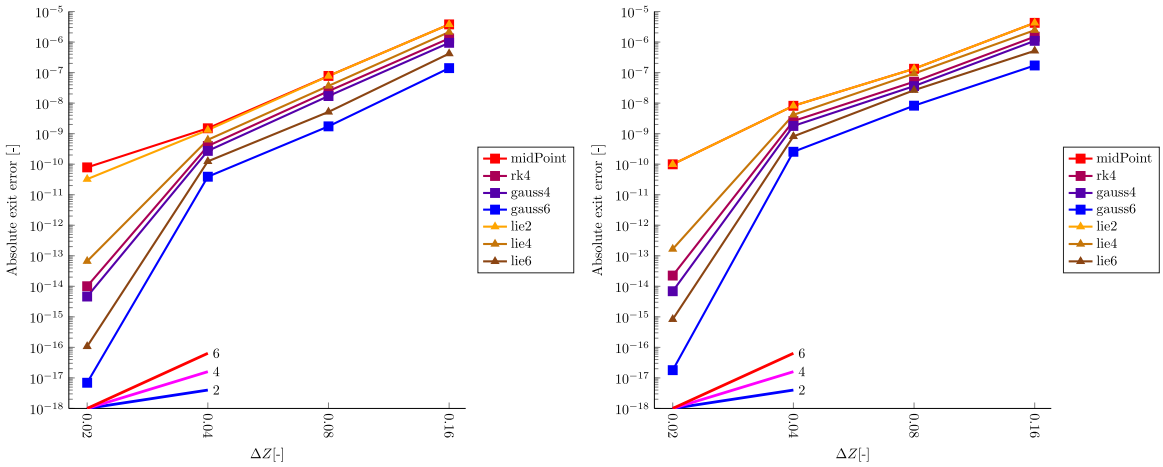

Fig. 9. Realistic case, cubic spline interpolation. Error comparison between ODE methods for X (left) and P_y (right). The straight lines in the bottom right corner correspond to the theoretical slopes of the error curves for different convergence orders.

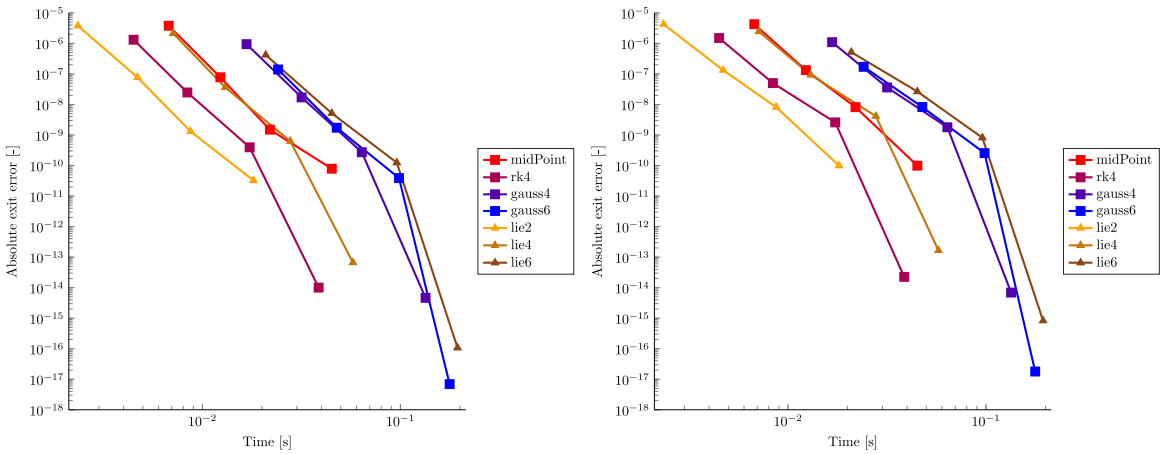

Fig. 10. Realistic case, cubic spline interpolation. Efficiency comparison between ODE methods for X (left) and P_y (right).

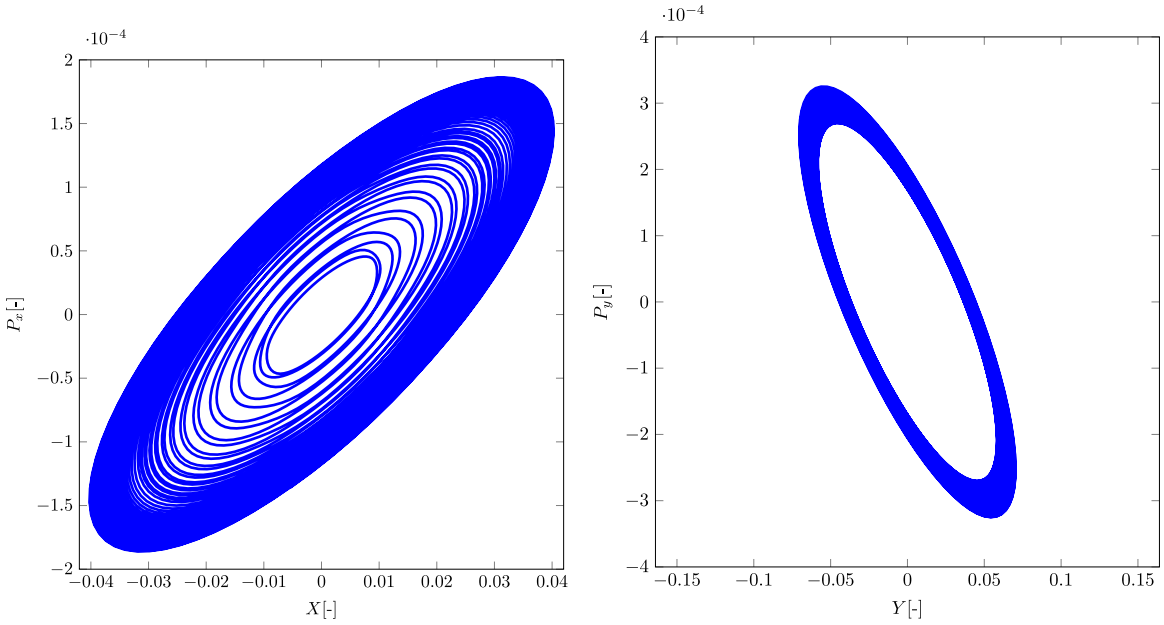

Fig. 11. Realistic case, cubic spline interpolation. Phase-space trajectories in the (X, P_x) (left) and (Y, P_y) (right) planes, $X_0 = 0.02$, $Y_0 = -0.04$. Fourth-order Lie method.

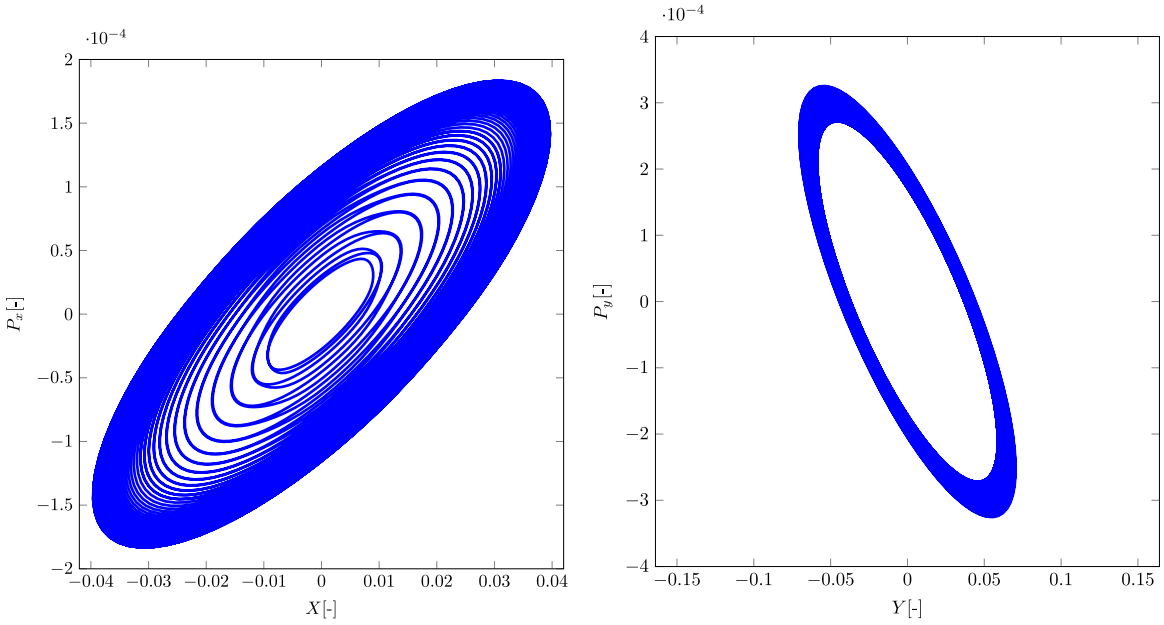

Fig. 12. Realistic case, cubic spline interpolation. Phase-space trajectories in the (X, P_x) (left) and (Y, P_y) (right) planes, $X_0 = 0.02$, $Y_0 = -0.04$. Fourth-order explicit Runge–Kutta method.

$\Delta Z = 0.04$. To check the stability of the motion, we consider the mechanical momentum P_x^M, plotted in Fig. 17 (left) for the different numerical methods. Notice that, in this and in the following plots of this section, the value of P_x^M computed at the end of the quadrupole is reported, sampling only one every 300 quadrupole couples. Similar results are obtained considering the mechanical momentum in the other transversal direction P_y^M. It can be noticed that all the methods produce the same oscillating trend. While all methods appear to compute stable orbits, the computed values of P_x^M and the resulting particle trajectories display significant differences. This can be seen better in Fig. 17 (right), where the differences with respect to the mechanical momentum computed using the reference sixth-order Gauss method are shown. In this case, it is apparent that larger deviations are obtained with the lower order methods. As in the shorter integration discussed previously, the differences in computed mechanical momentum values between the various numerical methods can be reduced either considering a particle travelling closer to the quadrupole axis, see Fig. 18 (left) or using a smaller integration step, see Fig. 18 (right). The size of the deviations of P_x^M from the reference values appears to be related more to the order of convergence of each method than to whether the specific method has symplectic properties or not.

A final test has been carried out, comparing the symplectic second and fourth-order Lie methods and the non-symplectic fourth-order Runge–Kutta method on a longer sequence of 1 500 000 focusing–defocusing quadrupole couples, using an integration step $\Delta Z = 0.04$. The results are shown in Fig. 19. In this case, the value of P_x^M computed at the end of the quadrupole is reported, sampling only one every 6000 quadrupole couples. Even in this very long integration, no unstable trends appear and the both symplectic

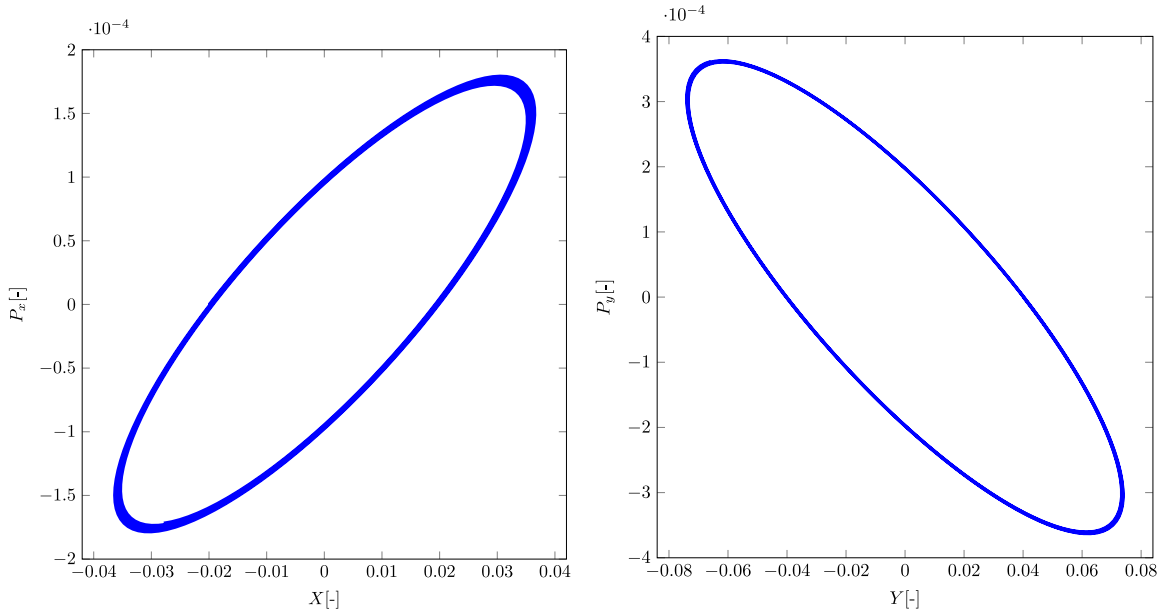

Fig. 13. Realistic case, second order harmonic, two generalized gradient derivatives, cubic spline interpolation. Phase-space trajectories in the (X, P_x) (left) and (Y, P_y) (right) planes, $X_0 = -0.02$, $Y_0 = 0.04$. Fourth-order Lie method.

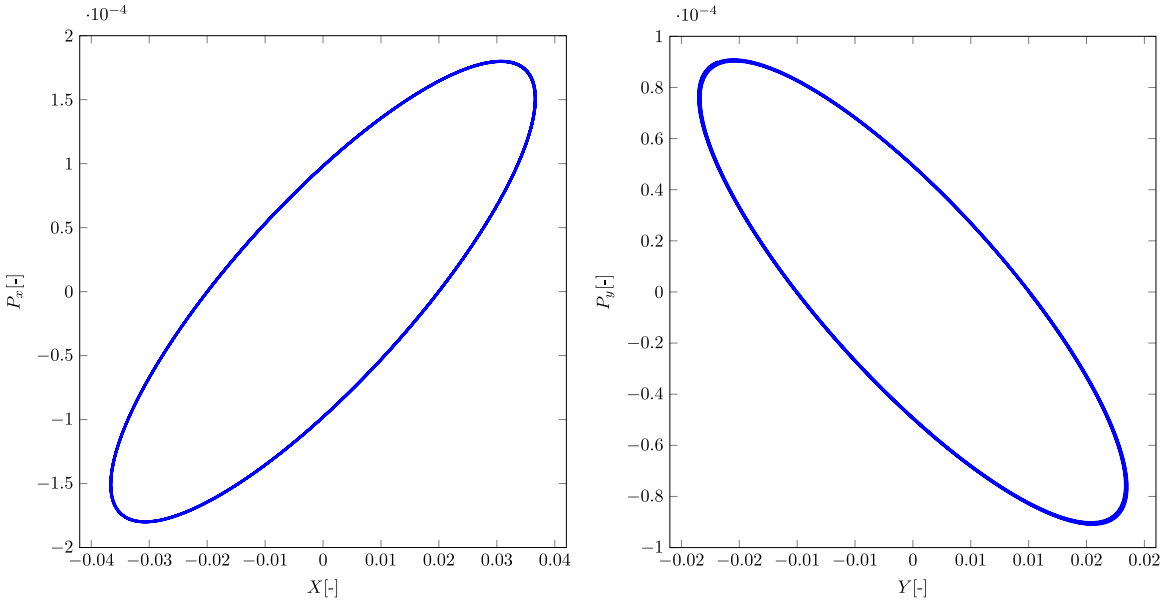

Fig. 14. Realistic case, cubic spline interpolation. Phase-space trajectories in the (X, P_x) (left) and (Y, P_y) (right) planes, $X_0 = -0.02$, $Y_0 = 0.01$. Fourth-order Lie method.

and non symplectic methods appear to behave in a qualitatively analogous fashion.

7. Nonlinear dependencies of exit positions and momenta on the initial values

The net effect of the quadrupole on charged particles crossing it can be approximately described by a linear relationship between the initial and final particle positions and momenta. Denoting quantities at the entrance of the quadrupole by the subscript *in* and quantities at the exit of the quadrupole by the subscript *out*, we can express the linear dependence as:

$$\boldsymbol{w}_{out}^{lin} = \boldsymbol{M}\, \boldsymbol{w}_{in}. \tag{51}$$

Here, $\boldsymbol{M}$ denotes a matrix computed using the slicing algorithm and thin quadrupole approximation described in [20]. Nonlinear effects are much smaller in amplitude and are mainly due to the regions in which the field is not constant in Z. In order to highlight these nonlinear effects, we compute the particle trajectories through the quadrupole and we then subtract the linear contribution determined using (51). Reference trajectories are computed by a sixth-order symplectic Gauss method with $\Delta Z = \Delta Z^{data}/10$ and cubic spline interpolation of the vector potential data (reconstructed using $ND = 16$ generalized gradient derivatives as in Section 6). In the following figures, the nonlinear trend of the reference trajectory will be represented by a purple line. We have considered again the vector potential of the realistic case of Section 6. Note that, since a reference length $L = 1$ m has been used to normalize the longitudinal coordinate z, the numerical values of Δz and ΔZ coincide. In Fig. 20, the nonlinear trend of X and P_x is shown, as computed from the reference trajectories of particles entering the quadrupole at different positions in the transversal plane and

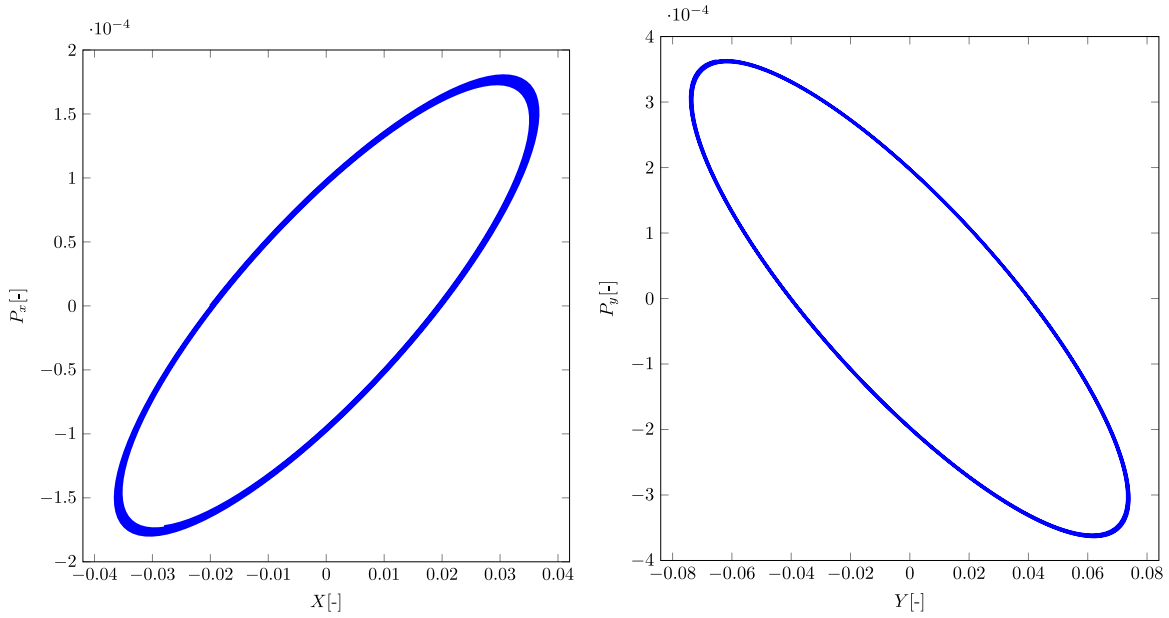

Fig. 15. Realistic case, second order harmonic, two generalized gradient derivatives, cubic spline interpolation. Phase-space trajectories in the (X, P_x) (left) and (Y, P_y) (right) planes, $X_0 = -0.02$, $Y_0 = 0.04$. Fourth-order explicit Runge–Kutta method.

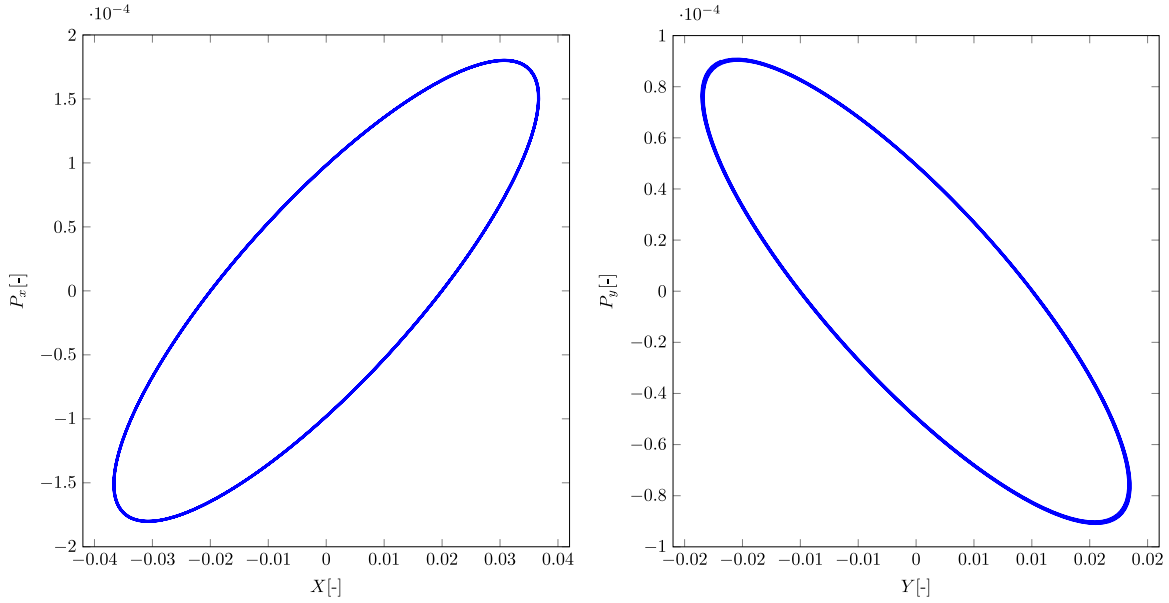

Fig. 16. Realistic case, cubic spline interpolation. Phase-space trajectories in the (X, P_x) (left) and (Y, P_y) (right) planes, $X_0 = -0.02$, $Y_0 = 0.01$. Fourth-order explicit Runge–Kutta method.

having null transversal momenta. Therefore, the particles are moving initially in a direction parallel to the longitudinal axis Z. It can be seen that the nonlinear effects are much stronger away from the quadrupole axis. Based on the previous results in this section, this is exactly the region in which the inaccuracies due to the field reconstruction procedure are most relevant. Therefore, a significant impact of the field reconstruction method on the accuracy of the approximation of nonlinear effects has to be expected for particles with initial data far from the quadrupole axis and that the shape and magnitude of the nonlinearities on the positions are different with respect to the ones on the momenta. As we will see later, this difference is due to the asymmetry of the field with respect to z.

In order to compare the various numerical methods with respect to their rendering of nonlinear effects, in the following test we then consider a set of particles whose initial positions, at the entrance of the quadrupole, are equally spaced along the Y-axis between -0.04 and 0.04 and whose initial momenta are $P_x = P_y = 0$. The nonlinear effects computed with cubic spline interpolation and second order Lie method, fourth order Lie method and fourth order Runge–Kutta method are displayed in Figs. 21–23, respectively. It can be seen that all methods converge to the reference result for decreasing ΔZ and for sufficiently small initial distances from the quadrupole axis. On the other hand, large values of the integration step result in big errors on the approximation of the nonlinear effects, thus showing again that sufficiently high resolution of the fringe field region is essential. Furthermore, as already mentioned in the discussion of Fig. 20, nonlinear effects become more relevant away from the axis and, in that region, the

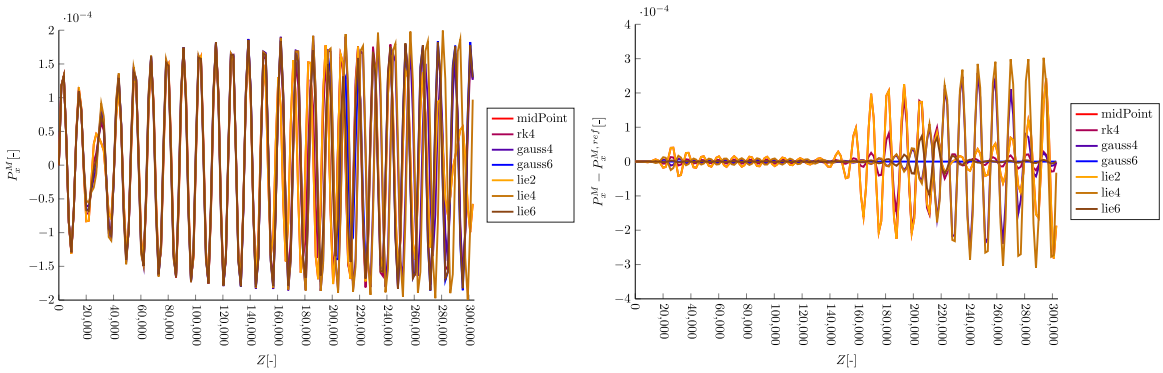

Fig. 17. Realistic case, cubic spline interpolation, 50 000 quadrupole couples, $X_0 = 0.02$, $Y_0 = -0.04$, $\Delta Z = 0.04$. Trend of P_x^M (left) and deviations of P_x^M with respect to the one computed with the sixth-order Gauss method (right) for the various numerical methods. Second-order Lie method and Midpoint method appear as superposed.

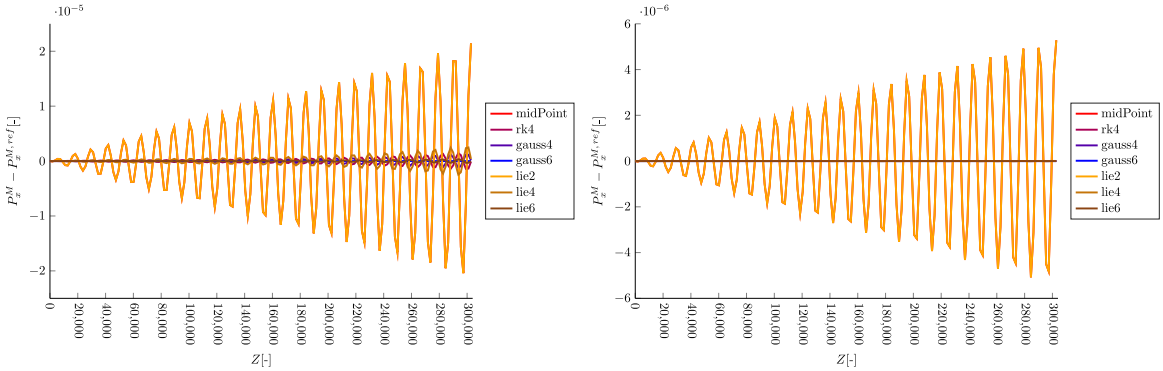

Fig. 18. Realistic case, cubic spline interpolation, 50 000 quadrupole couples, $X_0 = -0.02$, $Y_0 = 0.03$, $\Delta Z = 0.04$ (left) and $\Delta Z = 0.02$ (right). Deviations of P_x^M with respect to the one computed with the sixth-order Gauss method for the second and fourth-order Lie methods and the non-symplectic fourth-order Runge–Kutta method. Second-order Lie method and Midpoint method appear as superposed.

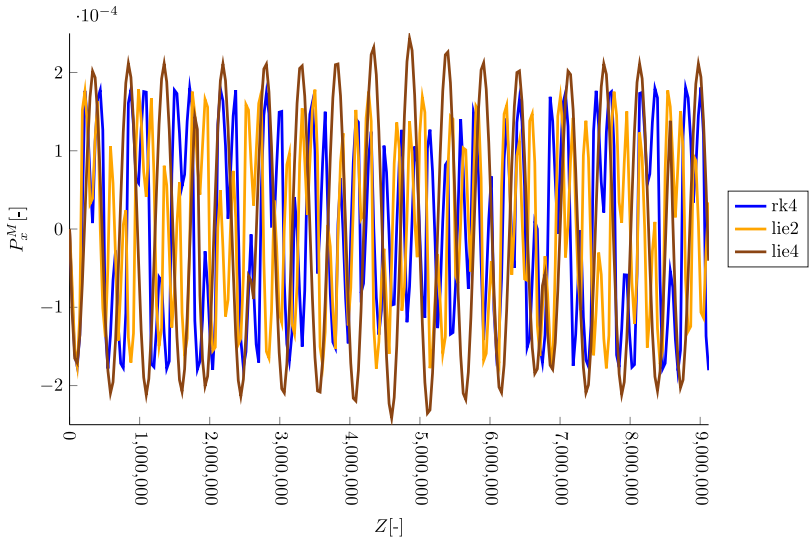

Fig. 19. Realistic case, cubic spline interpolation, $\Delta Z = 0.04$, 1 500 000 quadrupole couples, $X_0 = 0.02$, $Y_0 = -0.04$. P_x^M trend (one point each 6000 quadrupole couples) computed with second and fourth-order Lie methods and the non-symplectic fourth-order Runge–Kutta method.

quality of their approximation may suffer more from the errors on the reconstructed or interpolated field than from the error induced by the numerical integrator employed.

We then compare one of the methods used previously (specifically, the sixth order symplectic Gauss method) with the thin lens model currently used in SixTrack [6], which is based on integrated multipoles and therefore neglects the z-dependence of the field. The version of the thin lens method employed uses 500 slices. In Fig. 24, it can be seen that there is a good agreement between the two models the momentum nonlinearities, where the two lines are superposed, while the position nonlinearities are different. We attribute this difference to the asymmetry of the field in the z direction, which cannot be taken into account using integrated multipoles. Considering a set of particles starting at different positions in the transversal plane, it can be noticed that the thin model describe the position nonlinearities similarly to

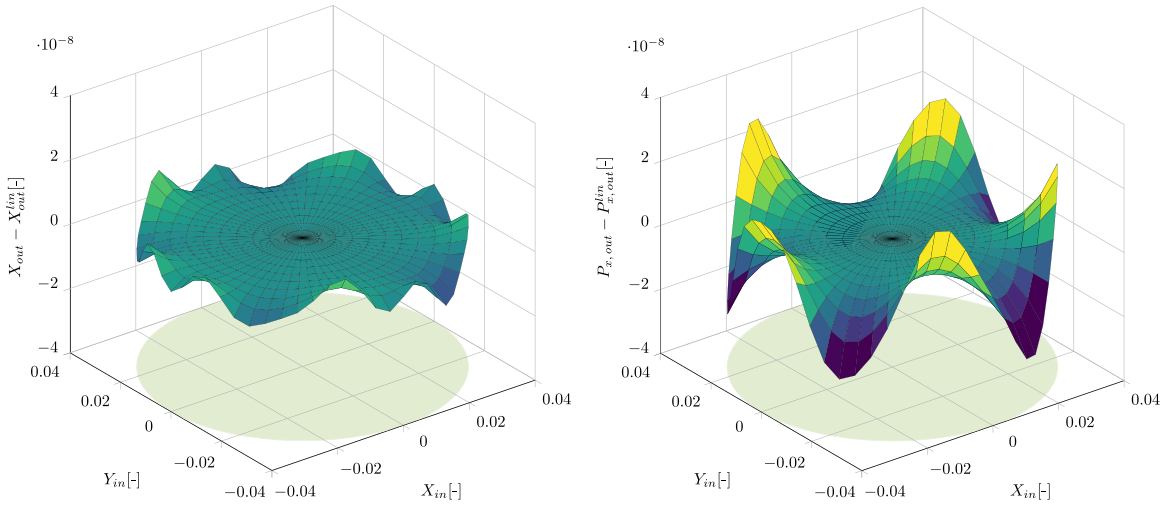

Fig. 20. Realistic case, nonlinearities of X and P_x for a set of particles starting at different positions in the transversal plane and null transversal momenta.

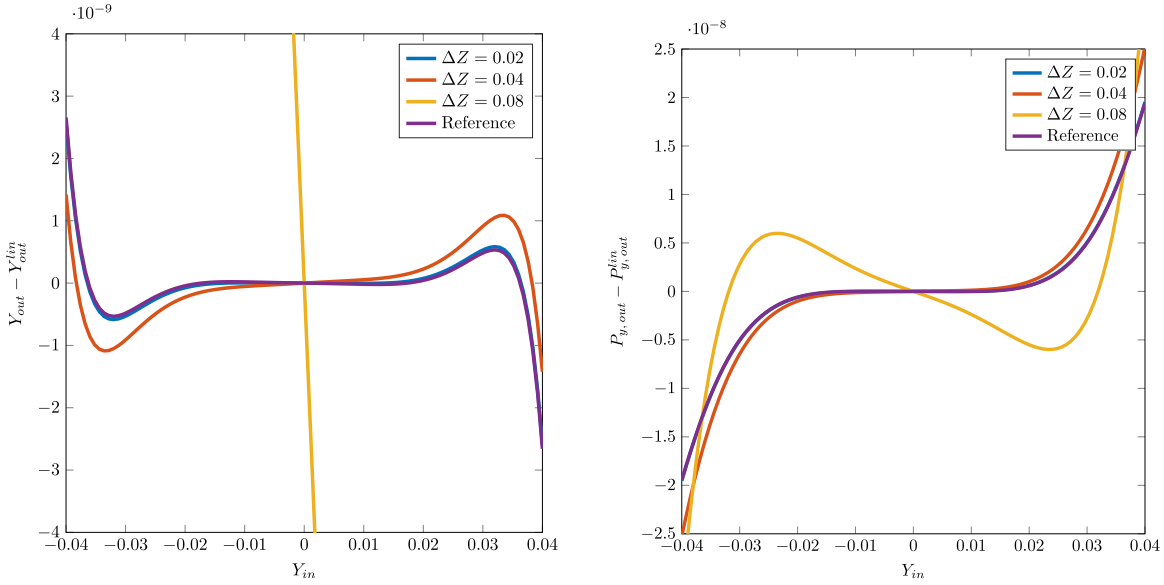

Fig. 21. Realistic case, cubic spline interpolation. Nonlinear part of positions (left) and momenta (right) computed using the second-order Lie method.

the momentum nonlinearities, whereas the ones computed by the reference method have a smaller magnitude and a more complex behaviour (see Fig. 25). If we instead consider a symmetric field, for example adding a specular quadrupole immediately after the first one, we obtain again comparable results for the position nonlinearities too, as can be seen in Fig. 26. In this latter case, where the field is symmetric and the results seem to be comparable, we can compute the differences between the two models. If we compare the maximum of the differences to the maximum of the nonlinearities, we see a difference of $\sim$ 5-10%, but the maxima correspond to different initial positions in the transversal plane, so that there is no fixed correspondence, for each entrance position, between the magnitude of the nonlinearities and the magnitude of the differences.

8. Conclusions and future developments

We have discussed and analysed several issues that arise in the numerical approximation of charged particles trajectories in magnetic quadrupoles.

We have shown that a specific gauge transformation allows to reduce by approximately 50% the computational cost of each vector potential evaluation, thus significantly enhancing the efficiency of any numerical approximation method for the trajectory simulation. The impact of the interpolation technique employed to compute magnetic vector potential values at arbitrary locations from gridded data has also been assessed, highlighting potential limitations in accuracy induced by insufficiently accurate interpolation methods, if high order time integration techniques are to be applied. However, cubic spline interpolation was found to be sufficient for preserving the accuracy of all the methods considered in this work over a wide range of values for the integration step.

We have then compared several high order integration techniques, which allow to maintain high accuracy even with relatively large integration step values, in order to assess their accuracy and efficiency for long-term simulations. Explicit high order Lie methods have been considered, along with implicit high order symplectic integrators and a more conventional, non-symplectic, explicit Runge–Kutta method. The tests presented in this work show that, for realistic vector potentials, the errors induced by the vector potential representation and interpolation become significant and reduce the highest possible accuracy that can be

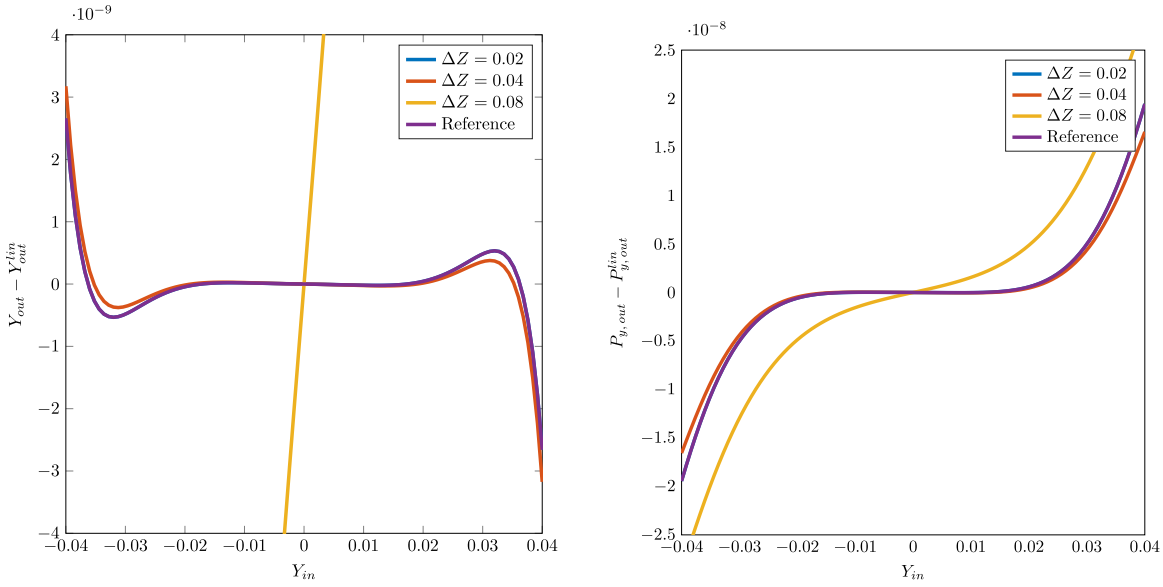

Fig. 22. Realistic case, cubic spline interpolation. Nonlinear part of positions (left) and momenta (right) computed using the fourth-order Lie method.

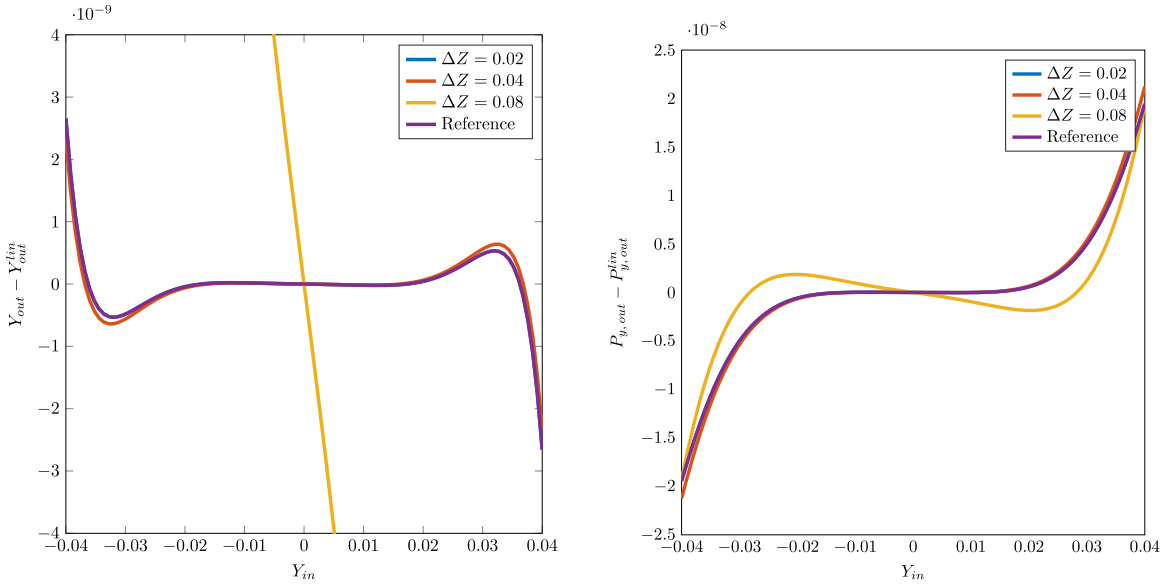

Fig. 23. Realistic case, cubic spline interpolation. Nonlinear part of positions (left) and momenta (right) computed using the fourth-order explicit Runge–Kutta method.

attained. Furthermore, since in realistic cases the magnetic vector potential evaluation is costlier, numerical methods which require less evaluations, such as the second-order Lie method, appear to be more competitive in terms of efficiency. On the other hand, if these errors could be reduced by different approaches for the vector field representation, higher order methods could be advantageous if a more precise approximation is required. The speed gain obtained by the horizontal-free Coulomb gauge would also allow to use more expensive methods. In particular, the explicit fourth-order Runge–Kutta appears to be the most efficient method and the fourth-order Lie the most efficient among symplectic methods. The results obtained also show that, for all the compared methods, even though their stability and formal accuracy properties would allow the use of large integration steps, these are to be discarded because they lead to insufficient resolution in the fringe field regions. All the methods studied in this paper yield convergent approximations of nonlinear effects, that are discarded when linear transfer maps are applied. However, the computation of these effects far from the quadrupole axis and with too large integration steps is also affected by the poor resolution of the fringe field and the errors in the vector potential reconstruction, respectively. A comparison of the results of a symplectic, high order integrator with those of the thin lens model of SixTrack showed a significant discrepancy with respect to the position nonlinearities, which can be attributed to the asymmetry of the field in the longitudinal direction z. Even when symmetric field is considered, a difference between the two models of $\sim$ 5-10% can be observed, but this difference depends on the initial position of the particle and it is not directly related to the magnitude of the nonlinear effect. As a future perspective, it is interesting to study the effect of these differences over the long-term tracking in the full accelerator.

All the computations carried out in this work used vector potential values sampled on a uniform grid along the longitudinal axis of the quadrupole. In order to increase efficiency, using vector potentials sampled over a non-uniform grid appears to be a straightforward and necessary improvement. In such way, it could

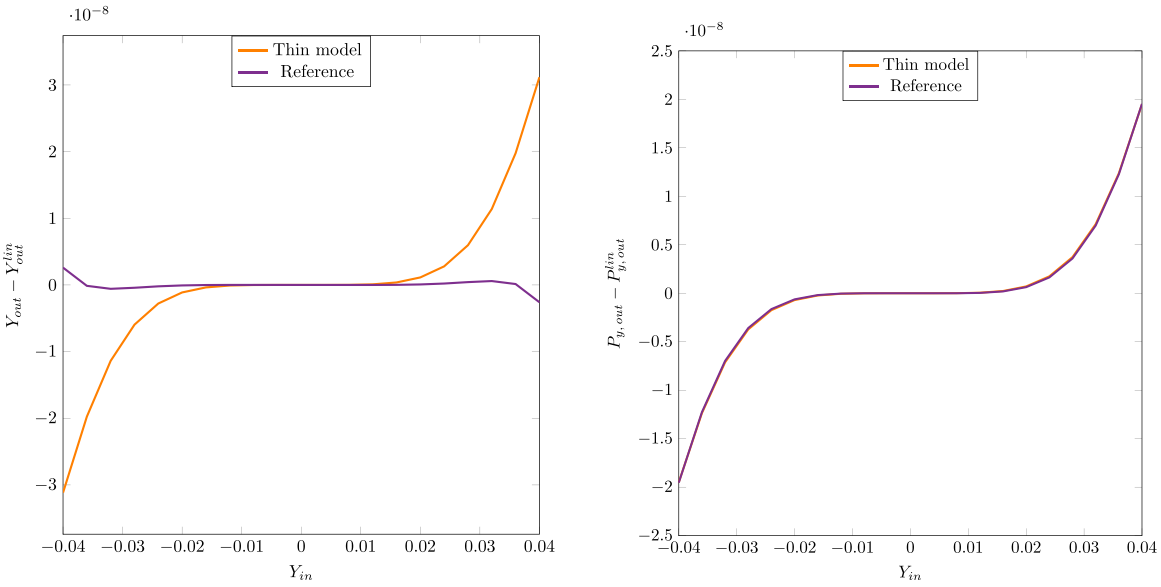

Fig. 24. Thin lens model. Nonlinear part of positions (left) and momenta (right). For the momenta the lines are superposed.

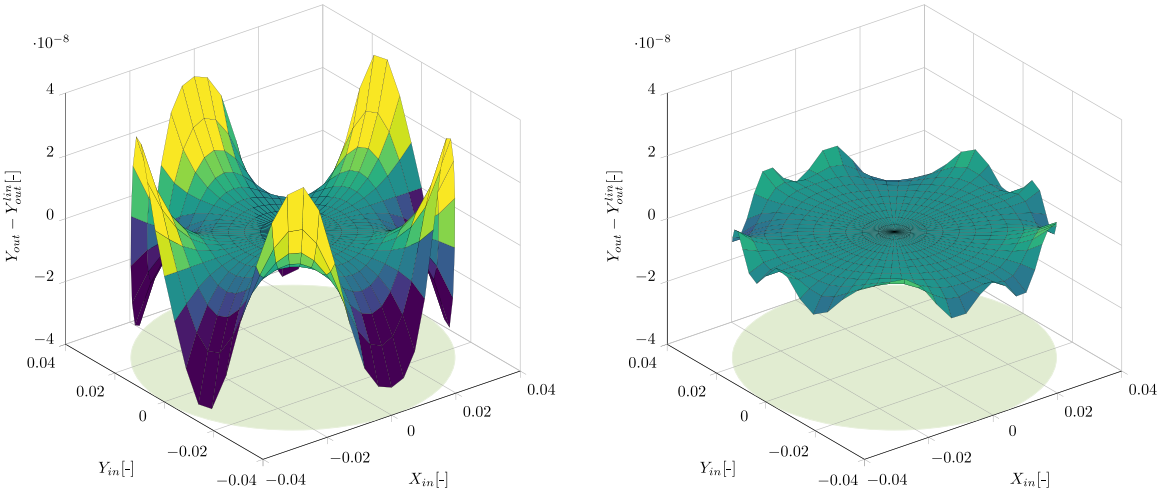

Fig. 25. Thin lens model. Position nonlinearities computed with the thin lens model (left) and with the sixth order symplectic Gauss method (right). The position nonlinearities produced by the thin lens model are larger and similar to the momentum nonlinearities.

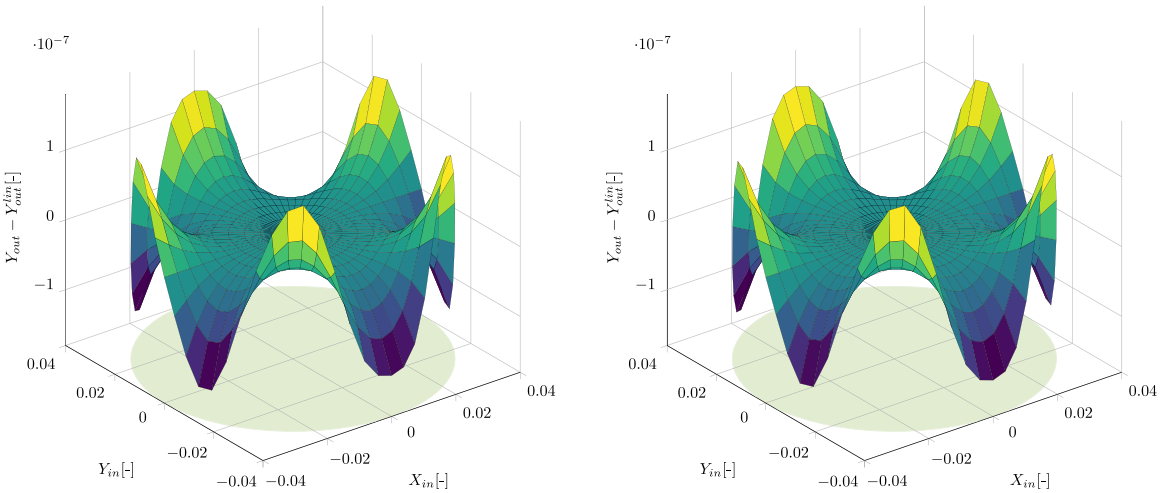

Fig. 26. Thin lens model, symmetric field obtained considering two adjacent specular quadrupoles. Position nonlinearities computed with the thin lens model (left) and with the sixth order symplectic Gauss method (right). In this case, where the field is symmetric with respect to the longitudinal axis z, the results of the two methods are comparable.

be possible to use a smaller step in the fringe field regions, where the vector potential has more complex shape, and a larger step where the field is uniform and has simpler structure.

An interesting aspect of the results obtained was the fact that non-symplectic methods appeared to be competitive with symplectic ones, even on relatively long integrations. A goal of future work is to understand whether more realistic test cases would actually highlight negative effects induced by non-symplectic methods and whether more detailed monitoring of the particle motion could be employed for this purpose. For example, in this work only the energy associated to the transverse variable was used to measure the good behaviour in long-term simulations. Other conserved quantities could also be used to compare the performance of the different methods.

Finally, given the degradation in accuracy that is induced by the vector potential approximation considered in this work, when the potential is to be computed far from the quadrupole axis, investigation of alternative approximations based on high order finite element approaches also seems an interesting possible development, in order to achieve a more reliable description of the particle trajectories in the large aperture case.

Acknowledgements

This paper contains an extension of results initially presented in the Master Thesis of A.S., discussed at Politecnico di Milano in 2016. A.S. was partially supported by CEA Saclay, where part of this work was carried out. The authors thank C. de Falco for several useful discussions on related topics. The authors are also grateful to E. Todesco and S. Izquierdo for providing the harmonics sampled on z of the HL-LHC interaction region quadrupole prototype.

References

[1] D.C. Carey, Appl. Opt. 27 (1988) 1002.
[2] E. Forest, Beam Dynamics, CRC Press, 1998.
[3] L. Rossi, Second International Particle Accelerator Conference, San Sebastian, 2011.
[4] Y. Wu, E. Forest, D. Robin, Phys. Rev. E 68 (4) (2003) 046502.
[5] B. Dalena, O. Gabouev, M. Giovannozzi, R.D. Maria, R. Appleby, A. Chancé, J. Payet, D. Brett, Tech. Rep. CERN-ACC-2014-0175, CERN, 2014.
[6] CERN, SixTrack - 6d Tracking Code, URL http://sixtrack.web.cern.ch/SixTrack/.
[7] F. Méot, Tech. rep., Brookhaven National Laboratory (BNL), 2012.
[8] D. Uriot, N. Pichoff, Tracewin, CEA Saclay, June.
[9] A. Dragt, Lie Methods for Nonlinear Dynamics with Applications to Accelerator Physics, University of Maryland, Center for Theoretical Physics, Department of Physics, 1997, URL http://www.physics.umd.edu/dsat/.
[10] Y. Cai, M. Giovannozzi, R. De Maria, Y. Nosochkov, F. Van Der Veken, Tech. rep., 2018.
[11] E. Hairer, C. Lubich, G. Wanner, Geometric Numerical Integration: Structure-Preserving Algorithms for Ordinary Differential Equations, Springer Science & Business Media, 2006.
[12] J. Corno, C. de Falco, H.D. Gersem, S. Schöps, Comput. Phys. Comm. 201 (2016) 1–7.
[13] K. Lipnikov, G. Manzini, F. Brezzi, A. Buffa, J. Comput. Phys. 230 (2) (2011) 305–328.
[14] M. Venturini, A. Dragt, Nucl. Instrum. Methods Phys. Res. A 427 (1) (1999) 387–392.
[15] W.H. Panofsky, M. Phillips, Classical Electricity and Magnetism, Addison Wesley, 1962.
[16] H. Yoshida, Phys. Lett. A 150 (5) (1990) 262–268.
[17] T. Pugnat, B. Dalena, Tech. rep., Commissariat à l'Énergie Atomique et aux Énergies Alternatives, 2015, unpublished.
[18] G. Kotkin, V.G. Serbo, Collection of Problems in Classical Mechanics: International Series of Monographs in Natural Philosophy, Vol. 31, Elsevier, 2013.
[19] ROXIE - Software for electromagnetic simulation and optimization of accelerator magnets, https://espace.cern.ch/roxie/default.aspx, 2018.
[20] H. Burkhardt, M. Giovannozzi, R.D. Maria, T. Risselada, Tech. rep. CERN-ACC-2013-0059, CERN, 2013.

A.9 Computation of beam based quantities with 3D final focus quadrupoles field in circular hadronic accelerators

Nuclear Inst. and Methods in Physics Research, A 978 (2020) 164350

Contents lists available at ScienceDirect

Nuclear Inst. and Methods in Physics Research, A

journal homepage: www.elsevier.com/locate/nima

Computation of beam based quantities with 3D final focus quadrupoles field in circular hadronic accelerators

T. Pugnat [a], B. Dalena [a,*], A. Simona [b], L. Bonaventura [b]

[a] CEA, Irfu, DACM, Université Paris-Saclay, F-91191, Gif-sur-Yvette, France
[b] MOX, Politecnico di Milano, Milano, Italy

ARTICLE INFO

Keywords:
Non-linear beam dynamics
Optics corrections
Chaotic motion

ABSTRACT

The computation of analytic and numerical beam based quantities are derived for full 3D representation of the quadrupoles magnetic field, which can be computed by finite element code or measured. The impact of this more accurate description of the non homogeneity of the field is estimated on beam based observables and non linear correctors strengths, and compared with the less accurate models in the case of HL-LHC.

1. Introduction

This paper presents the computation of beam based quantities (such as amplitude detuning and dynamic aperture) based on a 3D representation of the non homogeneity's of the quadrupole field, studying, in particular, the final focus quadrupoles of the high luminosity upgrade of LHC (HL-LHC [1]).

In general, allowed non linearities are stronger in the extremities than in the body of a magnet, as can be seen in Fig. 1, where the longitudinal profile of the harmonics from a short prototype of the large aperture (150 mm) final focus quadrupoles of HL-LHC project is shown. The presence of connectors on one side of the magnet has also been considered since they break the longitudinal symmetry of the field. In this paper, the orientation of the magnet follow the powering scheme for HL-LHC shown in Fig. 2.

The possibility to study the impact of magnet fringe fields on non-linear beam dynamics dates back to around the 90's [2,3]. More recently, analytical functions have been used to fit magnetic field data, computed with finite element codes or measured, with application to different projects [4,5]. Generalized Gradients based methods are also able to include magnetic data, measured or computed, in the non-linear transfer maps [6,7]. Its application to a photon source [8] have shown agreement of tracking simulations using magnetic field maps with tracking using machine optics model. Here, we fully link the Generalized Gradient technique to beam based observables, to study the impact of the 3 dimensional distribution of the field on the ring performance. We consider the case of HL LHC inner triplet where the gradient of the betatronic (β) function in a single quadrupole is not so small and the β function is very big. Therefore, beam based quantities like Amplitude Detuning and Dynamic Aperture, are dominated by the errors in these elements.

Combining the variation of this high β function in the same quadrupole and a non-uniform longitudinal distribution of the harmonic alongside the magnet can have a non-negligible weight on the model prediction and explain eventual discrepancy with beam based observables. In particular, this study quantifies the level of detail in the description of the field that has significant effect on commonly used beam based quantities, such as amplitude detuning, dynamic aperture and non linear correctors evaluations. An analytical calculations of the impact of the extremities of the inner triplet magnets of HL-LHC on detuning with amplitude, using first order Hamiltonian perturbation theory, can be found in [9]. In this paper, we derived it for the first time in terms of generalized gradients of the magnetic field, including also the dodecapole harmonics, and extend it to the numerical estimates of the same quantities studied in the previous paper and of the dynamic aperture, comparing it to more simplified models for the non-linear transfer maps.

Section 2 describes the analytical calculation for the variation of the phase-space transverse angular velocity with the amplitude of the particle (Amplitude Detuning) in terms of Generalized Gradients of the quadrupole. This beam dynamic quantity is widely used to define the performance and the non-linear correction in circular accelerators [10]. Beam based measurements of amplitude detuning are essential for the LHC commissioning [11].

Section 3 introduces the symplectic and efficient (mandatory for application to large hadron storage rings) non-linear transfer maps based on Generalized Gradients and compares it to the approximated models: the classical one, in which the non-linearities of the field are integrated along the magnet and uniformly distributed, and a first approximation of the longitudinal distribution of the high order harmonics, which splits the quadrupole into three parts (i.e. the body and the two extremities). The proposed 3D non-linear transfer map,

* Corresponding author.
E-mail addresses: thomas.pugnat@cea.fr (T. Pugnat), barbara.dalena@cea.fr (B. Dalena).

https://doi.org/10.1016/j.nima.2020.164350
Received 2 July 2020; Received in revised form 7 July 2020; Accepted 8 July 2020
Available online 10 July 2020
0168-9002/

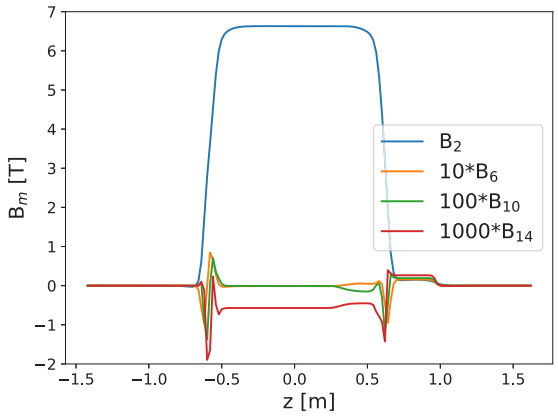

Fig. 1. Normal longitudinal harmonics sampled at $\Delta z = 2$ mm for the prototype of HL-LHC Inner Triplet quadrupole. Courtesy of E. Todesco and S. Izquierdo Bermudez.

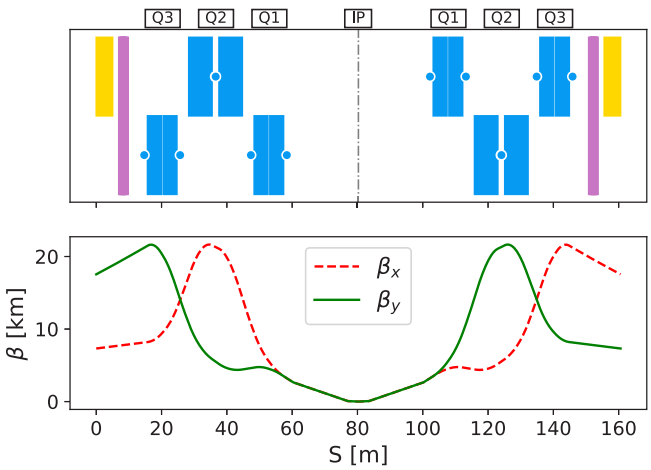

Fig. 2. Single aperture elements in the HL-LHC insertion regions. The three (splitted) quadrupoles composing each inner triplet (Q1, Q2 and Q3) are in blue, blue dots represent the position of the quadrupoles connectors, the first separation dipole is in yellow and the non-linear correctors are in purple (top panel). The horizontal and vertical β functions are shown in the bottom panel. (For interpretation of the references to color in this figure legend, the reader is referred to the web version of this article.)

called Lie2 since is derived using Lie Algebra techniques, consists of numerical integration of the two extremities using smaller steps. It has the advantage (with respect to the approximate models) to be able to take into account the derivatives of the field gradients, that are also sources of non-linearities.

Section 4 compares the analytical estimates of Amplitude Detuning (AD) with the tracking simulations using the three different transfer maps, corresponding to the models described in the previous section. This beam-based observable refers to the variation of the transverse Phase-Space angular frequency (i.e. the tune) with respect to the amplitude of the particle and it is the most direct measurement of beam non-linearities. The impact of the model on the correctors strength expected to correct this AD, is also quantified and compared to present strength specifications. Those correctors are used to correct locally non-linearities (i.e. reduce the beam Resonance Driving Terms (RDTs), Ref. [12]).

Section 5 repeats the comparison of the models on another beam dynamic quantity that is the Dynamic Aperture. It defines the region of stable motion of the particles against magnet non-linearities and is often used to define tolerances on magnets conception in the design phase of circular accelerators. Unlike Amplitude Detuning, there is no analytic calculation of Dynamic Aperture including field errors and corrections. Its computation relies on tracking simulations therefore an accurate, symplectic and efficient non linear transfer map is necessary for large hadrons storage rings, as the LHC.

2. Expression of the amplitude detuning with generalized gradients

Following Ref. [13], the Amplitude and Cross Detuning as a function of the normalized amplitude $2J_u$ ($u \in \{x, y\}$) is given by:

$$\Delta Q_u = \frac{1}{2\pi} \oint \frac{\partial \langle H_p \rangle}{\partial J_u} \mathrm{d}i \tag{1}$$

with $\langle H_p \rangle$ the perturbative part of the Hamiltonian, describing the non-homogeneity's of the field, and i the position along the ring. In this paper, the kinematic and second order terms will be neglected. Following Ref. [13], the equations for the Direct and Cross Amplitude Detuning for the harmonics b_4 and b_6 are:

$$\begin{aligned}\Delta Q_x = \frac{q}{2\pi p_0 c} \sum_i \Big[& \frac{3}{8}\left(\beta_x^2 \bar{b}_4\right)_i (2J_x) + \frac{5}{16}\left(\beta_x^3 \bar{b}_6\right)_i (2J_x)^2 \\ & - \frac{3}{4}\left(\beta_x \beta_y \bar{b}_4\right)_i (2J_y) + \frac{15}{16}\left(\beta_x \beta_y^2 \bar{b}_6\right)_i (2J_y)^2 \\ & - \frac{15}{8}\left(\beta_x^2 \beta_y \bar{b}_6\right)_i (2J_x 2J_y)\Big]\end{aligned} \tag{2}$$

$$\begin{aligned}\Delta Q_y = \frac{q}{2\pi p_0 c} \sum_i \Big[& \frac{3}{8}\left(\beta_y^2 \bar{b}_4\right)_i (2J_y) - \frac{5}{16}\left(\beta_y^3 \bar{b}_6\right)_i (2J_y)^2 \\ & - \frac{3}{4}\left(\beta_x \beta_y \bar{b}_4\right)_i (2J_x) - \frac{15}{16}\left(\beta_x^2 \beta_x \bar{b}_6\right)_i (2J_x)^2 \\ & + \frac{15}{8}\left(\beta_x \beta_y^2 \bar{b}_6\right)_i (2J_x 2J_y)\Big]\end{aligned} \tag{3}$$

where the $\bar{b}_n$ indicates that the relative high order field harmonics are averaged for the positions i belonging to the same element and are kept constant over the length of the magnet. They can be computed with finite element codes or measured with rotating coils. Using expression (14) of the Generalized Gradient and $H_p = -a_z - a_x p_x - a_y p_y$ being the perturbative Hamiltonian with the vector potential defined in Eq. (15), the previous equations can be extended to consider the gradient derivatives and different values for the field harmonics along the same element:

$$\begin{aligned}\Delta Q_x = \frac{q}{2\pi p_0 c} \sum_i \Big[& \frac{3}{8}\left(4\beta_x^2 C_{4,s}^{[0]} + 2\beta_x \alpha_x C_{2,s}^{[1]} - \frac{2}{3}\beta_x^2 C_{2,s}^{[2]}\right)_i (2J_x) \\ & - \frac{3}{4}\left(4\beta_x \beta_y C_{4,s}^{[0]} - \frac{1}{3}(\beta_x \alpha_y - \beta_y \alpha_x) C_{2,s}^{[1]}\right)_i (2J_y) \\ & + \frac{5}{16}\left(6\beta_x^3 C_{6,s}^{[0]} + \frac{3}{2}\beta_x^2 \alpha_x C_{4,s}^{[1]} - \frac{9}{20}\beta_x^3 C_{4,s}^{[2]}\right)_i (2J_x)^2 \\ & + \frac{15}{16}\left(6\beta_x \beta_y^2 C_{6,ts}^{[0]} + \frac{1}{5}\beta_y\left(\frac{\beta_y \alpha_x}{2} - 3\beta_x \alpha_y\right) C_{4,s}^{[1]} + \frac{3}{20}\beta_x \beta_y^2 C_{4,s}^{[2]}\right)_i \\ & \times (2J_y)^2 \\ & - \frac{15}{8}\left(6\beta_x^2 \beta_y C_{6,s}^{[0]} - \frac{1}{5}\beta_x\left(\frac{\beta_x \alpha_y}{2} - 3\beta_y \alpha_x\right) C_{4,s}^{[1]} - \frac{3}{20}\beta_x^2 \beta_y C_{4,s}^{[2]}\right)_i \\ & \times (2J_x 2J_y)\Big]\end{aligned} \tag{4}$$

$$\begin{aligned}\Delta Q_y = \frac{q}{2\pi p_0 c} \sum_i \Big[& \frac{3}{8}\left(4\beta_y^2 C_{4,s}^{[0]} - 2\beta_y \alpha_y C_{2,s}^{[1]} + \frac{2}{3}\beta_y^2 C_{2,s}^{[2]}\right)_i (2J_y) \\ & - \frac{3}{4}\left(4\beta_x \beta_y C_{4,s}^{[0]} - \frac{1}{3}(\beta_x \alpha_y - \beta_y \alpha_x) C_{2,s}^{[1]}\right)_i (2J_x) \\ & - \frac{5}{16}\left(6\beta_y^3 C_{6,s}^{[0]} - \frac{3}{2}\beta_y^2 \alpha_y C_{4,s}^{[1]} + \frac{9}{20}\beta_y^3 C_{4,s}^{[2]}\right)_i (2J_y)^2 \\ & - \frac{15}{16}\left(6\beta_x^2 \beta_y C_{6,s}^{[0]} - \frac{1}{5}\beta_x\left(\frac{\beta_x \alpha_y}{2} - 3\beta_y \alpha_x\right) C_{4,s}^{[1]} - \frac{3}{20}\beta_x^2 \beta_y C_{4,s}^{[2]}\right)_i \\ & \times (2J_x)^2 \\ & + \frac{15}{8}\left(6\beta_x \beta_y^2 C_{6,s}^{[0]} + \frac{1}{5}\beta_y\left(\frac{\beta_y \alpha_x}{2} - 3\beta_x \alpha_y\right) C_{4,s}^{[1]} + \frac{3}{20}\beta_x \beta_y^2 C_{4,s}^{[2]}\right)_i \\ & \times (2J_x 2J_y)\Big]\end{aligned} \tag{5}$$

From these equations, it appears clearly that the non-linearities act on amplitude detuning as weighted sum of the multipolar strengths with the Twiss parameters as weight powers. In regions where those weights can vary inside one magnet and/or have big values, not taking into consideration the longitudinal distribution of the non-linear harmonics can bias the prediction for the detuning with Amplitude. The same holds for the RDTs with also additional dependence on the phases advances.

3. The Lie2 non-linear transfer map

In order to describe the motion of the particles in a magnetic system, the transfer map of the system is required and in the case of multi-turn simulations in the large hadron collider, this map needs also to be symplectic. Using Lie Algebra formalism, a non-linear and symplectic transfer map takes the following expression:

$$M(\Delta\sigma) = \exp(-L : K :) \tag{6}$$

where L and K are respectively the length and the Hamiltonian of the system. In order to have the explicit dependence on z in the Hamiltonian, we consider the 8 dimensions Hamiltonian reported in Appendix A. Since the expression of the Hamiltonian contains the terms of the type $(p_{x,y} - a_{x,y})^2$, the system is not exactly solvable, so we use a transfer map approximated to the second order (that we call Lie2):

$$\begin{aligned} M(\Delta\sigma) = {} & \exp(\frac{-\Delta\sigma}{2} : K1 :)\exp(-\frac{\Delta\sigma}{2} : K2 :) \\ & \exp(-\frac{\Delta\sigma}{2} : K3 :)\exp(-\Delta\sigma : K4 :) \\ & \exp(-\frac{\Delta\sigma}{2} : K3 :)\exp(-\frac{\Delta\sigma}{2} : K2 :) \\ & \exp(-\frac{\Delta\sigma}{2} : K1 :) + O(\Delta\sigma^3) \\ = {} & M2 + O(\Delta\sigma^3) \end{aligned} \tag{7}$$

where $K1 = pz - \delta$, $K2 = a_z$, $K3 = \frac{(p_x - a_x)^2}{2(1+\delta)}$, $K4 = \frac{(p_y - a_y)^2}{2(1+\delta)}$, $: K : f = \langle K, f \rangle$ is the Lie operator defined by the Poisson brackets [14], and we have used the generating function given in [15] to simplify the terms K3 and K4. To optimize the computational speed this Lie2 transfer map is applied only at the two extremities of the quadrupoles magnet (which are the same of the magnet prototype). The central part of the quadrupole (called body) is treated in the hard hedge approximation since all the harmonics are expected to be constant (Refs. [16–18]). As specified in Ref. [19], this model also allows to consider the derivatives of the gradient in the simulation, another source of non-linearities which is not included in the hard edge approximation of the kicks. In the following, ND0 represents the case without derivatives of the field gradients, and ND6 the case with the derivatives up to the 6th. The impact of the number of derivatives (ND, derivative orders) is discussed in Appendix B, while details of the numerical implementation of the Lie2 transfer map and its integration in the SixTrack tracking code are reported in Appendix A.

This new map is compared with classical kicks models using hard hedge approximation applied on one optics configuration of the HL-LHC project. The goal is to verify if the harmonics longitudinal distribution have a measurable impact on beam-based observable. A schematic view of these three models is shown in Fig. 3. As a matter of convention, we use the notation of the magnetic length L and the normalized strength b_n where n is the order of the harmonic (2 for quadrupole, ...), etc, and indices T, CS, NC and B represent respectively the whole magnet, the connector and non-connector side, and the body.

In the Hard Edge model, called HE, the harmonic longitudinal distribution and their derivatives are neglected. The normalized integrated strength $b_{n,T}L_T$ is equally distributed on 16 multipolar kicks for each quadrupole.

In the model called HE+Heads, the normalized integrated strengths in the extremity (Head) of the quadrupole ($b_{n,CS}L_{CS}$ and $b_{n,NC}L_{NC}$) are

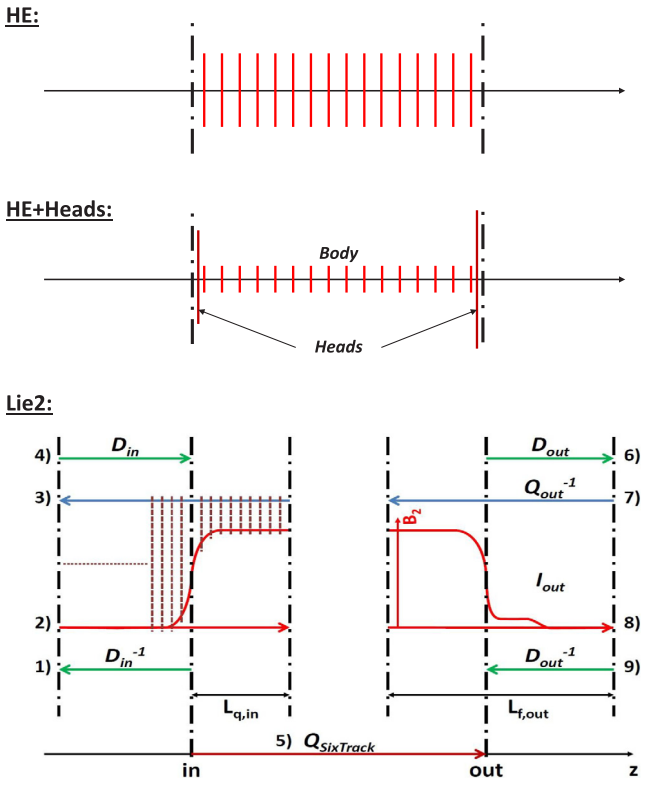

Fig. 3. Longitudinal representation of the Models.

estimated, respectively as $L_{NC/CS} = \int_{NC/CS} \frac{B_2}{B_{2,max}} dz$ and $\overline{b_{n,NC/CS}} = \int_{NC/CS} \frac{B_n}{B_{2,max} L_{NC/CS}} dz$, using the two halves of the longitudinal profile of the magnet prototype (where the Lie2 integration is also applied). The residual $b_{n,B}L_B$ (body part) is computed from the following equation and equally distributed on 16 multipolar kicks, as in the HE method. No random integrated strength is considered in the Heads in this approach.

$$b_{n,B}L_B = b_{n,T}L_T - (b_{n,CS}L_{CS} + b_{n,NC}L_{NC}) \tag{8}$$

$$L_B = L_T - (L_{CS} + L_{NC}) \tag{9}$$

It is worth noticing that the integrated strength in each Head is the same as in the Lie2 model and that the total integrated strength of the magnet is preserved for all the three models, except for the derivatives of the gradient.

4. Amplitude detuning

The Amplitude Detuning corresponds to the variation of the phase-space angular velocity as a function of the Betatron Amplitude. In this paper, we simulate the particles motion over 10^3 revolutions purely on the vertical or horizontal plane, without the dodecapole correction. The initial positions are set to be below the DA value (i.e. $0<2J_u \leq 0.05$ μm for a normalized emittance of 2.5 μm), and their initial momentum offset δ is 0. As a comparison, the maximum measured amplitude reached in the LHC is of the order of 0.3 μm for a β^* of 25 cm (see Refs. [11,20,21]).

For the sake of the graphic visibility, the b_4 multipole error components have been removed from the simulation. And the linear amplitude detuning from the main sextupole second order has been subtracted in the AD using the linear coefficient C1 (about $1.8 \pm 0.1 \times 10^{-2}$ μm^{-1} and $1.75 \pm 0.1 \times 10^{-2}$ μm^{-1}, in the x and y-planes respectively) compatible with the 1st order anharmonicity given by MADX PTC (Ref. [22]).

4.1. Amplitude detuning with all the harmonics

Fig. 4 shows the simulated Amplitude Detuning in both planes with all the non-linear errors (except for b_4) for all the models. The horizontal error bars correspond to the minimum and maximum amplitude over the 10^3 revolutions and are centered on the initial amplitude. The vertical error bars correspond to the uncertainty of the correction for linear detuning due to second order effects from main sextupoles. Table 1 shows the fitted values with respect to the predicted ones. For each model, the simulated AD is compared to the theoretical AD from Eqs. (4) and (5). The simulated detuning with amplitude is fitted with a 4th order polynomial (motivated by using smallest degree for the best score, and its robustness over fitting procedures).

It appears clearly in Fig. 4 and Table 1 that the Amplitude Detuning is sensible to the longitudinal distribution of the harmonics in the magnet, i.e. the model. This is also confirmed by the fact that the simulations agree well with the prediction up to an amplitude of $\sim 3.0 \times 10^{-2}$ μm.

The good agreement between the HE+Heads and the Lie2 ND0 model shows that one additional kick in each of the extremity gives a good approximation of the longitudinal distribution of the expected non-linearities. Nevertheless, the Lie2 model yields the best representation, if accuracy is more important than computational cost.

The discrepancy between the Lie2 models with and without derivatives (ND0 and ND6, respectively) shows an additional linear detuning generated by the 1st and 2nd derivatives of the b_2 harmonics, as expected from Eqs. (4) and (5). We just note that this effect is of the same order as the effect due to the 2nd-order Sextupoles for the ATS optics [23] with 15 cm β^*, foreseen for HL-LHC project.

4.2. Amplitude detuning for only the b_6 harmonics

In order to understand the origin of the discrepancy for amplitude higher than 3.0×10^{-2} μm in Fig. 4, the same analysis is repeated considering only the b_6 harmonics error in the final focus quadrupoles. Since the error are generated using random number as explained in 3, the second order AD will be different from the previous section. The results are shown in Fig. 5 and Table 2.

In this case, there is no discrepancy between the theory and the simulation for all the models. This comforts us in the idea that the previous discrepancy comes from higher order harmonics that are not taken into consideration in the analytic calculation.

4.3. Correction of the non-linearities

As mentioned in the previous section, the Detuning with Amplitude and similarly all the RDTs are sensitive to the longitudinal distribution of the high order field harmonics. Since the non-linear corrections are computed in order to cancel the main RDTs, as a result, the correctors strength used to correct them is also sensitive to the longitudinal distribution of the non-linearities.

In HL-LHC, there is one corrector on each side of each IP and their strength is computed using (Ref. [12]):

$$\begin{pmatrix} K_{n,Left}L \\ K_{n,Right}L \end{pmatrix} = \begin{pmatrix} \beta_{x,Left}^{n/2} & \beta_{x,Right}^{n/2} \\ \beta_{y,Left}^{n/2} & \beta_{y,Right}^{n/2} \end{pmatrix}^{-1} \sum_{i \in IP} b_{n,i} K_{r,i} L_i \begin{pmatrix} \beta_{x,i}^{n/2} \\ \beta_{y,i}^{n/2} \end{pmatrix} \quad (10)$$

As the exact values of the strength of each of the magnets errors are not known yet, the strength of the octupole and dodecapole correctors are computed for 60 different seeds, in which the uncertainty and random component of the errors for each magnets can vary according to Eq. (11).

$$b_n = b_{n_S} + \frac{\xi_U}{1.5} b_{n_U} + \xi_R b_{n_R} \quad (11)$$

It represents the sum of a systematic part b_{n_S} and two random parts b_{n_U} and b_{n_R}, normalized with respect to the reference magnet strength [24]. ξ_U and ξ_R denote random variables with Gaussian distribution truncated at 1.5 and 3σ, respectively. In particular, the ξ_U is kept constant for all the inner triplet magnets of the same type (to account for systematic errors coming from different production chains), while ξ_R changes for each magnet (to describe differences between each magnets).

Fig. 6 shows the correlation of the non-linear correctors strength at both sides of the high luminosity IPs for these 60 seeds. Since only the systematic component of the error as a longitudinal distribution (while the uncertainty and random component are equally distributed), it results in a systematic shift between the HE model and the others.

The octupole-like generated by b_2' and b_2'' produces a systematic shift in the octupole corrector strength of about 4% with respect to the b_4 corrector specification given in Ref. [12]. In the case of b_6 correction, the systematic shift is around 13%, always with respect to the present corrector specification.

The shift stays within the correctors specification also for the dodecapole corrector. The difference between the shift for the HE+Heads and the Lie2 models, as well as the effect of the gradients derivatives, is negligible in this case.

It is worth noticing that only the longitudinal distribution of the systematic part of the errors is studied in this paper. The random part of the harmonics is considered equally distributed in the magnet, since this random component is computed using 2D Monte Carlo simulations. Therefore, measurements of the longitudinal profile for all the harmonics (above all the ones that do not have a systematic component) is essential to be able to model them accurately in the calculation of the correction.

5. Dynamic aperture

Dynamic aperture (DA) is a quantity often used to define the performance of an accelerator against magnets imperfections. It is defined as the area of the stable phase-space region spanned by a particle in an accelerator and it is evaluated using particle tracking simulations [25] or measured by different techniques [26].

In this part, we study the impact of the three different models described in Section 3 on the computation of DA, focusing in particular on the effect of the b_6 correctors. The DA is computed simulating the particles motion over 10^4 revolutions with initial conditions distributed on a polar grid, so as to have 30 pairs of particles (different initial conditions) for each interval of 2 sigma (beam size) from 0 to 28. Eleven angles in the x–y phase space are scanned, where x and y are in units of linear beam dimensions. The initial momentum offset δ is set to $27.e^{-5}$ (which is equivalent to 2/3 of the LHC RF bucket design). The DA values are defined as the initial amplitudes (in number of beam size σ) of particles lost in 10^4 turns. This procedure for the DA simulations is the same used for LHC DA studies [27] and it was found to provide a precision of about 0.5 beam σ at 10^5 turns [28]. Since in the machine configurations we study in this paper the DA converges very quickly to its asymptotic value, we expect the same type of precision in the DA results of this comparison between models. The tracking simulations in the Lie2 case are performed considering up to two derivatives of the generalized gradient, since there is no significant difference in the tracking with two, four or six number of derivatives of the generalized gradients, see Appendix B.

5.1. DA as a function of angles in the x–y phase space

The DA values for the eleven phase space angles scanned in the simulations are shown in Fig. 7 for one configuration of the machine. The cases without and with b_6 correction are compared. DA without b_6 correction is pretty similar for all the model in the x and y plane, while it can differ up to 3 σ at around 40°. The impact of b_6 correction is different according to the model considered. There is no improvement in DA for the HE+heads model while can be significant for the HE or Lie2, according to the angle.

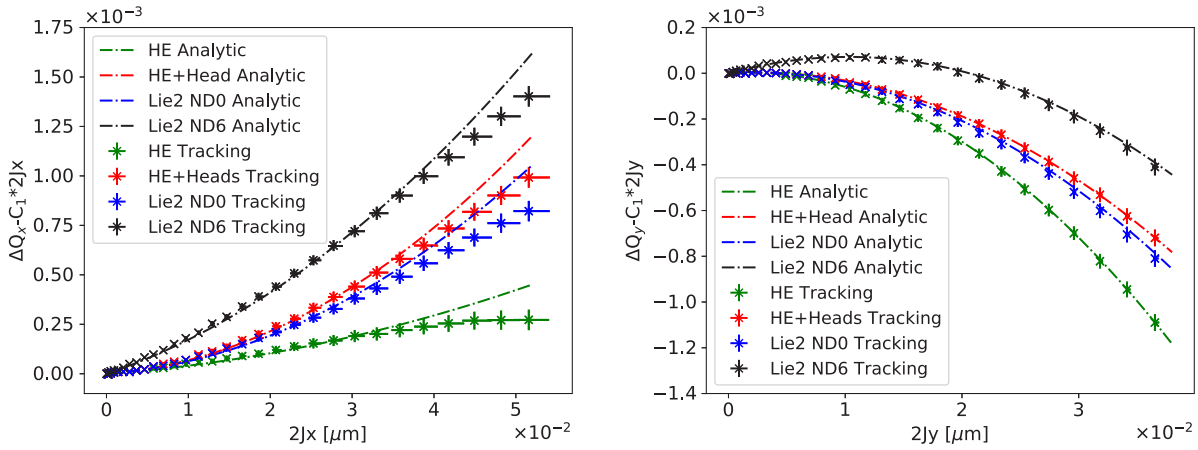

Fig. 4. Amplitude detuning for the horizontal (left) and the vertical plane (right).

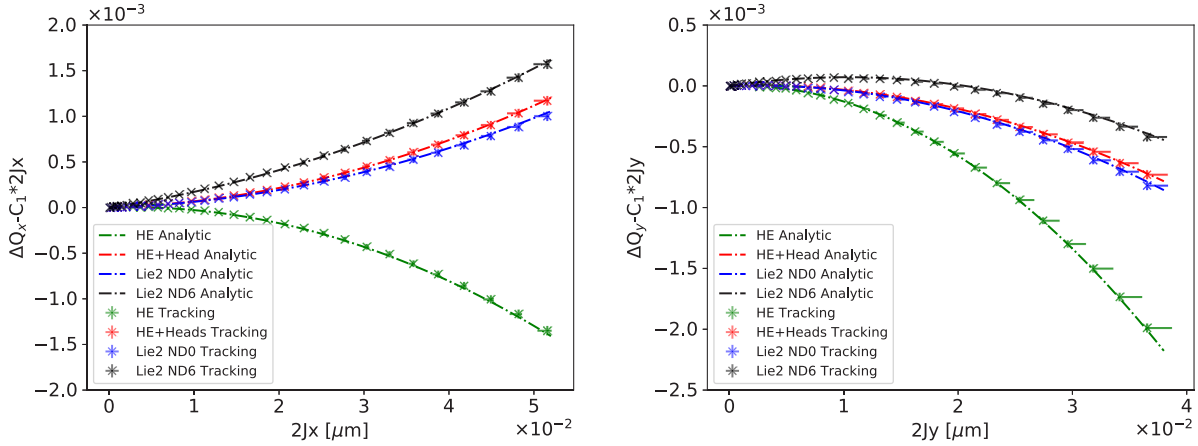

Fig. 5. Amplitude detuning for the horizontal plane (left) and the vertical plane (right).

Table 1
Amplitude detuning coefficients from Fig. 4 fitted with a 4th-order polynomial and for an Amplitude in μm.

	Analytic		Theory	
Case	$\partial Q_x/\partial(2J_x)$	$\partial^2 Q_x/2\partial(2J_x)^2$	$\partial Q_x/\partial(2J_x)$	$\partial^2 Q_x/2\partial(2J_x)^2$
HE	$(0.1 \pm 0.3) \times 10^{-3}$	0.08 ± 0.03	0	0.11
HE +Heads	$(0.1 \pm 0.4) \times 10^{-3}$	0.38 ± 0.03	0	0.39
Lie2 ND0	$(0.9 \pm 0.4) \times 10^{-3}$	0.22 ± 0.03	0	0.33
Lie2 ND6	$(9.2 \pm 0.4) \times 10^{-3}$	0.25 ± 0.03	10.9×10^{-3}	0.33
Case	$\partial Q_y/\partial(2J_y)$	$\partial^2 Q_y/2\partial(2J_y)^2$	$\partial Q_y/\partial(2J_y)$	$\partial^2 Q_y/2\partial(2J_y)^2$
HE	$(0.2 \pm 0.4) \times 10^{-3}$	-0.98 ± 0.05	0	−0.90
HE +Heads	$(0.0 \pm 0.4) \times 10^{-3}$	-0.63 ± 0.05	0	−0.62
Lie2 ND0	$(0.4 \pm 0.5) \times 10^{-3}$	-0.79 ± 0.06	0	−0.67
Lie2 ND6	$(10.7 \pm 0.4) \times 10^{-3}$	-0.67 ± 0.05	10.9×10^{-3}	−0.67

Table 2
Amplitude detuning coefficients from Fig. 5 fitted with a 4th-order polynomial and for an Amplitude in μm.

	Analytic		Theory	
Case	$\partial Q_x/\partial(2J_x)$	$\partial^2 Q_x/2\partial(2J_x)^2$	$\partial Q_x/\partial(2J_x)$	$\partial^2 Q_x/2\partial(2J_x)^2$
HE	$(0.8 \pm 0.3) \times 10^{-3}$	-0.64 ± 0.03	0	−0.58
HE +Heads	$(0.6 \pm 0.3) \times 10^{-3}$	0.38 ± 0.03	0	0.39
Lie2 ND0	$(0.7 \pm 0.4) \times 10^{-3}$	0.28 ± 0.03	0	0.33
Lie2 ND6	$(11.4 \pm 0.4) \times 10^{-3}$	0.34 ± 0.04	10.9×10^{-3}	0.33
Case	$\partial Q_y/\partial(2J_y)$	$\partial^2 Q_y/2\partial(2J_y)^2$	$\partial Q_y/\partial(2J_y)$	$\partial^2 Q_y/2\partial(2J_y)^2$
HE	$(-0.2 \pm 0.5) \times 10^{-3}$	-1.64 ± 0.07	0	−1.59
HE +Heads	$(-0.5 \pm 0.5) \times 10^{-3}$	-0.59 ± 0.06	0	−0.62
Lie2 ND0	$(-0.3 \pm 0.5) \times 10^{-3}$	-0.74 ± 0.07	0	−0.67
Lie2 ND6	$(11.0 \pm 0.4) \times 10^{-3}$	-0.80 ± 0.05	10.9×10^{-3}	−0.67

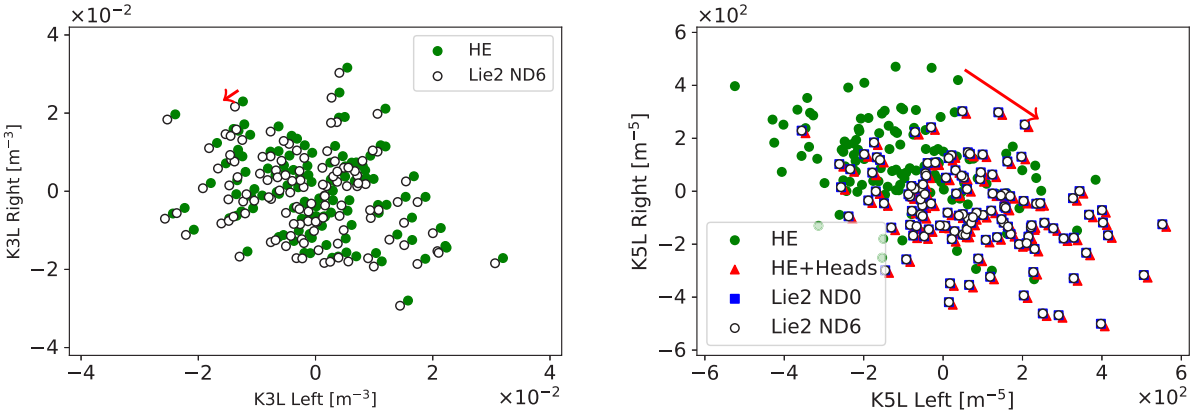

Fig. 6. Integrated strength of the b_4 (called K3L, left) and b_6 (called K5L right) corrector computed for different models in IR1 and IR5, with 60 seeds.

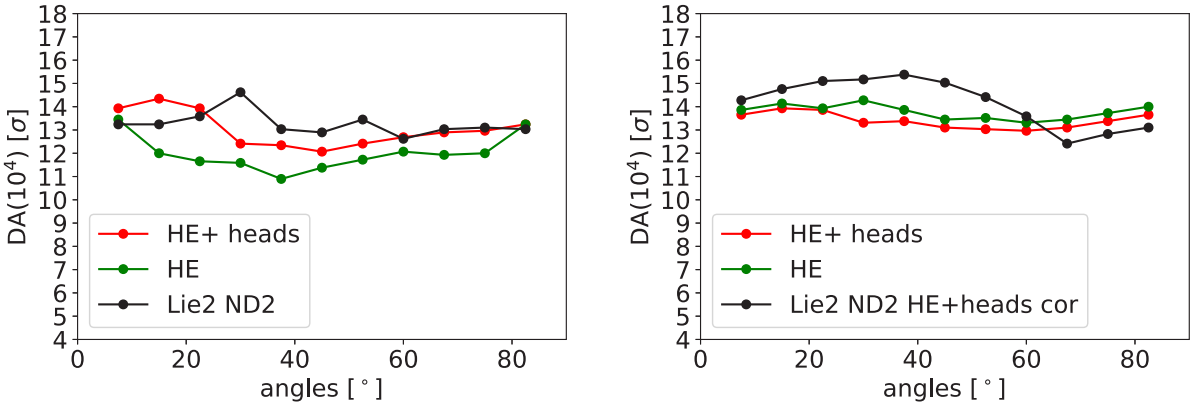

Fig. 7. DA at 10^4 as a function of phase space angles with b_6 correctors OFF (left), and with b_6 correctors ON (right) for one configuration of the machine. The HE+Heads model has been used to compute correction of b_6 in the case of Lie2 ND2 tracking.

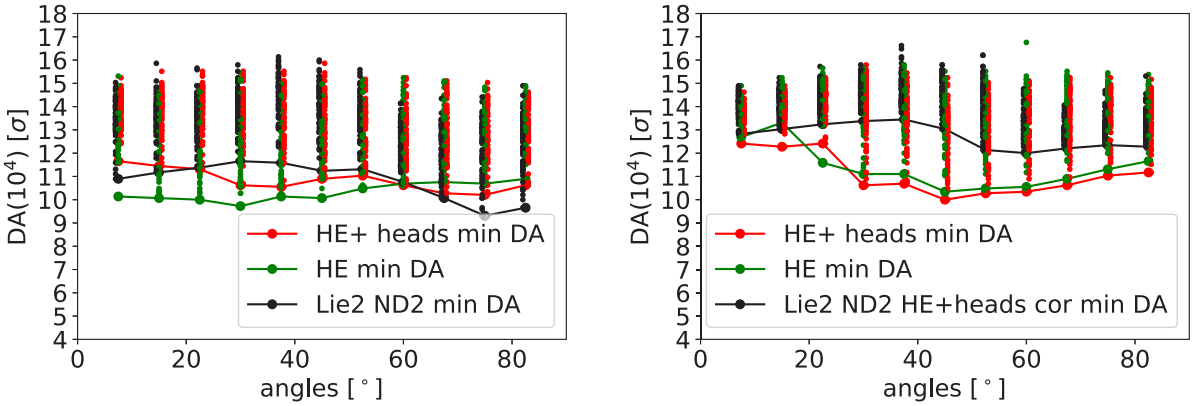

Fig. 8. DA at 10^4 as a function of phase space angles with b_6 correctors OFF (left), and with b_6 correctors ON (right). Dots represents the 60 different configurations of the machine according to random component of the magnets errors.

The statistics of all the 60 different configurations of the machine simulated is shown in Fig. 8. Dots represent the values corresponding to the 60 seeds, while the continuous line joins the minimum DA values for each angle. All high order fields errors are considered and correction for b_3, b_4, b_5, a_3, a_4, a_5 of the inner triplets, as well as b_3, b_4, b_5 of the arc dipole, are applied. The b_6 correction is included in the results shown in the right panel of Fig. 8. Its effect on DA is slightly different according to the angle and the model. A major positive impact of b_6 correction is visible towards the horizontal plane for the HE model. When the HE+Heads model is considered the gain in DA is smaller, and in particular the correction does not improve DA for angles around 40°. In the case of the Lie2 model the correction gives a positive impact towards the vertical plane. Averaging over the angles the impact of the b6 correction is of 0σ for the HE+Heads model, 1σ for the HE model and 2σ for the Lie2 model. Finally, a difference between Lie2 model and the two others is visible at 40° when looking at all machine configurations.

5.2. DA as a function of turn

Starting from the ensemble of initial amplitude of particles lost in the x–y phase space, which define the DA shown in the previous section,

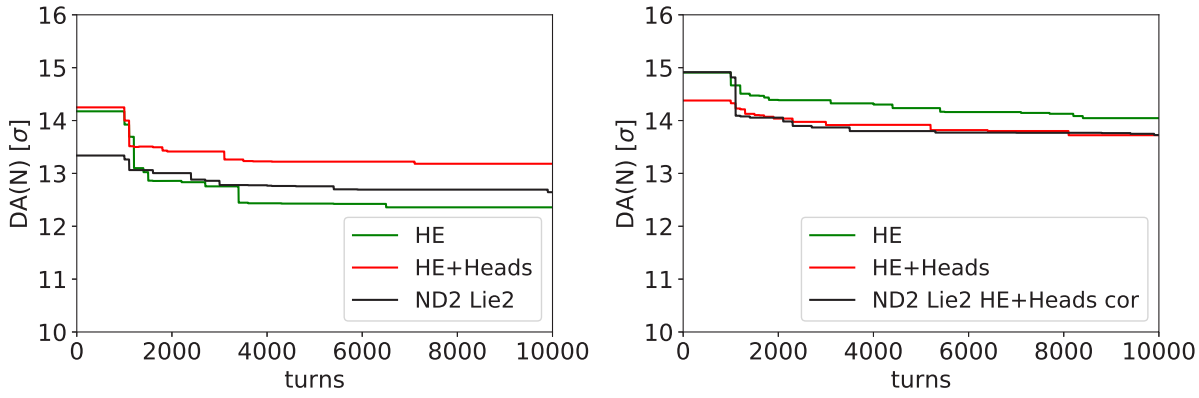

Fig. 9. DA as a function of particle revolutions (turns) with b_6 correctors OFF (left), and with b_6 correctors ON (right) for one machine configuration. The HE+Heads model is used to compute the correction in the Lie2 ND2 case.

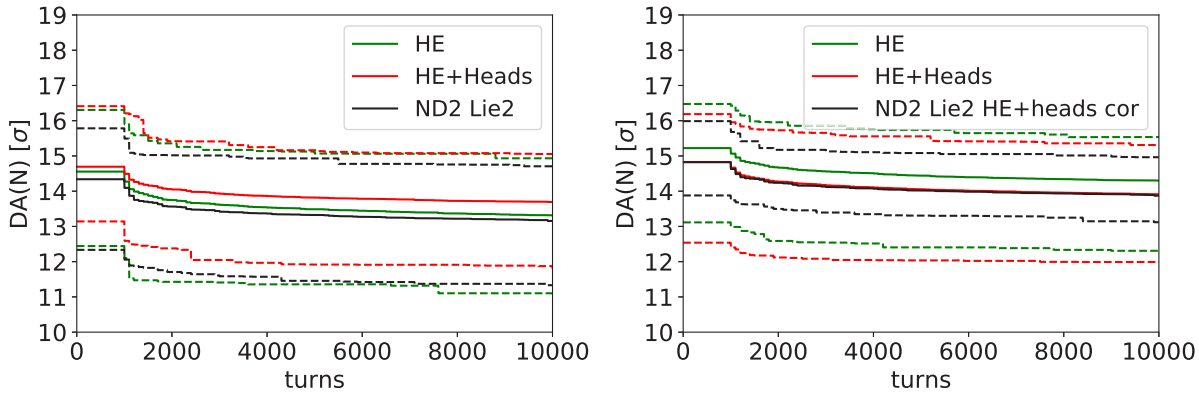

Fig. 10. DA as a function of particle revolutions (turns) with b_6 correctors OFF (left), and with b_6 correctors ON (right). The minimum and maximum (dashed lines) together with the mean values (full lines) over 60 different configurations of the machine according to random component of the magnets errors are shown for each model.

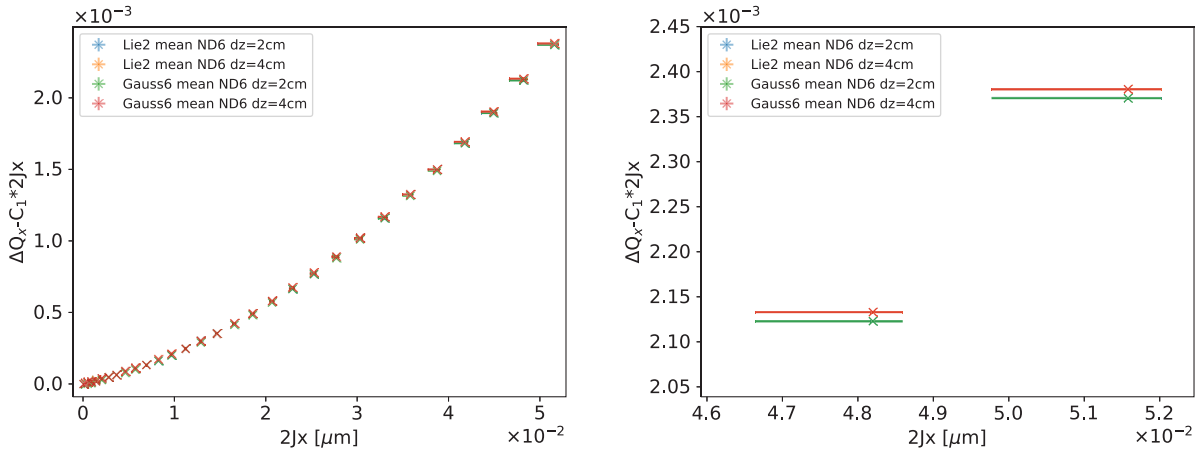

Fig. 11. Comparison of the Lie2 model (for ND6) with the referential model (Gauss6) from Ref. [19] on the Amplitude Detuning for two different step sizes in z. The right plot is a zoom over the high amplitude. For each step size, the value for the model are superposed.

a normalized area of stable motion can be defined following [26]:

$$DA(N) = \frac{2}{\pi}\int_0^{\pi/2} r_s(\theta; N)\mathrm{d}\theta \tag{12}$$

where N is the number of revolutions of the particle in the accelerator (called turns), r_s is the last stable particle (disregarding stability islands non-connected to the origin) and θ is the angle in the x–y phase space. Thus, a value of DA can be calculated for each turn, which is shown in Fig. 9 for one configuration of the machine. In this configuration of the machine (seed), the Lie2 model maintains a higher DA value for longer numbers of turns (above 2000). The impact of the b_6 correction varies according to the model as in the case of the DA vs angle. Once again when the b_6 correction is applied no improvement in the DA evolution is visible for the HE+Heads model.

Fig. 10 shows statistics from the 60 different machine configurations. As for the case DA at 10^4 revolutions as a function of the angle, the random part of the errors dominates over the systematic part, resulting in much less difference between the models when looking at their mean values. The only significant difference seems to be on the spread between the minimum and maximum DA values, which is reduced in the Lie2 model, as one can also glimpse in Fig. 8.

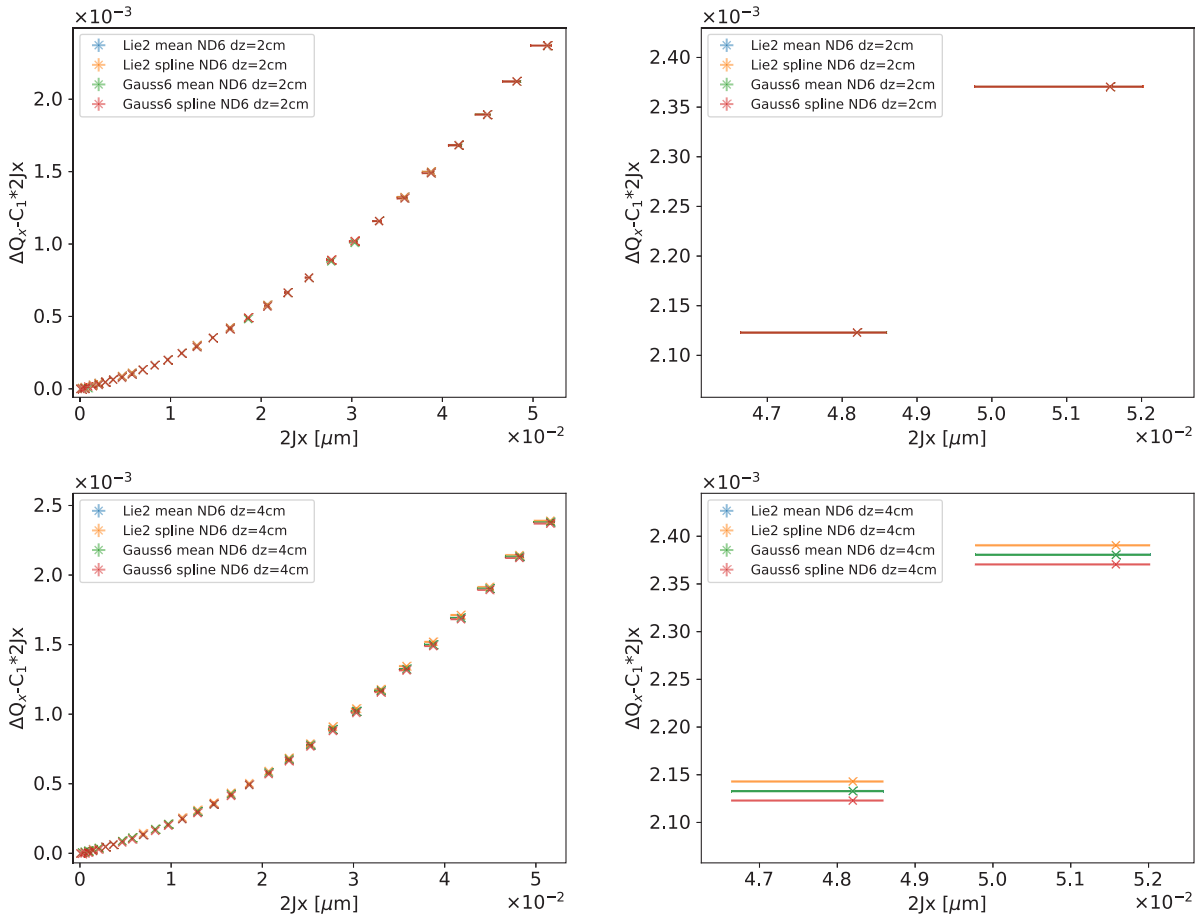

Fig. 12. Comparison of the Lie2 model (for ND6) with the referential model (Gauss6) from Ref. [19] on the Amplitude Detuning for $dz = 2\,\mathrm{cm}$ (top) and $4\,\mathrm{cm}$ (bottom). The right plot is a zoom over the high amplitude. All the points for $dz = 2\,\mathrm{cm}$ and the mean points for $dz = 4\,\mathrm{cm}$ are superposed.

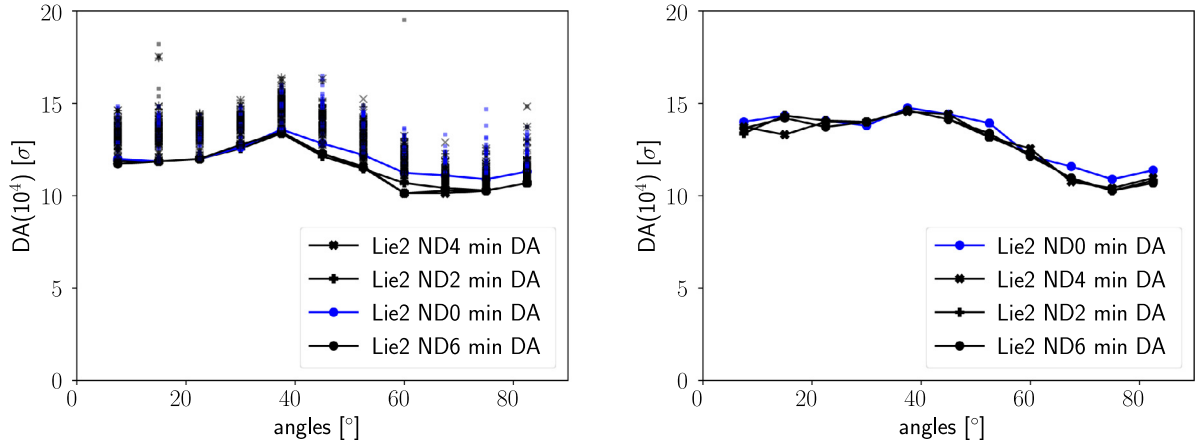

Fig. 13. DA as a function of phase space angles (with b_6 correction) for different numbers of gradients derivatives considered in the Lie2 model. All the 60 seeds simulated are shown on the left, while the comparison for one configuration of the machine is shown on the right.

6. Conclusion

An analytic expression for Amplitude Detuning and an accurate, symplectic and efficient non linear transfer map are derived, using the generalized gradients representation of the quadrupole vector potential. It allows to quantify the impact of 3D field distribution of the quadrupoles on machine performance, taking into account magnetic field detailed data.

Applied in the case of HL-LHC project, this impact is not negligible and has to be taken into account, especially when comparing computed with beam based measured values. The impact on the b_6 corrector strength can be up to about 13% with respect to the present corrector specification. The impact of the first and second derivatives of the quadrupole field (octupole-like) accounts for 4% of present octupole corrector specification. The modification to the corrector strength is in the present design specification, so no big impact is expected from the design point of view. Nevertheless, the accurate knowledge of the

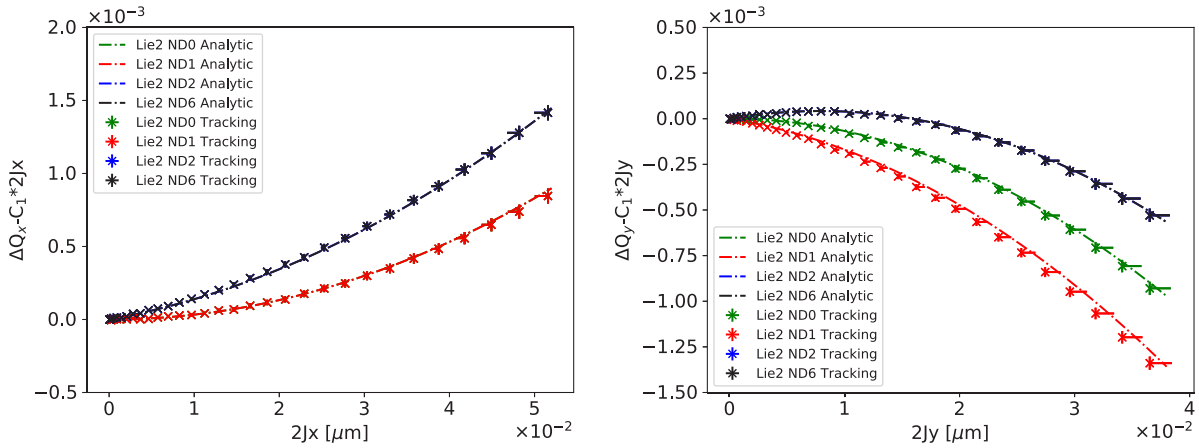

Fig. 14. Horizontal (left) and vertical (Right) Amplitude Detuning for different numbers of gradients derivatives considered in the Lie2 model. The Vector Potential is computed with the Horizontal Free Coulomb gauge (see Ref. [19]).

main field and field errors distribution of the final focus magnets is important to be able to reproduce the long term stability of the machine and the beam based observables in numerical simulations. In particular, being able to reproduce accurately the longitudinal profile of each of the harmonics of the final focus magnets is more important than higher order derivatives. The impact on the computation of dynamic aperture of the b_6 correction can be negligible or amount of about 2σ at 10^4 turns according to the model considered.

This impact, being weighted by the values of the betatronic function at the place where the field errors are located, is expected to be also important in the case of future hadronic circular colliders, such as FCC-hh [29] or more generally when the betatronic function vary a lot inside a magnet. Similarly, the impact of the longitudinal distribution of the field on feed-down effect due to crossing angle or magnet displacement, should also be studied in the future.

CRediT authorship contribution statement

T. Pugnat: Methodology, Software, Validation, Formal analysis, Writing - original draft, Writing - review & editing. **B. Dalena:** Conceptualization, Software, Validation, Writing - original draft, Writing - review & editing. **A. Simona:** Methodology, Software, Validation, Formal analysis. **L. Bonaventura:** Supervision, Writing - review & editing.

Declaration of competing interest

The authors declare that they have no known competing financial interests or personal relationships that could have appeared to influence the work reported in this paper.

Acknowledgments

The authors would like to thank S. Izquierdo-Bermudez and E. Todesco for providing the field harmonics computed with ROXIE of the inner triplet prototype for the HL-LHC project. The initial phase of the research leading to these results has received funding from the European Commissionhttp://dx.doi.org/10.13039/501100000780 under the FP7 project HiLumi LHC, GA no. 284404, co-funded by the DoE, USA and KEK, Japan. The whole work has been supported by CEA.

Appendix A. The Lie2 model and its interface with SixTrack

A.1. The symplectic map

The Lie2 model developed for this study is derived from the approximated Hamiltonian (Eq. (13)) of Ref. [15].

$$K = p_z - a_z - \delta + \frac{(p_x - a_x)^2 + (p_y - a_y)^2}{2(1+\delta)} \tag{13}$$

The vector potential is computed using the Generalized Gradient given by the following equation:

$$C_{n,*}^{[ND]}(z) = \frac{i^{ND}}{2^n n!}\frac{1}{\sqrt{2\pi}}\int_{-\infty}^{+\infty}\frac{k^{n+ND+1}}{I_n'(Rk)}\widehat{B}_{n,*}(R,k)e^{ikz}\mathrm{d}k \tag{14}$$

where the indices s and c correspond to the normal and skew harmonics, respectively. Using this formalism, the normalized vector potential, with respect to the charge q and the total momentum p_0 of the particle, is given by:

$$\begin{aligned}
a_x(x,y,z) &= \frac{q}{p_0 c}\sum_n^\infty\sum_l^\infty \frac{(-1)^l(n-1)!}{2^{2l}l!(l+n)!}\\
&\times\left[\sum_{p=0}^{n/2}\sum_{q=0}^{l}\binom{n}{2p}\binom{l}{q}(-1)^p x^{n+2(l-p-q)+1}y^{2(p+q)}C_{n,s}^{[2l+1]}(z)\right.\\
&\left.-\sum_{p=0}^{(n-1)/2}\sum_{q=0}^{l}\binom{n}{2p+1}\binom{l}{q}(-1)^p x^{n+2(l-p-q)}y^{2(p+q)+1}C_{n,c}^{[2l+1]}(z)\right]\\
a_y(x,y,z) &= \frac{q}{p_0 c}\sum_n^\infty\sum_l^\infty \frac{(-1)^l(n-1)!}{2^{2l}l!(l+n)!}\\
&\times\left[\sum_{p=0}^{n/2}\sum_{q=0}^{l}\binom{n}{2p}\binom{l}{q}(-1)^p x^{n+2(l-p-q)}y^{2(p+q)+1}C_{n,s}^{[2l+1]}(z)\right.\\
&\left.-\sum_{p=0}^{(n-1)/2}\sum_{q=0}^{l}\binom{n}{2p+1}\binom{l}{q}(-1)^p x^{n+2(l-p-q)-1}y^{2(p+q+1)}C_{n,c}^{[2l+1]}(z)\right]\\
a_z(x,y,z) &= \frac{-q}{p_0 c}\sum_n^\infty\sum_l^\infty \frac{(-1)^l(n-1)!(2l+n)}{2^{2l}l!(l+n)!}\\
&\times\left[\sum_{p=0}^{n/2}\sum_{q=0}^{l}\binom{n}{2p}\binom{l}{q}(-1)^p x^{n+2(l-p-q)}y^{2(p+q)+1}C_{n,s}^{[2l]}(z)\right.\\
&\left.-\sum_{p=0}^{(n-1)/2}\sum_{q=0}^{l}\binom{n}{2p+1}\binom{l}{q}(-1)^p x^{n+2(l-p-q)-1}y^{2(p+q)}C_{n,c}^{[2l]}(z)\right]
\end{aligned} \tag{15}$$

Following the technique proposed by H. Yoshida in Ref. [30], a 4D Lie map (Eq. (16)) of second order, that we call Lie2, has been

developed.

$$
\begin{aligned}
\begin{pmatrix} p_x \\ p_y \end{pmatrix}_{i+1/7} &= \begin{pmatrix} p_x \\ p_y \end{pmatrix}_{i} + \frac{dz}{2} \begin{pmatrix} \frac{\partial a_z(x_i,y_i,i)}{\partial x} \\ \frac{\partial a_z(x_i,y_i,i)}{\partial y} \end{pmatrix} - \begin{pmatrix} a_x\left(x_i, y_i, i\right) \\ \int \frac{\partial a_x\left(x_i, y_i, i\right)}{\partial y} \mathrm{d}x \end{pmatrix} \\
x_{i+2/7} &= x_{i+1/7} + \frac{dz}{2} \frac{p_{x,i+1/7}}{1+\delta} \\
\begin{pmatrix} p_x \\ p_y \end{pmatrix}_{i+3/7} &= \begin{pmatrix} p_x \\ p_y \end{pmatrix}_{i+2/7} + \begin{pmatrix} a_x\left(x_{i+2/7}, y_{i+2/7}, i\right) \\ \int \frac{\partial a_x\left(x_{i+2/7}, y_{i+2/7}, i\right)}{\partial y} \mathrm{d}x \end{pmatrix} \\
&\quad - \begin{pmatrix} \int \frac{\partial a_y\left(x_{i+2/7}, y_{i+2/7}, i\right)}{\partial x} \mathrm{d}y \\ a_y\left(x_{i+2/7}, y_{i+2/7}, i\right) \end{pmatrix} \\
y_{i+4/7} &= y_{i+3/7} + dz \frac{p_{y,i+3/7}}{1+\delta} \\
\begin{pmatrix} p_x \\ p_y \end{pmatrix}_{i+5/7} &= \begin{pmatrix} p_x \\ p_y \end{pmatrix}_{i+4/7} + \begin{pmatrix} \int \frac{\partial a_y\left(x_{i+4/7}, y_{i+4/7}, i\right)}{\partial y} \mathrm{d}x \\ a_y\left(x_{i+4/7}, y_{i+4/7}, i\right) \end{pmatrix} \\
&\quad - \begin{pmatrix} a_x\left(x_{i+4/7}, y_{i+4/7}, i\right) \\ \int \frac{\partial a_x\left(x_{i+4/7}, y_{i+4/7}, i\right)}{\partial y} \mathrm{d}x \end{pmatrix} \\
x_{i+6/7} &= x_{i+5/7} + \frac{dz}{2} \frac{p_{x,i+5/7}}{1+\delta} \\
\begin{pmatrix} p_x \\ p_y \end{pmatrix}_{i+1} &= \begin{pmatrix} p_x \\ p_y \end{pmatrix}_{i+6/7} + \begin{pmatrix} a_x\left(x_{i+6/7}, y_{i+6/7}, i\right) \\ \int \frac{\partial a_x\left(x_{i+6/7}, y_{i+6/7}, i\right)}{\partial y} \mathrm{d}x \end{pmatrix} \\
&\quad + \frac{dz}{2} \begin{pmatrix} \frac{\partial a_z\left(x_{i+6/7}, y_{i+6/7}, i\right)}{\partial x} \\ \frac{\partial a_z\left(x_{i+6/7}, y_{i+6/7}, i\right)}{\partial y} \end{pmatrix}
\end{aligned}
\tag{16}
$$

With this form, the Vector Potential can be computed by slices in z and saved in files, as Horner polynomial coefficients for each step i [19]. These files are then read by the SixTrack code once per simulation Refs. [31,32].

In Ref. [19] the accuracy and efficiency of different integration and interpolation methods were studied and compared, including the Lie2 model presented here. In this paper, we compare the tracking using the Lie2 transfer map with the reference model from [19], a 6th order Gauss method, using AD as figure of merit. Fig. 11 shows the impact on the AD for the two integration methods and two step sizes. A small difference of about 10^{-5} appears when going at amplitude higher than 0.02 μm, which is due to the step size in z. The two integration methods reproduce the same detuning with amplitude for a non-linear transfer map of 2 cm step size. In Fig. 12, two interpolation methods (mean and spline) are compared for two step sizes. The mean interpolation method seems more stable, with an error of the order of 10^{-5} which is also the precision of frequency analysis. We conclude that the step size in z has more impact on the precision of the model than the integration or the interpolation method chosen, which is also consistent with the results published in Ref. [19].

A.2. The interface of the Lie2 map with Sixtrack

The Head is the region of the magnet in which the harmonics vary along the magnetic axis z. On the contrary the body is the region of constant field (main and higher order harmonics) along z. In other terms the Heads are defined as $\{z \in \mathbb{R} \ : \ B_z(x,y,z) \neq 0, \ \forall\, x,y \in \mathbb{R}\}$, i.e. $\{z \in \mathbb{R} \ : \ A_x(x,y,z) \neq 0$ or $A_y(x,y,z) \neq 0, \ \forall\, x,y \in \mathbb{R}\}$. With this definition, an equivalent magnetic length is computed for each Head. In Fig. 3, this length is called $L_{q,*}$ (with $*$ being "*in*" and "*out*" for each extremity of the magnet, respectively).

As mentioned previously, the Lie2 model has been implemented in SixTrack (Ref. [32]). In order to add only the non-linear effects of the Fringe Field, and to leave the modelization of the linear part to SixTrack, the first step consists in identifying the beginning of the Hard-Edge quadrupole ("*in*" in Fig. 3). From this position, the particle are tracked back with an anti-Drift of length $L_{D,in} = L_{f,in} - L_{q,in}$, where $L_{f,*}$ is the total length in z of the Vector Potential Files for the first extremity ((1) in Fig. 3). The forward tracking is then done using the Lie2 map and the Horner coefficient from the first Vector Potential Files ((2) in Fig. 3). At the end of the Lie2 tracking, the linear part has to be removed by using an Half-Kick/Drift/Half-Kick anti quadrupole matrix for each step i ((3) in Fig. 3). The particle is back to the beginning of the Vector Potential File, a Drift of length $L_{D,in}$ returns it to the beginning of the Hard-Edge quadrupole ((4) in Fig. 3). SixTrack takes care of the tracking in the body of the magnet. At the end of the quadrupole, the sequence is reversed (from (6) to (9) in Fig. 3) with the second Vector Potential Files.

As the tracking takes a lot of time (small step size, number of harmonics, number of gradients derivatives, etc.), the speed of the routine is a major factor in the choice of the integrator. From [19], two integrators show a low computational time. Since the 4th Runge–Kutta is not symplectic, the Lie2 model is chosen for the SixTrack. A lot of improvements have been made in the optimization of the subroutine. In particular, since storage matrix for the vector potential coefficient (with Horner exponent as coordinate) are relatively sparse, they were saved as a Matrix Market Exchange format (Ref. [33]) also known as COO format (Ref. [34,35]). This reduces the memory size and increases the speed of Horner polynomial subroutines. Similarly, the power of the horizontal and vertical coordinates are computed beforehand in order to not repeat the same operation during tracking. This allows to multiply the speed of the tracking by a factor of two.

Appendix B. The impact of the derivatives

As discussed in Section 3, in the case of Lie2 the numbers of gradients derivatives (derivative orders) can be specified in the reconstruction of the vector potential used for the tracking. Fig. 13 shows the impact of different number of derivatives on DA. All 60 seeds and the line joining the minimum value for each angle are shown on the left panel, while the comparison for one configuration of the machine is shown on the right. All derivatives above the second do not change DA, meaning that only the first two derivatives can be used.

Fig. 14 shows a similar comparison for the Amplitude Detuning. It appears that the 1st derivative generates half of the 1st-order Amplitude Detuning. This is not observed for the Horizontal plane because of the Gauge used. In order to further speed-up tracking the horizontal-free Coulomb gauge is chosen, which requires in general between 20% and 25% less coefficients evaluation of the vector potential in Eq. (15) with respect to the azimuthal-free gauge [19]. Nevertheless for even number of derivatives (ND) all the gauges produce exactly the same magnetic field by definition, and as a consequence will result in the same amplitude detuning. It is also important to note that no significant discrepancy can be observed for a number of derivatives (derivative orders) higher than 2, as in the DA case.

References

[1] G. Apollinari, I. Bejar, O. Bruning, P. Fessia, M. Lamont, L. Rossi, T. Tavian, eds., High-Luminosity Large Hadron Collider (HL-LHC): Technical Design Report V. 0.1, Cern yellow report, CERN, Geneva, Switzerland, 2017, https://cds.cern.ch/record/2284929.

[2] E. Forest, J. Milutinovic, Leading order hard edge fringe fields effects, Nucl. Instrum. Methods A 269 (1988) 474–482, http://dx.doi.org/10.1016/0168-9002(88)90123-4.

[3] Y. Papaphilippou, J. Wei, R. Talman, Deflection in magnet fringe fields, Phys. Rev. E 67 (2003) 046502, http://dx.doi.org/10.1103/PhysRevE.67.046502.

[4] M. Patecki, R. Tomas, Effects of quadrupole fringe fields in final focus systems for linear colliders, Phys. Rev. Special Top. Accel. Beams 17 (2014) 101002, http://dx.doi.org/10.1103/PhysRevSTAB.17.101002.

[5] B.D. Muratori, J.K. Jones, A. Wolski, Analytical expressions for fringe fields in multipole magnets, Phys. Rev. Special Top. Accel. Beams 18 (2015) 064001, http://dx.doi.org/10.1103/PhysRevSTAB.18.064001.

[6] M. Venturini, A.J. Dragt, Accurate computation of transfer maps from magnetic field data, in: Accelerators, Spectrometers, Detectors and Associated Equipment, Nucl. Instrum. Methods Phys. Res. A 427 (1999) 387–392, http://dx.doi.org/10.1016/S0168-9002(98)01518-6.

[7] C.E. Mitchell, A.J. Dragt, Accurate transfer maps for realistic beam-line elements: Straight elements, Phys. Rev. Special Top. Accel. Beams 13 (2010) 064001, http://dx.doi.org/10.1103/PhysRevSTAB.13.064001.

[8] M. Borland, R.R. Lindberg, Modeling of dipole and quadrupole fringe-field effects for the advanced photon source upgrade lattice, in: Proc. of NAPAC, JACoW, Chicago, IL, USA, 2016, pp. 1119–1122, http://dx.doi.org/10.18429/JACoW-NAPAC2016-TUB2IO01, paper THPOA13.

[9] A.V. Bogomyagkov, E.B. Levichev, P.A. Piminov, A. Chancé, B. Dalena, J. Payet, R. De Maria, S. Fartoukh, M. Giovannozzi, Analysis of the Non-linear fringe effects of large aperture triplets for the hl-lhc project, in: Proc. 4th International Particle Accelerator Conference, JACoW, Shanghai, China, 2013, pp. 2615–2617, paper WEPEA049.

[10] E.H. Maclean, Modelling and Correction of the Non-Linear Transverse Dynamics of the LHC from Beam-Based Measurements (Ph.D. thesis), University of Oxford, United Kingdom, 2014, CERN-THESIS-2014-135.

[11] E.H. Maclean, R. Tomás, F.S. Carlier, M.S. Camillocci, J.W. Dilly, J. Coello de Portugal, E. Fol, K. Fuchsberger, A. Garcia-Tabares Valdivieso, M. Giovannozzi, M. Hofer, L. Malina, T.H.B. Persson, P.K. Skowronski, A. Wegscheider, New approach to LHC optics commissioning for the nonlinear era, Phys. Rev. Accel. Beams 22 (2019) 061004, http://dx.doi.org/10.1103/PhysRevAccelBeams.22.061004.

[12] M. Giovannozzi, S.D. Fartoukh, R. De Maria, Specification of a system of correctors for the triplets and separation dipoles of the LHC upgrades, in: Proc. 4th International Particle Accelerator Conference, JACoW, Shanghai, China, 2013, pp. 2612–2614, paper WEPEA048.

[13] S. White, E.H. Maclean, R. Tomas, Direct amplitude detuning measurement with ac dipole, Phys. Rev. Special Top. Accel. Beams 16 (2013) 071002, http://dx.doi.org/10.1103/PhysRevSTAB.16.071002.

[14] A.J. Dragt, F. Neri, G. Rangarajan, D. Douglas, L.M. Healy, R.D. Ryne, Lie algebraic treatment of linear and nonlinear beam dynamics, Ann. Rev. Nucl. Part. Sci. 38 (1988) 455, http://dx.doi.org/10.1146/annurev.ns.38.120188.002323.

[15] Y.K. Wu, E. Forest, D.S. Robin, Explicit symplectic integrator for s-dependent static magnetic field, Phys. Rev. E 68 (2003) 046502, http://dx.doi.org/10.1103/PhysRevE.68.046502.

[16] B. Dalena, O. Gabouev, J. Payet, A. Chancé, R. Brett, R.B. Appleby, R. De Maria, Fringe field modeling for the high luminosity LHC large aperture quadrupole, in: Proc. 5th International Particle Accelerator Conference, JACoW, Dresden, Germany, 2014, pp. 993–996, http://dx.doi.org/10.18429/JACoW-IPAC2014-TUPRO002, paper TUPRO002.

[17] T. Pugnat, B. Dalena, A. Simona, L. Bonaventura, R. De Maria, J. Molson, Accurate and efficient tracking in electromagnetic quadrupoles, in: Proc. 9th International Particle Accelerator Conference, JACoW, Vancouver, Canada, 2018, pp. 3207–3210, http://dx.doi.org/10.18429/JACoW-IPAC2018-THPAK004, paper THPAK004.

[18] T. Pugnat, B. Dalena, L. Bonaventura, A. Simona, R. De Maria, V. Olsen, Study of fringe fields effects from final focus quadrupoles on beam based measured quantities, in: Proc. 10th International Particle Accelerator Conference, JACoW, Melbourne, Australia, 2019, pp. 90–93, http://dx.doi.org/10.18429/JACoW-IPAC2019-MOPGW012, paper MOPGW012.

[19] A. Simona, L. Bonaventura, B. Dalena, T. Pugnat, High order time integrators for the simulation of charged particle motion in magnetic quadrupoles, Comput. Phys. Comm. 239 (2019) 33–52, http://dx.doi.org/10.1016/j.cpc.2019.01.018.

[20] E.H. Maclean, F. Carlier, M.S. Camillocci, K. Fuchsberger, M. Giovannozzi, T.H.B. Persson, R. Tomás, Report from LHC MDs 1391 and 1483: Tests of New Methods for Study of Nonlinear Errors in the LHC Experimental Insertions, Report CERN-ACC-NOTE-2018-0035, CERN, Geneva, Switzerland, 2017, http://cds.cern.ch/record/2314410.

[21] E.H. Maclean, F. Carlier, J.W. Dilly, M.S. Camillocci, E. Cruz Alaniz, B. Dalena, E. Fol, K. Fuchsberger, M. Giovannozzi, M. Hofer, L. Malina, T.H.B. Persson, J. Coello de Portugal, P. Skowronski, R. Tomás, A. Garcia-Tabares Valdivieso, A. Wegscheider, Report from LHC MD 2158: IR-Nonlinear Studies, Report, (CERN-ACC-NOTE-2018-0021) CERN, Geneva, Switzerland, 2018, http://cds.cern.ch/record/2306295.

[22] MAD - Methodical Accelerator Design, CERN - BE/ABP Accelerator Beam Physics Group, 2019, https://mad.web.cern.ch/mad.

[23] S. Fartoukh, Achromatic telescopic squeezing scheme and application to the LHC and its luminosity upgrade, Phys. Rev. Special Top. Accel. Beams 16 (2013) http://dx.doi.org/10.1103/PhysRevSTAB.16.111002.

[24] S. Fartoukh, O. Brüning, Field quality specification for the LHC main dipole magnets, Report, (LHC-Project-Report-501) CERN, 2001, https://cds.cern.ch/record/522049.

[25] E. Todesco, M. Giovannozzi, Dynamic aperture estimates and phase-space distortions in nonlinear betatron motion, Phys. Rev. E 53 (1996) 4067.

[26] E.H. Maclean, M. Giovannozzi, R.B. Appleby, Innovative method to measure the extend of the stable phase-space region of proton synchrotrons, Phys. Rev. Accel. Beams 22 (2019) 034002, http://dx.doi.org/10.1103/PhysRevAccelBeams.22.034002.

[27] S. Fartoukh, M. Giovannozzi, Dynamic aperture computation for the as-built CERN large hadron collider and impact of main dipoles sorting, Nucl. Instrum. Methods A 671 (2012) 10–23, http://dx.doi.org/10.1016/j.nima.2011.12.052.

[28] M. Hayes, E. McIntosh, F. Schmidt, The influence of computer errors on dynamic aperture results using sixtrack, LHC Project Note 309, CERN, Geneva, Switzerland, 2003, https://cds.cern.ch/record/692073/.

[29] A. Abada, M. Abbrescia, S.S. AbdusSalam, et al., Future Circular Collider Conceptual Design Report, Report, CERN, Geneva, Switzerland, 2019, https://fcc-cdr.web.cern.ch.

[30] H. Yoshida, Construction of higher order symplectic integrators, Phys. Lett. A 150 (5) (1990) 262–268, http://dx.doi.org/10.1016/0375-9601(90)90092-3.

[31] SixTrack - 6D Tracking Code, CERN - BE/ABP Accelerator Beam Physics Group, 2019, https://sixtrack.web.cern.ch/SixTrack.

[32] R. De Maria, J. Andersson, V.K.B. Olsen, L. Field, M. Giovannozzi, P.D. Hermes, N. Høimyr, G. Iadarola, S. Kostoglou, E.H. Maclean, E. McIntosh, A. Mereghetti, J. Molson, D. Pellegrini, T. Persson, M. Schwinzerl, B. Dalena, T. Pugnat, I. Zacharov, N. Sjobak, Sixtrack version 5: Status and new developments, in: Proc. 10th International Particle Accelerator Conference, JACoW, Melbourne, Australia, 2019, pp. 3200–3203, http://dx.doi.org/10.18429/JACoW-IPAC2019-WEPTS043, paper WEPTS043.

[33] Matrix Market Exchange Formats, Matrix Market - NIST, 2013, https://math.nist.gov/MatrixMarket/formats.html.

[34] I.P. Stanimirović, M.B. Tasić, Performance comparison of storage formats for sparse matrices, EMS Facta Univ. Ser. Math. Inform. 24 (2009) 39–51, https://facta.junis.ni.ac.rs/mai/mai24/fumi-24_39_51.pdf.

[35] R.F. Boisvert, R. Pozo, K.A. Remington, The matrix market exchange format: Initial design, NIST Interag./Internal Report (NISTIR) 5935 (1996) https://citeseerx.ist.psu.edu/viewdoc/download;jsessionid=E98EDA719761E27EFA4969791979893F?doi=10.1.1.34.3448&rep=rep1&type=pdf.